



12-1999

Understanding isothermal crystallization and subsequent melting behavior of syndiotactic polypropylene

Pitt Supaphol

Follow this and additional works at: https://trace.tennessee.edu/utk_graddiss

Recommended Citation

Supaphol, Pitt, "Understanding isothermal crystallization and subsequent melting behavior of syndiotactic polypropylene. " PhD diss., University of Tennessee, 1999.
https://trace.tennessee.edu/utk_graddiss/8925

This Dissertation is brought to you for free and open access by the Graduate School at TRACE: Tennessee Research and Creative Exchange. It has been accepted for inclusion in Doctoral Dissertations by an authorized administrator of TRACE: Tennessee Research and Creative Exchange. For more information, please contact trace@utk.edu.

To the Graduate Council:

I am submitting herewith a dissertation written by Pitt Supaphol entitled "Understanding isothermal crystallization and subsequent melting behavior of syndiotactic polypropylene." I have examined the final electronic copy of this dissertation for form and content and recommend that it be accepted in partial fulfillment of the requirements for the degree of Doctor of Philosophy, with a major in Polymer Engineering.

Joseph E. Spruiell, Major Professor

We have read this dissertation and recommend its acceptance:

Paul J. Phillips, Roberto S. Benson, Kevin M. Kit, Mark E. Dadmun

Accepted for the Council:

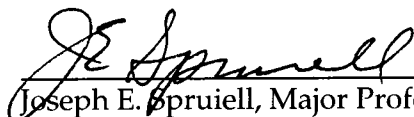
Carolyn R. Hodges

Vice Provost and Dean of the Graduate School

(Original signatures are on file with official student records.)

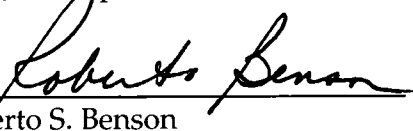
To the Graduate Council:

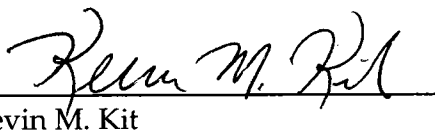
I am submitting herewith a dissertation written by Pitt Supaphol entitled "Understanding Isothermal Crystallization and Subsequent Melting Behavior of Syndiotactic Polypropylene." I have examined the final copy of this dissertation for form and content and recommend that it be accepted in partial fulfillment of the requirements for the degree of Doctor of Philosophy, with a major in Polymer Engineering.



Joseph E. Spruiell, Major Professor

We have read this dissertation
and recommend its acceptance:


Paul J. Phillips


Roberto S. Benson


Kevin M. Kit


Mark E. Dadmun

Accepted for the Council:


Associate Vice Chancellor and
Dean of The Graduate School

**UNDERSTANDING ISOTHERMAL CRYSTALLIZATION
AND SUBSEQUENT MELTING BEHAVIOR
OF SYNDIOTACTIC POLYPROPYLENE**

A Dissertation
Presented for the
Doctor of Philosophy
Degree
The University of Tennessee, Knoxville

Pitt Supaphol
December 1999

Copyright © Pitt Supaphol, 1999
All rights reserved

DEDICATION

This dissertation is dedicated to my parents,

Mr. Pin Supaphol

and

Mrs. Somchit Supaphol,

who have always given me unconditional love, support and
invaluable educational opportunities.

ACKNOWLEDGMENTS

I would like to express my sincere appreciation to my major advisor, Professor Joseph E. Spruiell, for his kindness, invaluable guidance and advice, and interesting discussion through the years I have been at UTK. A profound appreciation needs to be mentioned on the financial support that Professor Joseph E. Spruiell has kindly provided throughout the course of my Ph.D. studies. Sincere thankfulness is extended to all the members of my dissertation committee, Professor Paul J. Phillips, Professor Roberto S. Benson, Professor Kevin M. Kit, and Professor Mark E. Dadmun, for their support of this research work.

This research would not be completed without technical support provided by the staffs of the electronics and machine shops. Thanks are also extended to fellow students for their intellectual discussion and friendship, with the last making years of my residence in Knoxville a pleasant experience. Among them, Gary A. Holt, Jr., Imad M. Qashou, and Gyanendra Dutt will always be remembered.

My accomplishment would not have happened if lacking of support from my family in Thailand, comprising Mr. Pin Supaphol (my dad), Mrs. Somchit Supaphol (my mom), Jade Supaphol, M.D. (my younger brother), and Miss Pattaramanee Supaphol (my lovely, younger sister), who always give love and support through the years I am away from home.

ABSTRACT

Various issues related to isothermal quiescent crystallization and subsequent melting behavior of syndiotactic polypropylene (sPP) were investigated in this dissertation. On the study of isothermal melt- and cold-crystallization kinetics and subsequent melting behavior of sPP, the overall crystallization rate parameters for melt-crystallization process, when plotted as a function of crystallization temperature, exhibited an unmistakable double bell-shaped curve; whereas, those for cold-crystallization process showed the typical bell-shaped curve. Comparison of the overall crystallization rate parameters obtained for both melt- and cold-crystallization processes indicate that crystallization from the glassy state proceeds at a much greater rate than from the melt state. The multiple-melting behavior observed in subsequent melting endotherms is attributed to the contributions from: 1) melting of the secondary crystallites and their re-crystallization, 2) partial melting of the less stable fraction of the primary crystallites and their re-crystallization, 3) melting of the primary crystallites, and lastly 4) re-melting of the re-crystallized crystallites formed during the heating scan.

Analysis of the linear growth rate data of sPP#1 and other data sets taken from the literature in the context of the Lauritzen-Hoffman secondary nucleation theory suggested an unmistakable regime II-III transition at the crystallization temperature of 110°C. Regardless of the crystal structure, if the growth is assumed to occur on the *bc* plane, the lateral surface free energy $\sigma = 11.3 \text{ erg}\cdot\text{cm}^{-2}$ and the fold surface free energy $\sigma_e = 63.7 \pm 7.1 \text{ erg}\cdot\text{cm}^{-2}$ were found. On the other hand, if the growth is assumed to occur on the *ac* plane, the fold surface free energy is found to be $\sigma_e = 82.4 \pm 9.1 \text{ erg}\cdot\text{cm}^{-2}$, while the lateral surface free energy is the same as previously noted. The sensitivity of the crystal growth parameters on changes in the values of the input parameters was also investigated.

Isothermal crystallization behavior after partial or complete melting of syndiotactic polypropylene was also investigated. On subsequent crystallization after partial melting, the total concentration of predetermined nuclei was found to decrease with increasing fusion temperature and increasing time period the sample spent at a specific fusion temperature. On subsequent crystallization after complete melting, the total concentration of predetermined nuclei was found to approach a constant value, which is the concentration of infusible heterogeneous nuclei (e.g., impurities, catalyst residues, etc.) present originally in the sample. At a specific fusion temperature, the concentration of predetermined athermal nuclei was found to decrease exponentially with the time period spent in the melt.

Applicability of four macrokinetic models; namely the Avrami, Tobin, Malkin, and simultaneous Avrami models; in describing the time-dependent relative crystallinity data, using sPP as the model system, was tested using a non-linear multi-variable regression program. Based on the quality of the fit, only the Avrami, Malkin, and the simultaneous Avrami models were found to describe the experimental data well, resulting in the rejection of the Tobin model in describing isothermal crystallization data of sPP. Comparison of the Avrami kinetics parameters obtained from the program with those obtained from the traditional analytical procedure suggested that use of non-linear multi-variable regression program in data analysis is satisfactorily reliable.

Lastly, a technique of using differential scanning calorimeter (DSC) to study crystallization behavior and the kinetics of the process at high crystallization temperatures or low degrees of undercooling was proposed. The technique was carried out based on the observations of, and the measurements of the enthalpy of fusion from, the subsequent melting endotherms after isothermal crystallization for various time intervals. Comparison of the overall crystallization data obtained from this proposed

technique with those obtained from the traditional technique evidently indicated that the proposed technique of using information acquired from subsequent melting endotherms in studying crystallization kinetics is at least reliable and applicable to describe isothermal crystallization of sPP at the conditions studied. Apparent advantages and disadvantages of the proposed technique were also given.

TABLE OF CONTENTS

PART 1: GENERAL INTRODUCTION AND GENERAL REVIEW OF THEORETICAL BACKGROUND

1. GENERAL INTRODUCTION	2
2. GENERAL REVIEW OF THEORETICAL BACKGROUND	6
2.1. Overview of Polymer Crystallization	6
2.1.1. Basic Concept of Polymer Crystallization	6
2.1.2. Crystal Morphology	7
2.1.2.1. Fringed Micelle Morphology	7
2.1.2.2. Single Crystal Morphology	8
2.1.2.3. Spherulitic Morphology	9
2.1.2.4. Axialitic Morphology	10
2.1.2.5. Extended Chain Morphology	10
2.1.3. Concepts of Chain Folding	10
2.2. Theories of Microscopic Kinetics of Polymer Crystallization	13
2.2.1. Theories of Primary Nucleation	13
2.2.1.1. Thermodynamics Consideration of Homogeneous Thermal Nucleation	14
2.2.1.2. Thermodynamics Consideration of Heterogeneous Nucleation	17
2.2.1.3. Theory of the Nucleation Rate	19
2.2.2. Theories of Secondary Nucleation	20
2.2.2.1. Traditional Approach on Observing the Lamellar Thickness	21
2.2.2.2. The Lauritzen-Hoffman Secondary Nucleation Theory	22
2.2.2.2.1. Model Used in this Approach	22
2.2.2.2.2. Calculation of the Total Flux	25
2.2.2.2.3. Initial Lamellar Thickness	28
2.2.2.2.4. Retardation Factor	29
2.2.2.3. Theory of the Linear Growth Rate	31
2.2.2.3.1. Regime I Growth	31
2.2.2.3.2. Regime II Growth	33
2.2.2.3.3. Regime III Growth	34
2.2.2.3.4. Test of Regime	35
2.2.3. Theories of the Maximum Nucleation and Growth Rates	37

2.3. Theories of Macroscopic Kinetics of Polymer Crystallization	38
2.3.1. Kinetics of Isothermal Macroscopic Crystallization	38
2.3.1.1. Avrami Macrokinetic Model	39
2.3.1.2. Tobin Macrokinetic Model	41
2.3.1.3. Malkin Macrokinetic Model	42
2.3.1.4. Analysis of the Experimental Data	42
2.3.1.5. Other Macrokinetic Models	43
2.3.1.5.1. Simultaneous Avrami Macrokinetic Model	43
2.3.1.5.2. Ding-Spruiell Macrokinetic Model	46
2.3.1.5.3. Traditional Ziabicki Macrokinetic Model	50
2.3.1.6. Temperature Dependence of the Crystallization Rate Parameters	51
2.3.2. Kinetics of Non-isothermal Macroscopic Crystallization	52
2.3.2.1. Generalized Avrami Macrokinetic Models	52
2.3.2.2. Malkin Macrokinetic Model	55
2.3.2.3. Traditional Ziabicki Macrokinetic Model	56
2.3.2.4. Generalized Ziabicki Macrokinetic Model	58
2.4. Methods for the Determination of Equilibrium Melting Temperature	62
2.4.1. Flory-Vrij Extrapolation Method	63
2.4.2. Gibbs-Thomson Extrapolation Method	63
2.4.3. Hoffman-Weeks Extrapolation Methods	65
2.4.3.1. Linear Hoffman-Weeks Extrapolation Method	65
2.4.3.2. Non-linear Hoffman-Weeks Extrapolation Method	66
2.4.4. Data-fitting Methods	69
2.4.4.1. Data-fitting Method Based on Induction Time Data	69
2.4.4.2. Data-fitting Method Based on Linear Growth Rate Data	71
3. REFERENCES	73

PART 2: THERMAL PROPERTIES AND ISOTHERMAL CRYSTALLIZATION
OF SYNDIOTACTIC POLYPROPYLENES: DIFFERENTIAL SCANNING
CALORIMETRY AND OVERALL CRYSTALLIZATION KINETICS

1. ABSTRACT	78
2. INTRODUCTION	78
3. THEORETICAL BACKGROUND	79

4. EXPERIMENTAL DETIALS	82
4.1. Materials	82
4.2. Technique and Sample Preparation	82
4.3. Methods	84
5. RESULTS AND DISCUSSION	85
5.1. Glass Transition Temperature	85
5.2. Melting Behavior and Equilibrium Melting Temperature	87
5.3. Overall Crystallization Kinetics	97
5.3.1. Avrami Analysis	97
5.3.2. Regime Analysis	103
5.3.3. Construction of Crystallization Rate Function	109
5.3.4. Kinetic Crystallizability	111
6. CONCLUSIONS	113
7. REFERENCES	115

PART 3: REGIME CRYSTALLIZATION IN SYNDIOTACTIC
POLYPROPYLENES: RE-EVALUATION OF THE LITERATURE DATA

1. ABSTRACT	118
2. INTRODUCTION	118
3. THEORETICAL BACKGROUND	121
4. MATERIALS, LINEAR GROWTH RATE, AND INPUT DATA	124
5. ANALYSIS AND DISCUSSION OF LITERATURE DATA	130
5.1. Determication of Crystal Growth Parameters	130
5.2. Effect of Change in T_g	135
5.3. Effect of Change in $(T_m^0)_{100\%}$	138
5.4. Effect of Change in ΔH_f^0	141
5.5. Further Discussion of the Literature	141
6. FURTHER DISCUSSION ON THE T_m^0 VALUE USED IN THE ANALYSIS	143
7. SUMMARY AND CONCLUSIONS	146
8. REFERENCES AND NOTES	148

PART 4: CRYSTALLINE MEMORY EFFECT IN ISOTHERMAL
CRYSTALLIZATION OF SYNDIOTACTIC POLYPROPYLENE

1. ABSTRACT	151
-------------------	-----

2. INTRODUCTION	151
3. EXPERIMENTAL DETIALS	153
3.1. Materials	153
3.2. Sample Preparation and Experimental Methods	153
4. ANALYSIS, RESULTS AND DISCUSSION	154
4.1. Analysis of DSC Measurements	154
4.2. Effect of Crystallization Temperature	157
4.3. Effect of Heating Rate	162
4.4. Effect of Fusion Temperature	165
4.5. Effect of Holding Time	168
5. CONCLUSIONS	175
6. REFERENCES	179

PART 5: APPLICATION OF THE AVRAMI, TOBIN, MALKIN, AND
SIMULTANEOUS AVRAMI MACROKINETIC MODELS TO ISOTHERMAL
CRYSTALLIZATION OF SYNDIOTACTIC POLYPROPYLENE

1. ABSTRACT	181
2. INTRODUCTION	181
3. THEORETICAL BACKGROUND	183
4. EXPERIMENTAL DETIALS	186
4.1. Materials	186
4.2. Technique and Sample Preparation	186
4.3. Methods	188
5. RESULTS AND DISCUSSION	188
5.1. Isothermal Crystallization of sPP from the Melt	188
5.2. Application of the Avrami, Tobin, and Malkin Models	194
5.2.1. Isothermal Crystallization Kinetics Based on the Avrami Model	194
5.2.2. Isothermal Crystallization Kinetics Based on the Tobin Model	195
5.2.3. Isothermal Crystallization Kinetics Based on the Malkin Model	197
5.2.4. Comparison Between the Different Isothermal Macrokinetic Models	199
5.3. Application of the Simultaneous Avrami Model	202
5.4. Prediction of Isothermal Crystallization Kinetics	207
6. CONCLUSIONS	215
7. REFERENCES	217

PART 6: ON THE CRYSTALLIZATION AND MELTING BEHAVIOR IN
SYNDIOTACTIC POLYPROPYLENE: THE ORIGIN OF THE MULTIPLE
ENDOTHERMIC MELTING PHENOMENON

1. ABSTRACT	219
2. INTRODUCTION	219
3. EXPERIMENTAL DETIALS	223
3.1. Materials	223
3.2. Sample Preparation	223
3.3. Apparatus and Procedure	224
3.3.1. Differential Scanning Calorimetry (DSC)	224
3.3.2. Wide-angle X-ray Diffraction (WAXD)	224
4. RESULTS AND DISCUSSION	225
4.1. Dependence of Subsequent Melting Endotherms on Crystallization Temperature	225
4.2. Dependence of Subsequent Melting Endotherms on Crystallization Time Interval	235
4.3. Dependence of Subsequent Melting Endotherms on Heating Rate	243
5. CONCLUSIONS	252
6. REFERENCES	254

PART 7: ISOTHERMAL MELT- AND COLD-CRYSTALLIZATION KINETICS
AND SUBSEQUENT MELTING BEHAVIOR IN SYNDIOTACTIC
POLYPROPYLENE: A DIFFERENTIAL SCANNING CALORIMETRY STUDY

1. ABSTRACT	258
2. INTRODUCTION	258
3. THEORETICAL BACKGROUND	259
4. EXPERIMENTAL DETIALS	263
4.1. Materials	263
4.2. Sample Preparation and Technique	263
4.3. Methods	264
5. RESULTS	265
5.1. Crystallization Kinetics	265
5.2. Subsequent Melting Behavior	269
6. DISCUSSION	279
6.1. Temperature Dependence of Overall Crystallization Kinetics Parameters	279

6.2. Determination of the Equilibrium Melting Temperature	296
7. CONCLUSIONS	304
8. REFERENCES	306

PART 8: ISOTHERMAL CRYSTALLIZATION AND MELTING BEHAVIOR OF
SYNDIOTACTIC POLYPROPYLENE: A WAXD/SAXS/DSC STUDY

1. ABSTRACT	309
2. INTRODUCTION	309
3. EXPERIMENTAL DETIALS	310
3.1. Materials	310
3.2. Sample Preparation	310
3.3. Wide-angle X-ray Diffraction	311
3.4. Small-angle X-ray Scattering	311
3.5. Differential Scanning Calorimetry	312
4. RESULTS	312
5. DISCUSSION	320
6. CONCLUSIONS	336
7. REFERENCES	337

PART 9: USE OF DSC MELTING ENDOTHERMS FOR STUDYING
ISOTHERMAL BULK CRYSTALLIZATION OF SEMICRYSTALLINE
POLYMERS AT LOW DEGREES OF UNDERCOOLING: A CASE STUDY
IN SYNDIOTACTIC POLYPROPYLENE

1. ABSTRACT	340
2. INTRODUCTION	340
3. USE OF DSC IN STUDYING CRYSTALLIZATION OF POLYMERS	342
3.1. The General Technique of DSC	342
3.2. Determination of Crystallization Kinetics Parameters	346
4. EXPERIMENTAL DETIALS	348
4.1. Materials	348
4.2. Sample Preparation	348
4.3. Technique and Experimental Methods	349
5. RESULTS AND DISCUSSION	350
5.1. Origination of the Proposed Technique	350
5.2. Determination of Crystallization Kinetics Parameters	356

5.3. Further Discussion on the Temperature Dependence of the Induction Time	360
5.4. Further Discussion on the Temperature Dependence of the Crystallization Half-time	364
6. CONCLUSIONS	367
7. REFERENCES	369

PART 10: SUMMARY OF MAJOR CONCLUSIONS AND
RECOMMENDATIONS FOR FUTURE WORK

1. SUMMARY OF MAJOR CONCLUSIONS	372
2. RECOMMENDATIONS FOR FUTURE WORK	377
VITA	379

LIST OF TABLES

TABLE	PAGE
PART 1: GENERAL INTRODUCTION AND GENERAL REVIEW OF THEORETICAL BACKGROUND	
1-1. Phenomenal description of the Avrami exponent n_a (after reference [18])	40
1-2. Mathematical description of the Avrami isothermal crystallization rate constant k_a for different types of morphology and transient nucleation	45
1-3. Qualitative characteristic of the nucleation index m	49
PART 2: THERMAL PROPERTIES AND ISOTHERMAL CRYSTALLIZATION OF SYNDIOTACTIC POLYPROPYLENES: DIFFERENTIAL SCANNING CALORIMETRY AND OVERALL CRYSTALLIZATION KINETICS	
2-1. Characterization data of as-received syndiotactic polypropylene samples	83
2-2. Glass transition temperatures for syndiotactic polypropylene samples	86
2-3. Crystallization and melting data for syndiotactic polypropylene samples	91
2-4. Thermodynamic equilibrium melting points, β parameters, and corresponding calculated equilibrium melting points for 100% syndiotacticity for syndiotactic polypropylene samples	94
2-5. Overall crystallization kinetics data for syndiotactic polypropylene samples	99
2-6. Input parameters for calculation of parameters characteristic of crystal growth	106
2-7. Analysis of the crystallization times t_0 based on the modified growth rate theory	107
2-8. Kinetic characteristics of syndiotactic polypropylene samples and some other polymers	112
PART 3: REGIME CRYSTALLIZATION IN SYNDIOTACTIC POLYPROPYLENES: RE-EVALUATION OF THE LITERATURE DATA	
3-1. Materials characterization data for syndiotactic polypropylene samples used in the referenced literature	125
3-2. Linear spherulitic growth rate data for syndiotactic polypropylene samples used in the referenced literature	126

TABLE	PAGE
3-3. Input parameters for calculation of crystal growth parameters	129
3-4. Nucleation exponents and crystal growth parameters based on the traditional regime analysis for the case: $T_g = 267.0$ K, $(T_m^0)_{100\%} = 441.8$ K, and $\Delta H_f^0 = 8.0$ kJ·mol ⁻¹	133
3-5. Nucleation exponents and crystal growth parameters based on the traditional regime analysis for the case: $T_g = 273.2$ K, $(T_m^0)_{100\%} = 441.8$ K, and $\Delta H_f^0 = 8.0$ kJ·mol ⁻¹	137
3-6. Nucleation exponents and crystal growth parameters based on the traditional regime analysis for the case: $T_g = 273.2$ K, $(T_m^0)_{100\%} = 433.2$ K, and $\Delta H_f^0 = 8.0$ kJ·mol ⁻¹	140

PART 4: CRYSTALLINE MEMORY EFFECT IN ISOTHERMAL
CRYSTALLIZATION OF SYNDIOTACTIC POLYPROPYLENE

4-1. Effect of crystallization temperature T_c on crystallization half-time $t_{0.5}$, heat of crystallization ΔH_c , total concentration of predetermined nuclei N_{tot} and average spherulite diameter D . Conditions: $\phi = 80^\circ\text{C}\cdot\text{min}^{-1}$, $T_f = 190^\circ\text{C}$, and $t_h = 5$ min	160
4-2. Effect of heating rate ϕ on crystallization half-time $t_{0.5}$, heat of crystallization ΔH_c , total concentration of predetermined nuclei N_{tot} and average spherulite diameter D . Conditions: $T_f = 150^\circ\text{C}$, $t_h = 5$ min, and $T_c = 85^\circ\text{C}$	164
4-3. Effect of fusion temperature T_f on crystallization half-time $t_{0.5}$, heat of crystallization ΔH_c , total concentration of predetermined nuclei N_{tot} and average spherulite diameter D . Conditions: $\phi = 80^\circ\text{C}\cdot\text{min}^{-1}$, $t_h = 5$ min, and $T_c = 85^\circ\text{C}$	169
4-4. Effect of holding time t_h in the melt at 5 different fusion temperatures T_f , ranging from 145°C to 180°C , on crystallization half-time $t_{0.5}$, heat of crystallization ΔH_c , total concentration of predetermined nuclei N_{tot} and average spherulite diameter D . Conditions: $\phi = 80^\circ\text{C}\cdot\text{min}^{-1}$, and $T_c = 85^\circ\text{C}$	172
4-5. Summary of the relaxation time for the segregation of nucleation cluster τ , the initial concentration of predetermined athermal nuclei N_0 , and the initial total concentration of predetermined nuclei $N_{tot}(T_f, 0)$ for 5 different fusion temperatures T_f	177

PART 5: APPLICATION OF THE AVRAMI, TOBIN, MALKIN, AND
SIMULTANEOUS AVRAMI MACROKINETIC MODELS TO ISOTHERMAL
CRYSTALLIZATION OF SYNDIOTACTIC POLYPROPYLENE

5-1. Characterization data of as-received syndiotactic polypropylene samples	187
--	-----

TABLE	PAGE
5-2. Summary of the overall crystallization kinetics data for syndiotactic polypropylene samples based on the Avrami model	191
5-3. Summary of the overall crystallization kinetics data for syndiotactic polypropylene samples based on the Tobin model	196
5-4. Summary of the overall crystallization kinetics data for syndiotactic polypropylene samples based on the Malkin model	198
5-5. Theoretical description of the Avrami isothermal crystallization rate constant k_a for different types of morphology and transient nucleation mechanisms	204
5-6. Summary of the overall crystallization kinetics data for syndiotactic polypropylene samples based on the simultaneous Avrami model	206
5-7. The fitting parameters, as provided by the program, for the best possible fits of the respective rate parameters to Equation (5-8)	212
PART 6: ON THE CRYSTALLIZATION AND MELTING BEHAVIOR IN SYNDIOTACTIC POLYPROPYLENE: THE ORIGIN OF THE MULTIPLE ENDOTHERMIC MELTING PHENOMENON	
6-1. Variation of the initial temperature T_{int} , the minor peak temperature T_l , the low-melting peak temperature T_{ml} , the high-melting peak temperature T_{mh} , the end temperature T_{end} , and the enthalpy of fusion ΔH_f , as determined from Figure 6-1, with the crystallization temperature	230
6-2. Variation of the initial temperature T_{int} , the minor peak temperature T_l , the low-melting peak temperature T_{ml} , the high-melting peak temperature T_{mh} , the end temperature T_{end} , and the enthalpy of fusion ΔH_f , as determined from Figure 6-7, with the heating rate used to record the subsequent melting endotherms after complete crystallization at $T_c = 75^\circ\text{C}$	247
6-3. Variation of the low-melting peak temperature T_{ml} , the high-melting peak temperature T_{mh} , and the enthalpy of fusion ΔH_f , as determined from Figures 6-8 and 6-9, with the heating rate used to record the subsequent melting endotherms after partial crystallization at $T_c = 75^\circ\text{C}$ for 1.5 min and at $T_c = 95^\circ\text{C}$ for 15 min, respectively	251
PART 7: ISOTHERMAL MELT- AND COLD-CRYSTALLIZATION KINETICS AND SUBSEQUENT MELTING BEHAVIOR IN SYNDIOTACTIC POLYPROPYLENE: A DIFFERENTIAL SCANNING CALORIMETRY STUDY	
7-1. Summary of the overall crystallization kinetics parameters (e.g., the crystallization half-time $t_{0.5}$, the reciprocal half-time $t_{0.5}^{-1}$, the Avrami exponent n_a , the Avrami rate constant k_a , the Malkin exponent C_0 , and the Malkin rate constant C_1) for isothermal crystallization of sPP from the melt state	270

TABLE

PAGE

7-2.	Summary of the overall crystallization kinetics parameters (e.g., the crystallization half-time $t_{0.5}$, the reciprocal half-time $t_{0.5}^{-1}$, the Avrami exponent n_a , the Avrami rate constant k_a , the Malkin exponent C_0 , and the Malkin rate constant C_1) for isothermal crystallization of sPP from the glassy state	271
7-3.	Summary of the minor peak temperature T_l , the low-melting peak temperature T_{ml} , the high-melting peak temperature T_{mh} , enthalpy of crystallization ΔH_c , and enthalpy of fusion ΔH_f for isothermal crystallization of sPP from the melt state	275
7-4.	Summary of the minor peak temperature T_l , the low-melting peak temperature T_{ml} , the high-melting peak temperature T_{mh} , enthalpy of crystallization ΔH_c , and enthalpy of fusion ΔH_f for isothermal crystallization of sPP from the glassy state	276
7-5.	The fitting parameters, provided by the non-linear multi-variable regression program, for the best possible fits of the respective bulk crystallization rate parameters (e.g., $t_{0.5}^{-1}$, k_a , C_1 and $k_a^{1/n}$) according to Equation (7-13)	291
7-6.	The fitting parameters, provided by the non-linear multi-variable regression program, for the best possible fits of the respective bulk crystallization rate parameters (e.g., $t_{0.5}^{-1}$, k_a , C_1 and $k_a^{1/n}$) according to Equation (7-14)	292
7-7.	Summary of the equilibrium melting temperature T_m^{LHW} and the lamellar thickening ratio β as suggested by the <i>linear</i> Hoffman-Weeks extrapolative method, and the equilibrium melting temperature T_m^{NLHW} and the parameter a associated with the resulting T_m^{NLHW} value as suggested by the <i>non-linear</i> Hoffman-Weeks extrapolative method for the observed T_m - T_c data ranges specified	300
PART 8: ISOTHERMAL CRYSTALLIZATION AND MELTING BEHAVIOR OF SYNDIOTACTIC POLYPROPYLENE: A WAXD/SAXS/DSC STUDY		
8-1.	Experimental values of the WAXD degree of crystallinity χ_c^{WAXD} , the maximum scattering vector q_{max} , the long period L_B , the lamellar thickness l_c , and the melting temperature T_m	315
PART 9: USE OF DSC MELTING ENDOTHERMS FOR STUDYING ISOTHERMAL BULK CRYSTALLIZATION OF SEMICRYSTALLINE POLYMERS AT LOW DEGREES OF UNDERCOOLING: A CASE STUDY IN SYNDIOTACTIC POLYPROPYLENE		
9-1.	Induction time t_0 and overall Avrami crystallization kinetics data for syndiotactic polypropylene, as determined from the present technique (i.e., $t_{0.5}$, n_a , k_a) and the traditional technique (i.e., $t_{0.5}^*$, n_a^* , k_a^*)	358

LIST OF FIGURES

FIGURE	PAGE
PART 1: GENERAL INTRODUCTION AND GENERAL REVIEW OF THEORETICAL BACKGROUND	
1-1. Schematic diagram of the model used in the derivation of the Lauritzen-Hoffman secondary nucleation kinetics theory	23
1-2. Conceptual diagram illustrating the free energy of formation of a chain-folded nucleus on an existing growth surface	26
1-3. Schematic diagram illustrating mechanisms of linear growth rate data in Regimes I, II, and III, and corresponding appearance when performing a Lauritzen-Hoffman plot on the linear growth rate data	32
PART 2: THERMAL PROPERTIES AND ISOTHERMAL CRYSTALLIZATION OF SYNDIOTACTIC POLYPROPYLENES: DIFFERENTIAL SCANNING CALORIMETRY AND OVERALL CRYSTALLIZATION KINETICS	
2-1. Melting endotherms of sample sPP#4, recorded at the heating rate of $20^{\circ}\text{C}\cdot\text{min}^{-1}$, after isothermal crystallization at the specified temperature	88
2-2. Melting endotherms of sample sPP#4, recorded at the specified heating rates, after isothermal crystallization at 75°C	89
2-3. Melting temperatures as a function of crystallization temperatures for the sPP samples	93
2-4. Relative crystallinity as a function of time, and typical Avrami plots shown as the inset figure for sample sPP#3, isothermally crystallized at the specified temperatures: (\square) 80°C ; (\diamond) 85°C ; (\circ) 90°C ; (\triangle) 92.5°C ; (\times) 95°C	98
2-5. Half-time of crystallization as a function of crystallization temperatures. Reciprocal half-time is shown as a function of crystallization temperature in the inset figure. Key: (\square) sPP#1; (\diamond) sPP#2; (\circ) sPP#3; (\triangle) sPP#4; (\times) sPP#5	100
2-6. Avrami crystallization rate constant as a function of crystallization temperatures for the sPP samples: (\square) sPP#1; (\diamond) sPP#2; (\circ) sPP#3; (\triangle) sPP#4; (\times) sPP#5	102
2-7. Analysis of the half-times of crystallization based on the modified growth rate theory for the sPP samples: (\square) sPP#1; (\diamond) sPP#2; (\circ) sPP#3; (\triangle) sPP#4; (\times) sPP#5	104
2-8. Reciprocal half-times as a function of crystallization temperature for the sPP samples showing the comparison to the calculated curves based on Equation (2-10) (lines): (\square) sPP#1; (\diamond) sPP#2; (\circ) sPP#3; (\triangle) sPP#4; (\times) sPP#5	110

PART 3: REGIME CRYSTALLIZATION IN SYNDIOTACTIC
POLYPROPYLENES: RE-EVALUATION OF THE LITERATURE DATA

- 3-1. Spherulitic growth rates of syndiotactic polypropylene as a function of crystallization temperatures: (×) data of Miller and Seeley (sample 6H) [17,18]; (◆) data of Rodriguez-Arnold et al. (sample sPP(8)) [19,21,23]; (◇) data of Rodriguez-Arnold et al. (sample sPP(9)) [19,21,23]; (●) data of Supaphol et al. (sample sPP#1) [22] 127
- 3-2. Analysis of the spherulitic growth rates of syndiotactic polypropylene as a function of crystallization temperatures based on the Lauritzen and Hoffman secondary nucleation theory for the case $U^* = 1500 \text{ cal}\cdot\text{mol}^{-1}$, $T_\infty = T_g - 30 = 237.0 \text{ K}$, and $(T_m^0)_{100\%} = 441.8 \text{ K}$: (×) data of Miller and Seeley (sample 6H) [17,18]; (◆) data of Rodriguez-Arnold et al. (sample sPP(8)) [19,21,23]; (◇) data of Rodriguez-Arnold et al. (sample sPP(9)) [19,21,23]; (●) data of Supaphol et al. (sample sPP#1) [22] 131
- 3-3. The same plot as Figure 3-2 but without the data of Miller and Seeley (sample 6H) [17,18]. The regime II→III transition is clearly distinguishable in all three sets of data, and corresponds to the crystallization temperature of 110°C 132
- 3-4. Spherulitic growth rates of syndiotactic polypropylene as a function of crystallization temperatures: (◆) data of Rodriguez-Arnold et al. (sample sPP(8)) [19,21,23]; (◇) data of Rodriguez-Arnold et al. (sample sPP(9)) [19,21,23]; (●) data of Supaphol et al. (sample sPP#1) [22]; (----) predicted values based on the growth rate expression (e.g., Equation (3-1)) with appropriate G_0 and K_g values 136
- 3-5. Variation of the $K_{g,III}/K_{g,II}$ value as a result of changes in the seed equilibrium melting temperature T_m^0 of sample sPP#1. The seed T_m^0 value which results in the $K_{g,III}/K_{g,II}$ value of 2.0 (ca. 178°C) is supposed to be the true equilibrium melting temperature of sample sPP#1 145

PART 4: CRYSTALLINE MEMORY EFFECT IN ISOTHERMAL
CRYSTALLIZATION OF SYNDIOTACTIC POLYPROPYLENE

- 4-1. Relative crystallinity $\theta(t)$ as a function of time for sPP. The inset figure shows the original DSC crystallization exotherm as a function of time. Conditions: $\phi = 80^\circ\text{C}\cdot\text{min}^{-1}$, $T_f = 135^\circ\text{C}$, $t_h = 10 \text{ min}$, and $T_c = 85^\circ\text{C}$ 156
- 4-2. Effect of crystallization temperature T_c on the observed crystallization half-time $t_{0.5}$. The inset figure shows the effect of crystallization temperature T_c on the rate of overall crystallization (reciprocal half-time $t_{0.5}^{-1}$). Conditions: $\phi = 80^\circ\text{C}\cdot\text{min}^{-1}$, $T_f = 190^\circ\text{C}$, and $t_h = 5 \text{ min}$ 159
- 4-3. Effect of crystallization temperature T_c on the total concentration of predetermined nuclei N_{tot} and the average spherulite diameter D . Conditions: $\phi = 80^\circ\text{C}\cdot\text{min}^{-1}$, $T_f = 190^\circ\text{C}$, and $t_h = 5 \text{ min}$ 161

FIGURE	PAGE
4-4. Effect of heating rate ϕ on the observed crystallization half-time $t_{0.5}$. The inset figure shows the effect of heating rate ϕ on the rate of overall crystallization (reciprocal half-time $t_{0.5}^{-1}$). Conditions: $T_f = 150^\circ\text{C}$, $t_h = 5$ min, and $T_c = 85^\circ\text{C}$	163
4-5. Effect of heating rate ϕ on the total concentration of predetermined nuclei N_{tot} and the average spherulite diameter D . Conditions: $T_f = 150^\circ\text{C}$, $t_h = 5$ min, and $T_c = 85^\circ\text{C}$	166
4-6. Effect of fusion temperature T_f on the observed crystallization half-time $t_{0.5}$. The inset figure shows the effect of fusion temperature T_f on the rate of overall crystallization (reciprocal half-time $t_{0.5}^{-1}$). Conditions: $\phi = 80^\circ\text{C}\cdot\text{min}^{-1}$, $t_h = 5$ min, and $T_c = 85^\circ\text{C}$	167
4-7. Effect of fusion temperature T_f on the total concentration of predetermined nuclei N_{tot} and the average spherulite diameter D . Conditions: $\phi = 80^\circ\text{C}\cdot\text{min}^{-1}$, $t_h = 5$ min, and $T_c = 85^\circ\text{C}$	170
4-8. Effect of holding time t_h on the observed crystallization half-time $t_{0.5}$ for 5 different fusion temperatures T_f , ranging from 145°C to 180°C . Conditions: $\phi = 80^\circ\text{C}\cdot\text{min}^{-1}$, and $T_c = 85^\circ\text{C}$	171
4-9. Effect of holding time t_h on the total concentration of predetermined nuclei N_{tot} and the average spherulite diameter D . Conditions: $\phi = 80^\circ\text{C}\cdot\text{min}^{-1}$, $T_f = 180^\circ\text{C}$, and $T_c = 85^\circ\text{C}$	174
4-10. Plot of $\ln[N_{\text{tot}}(T_f, t_h) - N_{\text{tot}}(T_f, \infty)]$ versus holding time t_h for 5 different fusion temperatures T_f : (●) 145°C ; (○) 150°C ; (◆) 160°C ; (◇) 170°C ; and (▲) 180°C	176

PART 5: APPLICATION OF THE AVRAMI, TOBIN, MALKIN, AND
SIMULTANEOUS AVRAMI MACROKINETIC MODELS TO ISOTHERMAL
CRYSTALLIZATION OF SYNDIOTACTIC POLYPROPYLENE

5-1. Experimental relative crystallinity as a function of time of sPP#1 for 5 different crystallization temperatures: (○) 75°C ; (●) 80°C ; (◇) 85°C ; (◆) 90°C	189
5-2. Experimental relative crystallinity as a function of time of sPP#3 for 5 different crystallization temperatures: (○) 75°C ; (●) 80°C ; (◇) 85°C ; (◆) 90°C	190
5-3. Half-time of crystallization as a function of crystallization temperatures, with the inset figure illustrating the reciprocal half-time as a function of crystallization temperature: (○) sPP#1; (●) sPP#3	192

FIGURE

PAGE

5-4.	Relative crystallinity as a function of time of sPP#1 for 2 different crystallization temperatures: (○) 75°C; (◇) 85°C. The experimental data, shown as points, were fitted to the non-linear multi-variable regression program, where the best fits according to the Avrami, Tobin, and Malkin macrokinetic models are shown as the solid, dotted, and dashed lines	200
5-5.	Relative crystallinity as a function of time of sPP#3 for 2 different crystallization temperatures: (○) 75°C; (◇) 85°C. The experimental data, shown as points, were fitted to the non-linear multi-variable regression program, where the best fits according to the Avrami, Tobin, and Malkin macrokinetic models are shown as the solid, dotted, and dashed lines	201
5-6.	The best fitted curves of various crystallization rate parameters of sPP#1 to Equation (5-8). Keys: (●) $t_{0.5}^{-1}$; (○) k_a ; (◆) C_{1i} ; (▲) k_{ai} ; (△) k_{as}	210
5-7.	The best fitted curves of various crystallization rate parameters of sPP#3 to Equation (5-8). Keys: (●) $t_{0.5}^{-1}$; (○) k_a ; (◆) C_{1i} ; (▲) k_{ai} ; (△) k_{as}	211
5-8.	Relative crystallinity as a function of time of sPP#1 for 2 different crystallization temperatures: (○) 85°C; (●) 90°C. The experimental data, shown as points, are plotted along with the predicted curves using the Avrami, Malkin, and simultaneous Avrami macrokinetics models (shown as the solid, dotted, and dashed lines, respectively)	213
5-9.	Relative crystallinity as a function of time of sPP#3 for 2 different crystallization temperatures: (○) 85°C; (●) 90°C. The experimental data, shown as points, are plotted along with the predicted curves using the Avrami, Malkin, and simultaneous Avrami macrokinetics models (shown as the solid, dotted, and dashed lines, respectively)	214
 PART 6: ON THE CRYSTALLIZATION AND MELTING BEHAVIOR IN SYNDIOTACTIC POLYPROPYLENE: THE ORIGIN OF THE MULTIPLE ENDOTHERMIC MELTING PHENOMENON 		
6-1.	Subsequent melting endotherms (20°C·min ⁻¹) of sPP samples after isothermal crystallization from the melt at the specified temperature. Terminologies: T_1 = the minor peak temperature; T_{m1} = the low-melting peak temperature; T_{mh} = the high-melting peak temperature	226
6-2.	The procedure used in this study to determine characteristic temperatures from a subsequent melting endotherm. Terminologies: T_{int} = the initial temperature; T_1 = the minor peak temperature; T_{m1} = the low-melting peak temperature; T_{mh} = the high-melting peak temperature; T_{end} = the end temperature	228
6-3.	Variation of the initial temperature T_{int} , the minor peak temperature T_1 , the low-melting peak temperature T_{m1} , and the high-melting peak temperature T_{mh} , as determined from the subsequent melting endotherms in Figure 6-1, with the crystallization temperature	231

FIGURE	PAGE
6-4. Wide-angle x-ray diffractograms of sPP samples isothermally crystallized from the melt at the specified temperature corresponding to the conditions used for the thermal analysis shown in Figure 6-1	234
6-5. Subsequent melting endotherms ($20^{\circ}\text{C}\cdot\text{min}^{-1}$) of sPP samples after partial and complete crystallization at $T_c = 75^{\circ}\text{C}$ for different time intervals as indicated. Terminologies: T_1 = the minor peak temperature; T_{ml} = the low-melting peak temperature; T_{mh} = the high-melting peak temperature	236
6-6. Subsequent melting endotherms ($20^{\circ}\text{C}\cdot\text{min}^{-1}$) of sPP samples after partial and complete crystallization at $T_c = 95^{\circ}\text{C}$ for different time intervals as indicated. Terminologies: T_1 = the minor peak temperature; T_{ml} = the low-melting peak temperature; T_{mh} = the high-melting peak temperature	237
6-7. Subsequent melting endotherms of sPP samples recorded using different scanning rate ranging from 5 to $40^{\circ}\text{C}\cdot\text{min}^{-1}$ after complete crystallization at $T_c = 75^{\circ}\text{C}$. Terminologies: T_1 = the minor peak temperature; T_{ml} = the low-melting peak temperature; T_{mh} = the high-melting peak temperature	245
6-8. Subsequent melting endotherms of sPP samples recorded using different scanning rate ranging from 5 to $30^{\circ}\text{C}\cdot\text{min}^{-1}$ after partial crystallization at $T_c = 75^{\circ}\text{C}$ for 1.5 min. Terminologies: T_{ml} = the low-melting peak temperature; T_{mh} = the high-melting peak temperature	249
6-9. Subsequent melting endotherms of sPP samples recorded using different scanning rate ranging from 5 to $30^{\circ}\text{C}\cdot\text{min}^{-1}$ after partial crystallization at $T_c = 95^{\circ}\text{C}$ for 15 min. Terminologies: T_{ml} = the low-melting peak temperature; T_{mh} = the high-melting peak temperature	250
PART 7: ISOTHERMAL MELT- AND COLD-CRYSTALLIZATION KINETICS AND SUBSEQUENT MELTING BEHAVIOR IN SYNDIOTACTIC POLYPROPYLENE: A DIFFERENTIAL SCANNING CALORIMETRY STUDY	
7-1. Typical crystallization exotherm data of sPP sample isothermally crystallized at $T_c = 70^{\circ}\text{C}$ from the melt state	266
7-2. Typical relative crystallinity $\theta(t)$ as a function of crystallization time t , calculated from the raw crystallization exotherm data shown in Figure 7-1 according to Equation (7-6)	268
7-3. Subsequent melting endotherms ($20^{\circ}\text{C}\cdot\text{min}^{-1}$) of sPP samples after isothermal crystallization from the melt state at the specified temperatures. Terminologies: T_1 = the minor peak temperature; T_{ml} = the low-melting peak temperature; T_{mh} = the high-melting peak temperature	272

FIGURE

PAGE

- 7-4. Subsequent melting endotherms ($20^{\circ}\text{C}\cdot\text{min}^{-1}$) of sPP samples after isothermal crystallization from the glassy state at the specified temperatures. Terminologies: T_1 = the minor peak temperature; T_{ml} = the low-melting peak temperature; T_{mh} = the high-melting peak temperature 273
- 7-5. Variation of the minor peak temperature T_1 , the low-melting peak temperature T_{ml} , and the high-melting peak temperature T_{mh} , as determined from the subsequent melting endotherms after complete crystallization from both the melt and glassy states, with the crystallization temperature T_c . Keys: (\blacklozenge), (\bullet), and (\blacksquare) represent T_1 , T_{ml} , T_{mh} values for crystallization from the melt states; (\diamond), (\circ), and (\square) represent T_1 , T_{ml} , T_{mh} values for crystallization from the glassy states 277
- 7-6. Variation of the reciprocal half-time $t_{0.5}^{-1}$ as a function of crystallization temperature T_c : (\diamond) melt-crystallization data taken from reference [40], (\times) melt-crystallization data taken from reference [13], (\bullet) melt-crystallization data measured in this study, and (\circ) cold-crystallization data measured in this study. Different lines represent the best fits of the experimental data 280
- 7-7. Variation of the Avrami exponent n_a as a function of crystallization temperature T_c : (\diamond) melt-crystallization data taken from reference [40], (\times) melt-crystallization data taken from reference [13], (\bullet) melt-crystallization data measured in this study, and (\circ) cold-crystallization data measured in this study 284
- 7-8. Variation of the Malkin exponent C_0 as a function of crystallization temperature T_c : (\bullet) melt-crystallization data measured in this study, and (\circ) cold-crystallization data measured in this study 285
- 7-9. Variation of the Avrami rate constant k_a as a function of crystallization temperature T_c : (\diamond) melt-crystallization data taken from reference [40], (\times) melt-crystallization data taken from reference [13], (\bullet) melt-crystallization data measured in this study, and (\circ) cold-crystallization data measured in this study. Different lines represent the best fits of the experimental data 287
- 7-10. Variation of the Malkin rate constant C_1 as a function of crystallization temperature T_c : (\diamond) melt-crystallization data taken from reference [40], (\times) melt-crystallization data taken from reference [13], (\bullet) melt-crystallization data measured in this study, and (\circ) cold-crystallization data measured in this study. Different lines represent the best fits of the experimental data 288
- 7-11. Variation of $(1/n_a)\ln k_a$ as a function of the inversed crystallization temperature T_c^{-1} according to Equation (7-15). Keys: (\diamond) melt-crystallization data taken from reference [40], (\times) melt-crystallization data taken from reference [13], (\bullet) melt-crystallization data measured in this study, and (\circ) cold-crystallization data measured in this study 294

FIGURE

PAGE

- 7-12. Variation of $k_a^{1/n}$ as a function of the crystallization temperature T_c according to Equation (7-15). Keys: (\diamond) melt-crystallization data taken from reference [40], (\times) melt-crystallization data taken from reference [13], (\bullet) melt-crystallization data measured in this study, and (\circ) cold-crystallization data measured in this study 295
- 7-13. Variation of the low-melting peak temperature T_{ml} (or the melting temperature T_m of the primary crystals formed at T_c) as a function of the crystallization temperature T_c for isothermal crystallization from the melt state (\bullet), and corresponding *linear* and *non-linear* Hoffman-Weeks extrapolations shown as straight and curved lines, respectively. Keys: (\dashrightarrow) fitted line for the data range $40^\circ\text{C} \leq T_c \leq 95^\circ\text{C}$, (\dashleftarrow) fitted line for the data range $50^\circ\text{C} \leq T_c \leq 95^\circ\text{C}$, (\dashv) fitted line for the data range $60^\circ\text{C} \leq T_c \leq 95^\circ\text{C}$, (\dashv) fitted line for the data range $70^\circ\text{C} \leq T_c \leq 95^\circ\text{C}$, and (\dashrightarrow) fitted line for the data range $80^\circ\text{C} \leq T_c \leq 95^\circ\text{C}$ 297
- 7-14. Variation of the low-melting peak temperature T_{ml} (or the melting temperature T_m of the primary crystals formed at T_c) as a function of the crystallization temperature T_c for isothermal crystallization from the glassy state (\circ), and corresponding *linear* and *non-linear* Hoffman-Weeks extrapolations shown as straight and curved lines, respectively. Keys: (\dashrightarrow) fitted line for the data range $40^\circ\text{C} \leq T_c \leq 95^\circ\text{C}$, (\dashleftarrow) fitted line for the data range $50^\circ\text{C} \leq T_c \leq 95^\circ\text{C}$, (\dashv) fitted line for the data range $60^\circ\text{C} \leq T_c \leq 95^\circ\text{C}$, (\dashv) fitted line for the data range $70^\circ\text{C} \leq T_c \leq 95^\circ\text{C}$, and (\dashrightarrow) fitted line for the data range $80^\circ\text{C} \leq T_c \leq 95^\circ\text{C}$ 298

PART 8: ISOTHERMAL CRYSTALLIZATION AND MELTING BEHAVIOR OF
SYNDIOTACTIC POLYPROPYLENE: A WAXD/SAXS/DSC STUDY

- 8-1. WAXD diffractograms of sPP#4 samples isothermally crystallized at various crystallization temperatures T_c ranging from 30°C to 95°C 313
- 8-2. Azimuthally averaged SAXS profiles of sPP#4 samples isothermally crystallized at various crystallization temperatures T_c ranging from 30°C to 95°C 316
- 8-3. Lorentz-corrected SAXS profiles (Kratky plots) of sPP#4 samples isothermally crystallized at various crystallization temperatures T_c ranging from 30°C to 95°C . (Please see Figure 8-2 for legends.) 317
- 8-4. Subsequent melting thermograms observed in DSC using a heating rate of $20^\circ\text{C}\cdot\text{min}^{-1}$ for sPP#4 samples isothermally crystallized at various crystallization temperatures T_c ranging from 30°C to 95°C 319
- 8-5. Relations between the inverse lamellar thickness l_c^{-1} , the observed melting temperature T_m , and the crystallization temperature T_c obtained for sPP#4 samples isothermally crystallized at various crystallization temperatures T_c ranging from 60°C to 95°C . T_1 represents $T_m(l_c^{-1} \rightarrow 0)$, T_2 represents $T_c(l_c^{-1} \rightarrow 0)$, and T_3 represent T_m^{LHW} 322

8-6.	Plot of the observed melting temperature T_m as a function of the crystallization temperature T_c (without the data points at $T_c = 30, 40, \text{ and } 50^\circ\text{C}$). The long-dashed line is the <i>linear</i> HW extrapolation based on experimental data points (●). The solid line is the <i>non-linear</i> HW extrapolation calculated using $\beta^m = 1, a = 2.34, \text{ and } T_m^{\text{NLHW}} = 184.7^\circ\text{C}$. The short-dashed line is the <i>linear</i> HW extrapolation based on experimental data of this study (●) and those reported earlier in references 13 and 36 (not shown). The alternating-dashed line is the <i>non-linear</i> HW extrapolation calculated using $\beta^m = 1, a = 2.25, \text{ and } T_m^{\text{NLHW}} = 186.6^\circ\text{C}$	327
8-7.	Plots of the scaled observed melting temperature $M = T_m^0 / (T_m^0 - T_m)$ against the scaled crystallization temperature $X = T_m^0 / (T_m^0 - T_c)$ for various choices of the seeded equilibrium melting temperature T_m^0 for the observed $T_m - T_c$ data of this study (without the data points at $T_c = 30, 40, \text{ and } 50^\circ\text{C}$)	331
8-8.	Plots of the scaled observed melting temperature $M = T_m^0 / (T_m^0 - T_m)$ against the scaled crystallization temperature $X = T_m^0 / (T_m^0 - T_c)$ for various choices of the seeded equilibrium melting temperature T_m^0 for the observed $T_m - T_c$ data of this study (●) and those reported earlier in references 13 (□) and 36 (×)	333
8-9.	Plot of lamellar thickness l_c as a function of the crystallization temperature T_c (without the data points at $T_c = 30, 40, \text{ and } 50^\circ\text{C}$). The short- and long-dashed lines are the best fits of the experimental data (●) according to Equation (8-13) when T_m^0 is taken as 166.3°C and 184.7°C , respectively. The solid line is the estimated curve calculated according to Equation (8-13) using $\sigma_e^1 = \sigma_e^{\text{GT}} = 57.8 \text{ mJ}\cdot\text{m}^{-2}, T_m^0 = 184.7^\circ\text{C}, \Delta H_f^0 = 4.6 \text{ kJ}\cdot\text{mol}^{-1}, \text{ and } a = 2.34$	335

PART 9: USE OF DSC MELTING ENDOTHERMS FOR STUDYING
ISOTHERMAL BULK CRYSTALLIZATION OF SEMICRYSTALLINE
POLYMERS AT LOW DEGREES OF UNDERCOOLING: A CASE STUDY
IN SYNDIOTACTIC POLYPROPYLENE

9-1.	Typical crystallization exotherm data of sPP sample isothermally crystallized at $T_c = 77.5^\circ\text{C}$	343
9-2.	Typical relative crystallinity $\theta(t)$ as a function of crystallization time t , calculated from the raw data shown in Figure 9-1 according to Equation (9-2)	345
9-3.	DSC subsequent melting endotherms ($20^\circ\text{C}\cdot\text{min}^{-1}$) of sPP samples after partial crystallization at $T_c = 75^\circ\text{C}$ for different time intervals as indicated	351
9-4.	DSC subsequent melting endotherms ($20^\circ\text{C}\cdot\text{min}^{-1}$) of sPP samples after partial crystallization at $T_c = 95^\circ\text{C}$ for different time intervals as indicated	352

FIGURE	PAGE
9-5. Relative crystallinity $\theta(t)$ as a function of crystallization time t (in logarithmic scale) of sPP sample, calculated from enthalpy of fusion $\Delta H_{f,t}$ determined from subsequent melting endotherms after isothermal crystallization for various time intervals (cf. Figures 9-3 and 9-4) according to Equation (9-4), for 5 different crystallization temperatures T_c : (●) 75°C; (○) 90°C; (▲) 95°C; (△) 100°C; and (▼) 105°C	355
9-6. Induction time t_0 (cf. Table 9-1) as a function of crystallization temperature T_c of sPP. The dotted line 1 is the best fitted-curve drawn through the bulk of the data after Equation (9-13), while the dotted line 2 is drawn after Equation (9-14). Parameters of the fitted curves: $\tau_1 = 2.64 \times 10^{-8} \text{ min} \cdot \text{K}$, $K_1 = 4.31 \times 10^5 \text{ K}^2$, $\tau_2 = 4.81 \times 10^{-6} \text{ min}$, and $K_2 = 1.30 \times 10^7 \text{ K}^3$	363
9-7. Reciprocal half-time $t_{0.5}^{-1}$ as a function of crystallization temperature T_c for sPP. Keys: (●) the data measured from this study (cf. Table 9-1); and (△) the data measured from the traditional technique (cf. Table 2-5 in reference [19] (cf. Part 2)). The dotted line is the best fitted curve drawn through the bulk of the data after Equation (9-15). Parameters of the fitted curve: $\Psi_0 = 2.38 \times 10^{12} \text{ min}^{-1}$ and $K_3 = 6.38 \times 10^5 \text{ K}^2$	365

PART 1:
GENERAL INTRODUCTION AND GENERAL REVIEW OF
THEORETICAL BACKGROUND

1. GENERAL INTRODUCTION

The syndiotactic form of polypropylene (sPP) was first synthesized in the 1960s by Natta et al. [1,2] based on the $\text{AlR}_2\text{Cl}/\text{VCl}_4$ catalyst systems. Regardless of it having a fair level of syndiotactic content, the resulting polymer contained too high a level of regio-irregular defects (e.g., head-to-head/tail-to-tail types of defects) along the molecular chain. As a result, it was considered only a laboratory curiosity. It was not until the invention of Ewen et al. [3], who reported in 1988 that highly stereo-regular and regio-regular sPP can be synthesized using novel metallocene catalysis composed of isopropylidene(cyclo-pentadienyl)(9-fluorenyl)zirconium or hafnium dichloride and methylaluminoxane, that recurring interest of this polymer in terms of industrial applications has been realized. This is evidenced by an increase in the number of publications in the recent years in which industrial applications of sPP have been extensively explored in areas such as films [4,5], injection molding [6], and melt-spun fibers [7,8]. Other physical properties related to applications have also been investigated and reported [9,10].

In order to have a clear picture about what is happening during processing of this polymer, studies related to the crystallization process are of prime importance, owing to the fact that the resulting physical properties are strongly dependent on the morphology formed and the extent of crystallization. It is therefore very important to understand the processing-structure-property inter-relationships of the studied materials, which in this case is sPP. In recent years, investigations related to the chain conformation, crystal structure, morphology, and phase transitions in sPP have been extensively reported. These studies up to 1994 were reviewed and discussed in a publication by Rodriguez-Arnold et al. [11].

The general philosophy of this research is to gain more understanding of the fundamentals of isothermal quiescent crystallization and subsequent melting behavior of sPP. The general objectives of this research are (1) to understand isothermal melt- and cold-crystallization and subsequent melting behavior of sPP, and to determine related kinetics parameters associated with the crystallization process using appropriate macrokinetic models; (2) to investigate the crystal growth kinetics of quiescent crystallization of sPP under isothermal conditions, and to determine related kinetics parameters; (3) to determine under what conditions the information obtained from bulk isothermal measurements is not influenced by the effects of athermal nucleation, or in other words, to determine under what conditions the information obtained from bulk isothermal measurements is valid function of temperature only; and finally (4) to understand the capability and limitations of various macrokinetic models in describing the experimental data obtained under isothermal conditions.

This dissertation is organized into 9 parts. Part 1 deals with the general review of the theoretical background. Each of Parts 2 to 9 corresponds to a research paper which has either been accepted or submitted for publication in a scientific journal. As a result, the content in each of Parts 2 to 9 is self-explanatory.

The research described in Part 2 was carried out to establish a general understanding of the isothermal melt-crystallization and subsequent melting behavior of all the sPP resins acquired. The glass transition temperatures of these resins were also determined. The crystallization kinetics was investigated over a temperature range of ca. 60°C to 95°C. The traditional Avrami analysis was applied to obtain related kinetics parameters. The equilibrium melting temperature of these resins were also determined based on the linear Hoffman-Weeks extrapolative method. It should be noted that detailed analysis and discussion of the multiple-melting behavior of sPP based on the

results obtained from a combination of differential scanning calorimetry and wide-angle x-ray diffraction techniques can be found in Part 6.

Part 3 deals with the analysis and discussion of the kinetics of linear crystal growth rate data of sPP#1 resin, including data obtained from the literature, in the context of the Lauritzen-Hoffman secondary nucleation theory. The effects of changes in the input parameters characteristic to this theory on the resulting kinetics parameters were studied. The equilibrium melting temperature of sPP#1 resin was determined based on the analysis of the linear growth rate data using a data-fitting method.

The objective of the research described in Part 4 is to investigate isothermal crystallization behavior of sPP#4 after partial or complete melting using differential scanning calorimetry technique. Determination for the conditions of partial and complete melting were carried out by variation of fusion temperatures the samples were brought to melt and the time periods the samples spent at a specific fusion temperature. The most important character of partial melting is such that, upon subsequent cooling, the crystalline residues which survive due to insufficient fusion temperature and/or the time interval the sample spent at the fusion temperature can act as pre-determined athermal nuclei which greatly enhance the overall crystallization rate.

The analysis and discussion on the capability and limitations of various macrokinetic models; namely the Avrami, Tobin, Malkin, and simultaneous Avrami models; in describing the experimental data obtained under isothermal conditions were carried out on sPP#1 and sPP#3 resins in Part 5. For successful analysis of the experimental data according to these models, a non-linear multi-variable regression program was used to determine related kinetics parameters specific to each model. The applicability and reliability of the non-linear multi-variable regression program in the analysis of the experimental data were assured by comparison of the Avrami kinetics

parameters determined from the program with those determined based on a traditional analytical procedure.

The research described in Part 7 was to investigate in detail the isothermal melt- and cold-crystallization kinetics and subsequent melting behavior of sPP#1 resin using differential scanning calorimetry. The melt- and cold-crystallization kinetics were both investigated over a wide temperature range of ca. 8°C to 100°C. The overall crystallization kinetics was studied based on the Avrami and Malkin macrokinetic models using the non-linear multi-variable regression program, as described in Part 5. Detailed analysis and discussion on the determination of the equilibrium melting temperature of sPP#1 resin were carried out based on both linear and non-linear Hoffman-Weeks extrapolative methods.

The lamellar morphology of isothermally crystallized sPP#4 samples was investigated using wide-angle x-ray diffraction and small-angle x-ray scattering techniques. The results and discussion of this study are shown in Part 8. The melting behavior of these samples was also investigated using differential scanning calorimetry technique. Three methods for the determination of the equilibrium melting temperature, namely the Gibbs-Thomson, the linear and non-linear Hoffman-Weeks extrapolative methods, were employed to evaluate this important thermodynamic parameter. Discussion on the temperature dependence of the lamellar thickness of sPP#4 resin was also given.

In Part 9, a technique of using differential scanning calorimetry to study crystallization behavior and the kinetics of the process of semi-crystalline polymers at high crystallization temperatures or low degrees of undercooling, using sPP#4 resin as the model system, was proposed. The technique was carried out based on the observations of, and the measurements of the enthalpy of fusion from, the subsequent

melting endotherms after isothermal crystallization for various time intervals. This technique allows for an accurate determination of the induction time. It also gives an insight into the crystallization process as it occurs at different time intervals. The reliability and applicability of the technique were discussed by comparing the kinetics results with those obtained using the traditional technique.

2. GENERAL REVIEW OF THEORETICAL BACKGROUND

2.1. Overview of Polymer Crystallization

2.1.1. Basic Concept of Polymer Crystallization

In general, the term polymer is specifically used to describe high molecular weight substances which are made up by the repetition of a large number of small basic units, namely the repeating units. However, there exists an important problem of how high the molecular weight must be to be considered high enough to be called a polymer. It is experimentally accepted that the molecular weight dependence becomes very small when the number of repeating units exceed about 1,000 to 2,000, depending on the polymers.

Corresponding to the morphological aspect, polymers can be largely divided into two subcategories: amorphous polymers and semicrystalline polymers. Amorphous polymers are those whose molecules are intertwined or coiled up such that no regular, long-range arrangement is detected. Unlike the amorphous polymers, semicrystalline polymers contain both amorphous and crystalline domains. In the crystalline domains, the molecules are aligned in a three-dimensionally repetitive manner so that the molecules exhibit a high level of order.

However, it should be noted here that not all the polymers can crystallize. In general, stereo-regularity along the chain is required for crystallization to occur. However, several factors are still very important in this process. These factors comprise

the absence of the bulky side groups, the regularity of the molecular configurations, the regularity of the tacticity of the side groups, and the presence of vibrational and rotational motions in the molecular chains such that several conformations can be obtained.

2.1.2. Crystal Morphology

2.1.2.1. Fringed Micelle Morphology

This is a very early morphology proposed around 1930 based on x-ray diffraction results [12]. The early studies showed that, in both natural and synthetic polymers, there were some certain crystalline features present. However, the Bragg reflections of these samples are broader than those obtained from nonpolymeric low molecular weight substances. With the studies of the line broadening of those Bragg patterns, the picture of a polymer crystal about $100 \text{ \AA} \times 400 \text{ \AA}$ was developed. Hermann et al. [12] suggested the coexistence of two domains in the morphology, amorphous and crystalline domains, in the crystallization study of natural rubber. Crystalline domain is formed by the extension of the molecular chains along the chain axis. Each molecule was thought to travel from one crystallite to another by passing through the amorphous domain. The crystallites hence were thought of as physical crosslinks in the polymer solids and they were embedded in the amorphous matrix. Although this model had served an important role in explaining macroscopic properties of bulk polymers for decades, it was unsatisfactory to explain the development of the spherulitic microstructure, which is the common macroscopic feature of polymers crystallizing from the melt. This caused the demise of the concept of fringe micelle morphology.

2.1.2.2. Single Crystal Morphology

As early as 1938, Storks [13] suggested that thin film of gutta-percha (*trans*-polyisoprene) exhibited a chain-folded configuration. He pointed out the gutta-percha molecules may possibly fold back and forth by the rotational mechanism around single bonds. In 1957, Fischer [14], Till [15], and Keller [16] individually grew and observed the lamellar single crystals of linear polyethylene from dilute solution. All single crystals grown from dilute solution are in the form of thin platelets of ca. 100 Å in thickness. Based on the studies of electron diffraction experiments carried out by Fischer [14], Till [15], and Keller [16], the molecules are believed to align themselves normal to the lamellar platelets. Keller [16,17] suggested at this point that the molecules have to fold back and forth on themselves, which is in agreement with the earlier work by Storks [13].

The thickness of the single crystal platelets are relatively uniform from one polymer to another, which are in the order of ca. 100 Å. The lamellar thickness is dependent on the crystallization temperature and pressure in a roughly linear manner. It is also inversely dependent on the degree of undercooling, which is the difference between the melting point and the crystallization temperature.

Growth of the lamellae occur along the lateral surfaces of the single crystals. The growth is composed of the folding of molecules along these lateral faces to form folded ribbons parallel to the growing faces. The nature of the successive folding of the molecular chains is very questionable; thus, leading to two distinct subdivisions of the chain folding. These subdivisions can be discerned from the work by Reneker and Geil [18]. They suggested two possible distinctions in the chain folding of the successive fold plane which can be seen in the formation of flat or hollow pyramids. However, the hollow pyramidal crystals collapse due to the evaporation of the solvent during sample

preparation; leading to the presence of wrinkled, corrugated, and even pleated crystals [19,20], when observed by electron microscopy.

2.1.2.3. Spherulitic Morphology

When crystallization of a polymer from a concentrated solution or a melt is observed, spherulitic morphology is usually a common microstructural feature. Microscopically, spherulites consist of ribbonlike lamellae that grow out radially from the spherulitic nuclei until impingement occurs with other spherulites.

Spherulites develop from two distinct processes [19,21,22]. First, the primary crystallization may take place from a single crystal or a stack of single crystals to form a primary branching unit nuclei. Later, they evolve to sheaf-like morphology by the method of low-angle branching of the lamellae. Dendrites are examples of branched crystals obtained in the case that the crystallization rate is dependent on a growing direction. After that the sheaf-like morphology will advance to the final spherulitic shape. Secondary crystallization may later take place within each spherulite in order to transform a portion of the remnant amorphous material between the lamellae into crystalline material within that spherulite.

The size of spherulites ranges from as small as 1 μm to a few millimeters. An interesting aspect of spherulitic morphology is the birefringence effect. Under polarized light, spherulites show the typical Maltese cross, which is caused by the effect of the difference between the refractive indices observed along the radial direction n_r of the spherulite and that along the tangential direction n_t . Two different types of spherulites in this aspect are observed; positive and negative spherulites. Since the spherulitic birefringence is given by, $\Delta n = n_r - n_t$, positive spherulites show the highest refractive index in radial direction; whereas, negative spherulites show the highest refractive index in the tangential direction.

2.1.2.4. Axialitic Morphology

Axialites are microscopic aggregates of several crystal lamellar layers, stacked to form the final thickness which, in some cases, may exceed one micron. They exhibit different characteristics of polymer single crystals or spherulites dependent on the angle of view. They are considered to be intermediate in complexity between single crystals and spherulites, which are usually formed during crystallization from the concentrated solution or the melt. Axialites can crystallize in various macroscopic structures such as hedrites, which have hexagonally oriented fibrous lamellae which may incorporate a screw dislocation; ovoids, which have radially fibrous lamellae; and spiral ovoids, which have spirally oriented fibrous lamellae [23].

2.1.2.5. Extended Chain Morphology

In certain circumstances, crystallization of polymers, such as polyethylene, from a very slow crystallization at a temperature close to their melting points can be so arranged such that the molecules are aligned up with their ends being laid down in the same plane as well as their chains being in fully extended manner. Not only does slow crystallization at the vicinity of the melting point of the polymers allow this to occur, but crystallization of the melts under high pressure, of about 5,000 atm, and high orientation as the melt is cooling down also facilitates the formation of extended chain crystals. Mostly, fully extended morphology take place with the chains of molecular weight less than 10,000 and of which extended lengths are less than 1,000 Å being able to be seen.

2.1.3. Concepts of Chain Folding

There have been several approaches trying to elucidate the nature of the chain folding in lamellar crystals which can be seen in various structural morphologies obtained from concentrated solutions and the melt. Three possible assumptions have

been suggested by several authors: regular adjacent reentry, irregular adjacent reentry, and switchboard model. *Regular adjacent reentry* was proposed by Keller [16], in which he suggested the presence of the molecules folding back and forth contiguously on themselves. *Irregular adjacent reentry* was first proposed by Frank and Tosi [24]. They allowed the fluctuation in the size of the secondary nucleated stems to occur. This results in non-uniformity in the lamellar thickness of single crystals.

The other extreme model was proposed by Flory [25] which is known as the *switchboard model*. Unlike the adjacent reentry model, the switchboard model suggests that the molecules fold back and forth in a non-adjacent manner and sometimes some molecules may take place in several lamellae. This model suggests that the fold surface would be very rough due to the presence of loop chains. Tie molecules are also observed between different lamellae. This model is a somewhat better explanation to the question of the density defect of single crystals. It is known that the theoretical density of a single crystal obtained from x-ray diffraction is greater than the actual density of it. The difference is attributed to the amorphous zone arising from the presence of chain loops, tie molecules and loose ends. Some literature quotes that the crystallinity of a single crystal ranges from ca. 75% to ca. 85%, but that 100% crystallinity may be acquired by decomposing the fold surfaces of the single crystal by fuming nitric acid [23].

Experimentally, several arguments may be supportive of both the adjacent reentry and switch board models. The studies were made individually by Bank and Krimm [26] based on the presence of doublets in the IR spectrum, and by Spells et al. [27] based on the neutron scattering technique. Both groups studied the trajectory of molecules in a single crystal from a dilute solution of the mixture between deuterated and hydrogenous linear polyethylene. They obtained the similar conclusion that a

molecule needs to fold back and forth along the next adjacent (110) plane and this adjacent reentry manner of the molecule continues for at least two adjacent (110) planes [28].

In the case of crystallization from a highly concentrated solution and the melt, it is true that the content of amorphous region is considerably higher than that acquired from a dilute solution, and also the number of interlamellar links or tie molecules increases with increasing molecular weight of the polymer. Mandelkern [21] interestingly pointed out that the morphology from the melt is related to the lamellar structure as being seen from the dilute solutions, but in an even more complicated manner. The ordered structures, or the crystalline regions, are also observed of which some of the chains fold back to the originated crystallite but not mandatorily in juxtaposition to the original emergence, and others leave the originated crystallite and form a disordered amorphous or interzonal region but ultimately they will join a contiguous crystallite. This model is also known as *interzonal model*, which is similar to the switchboard model proposed by Flory [25].

A very supportive explanation to both interzonal and switchboard models, which are more suitable to the crystallization from the melt, is that the achievement for the molecules to be in the theoretically extended, close-packed arrangement is kinetically impossible. Although it is thermodynamically consonant to let that situation occur, the kinetic and mechanistic difficulties that must be overcome to accomplish this idealized equilibrium condition are enormous. The difficulty is the fact that the molecules must take a great deal of time in order to untwine themselves from the highly molecularly entangled melt. In addition, the fact that the crystallization inevitably occurs at temperatures well below the thermodynamic melting point indicates that crystallization occurs under non-equilibrium conditions. It is hence rare for the perfect

transformation from the disordered to the crystalline state to occur. With this problem, only a portion of the chains may achieve the conformation corresponding to the ideal crystal. Furthermore, once a portion of disordered molecules are trapped between the crystalline regions, it is very difficult for the molecules to undergo required conformational rearrangement to accomplish further deposition of a newly ordered structure on the surface of an existing crystallite. Detailed concepts of chain folding in polymer crystallization can be found in an excellent monograph by Keller [17].

2.2. Theories of Microscopic Kinetics of Polymer Crystallization

It is well established in crystallization of polymers from either solution or from melt that nucleation mechanisms play an important role. Nucleation mechanisms are divided roughly into two separate types: primary nucleation and secondary nucleation (i.e., subsequent crystal growth). Primary nucleation is defined as the origination of crystalline phase from the polymer solution or the melt. It can be categorized into two types dependent on the physical origins of the nucleus (i.e., chemical make-up of the nucleus when comparing with the crystallizing species): homogeneous nucleation and heterogeneous nucleation. Secondary nucleation is defined as a surface nucleation on an existing growth plane, which is responsible for further growth of the activated nucleus [29].

In the following paragraphs, the foundation of the concepts of both microscopic crystallization mechanisms (i.e., primary nucleation and the subsequent crystal growth) is briefly established.

2.2.1. Theories of Primary Nucleation

As mentioned previously, primary nucleation can be classified into two categories; homogeneous and heterogeneous nucleation, based on the chemical make-up

of the surface on which the critical nucleus is formed. Both types of nucleation mechanisms can be further categorized into either athermal [30] or thermal nucleation [31], depending whether or not the formation of nuclei in the polymeric bulk occurs simultaneously or throughout the crystallization process [29]. For general review in the subject of nucleation in polymers, interested readers are urged to consult excellent reviews by Price [32] and Wunderlich [29]. For advanced readers, a series of publications mainly by Ziabicki [33-37] offers a very thorough insight into the kinetics of various nucleation mechanisms using, however, rather complicated mathematical expressions.

2.2.1.1. Thermodynamics Consideration of Homogeneous Thermal Nucleation

Before going further into the discussion of thermodynamics consideration of the formation of homogeneous thermal nucleus in polymer crystallization, one ought to refer to the classical thermodynamic concept of nucleation given by Gibbs [38] for the crystallization, taking place without any volume constraint and without any compositional or chemical changes, of which the Gibbs free energy of the system is given by

$$\Delta G = G_{\text{crystal}} - G_{\text{melt}}, \quad (1-1a)$$

$$\Delta G = (H_{\text{crystal}} - H_{\text{melt}}) - T(S_{\text{crystal}} - S_{\text{melt}}^{\circ}), \quad (1-1b)$$

$$\Delta G = \Delta H - T\Delta S, \quad (1-1c)$$

where ΔG is the Gibbs free energy of crystallization, ΔH the enthalpy of crystallization, and ΔS the entropy of crystallization.

If crystallization ever followed Equation (1-1) strictly, the phase transformation would become possible as soon as ΔG becomes negative and homogeneous thermal nuclei would become evident throughout the bulk of the polymer melt as soon as the

temperature of the system has reached the *equilibrium melting temperature* T_m^0 at which point ΔG equals zero (i.e., at $\Delta G = 0$, $T_m^0 = \Delta H^0 / \Delta S^0$). On the contrary, crystallization of polymers from either the melt state or the concentrated solution always occurs at a finite temperature T_c lower than the theoretical melting temperature (i.e., T_m^0).

The reason for the undercooling can be explained based on the fact that crystallization can only occur after a stable nucleus is formed. In order for this to happen, the system has to overcome the energy barrier incurred by the difference of the chemical potential of the formed nucleus and that of the melt (i.e., the specific surface free energy). Thus, the Gibbs free energy of the system is given by [29]

$$\Delta G = \Delta G_c + \sum_i A_i \sigma_i, \quad (1-2)$$

where ΔG_c is the bulk Gibbs free energy of the phase transformation without the consideration of the surface effect, and A_i and σ_i the specific surface area and the corresponding specific surface free energy, respectively.

For better understanding of the thermodynamics of homogeneous thermal nucleation, let us consider a rectangular nucleus of thickness l containing v chains, each of which is separated from another by a distance a_0 in square array. It can hence be calculated that the volume of the nucleus is va_0^2l , the lateral surface area is $4la_0\sqrt{v}$, and the fold surface area is $2va_0^2$. Accordingly, the Gibbs free energy function can be mathematically shown as follows:

$$\Delta G = 4la_0\sqrt{v}\sigma + 2va_0^2\sigma_e - va_0^2l\Delta f, \quad (1-3)$$

where σ is the lateral surface free enthalpy per unit area, σ_e is the fold surface free energy per unit area, and Δf is the free enthalpy per unit volume of the crystal which also can be expressed as

$$\Delta f \approx \frac{\Delta H_f^0 \Delta T}{T_m^0}, \quad (1-4)$$

where ΔH_f^0 is the heat of fusion per unit volume at the equilibrium melting temperature T_m^0 and ΔT is the degree of supercooling. It is worth noting that the first two terms are inevitably positive and they can be counteracted by the third term when v , l and Δf are satisfactorily large enough.

The critical thickness of the nuclei l^* can be determined by differentiating Equation (1-3) with respect to the thickness and set the results equal to zero:

$$\frac{\partial \Delta G}{\partial a_0} = \frac{\partial \Delta G}{\partial l} = 0, \quad (1-5)$$

which results in

$$l^* = \frac{4\sigma_e}{\Delta f} \approx \frac{4\sigma_e T_m^0}{\Delta H_f^0 \Delta T}, \quad (1-6)$$

and
$$\Delta G^* = \frac{32\sigma^2\sigma_e}{(\Delta f)^2} \approx \frac{32\sigma^2\sigma_e (T_m^0)^2}{(\Delta H_f^0 \Delta T)^2}. \quad (1-7)$$

It is apparent from Equation (1-6) that the critical thickness l^* is proportional to the inverse of the undercooling. In other words, the critical thickness l^* increases monotonously with an increase in the temperature, and as the undercooling approaches zero (i.e., temperature approaches the theoretical melting temperature) the critical thickness l^* approaches an infinite value. Since it is well established in the literature [39-45] that local density fluctuations by way of conformational fluctuations of polymer segments are responsible for the formation of stable homogeneous nucleus (i.e., $l \geq l^*$), an induction time t_0 is necessary for the formation of stable crystals to occur at a given temperature.

Since, as mentioned previously, the critical thickness l^* is proportional to the inverse of the undercooling, as the temperature approaches the theoretical melting point the probability for the formation of stable nucleus decreases tremendously and approaches zero as temperature approaches the melting temperature; whereas, the

induction time t_0 required for the formation of stable nucleus increases and approaches an infinite value as the temperature approaches the melting temperature. It is not possible, however, to predict the induction time t_0 using the equilibrium theory.

2.2.1.2. Thermodynamics Consideration of Heterogeneous Nucleation

Thermodynamics consideration of heterogeneous nucleation was discussed extensively by Binsbergen [46-50], whose theoretical derivation is largely discussed in the following paragraphs. Let us again consider a polymeric nucleus of thickness l , of which width and layer thickness equal a_0 and b_0 , being nucleated on a preexisting flat heterogeneous surface. In this case, the Gibbs free energy of nucleation is given by

$$\Delta G = 2b_0l\sigma + 2a_0b_0\sigma_e + a_0l\Delta\sigma - a_0b_0\Delta f, \quad (1-8)$$

where $\Delta\sigma$ represents the difference in the interfacial free energy of the polymeric nucleus and that of the heterogeneous surface, while definitions of other quantities are the same as those mentioned previously.

By differentiation of Equation (1-8) with respect to the thickness and the stem dimensions and set the results equal to zero, one can determine quantities of the critical thickness and the critical Gibbs free energy:

$$\frac{\partial\Delta G}{\partial a_0} = \frac{\partial\Delta G}{\partial b_0} = \frac{\partial\Delta G}{\partial l} = 0, \quad (1-9)$$

which results in

$$l^* = \frac{4\sigma_e}{\Delta f} \approx \frac{4\sigma_e T_m^0}{\Delta H_f^0 \Delta T}, \quad (1-6)$$

and
$$\Delta G^* = \frac{16(\Delta\sigma)\sigma\sigma_e}{(\Delta f)^2} \approx \frac{16(\Delta\sigma)\sigma\sigma_e(T_m^0)^2}{(\Delta H_f^0 \Delta T)^2}. \quad (1-10)$$

Comparison made between the Gibbs free energy for the formation of homogeneous nucleus and that for the formation of the heterogeneous nucleus evidently

suggests that formation of heterogeneous nucleus is energetically more favorable than that of homogeneous counterpart. As a result, formation of heterogeneous nuclei of the same crystal thickness can occur at a much lower undercooling (i.e., higher temperature).

An important assumption made in the derivation of Equation (1-8) is that the heterogeneous surface is flat. In fact, heterogeneous nucleation on irregular or rough surfaces may be more energetically favorable than on flat surface. Indeed, the Gibbs free energy for the formation of heterogeneous nucleus on rough surfaces, which is given by [29]

$$\Delta G^* = \frac{8(\Delta\sigma)^2\sigma_c}{(\Delta f)^2} \approx \frac{8(\Delta\sigma)^2\sigma_c(T_m^0)^2}{(\Delta H_f^0\Delta T)^2}, \quad (1-11)$$

clearly agrees well with the aforementioned statement.

In Equations (1-10) and (1-11), it is assumed that the difference in the chemical potentials between the polymeric nucleus and the heterogeneous surface is large (i.e., $\Delta\sigma$ is large). However, as the heterogeneous surface becomes more efficient in nucleating the polymer nucleus (i.e., $\Delta\sigma$ gets smaller), the critical layer thickness of a nucleus approaches the molecular thickness, which further reduces the Gibbs free energy barrier for the formation of heterogeneous nucleus [29]:

$$\Delta G^* \approx \frac{4b_0\sigma\sigma_c T_m^0}{[\Delta H_f^0\Delta T - \frac{(\Delta\sigma)T_m^0}{b_0}]} \quad (1-12)$$

Interestingly, according to Equation (1-12), instead of being proportional to $(\Delta T)^{-2}$, the free enthalpy barrier for the formation of heterogeneous nucleus is now dependent on the inverse value of the undercooling.

A very special case which can be deduced from Equation (1-12) is when $\Delta\sigma$ equals zero. This can only happen when the chemical potential of the existing surface

and that of the nucleating (or crystallizing) polymeric species are identical, and this is in fact similar to the case of secondary nucleation (cf. Section 2.2.2) or to the case of homogeneous athermal nucleation (i.e., self-seeding nucleation).

2.2.1.3. Theory of the Nucleation Rate

The classical theory describing the temperature dependence of the rate of nucleation I was derived by Turnbull and Fisher [51], and it is given by

$$I = I_0 \exp\left(-\frac{\Delta G_\eta}{kT_c}\right) \exp\left(-\frac{\Delta G^*}{kT_c}\right), \quad (1-13)$$

where I_0 is a pre-exponential factor, k is the Boltzman constant, ΔG_η is the free energy barrier for the molecular transport across the phase boundary, and ΔG^* is the free energy barrier for the formation of a nucleus of critical size (cf. Equations (1-7), (1-10), (1-11), and (1-12)). In practice, the transport term, $\exp(-\Delta G_\eta/kT_c)$, is usually approximated by the William-Landel-Ferry (WLF) equation for viscous flow:

$$\exp\left(-\frac{\Delta G_\eta}{kT_c}\right) = \exp\left[-\frac{U^*}{R(T_c - T_\infty)}\right], \quad (1-14)$$

where U^* is the activation energy for the transportation of segments of molecules across the melt/solid surface boundary and T_∞ is the temperature where the molecular motion ceases (cf. Section 2.2.2.4). Consequently, Equation (1-13) can be re-written to be

$$I = I_0 \exp\left[-\frac{U^*}{R(T_c - T_\infty)}\right] \exp\left(-\frac{\Delta G^*}{kT_c}\right), \quad (1-15)$$

where ΔG^* may be one of the cases previously mentioned in Sections 2.2.1.1 and 2.2.1.2 (cf. Equations (1-7), (1-10), (1-11), and (1-12)).

Referring to Equation (1-15), the first exponential term, $\exp[-U^*/R(T_c - T_\infty)]$, corresponds to the diffusion of polymer molecules or segments of them across the phase boundary. The second exponential term, $\exp(-\Delta G^*/kT_c)$, relates to the formation of the

primary nucleus of the critical size. Obviously, this term relates directly to the primary nucleation rate I . Intuitively, from the competing contributions (i.e., $\exp[-U^*/R(T_c-T_\infty)]$ increases with increasing temperature, while $\exp(-\Delta G^*/kT_c)$ decreases) of the transport and primary nucleation terms, one expects that there should be a maximum in the nucleation rate data at a temperature somewhere between the glass transition temperature and the equilibrium melting temperature, when plotted as a function of the crystallization temperature. Indeed, maxima in the nucleation rate data (for various types of crystallizing materials) as a function of crystallization temperature are usually observed at $(0.3-0.7)T_m^0$ [52-55].

2.2.2. Theories of Secondary Nucleation

The polymer crystal growth or secondary nucleation kinetics theory introduced by Lauritzen and Hoffman [56-58] (i.e., the LH secondary nucleation theory) has been developed and revised repeatedly in subsequent publications essentially by Hoffman and his co-workers [59-64]. The theory suggests that polymers crystallize in three different regimes, as opposed to the classical theory of secondary nucleation in which the deposition of a single nucleus on a growth face is followed by a rapid lateral spreading process. The simplest way of understanding regime crystallization is to envisage the growth process as being composed of two different processes. The first is the deposition of the secondary nucleus on the growth face, while the second is the lateral spreading of polymer chains or segments of the chains across the growth face. Regime I is very similar to the notion of the classical theory in which the lateral spreading rate is much greater than that of the surface nucleation rate. Regime II is observed when the rates of the two processes are comparable, and Regime III occurs when the rate of secondary nucleation is greater than that of the lateral spreading.

The concepts leading to the LH secondary nucleation theory are summarized in detail in the following paragraphs, led by a discussion of the classical theory of secondary nucleation.

2.2.2.1. Traditional Approach on Observing the Lamellar Thickness

Experimentally, it is proven that secondary, rather than primary, nucleation plays an important role in the determination of lamellar thickness. Before development of the LH secondary nucleation theory, previous researchers had found out from the classical model, which is used to determine the lamellar thickness by primary nucleation process, that the Gibbs free enthalpy of formation is expressed as the following equation:

$$\Delta G = 2va_0^2\sigma_c + 2a_0l\sigma - va_0^2l\Delta f. \quad (1-16)$$

In Equation (1-6), the critical lamellar thickness was derived by differentiating Equation (1-3) according to the relationship in Equation (1-5). Hoffman et al. [59] suggested that the critical lamellar thickness derived in Equation (1-6) was obtained by assuming that v was very large. By proposing a different model, they also obtained the critical lamellar thickness by operating on Equation (1-16) with the relationship in Equation (1-5). This process gives

$$l^* = \frac{2\sigma_c}{\Delta f} \approx \frac{2\sigma_c T_m^0}{\Delta H_f^0 \Delta T}, \quad (1-17)$$

which is half the quantity obtained by the classical primary nucleation theory, and

$$\Delta G^* = \frac{4a_0\sigma\sigma_c}{\Delta f} \approx \frac{4a_0\sigma\sigma_c T_m^0}{\Delta H_f^0 \Delta T}, \quad (1-18)$$

which shows that the critical Gibbs free enthalpy function depends on $(\Delta T)^{-1}$ rather than with the $(\Delta T)^{-2}$ dependence acquired by the primary nucleation procedure. However, the lamellar thickness cannot equal to that specified by Equation (1-17), since once this is

substituted into melting point equation (usually referred to as the Gibbs-Thomson equation),

$$T_m = T_m^o \left(1 - \frac{2\sigma_e}{l\Delta H_f^o}\right), \quad (1-19)$$

the melting temperature becomes equal to the crystallization temperature, $T_m = T_c$. This means, at this particular lamellar thickness, the grown lamellae would melt at the same temperature. Consequently, the critical lamellar thickness has to be some number greater than the theoretical critical thickness. The actual critical lamellar thickness is thus given by

$$l^* = \frac{2\sigma_e}{\Delta f} + \delta l. \quad (1-20)$$

2.2.2.2. The Lauritzen-Hoffman Secondary Nucleation Theory

Lauritzen and Hoffman [56] was the first group who successfully determined the existence of δl on the presumption that the thickness of a folded chain is unchanged after the nucleation process has occurred. This approach is not aimed at studying the fluctuation in the lamellar thickness which leads to the roughness of the fold surface. It adopts the simple approximation of the adjacent reentry model proposed by Keller [16]; however, slight fluctuation in lamellar thickness may be allowed to occur (cf. Equation (1-20)) during isothermal growth.

2.2.2.2.1. Model Used in this Approach

Figure 1-1 shows the model used in the approach of Lauritzen and Hoffman [59] in which a_0 is the width of the molecular stem, b_0 is the thickness of a surface nucleus, l is the height of the nucleus which is kept stable at a particular crystallization temperature, and L is the total width of the crystal. Each stem is laid down along the g direction; whereas, the overall growth is in the G direction. With disregard of the chain ends'

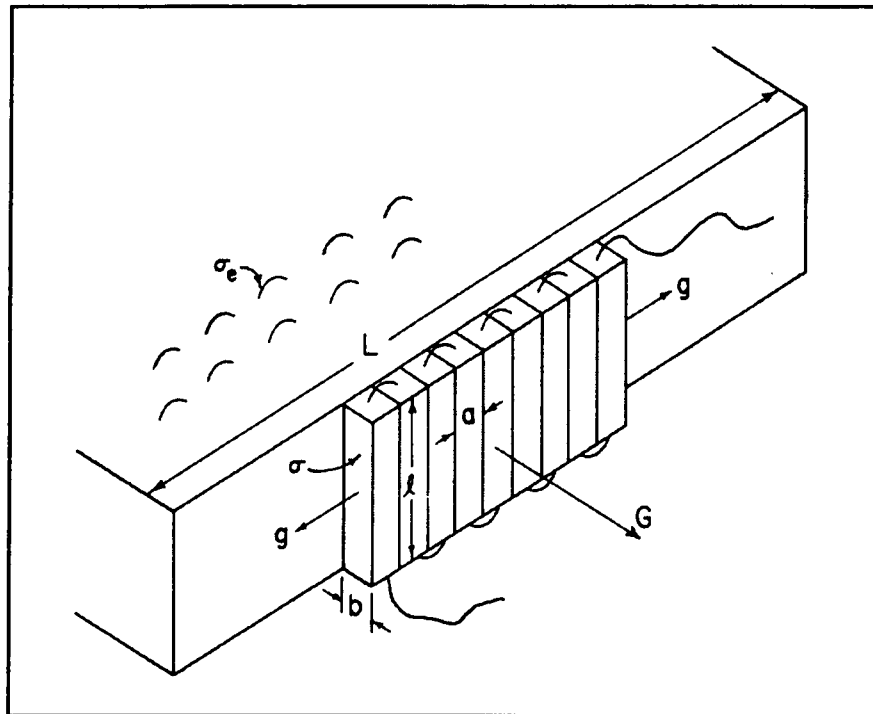


Figure 1-1. Schematic diagram of the model used in the derivation of the Lauritzen-Hoffman secondary nucleation kinetics theory.

effect, when v stems with $v_f = v - 1$ are formed, the Gibb's free enthalpy of formation can then be mathematically expressed as

$$\Delta G_v = 2b_0l\sigma + 2v_f a_0 b_0 \sigma_c - v a_0 b_0 l \Delta f, \quad (1-21)$$

and, for large quantity of v , Equation (1-21) becomes

$$\Delta G_v = 2b_0l\sigma + v a_0 b_0 (2\sigma_c - l\Delta f). \quad (1-22)$$

It is believed that the surface nucleus begins from a polymer segment or a set of segments, which may arise from the supercooled melt or from the solution, and attaches itself to the crystal substrate in order to form the first stem at the cost of $2b_0l\sigma$. The folding back on itself of the molecule then later occurs and crystallization in an adjacent manner to the first stem begins. The adjacent reentry model enters this mechanism since, if present, non-adjacent reentry will cost an extra free energy term $2b_0l\sigma$ in addition to the term $2a_0b_0\sigma_c$, which involves both adjacent and non-adjacent reentry mechanisms. A surface nucleus can be obtained by repeating that mechanism which grows in g direction. However, not only a single molecule may involve in the process, but other molecules can participate to complete the surface strip in order to obtain the substrate length L . Since there are many molecules involved in the completion step, it is very likely for their chain ends dangling out of the surface strip and this causes loose chain ends or cilia to exist.

At $v = 1$ or in the vicinity of $v = 1$, the maximum in free energy of formation of a molecular surface nucleus can be obtained. However, after the subsequential folding occurs, the free energy of formation will gradually reduce and approach the region of stability. Consequently, we can treat the case where a set of connected rate processes can be conceived to be a combination of the rates of forward and backward reactions between the states $v = 0$ and $v = 1$, namely A_0 and B_1 , and where all the subsequent forward and backward reactions are given by A and B as can be schematically shown in

Figure 1-2. The occupation numbers N_0, N_1, N_2, \dots will be employed here for $v = 0, 1, 2, \dots$. In general, this approach is referred to a nucleation-controlled process where the formation of a new growth surface must overcome a large energy barrier of the formation of the first stem or nucleus with the succeeding steps leading to the stable region.

2.2.2.2. Calculation of the Total Flux

In order to find a general steady-state expression for the flux S over the barrier to nucleation in terms of A_0, B_1, A and B and the occupation numbers N_0, N_1, \dots . The net flux of polymer from sites in liquid phase ($v = 0$) to the first step stem of polymer in the nucleus ($v = 1$) of a new layer of polymer crystal is defined as

$$S = N_0 A_0 - N_1 B_1. \quad (1-23)$$

In the formation of the first stem, two new surfaces will be created with the total cost in surface free energy of $2b_0 l \sigma$, less the free energy of fusion accounted for the elementary volume of $a_0 b_0 l$. In fact, the free energy of fusion is allotted by a fraction coefficient ψ to the activation free energy of the forward reaction, and the remainder to the backward reaction. Thus, the rate coefficients of the first step element can be expressed as

$$A_0 = \beta \exp \left\{ - \left(\frac{2b_0 l \sigma}{kT_c} \right) + \left[\frac{\psi a_0 b_0 l (\Delta f)}{kT_c} \right] \right\}, \quad (1-24)$$

$$B_1 = \beta \exp \left[- \frac{(1 - \psi) a_0 b_0 l (\Delta f)}{kT_c} \right], \quad (1-25)$$

where β is the retardation factor which accounts for the retardations to the molecular motion such as viscosity, surface transport, and so on.

In the formation of subsequent stems, no new lateral surface is involved, but each step does incur the cost in the free energy of creating a fold which is $2a_0 b_0 \sigma_e$, less the

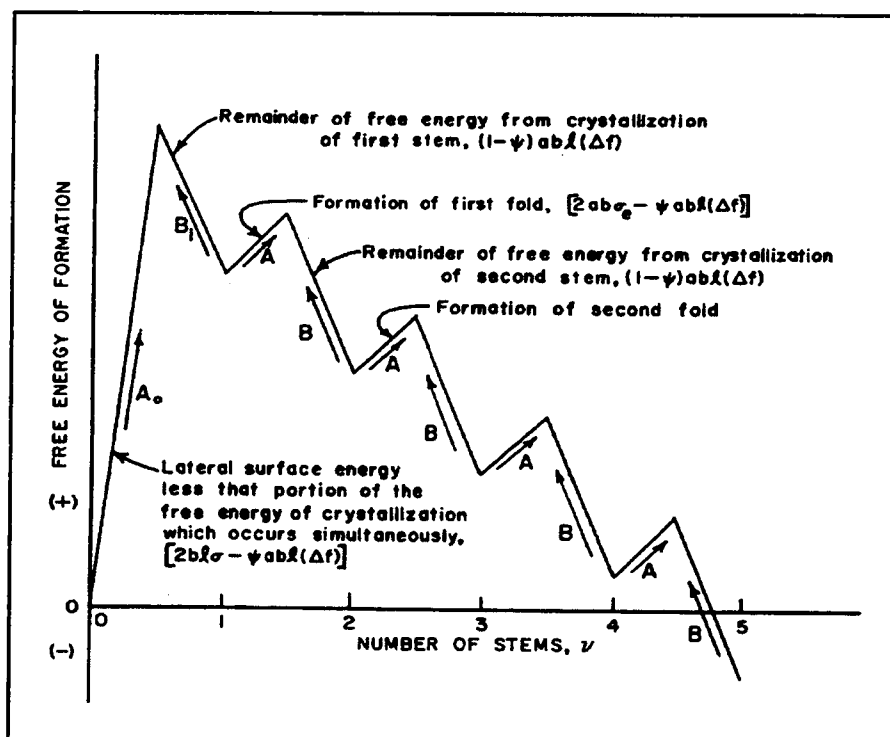


Figure 1-2. Conceptual diagram illustrating the free energy of formation of a chain-folded nucleus on an existing growth surface.

free energy of fusion. The acquisition of the rate constants are similar to the previous consideration; thus,

$$A = \beta \exp \left\{ -\left(\frac{2a_0 b_0 \sigma_c}{kT_c} \right) + \left[\frac{\psi a_0 b_0 l (\Delta f)}{kT_c} \right] \right\}, \quad (1-26)$$

$$B = \beta \exp \left[-\frac{(1-\psi) a_0 b_0 l (\Delta f)}{kT_c} \right]. \quad (1-27)$$

With the assumption that the portion of the free energy of fusion in the backward reaction rate being equal for all steps, the net rate of formation of nuclei of length l hence is

$$S(l) = \beta N_0 \exp \left\{ \frac{[-2b_0 l \sigma + \psi a_0 b_0 l (\Delta f)]}{kT_c} \right\} \times \left(1 - \exp \left\{ \frac{[-a_0 b_0 l (\Delta f) + 2a_0 b_0 \sigma_c]}{kT_c} \right\} \right). \quad (1-28)$$

The total flux S_T can be obtained by summing the flux terms of all possible values of l . It is assumed that possible values of l are increments of the monomer repeat length l_u , the summation can then be replaced by the integral

$$S_T = \left(\frac{1}{l_u} \right) \int_{\frac{2\sigma_c}{\Delta f}}^{\infty} S(l) dl, \quad (1-29a)$$

$$S_T = N_0 \left(\frac{\beta}{l_u} \right) P \exp \left(\frac{2a_0 b_0 \sigma_c \psi}{kT_c} \right) \exp \left[-\frac{4b_0 \sigma \sigma_c}{kT_c (\Delta f)} \right], \quad (1-29b)$$

where the lower limit of the integration accounts for the minimum possible thickness of crystal, and where

$$P = \frac{kT_c}{2b_0 \sigma - a_0 b_0 (\Delta f) \psi} - \frac{kT_c}{2b_0 \sigma + (1-\psi) a_0 b_0 (\Delta f)}. \quad (1-30)$$

The factor P is in cm, β is in *events* per second, and l_u is in cm, and S_T is consequently in *events*.

2.2.2.2.3. Initial Lamellar Thickness

The initial lamellar thickness l_g^* , which is actually the average value of l denoted by $\langle l \rangle_{avg}$, is calculated from the flux relating to

$$l_g^* = \frac{\left(\frac{1}{l_u}\right) \int_{\frac{2\sigma_c}{\Delta f}}^{\infty} l S(l) dl}{\left(\frac{1}{l_u}\right) \int_{\frac{2\sigma_c}{\Delta f}}^{\infty} S(l) dl}, \quad (1-31)$$

and the result of this average is found to be

$$l_g^* = \frac{2\sigma_c}{\Delta f} + \frac{kT_c}{2b_0\sigma} \cdot \frac{2 + \frac{(1-2\psi)a_0(\Delta f)}{2\sigma}}{\left[1 - \frac{a_0(\Delta f)\psi}{2\sigma}\right] \left[1 + \frac{a_0(\Delta f)(1-\psi)}{2\sigma}\right]}. \quad (1-32)$$

It is very obvious that the last term seems to be a function of ψ , which can be concisely termed to be δl . Though it is of interest to investigate the behavior of the total flux and the initial lamellar thickness for various ψ , it is clear that if $\psi = 1$, the last part of Equation (1-32) reduces to

$$\delta l = \frac{kT}{2b_0\sigma} \cdot \frac{\left(\frac{4\sigma}{a_0}\right) - \Delta f}{\left(\frac{2\sigma}{a_0}\right) - \Delta f}. \quad (1-33)$$

According to the denominator of Equation (1-33) and the fact that $\Delta f \equiv (\Delta H_f^0)(\Delta T)/T_m^0$ (i.e., Equation (1-4)), it is found that δl becomes infinite at the critical undercooling temperature;

$$\Delta T_c = \frac{2\sigma T_m^0}{(\Delta H_f^0)a_0}, \quad (1-34)$$

which is referred to as the δl catastrophe.

On the other hand, if $\psi = 0$, the last part of Equation (1-32) reduces to be

$$\delta l = \frac{kT_c}{2b_0\sigma} \cdot \frac{\left(\frac{4\sigma}{a_0}\right) + \Delta f}{\left(\frac{2\sigma}{a_0}\right) + \Delta f}. \quad (1-35)$$

This case is meaningfully interpreted that no δl catastrophe is being observed, and l_g^* falls continuously with decreasing temperature.

Physically, the significant change of the setting parameter ψ may be related to whether or not the polymer molecule is being absorbed on the surface prior to the actual crystallographic attachment being occurred. Here, when $\psi = 0$, the physical adsorption prior to the crystallization of a molecule, which attaches to a substrate face with zero momentum to that surface, occurs before the required crystallographic conformation of the chain does. This process would create the surface energy term $2bl\sigma$ before the compensating free energy of crystallization is released. On the contrary, when $\psi = 1$, the polymer molecule conforms itself directly from the melt onto the surface without prior adsorption of the molecule.

However, the theory as presented above accounts for only infinite long molecules; thus, no extreme cases, where $\psi = 0$ and $\psi = 1$, will be obtained. This is due to the fact that the nature of polymeric molecules are polydispersed and comprise finite chain lengths. Consequently, the condition, where $0 < \psi < 1$, is more likely to be found in real polymers.

2.2.2.2.4. Retardation Factor

As said earlier, the retardation factor β accounts for retardations to molecular motion, which result from the fact that molecules must transport from the undercooled melt to deposit on a substrate site. These retardations may arise from viscosity and surface transport, and the factor itself bears the unit of "events" per second. In real

polymeric systems, polymers can often be undercooled more than 100°C at which temperatures they become very viscous such that the retardations denoted by β plays an important role. In bulk polymeric systems, the jump rate to local motions can be expressed as the retardation function, which can be written as

$$\beta = \left(\frac{kT_c}{h}\right) J_1 \exp\left[-\frac{U^*}{R(T_c - T_\infty)}\right]. \quad (1-36)$$

The term $\exp[-U^*/R(T_c - T_\infty)]$ can be thought of as representing the temperature dependence of the segmental jump rate in polymeric molecules. In bulk polymers, the temperature T_∞ is obtained from experiments regarding viscosity of the bulk, at which all motion associated with viscous flow ceases, and T_∞ is related to the glass transition temperature T_g . The quantity U^* generally lies itself in the range 10-15% of 4,100 cal·mol⁻¹ (i.e., $U^* = 1,500$ cal·mol⁻¹ for iPS [65]) and T_∞ is always within about 5-10 K of being 50 K below T_g (i.e., $T_\infty = T_g - 30$ K for iPS [65]).

In the bulk polymer, the fluidity of the polymer can be governed by the temperature dependence of the jump rate, which is characterized by the exponential term, $\exp[-U^*/R(T_c - T_\infty)]$. In addition, the absolute value of the fluidity also depends on an extra term, which is molecular weight dependence term expressed by $M^{-3.4}$. It is nevertheless true that the jump rate term is not strongly dependent on the molecular weight. However, it is also the fact that the values of U^* and T_∞ applied to the crystallization process need not be exactly similar to those applied to bulk fluidity. It might be due to the fact that the values of U^* and T_∞ applicable to the crystallization process probably refer to motions near or in the proximity of a physical adsorbed layer of molecules deposited on the surface of the crystals.

The factor J_1 inserted in Equation (1-36) accounts for any explicit barriers which are not included in the exponential term and also dependent on temperature.

Compared to $\exp[-U^*/R(T_c - T_\infty)]$, the temperature dependence of J_1 is extremely small; hence, J_1 is commonly acting as a preexponential factor in the retardation function β .

2.2.2.3. Theory of the Linear Growth Rate

In the previous sections, it might be expected that the kinetics of the growth rate exhibits a temperature dependence similar to the rate of nucleation of new layers at the crystal edge, i.e. the total flux. In order to understand the whole process of crystallization theory, one needs only to relate the previous approach to the manner of completion of the layer to acquire the rate of advance by the molecular thickness. There have been three practical cases being proposed so far, namely regimes I, II, and III, which are shown in Figure 1-3.

2.2.2.3.1. Regime I Growth

Regime I growth is the case such that the rate of completion of a layer is so rapid that the nucleation rate of a new stem can not occur before completion of the first layer. The kinetics of the overall growth rate can be conceived to be nucleation controlled. Kinetically, a layer of thickness b_0 will advance at a speed;

$$G_1 = b_0 i L = \frac{b_0 S_T n_s}{N^o} = \frac{b_0 L S_T}{a_0 N^o}, \quad (1-37)$$

where i is the net surface nucleation rate, N^o is the Avogadro number and n_s is the number of sites or step elements corresponding to the length of the substrate, i.e., $n_s = L/a_0$. Substitution of Equations (1-29), (1-30), and (1-36) into Equation (1-37) leads to

$$G_1 = G_{1,0} \exp\left[-\frac{U^*}{R(T_c - T_\infty)}\right] \exp\left[-\frac{4b_0 \sigma \sigma_c}{kT_c (\Delta f)}\right], \quad (1-38)$$

for the polymeric bulk. The preexponential factor $G_{1,0}$ arises from the combination of factors not strongly dependent on temperature, which is expressed as

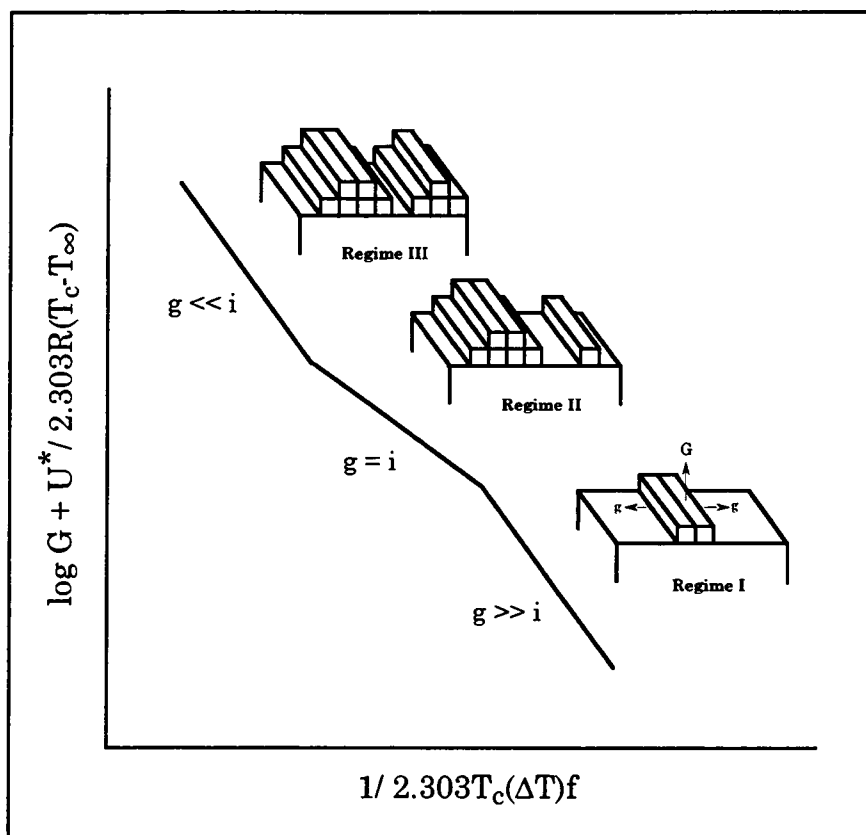


Figure 1-3. Schematic diagram illustrating mechanisms of linear growth rate data in Regimes I, II, and III, and corresponding appearance when performing a Lauritzen-Hoffman plot on the linear growth rate data.

$$G_{1,0} = b_0 \left(\frac{kT_c}{h} \right) n_s J_1 \exp\left(\frac{2a_0 b_0 \sigma_c \psi}{kT_c} \right). \quad (1-39)$$

In order to derive Equation (1-39), the parameter P was set equally to l_u for the bulk polymer. The factor J_1 might be 10^2 - 10^4 , and the exponential term varies from unity to 10^3 at its maximum. The factor $b_0(kT/h)$ is expected to be ca. 10^5 . As a result, the preexponential factor $G_{1,0}$ for regime I type crystallization should lie within several orders of magnitude of $10^4 n_s \text{ cm}\cdot\text{sec}^{-1}$ for bulk polymeric systems.

2.2.2.3.2. Regime II Growth

Regime II growth is the case for which the formation rate of nuclei on the substrate at a rate i is comparable to the spreading rate of the lateral growing step at a velocity g . Sanchez and DiMarzio [66] and Frank [67] showed independently that the linear growth rate of this regime is proportional to the square root of the surface nucleation rate, i.e., $(ig)^{1/2}$. The surface nucleation term i can be expressed as $i = S_T/N^o a_0$ bearing unit of $\text{cm}^{-1}\cdot\text{sec}^{-1}$, while g is in the unit of $\text{cm}\cdot\text{sec}^{-1}$. Then the linear growth rate of regime II can be expressed as

$$G_{II} = b_0 (ig)^{0.5} = b_0 \left(\frac{S_T g}{a_0 N^o} \right)^{0.5}. \quad (1-40)$$

Insertion of Equations (1-29), (1-30), and (1-36) into Equation (1-40) leads to the expression:

$$G_{II} = G_{II,0} \exp\left[-\frac{U^*}{R(T_c - T_\infty)} \right] \exp\left[-\frac{2b_0 \sigma \sigma_c}{kT_c (\Delta f)} \right], \quad (1-41)$$

where

$$G_{II,0} = b_0 \left(\frac{kT_c}{h} \right) J_1 \exp\left[\frac{a_0 b_0 \sigma_c (2\psi - 1)}{kT_c} \right], \quad (1-42)$$

where the parameter P is again set equal to l_u .

Seeing that from Equation (1-41) comparing to Equation (1-38) the regime II growth rate differs from the relevant expression for regime I by a factor of one-half in

the nucleation exponent. Also the ratio of the pre-exponential factors of regime I to regime II becomes

$$\frac{G_{I,0}}{G_{II,0}} = n_s \exp\left(\frac{a_0 b_0 \sigma_c}{kT_c}\right), \quad (1-43)$$

where results that $G_{I,0} \gg G_{II,0}$ for a given polymeric system.

2.2.2.3.3. Regime III Growth

First proposed by Phillips [68] and later being formulated by Hoffman [61], regime III growth can be conceived to be the reciprocal case to the regime I growth, where the rate of secondary nucleation is far faster than the completion rate of the layer. The rate of deposition of the secondary nucleus is so rapid that nuclei are formed on partly grown strips. This causes the growth rate to be proportional to the nucleation rate as for regime I. The growth rate for regime III can be formulated as

$$G_{III} = b_0 i L' = b_0 i n_s a_0 = \frac{b_0 L S_T}{a_0 N^o}, \quad (1-44)$$

where L' is the effective substrate length, and n_s is the average number of stems that are laid down in the niche adjacent to the newly created stem.

Substitution of Equations (1-29), (1-30), and (1-36) into Equation (1-44) leads to

$$G_{III} = G_{III,0} \exp\left[-\frac{U^*}{R(T_c - T_\infty)}\right] \exp\left[-\frac{4b_0 \sigma_c \psi}{kT_c(\Delta f)}\right], \quad (1-45)$$

where

$$G_{III,0} = b_0 \left(\frac{kT_c}{h}\right) n_s' J_1 \exp\left(\frac{2a_0 b_0 \sigma_c \psi}{kT_c}\right). \quad (1-46)$$

It is obvious that the ratio of Equation (1-39) to Equation (1-46) is

$$\frac{G_{I,0}}{G_{III,0}} = \frac{n_s}{n_s'} \equiv \frac{n_s}{3}. \quad (1-47)$$

2.2.2.3.4. Test of Regime

From the resemblance of the Equations (1-38), (1-41), and (1-45), a general expression of the three regimes can be presented as

$$G = G_0 \exp\left[-\frac{U^*}{R(T_c - T_\infty)}\right] \exp\left[-\frac{K_g}{T_c(\Delta T)f}\right], \quad (1-48)$$

where G_0 is a pre-exponential term which is not strongly dependent on temperature; K_g is the nucleation exponent and is defined as

$$K_g = \frac{j b_0 \sigma \sigma_e T_m^0}{k \Delta H_f^0}, \quad (1-49)$$

where j equals 2 for regime II and 4 for regimes I and III; and f is a factor used to correct for the temperature dependence of the heat of fusion and is given by [65]

$$f = \frac{2T_c}{(T_m^0 - T_c)}, \quad (1-50)$$

where, if the degree of undercooling is very small, i.e., the crystallization temperature is close to the thermodynamic melting point, f approaches unity. It is otherwise lower than unity and decreasing as the degree of undercooling increases.

Referring to Equation (1-48), the first exponential term, $\exp(-U^*/R(T_c - T_\infty))$, corresponds to the diffusion of polymer molecules or segments of them from the equilibrium melt onto the growth face. The second exponential term, $\exp(-K_g/T_c(\Delta T)f)$, relates to the formation of the critical nucleus on the growth face. Obviously, this term relates directly to the secondary nucleation rate i . Intuitively, from the competing contributions of the transport and nucleation terms, one expects that there should be a maximum in the growth rate data at a temperature somewhere between the glass transition temperature and the equilibrium melting temperature, when plotted as a function of the crystallization temperature. Indeed, maxima in the growth rate data as a function of crystallization temperature are usually observed at $(0.7-0.9)T_m^0$ [52-55].

As mentioned earlier, in each regime the linear growth rate G relates directly to the secondary nucleation rate i : $G \propto i^n$, where n equals 1 in regimes I and III, and 0.5 in regime II. Since the second exponential term in Equation (1-48) corresponds directly to the secondary nucleation rate, observation of the relationship between G and i can be examined by rearranging the logarithmic product of Equation (1-48), which results in the equation:

$$\log G + \frac{U^*}{2.303R(T_c - T_\infty)} = \log G_0 - \frac{K_g}{2.303T_c(\Delta T)f}. \quad (1-51)$$

In practice, the test of regimes can be done through the plot of $\log G + U^*/2.303R(T_c - T_\infty)$ versus $1/2.303T_c(\Delta T)f$ (i.e., hereafter the LH plot). This type of plot factors out the contribution of the transport term to the growth rate, and the slope equals the negative value of the nucleation exponent (i.e., slope = $-K_g$). According to Equation (1-51), regime I→II transition is evident when a downward change in slope is observed, whereas it is an upward change in slope that is observed in the transition from regime II to regime III.

In order to observe the distinction between regimes I and II, Lauritzen and Hoffman [58] has successfully shown that the parameter governing the differentiation between these two regimes is a dimensionless number presented as

$$Z = \frac{iL^2}{4g}. \quad (1-52)$$

It can be estimated from Equations (1-48) and (1-52) that observation of the ratio of the secondary nucleation and the spreading rate i/g can be done under certain limits from the experimental value of K_g obtained by analyzing data on a polymer. It is hence

$$Z = \frac{iL^2}{4g} \approx 10^3 \left(\frac{L}{2a_0} \right)^2 \exp\left[-\frac{X}{T_c(\Delta T)} \right], \quad (1-53)$$

where $X = K_g$ for test of regime I, $Z \leq 0.01$,

$X = 2K_g$ for test of regime II, $Z \geq 1$.

This criterion can be used to estimate the range of L values which are in accordance with regime I or regime II behavior. It can be done by analyzing the growth rate data to determine K_g . It is then from Equation (1-53) with the known value of K_g , the range of L values can be acquired. In general, such estimates give reasonable values of L for only one regime and totally unreliable values for the other; accordingly, a clear choice between the two regimes can be made. In real polymeric systems, the effective length L of a lamellae is believed to be controlled by a number of factors, which include impingements, noncrystallographic branching frequency, and accumulations of noncrystallizable impurities.

2.2.3. Theories of the Maximum Nucleation and Growth Rates

By using very slightly different forms of nucleation rate and growth rate functions:

$$I = I_0 \exp\left(-\frac{\Delta E}{RT_c}\right) \exp\left[-\frac{K_1(T_m^o)^2}{RT_c(\Delta T)^2}\right], \quad (1-54)$$

$$G = G_0 \exp\left(-\frac{\Delta E}{RT_c}\right) \exp\left[-\frac{K_2 T_m^o}{RT_c(\Delta T)}\right], \quad (1-55)$$

where ΔE relates to the activation energy for segmental transport across the interfacial boundary, K_1 and K_2 relates directly to the primary and secondary nucleation exponents defined previously, and other quantities are similar to previous definitions, Okui [52-55] was able to develop simplified equations to determine the temperatures, $T_{c,\max}^I$ and $T_{c,\max}^G$ where the nucleation rate and the growth rate exhibit the maxima, respectively.

For the maximum in the nucleation rate function,

$$\frac{T_{c,\max}^I}{T_m^o} = \frac{D^2 - D + 1}{D^2 + D + 1}, \quad (1-56)$$

where $D = \left(\frac{B+1}{B-1}\right)^{1/3}, \quad (1-57)$

$$B = \left(1 + \frac{K_1}{\Delta E}\right)^{1/2}. \quad (1-58)$$

For the maximum in the growth rate function,

$$\frac{T_{c,\max}^G}{T_m^o} = \frac{C}{C+1}, \quad (1-59)$$

where
$$C = \left(1 + \frac{\Delta E}{K_2}\right)^{1/2}. \quad (1-60)$$

By determining the K_1 and K_2 values from the primary nucleation rate and the growth rate data, the temperatures, $T_{c,\max}^I$ and $T_{c,\max}^G$, where the primary nucleation rate and the growth rate exhibit the maxima can be evaluated.

2.3. Theories of Macroscopic Kinetics of Polymer Crystallization

2.3.1. Kinetics of Isothermal Macroscopic Crystallization

Overall crystallization process in semi-crystalline polymers can be divided into two main processes: primary crystallization and secondary crystallization. Primary crystallization process is a macroscopic development of crystallinity as a result of two consecutive microscopic mechanisms: primary nucleation and subsequent crystal growth (i.e., secondary nucleation). Secondary crystallization process is mainly concerned with the crystallization of interfibrillar melt, which was rejected and trapped between the fibrillar structure formed during the growth of crystalline aggregates (e.g., axialites, spherulites, etc.) [69-71]. It should be noted that if the crystallization time becomes very long, other types of secondary crystallization (i.e., crystal perfection and crystal thickening) may become significant enough to increase the ultimate absolute crystallinity.

For the purpose of describing the macroscopic evolution of crystallinity under quiescent isothermal condition, a number of mathematical models [72-81] have been

proposed, based primarily on the notion of primary nucleation and subsequent crystal growth microscopic mechanisms, over the past sixty years. Even though the contributions from Kolmogoroff [72], Johnson and Mehl [73], Avrami [74-76], and Evans [77] are essentially similar, it is the work of Avrami that has received the most attention. Thereby, these contributions are frequently referred to as the *Avrami equation*. Derived based on different approaches, Tobin [78-80] and Malkin et al. [81] arrived at different mathematical models, which are also different from the Avrami model. Conclusively, the quiescent crystallization data of semi-crystalline polymers at a constant temperature can be mathematically described by these three distinctive models.

2.3.1.1. Avrami Macrokinetic Model

The overall crystallization kinetics is usually analyzed by use of the Avrami equation [72-77]. When applied to be used with a differential scanning calorimetry (DSC), it is assumed that the differential area under the crystallization curve with time corresponds to the dynamic changes in the conversion of mass from the melt phase to the solid phase. If χ_∞ and χ_t are the absolute crystallinity obtained at a particular crystallization condition and the dynamic crystallinity at arbitrary time t at the same crystallization condition, respectively, then the governing equation describing steady-state isothermal phase transformation (i.e., *Avrami equation*) can be written as

$$\frac{\chi_t}{\chi_\infty} = \theta(t) = 1 - \exp(-k_a t^{n_a}), \quad (1-61a)$$

where $\theta(t)$ denotes the relative crystallinity as a function of time, k_a the Avrami crystallization rate constant, and n_a the Avrami exponent of time. Both k_a and n_a are constants typical of a given crystalline morphology, and type of nucleation at a particular crystallization condition (cf. Table 1-1). It should be noted that, according to

Table 1-1. Phenomenal description of the Avrami exponent n_a (after reference [18]).

Type of crystallization	Type of nucleation	Avrami exponent, n_a
<i>A. linear Problem:</i>		
line	athermal	1
line	thermal	2
<i>B. two-dimensional problem:</i>		
ribbon	athermal	≤ 1
ribbon	thermal	≤ 2
circular	athermal	2
circular	thermal	3
circular, diffusion control	athermal	1
circular, diffusion control	thermal	2
circular	thermal, exhaustion	3 \rightarrow 2
<i>C. Three-dimensional problem:</i>		
fibrillar	athermal	≤ 1
fibrillar	thermal	≤ 2
circular lamellar	athermal	≤ 2
circular lamellar	thermal	≤ 3
spherical	athermal	3
spherical	thermal	4
spherical, diffusion control	athermal	3/2
spherical, diffusion control	thermal	5/2
spherical	thermal, exhaustion	4 \rightarrow 3
two-stage	athermal/thermal	fractional
branching fibrillar	athermal/thermal	1, 2 \rightarrow large
solid sheaf-like	athermal	≥ 5
solid sheaf-like	thermal	≥ 6
truncated spherical	athermal	2-3
truncated spherical	thermal	3-4

the original assumptions of the theory, the value of n_a should be integral, ranging from 1 to 4.

More generally, Equation (1-61a) can be written in two different forms, involving parameters characteristic of the nucleation and crystal growth microscopic mechanisms:

$$\theta(t) = 1 - \exp(-C_n N_0 G^n t^n), \quad (1-61b)$$

$$\theta(t) = 1 - \exp\left(-\frac{C_n}{n+1} I G^n t^{n+1}\right), \quad (1-61c)$$

where C_n is the shape factor, and N_0 is the number of predetermined nuclei (i.e., heterogeneous and, possibly, athermal nuclei) at the beginning of the crystallization process. It should be noted that Equation (1-61b) represents the isothermal phase transformation equation for the case of time-independent or instantaneous nucleation, whereas it is the case of time-dependent or sporadic nucleation for Equation (1-61c).

2.3.1.2. Tobin Macrokinetic Model

An important remark that has been made on the Avrami model is that the equation is only appropriate for the early stages of crystallization. In order to improve the Avrami model, Tobin [78-80] proposed a different expression describing phase transformation kinetics with growth site impingement. The original theory was written in a form of nonlinear Volterra integral equation, of which zeroth-order solution is given by

$$\theta(t) = \frac{k_t t^{n_t}}{1 + k_t t^{n_t}}, \quad (1-62)$$

where $\theta(t)$ is the relative crystallinity as a function of time, k_t the Tobin crystallization rate constant and n_t the Tobin exponent. Based on this proposition, the Tobin exponent of time n_t needs not be integral [79,80] and it is governed directly by different types of nucleation and growth mechanisms. It is worth noting that similar expression was first

considered by Rabesiaka and Kovacs [82] and it was found to give a good fit to their dilatometric data of linear PE for $\theta(t)$ up to 0.9.

2.3.1.3. Malkin Macrokinetic Model

Malkin et al. [81] developed a macrokinetic crystallization model based on the notions that crystallization is an autocatalytic process and that the overall crystallization rate equals the summation of the rate at which the degree of crystallinity varies as a result of emergence of the primary nuclei and the rate of variation in the degree of crystallinity as a result of crystal growth. The crystal growth is assumed to be proportional to the existing crystal surface, while the crystal surface is assumed to be a linear function of crystallinity. In crystallization under isothermal conditions, these approximations led to the following equation:

$$\theta(t) = 1 - \frac{C_0 + 1}{C_0 + \exp(C_1 t)} \quad (1-63)$$

where $\theta(t)$ is the relative crystallinity as a function of time. C_0 relates directly to the ratio of the linear growth rate G to the nucleation rate I (i.e., $C_0 \propto G/I$); whereas, C_1 relates directly to the overall crystallization rate (i.e., $C_1 = a \cdot I + b \cdot G$, where a and b are specific combined constants). Apparently, both C_0 and C_1 are temperature-dependent constants.

2.3.1.4. Analysis of the Experimental Data

Analysis of the experimental data based on the Avrami and the Tobin approaches are straight forward. The Avrami kinetics parameters, k_a and n_a , can be extracted from the least-square line fitted to the double logarithmic plot of $\ln[-\ln(1-\theta(t))]$ versus $\ln(t)$, where k_a is taken as the anti-logarithmic value of the y-intercept and n_a is simply the slope of the least-square line. Similarly, the Tobin crystallization kinetics parameters, k_t and n_t , can be extracted by drawing a least-square line fitted to the double

logarithmic plot of $\ln[\theta(t)/(1-\theta(t))]$ versus $\ln(t)$, where k_i is taken as the anti-logarithmic value of the y-intercept and n_i is simply the slope. It should be noted that, in both cases, the kinetics parameters will be calculated from the least-square line drawn through the bulk of the data in the range of $0.10 < \theta(t) < 0.80$. In the case of the Malkin approach, the authors proposed a short-cut method of determining their kinetics parameters, C_0 and C_1 , from those obtained from the Avrami analysis [81]:

$$C_0 = 4^{n_a} - 4, \quad (1-64)$$

$$C_1 = \ln(4^{n_a} - 2) \left(\frac{k_a}{\ln(2)} \right)^{1/n_a}. \quad (1-65)$$

2.3.1.5. Other Macrokinetics Models

2.3.1.5.1. Simultaneous Avrami Macrokinetic Model

One of the serious discrepancies which has been raised to question the applicability of the Avrami model is that, in most cases, the analysis of the experimental data based on the Avrami equation leads to fractional values of the Avrami exponent n_a . The non-integral observations of the Avrami exponent n_a may be explained as follows:

- 1) The discrepancies in the assumptions used in the derivation of the model;
- 2) Inaccuracy in the determination of the onset of the crystallization process (if the onset is set prematurely, the value of the Avrami exponent n_a will be greater than the actual value, while that of the rate constant k_a will be lesser);
- 3) Changes in the nucleation rate I and growth rate G during crystallization process (if the values decrease, the value of the Avrami exponent n_a will also decrease);
- 4) Changes in the morphology during crystallization process (i.e., sheaf-like to spherulitic). This may also include the occurrence of the secondary

crystallization in which internal changes in the crystal morphology are experimentally observed [69-71].

In addition to the above explanations, the fractional value of the Avrami exponent n_a may also be elucidated based on the hypothesis that crystalline aggregates grow concurrently from both instantaneous and sporadic nuclei (as opposed to growing from only one type of nuclei, assumed in the original theory), as previously mentioned elsewhere in this manuscript. Indeed, observation made on an optical microscope confirms that at a certain crystallization temperature a certain number of nuclei is activated instantaneously, while others are activated sporadically. Based on this experimental observation, the original Avrami equation can be modified to account for both types of transient nucleation. The modified equation is called the *simultaneous Avrami model*, which can be written as

$$\theta(t) = 1 - \exp(-k_{ai}t^n - k_{as}t^{n+1}), \quad (1-66a)$$

or in a more general equation as

$$\theta(t) = 1 - \exp(-C_n N_0 G^n t^n - \frac{C_n}{n+1} I G^n t^{n+1}), \quad (1-66b)$$

where $\theta(t)$ denotes the relative crystallinity as a function of time, and n the morphological dimensionality which ranges from 1 to 3 (i.e., rod, disc, and sphere). k_{ai} and k_{as} are the crystallization rate constants specific for instantaneous and sporadic nucleation, respectively (cf. Table 1-2). C_n and N_0 are the shape factor and the number of predetermined nuclei, respectively. It should be noted that a similar equation was first used to explain the fractional values of the Avrami exponent n_a by Banks et al. [83], but they concluded then that the equation was not satisfactory in accounting for the occurrence of the fractional values of n_a .

Table 1-2. Mathematical description of the Avrami isothermal crystallization rate constant k_a for different types of morphology and transient nucleation.

Crystal morphology	Morphological dimensionality, n	Instantaneous nucleation, k_{ai} (min^{-n})	Isothermal crystallization rate constant ^{a)} Sporadic nucleation, k_{as} ($\text{min}^{-(n+1)}$)
Rod	1	N_0GA	$1/2 \cdot IGA$
Disc	2	πN_0G^2D	$\pi/3 \cdot IG^2D$
Sphere	3	$4\pi/3 \cdot N_0G^3$	$\pi/3 \cdot IG^3$

a) A is constant area, D is the disc thickness, G is the linear crystal growth rate, N_0 is the concentration of predetermined nuclei, and I is the nucleation rate.

2.3.1.5.2. Ding-Spruiell Macrokinetic Model

Recently, Ding and Spruiell [84] have derived a generalized model for phase transformation in which the linear growth rate G and the nucleation rate I are considered to be arbitrary functions of time. Since it is found that their model may be a good explanation to various limitations to the traditional Avrami model, i.e., especially the experimentally observed fractional values of the Avrami exponent n_a , their mathematical derivation is briefly followed here. For simplicity, they imposed the following assumptions: 1) iso-volumetric approximation, 2) spherulitic morphology, 3) no impingement, and 4) no secondary crystallization within the already transformed spherulites.

If r is the radius of a transformed spherulite, v_{sp} is the volume of a spherulite, V_{sp} is the total volume transformed (into spherulites), V_a is the total volume untransformed, and the total volume of the sample is $V = V_{sp} + V_a$, the volume of a spherulite which was nucleated at arbitrary time τ and was measured at time t is

$$v_{sp}(t, \tau) = \int_{\tau}^t 4\pi \cdot \left(\int_{\tau}^{t'} G dt'' \right)^2 \cdot G \cdot dt', \quad (1-67)$$

and therefore the total transformed volume at time t which nucleated during the time interval $d\tau$ can be calculated as

$$dV_{sp} = v_{sp}(t, \tau) \cdot I \cdot V_a \cdot d\tau, \quad (1-68)$$

where I is the nucleation rate which has a unit of number of nuclei per unit volume untransformed materials per unit time.

By substituting Equation (1-67) into Equation (1-68), dividing the result with the total volume, and defining θ as the volume fraction of the transformed phase with respect to the total volume (i.e., $\theta = V_{sp}/V$), one arrives at

$$\left(\frac{1}{1-\theta}\right)d\theta = \left[\int_{\tau}^t 4\pi \cdot \left(\int_{\tau}^t G dt' \right)^2 \cdot G dt'' \right] \cdot I \cdot d\tau. \quad (1-69)$$

By integrating Equation (1-69) with respect to time, the total transformed volume (into spherulites) over the course of crystallization process can now be calculated, and it is given by

$$\ln\left(\frac{1}{1-\theta}\right) = \int_0^t \left[\int_{\tau}^t 4\pi \cdot \left(\int_{\tau}^t G dt' \right)^2 \cdot G dt'' \right] \cdot I \cdot d\tau. \quad (1-70)$$

In crystallization of polymers under isothermal conditions, the growth rate G is found to be constant, and this would further simplify Equation (1-70) to be

$$\ln\left(\frac{1}{1-\theta}\right) = \frac{4\pi}{3} G^3 \int_0^t (t-\tau)^3 \cdot I \cdot d\tau. \quad (1-71)$$

Equation (1-71) can be generalized to describe phase transformation of other morphological geometries (e.g., rod or disc) by using the traditional definition of the geometrical dimensionality concept (e.g., $n = 1$ for rod, $n = 2$ for disc, and $n = 3$ for sphere), thus Equation (1-71) transforms to

$$\ln\left(\frac{1}{1-\theta}\right) = C_n G^n \int_0^t (t-\tau)^n \cdot I \cdot d\tau, \quad (1-72)$$

where C_n is the shape factor (e.g., $C_2 = \pi$ and $C_3 = 4\pi/3$).

In order to further simplify Equation (1-72), Ding and Spruiell [84] brilliantly introduced a *nucleation rate function* to quantify the nucleation rate I as a function of time throughout the course of crystallization process. Intuitively, the nucleation rate function $I(t)$ is directly proportional to the availability of the untransformed volume, and it is given by

$$I(t) = I_c \cdot (1+m) \cdot t^m, \quad (1-73)$$

where I_c is defined as the *nucleation rate constant* [# of nuclei/(sec ^{$m+1$} ·cm³)] and it is a function of temperature but time independent, and m is defined as the *nucleation index*.

By substituting Equation (1-73) into Equation (1-72) and defining a B -function as

$$B(m+2, n) = \int_0^1 q^{m+2-1} \cdot (1-q)^{n-1} \cdot dq, \quad (1-74)$$

Equation (1-72) reduces to assume the following form:

$$\ln\left(\frac{1}{1-\theta}\right) = nC_n I_c G^n B(m+2, n) t^{n+m+1}. \quad (1-75)$$

By comparing Equation (1-75) with the logarithmic form of Equation (1-61), which is

$$\ln\left(\frac{1}{1-\theta}\right) = k_a t^{n_a}, \quad (1-76)$$

one is able to conclude that the Avrami crystallization rate k_a and the Avrami exponent n_a are given by

$$k_a = nC_n I_c G^n B(m+2, n), \quad (1-77)$$

$$n_a = n + m + 1. \quad (1-78)$$

Interestingly, in the cases where m equals 0 and -1 , Equation (1-75) reduces to the special cases of crystallization under sporadic nucleation and instantaneous nucleation [84], respectively.

According to Equation (1-78), the traditional sense of the Avrami exponent n_a to describe the dimensionality of the crystal geometry can be satisfied with the geometry or dimensionality index n , but, more importantly, abnormality in the observation of the Avrami exponent n_a (i.e., fractional values of n_a or values of n_a more than 4) can be now theoretically explainable by the introduction of the nucleation index m . Even though the nature of the nucleation index m is not entirely understood at the present time, Ding and Spruiell [84] were able to qualitatively characterize the nucleation index m in describing the nucleation mechanism throughout the crystallization process (cf. Table 1-3). It is worth noting that the iso-volumetric approximation can be alleviated by multiplying a

Table 1-3. Qualitative characteristic of the nucleation index m .

	Nucleation mechanism	Nature of the nucleation rate over crystallization time
$m = -1$	instantaneous	constant
$-1 < m < 0$	instantaneous and sporadic	gradually decreasing with time and approaching a constant value at a certain time
$m = 0$	sporadic	steadily increasing with time
$0 < m < 1$	sporadic	increasing with time
$m > 1$	sporadic	increasing strongly with time

density factor ρ_c/ρ_a (where ρ_c is the density of the crystalline portion and ρ_a is that of the amorphous portion) to the expectancy term.

2.3.1.5.3. Traditional Ziabicki Macrokinetic Model

Instead of describing the crystallization process with complicated mathematical models, Ziabicki [85-87] proposed that phase transformation kinetics can also be described by a first-order kinetic equation:

$$\frac{d\theta(t)}{dt} = K(T)[1 - \theta(t)], \quad (1-79)$$

where $\theta(t)$ is the relative crystallization as a function of time and $K(T)$ is a crystallization rate function which is only dependent on temperature. In the case of isothermal crystallization, function $K(T)$ can be replaced by the half-time of crystallization as a function of temperature (i.e., $K(T) = t_{0.5}^{-1}(T)$).

Based on Equation (1-79), Ziabicki [85-87] showed that the temperature dependence of the crystallization half-times can be described by a Gaussian function of the form:

$$t_{0.5}^{-1} = (t_{0.5})_{\min}^{-1} \exp\left[-4 \ln 2 \frac{(T_c - T_{\max})^2}{D^2}\right], \quad (1-80)$$

where T_{\max} is the temperature where the crystallization rate exhibits the maximum, $(t_{0.5})_{\min}$ the crystallization half-time at T_{\max} , and D the half-width of the crystallization rate (the reciprocal value of the crystallization half-time) curve. With use of the isokinetic approximation (i.e., the kinetics of primary nucleation and that of crystal growth are similar such that the ratio of crystal growth rate G to nucleation rate I is constant throughout the course of crystallization), integration of Equation (1-80) over the whole range of temperatures in which crystallization may occur ($T_g < T < T_m^0$) leads to an

important characteristic value describing the crystallization ability of the polymer, namely the kinetic crystallizability K^z :

$$\int_{T_c}^{T_c''} t_{0.5}^{-1}(T) dT \approx \frac{1.064D}{(t_{0.5})_{\min}} = K^z. \quad (1-81)$$

2.3.1.6. Temperature Dependence of the Crystallization Rate Parameters

The crystallization rate parameters (i.e., $t_{0.5}^{-1}$, k_a , C_1 , k_{ai} , or k_{as}) determined from limited experimental isothermal measurements can be used to estimate the corresponding values at other temperatures. The estimation can be carried out by virtue of the following facts:

- 1) The crystallization rate parameters determined based on different macrokinetic models exhibit a finite temperature dependence;
- 2) The crystallization rate parameters relate in one way or another to the crystal growth rate G and/or the nucleation rate I , especially the crystallization rate parameters of the Avrami and simultaneous Avrami models (cf. Table 1-2);
- 3) Since the temperature dependence of the crystal growth rate G and the nucleation rate I are well defined (cf. Equations (1-15) and (1-48)), the crystallization rate parameters should also have the similar temperature dependence, which can be written as

$$\Psi(T) = \Psi_0 \exp\left\{-\frac{\Theta}{R[T_c - (T_g - C_2)]} - \frac{K}{T_c(\Delta T)^f}\right\}, \quad (1-82)$$

where $\Psi(T)$ and Ψ_0 are the corresponding crystallization rate function (i.e., $t_{0.5}^{-1}$, k_a , C_1 , k_{ai} , or k_{as}) and the corresponding pre-exponential parameter (i.e., $(t_{0.5}^{-1})_0$, k_{a0} , C_{10} , k_{ai0} , or k_{as0}), respectively. Θ is a parameter related to the activation energy characterizing the molecular diffusion across the

melt/crystal interface, K is a parameter related to the secondary nucleation, while other parameters are the same as previously noted.

The temperature-dependent crystallization rate function $\Psi(T)$ can now be determined by directly fitting the experimentally measured values of the corresponding rate parameters collected at various crystallization temperatures to Equation (1-82).

2.3.2. Kinetics of Non-isothermal Macroscopic Crystallization

A number of mathematical models describing the evolution of the crystallinity under non-isothermal conditions have been proposed by way of modifying or extending in one way or another the existing isothermal macrokinetic models. Summary of some of the models is described in the following few paragraphs.

2.3.2.1. Generalized Avrami Macrokinetic Models

It is well discussed in the work by Patel and Spruiell [88] that the evolution of the crystallinity under non-isothermal conditions can be directly calculated using the generalized Avrami equation (cf. Equation (1-70)), in which case the knowledge of detailed mechanisms of nucleation and crystal growth over the course of crystallization process as a function of temperature for a particular cooling condition are indispensable. This has proven to be very tedious and time-consuming, therefore attempts have been made in order to modify the generalized Avrami equation to more practicable models which can be used to either directly fit the experimental data or to predict the evolution of the crystallinity at constant cooling rates from data taken from isothermal measurements.

The most commonly cited model is the one developed by Nakamura et al. [89,90]. They have generalized the Avrami macrokinetic model by adopting the

isokinetic approximation and assuming that the ultimate crystallinity is independent of the cooling process. This led to the following equation:

$$\theta(t) = 1 - \exp\left[-\left(\int_0^t K_n(T) dt\right)^{n_a}\right], \quad (1-83)$$

where the Nakamura rate function $K_n(T)$ relates to the Avrami rate function $k_a(T)$ or the crystallization half-time $t_{0.5}^{-1}(T)$ through the following equation:

$$K_n(T) = \sqrt[n_a]{k_a(T)} = \sqrt[n_a]{\ln 2} \cdot t_{0.5}^{-1}(T). \quad (1-84)$$

By using temperature as an independent variable, Equation (1-83) becomes

$$\theta(T, \phi) = 1 - \exp\left[-\left(\frac{1}{\phi} \int_{T_0}^T K_n(T) dT\right)^{n_a}\right], \quad (1-85)$$

where ϕ is the constant cooling rate, and T_0 is an arbitrary initial temperature (e.g. T_m°).

Usage of Equation (1-85) is twofold. First, it can be used to predict the evolution of crystallinity as a function of temperature when the average Avrami exponent n_a and the Avrami crystallization rate function $k_a(T)$ (from isothermal measurements) are known [88,91,92]. Second, it can also be used to estimate the Avrami kinetics parameters by directly fitting the experimental non-isothermal crystallization measurements to the equation using non-linear regression methods [93].

A slightly different form of mathematical model was derived by Kamal and Chu [94] based on the assumptions that non-isothermal crystallization may be treated as a sequence of isothermal crystallization steps [85] and that the secondary crystallization is negligible. This led to the equation of the form:

$$\theta(t) = 1 - \exp\left[-\int_0^t k_a(T) n_a t^{n_a-1} dt\right]. \quad (1-86)$$

By using temperature as an independent variable, Equation (1-86) becomes

$$\theta(T, \phi) = 1 - \exp\left[-\frac{1}{\phi} \int_{T_0}^T k_a(T) n_a \left(\frac{T_0 - T}{\phi}\right)^{n_a-1} dT\right], \quad (1-87)$$

where ϕ is the constant cooling rate, and T_0 is an arbitrary initial temperature (e.g. T_m°). Application of Equation (1-87) is similar to that of Equation (1-85).

Based on the mathematical derivation of Evans [77], Ozawa [95] extended the Avrami model to be able to describe the non-isothermal case. Mathematically, the relative crystallinity can be written as a function of cooling rate according to the following equation:

$$\theta(T, \phi) = 1 - \exp\left[-\frac{k_o(T)}{\phi^{n_o}}\right], \quad (1-88)$$

where $k_o(T)$ is the Ozawa crystallization rate function and n_o is the Ozawa exponent (which is similar to the Avrami exponent). Direct comparison of Equation (1-88) to Equation (1-85) and (1-87) suggests that the Ozawa rate function $k_o(T)$ may assume one of the following forms:

$$k_o(T) = \left(\int_{T_0}^T K_n(T) dT\right)^{n_o} = \left(\int_{T_0}^T \sqrt[n_o]{k_o(T)} dT\right)^{n_o}, \quad (1-89a)$$

$$k_o(T) = \int_{T_0}^T [k_o(T) n_o (T_0 - T)^{n_o - 1}] dT. \quad (1-89b)$$

Analysis based on Equation (1-88) can be performed through a double logarithmic plot of $\ln[-\ln(1-\theta(T))]$ versus $\ln(\phi)$ for a fixed temperature, of which the negative value of the slope yields the Ozawa exponent n_o . Practically, Ozawa model offers very limited use. It may only serve as a means of obtaining the Ozawa exponent (or Avrami exponent) from non-isothermal measurements, similar to some other proposed methods [96-98].

Patel and Spruiell [88] suggested that the differential form of the Nakamura model may be more useful in modelling of polymer processing than its integral form. The differential form of the Nakamura model is given by

$$\frac{d\theta}{dt} = n_o K(T) (1-\theta) [-\ln(1-\theta)]^{(n_o-1)/n_o}. \quad (1-90)$$

The integral and the differential Nakamura model are identical in terms of their predictions; however, it is precautionary that the differential equation requires a non-zero initial crystallinity condition for $n_a > 1$ [88]. In addition, according to their results on Nylon 6, Patel and Spruiell [88] found that Nakamura model (i.e., Equation (1-85)) gave a better fit to the experimental measurements than the Kamal model (i.e., Equation (1-87)).

2.3.2.2. Malkin Macrokinetic Model

Malkin et al. [81] developed a macrokinetic crystallization model based on the notions that crystallization is an autocatalytic process and that the overall crystallization rate equals the summation of the rate at which the degree of crystallinity varies as a result of emergence of the primary nuclei and the rate of variation in the degree of crystallinity as a result of crystal growth. The crystal growth is assumed to be proportional to the existing crystal surface, while the crystal surface is assumed to be a linear function of crystallinity. In crystallization under isothermal conditions, these approximations led to Equation (1-63). However, in crystallization under non-isothermal conditions, the generalized form is more practical and it can be written as [81,99]

$$\frac{d\theta}{dt} = K_m(1-\theta)(1+C_0\theta), \quad (1-91)$$

where K_m is a temperature-dependent constant related to the primary nucleation mechanism (i.e., $K_m \propto I$), and C_0 is also a temperature-dependent constant related directed to the ratio of the linear growth rate G to the nucleation rate I (i.e., $C_0 \propto G/I$).

Using Equations (1-54) and (1-55) as the platforms, temperature-dependences of the parameters K_m and C_0 may be formulated as

$$K_m = K_{m0} \exp\left(-\frac{\Delta E}{RT_c}\right) \exp\left[-\frac{K_1(T_m^0)^2}{RT_c(\Delta T)^2}\right], \quad (1-92a)$$

$$C_0 = C_{00} \exp\left[\frac{K_1(T_m^0)^2}{RT_c(\Delta T)^2} - \frac{K_2 T_m^0}{RT_c(\Delta T)}\right]. \quad (1-93a)$$

Instead of using the above equations which are supposed to be the most theoretically correct forms, Malkin et al. [99] formulated the temperature-dependences of the parameters K_m and C_0 to be

$$K_m = K_{m0} \exp\left(-\frac{\Delta E}{RT_c}\right) \exp\left[-\frac{K_1 T_m^0}{RT_c(\Delta T)}\right], \quad (1-92b)$$

$$C_0 = C_{00} \exp\left[-\frac{(K_2 - K_1) T_m^0}{RT_c(\Delta T)}\right]. \quad (1-93b)$$

Equation (1-91) along with Equations (1-92) and (1-93) can be used with proper energy equation to predict the evolution of crystallinity in the actual polymer processing [99].

2.3.2.3. Traditional Ziabicki Macrokinetic Model

Instead of describing the crystallization process with complicated mathematical models, Ziabicki [85-87] proposed that phase transformation kinetics can also be described by a first-order kinetic equation (i.e., Equation (1-79)), of which its integral form is given by

$$\theta(t) = 1 - \exp\left[-\int_0^t K(T) dt\right], \quad (1-94)$$

where $\theta(t)$ is the relative crystallization as a function of time and $K(T)$ is a crystallization rate function which is only dependent on temperature. By using temperature as an independent variable, Equation (1-94) becomes

$$\theta(T, \phi) = 1 - \exp\left[-\frac{1}{\phi} \int_{T_0}^T K(T) dT\right], \quad (1-95)$$

where ϕ is the constant cooling rate, and T_0 is an arbitrary initial temperature (e.g. T_m^0).

In the case of non-isothermal crystallization, functions $K(T)$ and $\theta(t)$ vary and are dependent on cooling rates studied. For a given cooling condition, Ziabicki [85-87] showed that the crystallization rate function $K(T)$ can be described by a Gaussian function of the form:

$$K(T) = K_{\max} \exp\left[-4 \ln 2 \frac{(T_c - T_{\max})^2}{D^2}\right], \quad (1-96)$$

where T_{\max} is the temperature where the crystallization rate is the maximum, K_{\max} the crystallization rate at T_{\max} and D the half-width of the crystallization rate-temperature function. With use of the isokinetic approximation, integration of Equation (1-96) over the whole range of temperatures, for a given cooling condition, in which crystallization may occur ($T_g < T < T_m^0$) leads to the kinetic crystallizability K^z parameter (cf. Equation (1-81)):

$$\int_{T_g}^{T_m^0} K(T) dT \approx 1.064 \cdot K_{\max} \cdot D = K^z. \quad (1-97)$$

In the case of non-isothermal crystallization studies in DSC where cooling rate is a variable, Equation (1-97) can be applied by replacing the crystallization rate function $K(T)$ with a derivative function of the relative crystallinity $\dot{\theta}_\phi(T)$ specific for each cooling rate studied (i.e., crystallization rate function at different cooling rate). Therefore, Equation (1-97) is re-written to be

$$\int_{T_g}^{T_m^0} \dot{\theta}_\phi(T) dT \approx 1.064 \cdot \dot{\theta}_{\max, \phi} \cdot D_\phi = K_\phi^z, \quad (1-98)$$

where $\dot{\theta}_{\max, \phi}$ and D_ϕ are the maximum crystallization rate and the half-width observed on corresponding derivative function $\dot{\theta}_\phi(T)$. According to Equation (1-98), K_ϕ^z is the kinetic crystallizability at an arbitrary cooling rate ϕ , the kinetic crystallizability at *unit*

cooling rate K^z can therefore be obtained by normalizing K^z_ϕ with ϕ (i.e., $K^z = K^z_\phi / \phi$). It should be noted that this procedure was first realized by Jeziorny [100].

2.3.2.4. Generalized Ziabicki Macrokinetic Model

Very recently, Ziabicki [101] developed a new macrokinetic model describing polymer crystallization kinetics in variable external conditions. The proposed model concerns not only the changes in temperature as a function of time, but also changes of other external variables, e.g., pressure, stress, and etc., as a function of time. The model emphasizes the effects of transient and athermal nucleation on the overall crystallization process which are found to be a strong function of the rate of change in the external conditions, instead of resting on the quasi-static approximation utilized in earlier non-isothermal macrokinetic models [85,86,89,90,94,95].

In his later paper, Ziabicki [102] applied the more general equations [101] to the case of non-isothermal crystallization of unstressed and unoriented polymers. In this case, the crystallization rate involving transient and athermal effects is only a function of temperature T and constant cooling rate ϕ . The model has been preliminarily applied to the cases of poly(ethylene terephthalate) (PET), isotactic polypropylene (iPP) [102,103], and more extensively to the case of poly(vinylidene fluoride) (PVDF) [103,104]. In the few following paragraphs, theory designated for crystallization of polymers under influence of changes in temperature [102-104] is briefly reviewed.

The Ziabicki macrokinetic model was developed based on the Avrami equation of phase transformation (i.e., Equation (1-61)) [72-77]. Instead of using the volume fraction of crystallinity:

$$\frac{\chi(t)}{\chi_\infty} = \theta(t) \in (0,1), \quad (1-99)$$

Ziabicki [101,102] brilliantly introduced a non-linear measure of crystallinity:

$$P(t) = [-\ln(1 - \theta(t))]^{1/n_a} \in (0, \infty), \quad (1-100)$$

where n_a is the Avrami exponent.

Differentiation of the non-linear measure of crystallinity $P(t)$ with respect to time t yields the non-linear crystallization rate:

$$\kappa(t) = \frac{dP(t)}{dt}, \quad (1-101)$$

which, in pure steady-state isothermal conditions, reduces to steady-state crystallization rate constant κ_{st} which relates directly to the Avrami rate constant k_a and to the reciprocal half-time $t_{0.5}^{-1}$:

$$\kappa_{st} = (k_a)^{1/n_a} = \sqrt[n_a]{\ln 2} \cdot t_{0.5}^{-1}. \quad (1-102)$$

According to Ziabicki's theory [101,102], in crystallization of polymers under non-isothermal conditions, the non-linear crystallization rate $\kappa(t)$ is assumed to take into account transient and athermal mechanisms, rather than only one in pure isothermal conditions. First, progress of crystallization is assumed to lag behind changes in external conditions which give rise to retardation of crystallization. This retardation of crystallization is caused by relaxation effects, which directly affect the crystallization mechanism mainly controlled by thermal nucleation. Secondly, athermal effects, which is proportional to the rate of change of external conditions, become dominant with increasing rate of change of external conditions, as sub-critical nuclei can become stable under the new conditions.

By assuming that athermal effects are only included in primary nucleation but not in secondary nucleation (i.e., homogeneous surface nucleation), the total non-linear crystallization rate $\kappa(t)$ is given by [101,102]

$$\kappa(t) = \kappa_{th}(t) + \kappa_{ath}(t) = \kappa_{th} \left[1 + \frac{I_{ath}}{I_{th}} \right]^{1/n_a} = \kappa_{th} [1 - B_{ath} \dot{T}]^{1/n_a}, \quad (1-103)$$

where I_{th} and I_{ath} are thermal and athermal nucleation rate, respectively, and B_{ath} is the athermal function.

It was shown by Ziabicki and Sajkiewicz [103] for the case of constant rate of change of temperature (i.e., constant cooling or heating rates \dot{T}) that thermal crystallization rate $\kappa_{th}(t, T(t))$ can be expanded in series and is given by

$$\kappa_{th}(t, T(t)) = \kappa_{st}(T(t)) [1 + A_1 \dot{T} + A_2 \dot{T}^2 + A_3 \dot{T}^3 + \dots], \quad (1-104)$$

where
$$A_1 = -\tau \left(\frac{\partial \ln \kappa_{st}}{\partial T} \right), \quad (1-104a)$$

$$A_2 = \tau^2 \left[\frac{1}{\kappa_{st}} \left(\frac{\partial^2 \kappa_{st}}{\partial T^2} \right) + \left(\frac{\partial \ln \kappa_{st}}{\partial T} \right) \left(\frac{\partial \ln \tau}{\partial T} \right) \right], \quad (1-104b)$$

and
$$A_3 = -\tau^3 \left\{ \frac{1}{\kappa_{st}} \left(\frac{\partial^3 \kappa_{st}}{\partial T^3} \right) + \frac{3}{\kappa_{st}} \left(\frac{\partial^2 \kappa_{st}}{\partial T^2} \right) \left(\frac{\partial \ln \tau}{\partial T} \right) + \left(\frac{\partial \ln \kappa_{st}}{\partial T} \right) \left[\left(\frac{\partial^2 \ln \tau}{\partial T^2} \right) + 2 \left(\frac{\partial \ln \tau}{\partial T} \right)^2 \right] \right\}. \quad (1-104c)$$

Evidently, the thermal crystallization rate $\kappa_{th}(t, T(t))$ is composed of the steady-state crystallization rate κ_{st} which is modified by the relaxation effects characterized by the relaxation parameter τ . Sajkiewicz [104] pointed out that the rate of non-isothermal crystallization can either be increased or decreased by the relaxation effect depending on the actual temperature. In the case of constant cooling (i.e., $\dot{T} < 0 = \phi$), the total crystallization rate is reduced by the relaxation effects for temperatures above the temperature of the maximum steady-state crystallization rate (i.e., $\partial \ln \kappa_{st} / \partial T < 0$). However, when the temperature is lower than the temperature of the maximum steady-state crystallization rate (i.e., $\partial \ln \kappa_{st} / \partial T > 0$), total crystallization rate during the constant cooling is expected to increase.

Ziabicki and Sajkiewicz [103] also showed that the athermal correction term can be written in a series expansion of the form:

$$[1 - B_{\text{ath}} \dot{T}]^{1/n_a} = 1 + B_1 \dot{T} + B_2 \dot{T}^2 + B_3 \dot{T}^3 + \dots, \quad (1-105)$$

where
$$B_1 = -\frac{B_{\text{ath}}}{n_a}, \quad (1-105a)$$

$$B_2 = \frac{(1 - n_a) B_{\text{ath}}^2}{n_a^2}, \quad (1-105b)$$

and
$$B_3 = \frac{(1 - n_a)(1 - 2n_a) B_{\text{ath}}^3}{n_a^3}. \quad (1-105c)$$

Substitution of Equations (1-104) and (1-105) into Equation (1-103) leads to the equation describing the non-linear crystallization rate $\kappa_{\text{th}}(t, T(t))$ as a function of the constant rate of changes of temperature:

$$\kappa(t, T(t)) = \kappa_{\text{st}} [1 + (A_1 + B_1) \dot{T} + (A_2 + B_2 + A_1 B_1) \dot{T}^2 + \dots]. \quad (1-106)$$

Due to the constancy of the rate of changes of temperature (i.e., conditions of constant cooling or heating rates), Equation (1-106) is integratable over the whole temperature range. According to Equations (1-100), (1-101) and (1-106), the complete non-linear measure of crystallinity $P(t)$ can therefore be written as

$$P(T(t)) = \frac{1}{\dot{T}} \int_{T(0)}^{T(t)} \kappa_{\text{st}}(T') [1 + (A_1(T') + B_1(T')) \dot{T} + (A_2(T') + B_2(T') + A_1(T') B_1(T')) \dot{T}^2 + \dots] dT'. \quad (1-107)$$

For simplicity in the experimental analysis, Equation (1-107) can be rearranged to the following form:

$$P(T(t)) \dot{T} = \int_{T(0)}^{T(t)} \kappa_{\text{st}}(T') dT' + \dot{T} \int_{T(0)}^{T(t)} (A_1(T') + B_1(T')) \kappa_{\text{st}}(T') dT' + \dots \quad (1-108a)$$

In the case of cooling at a constant rate from the melt (i.e., $\dot{T} = -|\dot{T}|$), the initial temperature $T(0)$ is any temperature higher than the final temperature $T(t)$. Therefore, Equation (1-108a) can be written as

$$-P(T(t)) \cdot |\dot{T}| = - \int_{T(t)}^{T(0)} \kappa_{st}(T') dT' + |\dot{T}| \int_{T(t)}^{T(0)} (A_1(T') + B_1(T')) \kappa_{st}(T') dT' + \dots \quad (1-108b)$$

Note that the choice of $T(0)$ is unimportant as long as it is located beyond the melting temperature of the polymer of interest (i.e., T_m^0).

According to Equation (1-108b), it is apparent that experimental non-isothermal measurements can be carried out through the plot of $-P \cdot |\dot{T}|$ versus $-|\dot{T}|$, of which the y-intercept and the initial slope are given by

$$\lim_{\dot{T} \rightarrow 0} (-P \cdot |\dot{T}|) = \int_{T(t)}^{T(0)} \kappa_{st}(T') dT', \quad (1-109)$$

and

$$\lim_{\dot{T} \rightarrow 0} \frac{d(-P \cdot |\dot{T}|)}{d(-|\dot{T}|)} = - \int_{T(t)}^{T(0)} (A_1(T') + B_1(T')) \kappa_{st}(T') dT', \quad (1-110)$$

respectively. According to Equation (1-109), the steady-state crystallization rate function $\kappa_{st}(T)$ is given by

$$\kappa_{st}(T) = - \frac{d}{dT} \left[\lim_{\dot{T} \rightarrow 0} (-P \cdot |\dot{T}|) \right]. \quad (1-111)$$

In addition, the term which is controlled by the transient and athermal effects can be evaluated from Equation (1-110) and is given by

$$A_1(T) + B_1(T) = \frac{1}{\kappa_{st}(T)} \frac{d}{dT} \left[\lim_{\dot{T} \rightarrow 0} \frac{d(-P \cdot |\dot{T}|)}{d(-|\dot{T}|)} \right]. \quad (1-112)$$

2.4. Methods for the Determination of Equilibrium Melting Temperature

Equilibrium melting temperature T_m^0 is one of the most important parameters in the study of polymer crystallization, especially in the study of microscopic kinetics of polymer crystallization (cf. Section 2.2). Since, by the definition (i.e., the melting temperature of fully extended crystals consisting of molecules of infinite molar mass), the equilibrium melting temperature T_m^0 is rather a theoretical parameter which

characterizes the driving force (i.e., the degree of undercooling ΔT) for crystallization of polymers at conditions deviated from the equilibrium condition, it cannot be measured directly. Due to its importance in the study of polymer crystallization, some methods for the determination of the equilibrium melting temperature T_m^0 are briefly reviewed.

2.4.1. Flory-Vrij Extrapolation Method

In this method, the melting temperatures for a series of low molecular mass homologs of the polymer in question are measured. According to the definition of the equilibrium melting temperature, crystals of these homologs have to grow until they are in equilibrium conditions (i.e., fully extended crystals). Extrapolation of the melting temperatures of these homologs to the infinite molar mass yields the equilibrium melting temperature T_m^0 [105]. Experimentally, the extrapolation can be done through the plot of the melting temperatures versus the inverse values of the molar mass of these homologs, whereas the T_m^0 value is taken as the y-intercept (i.e., at $1/M = 0$). The most obvious polymer system, to which this method can be applied, is high density polyethylene (HDPE), of which its T_m^0 value is determined from the extrapolation of a series of the melting temperatures of *n*-paraffins [106]. Detailed discussion on the determination of the T_m^0 value of HDPE in terms of both experimental and theoretical points of view can be found in a superb work by Kim [107].

2.4.2. Gibbs-Thomson Extrapolation Method

Even though it is theoretically postulated that, at equilibrium, crystallization of polymers would result in crystals of infinite thickness, experimental observation not only proves that crystallization can only occur at some temperatures lower than the equilibrium melting temperature, but also it proves that, often time, crystallization of polymers results in crystals of finite thickness. Consequently, the actual melting point

T_m is lower than the theoretical value T_m^0 , and related to the thickness of the crystals through the Gibbs-Thomson equation (cf. Section 2.2.2.1):

$$T_m = T_m^0 \left(1 - \frac{2\sigma_e}{l\Delta H_f^0} \right), \quad (1-19)$$

where σ_e is the fold surface free energy, l is the lamellar thickness (or the crystal thickness), and ΔH_f^0 is the enthalpy of fusion. Two important parameters which can be evaluated directly from the plot of T_m versus $1/l$ are the T_m^0 value from y-intercept and the σ_e value from the slope.

Taking into account the effect of variation in molar mass, Buckley and Kovacs [108] proposed that the Gibbs free energy for the formation of secondary nuclei (cf. Equation (1-16)) can be corrected by subtraction of the entropy of localization due to pairing of chain ends. The modified equation is similar to the Gibbs-Thomson equation with a correction term for the chain-end effect:

$$T_m = T_m^0 \left(1 - \frac{2\sigma_e}{l\Delta H_f^0} - \frac{RT_m^0}{\Delta H_f^0} \cdot \frac{\ln x}{x} \right), \quad (1-113)$$

where R is the universal gas constant and x is the degree of polymerization (i.e., the average number of the repeating units).

Experimentally, the lamellar thickness l of the crystals is measured from data taken from scanning electron microscopy (SEM) or small-angle x-ray scattering (SAXS) along with the knowledge of the absolute crystallinity (determined from differential scanning calorimetry (DSC), wide-angle x-ray diffraction (WAXD), density, or some combination of these techniques). The melting point is measured using DSC, however it is important to avoid any annealing (i.e., crystal thickening) or recrystallization of the original crystals during the heating scan. The methods used to prevent this from happening are to use 1) optimal heating rate which depends on the polymer system of

interest, 2) chemically etching away the folded surfaces and the amorphous regions, and 3) chemically crosslinking the amorphous portion.

Recently, Xu et al [109] questioned the reliability of the SAXS technique in measuring the lamellar thickness l (at least for the case of iPP), and hence the resulting T_m^0 value obtained from this method.

2.4.3. Hoffman-Weeks Extrapolation Methods

2.4.3.1. Linear Hoffman-Weeks Extrapolation Method

As mentioned previously in Section 2.2.2.1, the initial lamellar thickness has to be greater than the critical lamellar thickness calculated from the classical secondary nucleation theory by a factor of δl in order for the crystals to grow, which is given by

$$l^* = \frac{2\sigma_e}{\Delta f} + \delta l \approx \frac{2\sigma_e T_m^0}{\Delta H_f^0 \Delta T} + \delta l, \quad (1-20)$$

where l^* is the initial lamellar thickness and δl is a quantity related to very small thickening of the crystals and is a very weak function of temperature.

If the thickening behavior of the crystals can be expressed by the introduction of the thickening ratio $\beta = l/l^* \geq 1$ (for a coherent two-dimensional nucleation process), the observed melting point T_m of a crystal which has been thickened by a factor β can be expressed by

$$T_m = T_m^0 \left(1 - \frac{2\sigma_e}{\beta l^* \Delta H_f^0}\right). \quad (1-114)$$

In the case where β equals 1 or δl equals 0 (i.e., non-thickening), the melting point T_m of a crystal is related to its crystallization temperature T_c according to the equation:

$$T_c = T_m^0 \left(1 - \frac{2\sigma_e}{l^* \Delta H_f^0}\right). \quad (1-115)$$

Based on Equations (1-114) and (1-115), Hoffman and Weeks [110] were able to derive a very useful equation which allows determination of the equilibrium melting temperature T_m^0 from a series of melting temperatures T_m of crystals crystallized at crystallization temperatures T_c :

$$T_m = \frac{T_c}{2\beta} + T_m^0 \left(1 - \frac{1}{2\beta}\right). \quad (1-116)$$

According to Equation (1-116), linear extrapolation of T_m versus T_c data to the line $T_m = T_c$ yields the equilibrium melting temperature T_m^0 value, and yields the thickening ratio β as the slope. This type of plot is hereafter referred to as the *linear Hoffman-Weeks extrapolation*. The factor 2 in Equation (1-116) suggests that the thickness of the crystals undergoing melting is approximately doubled that of the initial critical thickness (cf. Equation (1-17)).

2.4.3.2. Non-linear Hoffman-Weeks Extrapolation Method

Theoretically, Equation (1-116) is only valid when the slope of the plot of observed T_m versus T_c is a constant value close to 0.5, at which condition the thickening ratio β is close to 1. Experimental observations on various polymer systems [107,110-113], however, have shown non-linearity in the observed T_m data when plotted over wide T_c range, thus raising a concern on the assumed constancy of the thickening ratio β . In fact, Weeks [114] has pointed out that the increase in observed T_m value with increasing crystallization time is a result of the increase in lamellar thickness, which has a logarithmic dependence on time. This simply means that the thickening effect is much more severe at higher T_c values (i.e, β increases with increase in T_c) where prolonged crystallization time is needed for complete crystallization.

If the observed T_m - T_c data are collected over wide enough temperature range, it is possible to divide curves T_m versus T_c into three regions as suggested by Alamo et al.

[113]. The first region corresponds to the lowest crystallization temperature range. Within this range, the thickness of the crystallites is less sensitive to changes in T_c , therefore observed T_m is essentially only slightly dependent on T_c . The second region corresponds to the highest crystallization temperature range. Within this range, prolonged crystallization time is needed in order to allow for the completion of the crystallization process. During this time period, the initial nuclei can undergo excessive thickening even before the bulk reaches 5-10% crystallinity [113]. The extent of thickening process is a function of both time and crystallization temperature. The third region corresponds to the temperature range intermediate to both extremes. In this range, linearity in the plot of observed T_m versus T_c is evident, and it is the region to which the linear Hoffman-Weeks procedure has been applied.

Even though the non-linearity in the observed T_m - T_c data over wide range of temperature was explained to some extent by Alamo et al. [113], it is the recent contribution by Marand et al. [115] that offers a new method of determining the T_m^0 value based on the observed T_m - T_c data in which the observed T_m data were taken from samples crystallized at different temperatures but with the same *a priori* lamellar thickening coefficient.

Based on the proposition made by Lauritzen and Passaglia [116] on stem length fluctuations during chain folding, the fold surface free energy associated with a nucleus of critical size σ_e^{GT} accounting for the extra lateral surface energy due to fold protrusion and for the mixing entropy associated with stems of different lengths (related to the σ_e quantity appeared in the Gibbs-Thomson equation) can be expressed as a function of undercooling as

$$\sigma_e^{GT} = \sigma_e^l(1 + \zeta\Delta T), \quad (1-117)$$

where σ_e^1 is the interfacial energy associated with the basal plane of the mature crystallite and can be estimated from the slope of l^* versus $1/\Delta T$ [59,64], and ζ is a small positive constant.

Based on Equation (1-117), Marand et al. [115] re-wrote the equation for the initial lamellar thickness (i.e., Equation (1-20)) to be

$$l^* = \frac{2\sigma_e^1 T_m^o}{\Delta H_f^o \Delta T} + \frac{2\sigma_e^1 \zeta T_m^o}{\Delta H_f^o} + \delta l = \frac{D_1}{\Delta T} + D_2, \quad (1-118)$$

where D_1 and D_2 are constants, and all other parameters are the same as previously defined. Equation (1-118) is able to explain the discrepancy between the thickening parameter measured experimentally (i.e., D_2 in Equation (1-118)) and that calculated based on theoretical consideration (i.e., δl in Equation (1-20)) [115].

With the combinations of Equations (1-19), (1-117) and (1-118), Marand et al. [115] proposed a new method, so-called the *non-linear Hoffman-Weeks extrapolation*, for the analysis of experimental T_m - T_c data based on the equation of the form:

$$\frac{T_m^o}{T_m^o - T_m} = \beta^m \frac{\sigma_e^1}{\sigma_e^{GT}} \left[\frac{T_m^o}{T_m^o - T_c} + \frac{D_2 \Delta H_f^o}{2\sigma_e^1} \right], \quad (1-119a)$$

or in a simpler form:

$$M = \beta^m \frac{\sigma_e^1}{\sigma_e^{GT}} (X + a), \quad (1-119b)$$

where β^m is the thickening coefficient (cf. β in Equation (1-116)), and all other parameters are the same as previously defined. It is worth noting that for most cases it is safe to assume that $\sigma_e^1 = \sigma_e^{GT}$. Precautionary remarks about using the non-linear Hoffman-Weeks procedure were addressed in detail in the original publication by Marand et al. [115].

In order to apply Equation (1-119) to real polymer systems, it is required that the observed T_m data be collected from samples crystallized at different temperatures but

having the same lamellar thickening coefficient β^m . Due to the fact that the rate of isothermal lamellar thickening increases, while the overall rate of crystallization decreases, with increasing crystallization temperature, measurement of the observed T_m data under the aforementioned condition is unpractical. To solve this problem, Xu et al. [109], in a successful attempt of applying the non-linear Hoffman-Weeks procedure to the case of iPP synthesized with Ziegler-Natta catalysts, obtained the observed T_m data of non-thickened crystals (i.e., $\beta^m = 1$) by extrapolation of the T_m values of thickened crystals to zero crystallinity. The same procedure is repeated to collect the observed T_m data at other crystallization temperatures T_c .

For each set of the observed T_m - T_c data, corresponding values of M and X in Equation (1-119) can be calculated for a given choice of the equilibrium melting temperature T_m^0 . For the case of $\sigma_e^1 = \sigma_e^{GT}$, the *actual* equilibrium melting temperature T_m^0 is taken as the seed T_m^0 value which results in the plot of M versus X being a straight line with slope of unity (i.e., $\beta^m = 1$) and intercept of a (i.e., $a = D_2\Delta H_f^0/2\sigma_e^1$). It should be noted that this method was successfully tested for the case of linear polyethylene (HDPE) by comparing with the theoretical approach by Flory and Vrij [105].

2.4.4. Data-fitting Methods

2.4.4.1. Data-fitting Method Based on Induction Time Data

Recently, a new method for the determination of the equilibrium melting temperature T_m^0 based on the measurements of nucleation induction times, defined as the time interval the polymer takes from the beginning of isothermal crystallization to the moment when stable nuclei are formed, was proposed by Lednicky and Muchova [117]. The theory of nucleation induction time by Lednicky and Muchova [117-122] was derived based on the classical theories of primary nucleation [29,32] (cf. Section (2.1)), and offers a way to quantitatively relate the theories to the experimental results. The

main application of the theory is to assess the nature of primary nucleation on foreign surfaces [121,122], e.g., fibers, fillers, etc.

In general, crystallization of polymers from the melt often starts with primary nucleation due to the presence of foreign surfaces, provided that prolonged melting is carried out to ensure complete melting. In heterogeneous nucleation, two mechanisms are involved [117,119,121]: 1) formation of the first layer on the foreign surface which is characterized by the difference in the surface energies (cf. Section 2.2.1.2), and 2) formation of the subsequent layers until the nucleus of critical size is established and the growth process occurs. The induction time t_i can be expressed as a summation of the time periods for the formation of the first layer (denoted t_h) and for the formation of the subsequent layers (denoted t_s).

Since the time characteristic for each mechanism is inversely proportional to the number of segments capable of nucleation [117,119,121], the equation describing the induction time is given by

$$t_i = t_h + t_s, \quad (1-120)$$

in which
$$t_h = E_1 \exp\left(\frac{\Delta G_n}{kT}\right) \exp\left(\frac{16(\Delta\sigma)\sigma\sigma_c(T_m^0)}{kT(\Delta H_f^0\Delta T)^2}\right), \quad (1-121)$$

$$t_s = E_2 \left[\frac{2(\Delta\sigma)T_m^0}{(\Delta H_f^0\Delta T)b_0} - 1 \right] \exp\left(\frac{\Delta G_n}{kT}\right) \exp\left(\frac{4b_0\sigma\sigma_c T_m^0}{kT(\Delta H_f^0\Delta T)}\right), \quad (1-122)$$

where E_1 and E_2 are proportionality constants, and the other quantities are the same as previously defined.

Muchova and Lednicky [117,121] showed that in some certain circumstances only one of the constituent terms dominates. Specifically, for sufficiently high crystallization temperatures, when the number of subsequent layers is much higher than unity (in order for the nucleus to be energetically stable), the time for the formation of

the first layer t_h can be neglected. In such a case, the induction time t_i can be approximated by

$$t_i = E_2 \left[\frac{2(\Delta\sigma)T_m^0}{(\Delta H_f^0 \Delta T) b_0} \right] \exp\left(\frac{\Delta G_\eta}{kT}\right) \exp\left(\frac{4b_0 \sigma \sigma_c T_m^0}{kT(\Delta H_f^0 \Delta T)}\right). \quad (1-123)$$

For some lower crystallization temperatures where the number of critical layer approaches unity, the time for the formation of subsequent layers t_s can now be neglected. The induction time t_i is therefore given by

$$t_i = E_1 \exp\left(\frac{\Delta G_\eta}{kT}\right) \exp\left(\frac{16(\Delta\sigma)\sigma\sigma_c(T_m^0)}{kT(\Delta H_f^0 \Delta T)^2}\right). \quad (1-124)$$

If the measured data are of high quality, the best fit of either Equation (1-123) or (1-124) to the induction time data measured in a certain range of crystallization temperatures where either equation can be approximated can be used to determine the equilibrium melting temperature T_m^0 . If the induction time data can be measured very precisely, the T_m^0 value obtained will become more accurate.

2.4.4.2. Data-fitting Method Based on Linear Growth Rate Data

Recently, Huang et al. [112] suggested that analysis of the linear growth rate data of polymers in the context of the LH secondary nucleation theory can only be carried out successfully when the equilibrium melting temperature T_m^0 for the polymer of interest can be determined accurately. They also suggested that the T_m^0 value for the polymer of interest can be evaluated directly from the growth rate data, using the LH secondary nucleation theory as basis (cf. Equation (1-48)).

By considering T_m^0 as a variable, a seed T_m^0 value is first chosen and then the traditional LH plot (i.e., $\log G + U/2.303R(T_c - T_\infty)$ versus $1/2.303T_c(\Delta T)f$) for each regime is constructed based on the seed T_m^0 value. From the linear regression, the values of the nucleation exponent K_g (i.e., the negative value of the slope) and the intercept (i.e., $\log G_0$)

corresponding to the seed T_m^0 value are obtained. They assumed that the true T_m^0 value for the polymer of interest is taken as the seed T_m^0 value which gives the lowest variance between the experimental values (i.e., the LHS of Equation (1-51)) and the linear regression values (i.e., the RHS of Equation (1-51)). Their proposed method is hereafter called the *data-fitting procedure*. So far, this method has been successfully applied to the cases of poly(pivalolactone) [112] and its blends [112,123], isotactic polystyrene (iPS) [124], poly(L-lactide-co-meso-lactide) copolymers [125], and isotactic polypropylene (iPP) [109].

An alternative method for determining the true T_m^0 value for the polymer of interest can be determined based on the theoretical requirement of the ratios $K_{g,I}/K_{g,II} = K_{g,III}/K_{g,II} = 2.0$, provided that either regime I→II or regime II→III transition exists within the temperature range of interest. By assuming that the LH secondary nucleation theory is applicable to describe the temperature dependence of the growth rate data of polymers other than that of polyethylene which is the basis for the development of the theory and that the measured growth rate data is of high quality, the true T_m^0 value for the polymer of interest is taken as the seed T_m^0 value which results in the ratio of the corresponding nucleation exponents of 2.0. Xu et al. [109] applied both alternative approaches of the data-fitting procedure on the growth rate data of iPP, and found that the resulting T_m^0 values determined from both approaches are comparable (ca. 215°C).

3. REFERENCES

- [1] Natta, G.; Pasquon, I.; Corradini, P.; Peraldo, M.; Pegoraro, M.; and Zambelli, A. *Rend. Acc. Naz. Lincei*. **1960**, *28*, 539.
- [2] Natta, G.; Pasquon, I.; and Zambelli, A. *J. Am. Chem. Soc.* **1962**, *84*, 1488.
- [3] Ewen, J.A.; Johns, R.L.; Razavi, A.; and Ferrara, J.D. *J. Am. Chem. Soc.* **1988**, *110*, 6255.
- [4] Schardl, J.; Sun, L.; Kimura, S.; and Sugimoto, R. *SPE-ANTEC Proc.* **1995**, 3414.
- [5] Schardl, J.; Sun, L.; Kimura, S.; and Sugimoto, R. *J. Plastic Film & Sheeting* **1996**, *12*, 157.
- [6] Sun, L.; Shamshoum, E.; and DeKunder, G. *SPE-ANTEC Proc.* **1996**, 1965.
- [7] Gownder, M. *SPE-ANTEC Proc.* **1998**, 1511.
- [8] Sura, R.K.; Desai, P.; and Abhiraman, A.S. *SPE-ANTEC Proc.* **1999**, 1764.
- [9] Wheat, W.R. *SPE-ANTEC Proc.* **1995**, 2275.
- [10] Wheat, W.R. *SPE-ANTEC Proc.* **1997**, 565.
- [11] Rodriguez-Arnold, J.; Bu, Z.; and Cheng, S.Z.D. *J. Macromol. Sci.-Rev. Macromol. Chem. Phys.* **1995**, *C35*, 117.
- [12] Hermann, K.; Gerngoss, O.; and Abitz, W. *Z. Phys. Chem.* **1930**, *10*, 371.
- [13] Storcks, K.H. *J. Am. Chem. Soc.* **1938**, *60*, 1753.
- [14] Fischer, E.W. *Z. Naturf.* **1957**, *A12*, 753.
- [15] Till, P.H. *J. Polym. Sci.* **1957**, *24*, 30.
- [16] Keller, A. *Phil. Mag.* **1957**, *2*, 1171.
- [17] Keller, A. In *Sir Charles Frank FRS, OBE: An Eightieth Birthday Tribute*; Chambers, R.G., Ed.; Adam Hilger: Bristol, 1991; pp 265-306.
- [18] Reneker, D.H. and Geil, P.H. *J. Appl. Phys.* **1960**, *31*, 1916.
- [19] Fava, R.A. *J. Polym. Sci., Macromol. Rev.* **1971**, *5*, 1.
- [20] Geil, P.H. In *Polymer Single Crystals*; John Wiley & Sons: New York, 1973.
- [21] Mandelkern, L. In *An Introduction to Macromolecules*; Springer-Verlag: New York, 1972.
- [22] Bassett, D.C. In *Principles of Polymer Morphology*; Cambridge University Press: Cambridge, 1981.
- [23] Rabek, J.F. In *Experimental Methods in Polymer Chemistry*; John Wiley & Sons: Chichester, 1980.
- [24] Frank, F.C. and Tosi, M. *Proc. Res. Soc.* **1961**, *A263*, 323.
- [25] Flory, P.J. *J. Am. Chem. Soc.* **1962**, *84*, 2857.
- [26] Bank, I.M. and Krimm, S. *J. Polym. Sci., A-2: Polym. Phys.* **1969**, *7*, 1785.
- [27] Spells, S.J.; Sadler, D.M.; and Keller, A. *Polymer* **1980**, *21*, 1121.
- [28] Phillips, P.J. *Rep. Prog. Phys.* **1990**, *53*, 549.
- [29] Wunderlich, B. In *Macromolecular Physics*; Academic Press: New York, 1976; Vol. 2.
- [30] Janeschitz-Kriegl, H.; Ratajski, E.; and Wippel, H. *Colloid Polym. Sci.* **1999**, *277*, 217.
- [31] Janeschitz-Kriegl, H. *Colloid Polym. Sci.* **1997**, *275*, 1121.

- [32] Price, F.P. In *Nucleation*; Zettlemoyer, A.C., Ed.; Marcel Dekker: New York, 1969; Chapter 8.
- [33] Ziabicki, A. *J. Chem. Phys.* **1968**, *48*, 4368.
- [34] Ziabicki, A. *J. Chem. Phys.* **1968**, *48*, 4374.
- [35] Ziabicki, A. *J. Chem. Phys.* **1977**, *66*, 1638.
- [36] Ziabicki, A. and Jarecki, L. *J. Chem. Phys.* **1984**, *80*, 5751.
- [37] Ziabicki, A. *J. Chem. Phys.* **1986**, *85*, 3042.
- [38] Gibbs, J.W. *Trans. Conn. Acad.* **1878**, *3*, 343.
- [39] Imai, M.; Mori, T.; Mizukami, K.; Kaji, K.; and Kanaya, T. *Polymer* **1992**, *33*, 4451.
- [40] Imai, M.; Mori, T.; Mizukami, K.; Kaji, K.; and Kanaya, T. *Polymer* **1992**, *33*, 4457.
- [41] Imai, M.; Kaji, K.; and Kanaya, T. *Phys. Rev. Lett.* **1993**, *71*, 4162.
- [42] Imai, M.; Kaji, K.; and Kanaya, T. *Macromolecules* **1994**, *27*, 7103.
- [43] Imai, M.; Kaji, K.; Kanaya, T.; and Sakai, Y. *Phys. Rev., Condensed Matter* **1995**, *52*, 12696.
- [44] Takeuchi, H. *J. Chem. Phys.* **1998**, *109*, 5614.
- [45] Terrill, N.J.; Fairclough, P.A.; Towns-Andrews, E.; Komanschek, B.U.; Young, R.J.; and Ryan, A.J. *Polymer* **1998**, *39*, 2381.
- [46] Binsbergen, F.L. *Kolloid Z. Z. Polym.* **1970**, *237*, 289.
- [47] Binsbergen, F.L. *Polymer* **1970**, *11*, 253.
- [48] Binsbergen, F.L. *Kolloid Z. Z. Polym.* **1970**, *238*, 389.
- [49] Binsbergen, F.L. and DeLange, B.G.M. *Polymer* **1970**, *11*, 309.
- [50] Binsbergen, F.L. *J. Polym. Sci., Polym. Phys.* **1973**, *11*, 117.
- [51] Turnbull, D. and Fisher, J.C. *J. Chem. Phys.* **1949**, *17*, 71.
- [52] Okui, N. *Polym. J.* **1987**, *19*, 1309.
- [53] Okui, N. *Polymer* **1990**, *31*, 92.
- [54] Okui, N. *Polym. Bull.* **1990**, *23*, 111.
- [55] Okui, N. *J. Mat. Sci.* **1990**, *25*, 1623.
- [56] Lauritzen Jr., J.I. and Hoffman, J.D. *J. Res. Nat'l. Bur. Stand.* **1960**, *A64*, 73.
- [57] Hoffman, J.D. and Lauritzen Jr., J.I. *J. Res. Nat'l. Bur. Stand.* **1961**, *A65*, 297.
- [58] Lauritzen Jr., J.I. and Hoffman, J.D. *J. Appl. Phys.* **1973**, *44*, 4340.
- [59] Hoffman, J.D.; Davis, G.T.; and Lauritzen Jr., J.I. In *Treatise on Solid State Chemistry*; Hannay, N.B., Ed.; Plenum Press: New York, 1976; Vol. 3; Chapter 7.
- [60] Hoffman, J.D. *Polymer* **1982**, *23*, 656.
- [61] Hoffman, J.D. *Polymer* **1983**, *24*, 3.
- [62] Hoffman, J.D. and Miller, R.L. *Macromolecules* **1988**, *21*, 3038.
- [63] Hoffman, J.D. *Polymer* **1992**, *33*, 2643.
- [64] Hoffman, J.D. and Miller, R.L. *Polymer* **1997**, *38*, 3151.
- [65] Suzuki, T. and Kovacs, A.J. *Polymer J.* **1970**, *1*, 82.

- [66] Sanchez, I.C. and DiMarzio, E.A. *J. Chem. Phys.* **1971**, *55*, 893.
- [67] Frank, F.C. *J. Cryst. Growth* **1974**, *22*, 233.
- [68] Phillips, P.J. *ACS Polym. Prepr.* **1979**, *20*, 438.
- [69] Keith, H.D. and Padden, F.J. *J. Appl. Phys.* **1964**, *35*, 1270.
- [70] Keith, H.D. and Padden, F.J. *J. Appl. Phys.* **1964**, *35*, 1286.
- [71] Verma, R.; Marand, H.; and Hsiao, B. *Macromolecules* **1996**, *29*, 7767.
- [72] Kolmogoroff, A.N. *Izvestiya Akad. Nauk USSR, Ser. Math.* **1937**, *1*, 355.
- [73] Johnson, W.A. and Mehl, K.F. *Trans. Am. Inst. Mining Met. Eng.* **1939**, *135*, 416.
- [74] Avrami, M. *J. Chem. Phys.* **1939**, *7*, 1103.
- [75] Avrami, M. *J. Chem. Phys.* **1940**, *8*, 212.
- [76] Avrami, M. *J. Chem. Phys.* **1941**, *9*, 177.
- [77] Evans, U.R. *Trans. Faraday Soc.* **1945**, *41*, 365.
- [78] Tobin, M.C. *J. Polym. Sci., Polym. Phys.* **1974**, *12*, 399.
- [79] Tobin, M.C. *J. Polym. Sci., Polym. Phys.* **1976**, *14*, 2253.
- [80] Tobin, M.C. *J. Polym. Sci., Polym. Phys.* **1977**, *15*, 2269.
- [81] Malkin, A.Y.; Beghishev, V.P.; Keapin, I.A.; and Bolgov, S.A. *Polym. Eng. Sci.* **1984**, *24*, 1396.
- [82] Rabesiaka, J. and Kovacs, A.J. *J. Appl. Phys.* **1961**, *32*, 2314.
- [83] Banks, W.; Sharples, A.; and Hay, J.N. *J. Polym. Sci.* **1964**, *A2*, 4059.
- [84] Ding, Z. and Spruiell, J.E. *J. Polym. Sci., Polym. Phys.* **1997**, *35*, 1077.
- [85] Ziabicki, A. *Appl. Polym. Symp.* **1967**, *6*, 1.
- [86] Ziabicki, A. *Polymery* **1967**, *12*, 405.
- [87] Ziabicki, A. In *Fundamentals of Fiber Spinning*; John Wiley & Sons: New York, 1976.
- [88] Patel, R.M. and Spruiell, J.E. *Polym. Eng. Sci.* **1991**, *31*, 730.
- [89] Nakamura, K.; Watanabe, T.; and Katayama, K. *J. Appl. Polym. Sci.* **1972**, *16*, 1077.
- [90] Nakamura, K.; Katayama, K.; and Amano, T. *J. Appl. Polym. Sci.* **1973**, *17*, 1031.
- [91] Hammami, A.; Spruiell, J.E.; and Mehrotra, A.K. *Polym. Eng. Sci.* **1995**, *35*, 797.
- [92] Lawrence, S.S. and Shinozaki, D.M. *Polym. Eng. Sci.* **1997**, *37*, 1825.
- [93] Wesson, R.D. *Polym. Eng. Sci.* **1994**, *34*, 1157.
- [94] Kamal, M.R. and Chu, E. *Polym. Eng. Sci.* **1983**, *23*, 27.
- [95] Ozawa, T. *Polymer* **1971**, *12*, 150.
- [96] Harnisch, K. and Muschik, H. *Colloid Polym. Sci.* **1983**, *261*, 908.
- [97] Caze, C.; Devaux, E.; Crespy, A.; and Cavrot, J.P. *Polymer* **1997**, *38*, 497.
- [98] Chuah, K.P.; Gan, S.N.; and Chee, K.K. *Polymer* **1999**, *40*, 253.
- [99] Malkin, A.Y.; Beghishev, V.P.; Keapin, I.A.; and Andrianova, Z.S. *Polym. Eng. Sci.* **1984**, *24*, 1402.
- [100] Jeziorny, A. *Polymer* **1978**, *19*, 1142.

- [101] Ziabicki, A. *Colloid Polym. Sci.* **1996**, 274, 209.
- [102] Ziabicki, A. *Colloid Polym. Sci.* **1996**, 274, 705.
- [103] Ziabicki, A. and Sajkiewicz, P. *Colloid Polym. Sci.* **1998**, 276, 680.
- [104] Sajkiewicz, P. *Polymer* **1999**, 40, 1433.
- [105] Flory, P.J. and Vrij, A. *J. Am. Chem. Soc.* **1963**, 85, 3548.
- [106] Mandelkern, L.; Prasad, A.; Alamo, R.G.; and Stack, G.M. *Macromolecules* **1990**, 23, 3696.
- [107] Kim, M.-H. In *Ph.D. Dissertation*, The University of Tennessee at Knoxville, 1996.
- [108] Buckley, C.P. and Kovacs, A.J. *Colloid Polym. Sci.* **1976**, 254, 695.
- [109] Xu, J.; Srinivas, S.; Marand, H.; and Agarwal, P. *Macromolecules* **1998**, 31, 8230.
- [110] Hoffman, J.D. and Weeks, J.J. *J. Res. Nat'l. Bur. Stand.* **1962**, A66, 13.
- [111] Lemstra, P.J.; Kooistra, T.; and Challa, G. *J. Polym. Sci., Polym. Phys.* **1972**, 10, 823.
- [112] Huang, J.; Prasad, A.; and Marand, H. *Polymer* **1994**, 35, 1896.
- [113] Alamo, R.G.; Viers, B.D.; and Mandelkern, L. *Macromolecules* **1995**, 28, 3205.
- [114] Weeks, J.J. *J. Res. Nat'l. Bur. Stand.* **1963**, A67, 441.
- [115] Marand, H.; Xu, J.; and Srinivas, S. *Macromolecules* **1998**, 31, 8219.
- [116] Lauritzen Jr., J.I. and Passaglia, E. *J. Res. Nat'l. Bur. Stand.* **1967**, A61, 261.
- [117] Lednicky, F. and Muchova, M. *J. Macromol. Sci.-Phys.* **1996**, B35, 681.
- [118] Lednicky, F. and Muchova, M. *Collect. Czech. Chem. Commun.* **1993**, 58, 2444.
- [119] Muchova, M. and Lednicky, F. *J. Macromol. Sci.-Phys.* **1995**, B34, 55.
- [120] Lednicky, F. and Muchova, M. *J. Macromol. Sci.-Phys.* **1995**, B34, 75.
- [121] Muchova, M. and Lednicky, F. *Polymer* **1996**, 37, 3031.
- [122] Muchova, M. and Lednicky, F. *Polymer* **1996**, 37, 3037.
- [123] Huang, J. and Marand, H. *Macromolecules* **1997**, 30, 1069.
- [124] Iler, H.D. In *Ph.D. Dissertation*, Virginia Institute of Technology and State University, 1995.
- [125] Huang, J.; Lisowski, M.S.; Runt, J.; Hall, E.S.; Kean, R.T.; Buehler, N.; and Lin, J.S. *Macromolecules* **1998**, 31, 2593.

PART 2:
THERMAL PROPERTIES AND ISOTHERMAL CRYSTALLIZATION
OF SYNDIOTACTIC POLYPROPYLENES: DIFFERENTIAL
SCANNING CALORIMETRY AND OVERALL CRYSTALLIZATION
KINETICS

1. ABSTRACT

Isothermal crystallization and subsequent melting behavior of five samples of syndiotactic polypropylene are presented. Crystallization studies were carried out in the temperature range of 60°C to 97.5°C using a differential scanning calorimeter (DSC). Subsequent DSC scans of isothermally crystallized samples exhibited double melting endotherms. The high-melting peak was concluded to be the result of the melting of crystals formed by recrystallization during the reheating process. Overall crystallization kinetics was studied based on the traditional Avrami analysis. Analysis of crystallization times based on the modified growth rate theory suggested that, within the crystallization temperature range studied, the syndiotactic polypropylenes crystallize in regime III. Kinetic crystallizability parameters were also evaluated, and were found to be in the range of $0.41^{\circ}\text{C}\cdot\text{sec}^{-1}$ to $2.14^{\circ}\text{C}\cdot\text{sec}^{-1}$.

2. INTRODUCTION

Since the mid-1950s, the invention of Ziegler-Natta catalysis [1-3] has opened up a new era in the synthesis of polyolefins. In 1958, isotactic polypropylene (iPP) was successfully synthesized, and later became one of the most widely used and studied polymers. In the 1960s, the syndiotactic form of polypropylene was successfully synthesized [4,5] based on the $\text{AlR}_2\text{Cl}/\text{VCl}_4$ catalyst systems. Even though the resulting polymer possessed a fair level of syndiotactic content, it contained too high a level of regio-irregular defects (e.g., head-to-head/tail-to-tail type defects). As a result, the properties of the obtained polymer were inferior to those of its isotactic counterpart.

In 1988, Ewen et al. [6] reported that highly stereoregular and regioregular sPP can be polymerized using a catalyst system composed of isopropylidene(cyclopentadienyl)(9-fluorenyl)zirconium or hafnium dichloride and methylaluminoxane. The discovery of these new metallocene catalyst systems helped open up a new route for the

production of sPP with much improved purity and yields, and produced renewed interest in the properties and possible applications of this "second generation" sPP.

It is well known that molecular characteristics, such as molecular weight, molecular weight distribution, stereoregularity, and regioregularity greatly influence the crystallization behavior and resulting morphology of polymers. It is therefore necessary to understand and obtain enough information on basic crystallization characteristics of the polymers of interest before further studies are carried out. In this study, the isothermal bulk crystallization kinetics as well as melting behavior of sPPs is examined using a differential scanning calorimeter.

3. THEORETICAL BACKGROUND

Bulk isothermal crystallization kinetics was studied by following the exotherms recorded in the DSC7. When used to follow the crystallization of polymers, what DSC measures is the heat flow \dot{Q} released due to the exothermic nature of the crystallization process. The heat flow is directly proportional to the weight of the sample w the enthalpy of crystallization ΔH_c and the overall crystallization rate $\dot{\theta}(t)$. Theoretically, ΔH_c is a product of the absolute crystallinity χ_c and the crystallization enthalpy of an infinitely thick extended chain crystal of a perfect crystal (i.e., 100% crystallinity) ΔH_c^0 . Ideally, ΔH_c^0 is also equal to the enthalpy of fusion of a perfect crystal ΔH_f^0 ; thus, they can be used interchangeably. Consequently, one may write the equation of heat flow as

$$\dot{Q} \propto w \cdot \chi_c \cdot \Delta H_f^0 \cdot \dot{\theta}(t). \quad (2-1)$$

By setting $\dot{q} = \dot{Q} / (c_1 w \cdot \chi_c \cdot \Delta H_f^0)$ (where c_1 is a proportionality constant), the relative crystallinity as a function of time $\theta(t)$, can be obtained by integrating the normalized heat flow $\dot{q}(t)$, over the course of the crystallization process. One finally gets

$$\theta(t) = \int_0^t \dot{\theta}(t) dt = \int_0^t \dot{q}(t) dt. \quad (2-2)$$

Analysis of isothermal bulk crystallization kinetics is usually performed using the Avrami equation [7], which is normally written in the form:

$$\theta(t) = 1 - \exp(-kt^n), \quad (2-3)$$

where k denotes the bulk crystallization rate constant, and n the Avrami exponent. Both k and n are constants typical of a given morphology and primary nucleation type. It should be noted that t is the time spent during the course of crystallization measured from the onset of crystallization (the incubation time is excluded). In practice, Equation (2-3) is usually written in its logarithmic form:

$$\ln[-\ln(1-\theta(t))] = \ln k + n \ln(t). \quad (2-4)$$

According to Equation (2-4), when plotting $\ln[-\ln(1-\theta(t))]$ against $\ln(t)$, the values of n and k can readily be extracted and taken as the slope and the anti-logarithmic value of the y-intercept.

Based on Equation (2-3), if the time the polymer spends from the beginning of the crystallization process to the time at which a certain amount of relative crystallinity has developed is known (denoted t_θ : for example, if $\theta = 0.50$, $t_{0.5}$ is the half-time of crystallization), k can also be directly calculated. By rearranging Equation (2-3), one arrives at

$$k = \frac{-\ln(1-\theta)}{t_\theta^n}. \quad (2-5)$$

If $\theta = 0.5$, Equation (2-5) converts into a more familiar equation, which reads

$$k = \frac{\ln 2}{t_{0.5}^n}. \quad (2-6)$$

Since the crystallization time t_θ can be obtained directly from the experimental data, it can be adapted to investigate the regime behavior (based on the growth rate theory by Hoffman et al. [8,9]) in the isothermal crystallization of polymers, as

described below. According to the Lauritzen and Hoffman theory, the spherulite growth rate G is given as

$$G = G_0 \exp\left(-\frac{U^*}{R(T_c - T_\infty)} - \frac{K_g}{T_c(\Delta T)f}\right), \quad (2-7)$$

where G_0 is a preexponential term which is not strongly dependent on temperature. U^* is the activation energy of the elementary jump process which governs the mobility of the polymer with respect to the temperature and is commonly given by a universal value of 6,276 J·mol⁻¹ [8], T_c is the crystallization temperature, T_∞ is the temperature where the molecular reptation is essentially zero and is frequently assumed to be $T_g - 30$, R is the gas constant, ΔT is the degree of undercooling (i.e., $\Delta T = T_m^0 - T_c$), and f is a factor used to correct for the temperature dependence of the heat of fusion (i.e., $f = 2T_c/(T_c + T_m^0)$). It should be noted that U^* and T_∞ are the WLF (Williams-Landel-Ferry) parameters. K_g is the nucleation exponent, and is defined as

$$K_g = \frac{j b_0 \sigma \sigma_e T_m^0}{k \Delta H_f^0}, \quad (2-8)$$

where j equals 2 for regime II and 4 for regimes I and III, b_0 denotes the crystal layer thickness along the growth direction, σ and σ_e the lateral and fold surface free energy, respectively, T_m^0 the equilibrium melting temperature, k the Boltzmann's constant, and ΔH_f^0 the heat of fusion.

In the case of overall crystallization kinetics, the growth rate theory can be applied by use of the following relationship (provided that the nucleation is mainly instantaneous and the growth is spherulitic in nature):

$$k = \frac{4}{3} \pi G^3 N_0, \quad (2-9)$$

where N_0 is the number of nucleation sites which is essentially constant for instantaneous nucleation type. Substitution of Equation (2-7) into Equation (2-9) and

equating the product with Equation (2-5) gives the following relationship between t_0 and G :

$$t_0^{-1} = A_1 G_0 \exp\left(-\frac{U^*}{R(T_c - T_\infty)} - \frac{K_g}{T_c(\Delta T)f}\right), \quad (2-10)$$

where A_1 is an arbitrary proportionality constant, and

$$\log(t_0^{-1}) = A_2 - \frac{U^*}{2.303R(T_c - T_\infty)} - \frac{K_g}{2.303T_c(\Delta T)f}, \quad (2-11)$$

where $A_2 = \log A_1 + \log G_0$, and

$$\log(t_0^{-1}) + \frac{U^*}{2.303R(T_c - T_\infty)} = A_2 - \frac{K_g}{2.303T_c(\Delta T)f}. \quad (2-12)$$

According to Equation (2-12), construction of $\log(t_0^{-1}) + U^*/2.303R(T_c - T_\infty)$ versus $1/2.303T_c(\Delta T)f$ plot serves as the regime test for the case of instantaneous nucleation with three dimensional growth. The slope of such a plot is equal to $-K_g$.

4. EXPERIMENTAL DETAILS

4.1. Materials

The sPPs used in this study were supplied in the pellet form by Fina Oil and Chemical Company in La Porte, Texas. Molecular characterization of these materials was kindly performed by Dr. Roger A. Phillips and his coworkers at Montell USA, Inc. in Elkton, Maryland. The results are listed in Table 2-1. It should be noted that sPP#2, sPP#3, and sPP#5 exhibit a bimodal molecular weight distribution, which results in an unusually high degree of polydispersity.

4.2. Technique and Sample Preparation

A Perkin-Elmer Series 7 Differential Scanning Calorimeter (DSC7) was used to follow the isothermal crystallization as well as related thermal characteristics in this study. The DSC7 equipped with internal liquid nitrogen cooling unit dependably

Table 2-1. Characterization data of as-received syndiotactic polypropylene samples.

Sample	Intrinsic Viscosity (dl·g ⁻¹)	M _n (daltons)	M _w (daltons)	M _z (daltons)	M _w /M _n	Racemic Pentads [%rrrr]	Racemic Triads [%rrr]	Racemic Dyads [%r]	Ethylene Content (% by Wt.)
sPP#1	1.61	76 200	165 000	290 000	2.15	77.10	87.31	91.42	1.3
sPP#2	1.80	52 300	195 000	450 000	3.73	74.55	83.09	87.36	0.6
sPP#3	1.32	37 300	133 000	308 000	3.55	74.61	83.73	88.29	0.5
sPP#4	1.61	81 300	171 000	294 000	2.10	74.63	84.37	89.24	0.3
sPP#5	1.52	47 000	165 000	406 000	3.51	75.28	85.09	90.00	0.2

provided a cooling rate up to $200^{\circ}\text{C}\cdot\text{min}^{-1}$. Temperature calibration was performed using indium as a standard; it has the following thermal properties: $T_m^{\circ} = 156.6^{\circ}\text{C}$ and $\Delta H_f^{\circ} = 28.5 \text{ J}\cdot\text{g}^{-1}$. The consistency of the temperature calibration was checked every other run to ensure reliability of the data obtained. To make certain that thermal lag between the polymeric sample and the DSC sensors is kept to a minimum, each sample holder was loaded with a single disc, weighing around $4.9 \pm 0.3 \text{ mg}$. A hole-puncher was used to cut the disc from a film. The film was prepared by melt-pressing virgin pellets, placed between a pair of Kapton films which in turn were sandwiched between a pair of stainless steel platens, in a Wabash compression molding machine at 190°C under a pressure of 67 kpsi. After ten minutes holding time, the film, approximately $280 \mu\text{m}$ thick, was taken out and immediately submerged in an ice-water bath, while it was still between the two steel platens. This treatment assumes that previous thermal and mechanical histories were essentially erased, and provides a controlled condition for the film.

4.3. Methods

The experiment started with heating the sample from -40°C at a scanning rate of $80^{\circ}\text{C}\cdot\text{min}^{-1}$ to 190°C , and was held there for 5 min before quenching at a cooling rate of $200^{\circ}\text{C}\cdot\text{min}^{-1}$ to a desired isothermal crystallization temperature T_c . The 5 min holding time at 190°C is necessary to erase the previous crystalline and orientation memories. At each crystallization temperature, the crystallization process was closely monitored. It was assumed that the crystallization finished when the exothermic trace converged to a horizontal baseline, at which point the DSC was programmed to quench the sample to $T_c - 10^{\circ}\text{C}$. After one minute holding time, the sample was heated at a scanning rate of $20^{\circ}\text{C}\cdot\text{min}^{-1}$ to observe its melting behavior. The relationship of the melting point observed and the crystallization temperature was also considered by preparing a

Hoffman and Weeks plot [10]. It should also be noted that each experimental run was performed on a fresh sample.

In this study, the glass transition temperature of each sPP sample was also investigated. The experiment started by melting a sample, which was encapsulated in a DSC sample holder, in a Mettler FP 82 hot stage, temperature of which was preset at 190°C. After a 5 min holding time, the sample was immediately quenched and submerged in liquid nitrogen for 3 min. The sample was then transferred as quickly as possible to the DSC cell, temperature of which was preset at -40°C. As soon as the heat flow became stable, the sample was heated at a heating rate of 20°C·min⁻¹. The glass transition temperature was then taken as the mid-point of the specific heat jump in the glass transition region [11].

5. RESULTS AND DISCUSSION

5.1. Glass Transition Temperature

The measured glass transition temperatures are listed in Table 2-2 for each sample. Other relevant data are also tabulated, such as the extrapolated glass transition onset T_{g0} , the extrapolated end-point T_{ga} and the specific heat jump ΔC_p . According to Table 2-2, ΔC_p lies in the range of 0.41 to 0.49 J·g⁻¹·K⁻¹. The value of T_g for each sample does not vary much, and it is likely that all values are within experimental error of the average value of $-6.1 \pm 0.4^\circ\text{C}$ (267.0 ± 0.4 K). The glass transition temperatures of sPP have been reported by a number of authors. Miller and Seeley [12] used two different methods, DSC and an automated torsional braid, and came up with the values of 0°C and 3°C, respectively. Haftka and Könnecke [13] determined the T_g of an sPP sample with 92.4% syndiotacticity (racemic pentads) to be 0°C by slow-cooling at 20°C min⁻¹ in a DSC. Recently, Eckstein et al. [14] has reported the T_g values of sPP samples with 79.6% and 92.0% syndiotacticity (racemic pentads) to be 0°C and 3.3°C,

Table 2-2. Glass transition temperatures for syndiotactic polypropylene samples.

Sample	T_{go} (°C)	T_{ga} (°C)	ΔC_p (J·g ⁻¹ ·K ⁻¹)	T_g (°C)
sPP#1	-8.94	-3.42	0.43	-6.05
sPP#2	-8.34	-3.81	0.41	-5.98
sPP#3	-8.84	-4.42	0.42	-6.52
sPP#4	-8.27	-3.03	0.47	-5.60
sPP#5	-9.61	-3.73	0.49	-6.47

respectively, using a DSC. They did the experiment by first quenching the samples at $200^{\circ}\text{C}\cdot\text{min}^{-1}$ to -60°C and then determined the T_g values upon subsequent heating at $20^{\circ}\text{C}\cdot\text{min}^{-1}$.

5.2. Melting Behavior and Equilibrium Melting Temperature

Figure 2-1 presents a set of DSC heating thermograms which were collected at a heating rate of $20^{\circ}\text{C}\cdot\text{min}^{-1}$ for sPP#4 samples isothermally crystallized at specified temperatures. It is apparent that the DSC endotherms exhibit double melting peaks, which are distinguishable at crystallization temperature below 90°C . Moreover, with an increase in crystallization temperature, the low-melting peak seems to increase in its size and sharpness, and moves to higher temperature. On the contrary, the high-melting peak gets smaller as the crystallization temperature increases, and disappears when $T_c \geq 90^{\circ}\text{C}$. This is, in general, consistent with earlier published results by other authors [15-18]. Another interesting melting characteristic of sPP, which can be observed directly from its melting endotherms, is that, upon reheating, the melting starts at a temperature close to its crystallization temperature (ca. $\approx T_c + 7^{\circ}\text{C}$). This phenomenon was verified very recently by Schmidtke et al. [18]. It is now believed that the melting starts slightly after T_c [18] and it is followed by a recrystallization [15,18] in the range of the first melting endotherm, resulting in the appearance of the second endotherm. However, the phenomenon is less pronounced at high T_c .

To account for the effect of heating rate on the melting behavior of sPP, a separate qualitative experiment on sPP#4 is performed, the result of which is presented in Figure 2-2. In this experiment, each sample was isothermally crystallized at 75°C , then its melting thermogram was recorded at 6 different scanning rates, ranging from 5 to $40^{\circ}\text{C}\cdot\text{min}^{-1}$. It is evident, according to Figure 2-2, that the areal fraction of the high-melting endotherm decreases with increasing heating rate, while the area of the lower

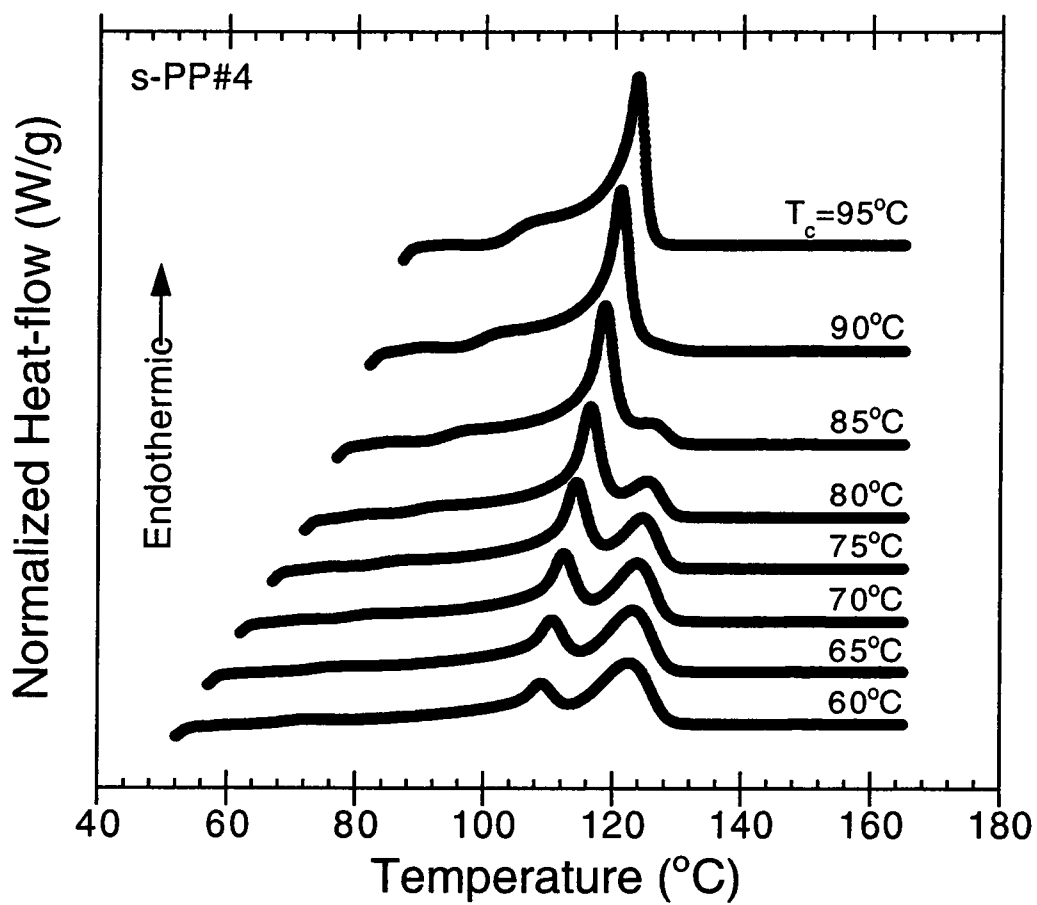


Figure 2-1. Melting endotherms of sample sPP#4, recorded at the heating rate of $20^{\circ}\text{C}\cdot\text{min}^{-1}$, after isothermal crystallization at the specified temperature.

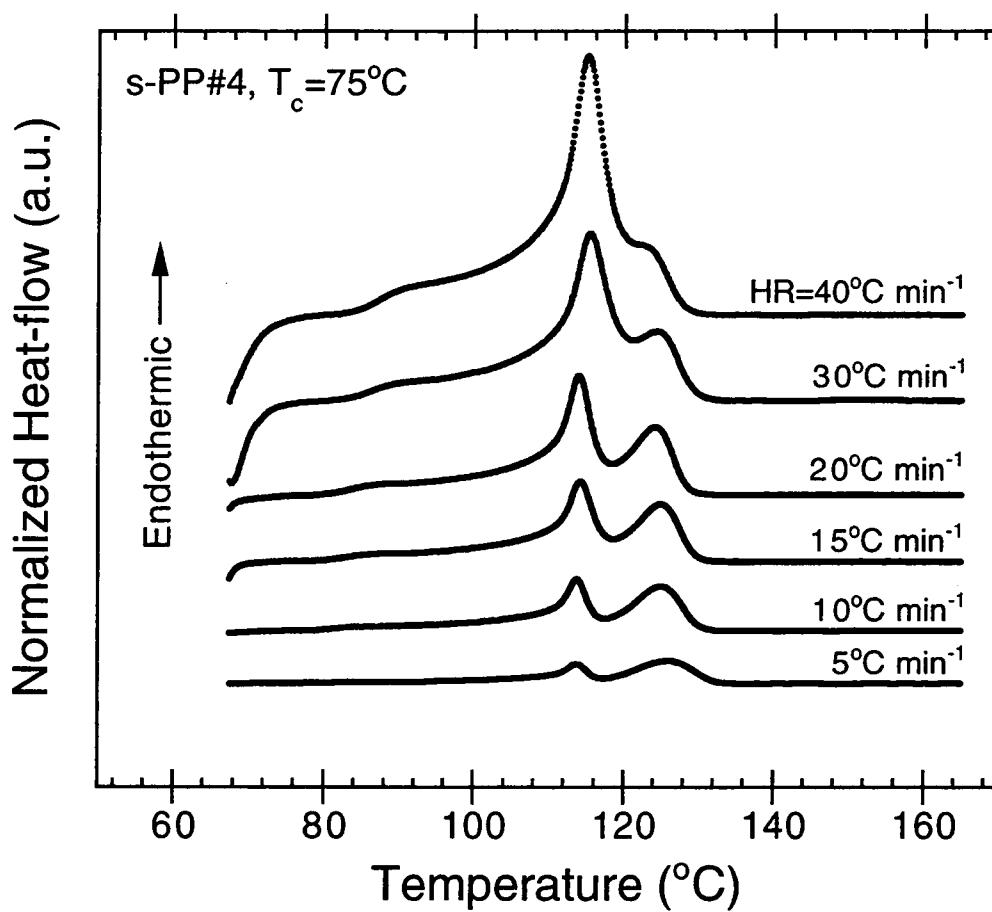


Figure 2-2. Melting endotherms of sample sPP#4, recorded at the specified heating rates, after isothermal crystallization at 75°C.

melting peak increases. This finding is in a very good agreement with earlier reports [16-18], and confirms the suggestion that the high-melting endotherm is in fact a result of a recrystallization process that occurred during the melting of the polymer. As was pointed out by Rodriguez-Arnold and her coworkers [16], the heating rate used to obtain a melting endotherm plays a major role in the melting point observed. The observed melting points when the heating rate is either lower or greater than $20^{\circ}\text{C}\cdot\text{min}^{-1}$ are greater in value than that obtained at $20^{\circ}\text{C}\cdot\text{min}^{-1}$. They suggested that it is the annealing effect that contributes to the increase in the melting point at the lower heating rates, whereas it is the instrumental thermal lag at the higher heating rates. A similar trend is also observed in the present study. This is the justification for the experiment to be conducted at the heating rate of $20^{\circ}\text{C}\cdot\text{min}^{-1}$.

Complete experimental data taken from crystallization exotherms and subsequent melting endotherms for all sPP samples are listed in Table 2-3. It is clearly seen, according to Table 2-3, that peak temperature values T_{mh} of the high-melting endotherms for all sPP samples are less dependent on the crystallization temperature than those T_{ml} of the low-melting ones. Furthermore, it is apparent that both enthalpy of crystallization ΔH_c and enthalpy of fusion ΔH_f increases with increasing T_c , whereas the difference between the two quantities decreases. For example, for sPP#1 the difference between ΔH_f and ΔH_c is as much as 20.4% at $T_c = 60^{\circ}\text{C}$, as opposed to 10.2% at $T_c = 95^{\circ}\text{C}$; and for sPP#5 it is 20.5% at $T_c = 70^{\circ}\text{C}$, as opposed to 16.2% at $T_c = 97.5^{\circ}\text{C}$. Along with the result shown in Figure 2-2, this suggests that the low-melting endotherms most likely are a result of the crystals formed at T_c , whereas the high-melting ones are a result of the recrystallization of metastable crystals melted in the course of the first melting peak. It also suggests that the once-molten crystals are less likely to recrystallize when T_c is increased. In addition, the temperature dependence of ΔH_f may, to some extent, account for the difference between ΔH_f and ΔH_c [18].

Based on the hypothesis drawn previously that the values of the low-melting peaks correspond to the melting of the crystals formed at a specified T_c , the T_m values listed in Table 2-3 are now considered as the melting points T_m of the samples crystallized at T_c . According to a theory derived by Hoffman and Weeks [10], the equilibrium melting temperature T_m^0 ; that is the melting temperature of infinitely extended crystals, can be obtained by linear extrapolation of T_m versus T_c data to the line $T_m = T_c$. Mathematically, they arrived at the following equation:

$$T_m = \frac{T_c}{2\beta} + T_m^0 \left[1 - \frac{1}{2\beta}\right], \quad (2-13)$$

where β is the "thickening ratio." In other words, β indicates the ratio of the thickness of the mature crystal l_c to that of the initial one l_c^* ; therefore, $\beta = l_c/l_c^*$, which is supposed to always be greater than or equal to 1. It should be noted that the factor 2 in Equation (2-13) suggests that the thickness of the crystals undergoing melting is approximately doubled that of the initial critical thickness.

Figure 2-3 shows the plots of T_m versus T_c for all sPP samples. It is evident that T_m values for all of the samples exhibit a linear relationship with T_c , at least in the temperature range of interest. The intersection of a least square line, fit to the data set for each sample, with the line $T_m = T_c$ provides the values of T_m^0 . The slope of the least square line, which equals 0.5β , can also be used to calculate the β parameter (i.e., $\beta = 0.5 \times \text{slope}^{-1}$). These values, along with the correlation coefficient, r^2 , of the fit, are reported in Table 2-4. The results show that the T_m^0 values lie between 146.1°C to 148.3°C (419.3 K to 421.4 K). The slopes of the least square lines range from 0.41 to 0.47, which agree extremely well with the published result by Balbontin et al. [19]. Derived from the slopes of the least square lines, the lamellar thickening parameter β is found to be roughly 1, which is in a very good agreement with other reports [13,19]. In addition, the value of β near 1 guarantees that the extrapolation is valid and gives a reliable T_m^0 value,

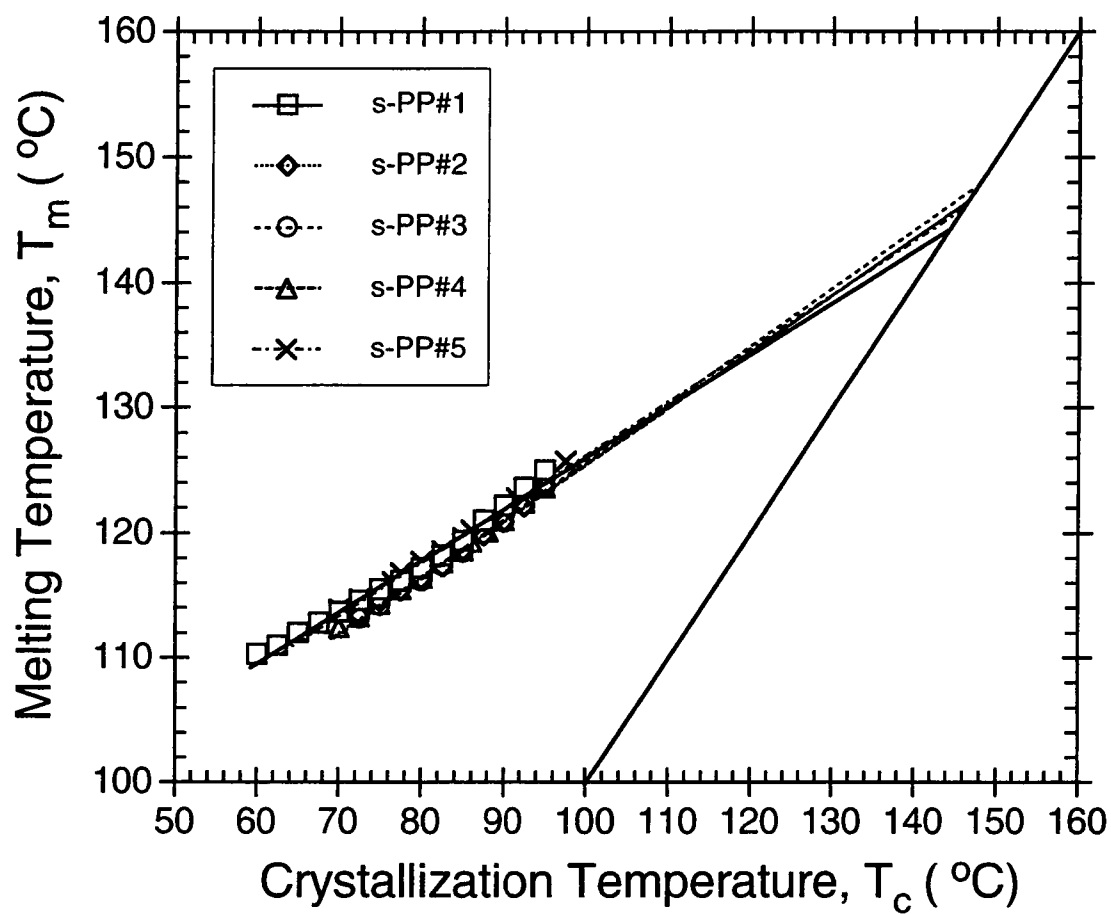


Figure 2-3. Melting temperatures as a function of crystallization temperatures for the sPP samples.

Table 2-4. Thermodynamic equilibrium melting points, β parameters, and corresponding calculated equilibrium melting points for 100% syndiotactic polypropylene samples.

Sample	[%rrrr]	[%rrr]	[%r]	T_m^0 (°C)	T_m^0 (K)	slope	β	r^2	$(T_m^0)_{100\%}$ (°C)	$(T_m^0)_{100\%}$ (K)
sPP#1	77.10	87.31	91.42	146.1	419.3	0.41	1.2	0.988	163.2	436.3
sPP#2	74.55	83.09	87.36	146.6	419.7	0.45	1.1	0.994	172.9	446.0
sPP#3	74.61	83.73	88.29	148.3	421.4	0.47	1.1	0.995	172.6	445.7
sPP#4	74.63	84.37	89.24	146.4	419.5	0.45	1.1	0.998	168.3	441.4
sPP#5	75.28	85.09	90.00	146.4	419.5	0.43	1.2	0.997	166.6	439.7

since the T_m values observed for different T_c values are not affected greatly by the annealing process.

There are a number of reported values of T_m^0 available in the literature [12,13,15-21]. These values scatter in a wide range, depending on the syndiotacticity level of the sample used. By lacking a common basis of reporting the degree of syndiotacticity, it is quite difficult to compare the reported values together. Recently, the level of NMR racemic pentads [%*rrrr*] has been used more frequently to represent the degree of syndiotacticity in sPP samples. Therefore, only those published T_m^0 values with known [%*rrrr*] will be reported with the syndiotacticity level in parentheses: they are 168°C (92%) [15], 160°C (86%) [16], 155°C to 170°C (87% to 95%) [17], 166°C (91%) [18], and 150°C to 186°C (89% to 95%) [19]. Comparing with these values, the result (146°C to 148°C) seems reasonable when considering that the syndiotacticity level lies in the range of 75% to 77%.

As can be seen, the observed T_m^0 values exhibit a strong correlation with the syndiotacticity in the samples. In an attempt to correlate the dependence of observed T_m^0 values as a function of syndiotacticity level, Miller [22] modified the original Flory theory for the depression of melting point in copolymers [23,24] to be used in this fashion, and it has been applied by several authors [12,17,19]. The model assumes that a sPP chain has a random arrangement of syndiotactic dyads, which are crystallizable, and isotactic ones, which are not. Mathematically, this model reads

$$\frac{1}{T_m^0} - \frac{1}{(T_m^0)_{100\%}} = -\left(\frac{R}{\Delta H_f^0}\right) \ln p_r, \quad (2-14)$$

where $(T_m^0)_{100\%}$ and ΔH_f^0 are the equilibrium melting temperature and the equilibrium enthalpy of fusion of a sPP with 100% syndiotacticity level, respectively. R is the gas constant, and p_r is the fraction of the monomer units which are syndiotactically bonded. In this case, p_r is substituted by the racemic dyads [%*r*].

According to Equation (2-14), $(T_m^0)_{100\%}$ can readily be calculated if all other variables are known. The only parameter which poses a problem with is ΔH_f^0 , due to the scattering in the reported values which range from 3.1 kJ·mol⁻¹ [12] to 8.3 kJ·mol⁻¹ [13]. Most recent studies have reported ΔH_f^0 values in the range of 7.7 kJ·mol⁻¹ [18] to 8.0 kJ·mol⁻¹ [16], which is very close to the value of 8.3 kJ·mol⁻¹ reported earlier by Haftka and Könnecke [13]. In this study, a ΔH_f^0 value of 8.0 kJ·mol⁻¹ (190.4 J·g⁻¹) is used in the calculation, the result of which is also listed as the last two columns in Table 2-4. According to Table 2-4, it is evident that $(T_m^0)_{100\%}$ ranges from 163.2°C to 172.9°C (436.3 K to 446.0 K), with the average value of $168.7 \pm 4.1^\circ\text{C}$ (441.8 ± 4.1 K). Reported values of $(T_m^0)_{100\%}$ in the literature are 220°C [12] and 214°C [19], which may be overestimated. Comparison of the $(T_m^0)_{100\%}$ values may lead to a misleading conclusion, since different authors often use different values of necessary parameters, especially those of p_r and ΔH_f^0 . Consequently, the $(T_m^0)_{100\%}$ values were re-calculated using $\Delta H_f^0 = 8.0$ kJ·mol⁻¹ based on data of known [%*r*] available in the literature [16,17,19]. The average calculated values of $(T_m^0)_{100\%}$ are $173.5 \pm 1.3^\circ\text{C}$ (for [16]), $165.0 \pm 5.1^\circ\text{C}$ (for [17]), and $173.6 \pm 10.9^\circ\text{C}$ (for [19]). Based on these values, the result seems very reasonable.

The $(T_m^0)_{100\%}$ values were also re-calculated using the ΔH_f^0 value of 8.3 kJ·mol⁻¹ (196.6 J·g⁻¹). The new $(T_m^0)_{100\%}$ values were found to lie in the range of 162.6°C to 172.0°C with the average value of $168.0 \pm 4.0^\circ\text{C}$ (441.1 ± 4.0 K). The $(T_m^0)_{100\%}$ values were also re-calculated based on the same data sets considered in the previous paragraph. The average recalculated values of $(T_m^0)_{100\%}$ are $173.1 \pm 1.0^\circ\text{C}$ (for [16]), $164.8 \pm 5.2^\circ\text{C}$ (for [17]), and $173.4 \pm 10.9^\circ\text{C}$ (for [19]). Based on these calculated values, it is possible to conclude that the lower the value of ΔH_f^0 used in the calculation, the higher the estimated $(T_m^0)_{100\%}$ value.

5.3. Overall Crystallization Kinetics

5.3.1. Avrami Analysis

As described previously, DSC is often used to follow the overall isothermal crystallization by measuring the heat flow released during the crystallization process, according to Equation (2-1). Combined with Equation (2-2), the relative crystallinity $\theta(t)$ as a function of reaction time t can be determined. Figure 2-4 illustrates relative crystallinity as a function of time for sPP#3 samples isothermally crystallized at T_c ranging from 80°C to 95°C. Based on the Avrami model [7] expressed as Equation (2-3), the data similar to those shown in Figure 2-4 can be analyzed according to the Avrami equation in its logarithmic form (i.e., Equation (2-4)). By performing a least square fit in the range of 10% to 80% relative crystallinity to the Avrami plots such as those shown as the inset figure in Figure 2-4, the Avrami exponent n and the rate constant k can readily be extracted. In practice, these kinetics parameters, together with Equation (2-3), can be used to simulate the crystallization process at a given T_c , as shown by the solid lines in Figure 2-4. The other important parameter is the half-time of crystallization $t_{0.5}$ which is the time taken from the onset of the crystallization until 50% completion, and can be extracted directly from the plot of $\theta(t)$ versus time t . Table 2-5 lists all of the kinetics results for all of the sPP samples.

Figure 2-5 shows the plots of the crystallization half-times and their reciprocal values against the crystallization temperature. It is evident that the rate of the crystallization falls in the following sequence: sPP#5 > sPP#3 > sPP#2 > sPP#4 > sPP#1, although sPP#2 seems to crystallize a little bit faster than sPP#3 at $T_c < 78^\circ\text{C}$. It is not possible, at least at this point, to find a reason why these sPP samples crystallize in that sequence. As is well known, there are a number of factors affecting the crystallization of polymers. They include stereoregularity, regioregularity, molecular weight, molecular weight distribution, kind and quantity of nucleation agent used, and

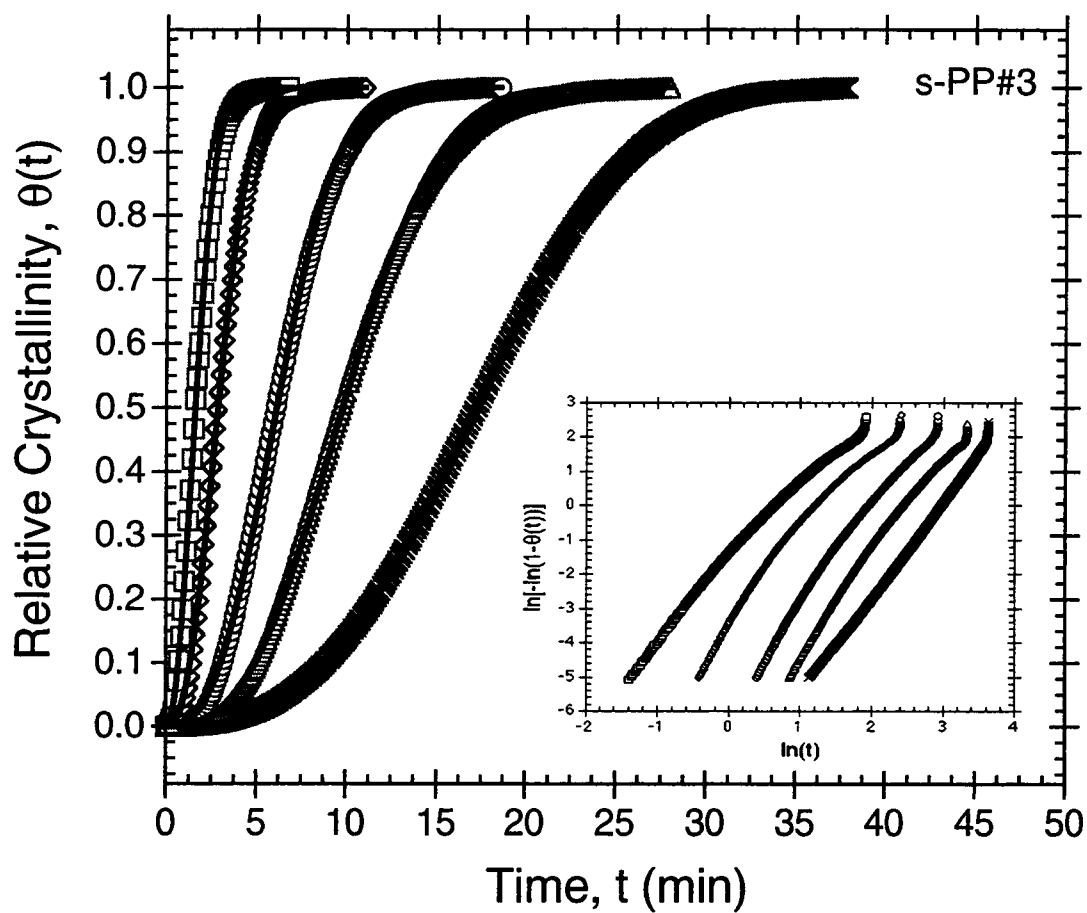


Figure 2-4. Relative crystallinity as a function of time, and typical Avrami plots shown as the inset figure for sample sPP#3, isothermally crystallized at the specified temperatures: (□) 80°C; (◇) 85°C; (○) 90°C; (△) 92.5°C; (×) 95°C.

Table 2-5. Overall crystallization kinetics data for syndiotactic polypropylene samples.

Sample T_c (°C)	sPP#1			sPP#2			sPP#3			sPP#4			sPP#5		
	$t_{0.5}$ (min)	n	k (min^{-n})	$t_{0.5}$ (min)	n	k (min^{-n})	$t_{0.5}$ (min)	n	k (min^{-n})	$t_{0.5}$ (min)	n	k (min^{-n})	$t_{0.5}$ (min)	n	k (min^{-n})
60.0	1.67	2.68	1.77×10^1	-	-	-	-	-	-	-	-	-	-	-	-
62.5	1.70	2.74	1.64×10^1	-	-	-	-	-	-	-	-	-	-	-	-
65.0	1.75	2.57	1.66×10^1	-	-	-	-	-	-	-	-	-	-	-	-
67.5	1.83	2.59	1.46×10^1	-	-	-	-	-	-	-	-	-	-	-	-
70.0	1.98	2.68	1.11×10^1	-	-	-	-	-	-	-	-	-	-	-	-
72.5	2.18	2.73	8.22×10^2	0.81	2.54	1.17	0.84	2.26	1.02	1.24	2.14	4.40×10^1	0.45	2.01	3.58
75.0	2.45	2.80	5.56×10^2	0.94	2.44	7.87×10^1	1.04	2.15	6.30×10^1	1.33	2.05	3.87×10^1	0.54	2.05	2.40
76.5	-	-	-	-	-	-	-	-	-	1.56	2.10	2.68×10^1	0.63	2.14	1.82
77.5	2.92	2.97	2.88×10^2	1.19	2.38	4.53×10^1	1.18	2.11	4.89×10^1	-	2.11	1.72×10^1	0.69	2.21	1.57
80.0	3.50	3.07	1.47×10^2	1.67	2.33	2.07×10^1	1.58	2.17	2.53×10^1	1.92	2.11	1.72×10^1	0.72	2.29	1.47
82.5	4.81	3.22	4.36×10^3	2.47	2.22	9.13×10^2	1.96	2.34	1.40×10^1	2.69	2.13	8.25×10^2	0.88	2.37	9.09×10^1
85.0	5.78	3.05	3.30×10^3	3.47	2.35	3.66×10^2	2.82	2.48	5.14×10^2	3.15	2.14	5.83×10^2	1.16	2.57	4.62×10^1
86.0	-	-	-	-	-	-	-	-	-	4.26	2.21	2.78×10^2	1.48	2.69	2.32×10^1
87.5	7.65	2.97	1.66×10^3	4.58	2.36	1.88×10^2	3.85	2.49	2.35×10^2	5.40	2.23	1.60×10^2	1.85	2.88	1.14×10^1
88.0	-	-	-	-	-	-	-	-	-	7.32	2.23	8.04×10^3	2.11	2.76	8.47×10^2
90.0	11.40	2.96	5.19×10^4	7.32	2.40	5.72×10^3	6.08	2.67	5.48×10^3	7.44	2.13	9.48×10^3	3.61	2.75	1.99×10^2
91.5	-	-	-	-	-	-	-	-	-	9.80	2.52	2.21×10^3	4.59	2.88	8.45×10^3
92.5	19.40	2.47	4.39×10^4	13.48	2.25	1.95×10^3	9.71	2.74	1.33×10^3	16.35	2.57	5.35×10^4	6.16	2.98	3.02×10^3
95.0	28.30	2.41	2.23×10^4	21.57	2.32	5.68×10^4	17.23	2.87	1.98×10^4	30.37	2.88	3.76×10^5	10.89	3.09	4.37×10^4
97.5	-	-	-	-	-	-	-	-	-	15.34	3.27	-	15.34	3.27	9.32×10^5

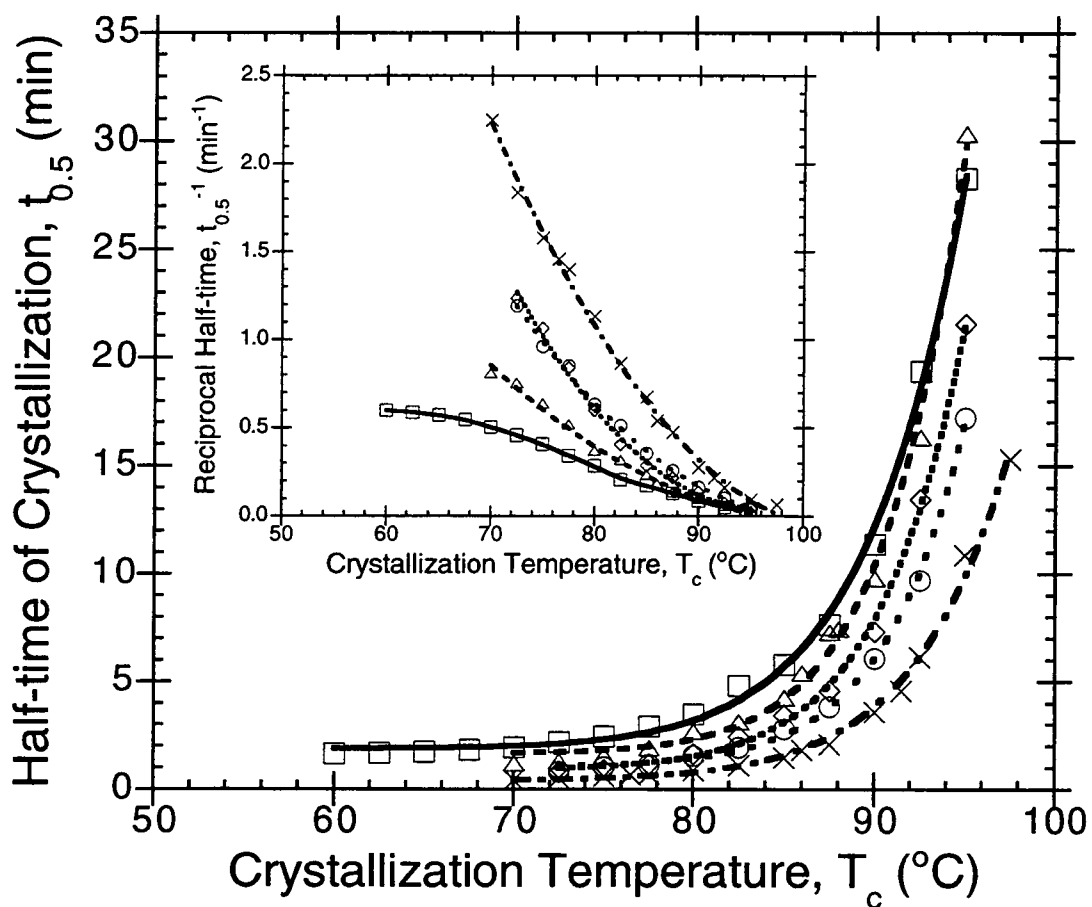


Figure 2-5. Half-time of crystallization as a function of crystallization temperatures. Reciprocal half-time is shown as a function of crystallization temperature in the inset figure. Keys: (□) sPP#1; (◇) sPP#2; (○) sPP#3; (△) sPP#4; (×) sPP#5.

presence of impurities. The crystallization behavior, in terms of growth rate and nucleation rate measurement, of these sPP samples will be investigated more extensively, and will be of future publication. With those results, it will then be possible to conclude with a higher level of confidence what is controlling the isothermal crystallization behavior of these sPP samples.

According to Table 2-5, the Avrami exponent n does not seem to exhibit a definite overall correlation with T_c , though samples sPP#3, sPP#4 and sPP#5 exhibit a slight gradual increase of n with an increase in crystallization temperature. For all of the sPP samples, n ranges from 2.01 to 3.27. More specifically, n ranges from 2.41 to 3.22 for sPP#1; from 2.22 to 2.54 for sPP#2; from 2.15 to 2.87 for sPP#3; from 2.05 to 2.88 for sPP#4; and finally from 2.01 to 3.27 for sPP#5. The result seems to fall in a comparable range of the values reported in the literature: they are 1.91 to 3.34 by Rodriguez-Arnold et al. [16], and 1.81 to 3.86 by Balbontin et al. [19]. Along with the plots of $t_{0.5}$ and $t_{0.5}^{-1}$ versus T_c as shown in Figure 2-5, the plot of the crystallization rate constant k shown in Figure 2-6, shows that sPP samples crystallize slower with an increase in T_c , at least in the range of T_c investigated. In an earlier paper [25], it is found that the plot of $t_{0.5}^{-1}$ (for sPP#1 sample) against T_c exhibits a double bell-shaped curve, while that of the linear growth rate against T_c shows the typical bell-shaped curve. Based on the growth rate theory [8,9], the bell-shaped curve can be described as a result of the nucleation control effect at high T_c (low undercooling, $\Delta T = (T_m^0)_{100\%} - T_c$), and diffusion control at low T_c (high ΔT). It is apparent according to the result shown in Figures 2-5 and 2-6 that, within the T_c range of interest, all of the sPP samples crystallize in the nucleation-controlled range.

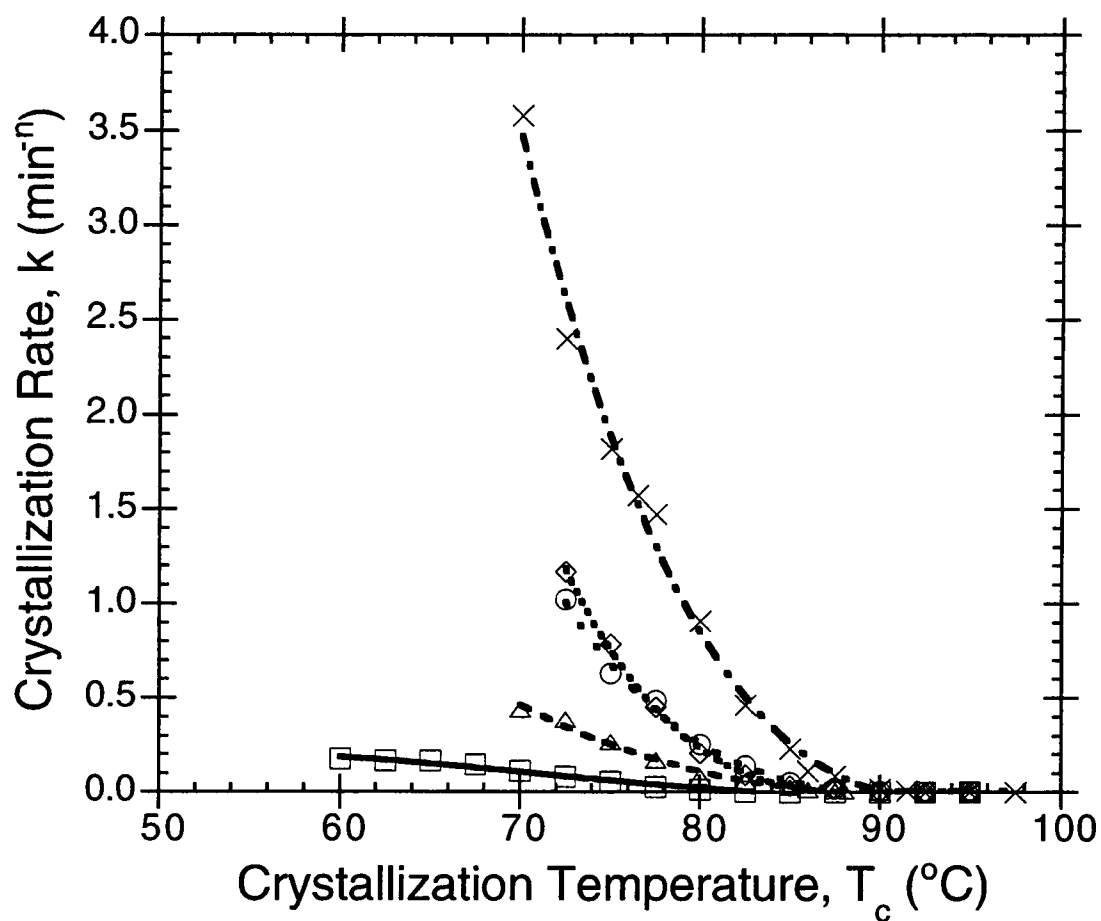


Figure 2-6. Avrami crystallization rate constant as a function of crystallization temperatures for the sPP samples: (\square) sPP#1; (\diamond) sPP#2; (\circ) sPP#3; (\triangle) sPP#4; (\times) sPP#5.

5.3.2. Regime Analysis

As discussed previously in the theoretical section, the growth rate theory [8,9] can also be tested by using t_0 values taken directly from the experimental data, obtained from the DSC experiments. At this moment, the relationship between the half-time of crystallization $t_{0.5}$ and crystallization temperature T_c is focused. Since a preliminary observation under a polarized light microscope suggested that all of the sPP samples crystallize mainly in a three dimensional, instantaneous fashion, within the T_c range of interest, construction of $\log(t_{0.5}^{-1}) + U^*/2.303R(T_c - T_\infty)$ versus $1/2.303T_c(\Delta T)f$, as shown in Figure 2-7 for all of the sPP samples, serves as the regime test. The parameters used are as follows: $T_\infty = 237$ K ($T_g = 267$ K), $(T_m^0)_{100\%} = 441.8$ K, and $U^* = 6,276$ J·mol⁻¹. It is apparent that the bulk of the data for all of the sPP samples fit a straight line, with the correlation coefficients r^2 of 0.998 or better. Since earlier reports [16,25-27] have suggested that the regime II→regime III transition should occur at $T_c \approx 110^\circ\text{C}$ (i.e., $\Delta T \approx 50^\circ\text{C}$), it is possible to conclude with a high level of confidence that the data, in the T_c range of interest, represent crystallization in regime III. From the slopes of the plots, the nucleation exponents K_g are found to range from 5.69×10^5 K² to 7.03×10^5 K².

Once K_g values have been determined, other parameters characteristic of crystal growth can be estimated. First, $\sigma\sigma_c$ can be calculated from Equation (2-8), provided that other parameters are known. By referring to Equation (2-8), the only unknown parameter is the layer thickness b_0 which can be estimated from the unit cell parameters. It is therefore imperative to know the crystallographic form and lattice dimensions of the sPP samples, crystallized in the temperature range of interest. Based on the WAXD results [28], it is obvious that all of the sPP samples crystallize in the high temperature orthorhombic form II (Cell II) as determined by Lotz and coworkers [29], especially when $T_c < 110^\circ\text{C}$. The unit cell of this orthorhombic modification occupies the space group $Pca2_1$, with the axis dimensions: $a = 14.50$ Å, $b = 5.60$ Å, and $c = 7.40$ Å. This

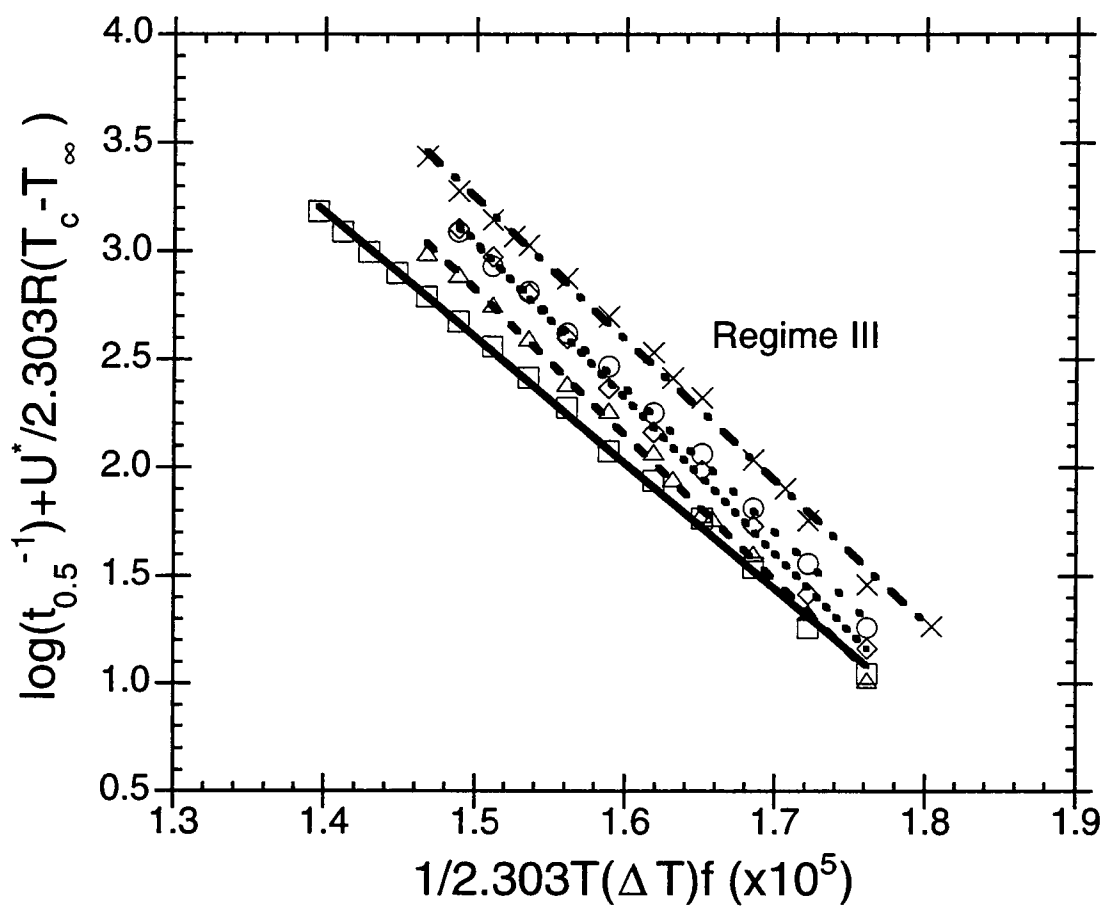


Figure 2-7. Analysis of the half-times of crystallization based on the modified growth rate theory for the sPP samples: (\square) sPP#1; (\diamond) sPP#2; (\circ) sPP#3; (\triangle) sPP#4; (\times) sPP#5.

structure is particularly characterized by the existence of helices of opposite hands with chain axes in $(0, 0, z)$ and $(\frac{1}{2}, 0, z)$.

By assuming that (010) or (200) is the growth plane, it is possible to estimate the molecular width a_0 and the layer thickness b_0 . At this point, it is possible to calculate the lateral and fold surface free energy, σ and σ_e , separately, but one first has to estimate the σ value based on the modified Thomas-Staveley equation [30]:

$$\sigma = \alpha \Delta H_f^0 \sqrt{a_0 b_0}, \quad (2-15)$$

where $a_0 b_0$ is a cross-sectional area of one chain molecule, and α is a universal parameter related to the chemical nature of the polymer, and often taken to be 0.1. Now, the fold surface free energy σ_e can be calculated from $\sigma \sigma_e / \sigma$ (cf. $\sigma \sigma_e$ is evaluated from K_g according to Equation (2-8)). Once the σ_e parameter has been calculated, the average work of chain folding \bar{q} which is defined as

$$\bar{q} = 2a_0 b_0 \sigma_e, \quad (2-16)$$

can also be calculated. All of the input parameters necessary for the calculation based on the growth rate theory and the results of the calculation for all of the sPP samples are listed separately in Tables 2-6 and 2-7.

According to Table 2-6, the lateral surface free energy σ is estimated to be 11.3 erg·cm⁻² (mJ·m⁻²) for both (010) and (200) growth planes. This value is in a good agreement with the reported value of 11 erg·cm⁻² by Rodriguez-Arnold et al. [27], and this value is also close to those estimated for isotactic polypropylene (iPP) and polyethylene (HDPE) [26], which are 11.5 erg·cm⁻² and 11.1 erg·cm⁻² to 14.1 erg·cm⁻², respectively. According to the last four columns in Table 2-7 where the half-time of crystallization $t_{0.5}$ was used in the analysis of the regime crystallization, the fold surface free energy σ_e lies in the range of 124.5 erg·cm⁻² to 153.9 erg·cm⁻² when assuming that (010) is the growth plane, and 96.2 erg·cm⁻² to 118.9 erg·cm⁻² when assuming that (200) is

Table 2-6. Input parameters for calculation of parameters characteristic of crystal growth.

Parameter	Value	Remarks
Heat of fusion, ΔH_f^0	$1.77 \times 10^9 \text{ erg}\cdot\text{cm}^{-3}$	Ref. 16 and Ref. 29
Glass transition temperature, T_g	-6.1°C or 267.0 K	This work
Equilibrium melting temperature, $(T_m^0)_{100\%}$	168.7°C or 441.8 K	This work
Boltzmann's constant, k	$1.380 \times 10^{-16} \text{ erg}\cdot\text{molecule}^{-1}\cdot\text{K}^{-1}$	
	For (010) growth plane	
Molecular width, a_0	$7.25 \times 10^{-8} \text{ cm}$	Estimated from Ref. 29
Layer thickness, b_0	$5.60 \times 10^{-8} \text{ cm}$	Estimated from Ref. 29
Cross-sectional area of chain, $a_0 b_0$	$4.06 \times 10^{-15} \text{ cm}^2$	Estimated from Ref. 29
Lateral surface free energy, σ	$11.3 \text{ erg}\cdot\text{cm}^{-2}$	From $\sigma = 0.1 \Delta H_f^0 (a_0 b_0)^{0.5}$
	For (200) growth plane	
Molecular width, a_0	$5.60 \times 10^{-8} \text{ cm}$	Estimated from Ref. 29
Layer thickness, b_0	$7.25 \times 10^{-8} \text{ cm}$	Estimated from Ref. 29
Cross-sectional area of chain, $a_0 b_0$	$4.06 \times 10^{-15} \text{ cm}^2$	Estimated from Ref. 29
Lateral surface free energy, σ	$11.3 \text{ erg}\cdot\text{cm}^{-2}$	From $\sigma = 0.1 \Delta H_f^0 (a_0 b_0)^{0.5}$

Table 2-7. Analysis of the crystallization times t_0 based on the modified growth rate theory.

Sample	$t_{0.1}$		$t_{0.2}$		$t_{0.5}$	
	K_g (K^2)	$\sigma\sigma_e$ ($\text{erg}^2\text{-cm}^{-4}$)	K_g (K^2)	$\sigma\sigma_e$ ($\text{erg}^2\text{-cm}^{-4}$)	K_g (K^2)	$\sigma\sigma_e$ ($\text{erg}^2\text{-cm}^{-4}$)
sPP#1	5.80×10^5	1433.6	5.82×10^5	1438.2	5.69×10^5	1405.3
sPP#2	7.11×10^5	1755.0	7.13×10^5	1759.7	7.03×10^5	1737.1
sPP#3	7.00×10^5	1728.4	6.86×10^5	1694.1	6.49×10^5	1603.5
sPP#4	6.99×10^5	1726.1	6.89×10^5	1701.7	6.57×10^5	1623.0
sPP#5	7.01×10^5	1731.1	6.81×10^5	1682.1	6.40×10^5	1580.8
			For (010) growth plane			
sPP#1	5.80×10^5	1107.3	5.82×10^5	1110.9	5.69×10^5	1085.5
sPP#2	7.11×10^5	1355.6	7.13×10^5	1359.2	7.03×10^5	1341.8
sPP#3	7.00×10^5	1335.0	6.86×10^5	1308.5	6.49×10^5	1238.6
sPP#4	6.99×10^5	1333.2	6.89×10^5	1314.4	6.57×10^5	1253.6
sPP#5	7.01×10^5	1337.1	6.81×10^5	1299.3	6.40×10^5	1221.0
			For (200) growth plane			
sPP#1	5.80×10^5	98.1	5.82×10^5	98.4	5.69×10^5	96.2
sPP#2	7.11×10^5	120.1	7.13×10^5	120.4	7.03×10^5	118.9
sPP#3	7.00×10^5	118.3	6.86×10^5	116.0	6.49×10^5	109.8
sPP#4	6.99×10^5	118.1	6.89×10^5	116.5	6.57×10^5	111.1
sPP#5	7.01×10^5	118.5	6.81×10^5	115.1	6.40×10^5	108.2
			\bar{q} ($\text{kcal}\cdot\text{mol}^{-1}$)	σ_e ($\text{erg}\cdot\text{cm}^{-2}$)	\bar{q} ($\text{kcal}\cdot\text{mol}^{-1}$)	σ_e ($\text{erg}\cdot\text{cm}^{-2}$)
sPP#1		14.8	14.9	127.5	14.9	124.5
sPP#2		18.2	18.2	155.9	18.2	153.9
sPP#3		17.9	17.5	150.1	17.5	142.1
sPP#4		17.9	17.6	150.8	17.6	143.8
sPP#5		17.9	17.4	149.1	17.4	140.1
sPP#1		11.5	11.5	98.4	11.5	96.2
sPP#2		14.0	14.1	120.4	14.1	118.9
sPP#3		13.8	13.6	116.0	13.6	109.8
sPP#4		13.8	13.6	116.5	13.6	111.1
sPP#5		13.9	13.5	115.1	13.5	108.2
			\bar{q} ($\text{kcal}\cdot\text{mol}^{-1}$)	σ_e ($\text{erg}\cdot\text{cm}^{-2}$)	\bar{q} ($\text{kcal}\cdot\text{mol}^{-1}$)	σ_e ($\text{erg}\cdot\text{cm}^{-2}$)
sPP#1		14.6	14.9	124.5	14.9	124.5
sPP#2		18.0	18.2	153.9	18.2	153.9
sPP#3		16.6	17.5	150.1	17.5	142.1
sPP#4		16.8	17.6	150.8	17.6	143.8
sPP#5		16.4	17.4	149.1	17.4	140.1

the growth plane. The work of chain folding \bar{q} was also calculated, and was found to be in the range of 14.6 kcal·mol⁻¹ to 18.0 kcal·mol⁻¹ when assuming that (010) is the growth plane, and 11.2 kcal·mol⁻¹ to 13.9 kcal·mol⁻¹ when assuming that (200) is the growth plane.

Since these values seem rather high when comparing to the values estimated ($\sigma_e = 49.9$ erg·cm⁻² and $\bar{q} = 5.8$ kcal·mol⁻¹) by Clark and Hoffman [26], and the reported values ($\sigma_e = 42-47$ erg·cm⁻² and $\bar{q} = 4.8-5.7$ kcal·mol⁻¹) by Rodriguez-Arnold et al. [27], it now becomes questionable whether or not the calculation was correct. An attempt to confirm the correctness of the calculation was done by re-evaluating the available growth rate data (for sPP#1) [25] and those by Miller and Seeley [12] using the same input parameters as used in this study, and found that, evaluated from growth data, σ_e lies in the range of 75.8 erg·cm⁻² to 85.8 erg·cm⁻² when assuming that (010) is the growth plane, and 54.6 erg·cm⁻² to 61.7 erg·cm⁻² when assuming that (200) is the growth plane. Likewise, \bar{q} was found to be in the range of 8.9 kcal·mol⁻¹ to 10.0 kcal·mol⁻¹ when assuming that (110) is the growth plane, and 6.4 kcal·mol⁻¹ to 7.2 kcal·mol⁻¹ when assuming that (200) is the growth plane. These values indicate that there should be nothing wrong with the calculation procedure in the present study. The discrepancy between the growth parameters analyzed from the bulk kinetics and those from the growth kinetics may result from the fact that the bulk kinetics also includes the nucleation kinetics, which is totally ignored when growth kinetics was analyzed.

Table 2-7 summarizes the growth parameters analyzed from crystallization times at 10% and 20% relative crystallinity, $t_{0.1}$ and $t_{0.2}$, respectively. The results seem to decrease in value corresponding to the crystallization times, t_θ , in the following order: $t_{0.1} > t_{0.2} > t_{0.5}$.

5.3.3. Construction of Crystallization Rate Function

Measurement of the crystallization times t_0 is not always possible especially in the lower crystallization temperature range. According to the growth theory, crystallization of polymers at low temperatures or high degrees of undercooling usually occurs in regime III. If the crystallization time data in this temperature range are available, they can be used to estimate the crystallization time values at other temperatures. This can be done by the use of Equation (2-10), which states the relationship of the reciprocal value of the crystallization time and the temperature. Provided that T_m^0 and T_g are known, the only unknown parameters are A_1G_0 and K_g , which can readily be obtained from the regime plot where A_1G_0 is the anti-logarithmic value of the y-intercept ($A_1G_0 = 10^{(\text{y-intercept value})}$) and K_g is the negative value of the slope ($K_g = -\text{slope}$). This can be demonstrated by taking the case of sPP#1 as an example.

According to the regime plot (analyzed for the half-time data) of the sPP#1 sample, the values of A_1G_0 and K_g are 2.06×10^{11} and 5.69×10^5 , respectively. Substitution of these values into Equation (2-10) leads to the expression of the half-time of crystallization as a function of temperature:

$$(t_{0.5}^{-1})_{\text{III}} (\text{min}^{-1}) = 2.06 \times 10^{11} \exp\left(-\frac{754.83}{(T_c - T_\infty)} - \frac{5.69 \times 10^5}{T_c(\Delta T)f}\right). \quad (2-17)$$

The expressions of crystallization times as a function of temperature for all of the samples can also be obtained in the similar fashion as shown above. Figure 2-8 shows both the experimental and predicted values of the reciprocal half-times as a function of temperature for all of the sPP samples. Apparently, the maxima in all of the plots occur near 60°C.

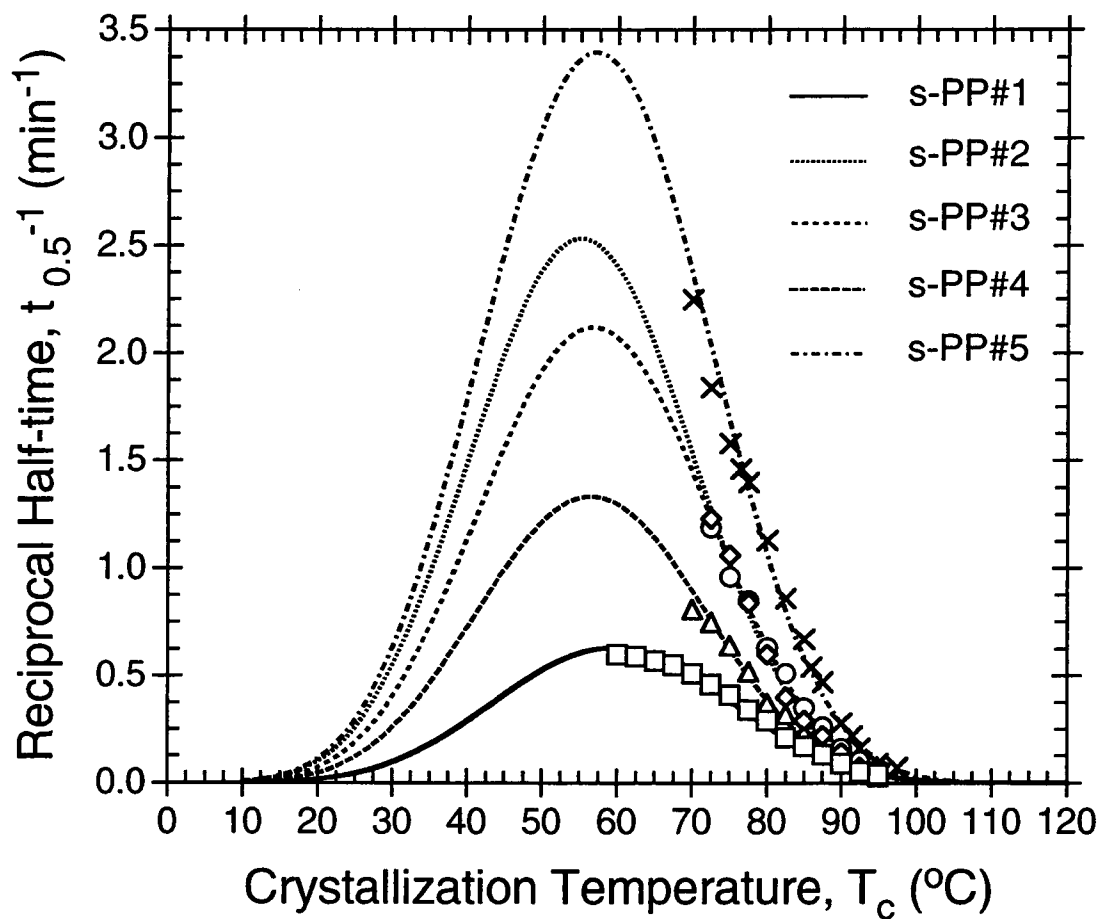


Figure 2-8. Reciprocal half-times as a function of crystallization temperature for the sPP samples showing the comparison to the calculated curves based on Equation (2-10) (lines): (\square) sPP#1; (\diamond) sPP#2; (\circ) sPP#3; (\triangle) sPP#4; (\times) sPP#5.

5.3.4. Kinetic Crystallizability

The temperature dependence of the crystallization half-times was introduced as early as in 1967 by Ziabicki [31-33] and can be described by a Gaussian function of the form:

$$t_{0.5}^{-1} = (t_{0.5})_{\min}^{-1} \exp\left[-4 \ln 2 \frac{(T_c - T_{\max})^2}{D^2}\right], \quad (2-18)$$

where T_{\max} is the temperature where the crystallization is the maximum, $(t_{0.5})_{\min}$ the crystallization half-time at T_{\max} , and D the half-width of the crystallization rate (the reciprocal value of the crystallization half-time) curve. With use of the isokinetic approximation, integration of Equation (2-18) over the whole range of temperatures in which crystallization may occur ($T_g < T < T_m^0$) leads to an important characteristic value describing the crystallization ability of the polymer, namely the kinetic crystallizability κ^2 :

$$\int_{T_g}^{T_m^0} t_{0.5}^{-1}(T) dT \approx \frac{1.064D}{(t_{0.5})_{\min}} = \kappa^2. \quad (2-19)$$

In practice, T_{\max} , $(t_{0.5})_{\min}$, and D may be measured from a curve such as that shown in Figure 2-8. Table 2-8 lists the T_{\max} , $(t_{0.5})_{\min}$, D , and κ^2 values for all of the sPP samples. The characteristic values of some other polymers [33] are also listed for comparison. The practical meaning of the G parameter is to characterize the ability of the polymer in crystallizing when it is cooled from the melting temperature to the glass transition temperature at a constant cooling rate [33]. The higher the κ^2 values, the more readily the polymer crystallizes. Based on the κ^2 values listed in Table 2-8, the crystallization ability of the sPP samples falls in the following order: sPP#5 > sPP#2 > sPP#3 > sPP#4 > sPP#1. When comparing with some other polymers listed in Table 2-8, the crystallization ability of these polymers fall in the following sequence: Nylon 66 > iPP > Nylon 6 > sPP > iPS.

Table 2-8. Kinetic characteristics of syndiotactic polypropylene samples and some other polymers.

	T_m^0 (°C)	T_g (°C)	T_{max} (°C)	$(t_{0.5})_{min}$ (sec)	D (°C)	κ^2 (°C·sec ⁻¹)
sPP#1	146.1	-6.1	60.0	95.2	36.9	0.41
sPP#2	146.6	-6.0	55.0	23.7	34.7	1.56
sPP#3	148.3	-6.5	57.0	28.3	35.6	1.34
sPP#4	146.4	-5.6	56.5	45.0	35.5	0.84
sPP#5	146.4	-6.5	57.0	17.7	35.6	2.14
iPS ^{a)}	240	100	170	185	40	0.16
Nylon 6 ^{a)}	228	45	146	5	46	6.8
Nylon 66 ^{a)}	264	45	150	0.42	80	139
iPP ^{a)}	180	-20	65	1.25	60	35

^{a)} Data taken from Table 2.5 in reference 33

6. CONCLUSIONS

The average glass transition temperature for all of the sPP samples used was determined to be $-6.1 \pm 0.4^\circ\text{C}$ (267.0 ± 0.4 K). Observation of subsequent melting of the sPP samples after isothermal crystallization at specified crystallization temperatures showed the existence of two endotherms whose position on the temperature axis and heat absorbed depended significantly on the crystallization temperature and the heating rate used. The result suggested that, at least in the crystallization range of interest (from 60°C to 97.5°C), the low-melting endotherms correspond to the melting of crystalline aggregates formed at specified crystallization temperature, whereas the high-melting ones are the result of the melting of crystalline aggregates which formed by recrystallization during heating. The typical Hoffman-Weeks extrapolation suggested that the equilibrium melting temperature T_m^0 lies in the range of 146.1°C to 148.3°C (419.3 K to 421.4 K). Finally, the equilibrium melting temperature of 100% syndiotacticity (T_m^0)_{100%} was estimated to be $168.7 \pm 4.1^\circ\text{C}$ (441.8 ± 4.1 K), which is the average value determined from the sPP samples studied.

The half-times of crystallization $t_{0.5}$ revealed that the rate of the crystallization for all of the sPP samples is in the following order: sPP#5 > sPP#3 > sPP#2 > sPP#4 > sPP#1. The Avrami index n does not seem to have a significant relationship with the crystallization temperature, at least in the temperature range of interest, and ranges from 2.01 to 3.27. The crystallization rate constant k agrees extremely well with what was observed by the half-time of crystallization. The plot of $\log(t_0^{-1}) + U^*/2.303R(T_c - T_\infty)$ against $1/2.303T_c(\Delta T)f$, serving as a regime test based on the growth rate theory, for t_0 at $\theta = 0.10, 0.20,$ and 0.50 clearly showed straight lines for all of the sPP samples. It was assumed that sPP samples crystallize in Regime III within the studied temperature range (60°C to 97.5°C).

The ability of the sPP samples to crystallize was determined by the kinetic crystallizability parameters κ^z which ranges from $0.41^\circ\text{C}\cdot\text{sec}^{-1}$ to $2.14^\circ\text{C}\cdot\text{sec}^{-1}$. Based on this parameter, the crystallizability of all of the sPP samples is in the following sequence: sPP#5 > sPP#2 > sPP#3 > sPP#4 > sPP#1. Comparison with some other polymers reveals that syndiotactic polypropylene crystallizes much slower than Nylon 6, isotactic polypropylene, and Nylon 66, while it crystallizes faster than isotactic polystyrene.

7. REFERENCES

- [1] K. Ziegler, E. Holzkamp, H. Breil, and H. Martin, *Angew. Chem.*, **67**, 541 (1955).
- [2] G. Natta, *J. Polym. Sci.*, **16**, 143 (1955).
- [3] G. Natta, P. Pino, P. Corradini, F. Danusso, E. Mantica, G. Mazzanti, and G. Moraglio, *J. Am. Chem. Soc.*, **77**, 1708 (1955).
- [4] G. Natta, I. Pasquon, and A. Zambelli, *J. Am. Chem. Soc.*, **84**, 1488 (1962).
- [5] J. Boor, Jr., and E.A. Youngman, *J. Polym. Sci., Polym. Chem.*, **4**, 1861 (1966).
- [6] J.A. Ewen, R.L. Johns, A. Razavi, and J.D. Ferrara, *J. Am. Chem. Soc.*, **110**, 6255 (1988).
- [7] M. Avrami, *J. Chem. Phys.*, **7**, 1103 (1939); *ibid.*, **8**, 212 (1940); *ibid.*, **9**, 177 (1941).
- [8] J.D. Hoffman, G.T. Davis, and J.I. Lauritzen, Jr., In *Treatise on Solid State Chemistry*, Vol. 3, N.B. Hannay (Ed.), Plenum Press, New York, 1976, Chapter 7.
- [9] J.D. Hoffman, *Polymer*, **24**, 3 (1983).
- [10] J.D. Hoffman and J.J. Weeks, *J. Res. Nat'l. Bur. Stand.*, **A66**, 13 (1962).
- [11] V.B.F. Mathot, In *Calorimetry and Thermal Analysis of Polymers*, Carl Hanser Verlag, Munich, 1994, p. 173.
- [12] R.L. Miller and E.G. Seeley, *J. Polym. Sci., Polym. Phys.*, **20**, 2297 (1982).
- [13] S. Haftka and K. Könnecke, *J. Macromol. Sci., Phys.*, **B30(4)**, 319 (1991).
- [14] A. Eckstein, C. Friedrich, A. Lobbrecht, R. Spitz, and R. Mülhaupt, *Acta Polymer.*, **48**, 41 (1997).
- [15] A. Marigo, C. Marega, R. Zannetti, A. Celli, and G. Paganetto, *Macromol. Rapid Commun.*, **15**, 225 (1994).
- [16] J. Rodriguez-Arnold, A. Zhang, S.Z.D. Cheng, A.J. Lovinger, E.T. Hsieh, P. Chu, T.W. Johnson, K.G. Honnell, R.G. Geerts, S.J. Palackal, G.R. Hawley, and M.B. Welch, *Polymer*, **35(9)**, 1884 (1994).
- [17] H. Uehara, Y. Yamazaki, C. Otake, and T. Kanamoto, *Kobunshi Ronbunshu*, **51(9)**, 597 (1994).
- [18] J. Schmidtke, G. Strobl, and T. Thurn-Albrecht, *Macromolecules*, **30**, 5804 (1997).
- [19] G. Balbontin, D. Dainelli, M. Galimberti, and G. Paganetto, *Makromol. Chem.*, **193**, 693 (1992).
- [20] J. Boor, Jr., and E.A. Youngman, *J. Polym. Sci., Polym. Lett.*, **3**, 577 (1965).
- [21] E.A. Youngman and J. Boor, Jr., *Macromol. Rev.*, **2**, 33 (1967).
- [22] R.L. Miller, *J. Polym. Sci.*, **57**, 975 (1962).
- [23] P.J. Flory, *J. Chem. Phys.*, **17**, 223 (1949).
- [24] P.J. Flory, *Trans. Faraday Soc.*, **51**, 848 (1955).
- [25] P. Supaphol, J.-J. Hwu, P.J. Phillips, and J.E. Spruiell, *SPE-ANTEC Proc.*, 1759 (1997).
- [26] E.J. Clark and J.D. Hoffman, *Macromolecules*, **17**, 878 (1984).

- [27] J. Rodriguez-Arnold, Z. Bu, S.Z.D. Cheng, E.T. Hsieh, T.W. Johnson, R.G. Geerts, S.J. Palackal, G.R. Hawley, and M.B. Welch, *Polymer*, **35**(24), 5194 (1994).
- [28] P. Supaphol and J.E. Spruiell, *in preparation*.
- [29] B. Lotz, A.J. Lovinger, and R.E. Cais, *Macromolecules*, **21**, 2375 (1988).
- [30] D.G. Thomas and L.A.K. Staveley, *J. Chem. Soc.*, 4569 (1952).
- [31] A. Ziabicki, *Appl. Polym. Symp.*, **6**, 1 (1967).
- [32] A. Ziabicki, *Polymery*, **12**, 405 (1967).
- [33] A. Ziabicki, In *Fundamentals of Fiber Spinning*, John Wiley & Sons, New York, 1976, page 112-114.

PART 3:
REGIME CRYSTALLIZATION IN SYNDIOTACTIC
POLYPROPYLENES: RE-EVALUATION OF THE LITERATURE DATA

1. ABSTRACT

The Lauritzen and Hoffman secondary nucleation theory was applied to linear growth rate data of syndiotactic polypropylene taken from the literature. Observation of the distinctive upward change of slope in plots of $\log G + U^*/2.303R(T_c - T_\infty)$ versus $1/2.303T_c(\Delta T)f$ suggested the regime II→III transition at the crystallization temperature of 110°C. Based on the input parameters judged to be the most accurate, the ratios of $K_{g,III}/K_{g,II}$ were found to range from 1.7 to 2.2. Regardless of the crystal structure, if the growth is assumed to occur on the *bc* plane, the lateral surface free energy $\sigma = 11.3$ erg·cm⁻² and the fold surface free energy $\sigma_e = 63.7 \pm 7.1$ erg·cm⁻² were found. The latter leads to the average work of chain folding of $\bar{q} = 7.4 \pm 0.8$ kcal·mol⁻¹. If the growth is assumed to occur on the *ac* plane, the fold surface free energy is found to be $\sigma_e = 82.4 \pm 9.1$ erg·cm⁻², while the lateral surface free energy is the same as previously noted. In this case, the work of chain folding of $\bar{q} = 9.6 \pm 1.1$ kcal·mol⁻¹ is found. These values are applicable to both regimes II and III. A detailed evaluation of the effects of changes in input parameters was also carried out.

2. INTRODUCTION

The polymer crystal growth or secondary nucleation kinetics theory introduced by Lauritzen and Hoffman [1-3] (i.e., the LH secondary nucleation theory) has been developed and revised repeatedly in subsequent publications essentially by Hoffman and his co-workers [4-10]. The theory suggests that polymers crystallize in three different regimes, as opposed to the classical theory of secondary nucleation in which the deposition of a single nucleus on a growth face is followed by a rapid lateral spreading process. The simplest way of understanding regime crystallization is to envisage the growth process as being composed of two different processes. The first is the deposition of the secondary nucleus on the growth face, while the second is the

lateral spreading of polymer chains or segments of the chains across the growth face. Regime I is very similar to the notion of the classical theory in which the lateral spreading rate is much greater than that of the surface nucleation rate. Regime II is observed when the rates of the two processes are comparable, and Regime III occurs when the rate of secondary nucleation is greater than that of the lateral spreading.

Fundamentally, a regime transition is observed as a break in the growth rate data with respect to the crystallization temperature or, to be exact, the degree of undercooling. In the highest temperature regime, where regime I is observed, the growth rate G is directly proportional to the secondary nucleation rate i (i.e., $G \propto i$). At moderate undercoolings, where regime II is observed, multiple surface nucleation occurs on a growth face, resulting in growth rate being dependent on the square root of the secondary nucleation rate (i.e., $G \propto \sqrt{i}$). As the undercooling is further decreased, multiple surface nucleation becomes so prolific that the niche separation approaches the size of a single stem, and the dependence of the growth rate and the surface nucleation rate switches back to that of regime I (i.e., $G \propto i$). Due to the relationship of the growth rate on the secondary nucleation rate in all three regimes, it is obvious that one should observe a downward break in the growth rate data at the point where the regime I→II transition occurs, and an upward break where regime II→III transition occurs.

Based on the growth rate studies in various laboratories, the presence of a regime I→II transition has been observed in polyethylene [4], and poly(L-lactic acid) [11]. Regime II→III transitions have been observed in polyethylene [6], isotactic polypropylene (iPP) [7], and poly(oxymethylene) [12]. The appearance of all of the three regimes was first observed in the studies of fractions of *cis*-polyisoprene by Phillips and Vatansever [13]. Recently, regime crystallization kinetics in polyethylene was discussed in a great deal of detail both theoretically and experimentally by Hoffman and Miller [10]. In the case where the growth rate data is not available or is too time-consuming to

obtain, the overall crystallization rate (denoted t_{θ}^{-1} : the reciprocal value of the time taken from the onset of the crystallization process to reach a certain value of relative crystallinity θ), obtained directly from the bulk crystallization, can also be used to observe regime crystallization in polymers. This type of study has been applied in various polymer systems, such as polyethylene [14,15], and crosslinked polyethylene [16].

Miller and Seeley [17,18] were the first group to conduct spherulitic growth rate measurements on syndiotactic polypropylene (sPP). They studied a sample having racemic dyad concentration of 71.7% over the crystallization temperature range of 97.4°C to 137.3°C. By assuming that the sPP crystallized in regime II, and using values of the glass transition temperature T_g , the equilibrium melting temperature T_m^0 , and the enthalpy of fusion ΔH_f^0 , of 0°C, 161°C and 3.14 kJ·mol⁻¹, respectively, the lateral and fold surface free energies, σ and σ_e , were estimated to be 4.4 erg·cm⁻² (1 erg·cm⁻² = 1 mJ·m⁻²) and 58 erg·cm⁻², respectively. They also calculated the average work of chain folding \bar{q} to be 6.8 kcal·mol⁻¹. Later in 1984, Clark and Hoffman [7] re-examined the growth rate data published by Miller and Seeley [17,18], and estimated σ_e to be 49.9 erg·cm⁻² and \bar{q} to be 5.8 kcal·mol⁻¹, using the same value of T_m^0 . They also suggested that a regime II→regime III transition should occur somewhere in the crystallization temperature range of 110°C to 115°C, or at the undercooling ΔT of around 50°C. It was not clear, however, how they came up with these estimates.

In 1994, Rodriguez-Arnold and her co-workers [19] performed a spherulitic growth rate measurement on two fractions of sPP samples with racemic pentads [%rrrrr] in the range of 86% to 87%. They indeed found a discontinuity in the growth rate data at the crystallization temperature T_c of 110°C. Since T_m^0 of these two fractions were estimated to be 160°C, this results in the regime II→III transition at the undercooling of

50°C, similar to the value estimated by Clark and Hoffman [7]. Based on their earlier value of ΔH_f^0 for 100% crystallinity of 8.0 kJ·mol⁻¹ [20], and T_g of 0°C [17], they estimated that σ is approximately 11.2 erg·cm⁻², σ_e being in the range of 42.2 erg·cm⁻² to 47.7 erg·cm⁻², and \bar{q} being between 4.9 kcal·mol⁻¹ and 5.6 kcal·mol⁻¹ [19,21]. Recently, it has been confirmed [22] that a spherulitic growth rate measurement on a sPP sample of 77.1% syndiotacticity (racemic pentads) over the temperature range of 45°C to 125°C. The result also confirmed that the regime II→III transition in sPP occurs at $T_c = 110^\circ\text{C}$. However, calculation of the parameters characteristic of the growth theory was not carried out.

It is known that the parameters characteristic of the growth theory (e.g., σ , σ_e , and \bar{q}) are very sensitive to the input parameters used to calculate them (e.g., T_g , T_m^0 , and ΔH_f^0). Comparison of these growth parameters obtained from different authors may lead to an ambiguous conclusion, since often times they used different input parameters. In this study, these published spherulitic growth rate data [17,18,22,23] are re-analyzed, and all the parameters characteristic of the growth theory are re-evaluated using the same input parameters. The sensitivity of crystal growth parameters (e.g., σ , σ_e , and \bar{q}) to changes in the input parameters (e.g., T_g , T_m^0 , and ΔH_f^0) is also examined.

3. THEORETICAL BACKGROUND

In the context of the LH secondary nucleation theory [1-10], the linear growth rate G of a crystalline aggregate (e.g., spherulite or axialite) for each regime is dependent on the degree of undercooling ΔT and is defined by the following equation:

$$G = G_0 \exp\left(-\frac{U^*}{R(T_c - T_\infty)} - \frac{K_g}{T_c(\Delta T)f}\right), \quad (3-1)$$

where G_0 is a preexponential term which is not strongly dependent on temperature. U^* is the activation energy for the transportation of segments of molecules across the

melt/solid surface boundary and usually given by a universal value of $1500 \text{ cal}\cdot\text{mol}^{-1}$, T_c is the crystallization temperature, T_∞ is the temperature where the molecular motion ceases (i.e., $T_\infty = T_g - 30$), R is the universal gas constant, ΔT is the degree of undercooling (i.e., $\Delta T = T_m^0 - T_c$), and f is a factor used to correct for the temperature dependence of the heat of fusion (i.e., $f = 2T_c/(T_c + T_m^0)$). K_g is the nucleation exponent, and is defined as

$$K_g = \frac{j b_0 \sigma \sigma_c T_m^0}{k \Delta H_f^0}, \quad (3-2)$$

where j equals 2 for regime II and 4 for regimes I and III, b_0 denotes the crystal layer thickness along the growth direction, σ and σ_c are the lateral and fold surface free energy, respectively, T_m^0 is the equilibrium melting temperature, k is the Boltzmann's constant, and ΔH_f^0 is the equilibrium heat of fusion.

Referring to Equation (3-1), the first exponential term, $\exp(-U^*/R(T_c - T_\infty))$, corresponds to the diffusion of polymer molecules or segments of them from the equilibrium melt onto the growth face. The second exponential term, $\exp(-K_g/T_c(\Delta T)f)$, relates to the formation of the critical nucleus on the growth face. Obviously, this term relates directly to the secondary nucleation rate i . Intuitively, from the competing contributions of the transport and nucleation terms, one expects that there should be a maximum in the growth rate data at a temperature somewhere between the glass transition temperature and the equilibrium melting temperature, when plotted as a function of the crystallization temperature. Indeed, maxima in the growth rate data as a function of crystallization temperature are usually observed at $(0.7 - 0.8) T_m^0$ [7].

As mentioned earlier, in each regime the linear growth rate G relates directly to the secondary nucleation rate i : $G \propto i^n$, where n equals 1 in regimes I and III, and 0.5 in regime II. Since the second exponential term in Equation (3-1) corresponds directly to the secondary nucleation rate, observation of the relationship between G and i can be examined according to the logarithmic product of Equation (3-1):

$$\log G + \frac{U^*}{2.303R(T_c - T_\infty)} = \log G_0 - \frac{K_g}{2.303T_c(\Delta T)f} \quad (3-3)$$

In practice, the test of regimes can be done through the plot of $\log G + U^*/2.303R(T_c - T_\infty)$ versus $1/2.303T_c(\Delta T)f$ (i.e., hereafter the LH plot). This type of plot factors out the contribution of the transport term to the growth rate, and the slope equals the negative value of the nucleation exponent (i.e., slope = $-K_g$). According to Equation (3-3), regime I→II transition is evident when a downward change in slope is observed, whereas it is an upward change in slope that is observed in the transition from regime II to regime III.

Once the nucleation exponent K_g values have been determined, other parameters characteristic of crystal growth can be estimated. First, $\sigma\sigma_c$ can be calculated from Equation (3-2), provided that other parameters are known. By referring to Equation (3-2), the only unknown parameter is the layer thickness b_0 which can be estimated from the unit cell parameters. It is therefore imperative to know into what type of crystallographic form sPP samples crystallize in the temperature range of interest. Based on the preliminary WAXD results [24], it is obvious that all of the sPP samples crystallize mainly in the high temperature orthorhombic form II (Cell II) as determined by Lotz and coworkers [25], especially when $60^\circ\text{C} < T_c < 110^\circ\text{C}$. The unit cell of this orthorhombic modification has space group symmetry $Pca2_1$, with the axis dimensions: $a = 14.50 \text{ \AA}$, $b = 5.60 \text{ \AA}$, and $c = 7.40 \text{ \AA}$. This structure is characterized by the existence of helices of opposite hands with chain axes in $(0, 0, z)$ and $(\frac{1}{2}, 0, z)$. However, when $T_c > 110^\circ\text{C}$, it is a combination of the high temperature orthorhombic form II (Cell II) [25] and form III (Cell III) [25,26] which exists after crystallization. Cell III is characterized by full antichirality along both the a and b axes, with the unit cell having a doubled b axis ($b = 11.2 \text{ \AA}$), and space group symmetry $Ibca$.

By assuming that (010) or (200) is the growth plane for Cell II (or (020) or (200) for Cell III) (i.e., the ac growth plane or the bc growth plane, respectively), it is possible

to estimate the molecular width a_0 and the layer thickness b_0 . At this point, it is possible to calculate the lateral and fold surface free energy, σ and σ_e , separately, but one first has to estimate the σ based on the modified Thomas-Staveley equation [27]:

$$\sigma = \alpha \Delta H_f^0 \sqrt{a_0 b_0}, \quad (3-4)$$

where $a_0 b_0$ is a cross-sectional area of one chain molecule, and α is a universal parameter related to the chemical nature of the polymer, and often taken to be 0.1. It is worth noting that the choice of $\alpha = 0.1$ may be justified for the case of sPP based on the fact that the σ_e values estimated by Rodriguez-Arnold et al. [19-21] based on the modified Thomas-Staveley method (using $\alpha = 0.1$) and the Gibbs-Thomson method are comparable within an experimental error. Once σ is known, the fold surface free energy σ_e can be calculated from $\sigma \sigma_e / \sigma$. Finally, the average work of chain folding \bar{q} which is defined as

$$\bar{q} = 2\alpha_0 b_0 \sigma_e, \quad (3-5)$$

can also be calculated.

4. MATERIALS, LINEAR GROWTH RATE, AND INPUT DATA

Four sets of linear growth rate data for syndiotactic polypropylene spherulites were taken from the literature [17-23] for re-analysis in this study. The materials characterization data for sPP samples examined are summarized in Table 3-1. The spherulitic growth rate data for these samples are listed in Table 3-2. It is noteworthy that the listing of these data is for future reference only.

Figure 3-1 represents the relationship between the spherulitic growth rate and the crystallization temperature for all of the sPP samples examined. It is evident that the growth rate for sPP#1 exhibits the typical bell-shaped dependence with the temperature, and the maximum in the growth rate data occurs at $T_c \approx 70^\circ\text{C}$. The growth rate data for

Table 3-1. Materials characterization data for syndiotactic polypropylene samples used in the referenced literature.

Sample	M_n (daltons)	M_w (daltons)	M_z (daltons)	M_w/M_n	Racemic Pentads [% rrrr]	Racemic Triads [% rr]	Racemic Dyads [% r]	Data Source
6H	-	-	-	-	-	64	72	Miller and Seeley [17,18]
sPP(8)	76 800	84 500	-	1.1	86	92	94	Rodriguez-Arnold et al. [19-21]
sPP(9)	132 000	158 400	-	1.2	87	92	95	Rodriguez-Arnold et al. [19-21]
sPP#1	76 200	165 000	290 000	2.2	77	87	91	Supaphol et al. [22]

Table 3-2. Linear spherulitic growth rate data for syndiotactic polypropylene samples used in the referenced literature.

Sample Label	6H		sPP(8)		sPP(9)		sPP#1	
	T_c (°C)	G ($\mu\text{m}\cdot\text{min}^{-1}$)	T_c (°C)	G ($\mu\text{m}\cdot\text{min}^{-1}$)	T_c (°C)	G ($\mu\text{m}\cdot\text{min}^{-1}$)	T_c (°C)	G ($\mu\text{m}\cdot\text{min}^{-1}$)
	97.4	7.32	101.0	9.12	100.0	5.82	45.0	1.55
	101.4	7.42	102.0	7.74	101.0	4.79	50.0	2.15
	104.4	4.92	103.0	6.74	102.0	4.18	55.0	3.32
	105.4	4.28	104.0	5.99	103.0	3.48	60.0	3.75
	109.4	4.22	105.0	5.18	104.0	3.11	65.0	4.29
	113.4	1.83	106.0	4.62	105.0	2.68	70.0	4.24
	117.4	1.61	107.0	3.95	106.0	2.18	75.0	4.17
	121.4	0.94	108.0	3.10	108.0	1.69	80.0	3.80
	125.4	0.44	109.0	2.67	110.0	1.16	85.0	2.78
	129.4	0.27	111.0	1.84	111.0	1.07	90.0	1.92
	133.4	0.10	113.0	1.41	112.0	0.94	95.0	1.38
	137.3	0.02	116.0	1.03	113.0	0.80	100.0	0.72
					114.0	0.72	105.0	0.48
					115.0	0.63	110.0	0.21
					116.0	0.55	115.0	0.11
					118.0	0.42	120.0	0.08
							125.0	0.04

Data Source Miller and Seeley [17,18] Rodriguez-Arnold et al. [19,21,23] Rodriguez-Arnold et al. [19,21,23] Supaphol et al. [22]

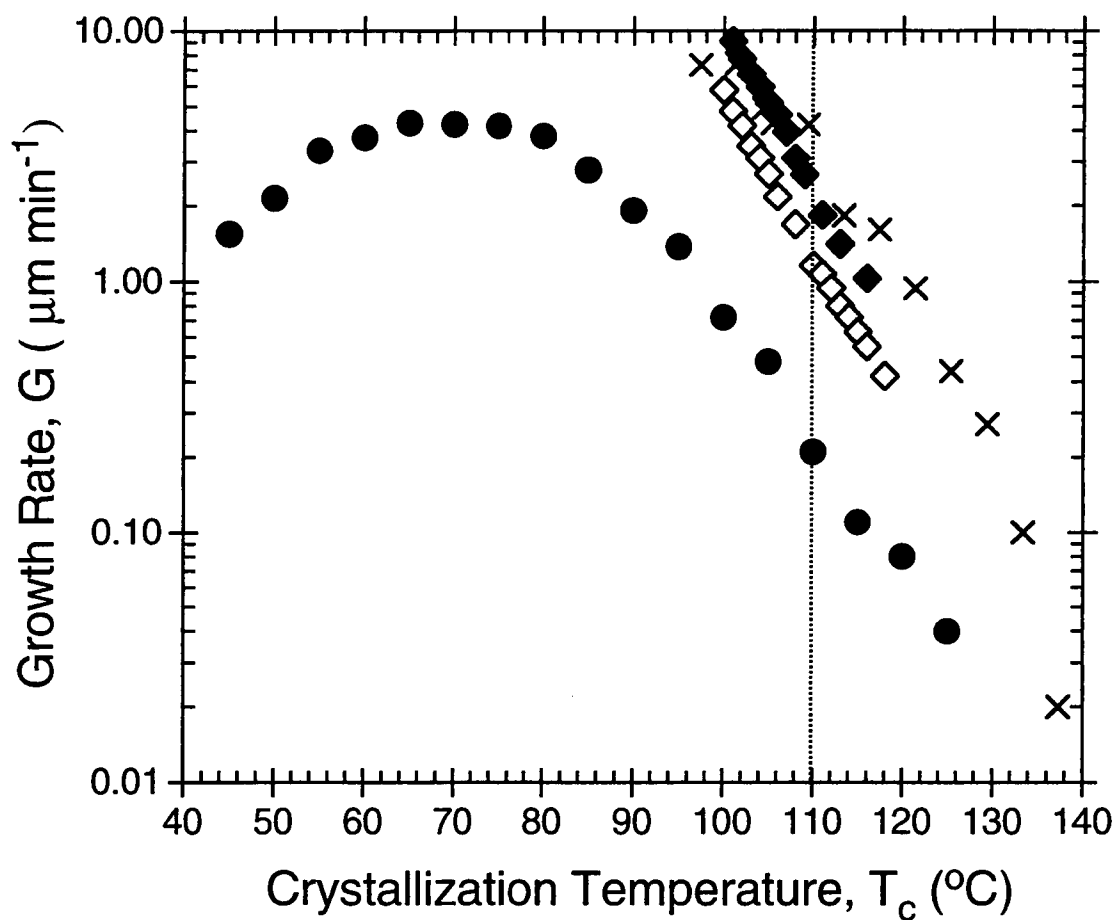


Figure 3-1. Spherulitic growth rates of syndiotactic polypropylene as a function of crystallization temperatures: (x) data of Miller and Seeley (sample 6H) [17,18]; (♦) data of Rodriguez-Arnold et al. (sample sPP(8)) [19,21,23]; (◇) data of Rodriguez-Arnold et al. (sample sPP(9)) [19,21,23]; (●) data of Supaphol et al. (sample sPP#1) [22].

6H, sPP(8), and sPP(9) samples are clearly in the high temperature region (low degree of undercooling) where the secondary nucleation is the rate determining process. From the figure, it is apparent that the rate of crystallization falls in the following order: sPP(8) > sPP(9) > sPP#1. That sPP(8) crystallizes faster than sPP(9) appears to be due to the fact that the average molecular weight for sPP(8) is much lower than that of sPP(9) when other parameters are comparable. On the other hand, it may be the broader molecular weight distribution or the lower degree of syndiotacticity (racemic pentads [%*rrrr*]) that accounts for the slowest crystallization rate observed in sPP#1. It is noteworthy that the crystallization rate of 6H is not discussed here, since the WAXD scan of 6H sample (cf. Figure 12 in reference 18) shows peaks characteristic of iPP. This can only be construed that the isotactic segments also take part in the crystallization process in 6H sample, since its racemic dyad content is only 72%.

The input parameters used in this analysis for the calculation of crystal growth parameters were selected after careful evaluation of available data in the literature and are listed in Table 3-3. The most questionable literature data are the values of equilibrium melting temperature T_m^0 and enthalpy of fusion ΔH_f^0 , which are strongly dependent on the degree of syndiotacticity. The melting temperature used in this study will be the estimated value (please see reference 28 (cf. Part 2) for more detail) for a sPP sample exhibiting 100% syndiotacticity (denoted $(T_m^0)_{100\%}$), which is 168.7°C (441.8 K). The value of ΔH_f^0 is taken as the published value by Rodriguez-Arnold and her coworkers [19-21], which is 8.0 kJ·mol⁻¹ (i.e., 1.77×10⁹ erg·cm⁻³). Table 3-3 summarizes the values for enthalpy of fusion [19-21], glass transition temperature [28], equilibrium melting temperature for a 100% syndiotactic sample [28], and unit cell parameters [25,26]. Based on these input parameters, the lateral surface free energy σ can be first estimated from Equation (3-4) and was found to be 11.3 erg·cm⁻².

Table 3-3. Input parameters for calculation of crystal growth parameters.

Parameter	Value	Remarks
Heat of fusion, ΔH_f^0	$1.77 \times 10^9 \text{ erg}\cdot\text{cm}^{-3}$	Ref. 19-21
Glass transition temperature, T_g	-6.1°C or 267.0 K	Ref. 28
Equilibrium melting temperature, $(T_m^0)_{100\%}$	168.7°C or 441.8 K	Ref. 28
Boltzmann's constant, k	$1.380 \times 10^{-16} \text{ erg}\cdot\text{molecule}^{-1}\cdot\text{K}^{-1}$	
	For (010) growth plane	
Molecular width, a_0	$7.25 \times 10^{-8} \text{ cm}$	Estimated from Ref. 25 and 26
Layer thickness, b_0	$5.60 \times 10^{-8} \text{ cm}$	Estimated from Ref. 25 and 26
Cross-sectional area of chain, $a_0 b_0$	$4.06 \times 10^{-15} \text{ cm}^2$	Estimated from Ref. 25 and 26
Lateral surface free energy, σ	$11.3 \text{ erg}\cdot\text{cm}^{-2}$	From $\sigma = 0.1 \Delta H_f^0 (a_0 b_0)^{0.5}$
	For (200) growth plane	
Molecular width, a_0	$5.60 \times 10^{-8} \text{ cm}$	Estimated from Ref. 25 and 26
Layer thickness, b_0	$7.25 \times 10^{-8} \text{ cm}$	Estimated from Ref. 25 and 26
Cross-sectional area of chain, $a_0 b_0$	$4.06 \times 10^{-15} \text{ cm}^2$	Estimated from Ref. 25 and 26
Lateral surface free energy, σ	$11.3 \text{ erg}\cdot\text{cm}^{-2}$	From $\sigma = 0.1 \Delta H_f^0 (a_0 b_0)^{0.5}$

5. ANALYSIS AND DISCUSSION OF LITERATURE DATA

5.1. Determination of Crystal Growth Parameters

The sPP growth rate data of Rodriguez-Arnold et al. [19,21,23] and Supaphol et al. [22] are available in a wide enough temperature range to exhibit the regime II→III transition, as evidenced by observation of a change in slope in each of the data sets for sPP(8), sPP(9) and sPP#1 samples shown in Figure 3-2. The input parameters used in the plot are $U^* = 1500 \text{ cal}\cdot\text{mol}^{-1}$, $T_\infty = T_g - 30 = 237.0 \text{ K}$ [28], and $(T_m^0)_{100\%} = 441.8 \text{ K}$ [28]. Even though the growth rate data of Miller and Seeley [17,18] does not exhibit any discontinuity in the slope, Clark and Hoffman [7] suggested that these data are in regime II and can be analyzed accordingly.

With the absence of the 6H data, the regime II→III transition can be graphically distinguished in the data set for sPP(8), sPP(9) and sPP#1 samples, as illustrated in Figure 3-3. This transition corresponds to the crystallization temperature of 110°C , which is in very good agreement with the predicted value by Clark and Hoffman [7]. As mentioned previously, for each data set the nucleation exponent K_g for either regime II or regime III can be extracted directly from the slope of the plot (i.e., $K_g = -\text{slope}$). It is worth noting that the correlation coefficients r^2 of the straight lines fit to the bulk of the data are 0.984 or better. In addition, G_0 correspondent to either regime II or regime III can also be extracted from the y-interception of the plot (i.e., $G_0 = 10^{(\text{y-intercept value})}$). Once K_g is determined from the slope, the value of σ_e can be determined from $\sigma\sigma_e/\sigma$, where $\sigma\sigma_e$ can be calculated based on Equation (3-2), and σ is already estimated to be $11.3 \text{ erg}\cdot\text{cm}^{-2}$ (depend markedly on the choice of ΔH_f^0 and the α parameter), which is a bit lower than the reported value of iPP (ca. $11.5 \text{ erg}\cdot\text{cm}^{-2}$). Finally, the \bar{q} value can also be calculated from Equation (3-5). Table 3-4 summarizes the values of K_g , $\sigma\sigma_e$, σ_e , \bar{q} , and G_0 , calculated based on the input parameters summarized in Table 3-3.

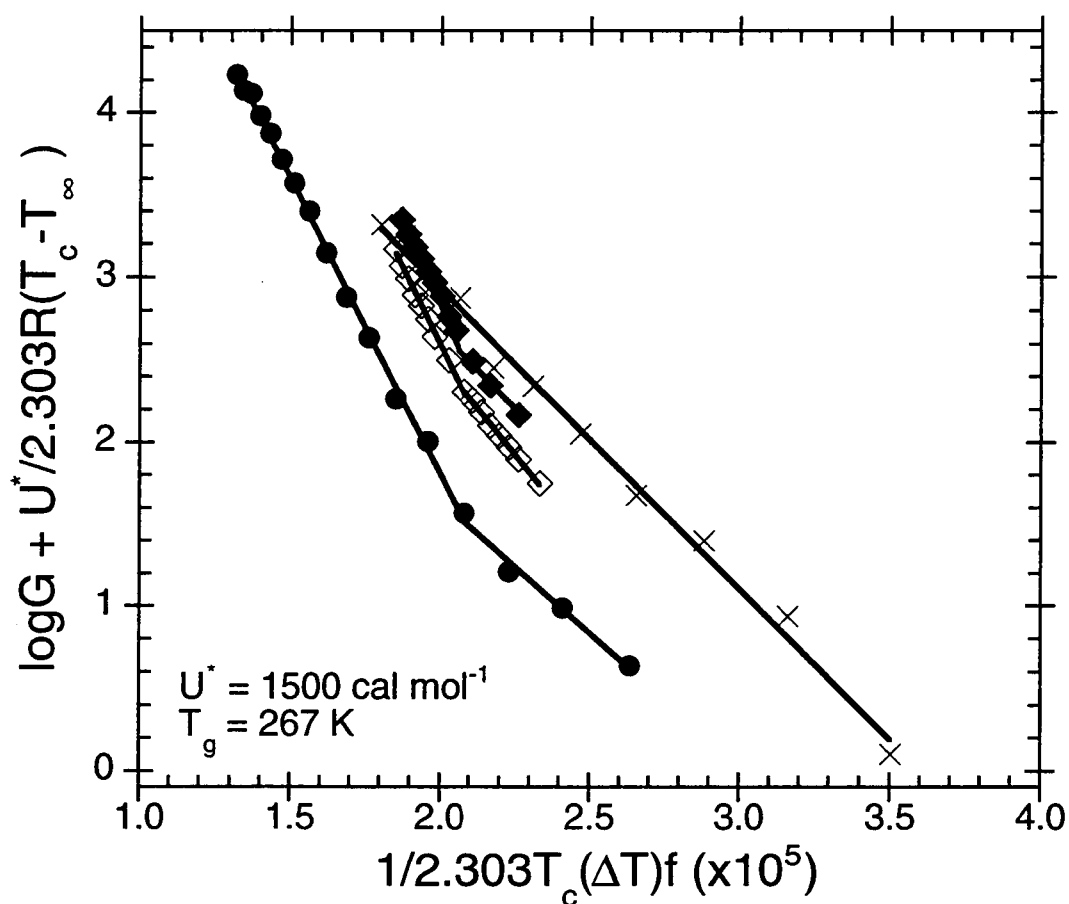


Figure 3-2. Analysis of the spherulitic growth rates of syndiotactic polypropylene as a function of crystallization temperatures based on the Lauritzen and Hoffman secondary nucleation theory for the case $U^* = 1500 \text{ cal}\cdot\text{mol}^{-1}$, $T_\infty = T_g - 30 = 237.0 \text{ K}$, and $(T_m^0)_{100\%} = 441.8 \text{ K}$: (x) data of Miller and Seeley (sample 6H) [17,18]; (◆) data of Rodriguez-Arnold et al. (sample sPP(8)) [19,21,23]; (◇) data of Rodriguez-Arnold et al. (sample sPP(9)) [19,21,23]; (●) data of Supaphol et al. (sample sPP#1) [22].

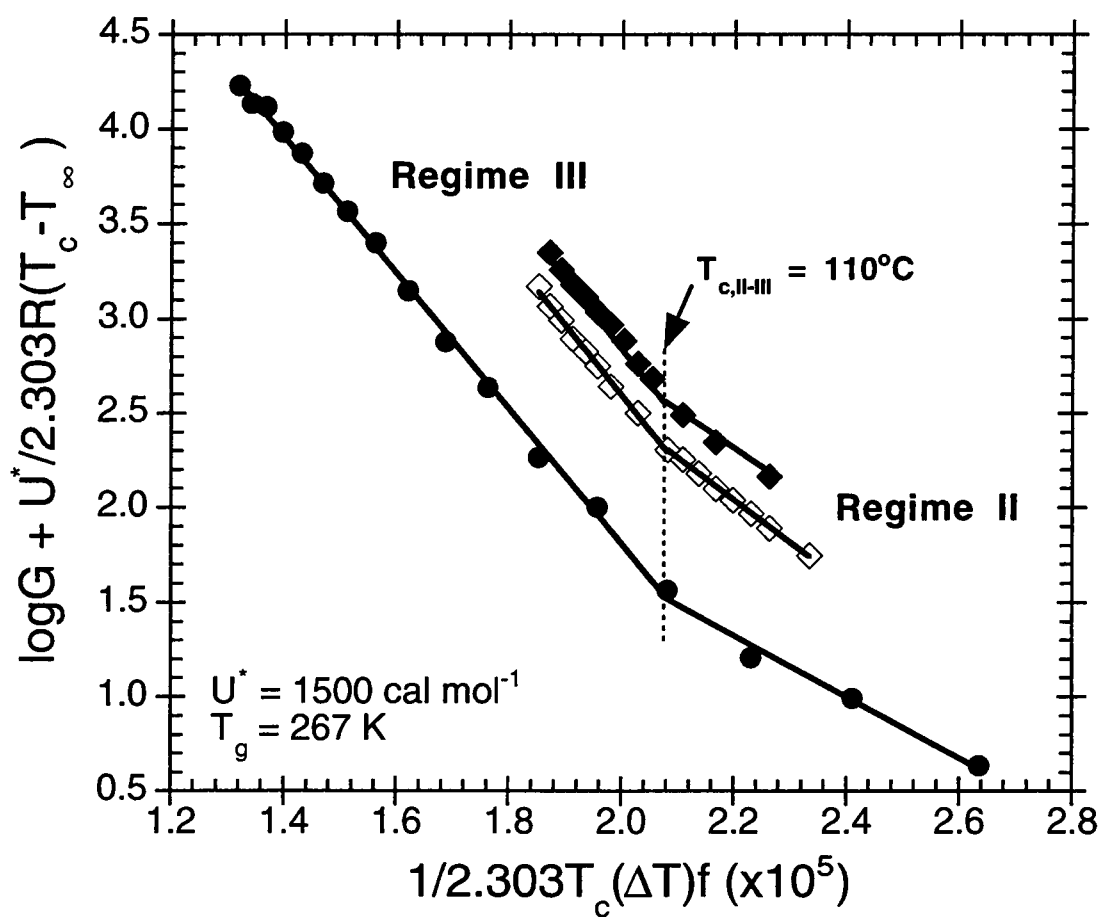


Figure 3-3. The same plot as Figure 3-2 but without the data of Miller and Seeley (sample 6H) [17,18]. The regime II→III transition is clearly distinguishable in all three sets of data, and corresponds to the crystallization temperature of 110°C .

Table 3-4. Nucleation exponents and crystal growth parameters based on the traditional regime analysis for the case: $T_g = 267.0$ K, $(T_m^0)_{100\%} = 441.8$ K, and $\Delta H_f^0 = 8.0$ kJ·mol⁻¹.

Sample	The <i>ac</i> growth plane				The <i>bc</i> growth plane				$G_{0,III}/G_{0,II}$	$K_{g,III}/K_{g,II}$
	K_g^s (K ²)	$\sigma\sigma_e$ (erg ² ·cm ⁻⁴)	σ_e (erg·cm ⁻³)	\bar{q} (kcal·mol ⁻¹)	$\sigma\sigma_e$ (erg ² ·cm ⁻⁴)	σ_e (erg·cm ⁻³)	\bar{q} (kcal·mol ⁻¹)	G_0 ($\mu\text{m}\cdot\text{min}^{-1}$)		
6H	1.83×10^5	901.6	79.9	9.3	696.4	61.7	7.2	3.82×10^6		
sPP(8)	2.08×10^5	1025.5	90.9	10.6	792.1	70.2	8.2	7.24×10^6	1.45×10^3	1.7
sPP(9)	2.24×10^5	1107.2	98.1	11.5	855.2	75.8	8.9	9.34×10^6	1.05×10^3	1.7
sPP#1	1.61×10^5	797.3	70.7	8.3	615.9	54.6	6.4	7.52×10^4	1.21×10^4	2.2
sPP(8)	3.57×10^5	881.8	78.1	9.1	681.1	60.4	7.1	1.05×10^{10}		
sPP(9)	3.70×10^5	913.5	81.0	9.5	705.6	62.5	7.3	9.76×10^9		
sPP#1	3.58×10^5	883.0	78.2	9.1	682.0	60.4	7.1	9.07×10^8		

As shown in Figure 3-3, the lines drawn through all sets of data within a given regime are roughly parallel. This is evidenced in the K_g values, taken directly from the slope of each line fit through each set of data. In the case of regime II, K_g values lie in the range of $1.61 \times 10^5 \text{ K}^2$ to $2.24 \times 10^5 \text{ K}^2$, whereas they are $3.57 \times 10^5 \text{ K}^2$ to $3.70 \times 10^5 \text{ K}^2$ in regime III. The ratios of $K_{g,III}/K_{g,II}$ are in the range of 1.7 to 2.2, which are close to the theoretical value of 2. Table 3-4 also lists the G_0 values estimated for regimes II and III. The ratios of $G_{0,III}/G_{0,II}$ were also calculated and were found to be 1.05×10^3 to 1.21×10^4 . In iPP, Clark and Hoffman [7] found that $G_{0,III}/G_{0,II}$ values lie in the range of 3×10^3 to 3×10^4 . Theoretically, the $G_{0,III}/G_{0,II}$ value can be calculated based on Equation (27a) in reference 6. Due to the lack of input information, it is not possible to calculate the theoretical $G_{0,III}/G_{0,II}$ ratio at this point.

Assuming that the crystal growth is on the (010) plane for Cell II (or (020) plane for Cell III) (i.e., the *ac* growth plane), for regime II values of $\sigma\sigma_e = 957.9 \pm 136.4 \text{ erg}^2 \cdot \text{cm}^{-4}$, $\sigma_e = 84.9 \pm 12.1 \text{ erg} \cdot \text{cm}^{-2}$, and $\bar{q} = 9.9 \pm 1.4 \text{ kcal} \cdot \text{mol}^{-1}$ are evaluated, and they are $\sigma\sigma_e = 892.7 \pm 18.0 \text{ erg}^2 \cdot \text{cm}^{-4}$, $\sigma_e = 79.1 \pm 1.6 \text{ erg} \cdot \text{cm}^{-2}$, and $\bar{q} = 9.2 \pm 0.2 \text{ kcal} \cdot \text{mol}^{-1}$ for regime III. In addition, when assuming that the crystal growth is on the (200) plane for either Cell II or Cell III (i.e., the *bc* growth plane), for regime II values of $\sigma\sigma_e = 739.9 \pm 105.3 \text{ erg}^2 \cdot \text{cm}^{-4}$, $\sigma_e = 65.6 \pm 9.3 \text{ erg} \cdot \text{cm}^{-2}$, and $\bar{q} = 7.7 \pm 1.1 \text{ kcal} \cdot \text{mol}^{-1}$ are evaluated, and they are $\sigma\sigma_e = 689.6 \pm 13.9 \text{ erg}^2 \cdot \text{cm}^{-4}$, $\sigma_e = 61.1 \pm 1.2 \text{ erg} \cdot \text{cm}^{-2}$, and $\bar{q} = 7.1 \pm 0.1 \text{ kcal} \cdot \text{mol}^{-1}$ for regime III. Obviously, the values calculated for the *bc* growth plane are lower, and appear to be comparable to the values reported for iPP (i.e., $\sigma\sigma_e = 740 - 790 \text{ erg}^2 \cdot \text{cm}^{-4}$, $\sigma_e = 65 - 70 \text{ erg} \cdot \text{cm}^{-2}$, and $\bar{q} = 6.4 - 6.8 \text{ kcal} \cdot \text{mol}^{-1}$) [7].

After the values of K_g and G_0 were identified, the growth rate function $G(T)$ can now be constructed with use of Equation (3-1). This can be demonstrated by taking the

case of sPP#1 as an example. According to the values of K_g and G_0 listed in Table 3-4, the growth rate function $G(T)$ for sPP#1 can be defined by the following expressions:

$$G_{II} = 7.52 \times 10^4 \exp\left(-\frac{754.83}{(T_c - T_\infty)} - \frac{1.61 \times 10^5}{T_c(\Delta T)f}\right), \quad (3-6)$$

which is valid at $T_c \geq 110^\circ\text{C}$, and

$$G_{III} = 9.07 \times 10^8 \exp\left(-\frac{754.83}{(T_c - T_\infty)} - \frac{3.58 \times 10^5}{T_c(\Delta T)f}\right), \quad (3-7)$$

which is valid at $T_c \leq 110^\circ\text{C}$. It should be noted that the crystal growth rate G denoted in Equations (3-6) and (3-7) is given in the unit of $[\mu\text{m}\cdot\text{min}^{-1}]$. The growth rate expressions for sPP(8) and sPP(9) can also be obtained in a similar fashion as shown here. Figure 3-4 shows the relationship between the linear growth rate of sPP(8), sPP(9) and sPP#1 samples and the crystallization temperature, with the calculated values (e.g., from Equations (3-6) and (3-7) for sPP#1) shown as the dotted curves. Interestingly, each calculated growth rate curve (with an exception of sample 6H) exhibits a maximum at $T_c \approx 70^\circ\text{C}$, similar to that observed in the raw data of sample sPP#1. Consequently, this would make the maximum in $G(T)$ for sPP occur at ca. $0.78(T_m^0)_{100\%}$.

5.2. Effect of Change in T_g

A number of authors measured the glass transition temperature of sPP samples to be around 0°C (i.e., 273.2 K) [17,18,29], and it has also been used in the regime analysis by Miller and Seeley [17,18] and Rodriguez-Arnold et al. [19,21]. Accordingly, data analysis for the use of $T_g = 273.2$ K as input parameter is examined, while all other parameters are kept unchanged. The input parameters thus are $T_\infty = T_g - 30 = 243.2$ K, $(T_m^0)_{100\%} = 441.8$ K, and $\Delta H_f^0 = 8.0$ kJ·mol⁻¹. Obviously, a slight increase in the T_g value (from 267.0 K to 273.2 K, equivalent to 2.3% increase in T_g value) causes a slight increase in the evaluated values of K_g and G_0 , as shown in Table 5. This change in T_g does not

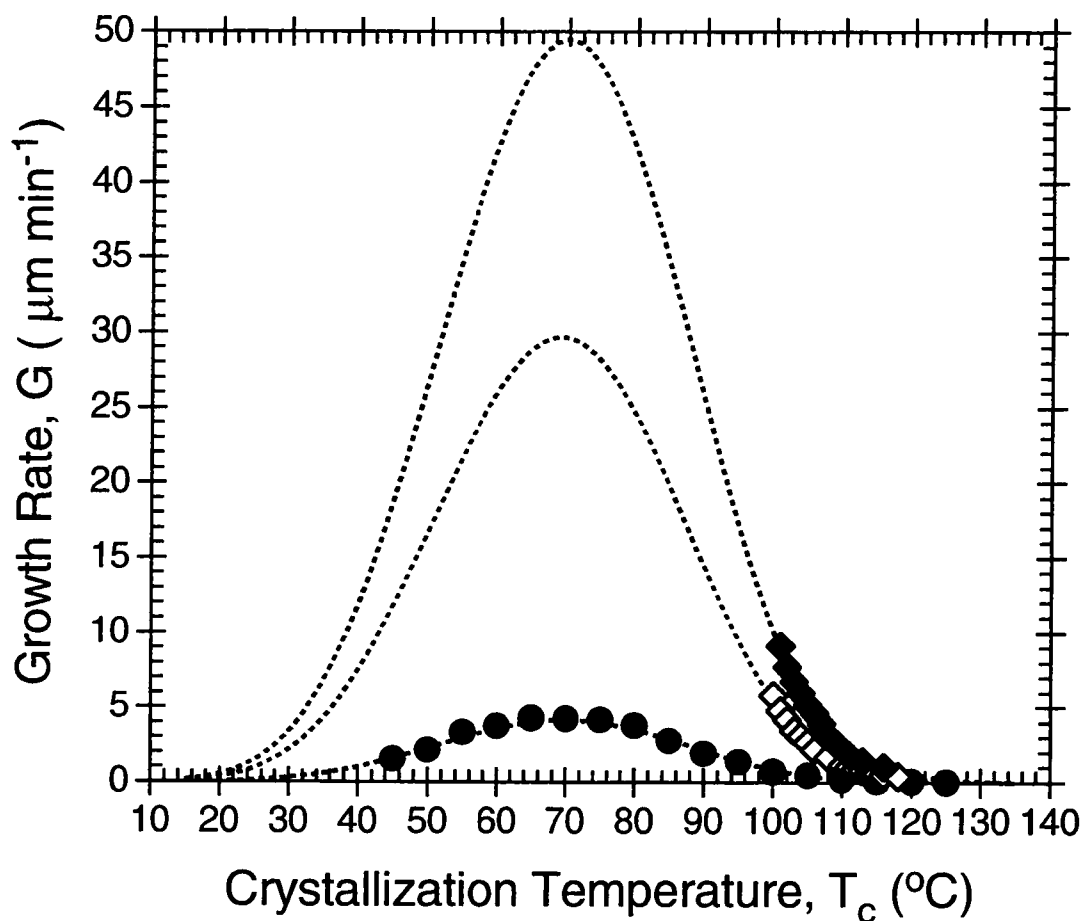


Figure 3-4. Spherulitic growth rates of syndiotactic polypropylene as a function of crystallization temperatures: (◆) data of Rodriguez-Arnold et al. (sample sPP(8)) [19,21,23]; (◇) data of Rodriguez-Arnold et al. (sample sPP(9)) [19,21,23]; (●) data of Supaphol et al. (sample sPP#1) [22]; (—) predicted values based on the growth rate expression (e.g., Equation (3-1)) with appropriate G_0 and K_g values.

Table 3-5. Nucleation exponents and crystal growth parameters based on the traditional regime analysis for the case: $T_g = 273.2$ K, $(T_m^0)_{100\%} = 441.8$ K, and $\Delta H_f^0 = 8.0$ kJ·mol⁻¹.

Sample	The <i>ac</i> growth plane			The <i>bc</i> growth plane			G_0 ($\mu\text{m}\cdot\text{min}^{-1}$)	$G_{0,\text{III}}/G_{0,\text{II}}$	$K_{g,\text{III}}/K_{g,\text{II}}$
	K_g (K ²)	$\sigma\sigma_e$ (erg ² ·cm ⁻⁴)	\bar{q} (kcal·mol ⁻¹)	$\sigma\sigma_e$ (erg ² ·cm ⁻⁴)	σ_e (erg·cm ⁻²)	\bar{q} (kcal·mol ⁻¹)			
6H	1.85×10^5	915.3	81.1	707.0	62.7	7.3	5.51×10^6		
sPP(8)	2.12×10^5	1045.8	92.7	807.8	71.6	8.4	1.11×10^7	1.64×10^3	1.7
sPP(9)	2.28×10^5	1127.0	99.9	870.5	77.1	9.0	1.42×10^7	1.19×10^3	1.7
sPP#1	1.65×10^5	813.0	72.0	628.0	55.7	6.5	1.10×10^5	3.38×10^4	2.3
				Regime II					
sPP(8)	3.64×10^5	898.3	79.6	693.9	61.5	7.2	1.81×10^{10}		
sPP(9)	3.77×10^5	930.1	82.4	718.4	63.7	7.4	1.69×10^{10}		
sPP#1	3.84×10^5	949.2	84.1	733.2	65.0	7.6	3.71×10^9		
				Regime III					

however have an effect on the position of the regime II→III transition observed. In addition, the ratio of $K_{g,III}/K_{g,II}$ remains essentially unchanged.

According to Table 3-5, assuming that the crystal growth is on the (010) plane for Cell II (or (020) plane for Cell III) (i.e, the *ac* growth plane), for regime II values of $\sigma\sigma_e = 975.3 \pm 138.9 \text{ erg}^2\cdot\text{cm}^{-4}$, $\sigma_e = 86.4 \pm 12.3 \text{ erg}\cdot\text{cm}^{-2}$, and $\bar{q} = 10.1 \pm 1.4 \text{ kcal}\cdot\text{mol}^{-1}$ are evaluated, and they are $\sigma\sigma_e = 925.9 \pm 25.7 \text{ erg}^2\cdot\text{cm}^{-4}$, $\sigma_e = 82.0 \pm 2.3 \text{ erg}\cdot\text{cm}^{-2}$, and $\bar{q} = 9.6 \pm 0.3 \text{ kcal}\cdot\text{mol}^{-1}$ for regime III. Furthermore, when assuming that the crystal growth is on the (200) plane for either Cell II or Cell III (i.e, the *bc* growth plane), for regime II values of $\sigma\sigma_e = 753.3 \pm 107.3 \text{ erg}^2\cdot\text{cm}^{-4}$, $\sigma_e = 66.8 \pm 9.5 \text{ erg}\cdot\text{cm}^{-2}$, and $\bar{q} = 7.8 \pm 1.1 \text{ kcal}\cdot\text{mol}^{-1}$ are evaluated, and they are $\sigma\sigma_e = 715.2 \pm 19.8 \text{ erg}^2\cdot\text{cm}^{-4}$, $\sigma_e = 63.4 \pm 1.8 \text{ erg}\cdot\text{cm}^{-2}$, and $\bar{q} = 7.4 \pm 0.2 \text{ kcal}\cdot\text{mol}^{-1}$ for regime III. By comparing the average values of corresponding parameters reported in Table 3-5 with those in Table 3-4, it can be concluded qualitatively that a 2.3% increase in T_g results in an approximate 2.9% increase in K_g value, and about 2.6% increase in $\sigma\sigma_e$, σ_e , and \bar{q} values.

5.3. Effect of Change in $(T_m^0)_{100\%}$

A number of authors [17,18,20,21,29,30] have reported T_m^0 values of sPP samples with different syndiotacticity levels. Only reported values with known concentration of racemic pentads [%*rrrr*] will be discussed here. These values of T_m^0 , with the syndiotacticity level in parentheses, are 160°C (86%) [20,21] and 150°C to 186°C (89% to 95%) [30]. Obviously, the T_m^0 values are strongly dependent on the syndiotacticity levels. Theoretically, the T_m^0 value measured for a sPP sample with a particular syndiotacticity level is presumably the melting point of 100% crystallinity crystals. In terms of regime analysis, using different T_m^0 values in the analysis may lead to anomalous results, since the crystal growth parameters are very sensitive to the T_m^0 values (as will be shown subsequently). With this in mind, use of $(T_m^0)_{100\%}$ in the

analysis is thus preferable, and this is why the $(T_m^0)_{100\%}$ value of 168.7°C (441.8 K) [28] has been used in this study.

To illustrate the effect of change in the $(T_m^0)_{100\%}$, the value of 160°C (433.2 K) is used in the analysis. It is worth noting that this value was used in the analysis by Rodriguez-Arnold et al. [19,21], and it is very close to the value of 161°C (434.2 K) used by Miller and Seeley [17,18]. The input parameters used in this case thus are $T_\infty = T_g - 30 = 243.2$ K, $(T_m^0)_{100\%} = 433.2$ K, and $\Delta H_f^0 = 8.0$ kJ·mol⁻¹. Obviously, the decrease in the $(T_m^0)_{100\%}$ value (from 441.8 K to 433.2 K, equivalent to roughly 2.0% decrease in $(T_m^0)_{100\%}$ value) causes a marked decrease in the values of K_g and G_0 , as shown in Table 3-6. This change in $(T_m^0)_{100\%}$ does not however have an effect on the position of the regime II→III transition observed. The ratios of $K_{g,III}/K_{g,II}$ are found to lie between 1.7 and 2.7.

According to Table 3-6, assuming that the crystal growth is on the (010) plane for Cell II (or (020) plane for Cell III) (i.e, the *ac* growth plane), for regime II values of $\sigma\sigma_e = 662.1 \pm 115.4$ erg²·cm⁻⁴, $\sigma_e = 58.7 \pm 10.2$ erg·cm⁻², and $\bar{q} = 6.9 \pm 1.2$ kcal·mol⁻¹ are evaluated, and they are $\sigma\sigma_e = 690.6 \pm 37.3$ erg²·cm⁻⁴, $\sigma_e = 61.2 \pm 3.3$ erg·cm⁻², and $\bar{q} = 7.2 \pm 0.4$ kcal·mol⁻¹ for regime III. Additionally, when assuming that the crystal growth is on the (200) plane for either Cell II or Cell III (i.e, the *bc* growth plane), for regime II values of $\sigma\sigma_e = 511.4 \pm 89.1$ erg²·cm⁻⁴, $\sigma_e = 45.3 \pm 7.9$ erg·cm⁻², and $\bar{q} = 5.3 \pm 0.9$ kcal·mol⁻¹ are evaluated, and they are $\sigma\sigma_e = 533.4 \pm 28.8$ erg²·cm⁻⁴, $\sigma_e = 47.3 \pm 2.6$ erg·cm⁻², and $\bar{q} = 5.5 \pm 0.3$ kcal·mol⁻¹ for regime III. By comparing the average values of corresponding parameters reported in Table 3-6 with those in Table 3-5, it can be concluded qualitatively that a 2.0% decrease in $(T_m^0)_{100\%}$ value results in an approximate 29.6% decrease in K_g value, and about 29.3% decrease in $\sigma\sigma_e$, σ_e , and \bar{q} values. In addition, the result suggests that a 1°C change in $(T_m^0)_{100\%}$ value leads to approximately 4.4% change in K_g , $\sigma\sigma_e$, σ_e , and \bar{q} values.

Table 3-6. Nucleation exponents and crystal growth parameters based on the traditional regime analysis for the case: $T_g = 273.2$ K, $(T_m^0)_{100\%} = 433.2$ K, and $\Delta H_f^0 = 8.0$ kJ·mol⁻¹.

Sample	The <i>ac</i> growth plane				The <i>bc</i> growth plane				$G_{0,III}/G_{0,II}$	$K_{g,III}/K_{g,II}$	
	K_g (K ³)	$\sigma\sigma_e$ (erg ² ·cm ⁻⁴)	σ_e (erg·cm ⁻²)	\bar{q} (kcal·mol ⁻¹)	$\sigma\sigma_e$ (erg ² ·cm ⁻⁴)	σ_e (erg·cm ⁻²)	\bar{q} (kcal·mol ⁻¹)	G_0 ($\mu\text{m}\cdot\text{min}^{-1}$)			
6H	1.15×10^5	581.6	51.5	6.0	449.2	39.8	4.7	4.77×10^5			
sPP(8)	1.45×10^5	732.3	64.9	7.6	565.6	50.1	5.9	1.40×10^6	7.16×10^2	1.8	
sPP(9)	1.56×10^5	786.5	69.7	8.1	607.5	53.8	6.3	1.49×10^6	5.61×10^2	1.7	
sPP#1	1.09×10^5	547.9	48.5	5.7	423.2	37.5	4.4	1.72×10^4	2.08×10^4	2.7	
					Regime II						
sPP(8)	2.62×10^5	658.7	58.4	6.8	508.8	45.1	5.3	1.00×10^9			
sPP(9)	2.71×10^5	681.4	60.4	7.1	526.3	46.6	5.5	8.34×10^8			
sPP#1	2.90×10^5	731.6	64.8	7.6	565.1	50.1	5.9	3.57×10^8			
					Regime III						

5.4. Effect of Change in ΔH_f^0

Intuitively, one can predict based on Equations (3-1), (3-2), (3-4), and (3-5) that the change in ΔH_f^0 value does not affect K_g , σ_e and \bar{q} values. Only the σ parameter is found to be sensitive to the change in ΔH_f^0 value. If other input parameters are kept unchanged ($T_\infty = T_g - 30 = 243.2$ K and $(T_m^0)_{100\%} = 433.2$ K), the change of ΔH_f^0 from 8.0 kJ·mol⁻¹ [19-21] to 8.3 kJ·mol⁻¹ [29] leads to a change of lateral surface free energy from 11.3 erg·cm⁻² to 11.7 erg·cm⁻². This corresponds to 3.5% increase in the σ value, as a result of 3.3% increase in the ΔH_f^0 value. In addition, if the ΔH_f^0 value of 3.1 kJ·mol⁻¹ [17,18] is used instead, the σ value decreases from 11.3 erg·cm⁻² to 4.4 erg·cm⁻², which equals the reported value by Miller and Seeley [17,18]. This corresponds to a 61.1% decrease in the σ value, as a result of 60.8% decrease in the ΔH_f^0 value. Based on these results, it can be construed that a 1% change in the ΔH_f^0 value causes a 1% change in the resulting σ value. It is worth noting that the K_g , σ_e and \bar{q} values are the same set as those reported in Table 3-6.

5.5. Further Discussion of the Literature

Miller and Seeley [17,18] analyzed their data based on regime II crystallization using the following input parameters: $T_g = 273.2$ K, $(T_m^0)_{100\%} = 434.2$ K, and $\Delta H_f^0 = 3.1$ kJ·mol⁻¹. They found the crystal growth parameters to be: $\sigma = 4.4$ erg·cm⁻², $\sigma\sigma_e = 256$ erg²·cm⁻⁴, $\sigma_e = 58$ erg·cm⁻², and $\bar{q} = 6.8$ kcal·mol⁻¹. Determination of the crystal growth parameters based on their use of input parameters reveals that $\sigma = 4.4$ erg·cm⁻², $\sigma\sigma_e = 241.9$ erg²·cm⁻⁴, $\sigma_e = 54.7$ erg·cm⁻², and $\bar{q} = 6.4$ kcal·mol⁻¹, when considering that (010) or (020) is the growth plane based on either Cell II or Cell III (i.e., the *ac* growth plane), respectively; and they are $\sigma = 4.4$ erg·cm⁻², $\sigma\sigma_e = 186.9$ erg²·cm⁻⁴, $\sigma_e = 42.2$ erg·cm⁻², and $\bar{q} = 4.9$ kcal·mol⁻¹, when considering that (200) is the growth plane based on either Cell II or Cell III (i.e., the *bc* growth plane). At the time of their publication though, only the

high temperature orthorhombic form I (Cell I) [31] was available, and they accordingly assumed that the growth plane occurred on the (110) plane, which is not. With this in mind, re-evaluation of the crystal growth parameters, based on $a_0 = 7.77 \times 10^{-8}$ cm and $b_0 = 5.22 \times 10^{-8}$ cm, indicates that $\sigma = 4.4$ erg·cm⁻², $\sigma\sigma_e = 259.5$ erg²·cm⁻⁴, $\sigma_e = 58.7$ erg·cm⁻², and $\bar{q} = 6.9$ kcal·mol⁻¹, which is extremely close to their published values.

In the case of Rodriguez-Arnold et al. [19,21], instead of performing a typical LH regime plot, they analyzed their data by a construction of the modified regime plot $\log G - \log \Delta T + U^*/2.303R(T_c - T_\infty)$ versus $1/2.303T_c(\Delta T)^f$. In this case, K_g and G_0 can still be obtained as they normally would with the traditional plot. In their analysis, the input parameters are: $T_g = 273.2$ K, $(T_m^0)_{100\%} = 433.2$ K, and $\Delta H_f^0 = 8.0$ kJ·mol⁻¹. Since they proposed that the growth occurs on the (200) plane (i.e., the *bc* growth plane), re-analysis of their data is carried out accordingly, and it indicates that the crystal growth parameters for sPP(8) and sPP(9) samples, based on K_g values taken from the modified regime plots, are $\sigma = 11.3$ erg·cm⁻², $\sigma\sigma_e = 460.4 - 527.9$ erg²·cm⁻⁴, $\sigma_e = 42.4 - 46.8$ erg·cm⁻², and $\bar{q} = 4.8 - 5.5$ kcal·mol⁻¹. These values are found to be in a good agreement with their original results (i.e., $\sigma = 11.2$ erg·cm⁻², $\sigma\sigma_e = 465.9 - 537.6$ erg²·cm⁻⁴, $\sigma_e = 41.8 - 47.7$ erg·cm⁻², and $\bar{q} = 4.9 - 5.6$ kcal·mol⁻¹) [19,21]. Apparently, the values obtained for sPP(8) and sPP(9) using the modified regime analysis are much lower than those obtained using the traditional approach (cf. Table 3-6). Qualitatively, the difference in the obtained values accounts for a 12.0% decrease in K_g value, and about 12.6% decrease in $\sigma\sigma_e$, σ_e , and \bar{q} values.

Even though the theoretical background of the modified regime analysis applied by Rodriguez-Arnold et al. [19,21] is not entirely clear, it is interesting to analyze the linear growth rate data based on the reference input parameters (i.e., $T_g = 267.0$ K, $(T_m^0)_{100\%} = 441.8$ K, and $\Delta H_f^0 = 8.0$ kJ·mol⁻¹) using the modified regime analysis and

compare the results with those analyzed using the traditional approach which are listed in Table 3-4. Assuming that the crystal growth is on the (010) plane for Cell II (or (020) plane for Cell III) (i.e., the *ac* growth plane), values of $\sigma\sigma_e = 839.4 \pm 129.5 \text{ erg}^2\cdot\text{cm}^{-4}$, $\sigma_e = 74.4 \pm 11.5 \text{ erg}\cdot\text{cm}^{-2}$, and $\bar{q} = 8.7 \pm 1.3 \text{ kcal}\cdot\text{mol}^{-1}$ are found for regime II, and they are $\sigma\sigma_e = 807.8 \pm 30.8 \text{ erg}^2\cdot\text{cm}^{-4}$, $\sigma_e = 71.6 \pm 2.7 \text{ erg}\cdot\text{cm}^{-2}$, and $\bar{q} = 8.4 \pm 0.3 \text{ kcal}\cdot\text{mol}^{-1}$ for regime III. In addition, when assuming that the crystal growth is on the (200) plane for either Cell II or Cell III (i.e, the *bc* growth plane), values of $\sigma\sigma_e = 648.3 \pm 100.0 \text{ erg}^2\cdot\text{cm}^{-4}$, $\sigma_e = 57.5 \pm 8.9 \text{ erg}\cdot\text{cm}^{-2}$, and $\bar{q} = 6.7 \pm 1.0 \text{ kcal}\cdot\text{mol}^{-1}$ are determined for regime II, and they are $\sigma\sigma_e = 623.9 \pm 23.8 \text{ erg}^2\cdot\text{cm}^{-4}$, $\sigma_e = 55.3 \pm 2.1 \text{ erg}\cdot\text{cm}^{-2}$, and $\bar{q} = 6.5 \pm 0.2 \text{ kcal}\cdot\text{mol}^{-1}$ for regime III. It is obvious that the crystal growth parameters obtained using the modified regime analysis are much lower than those obtained using the traditional approach (cf. Table 3-4). Qualitatively, the difference in the obtained values accounts for a 10.7% decrease in K_g value, and about 11.2% decrease in $\sigma\sigma_e$, σ_e , and \bar{q} values.

6. FURTHER DISCUSSION ON THE T_m^0 VALUE USED IN THE ANALYSIS

Recently, Huang et al. [32] suggested that analysis of the linear growth rate data of polymers in the context of the LH secondary nucleation theory can only be carried out successfully when the equilibrium melting temperature T_m^0 for the polymer of interest can be determined accurately. They also suggested that the T_m^0 value for the polymer of interest can be evaluated directly from the growth rate data, using the LH secondary nucleation theory as basis. By considering T_m^0 as a variable, they assumed that the true T_m^0 value for the polymer of interest is taken as the value which gives the lowest variance between the experimental values (i.e., the LHS values of Equation (3-3)) and the linear regression values (i.e, the RHS values of Equation (3-3)). Their proposed method is hereafter called the "data-fitting" procedure. So far, this method has successfully been applied to the cases of poly(pivalolactone) [32] and its blends [32,33], isotactic

polystyrene [34], poly(L-lactide-co-meso-lactide) copolymers [35], and isotactic polypropylene [36].

An alternative method in determining the true T_m^0 value for the polymer of interest can be determined based on the theoretical requirement of the ratios $K_{g,I}/K_{g,II} = K_{g,III}/K_{g,II} = 2.0$, provided that either regime I→II or regime II→III transition exists within the temperature range of interest. By assuming that the LH secondary nucleation theory is applicable to describe the temperature dependence of the growth rate data of polymers other than that of polyethylene which is the basis for the development of the theory and that the measured growth rate data is of high quality, the true T_m^0 value for the polymer of interest is taken as the value which results in the ratio of the corresponding nucleation exponents of 2.0. Xu et al. [36] applied both alternative approaches of the data-fitting procedure on the growth rate data of isotactic polypropylene, and found that the resulting T_m^0 values from both approaches are comparable (ca. 215°C).

In this study, the second alternative approach of the data-fitting procedure for the determination of the equilibrium melting temperature T_m^0 is applied to analyze the growth rate data of sPP#1. By varying the seed T_m^0 value (whereas $U^* = 1500 \text{ cal}\cdot\text{mol}^{-1}$ and $T_\infty = 267 - 30 \text{ K}$), the corresponding value of $K_{g,III}/K_{g,II}$ also varies, and it is found to decrease with increasing seed T_m^0 value (cf. Figure 3-5). According to Figure 3-5, the true T_m^0 value which results in the value of $K_{g,III}/K_{g,II}$ of 2.0 is approximately 178°C. Based on this new T_m^0 value, the resulting nucleation parameters, $K_{g,II}$ or $0.5K_{g,III}$, were found to be $2.36 \times 10^5 \text{ K}^2$. Using the same input parameters summarized in Table 3-3, the crystal growth parameters characteristic of the LH growth theory can be calculated accordingly. Assuming that growth occurs on the ac plane, values of $\sigma\sigma_e = 1109.0 \text{ erg}^2\cdot\text{cm}^{-4}$, $\sigma_e = 101.2 \text{ erg}\cdot\text{cm}^{-2}$, and $\bar{q} = 11.8 \text{ kcal}\cdot\text{mol}^{-1}$ are found, whereas they are $\sigma\sigma_e =$

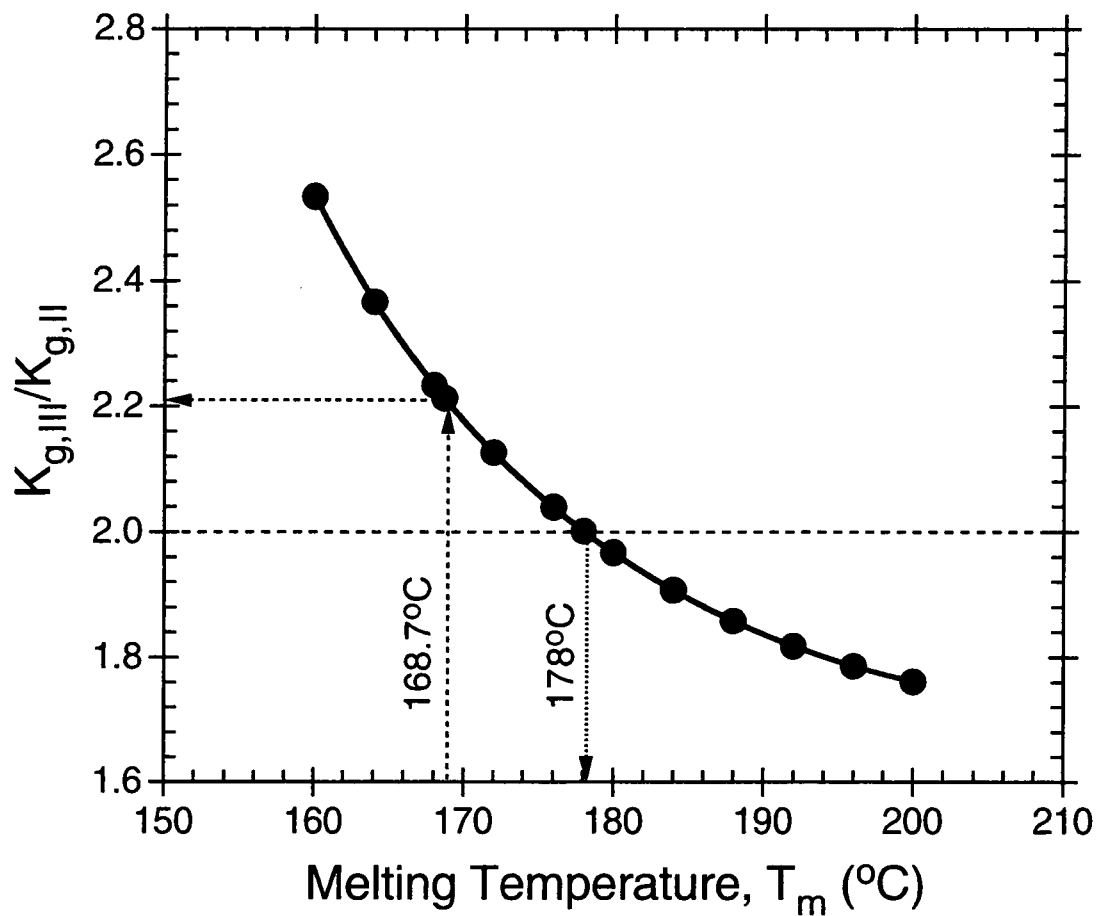


Figure 3-5. Variation of the $K_{g,III}/K_{g,II}$ value as a result of changes in the seed equilibrium melting temperature T_m^0 of sample sPP#1. The seed T_m^0 value which results in the $K_{g,III}/K_{g,II}$ value of 2.0 (ca. 178°C) is supposed to be the true equilibrium melting temperature of sample sPP#1.

856.6 erg²·cm⁻⁴, $\sigma_e = 78.2$ erg·cm⁻², and $\bar{q} = 9.1$ kcal·mol⁻¹ when assuming that growth occurs on the *bc* plane. Clearly, these values are much greater than those listed in Table 3-4, due to the effect of the much higher T_m^0 value used (i.e., 178°C versus 168.7°C).

One of the precautionary notes given by Huang et al. [32] is that the data-fitting procedure may only be applicable for growth rate data measured in a temperature range far from the glass transition temperature (i.e., in the nucleation control region) in order to minimize the influence from the transport term. Since the raw data of sPP#1 cover both regions, the effect of changes in parameters governing the transport term (i.e., U^* and T_∞) should also be considered. Qualitatively, an increase of 2.3% in T_g value resulted in an increase of 3.9% in the resulting T_m^0 value and of approximately 30% in all of the corresponding crystal growth parameters, whereas an increase of 8.3% in U^* value resulted in an increase of 2.3% in the resulting T_m^0 value and of approximately 17% in all of the corresponding crystal growth parameters [37]. Due to the fact that the T_m^0 value estimated from the data-fitting method is much greater than the one estimated previously [28] (cf. Part 2), more careful investigation is currently underway.

7. SUMMARY AND CONCLUSIONS

Spherulitic growth rate data of syndiotactic polypropylenes were taken from the literature and analyzed based on the traditional LH regime plot of $\log G + U^*/2.303R(T_c - T_\infty)$ versus $1/2.303T_c(\Delta T)f$. The input parameters used in the analysis were $T_g = 267.0$ K, $(T_m^0)_{100\%} = 441.8$ K, and $\Delta H_f^0 = 8.0$ kJ·mol⁻¹. Except for the data of 6H sample, all of the straight lines drawn through the bulk of data of sPP(8), sPP(9), and sPP#1 samples exhibited an unmistakable upward change in slopes, corresponding to the regime II→III transition, at the crystallization temperature of 110°C. The ratios of the $K_{g,III}/K_{g,II}$ were found to be in the range of 1.7 to 2.2. Based on these input parameters, the average values of the crystal growth parameters, regardless of the regime considered, were

found to be $\sigma = 11.3 \text{ erg}\cdot\text{cm}^{-2}$, $\sigma\sigma_e = 930.0 \pm 103.1 \text{ erg}^2\cdot\text{cm}^{-4}$, $\sigma_e = 82.4 \pm 9.1 \text{ erg}\cdot\text{cm}^{-2}$, and $\bar{q} = 9.6 \pm 1.1 \text{ kcal}\cdot\text{mol}^{-1}$, when assuming that growth occurs on the *ac* plane. But when assuming that growth occurs on the *bc* plane, they were $\sigma\sigma_e = 718.3 \pm 79.6 \text{ erg}^2\cdot\text{cm}^{-4}$, $\sigma_e = 63.7 \pm 7.1 \text{ erg}\cdot\text{cm}^{-2}$, and $\bar{q} = 7.4 \pm 0.8 \text{ kcal}\cdot\text{mol}^{-1}$.

The growth rate data were also analyzed based on the modified regime plot of $\log G - \log \Delta T + U/2.303R(T_c - T_\infty)$ versus $1/2.303T_c(\Delta T)f$, as suggested by Rodriguez-Arnold and her coworkers [19,21] using the same set of input parameters. Based on this analysis, the position of the regime II→III transition and the ratios of the $K_{g,III}/K_{g,II}$ were essentially unaffected. Only the parameters characteristic of the crystal growth were found to be lower in their values; these exhibited as much as 10.7% decrease in K_g value and about 11.2% decrease in $\sigma\sigma_e$, σ_e , and \bar{q} values. Specifically, the average values of the crystal growth parameters regardless of the regime considered were found to be $\sigma = 11.3 \text{ erg}\cdot\text{cm}^{-2}$, $\sigma\sigma_e = 825.8 \pm 94.8 \text{ erg}^2\cdot\text{cm}^{-4}$, $\sigma_e = 73.2 \pm 8.4 \text{ erg}\cdot\text{cm}^{-2}$, and $\bar{q} = 8.6 \pm 1.0 \text{ kcal}\cdot\text{mol}^{-1}$, when assuming that the *ac* plane is the growth plane. But when assuming that the *bc* plane is the growth plane, they were $\sigma\sigma_e = 637.9 \pm 73.2 \text{ erg}^2\cdot\text{cm}^{-4}$, $\sigma_e = 56.5 \pm 6.5 \text{ erg}\cdot\text{cm}^{-2}$, and $\bar{q} = 6.6 \pm 0.8 \text{ kcal}\cdot\text{mol}^{-1}$.

The measured crystal growth parameters were found to be sensitive to the values of the input parameters used, especially the equilibrium melting temperature. Qualitatively, it is found that a 2.3% change in T_g value leads to an approximately 2.9% change in K_g value, and around 2.6% change in $\sigma\sigma_e$, σ_e , and \bar{q} values. In the case of $(T_m^0)_{100\%}$, it is found that a 2.0% change in its value causes a 29.6% change in K_g value, and around 29.3% change in $\sigma\sigma_e$, σ_e , and \bar{q} values. Alternatively, a 1°C change in $(T_m^0)_{100\%}$ value causes an approximately 4.4% change in K_g , $\sigma\sigma_e$, σ_e , and \bar{q} values. Lastly, a 1% change in ΔH_f^0 value results in a roughly 1% change in σ value, while other parameters are unaffected.

8. REFERENCES AND NOTES

- [1] J.I. Lauritzen Jr., and J.D. Hoffman, *J. Res. Natl. Bur. Stand.*, **A64**, 73 (1960).
- [2] J.D. Hoffman and J.I. Lauritzen Jr., *J. Res. Natl. Bur. Stand.*, **A65**, 297 (1961).
- [3] J.I. Lauritzen Jr., and J.D. Hoffman, *J. Appl. Phys.*, **44**, 4340 (1973).
- [4] J.D. Hoffman, G.T. Davis, and J.I. Lauritzen Jr., In *Treatise on Solid State Chemistry*, Vol. 3, N.B. Hannay (Ed.), Plenum Press, New York, 1976, Chapter 7.
- [5] J.D. Hoffman, *Polymer*, **23**, 656 (1982).
- [6] J.D. Hoffman, *Polymer*, **24**, 3 (1983).
- [7] E.J. Clark and J.D. Hoffman, *Macromolecules*, **17**, 878 (1984).
- [8] J.D. Hoffman and R.L. Miller, *Macromolecules*, **21**, 3038 (1988).
- [9] J.D. Hoffman, *Polymer*, **33**, 2643 (1992).
- [10] J.D. Hoffman and R.L. Miller, *Polymer*, **38**, 3151 (1997).
- [11] R. Vasanthakumari and A.J. Pennings, *Polymer*, **24**, 175 (1983).
- [12] Z. Pelzbauer and A. Galeski, *J. Polym. Sci.*, **C38**, 23 (1972).
- [13] P.J. Phillips and N. Vatansever, *Macromolecules*, **20**, 2138 (1987).
- [14] J.G. Fatou, C. Marco, and L. Mandelkern, *Polymer*, **31**, 1685 (1990).
- [15] P. Supaphol and J.E. Spruiell, *J. Polym. Sci., Polym. Phys.*, **36**, 681 (1998).
- [16] P.J. Phillips and W.S. Lambert, *Macromolecules*, **23**, 2075 (1990).
- [17] R.L. Miller and E.G. Seeley, *J. Polym. Sci., Polym. Phys.*, **20**, 2297 (1982).
- [18] E.G. Seeley, In *M.S. Thesis*, Central Michigan University, 1982.
- [19] J. Rodriguez-Arnold, Z. Bu, S.Z.D. Cheng, E.T. Hsieh, T.W. Johnson, R.G. Geerts, S.J. Palackal, G.R. Hawley, and M.B. Welch, *Polymer*, **35**(24), 5194 (1994).
- [20] J. Rodriguez-Arnold, A. Zhang, S.Z.D. Cheng, A.J. Lovinger, E.T. Hsieh, P. Chu, T.W. Johnson, K.G. Honnell, R.G. Geerts, S.J. Palackal, G.R. Hawley, and M.B. Welch, *Polymer*, **35**(9), 1884 (1994).
- [21] J. Rodriguez-Arnold, In *Ph.D. Dissertation*, University of Akron, 1994.
- [22] P. Supaphol, J.J. Hwu, P.J. Phillips, and J.E. Spruiell, *SPE-ANTEC Proc.*, 1759 (1997).
- [23] Since Rodriguez-Arnold et al. did not publish their growth rate data of the two studied sPP fractions (labeled as sPP(76.8k) and sPP(132.0k) in reference 19 or sPP(8) and sPP(9) in reference 20) in their original publication [19] and only partial data are available in reference 21, I obtained their data by back-calculation (using the same parameters as theirs: $T_m^o = 160^\circ\text{C}$, $T_g = 0^\circ\text{C}$, and $\Delta H_f^o = 8.0 \text{ kJ}\cdot\text{mol}^{-1}$) from their results shown as Figure 4 in reference 19 or Figure 6.4 in reference 21. In addition, I also back-calculated (using $T_m^o = 160^\circ\text{C}$) the growth rate data from their results shown as Figure 3 in reference 19 or Figure 6.3 in reference 21. These regenerated data were averaged, and later compared with their original data partially listed in Table 6.1 in reference 21.
- [24] P. Supaphol and J.E. Spruiell, *in preparation*.
- [25] B. Lotz, A.J. Lovinger, and R.E. Cais, *Macromolecules*, **21**, 2375 (1988).
- [26] A.J. Lovinger, B. Lotz, and D.D. Davis, *ACS Polym. Prepr.*, **33**, 270 (1992).
- [27] D.G. Thomas and L.A.K. Staveley, *J. Chem. Soc.*, 4569 (1952).

- [28] P. Supaphol and J.E. Spruiell, *J. Appl. Polym. Sci.*, accepted on April 16, 1999.
- [29] S. Haftka and K.Könnecke, *J. Macromol. Sci., Phys.*, **B30(4)**, 319 (1991).
- [30] G. Balbontin, D. Dainelli, M. Galimberti, and G. Paganetto, *Makromol. Chem.*, **193**, 693 (1992).
- [31] P. Corradini, G. Natta, P. Garis, and P.A. Temussi, *J. Polym. Sci.*, **C16**, 2477 (1967).
- [32] J. Huang, A. Prasad, and H. Marand, *Polymer*, **35(9)**, 1896 (1994).
- [33] J. Huang and H. Marand, *Macromolecules*, **30**, 1069 (1997).
- [34] H.D. Iler, In *Ph.D. Dissertation*, Virginia Institute of Technology and State University, 1995.
- [35] J. Huang, M.S. Lisowski, J. Runt, E.S. Hall, R.T. Kean, N. Buehler, and J.S. Lin, *Macromolecules*, **31**, 2593 (1998).
- [36] J. Xu, S. Srinivas, H. Marand, and P. Agarwal, *Macromolecules*, **31**, 8230 (1998).
- [37] P. Supaphol and J.E. Spruiell, *ACS-PMSE Prepr.*, **81**, 252 (1999).

PART 4:

**CRYSTALLINE MEMORY EFFECT IN ISOTHERMAL
CRYSTALLIZATION OF SYNDIOTACTIC POLYPROPYLENE**

1. ABSTRACT

Isothermal crystallization behavior after partial or complete melting of syndiotactic polypropylene was investigated by differential scanning calorimetry (DSC). On partial melting, the total concentration of predetermined nuclei was found to decrease with increasing fusion temperature and increasing time period the sample spent at a specific fusion temperature. A significant effect of the rate of heating to the fusion temperature was also observed. On complete melting, the total concentration of predetermined nuclei was found to approach a constant value, which is the concentration of infusible heterogeneous nuclei (e.g., impurities, catalyst residues, etc.) present originally in the sample. At a specific fusion temperature, the concentration of predetermined athermal nuclei was found to decrease exponentially with the time period spent in the melt.

2. INTRODUCTION

It is known that crystallization of polymers is mainly controlled by nucleation and growth mechanisms. Since it is well established that the rate of crystal growth is primarily a function of crystallization temperature T_c , it can then be considered a constant when considering crystallization under isothermal conditions. The nucleation mechanism and rate are quite variable and much less well understood. It is known, however, that the nucleation rate depends on the number of infusible heterogeneous nuclei present in the polymer (e.g., impurities, catalyst residues, etc.) and the thermal history of the sample, as well as the crystallization temperature T_c . Because of its importance in determining overall crystallization kinetics and morphology, it is necessary to understand the nucleation mechanism and rate better. It is therefore very important that the influences of impurities, additives, nucleating agents, and especially "crystalline memory" be evaluated. The latter refers to clusters of molecules that retain

their crystal structure due to insufficient temperature or holding time at the fusion temperature. If these are retained at the crystallization temperature, they can act as nuclei provided they exceed the critical nucleus size. In practice, the crystalline memory can be erased by melting the polymer at a sufficiently high fusion temperature T_f for a certain period of time. Such temperature is usually greater than the polymer's equilibrium melting temperature ($T_f > T_m^0$). If the melting temperature or the holding time in the melt is insufficient (i.e., partial melting), upon subsequent cooling the crystalline residues can act as predetermined athermal nucleation sites which greatly enhance the overall crystallization rate. This phenomenon is also referred to as "self-nucleation."

In actual polymer processing, the polymer sample is not only subjected to thermal treatment, but also to mechanical treatment. Such mechanical deformation can lead to molecular orientation which also increases nucleation rate. This effect is referred to as "orientation memory." Both types of memory can greatly affect the crystallization behavior upon subsequent cooling of the sample. To eliminate both kinds of memory effects, it is necessary to keep the sample at a sufficiently high fusion temperature for a sufficiently long time period (depending on the fusion temperature T_f used) in order to eradicate as many traces of crystalline and oriented structures as possible. In some cases, one may wish to use these memory effects to control the overall crystallization rate or morphology of the crystallized polymer. Thus, one needs to understand the character of these effects in detail.

Due to their important influence on the crystallization behavior of polymers, memory effects (crystalline and orientation memories) have been of considerable interest and have been studied by several investigators [1-12]. However, no studies have appeared on memory effects in syndiotactic polypropylene. In this study, the effect of crystalline memory on isothermal crystallization characteristics of syndiotactic polypropylene (sPP) is thoroughly investigated.

3. EXPERIMENTAL DETAILS

3.1. Materials

The sPP sample used in this study was synthesized using a metallocene catalyst and was produced commercially in the pellet form by Fina Oil and Chemical Company of La Porte, Texas. Molecular characterization data, which were kindly performed by Dr. Roger A. Phillips and his group at Montell USA, Inc. in Elkton, Maryland, shows the following molecular weight information: $M_n = 76,200$ daltons, $M_w = 165,000$ daltons, $M_z = 290,000$ daltons, and $M_w/M_n = 2.2$. In addition, the syndiotacticity measured by ^{13}C NMR shows the racemic dyad content [%*r*] to be 91.4%, the racemic triad content [%*rr*] to be 87.3%, and the racemic pentad content [%*rrrr*] to be 77.1%.

3.2. Sample preparation and experimental methods

Sliced pellets were melt-pressed between a pair of Kapton films, which in turn were sandwiched between a pair of thick metal plates, in a Wabash compression molding machine preset at 190°C under a pressure of 67 kpsi. After ten minutes holding time, a film of 275 μm thickness was taken out and allowed to cool at ambient condition down to room temperature between the two metal plates. This treatment assumes that previous thermo-mechanical history was essentially erased, and provides a standard crystalline memory condition for the experiments.

In this study, a Perkin-Elmer Series 7 Differential Scanning Calorimeter (DSC-7) was used to follow isothermal crystallization behavior of sPP. The DSC-7 equipped with internal liquid nitrogen cooling unit reliably provided a cooling rate up to 200°C·min⁻¹. Temperature calibration was performed using an indium standard ($T_m^0 = 156.6^\circ\text{C}$ and $\Delta H_f^0 = 28.5 \text{ J}\cdot\text{g}^{-1}$). The consistency of the temperature calibration was checked every other run to ensure reliability of the data obtained. To make certain that thermal lag between the polymer sample and the DSC sensors is kept to a minimum,

each sample holder was loaded with a single disc, weighing 4.5 ± 0.3 mg, which was cut from the standard film already prepared. It is noteworthy that each sample was used only once and all the runs were carried out under nitrogen purge.

The experiments started with heating the sample from -40°C at a certain heating rate ϕ , ranging from $5^\circ\text{C}\cdot\text{min}^{-1}$ to $80^\circ\text{C}\cdot\text{min}^{-1}$, to a specified fusion temperature T_f . It should be noted that T_f is taken such that it is always greater than the highest melting point observed. For the purposes of this study, the highest observed melting point was taken to be approximately 125°C , which is the peak temperature observed from the melting endotherm of a sample isothermally crystallized at 95°C using a scanning rate of $20^\circ\text{C}\cdot\text{min}^{-1}$. The sample was then held at T_f for a certain holding time period t_h ranging from 3 to 300 min. After that, it was rapidly cooled at $200^\circ\text{C}\cdot\text{min}^{-1}$ from T_f to a fixed crystallization temperature T_c (cf. $T_c = 85^\circ\text{C}$), where it was left until the crystallization process was completed (approximately 15 min). The purpose of this study is to investigate the effect of changes in ϕ , T_f , and t_h on the crystalline memory behavior in isothermal crystallization of sPP.

4. ANALYSIS, RESULTS AND DISCUSSION

4.1. Analysis of DSC Measurements

DSC is an excellent device for following thermal transitions of polymers. When used to follow crystallization of polymers, what DSC measures is the heat flow \dot{Q} released due to the exothermic nature of the crystallization process. Intuitively, heat flow is directly proportional to the weight of the sample w , the heat of crystallization ΔH_c and the overall crystallization rate $\dot{\theta}(t)$. The crystallization enthalpy is a product of the absolute crystallinity χ_c and the enthalpy of crystallization of an infinitely thick crystal ΔH_c^0 (i.e., 100% crystalline sample). Consequently, an equation for the heat flow may be written as

$$\dot{Q} = c_1 \cdot w \cdot \chi_c \cdot \Delta H_c^0 \cdot \dot{\theta}(t), \quad (4-1)$$

where c_1 is a combined physical constant specific for each DSC used.

By setting $\dot{q} = \dot{Q}/(c_1 \cdot w \cdot \chi_c \cdot \Delta H_c^0)$, the relative crystallinity $\theta(t)$ can be obtained by integration of the transient normalized heat flow $\dot{q}(t)$ over the course of the crystallization. One finally gets

$$\theta(t) = \int_0^t \dot{\theta}(t) dt = \int_0^t \dot{q}(t) dt. \quad (4-2)$$

Figure 4-1 illustrates the plot of relative crystallinity as a function of time for sPP, which was melted at a fusion temperature T_f of 135°C for a holding time t_h of 10 min before being isothermally crystallized at $T_c = 85^\circ\text{C}$. The raw DSC exotherm is shown as the inset figure. An important parameter, which can easily be obtained from the plot similar to Figure 4-1, is the crystallization half-time $t_{0.5}$. The crystallization half-time is defined as the time spent from the onset of the crystallization to the point where the crystallization is 50% complete. It should be noted that the reciprocal of the half-time value (i.e., $t_{0.5}^{-1}$) is usually used to describe the overall rate of the crystallization process.

Analysis of isothermal bulk crystallization kinetics is often performed using the Avrami theory of phase transformation [13], which is normally written in the form:

$$1 - \theta(t) = \exp(-kt^n), \quad (4-3)$$

where k denotes the bulk crystallization rate constant, and n the Avrami exponent. Both k and n are constants typical of a given morphology and nucleation type. It should be noted that t is the time elapsed during the course of crystallization since the onset of crystallization (incubation time is excluded).

The bulk crystallization rate constant k can be deduced directly from the crystallization half-time $t_{0.5}$ through the following equation (by substitution of 0.5 for $\theta(t)$ in Equation (4-3)):

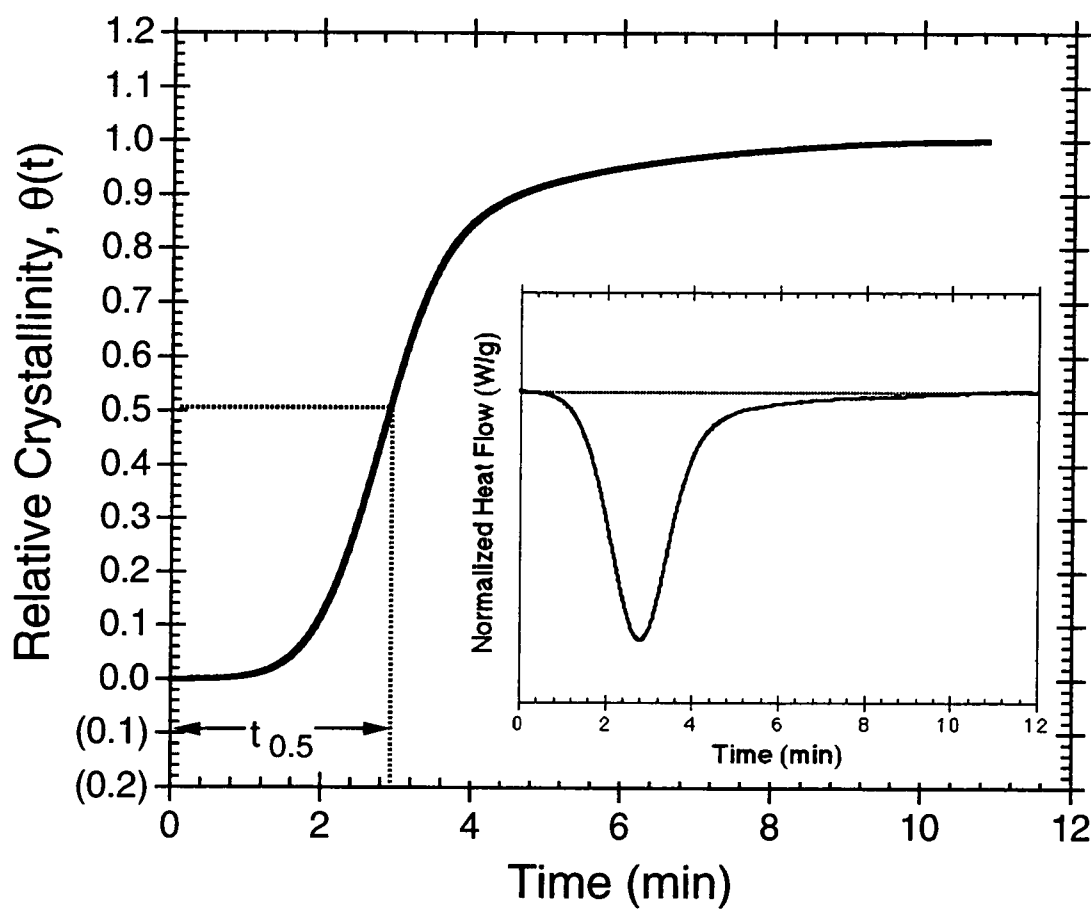


Figure 4-1. Relative crystallinity $\theta(t)$ as a function of time for sPP. The inset figure shows the original DSC crystallization exotherm as a function of time. Conditions: $\phi = 80^\circ\text{C}\cdot\text{min}^{-1}$, $T_i = 135^\circ\text{C}$, $t_h = 10$ min, and $T_c = 85^\circ\text{C}$.

$$k = \frac{\ln 2}{(t_{0.5})^n}. \quad (4-4)$$

In the case of predetermined nucleation and three dimensional growth (cf. later), the crystallization rate constant k is directly proportional to the total concentration of predetermined nuclei N_{tot} through the following equation:

$$k = \frac{4\pi}{3} N_{\text{tot}} G^3. \quad (4-5)$$

Based on Equations (4-4) and (4-5), the total concentration of predetermined nuclei N_{tot} can be calculated directly from the crystallization half-time $t_{0.5}$, according to the following equation:

$$N_{\text{tot}} = \frac{3}{4\pi G^3} \cdot \frac{\ln 2}{(t_{0.5})^3}. \quad (4-6)$$

Once the value of N_{tot} is determined, the average spherulite size D can also be calculated based on the following relationship:

$$D = \left(\frac{6}{\pi N_{\text{tot}}} \right)^{\frac{1}{3}}. \quad (4-7)$$

4.2. Effect of Crystallization Temperature

Investigations on the bulk crystallization kinetics of this particular sPP sample was recently performed, and the results were earlier reported [14,15] (cf. Part 2). Only the data taken for the crystallization temperature T_c range of 60°C to 95°C will be presented and discussed in this study. Each sample was cut in the form of a disc from a film prepared based on the same procedure as mentioned previously in the experimental section, and was put in a DSC sample holder. The sample was heated in a well calibrated DSC-7 from -40°C to $T_f = 190^\circ\text{C}$ at a heating rate ϕ of 80°C·min⁻¹ and was held at $T_f = 190^\circ\text{C}$ for a holding period t_h of 5 min before being quenched at a rate of 200°C·min⁻¹ to a desired crystallization temperature T_c .

Figure 4-2 shows the plot of crystallization half-time $t_{0.5}$ as a function of crystallization temperature T_c . The plot clearly shows an increase of $t_{0.5}$ value with increasing T_c within the T_c range of interest. This means that the rate of isothermal crystallization (i.e., the reciprocal value of the crystallization half-time $t_{0.5}^{-1}$) decreases as T_c increases (as shown in the inset figure of Figure 4-2). Previous results [14,15] (cf. Part 2) suggested that sPP crystallizes primarily in three dimensional growth and instantaneous nucleation at predetermined sites (within T_c range of interest); therefore, it is legitimate to calculate the total concentration of predetermined nuclei N_{tot} and the average spherulite diameter D by applying Equations (4-6) and (4-7) to the $t_{0.5}$ data obtained directly from the crystallization exotherms. The linear growth rate G as a function of crystallization temperature T_c can be approximated based on the following equation [16] (cf. Part 3):

$$G = 9.1 \times 10^8 \exp\left(-\frac{754.8}{T_c - 237.0} - \frac{3.6 \times 10^5}{T_c(441.8 - T_c)f}\right), \quad (4-8)$$

where $f = 2T_c/(T_c + 441.8)$. It should be noted that Equation (4-8) is valid only in the temperature range where $T_c \leq 110^\circ\text{C}$, and the unit of the crystal growth rate G is in $[\mu\text{m} \cdot \text{min}^{-1}]$.

Table 4-1 summarizes the effect of crystallization temperature T_c on crystallization half-time $t_{0.5}$, heat of crystallization ΔH_c , total concentration of predetermined nuclei N_{tot} , and average spherulite diameter D . Evidently, as the T_c value increases the total concentration of predetermined nuclei N_{tot} decreases monotonically; whereas, the average spherulite diameter D is found to be an increasing function of T_c (cf. Figure 4-3). In addition, the heat of crystallization ΔH_c is also found to increase with increasing T_c , suggesting that the absolute crystallinity is an increasing function of the crystallization temperature T_c , at least within the T_c range studied.

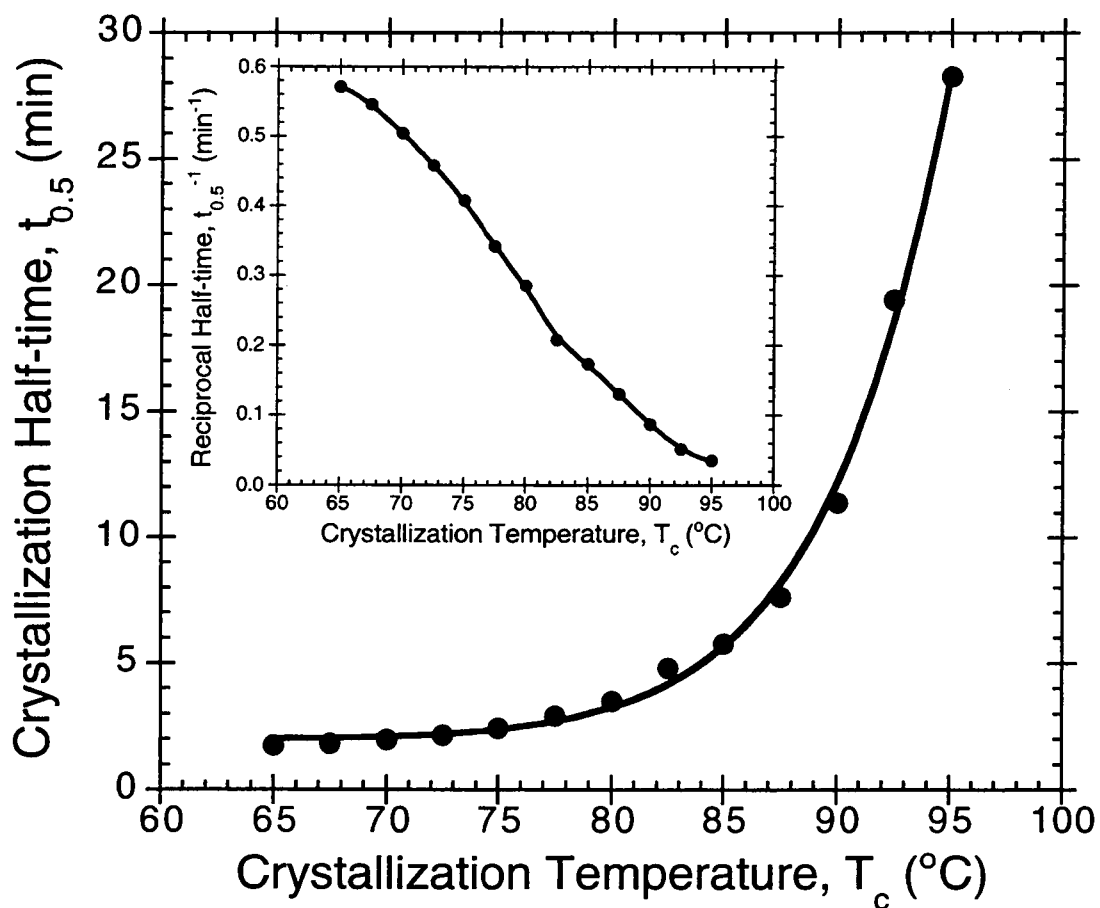


Figure 4-2. Effect of crystallization temperature T_c on the observed crystallization half-time $t_{0.5}$. The inset figure shows the effect of crystallization temperature T_c on the rate of overall crystallization (reciprocal half-time $t_{0.5}^{-1}$). Conditions: $\phi = 80^\circ\text{C}\cdot\text{min}^{-1}$, $T_f = 190^\circ\text{C}$, and $t_h = 5$ min.

Table 4-1. Effect of crystallization temperature T_c on crystallization half-time $t_{0.5}$, heat of crystallization ΔH_c , total concentration of predetermined nuclei N_{tot} , and average spherulite diameter D . Conditions: $\phi = 80^\circ\text{C}\cdot\text{min}^{-1}$, $T_f = 190^\circ\text{C}$, and $t_h = 5$ min.

T_c ($^\circ\text{C}$)	$t_{0.5}$ (min)	ΔH_c ($\text{J}\cdot\text{g}^{-1}$)	N_{tot} (nuclei $\cdot\text{cm}^{-3}$)	D (μm)
65.0	1.75	28.0	4.9×10^8	16
67.5	1.83	28.7	3.9×10^8	17
70.0	1.98	29.3	3.0×10^8	18
72.5	2.18	30.1	2.3×10^8	20
75.0	2.45	30.7	1.8×10^8	22
77.5	2.92	31.5	1.2×10^8	25
80.0	3.50	31.9	8.9×10^7	28
82.5	4.81	32.1	4.5×10^7	35
85.0	5.78	33.4	3.7×10^7	37
87.5	7.65	34.5	2.4×10^7	43
90.0	11.40	35.2	1.2×10^7	55
92.5	19.40	35.5	4.2×10^6	77
95.0	28.30	36.1	2.6×10^6	90

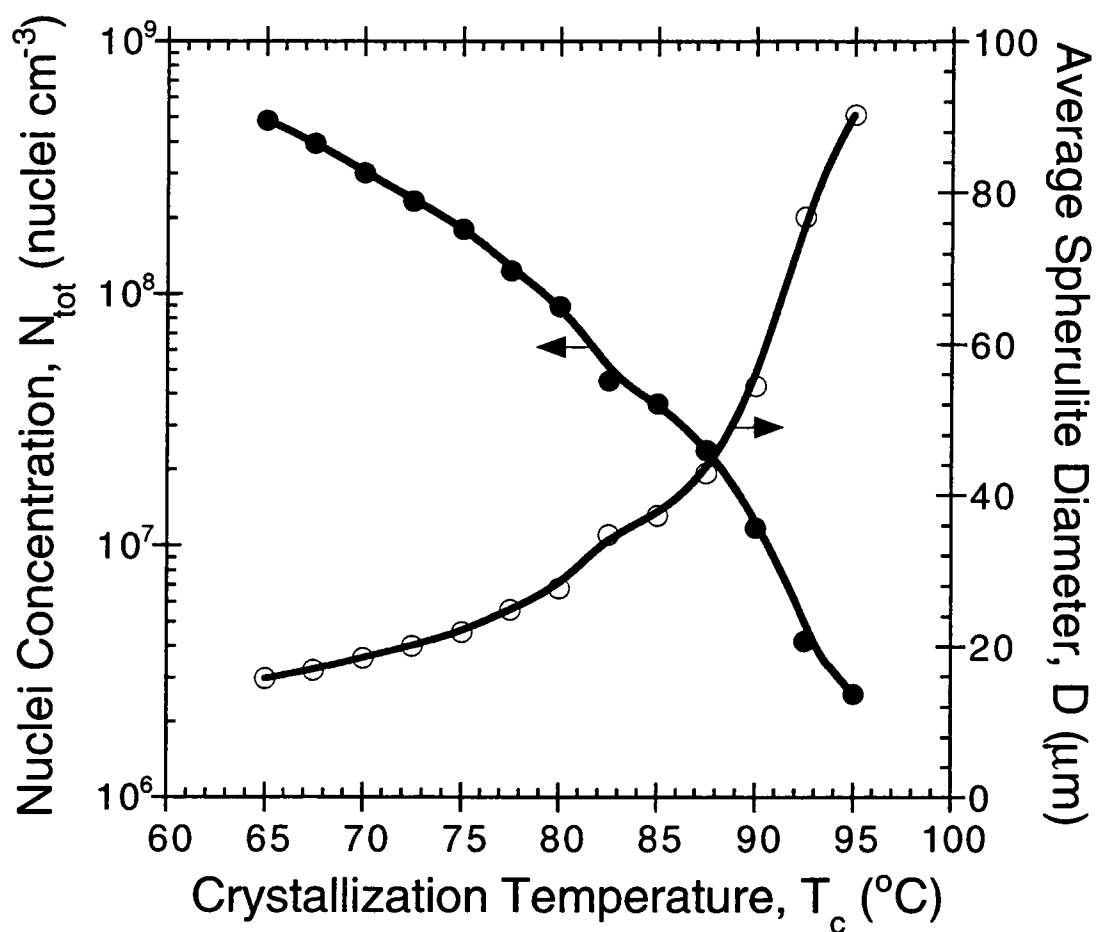


Figure 4-3. Effect of crystallization temperature T_c on the total concentration of predetermined nuclei N_{tot} and the average spherulite diameter D . Conditions: $\phi = 80^\circ\text{C}\cdot\text{min}^{-1}$, $T_f = 190^\circ\text{C}$, and $t_h = 5$ min.

As mentioned previously in the experimental section, it is necessary to find a crystallization temperature which gives a reliable crystallization exotherm, and the completion of crystallization does not take too long. By looking at all of the crystallization exotherms taken for this experiment, a $T_c = 85^\circ\text{C}$ was chosen as the standard crystallization temperature, since crystallization is completed within 15 min and it gives a low noise-to-signal ratio crystallization exotherm, which provides an optimal balance between the accuracy of the measurements and total time needed to complete the experiments.

4.3. Effect of Heating Rate

In this experiment, the samples were heated from -40°C to $T_f = 150^\circ\text{C}$ at 6 different heating rates ϕ ranging from $5^\circ\text{C}\cdot\text{min}^{-1}$ to $80^\circ\text{C}\cdot\text{min}^{-1}$. The samples were held at $T_f = 150^\circ\text{C}$ for a holding time t_h of 5 min before being brought down to isothermally crystallize at $T_c = 85^\circ\text{C}$. Figure 4-4 illustrates the effect of heating rate ϕ on the crystallization half-time $t_{0.5}$, obtained directly from the resulting DSC exotherms. Evidently, the observed $t_{0.5}$ value or the rate of isothermal crystallization (shown in Figure 4-4 as the inset figure) seems to have a strong correlation with the heating rate used when $\phi \leq 20^\circ\text{C}\cdot\text{min}^{-1}$, and is seemingly independent of the heating rate used when $\phi \geq 20^\circ\text{C}\cdot\text{min}^{-1}$. The result is very interesting in the sense that it clearly demonstrates that low heating rates (i.e., $\phi \leq 20^\circ\text{C}\cdot\text{min}^{-1}$) affect, to some extent, the original crystallinity of the sample during a DSC heating scan.

By assuming that the linear growth rate G is independent of the nucleation mechanism and is therefore constant (i.e., based on Equation (4-8), $G = 2.86 \mu\text{m}\cdot\text{min}^{-1}$ at $T_c = 85^\circ\text{C}$), the total concentration of predetermined nuclei N_{tot} and the average spherulite diameter D can directly be estimated based on Equations (4-6) and (4-7). Table 4-2 summarizes the effect of heating rate ϕ on crystallization half-time $t_{0.5}$, heat of

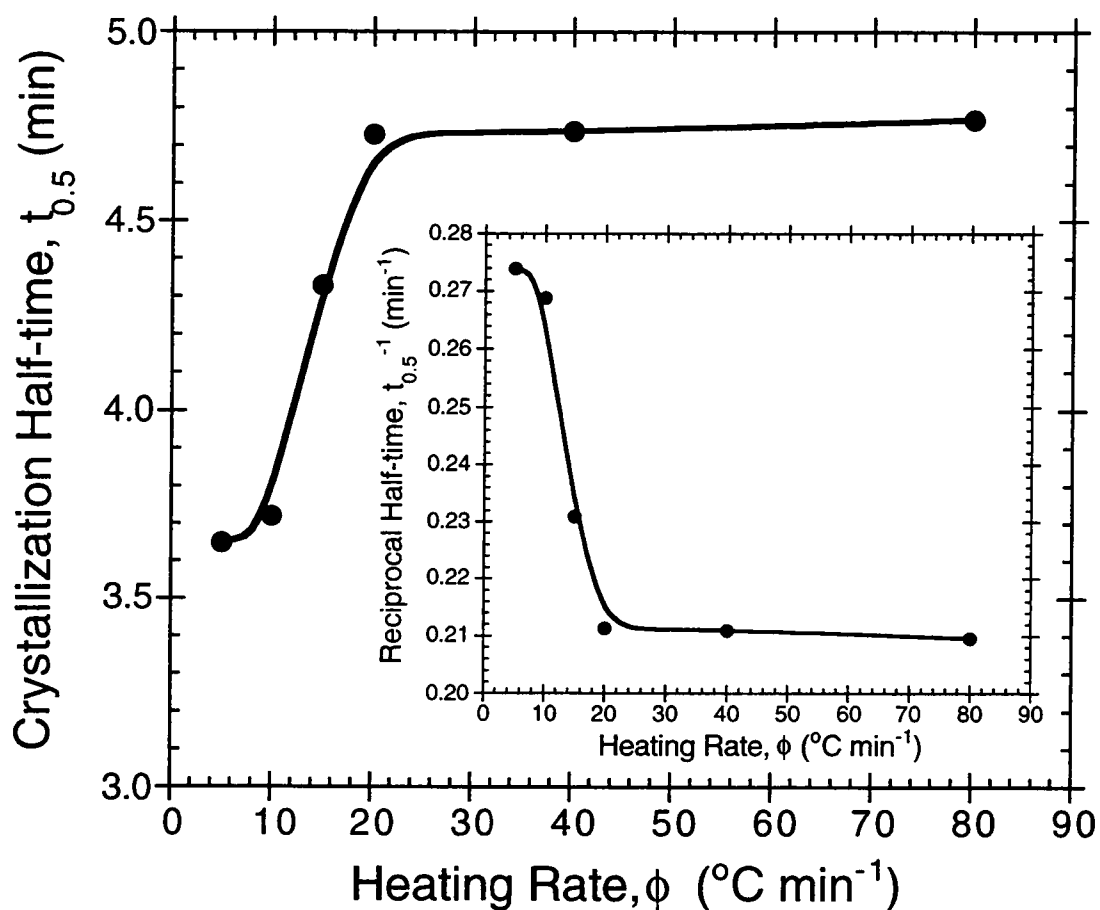


Figure 4-4. Effect of heating rate ϕ on the observed crystallization half-time $t_{0.5}$. The inset figure shows the effect of heating rate ϕ on the rate of overall crystallization (reciprocal half-time $t_{0.5}^{-1}$). Conditions: $T_i = 150^{\circ}\text{C}$, $t_h = 5$ min, and $T_c = 85^{\circ}\text{C}$.

Table 4-2. Effect of heating rate ϕ on crystallization half-time $t_{0.5}$, heat of crystallization ΔH_c , total concentration of predetermined nuclei N_{tot} , and average spherulite diameter D . Conditions: $T_i = 150^\circ\text{C}$, $t_h = 5$ min, and $T_c = 85^\circ\text{C}$

ϕ ($^\circ\text{C}\cdot\text{min}^{-1}$)	$t_{0.5}$ (min)	ΔH_c ($\text{J}\cdot\text{g}^{-1}$)	N_{tot} (nuclei $\cdot\text{cm}^{-3}$)	D (μm)
5	3.65	31.1	1.5×10^8	24
10	3.72	32.3	1.4×10^8	24
15	4.33	31.6	8.7×10^7	28
20	4.73	31.9	6.7×10^7	31
40	4.74	32.4	6.7×10^7	31
80	4.77	32.3	6.5×10^7	31

crystallization ΔH_c , total concentration of predetermined nuclei N_{tot} , and average spherulite diameter D . Apparently, for the case of $\phi \leq 20^\circ\text{C}\cdot\text{min}^{-1}$, as the ϕ value increases the total concentration of predetermined nuclei N_{tot} decreases monotonically; whereas, the average spherulitic diameter D is found to be an increasing function of ϕ (see Figure 4-5). On the other hand, in the range where $\phi \geq 20^\circ\text{C}\cdot\text{min}^{-1}$, both N_{tot} and D values do not seem to change with the heat rate ϕ used.

The result suggests that when low heating rates (i.e., $\phi \leq 20^\circ\text{C}\cdot\text{min}^{-1}$) are used in a DSC heating scan, the original crystalline structure is affected such that the sample may need to be kept in the melt for a longer holding time period in order to eliminate the previous crystalline memory. The reason why the original crystalline structure is affected by low heating rates is not entirely clear, but it may be a result of crystal thickening or recrystallization of some imperfect crystals originally present in the sample. Importantly, it has to be kept in mind that low heating rates used in an observation of melting behavior of a polymer may lead to anomalous results, as demonstrated by this experiment (as reflected by the increase in total concentration of predetermined nuclei N_{tot}) when the heating rate used was lower than $20^\circ\text{C}\cdot\text{min}^{-1}$.

4.4. Effect of Fusion Temperature

In this experiment, the samples were heated from -40°C to a specified fusion temperature T_f , ranging from 128°C to 200°C , at a heating rate ϕ of $80^\circ\text{C}\cdot\text{min}^{-1}$. The samples were kept at the fusion temperature T_f for a holding time t_h of 5 min before being brought down to isothermally crystallize at $T_c = 85^\circ\text{C}$. Figure 6 shows the plot of the crystallization half-time $t_{0.5}$, obtained directly from the resulting DSC exotherms, as a function of fusion temperature T_f . Apparently, the observed $t_{0.5}$ value or the rate of isothermal crystallization (shown in Figure 4-6 as the inset figure) seems to have a strong

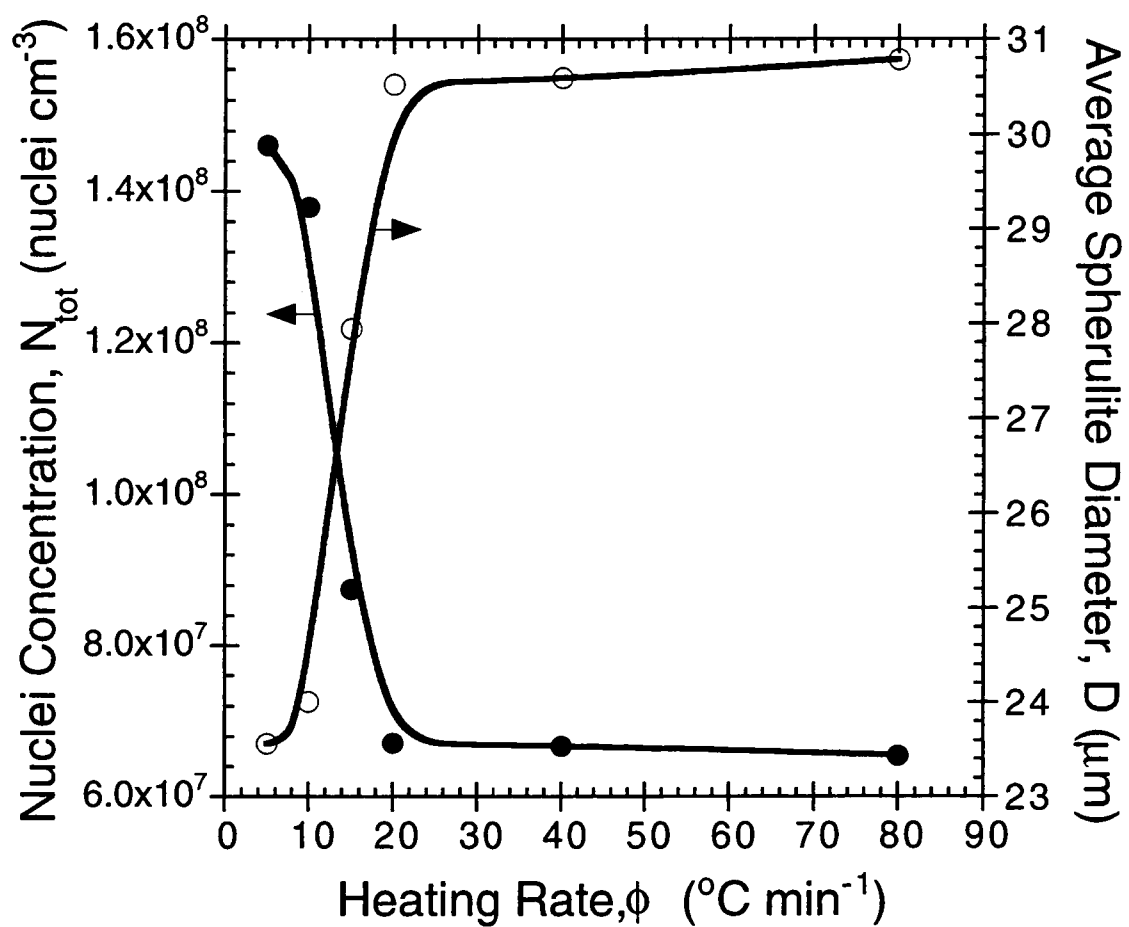


Figure 4-5. Effect of heating rate ϕ on the total concentration of predetermined nuclei N_{tot} and the average spherulite diameter D . Conditions: $T_f = 150^{\circ}\text{C}$, $t_h = 5$ min, and $T_c = 85^{\circ}\text{C}$.

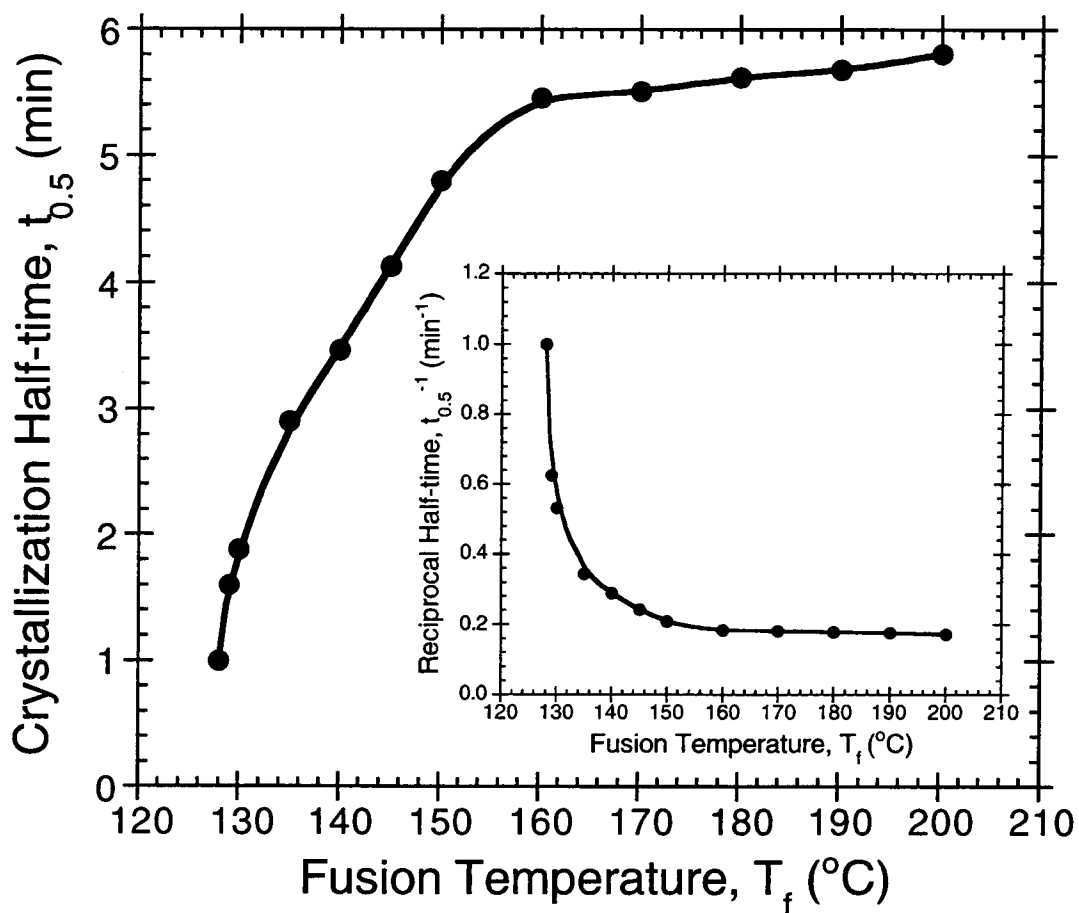


Figure 4-6. Effect of fusion temperature T_f on the observed crystallization half-time $t_{0.5}$. The inset figure shows the effect of fusion temperature T_f on the rate of overall crystallization (reciprocal half-time $t_{0.5}^{-1}$). Conditions: $\phi = 80^\circ\text{C}\cdot\text{min}^{-1}$, $t_h = 5$ min, and $T_c = 85^\circ\text{C}$.

correlation with the fusion temperature used, especially in the range where $T_f \leq 160^\circ\text{C}$, and it becomes independent of the fusion temperature used when $T_f \geq 160^\circ\text{C}$.

Based on Equations (4-6) and (4-7), the total concentration of predetermined nuclei N_{tot} and the average spherulite diameter D can be directly calculated. Table 4-3 summarizes the effect of fusion temperature T_f on crystallization half-time $t_{0.5}$, heat of crystallization ΔH_c , total concentration of predetermined nuclei N_{tot} , and average spherulite diameter D . Apparently, for the case of $T_f \leq 160^\circ\text{C}$, as the T_f value increases the average number of predetermined nuclei N_{tot} decreases monotonically; whereas, the average spherulitic diameter D is found to be an increasing function of T_f (see Figure 4-7). On the other hand, when $T_f \geq 160^\circ\text{C}$, both N_{tot} and D values do not seem to vary much with T_f . This suggests that prolonged melting of sPP at $T_f > 160^\circ\text{C}$ is mandatory in order for any measurement on crystallization behavior to be free from the influence of the predetermined athermal nuclei (i.e., the nuclei that were present as a result of an earlier crystallization process).

4.5. Effect of Holding Time

In this experiment, the samples were heated from -40°C to a specified fusion temperature T_f , ranging from 145°C to 180°C , at a heating rate ϕ of $80^\circ\text{C}\cdot\text{min}^{-1}$. The samples were held at a specific fusion temperature T_f for a series of holding times t_h , ranging from 3 min to 300 min, before being quenched to the isothermal crystallization temperature T_c of 85°C . Figure 4-8 shows the plot of the crystallization half-time $t_{0.5}$, obtained directly from the resulting DSC exotherms, as a function of holding time t_h for 5 different fusion temperatures T_f . Apparently, for each fusion temperature T_f , the $t_{0.5}$ value is found to increase with increasing holding time t_h .

Based on Equations (4-6) and (4-7), the total concentration of predetermined nuclei N_{tot} and the average spherulite diameter D can be directly calculated. Table 4-4

Table 4-3. Effect of fusion temperature T_f on crystallization half-time $t_{0.5}$, heat of crystallization ΔH_c , total concentration of predetermined nuclei N_{tot} , and average spherulite diameter D . Conditions: $\phi = 80^\circ\text{C}\cdot\text{min}^{-1}$, $t_h = 5$ min, and $T_c = 85^\circ\text{C}$.

T_f ($^\circ\text{C}$)	$t_{0.5}$ (min)	ΔH_c ($\text{J}\cdot\text{g}^{-1}$)	N_{tot} (nuclei $\cdot\text{cm}^{-3}$)	D (μm)
128	1.00	26.3	7.1×10^9	6
129	1.60	31.4	1.7×10^9	10
130	1.88	31.3	1.1×10^9	12
135	2.90	32.3	2.9×10^8	19
140	3.47	33.7	1.7×10^8	22
145	4.13	33.2	1.0×10^8	27
150	4.80	33.2	6.4×10^7	31
160	5.46	34.0	4.4×10^7	35
170	5.51	34.6	4.2×10^7	36
180	5.62	34.5	4.0×10^7	36
190	5.68	34.5	3.9×10^7	37
200	5.71	34.4	3.8×10^7	37

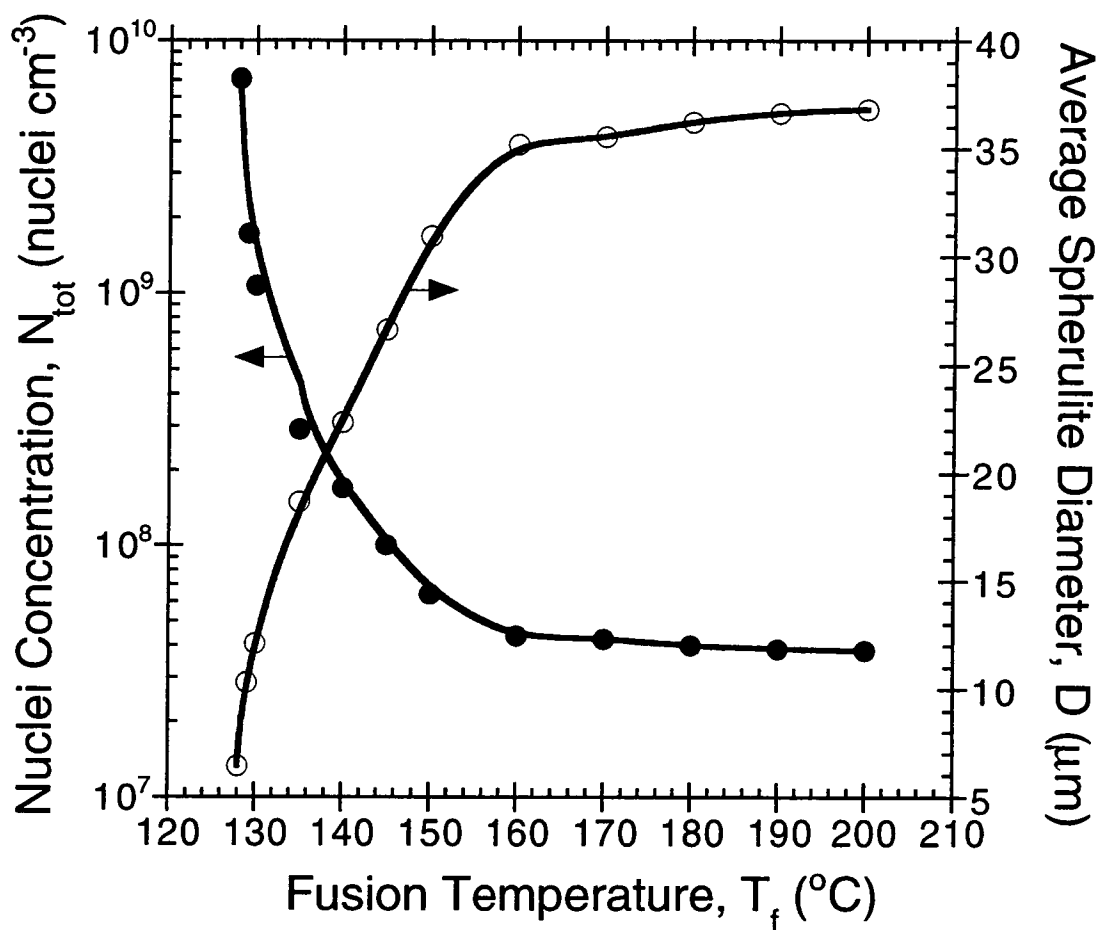


Figure 4-7. Effect of fusion temperature T_f on the total concentration of predetermined nuclei N_{tot} and the average spherulite diameter D . Conditions: $\phi = 80^\circ\text{C}\cdot\text{min}^{-1}$, $t_h = 5$ min, and $T_c = 85^\circ\text{C}$.

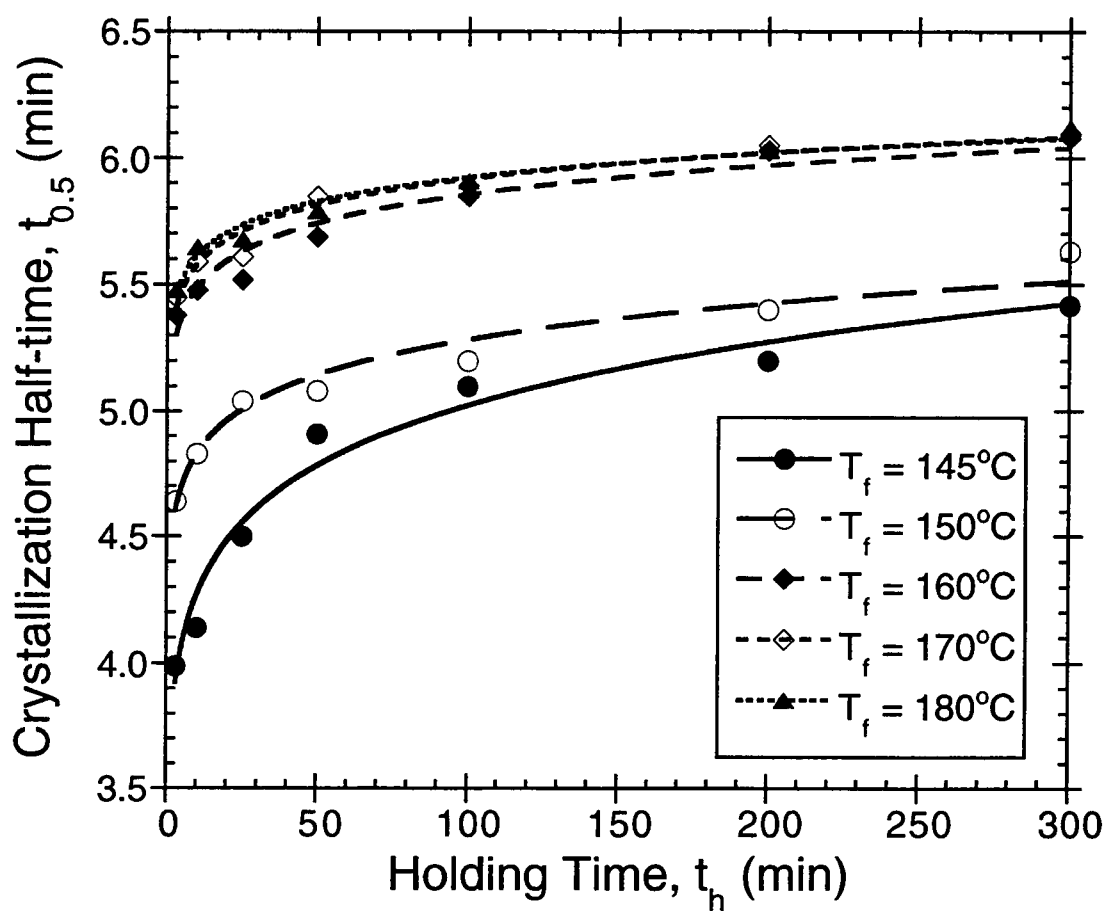


Figure 4-8. Effect of holding time t_h on the observed crystallization half-time $t_{0.5}$ for 5 different fusion temperatures T_f , ranging from 145°C to 180°C . Conditions: $\phi = 80^\circ\text{C}\cdot\text{min}^{-1}$, and $T_c = 85^\circ\text{C}$.

Table 4-4. Effect of holding time t_h in the melt at 5 different fusion temperatures T_f , ranging from 145°C to 180°C, on crystallization half-time $t_{0.5}$, heat of crystallization ΔH_c , total concentration of predetermined nuclei N_{tot} , and average spherulite diameter D . Conditions: $\phi = 80^\circ\text{C}\cdot\text{min}^{-1}$, and $T_c = 85^\circ\text{C}$.

T_f (°C)	t_h (min)	$t_{0.5}$ (min)	ΔH_c (J·g ⁻¹)	N_{tot} (nuclei·cm ⁻³)	D (μm)
145	3	3.99	32.3	1.1×10^8	26
	10	4.14	32.1	1.0×10^8	27
	25	4.50	33.6	7.8×10^7	29
	50	4.91	35.1	6.0×10^7	32
	100	5.10	35.5	5.4×10^7	33
	200	5.20	34.9	5.1×10^7	34
	300	5.42	33.4	4.5×10^7	35
150	3	4.64	33.1	7.1×10^7	30
	10	4.83	32.9	6.3×10^7	31
	25	5.04	33.7	5.5×10^7	33
	50	5.08	34.6	5.4×10^7	33
	100	5.20	34.6	5.1×10^7	34
	200	5.40	33.2	4.5×10^7	35
	300	5.63	35.4	4.0×10^7	36
160	3	5.38	33.8	4.6×10^7	35
	10	5.48	35.6	4.3×10^7	35
	25	5.52	35.3	4.2×10^7	36
	50	5.69	34.8	3.9×10^7	37
	100	5.85	36.0	3.5×10^7	38
	200	6.03	34.5	3.2×10^7	39
	300	6.08	36.0	3.2×10^7	39
170	3	5.45	33.4	4.6×10^7	35
	10	5.59	30.9	4.5×10^7	35
	25	5.61	33.2	4.5×10^7	35
	50	5.85	34.6	4.2×10^7	36
	100	5.89	35.4	4.2×10^7	36
	200	6.05	34.6	3.2×10^7	39
	300	6.10	34.5	3.1×10^7	39
180	3	5.48	34.6	4.3×10^7	35
	10	5.65	35.9	3.9×10^7	36
	25	5.68	33.8	3.9×10^7	37
	50	5.79	34.6	3.7×10^7	37
	100	5.91	35.9	3.4×10^7	38
	200	6.03	33.9	3.2×10^7	39
	300	6.12	34.9	3.1×10^7	40

summarizes the effect of holding time t_h on crystallization half-time $t_{0.5}$, heat of crystallization ΔH_c , total concentration of predetermined nuclei N_{tot} , and average spherulite diameter D for 5 different fusion temperatures T_f . Evidently, for a particular value of T_f , the total concentration of predetermined nuclei N_{tot} is found to decrease with increasing holding time t_h ; whereas, the average spherulite diameter D is an increasing function of t_h (shown, as an example, in Figure 4-9 for the case of $T_f = 180^\circ\text{C}$).

Based on the plot of N_{tot} versus t_h shown in Figure 4-9, it is intuitive to interpret that the total average number of predetermined nuclei per unit volume N_{tot} is a certain decreasing function with the holding time t_h for a particular fusion temperature T_f . Recently, Ziabicki and Alfonso [17,18] proposed that the total concentration of predetermined nuclei is an exponential decay function with the residence time in the melt, which reads

$$N_{tot}(T_f, t_h) = N_0 \exp\left[-\frac{t_h}{\tau(T_f)}\right] + N_{het}, \quad (4-9)$$

where N_{tot} is the total concentration of predetermined nuclei and is a function of both T_f and t_h , N_0 the initial concentration of predetermined athermal nuclei (as a result of residual crystalline structure), and τ the relaxation time for the dis-association of nucleation cluster. Furthermore, N_{het} denotes the concentration of infusible heterogeneous nuclei (e.g., impurities, catalyst residues, etc.), and can be obtained by extrapolation of the plot of N_{tot} versus t_h to infinite holding time. Thus,

$$N_{het} = N_{tot}(T_f, \infty). \quad (4-10)$$

Mathematical rearrangement of Equations (4-9) and (4-10) results in the following equation:

$$N_{tot}(T_f, t_h) - N_{tot}(T_f, \infty) = N_0 \exp\left[-\frac{t_h}{\tau(T_f)}\right]. \quad (4-11)$$

Equation (4-11) can also be written in its logarithmic form:

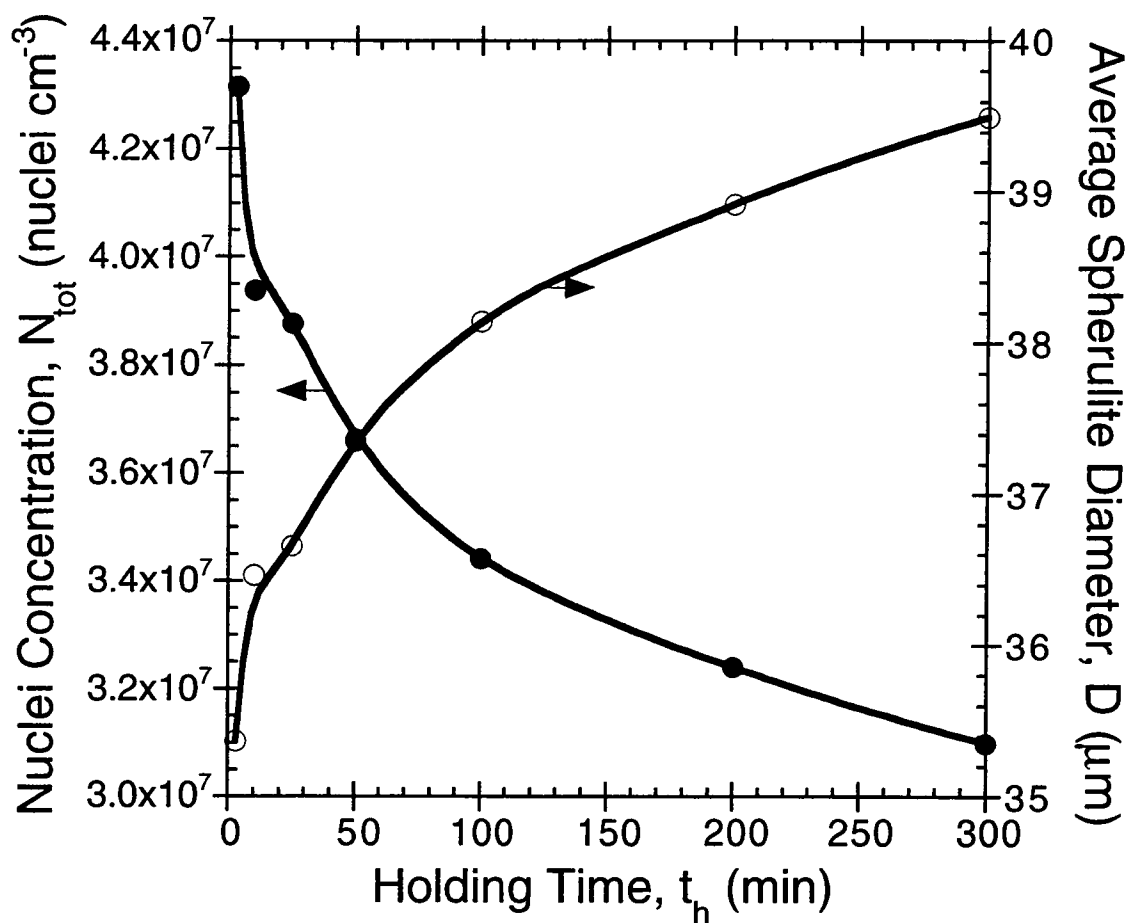


Figure 4-9. Effect of holding time t_h on the total concentration of predetermined nuclei N_{tot} and the average spherulite diameter D . Conditions: $\phi = 80^\circ\text{C}\cdot\text{min}^{-1}$, $T_f = 180^\circ\text{C}$, and $T_c = 85^\circ\text{C}$.

$$\ln[N_{\text{tot}}(T_f, t_h) - N_{\text{tot}}(T_f, \infty)] = \ln N_0 - \frac{1}{\tau(T_f)} t_h. \quad (4-12)$$

Based on Equation (4-12), it is clear that the relaxation time τ can be extracted directly from the plot of $\ln[N_{\text{tot}}(T_f, t_h) - N_{\text{tot}}(T_f, \infty)]$ against t_h , where τ is taken as the reciprocal value of the slope (i.e., $\tau(T_f) = \text{slope}^{-1}$). In addition, the initial concentration of predetermined athermal nuclei N_0 can also be estimated directly from the plot (i.e., $N_0 = e^{(\text{y-intercept})}$).

Based on the plot of N_{tot} versus t_h illustrated in Figure 4-9, the concentration of the infusible heterogeneous nuclei N_{het} was approximately estimated to be 3.0×10^7 nuclei-cm⁻³. Combined with the calculated values of N_{tot} listed in Table 4-4, the plots of $\ln[N_{\text{tot}}(T_f, t_h) - N_{\text{tot}}(T_f, \infty)]$ versus t_h for 5 different fusion temperatures T_f can be drawn as shown in Figure 4-10. The values of N_0 and $\tau(T_f)$ which were obtained from Figure 4-10 are summarized in Table 4-5. As expected, the relaxation time τ is a certain decreasing function of T_f (with the exception of the data at $T_f = 150^\circ\text{C}$).

5. CONCLUSIONS

Isothermal crystallization behavior of sPP after partial or complete melting has been investigated by DSC. On partial melting, the total concentration of predetermined nuclei N_{tot} was found to decrease with increasing fusion temperature T_f up to a critical value (i.e., $T_f \approx 160^\circ\text{C}$) where the N_{tot} value approaches a constant (i.e., complete melting). At a specific fusion temperature T_f , the total concentration of predetermined nuclei N_{tot} was found to be a certain decay function with the holding time t_h , characterized by a relaxation time τ , and it was also found to approach a constant value as the holding time t_h becomes long (i.e., complete melting). This constant value of total concentration of predetermined nuclei N_{tot} observed after prolonged melting of the sample at sufficiently high fusion temperature (i.e., $T_f > 160^\circ\text{C}$) is the concentration of infusible heterogeneous nuclei N_0 (e.g., impurities, catalyst residues, etc.), and was

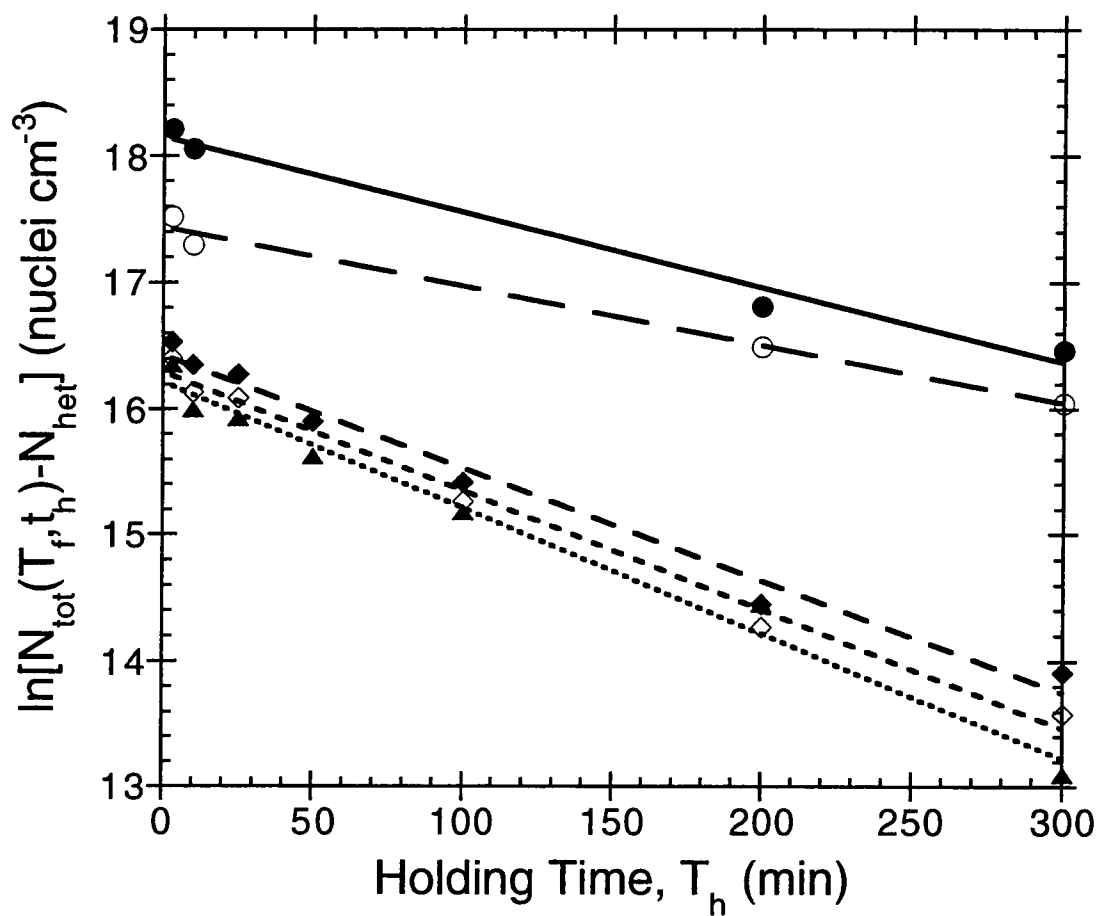


Figure 4-10. Plot of $\ln[N_{\text{tot}}(T_f, t_h) - N_{\text{tot}}(T_f, \infty)]$ versus holding time t_h for 5 different fusion temperatures T_f : (●) 145°C ; (○) 150°C ; (◆) 160°C ; (◇) 170°C ; and (▲) 180°C .

Table 4-5. Summary of the relaxation time for the segregation of nucleation cluster τ , the initial concentration of predetermined athermal nuclei N_0 , and the initial total concentration of predetermined nuclei $N_{\text{tot}}(T_f, 0)$ for 5 different fusion temperatures T_f .

T_f (°C)	$\tau(T_f)$ (min)	N_0 (nuclei·cm ⁻³)	$N_{\text{tot}}(T_f, 0)^{\text{a)}}$ (nuclei·cm ⁻³)
145	167.9	7.6×10^7	1.1×10^8
150	214.2	3.7×10^7	6.7×10^7
160	111.8	1.4×10^7	4.4×10^7
170	106.0	1.2×10^7	4.2×10^7
180	100.3	1.1×10^7	4.1×10^7

^{a)} $N_{\text{tot}}(T_f, 0) = N_0 + 3.0 \times 10^7$

approximated to be 3.0×10^7 nuclei-cm⁻³ for this particular sPP sample. The relaxation time τ was also found to be a certain decreasing function of fusion temperature T_f , which ranges from 168 min at $T_f = 145^\circ\text{C}$ to 100 min at $T_f = 180^\circ\text{C}$.

6. REFERENCES

- [1] B. Wunderlich, In *Macromolecular Physics*, Vol. 2, Academic Press, New York, 1976, pages 52-70.
- [2] E. Turska and S. Gogolewski, *J. Appl. Polym. Sci.*, **19**, 637 (1975).
- [3] Y.P. Khanna and A.C. Reimschuessel, *J. Appl. Polym. Sci.*, **35**, 2259 (1988).
- [4] Y.P. Khanna, A.C. Reimschuessel, A. Banerjie, and C. Altman, *Polym. Eng. Sci.*, **28**, 1600 (1988).
- [5] Y.P. Khanna, R. Kumar, and A.C. Reimschuessel, *Polym. Eng. Sci.*, **28**, 1607 (1988).
- [6] Y.P. Khanna, R. Kumar, and A.C. Reimschuessel, *Polym. Eng. Sci.*, **28**, 1612 (1988).
- [7] Y.P. Khanna, W.P. Kuhn, J.E. Macur, A.F. Messa, N.S. Murthy, A.C. Reimschuessel, R.L. Schneider, J.P. Sibilialia, A.J. Signorelli, and T.J. Taylor, *J. Polym. Sci., Polym. Phys.*, **33**, 1023 (1995).
- [8] N.A. Mehl and L. Rebenfeld, *Polym. Eng. Sci.*, **32**, 1451 (1992).
- [9] B. Fillon, J.C. Wittmann, B. Lotz, and A. Thierry, *J. Polym. Sci., Polym. Phys.*, **31**, 1383 (1993).
- [10] B. Fillon, B. Lotz, A. Thierry, and J.C. Wittmann, *J. Polym. Sci., Polym. Phys.*, **31**, 1395 (1993).
- [11] B. Fillon, A. Thierry, J.C. Wittmann, and B. Lotz, *J. Polym. Sci., Polym. Phys.*, **31**, 1407 (1993).
- [12] G.C. Alfonso and P. Scardigli, *Macromol. Symp.*, **118**, 323 (1997).
- [13] M. Avrami, *J. Chem. Phys.*, **7**, 1103 (1939); *ibid.*, **8**, 212 (1940); *ibid.*, **9**, 177 (1941).
- [14] P. Supaphol, J.J. Hwu, P.J. Phillips, and J.E. Spruiell, *SPE-ANTEC Proc.*, 1759 (1997).
- [15] P. Supaphol and J.E. Spruiell, *J. Appl. Polym. Sci.*, accepted on April 16, 1999.
- [16] P. Supaphol and J.E. Spruiell, *Polymer*, accepted on March 25, 1999.
- [17] A. Ziabicki and G.C. Alfonso, *Colloid Polym. Sci.*, **272**, 1027 (1994).
- [18] G.C. Alfonso and A. Ziabicki, *Colloid Polym. Sci.*, **273**, 317 (1995).

PART 5:

**APPLICATION OF THE AVRAMI, TOBIN, MALKIN, AND
SIMULTANEOUS AVRAMI MACROKINETIC MODELS TO
ISOTHERMAL CRYSTALLIZATION OF SYNDIOTACTIC
POLYPROPYLENES**

1. ABSTRACT

Various macrokinetic models; namely the Avrami, Tobin, Malkin, and simultaneous Avrami models; have been applied to describe the primary crystallization of syndiotactic polypropylene under isothermal conditions. Analysis of the experimental data was carried out using a direct fitting method, such that the experimental data were directly fitted to each macrokinetic model using a non-linear multi-variable regression program. Comparison of the kinetics parameters obtained from the program to those obtained from the traditional analytical procedure suggested that applicability and reliability of the direct fitting method is satisfactory. Prediction of the time-dependent relative evolution of crystallinity at other crystallization temperatures was demonstrated, based on the bulk kinetics parameters obtained from the analysis.

2. INTRODUCTION

The overall crystallization process in semi-crystalline polymers can be divided into two main processes: primary crystallization and secondary crystallization. The primary crystallization process is the macroscopic development of crystallinity as a result of two consecutive microscopic mechanisms: primary nucleation and secondary nucleation (i.e., subsequent crystal growth). The secondary crystallization process is mainly concerned with the crystallization of interfibrillar melt, which was rejected and trapped between the fibrillar structure formed during the growth of crystalline aggregates (e.g., axialites, spherulites, etc.) [1-3]. It should be noted that if the crystallization time becomes very long, other types of secondary crystallization (i.e., crystal perfection and crystal thickening) may become significant enough to increase the ultimate absolute crystallinity.

For the purpose of describing the macroscopic evolution of crystallinity under quiescent isothermal conditions, a number of mathematical models [4-13] have been proposed, based primarily on the notion of primary nucleation and subsequent crystal growth microscopic mechanisms, over the past sixty years. Even though the contributions from Kolmogoroff [4], Johnson and Mehl [5], Avrami [6-8], and Evans [9] are essentially similar, it is the work of Avrami that has received the most attention. Thereby, these contributions are frequently referred to as the "Avrami equation." Based on different approaches, Tobin [10-12] and Malkin et al. [13] arrived at different mathematical models, which are also different from the Avrami model. Consequently, the quiescent crystallization data of semi-crystalline polymers at a constant temperature can be mathematically described by these three distinct models.

Unlike the Avrami model, use of the Tobin and Malkin models to analyze the isothermal crystallization data of semi-crystalline polymers is scarce. Critical descriptive comparisons between the Avrami and Tobin models were performed on the isothermal crystallization data of poly(ethylene terephthalate) (PET), poly(phenylene sulfide) (PPS) [14], medium density polyethylene (MDPE), and poly(oxyethylene) (POM) [15]. On the other hand, critical descriptive comparisons between the Avrami and Malkin models were performed on isothermal crystallization data of polyethylene (PE), isotactic polypropylene (iPP), poly(ethylene terephthalate) (PET), poly(propylene oxide) (PPO), and polyurethane (PU) [13].

To the best of my knowledge, critical analysis of the experimental data, and hence the descriptive comparison of the results, using all three models has not been described in the literature thus far. Therefore, in the present study, all three macrokinetic models are used to analyze the isothermal crystallization data of syndiotactic polypropylene (sPP). The experimental data are fitted to each respective model using a non-linear multi-variable regression program. The goodness of the fit

suggests the applicability of the model in describing the isothermal crystallization data of sPP.

3. THEORETICAL BACKGROUND

The overall crystallization kinetics of polymers is usually analyzed by use of the Avrami equation [4-9]. When applied to be used with a differential scanning calorimetry (DSC), it is assumed that the differential area under the crystallization curve with time corresponds to the dynamic changes in the conversion of mass from the melt phase to the solid phase. If χ_∞ and χ_t are the maximum crystallinity obtained for particular crystallization condition and the dynamic crystallinity at arbitrary time t for the same crystallization condition, respectively, then the governing Avrami equation can be written as

$$\frac{\chi_t}{\chi_\infty} = \theta(t) = 1 - \exp(-k_a t^{n_a}), \quad (5-1)$$

where $\theta(t)$ denotes the relative crystallinity as a function of time, k_a the Avrami crystallization rate constant, and n_a the Avrami exponent of time. Both k_a and n_a are constants typical of a given crystalline morphology and type of nucleation for a particular crystallization condition [16]. It should be noted that, according to the original assumptions of the theory, the value of n_a should be integral, ranging from 1 to 4.

In the study of isothermal crystallization using DSC, the rate of evolution of the heat of crystallization as a function of time and the relative extent of crystallization $\theta(t)$ are related to one another according to the following equation:

$$\theta(t) = \frac{\int_0^t \left(\frac{dH_c}{dt}\right) dt}{\Delta H_c}, \quad (5-2)$$

where t represents an arbitrary time during the course of isothermal crystallization process, dH_c the enthalpy of crystallization released during an infinitesimal time interval

dt , and ΔH_c the overall enthalpy of crystallization for a specific crystallization temperature T_c .

An important remark that has been made on the Avrami model is that the equation is only appropriate for the early stages of crystallization. In order to improve the Avrami model, Tobin [10-12] proposed a different expression describing phase transformation kinetics with growth site impingement. The original theory was written in a form of nonlinear Volterra integral equation, of which zeroth-order solution is given by

$$\theta(t) = \frac{k_i t^{n_i}}{1 + k_i t^{n_i}}, \quad (5-3)$$

where $\theta(t)$ is the relative crystallinity as a function of time, k_i the Tobin crystallization rate constant and n_i the Tobin exponent. Based on this proposition, the Tobin exponent of time n_i needs not be integral [11-12] and it is governed directly by different types of nucleation and growth mechanisms. It is worth noting that a similar expression was considered by Rabesiaka and Kovacs [17] and it was found to give a good fit to their dilatometric data of linear PE for $\theta(t)$ up to 0.9.

Derived based on the notion that the overall crystallization rate equals the summation of the rate at which the degree of crystallinity varies as a result of emergence of the primary nuclei and the rate of variation in the degree of crystallinity as a result of crystal growth, Malkin et al. [13] proposed a totally different form of a macrokinetic equation, which reads

$$\theta(t) = 1 - \frac{C_0 + 1}{C_0 + \exp(C_1 t)}, \quad (5-4)$$

where $\theta(t)$ is the relative crystallinity as a function of time. C_0 relates directly to the ratio of the linear growth rate G to the nucleation rate I (i.e., $C_0 \propto G/I$) and C_1 relates

directly to the overall crystallization rate (i.e., $C_1 = a \cdot I + b \cdot G$, where a and b are specific constants). Apparently, both C_0 and C_1 are temperature-dependent constants.

Analysis of the experimental data based on the Avrami and Tobin approaches are straight forward. The Avrami kinetics parameters, k_a and n_a , can be extracted from the least-square line fitted to the double logarithmic plot of $\ln[-\ln(1-\theta(t))]$ versus $\ln(t)$; k_a is the anti-logarithmic value of the y-intercept and n_a is the slope of the least-square line. Similarly, the Tobin crystallization kinetics parameters, k_t and n_t , can be extracted by drawing a least-square line fitted to the double logarithmic plot of $\ln[\theta(t)/(1-\theta(t))]$ versus $\ln(t)$; here k_t is the anti-logarithmic value of the y-intercept and n_t is the slope. It should be noted that, in both cases, the kinetics parameters are calculated from the least-square line drawn through the bulk of the data in the range of $0.10 < \theta(t) < 0.80$. In the case of the Malkin approach, the authors proposed a short-cut method of determining their kinetics parameters, C_0 and C_1 , from those obtained from the Avrami analysis [13]:

$$C_0 = 4^{n_a} - 4, \quad (5-5)$$

and

$$C_1 = \ln(4^{n_a} - 2) \left(\frac{k_a}{\ln(2)} \right)^{1/n_a}. \quad (5-6)$$

In light of this being the computational age, a computer seems to be an indispensable tool in almost every aspect of our lives. Instead of analyzing the experimental data using the traditional procedure mentioned earlier, a non-linear multi-variable regression program is utilized to directly fit the experimental data to the three aforementioned macrokinetic models. The goodness of the fit is described by the chi-square parameter χ^2 [18], in which the lower the value the better the fit. In addition, the corresponding kinetics parameters required by each model are automatically provided by the program once the best fit was determined. The applicability and reliability of the

program were verified by comparing the Avrami kinetics parameters obtained based on the traditional procedure with those provided by the program.

4. EXPERIMENTAL DETAILS

4.1. Materials

The two sPP samples used in this study were supplied in pellet form by Fina Oil and Chemical Company in La Porte, Texas. Molecular characterization of these materials was kindly performed by Dr. Roger A. Phillips and his coworkers at Montell USA, Inc. in Elkton, Maryland. The results are listed in Table 5-1. It should be noted that sPP#3 has a bimodal molecular weight distribution, which results in an unusually high degree of polydispersity.

4.2. Technique and Sample Preparation

A Perkin-Elmer Series 7 Differential Scanning Calorimeter (DSC7) was used to follow the isothermal crystallization in this study. The DSC7 equipped with an internal liquid nitrogen cooling unit dependably provided a cooling rate up to $200^{\circ}\text{C}\cdot\text{min}^{-1}$. Temperature calibration was performed using indium as a standard; it has the following thermal properties: $T_m^{\circ} = 156.6^{\circ}\text{C}$ and $\Delta H_f^{\circ} = 28.5 \text{ J}\cdot\text{g}^{-1}$. The consistency of the temperature calibration was checked every other run to ensure reliability of the data obtained. To make certain that thermal lag between the polymeric sample and the DSC sensors is kept to a minimum, each sample holder was loaded with a single disc, weighing around $4.9 \pm 0.3 \text{ mg}$. A hole-puncher was used to cut the disc from a film. The film was prepared by melt-pressing virgin pellets, placed between a pair of Kapton films which in turn were sandwiched between a pair of stainless steel platens, in a Wabash compression molding machine at 190°C under a pressure of 67 kpsi. After ten minutes holding time, the film, approximately $280 \mu\text{m}$ thick, was taken out and immediately submerged in an ice-water bath while it was still between the two steel

Table 5-1. Characterization data of as-received syndiotactic polypropylene samples.

Sample	Intrinsic Viscosity (dl·g ⁻¹)	M _n	M _w	M _z	M _w /M _n	Racemic Pentads [%rrrr]	Racemic Triads [%rr]	Racemic Dyads [%r]	Ethylene Content (% by Wt.)
sPP#1	1.61	76 200	165 000	290 000	2.2	77.1	87.3	91.4	1.3
sPP#3	1.32	37 300	133 000	308 000	3.6	74.6	83.7	88.3	0.5

platens. By this treatment, it can be assumed that previous thermal and mechanical histories were essentially erased, providing a controlled condition for the film.

4.3. Methods

The experiment started by heating the sample from -40°C at a scanning rate of $80^{\circ}\text{C}\cdot\text{min}^{-1}$ to 190°C , and holding it there for 5 min before quenching at a cooling rate of $200^{\circ}\text{C}\cdot\text{min}^{-1}$ to a desired isothermal crystallization temperature T_c . It should be noted that melting of a sample at 190°C for at least 5 min is necessary and ample to ensure complete melting [19] (cf. Part 4). It was assumed that the crystallization finished when the exothermic trace converged to a horizontal baseline. The crystallization exotherms were then recorded for further analysis.

5. RESULTS AND DISCUSSION

5.1. Isothermal Crystallization of sPP from the Melt

By assuming that the evolution of the crystallinity is linearly proportional to the evolution of heat released during isothermal crystallization in the DSC, the relative evolution of the crystallinity as a function of time $\theta(t)$ can thus be calculated by integration of the crystallization exothermic traces according to Equation (5-2). The relative crystallinity as a function of time $\theta(t)$ of sPP#1 and sPP#3 samples are respectively plotted in Figures 5-1 and 5-2 for 4 different crystallization temperatures T_c ranging from 75°C to 90°C . Clearly, the time to reach the ultimate crystallinity increases with increasing crystallization temperature. An important kinetics parameter which can be taken directly from the $\theta(t)$ versus time t curve is the half-time of crystallization $t_{0.5}$, which is defined as the time taken from the onset of the crystallization until 50% completion. A summary of the crystallization half-time $t_{0.5}$ values for both sPP samples are listed in Table 5-2, whereas the plots of $t_{0.5}$ versus T_c (including the plots of its reciprocal value $t_{0.5}^{-1}$ versus T_c) are shown in Figure 5-3.

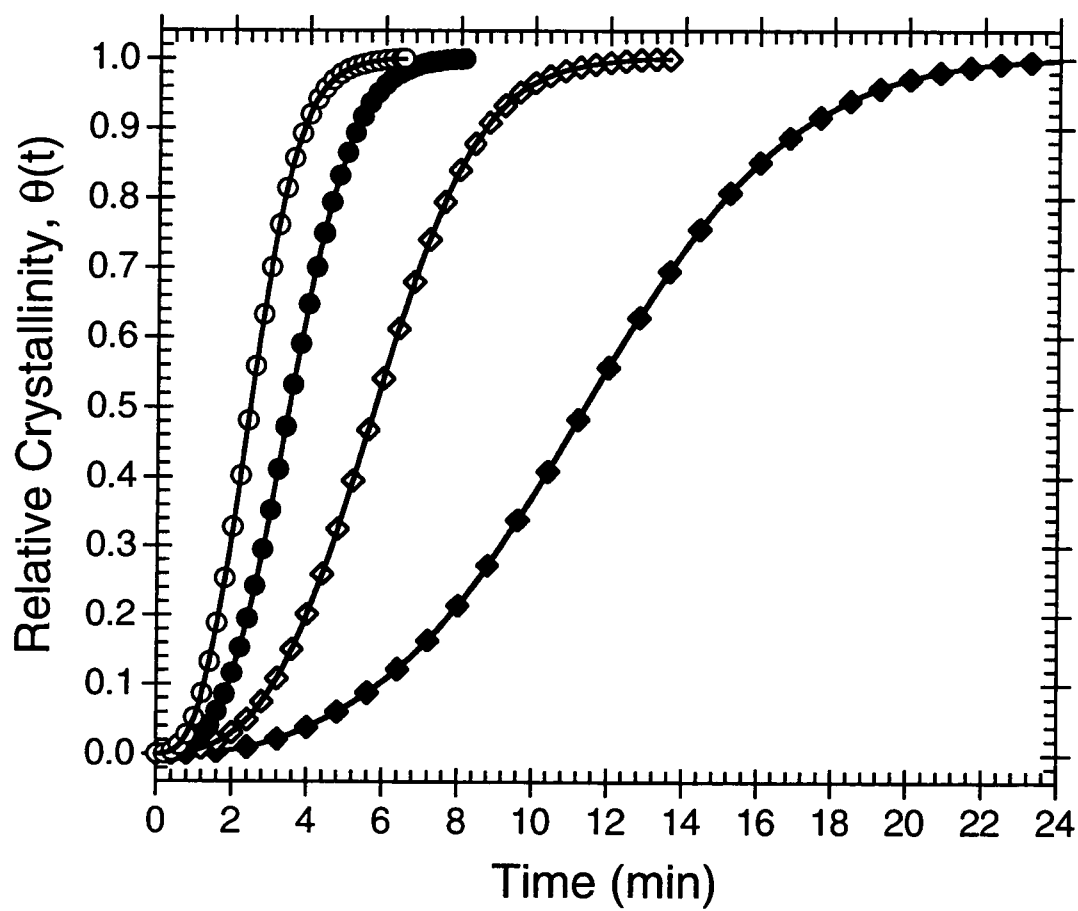


Figure 5-1. Experimental relative crystallinity as a function of time of sPP#1 for 5 different crystallization temperatures: (○) 75°C; (●) 80°C; (◇) 85°C; (◆) 90°C.

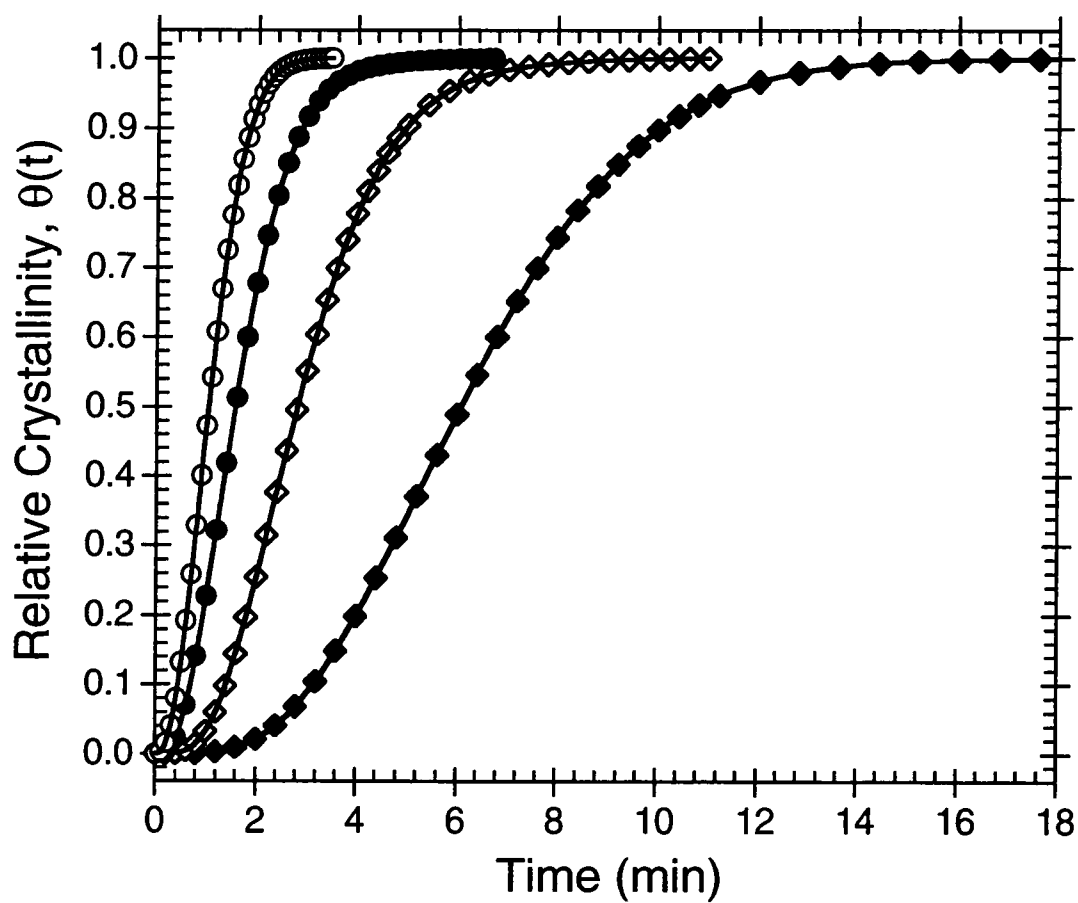


Figure 5-2. Experimental relative crystallinity as a function of time of sPP#3 for 5 different crystallization temperatures: (○) 75°C; (●) 80°C; (◇) 85°C; (◆) 90°C.

Table 5-2. Summary of the overall crystallization kinetics data for syndiotactic polypropylene samples based on the Avrami model.

Sample T_c (°C)	sPP#1					sPP#3								
	$t_{0.5}$ (min)	k_a^* (min^{-n})	n_a	k_a^{**} (min^{-n})	χ^2	n_a^{**}	k_a^{**} (min^{-n})	$t_{0.5}$ (min)	k_a^* (min^{-n})	n_a	k_a (min^{-n})	χ^2	n_a^{**}	k_a^{**} (min^{-n})
60.0	1.67	1.73×10^{-1}	2.71	1.75×10^{-1}	0.004	2.68	1.77×10^{-1}	-	-	-	-	-	-	-
62.5	1.70	1.63×10^{-1}	2.72	1.65×10^{-1}	0.007	2.74	1.64×10^{-1}	-	-	-	-	-	-	-
65.0	1.75	1.65×10^{-1}	2.56	1.66×10^{-1}	0.002	2.57	1.66×10^{-1}	-	-	-	-	-	-	-
67.5	1.83	1.48×10^{-1}	2.56	1.48×10^{-1}	0.016	2.59	1.46×10^{-1}	-	-	-	-	-	-	-
70.0	1.98	1.15×10^{-1}	2.63	1.14×10^{-1}	0.018	2.68	1.11×10^{-1}	-	-	-	-	-	-	-
72.5	2.18	8.71×10^{-2}	2.66	8.62×10^{-2}	0.018	2.73	8.22×10^{-2}	0.84	1.02	2.22	1.02	0.003	2.26	1.02
75.0	2.45	6.04×10^{-2}	2.72	5.95×10^{-2}	0.022	2.80	5.56×10^{-2}	1.04	6.38×10^{-1}	2.12	6.30×10^{-1}	0.004	2.15	6.30×10^{-1}
77.5	2.92	3.07×10^{-2}	2.91	3.06×10^{-2}	0.011	2.97	2.88×10^{-2}	1.18	4.96×10^{-1}	2.07	4.91×10^{-1}	0.009	2.11	4.89×10^{-1}
80.0	3.50	1.60×10^{-2}	3.01	1.59×10^{-2}	0.014	3.07	1.47×10^{-2}	1.58	2.69×10^{-1}	2.07	2.64×10^{-1}	0.051	2.17	2.53×10^{-1}
82.5	4.81	4.79×10^{-3}	3.17	4.75×10^{-3}	0.012	3.22	4.36×10^{-3}	1.96	1.58×10^{-1}	2.20	1.53×10^{-1}	0.123	2.34	1.40×10^{-1}
85.0	5.78	3.65×10^{-3}	2.99	3.64×10^{-3}	0.014	3.05	3.30×10^{-3}	2.82	6.38×10^{-2}	2.30	6.11×10^{-2}	0.154	2.48	5.14×10^{-2}
87.5	7.65	1.90×10^{-3}	2.90	1.90×10^{-3}	0.059	2.97	1.66×10^{-3}	3.85	3.20×10^{-2}	2.28	3.06×10^{-2}	0.226	2.49	2.35×10^{-2}
90.0	11.40	5.29×10^{-4}	2.95	5.32×10^{-4}	0.023	2.96	5.19×10^{-4}	6.08	7.09×10^{-3}	2.54	6.86×10^{-3}	0.076	2.67	5.48×10^{-3}
92.5	19.40	7.36×10^{-4}	2.31	7.10×10^{-4}	0.116	2.47	4.39×10^{-4}	9.71	1.80×10^{-3}	2.62	1.75×10^{-3}	0.062	2.74	1.33×10^{-3}
95.0	28.30	2.49×10^{-4}	2.37	2.50×10^{-4}	0.025	2.41	2.23×10^{-4}	17.23	1.88×10^{-4}	2.88	1.89×10^{-4}	0.002	2.87	1.98×10^{-4}

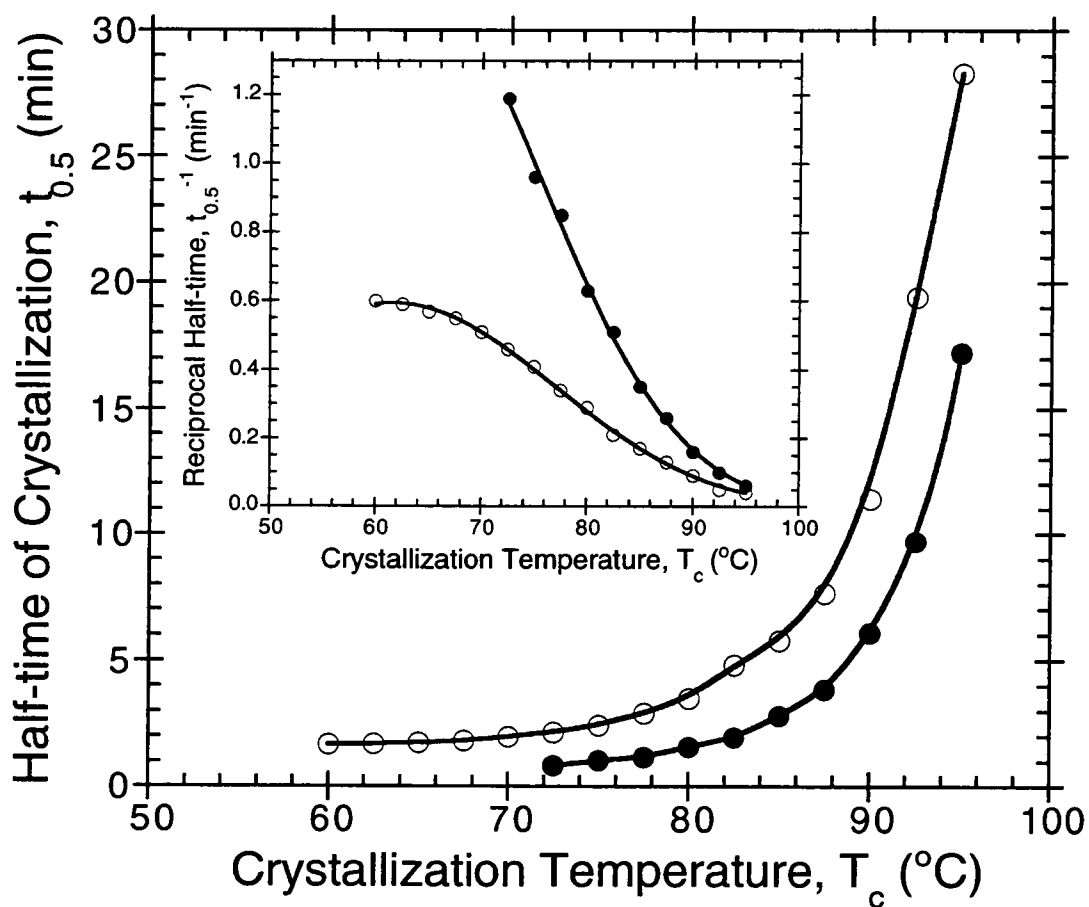


Figure 5-3. Half-time of crystallization as a function of crystallization temperatures, with the inset figure illustrating the reciprocal half-time as a function of crystallization temperature: (○) sPP#1; (●) sPP#3.

According to Figure 5-3, it is evident that for each sPP sample the crystallization half-time $t_{0.5}$ increases with increasing crystallization temperature. The most fundamental representation of the bulk crystallization kinetics data is to plot the reciprocal of the half-time of crystallization $t_{0.5}^{-1}$ against the crystallization temperature. Such plots are illustrated as inset figure of Figure 5-3. If the crystallization half-time data can be collected with minimal degree of error over the whole temperature range (i.e., $T_g < T_c < T_m^0$), the plot of $t_{0.5}^{-1}$ versus T_c should exhibit the typical bell-shaped curve, which can be described as a result of the nucleation control effect at low undercooling and diffusion control effect at high undercooling. Indeed, a double bell-shaped curve on the plot of $t_{0.5}^{-1}$ versus T_c was observed for the crystallization half-time data of sPP#1 [20] (cf. Part 7). An explanation of two maxima observed on the plot of $t_{0.5}^{-1}$ versus T_c is not known at this point and a matter of an ongoing investigation (cf. Part 7 for more detail). By comparing the plots of $t_{0.5}^{-1}$ versus T_c for both sPP samples shown in Figure 5-3 with earlier result [20], it is apparent that, within the temperature range of interest in this study (i.e., $60^\circ\text{C} < T_c < 95^\circ\text{C}$), both samples crystallize in the region where nucleation is the rate determining factor. It is important to note that one of the maxima clearly seen on the plot of $t_{0.5}^{-1}$ versus T_c [20] for the whole range of temperature for sPP#1 was at 60°C , corresponding to the maximum on the inset.

The result shown in Figure 5-3 also suggests that sPP#3 crystallizes faster than sPP#1 even though its syndiotacticity level is a bit lower (cf. Table 5-1). This can be explained based on the facts that sPP#3 has a lower level of ethylene content (i.e., comonomer defects) in its molecular chains and that sPP#3 consists of molecular chains of relatively lower molecular mass.

5.2. Application of the Avrami, Tobin, and Malkin Models

Instead of performing the data analysis in the traditional way, the experimental data were fitted iteratively to the respective macrokinetic models with the use of a non-linear multi-variable regression program. As mentioned previously, the goodness of the fit can be determined from the χ^2 values [18], in which the lower the value observed the better the quality of the fit. The respective kinetics parameters were also provided by the program once the best fit was determined.

5.2.1. Isothermal Crystallization Kinetics Based on the Avrami Model

The analysis based on the Avrami model can be done by fitting the $\theta(t)$ function obtained for each crystallization temperature to Equation (5-1). The Avrami exponent n_a , the crystallization rate constant k_a , and the χ^2 parameter, provided by the program, are summarized in Table 5-2. The exponent n_a for primary crystallization are found to range from 2.31 to 3.17 for sPP#1 (with the average value of 2.75 ± 0.2), and 2.07 to 2.88 for sPP#3 (with the average value of 2.33 ± 0.3). This may correspond to a two dimensional growth with a combination of thermal and athermal nucleation (as a result of the fractional n_a values observed) [16]. Intuitively, the temperature dependence of the exponent n_a , within the nucleation control region (i.e., $60^\circ\text{C} < T_c < 95^\circ\text{C}$), should be such that n_a decreases with decreasing temperature. This may be explained based on the fact that the number of athermal nuclei increases tremendously as the temperature decreases [19,21]. In other words, as the crystallization temperature decreases the number of athermal nuclei which become stable at that temperature also increases, resulting in the nucleation mechanism becoming more instantaneous in time and causing the Avrami exponent n_a to decrease. Indeed, the decrease in n_a value with decreasing temperature can be observed from the results listed in Table 5-2, especially in the case of sPP#3.

According to Table 5-2, the crystallization rate constant k_a exhibits extreme sensitivity to the change in crystallization temperature, increasing with decreasing temperature. This is because sPP crystallizes faster at lower temperature. This observation is only true when the temperature is in the range where nucleation is the rate determining factor (i.e., $60^\circ\text{C} < T_c < 95^\circ\text{C}$ for sPP). A similar implication was addressed earlier based on the fact that the reciprocal half-time $t_{0.5}^{-1}$ also exhibits the same trend (cf. the inset figure of Figure 5-2). Indeed, the rate constant k_a can be calculated directly from the reciprocal half-time $t_{0.5}^{-1}$ value (i.e., $k_a^* = \ln 2 (t_{0.5}^{-1})^n$); the calculated rate constant values k_a^* are also summarized for comparison in Table 5-2. Obviously, there is a good agreement between the rate constant obtained from the fit, k_a , and that obtained from the calculation, k_a^* . In addition, at the same temperature, sPP#3 has a larger value of k_a than does sPP#1, suggesting that sPP#3 crystallizes more readily as previously seen based on the $t_{0.5}^{-1}$ values.

Verification of the applicability and reliability of the fitting procedure in describing the isothermal crystallization data of sPP can be performed by comparison of the Avrami kinetics parameters, n_a and k_a , provided by the program to the ones obtained based on the traditional method [22] (cf. Part 2: listed in Table 5-2 as n_a^{**} and k_a^{**} , respectively). Apparently, extremely good agreement of the kinetics parameters obtained from the two different methods is obtained. This suggests that the fitting method can be used to analyze the isothermal crystallization data of sPP with a high level of confidence, and that it should also be applicable to other polymeric systems of similar molecular complexity.

5.2.2. Isothermal Crystallization Kinetics Based on the Tobin Model

The analysis based on the Tobin model can be performed by fitting the $\theta(t)$ function obtained for each crystallization temperature to Equation (5-3). Table 5-3

Table 5-3. Summary of the overall crystallization kinetics data for syndiotactic polypropylene samples based on the Tobin model.

Sample T_c (°C)	sPP#1					sPP#3				
	$t_{0.5}$ (min)	k_t^* (min^{-n})	n_t	k_t (min^{-n})	χ^2	$t_{0.5}$ (min)	k_t^* (min^{-n})	n_t	k_t (min^{-n})	χ^2
60.0	1.67	1.16×10^{-1}	4.19	1.35×10^{-1}	0.989	-	-	-	-	-
62.5	1.70	1.05×10^{-1}	4.25	1.21×10^{-1}	0.880	-	-	-	-	-
65.0	1.75	1.15×10^{-1}	3.86	1.31×10^{-1}	0.710	-	-	-	-	-
67.5	1.83	8.90×10^{-2}	4.00	1.01×10^{-1}	0.927	-	-	-	-	-
70.0	1.98	6.03×10^{-2}	4.11	6.80×10^{-2}	0.931	-	-	-	-	-
72.5	2.18	3.93×10^{-2}	4.15	4.38×10^{-2}	0.462	0.84	1.85	3.52	2.07	0.253
75.0	2.45	2.24×10^{-2}	4.24	2.48×10^{-2}	0.488	1.04	8.77×10^{-1}	3.36	9.69×10^{-1}	0.342
77.5	2.92	7.98×10^{-3}	4.51	9.02×10^{-3}	0.615	1.18	5.88×10^{-1}	3.29	6.52×10^{-1}	0.363
80.0	3.50	2.96×10^{-3}	4.65	3.33×10^{-3}	0.696	1.58	2.22×10^{-1}	3.30	2.42×10^{-1}	0.350
82.5	4.81	4.81×10^{-4}	4.86	5.40×10^{-4}	0.932	1.96	9.68×10^{-2}	3.47	1.04×10^{-1}	0.298
85.0	5.78	3.03×10^{-4}	4.62	3.42×10^{-4}	0.790	2.82	2.35×10^{-2}	3.62	2.49×10^{-2}	0.223
87.5	7.65	1.06×10^{-4}	4.50	1.20×10^{-4}	1.055	3.85	8.02×10^{-3}	3.58	8.49×10^{-3}	0.153
90.0	11.40	1.51×10^{-5}	4.56	1.73×10^{-5}	1.419	6.08	7.80×10^{-4}	3.96	8.45×10^{-4}	0.326
92.5	19.40	2.27×10^{-5}	3.61	2.43×10^{-5}	0.518	9.71	9.50×10^{-5}	4.07	1.04×10^{-4}	0.293
95.0	28.30	3.71×10^{-6}	3.74	4.21×10^{-6}	0.965	17.23	3.25×10^{-6}	4.44	3.71×10^{-6}	0.779

summarizes the Tobin kinetics parameters, n_t and k_t , as well as the χ^2 parameter. The Tobin exponent n_t for primary crystallization are found to range from 3.61 to 4.86 for sPP#1, and 3.29 to 4.44 for sPP#3. By comparison, it is apparent that at an arbitrary crystallization temperature the Avrami exponent n_a is consistently lower in value than the Tobin exponent n_t . By taking the average of the difference between the two values, it can be concluded, based on the experimental observation, that $n_t \approx n_a + 1.3$, which is in general accordance with observations by other researchers [14,15].

According to Table 5-3, the Tobin rate constant k_t clearly exhibits a similar trend to the Avrami rate constant k_a in that it is greater in its value at low crystallization temperature than that at high temperature. However, the change in the k_t value seems to be more sensitive to the change in the temperature than that exhibited by the Avrami rate constant k_a . According to Equation (5-3), the Tobin rate constant k_t can also be calculated from the reciprocal half-time $t_{0.5}^{-1}$ value (i.e., $k_t^* = (t_{0.5}^{-1})^n$). The calculated value k_t^* are also listed for comparison in Table 5-3. The discrepancy between the rate constant obtained from the fit, k_t , and that obtained from the calculation, k_t^* , of as much as 15% is found, as opposed to around a 3% difference in the k_a and k_a^* values. This suggests that the experimental data of sPP can be fitted to the Avrami model better than to the Tobin model. This can be confirmed based on the fact that the χ^2 parameters listed in Table 3 are much greater than those listed in Table 5-2.

5.2.3. Isothermal Crystallization Kinetics Based on the Malkin Model

The analysis based on the Malkin model can be carried out by fitting the $\theta(t)$ function obtained for each crystallization temperature to Equation (5-4). The kinetics parameters characteristic of the Malkin model, C_0 and C_1 , as well as the χ^2 parameter are listed in Table 5-4. The C_0 parameter is found to range from 25.11 to 107.27 for sPP#1, and 15.43 to 66.91 for sPP#3. Fundamentally, the C_0 parameter, which relates directly

Table 5-4. Summary of the overall crystallization kinetics data for syndiotactic polypropylene samples based on the Malkin model.

Sample T_c (°C)	sPP#1				sPP#3					
	C_0	C_1 (min^{-1})	χ^2	C_0^*	C_1^* (min^{-1})	C_0	C_1 (min^{-1})	χ^2	C_0^*	C_1^* (min^{-1})
60.0	49.90	2.37	0.066	38.74	2.26	-	-	-	-	-
62.5	51.56	2.34	0.055	39.65	2.23	-	-	-	-	-
65.0	38.70	2.11	0.064	31.01	2.04	-	-	-	-	-
67.5	38.80	2.02	0.072	30.63	1.94	-	-	-	-	-
70.0	44.44	1.93	0.088	34.47	1.84	-	-	-	-	-
72.5	46.85	1.77	0.052	36.04	1.69	20.98	3.69	0.033	17.79	3.66
75.0	52.18	1.62	0.064	39.61	1.53	17.05	2.79	0.049	14.87	2.81
77.5	70.62	1.46	0.047	52.36	1.38	15.43	2.39	0.067	13.61	2.43
80.0	83.04	1.27	0.057	60.60	1.19	15.64	1.78	0.140	13.67	1.80
82.5	107.27	0.97	0.104	76.65	0.91	20.35	1.55	0.242	17.05	1.53
85.0	80.65	0.76	0.048	59.18	0.72	25.06	1.14	0.261	20.35	1.11
87.5	69.58	0.56	0.026	51.65	0.53	24.25	0.83	0.322	19.69	0.81
90.0	74.95	0.38	0.057	55.65	0.36	38.35	0.60	0.167	29.77	0.57
92.5	25.11	0.17	0.235	20.57	0.16	44.12	0.39	0.126	33.80	0.37
95.0	27.91	0.12	0.079	22.83	0.12	66.91	0.25	0.059	50.52	0.23

to the n_a value through Equation (5-5), should exhibit a similar temperature dependence to that of the Avrami exponent n_a . Indeed, such a trend can be deduced from the results listed in Table 5-4, especially in the case of sPP#3. According to Table 5-4, the Malkin rate constant C_1 also exhibits a temperature dependence in a similar fashion as do the crystallization rate constants characteristic of both the Avrami and Tobin models.

Unlike the Avrami and the Tobin models, there is no direct analytical procedure for the determination of the Malkin kinetics parameters. Without the direct fitting method utilized in this study, the Malkin kinetics parameters, C_0 and C_1 , can only be estimated from the Avrami kinetics parameters, n_a and k_a , through the relationships set forth in Equations (5-5) and (5-6). The estimated Malkin kinetics parameters are also listed in Table 5-4, where they are denoted as C_0^* and C_1^* , respectively. Evidently, the estimated rate constant C_1^* is found to be in a good agreement with that obtained from the direct fitting method C_1 . Like the other two rate constants, the Malkin rate constant C_1 can also be calculated directly from the reciprocal half-time $t_{0.5}^{-1}$ value (i.e., $C_1 = \ln(4^n - 2)(t_{0.5}^{-1})$). Though not listed in Table 5-4, the C_1 values calculated from the $t_{0.5}^{-1}$ values are found to be almost identical to the estimated Malkin crystallization rate values C_1^* .

5.2.4. Comparison Between the Different Isothermal Macrokinetic Models

The quality of the model in describing the experimental isothermal measurements is numerically represented by the χ^2 parameter, in which the lower the value the better the quality of the fit. By comparing the values of the χ^2 parameter listed in Tables 5-2 to 5-4, it can be concluded that only the Avrami and the Malkin models are suitable to describe the primary process of the isothermal evolution of crystallinity in sPP well. This is accented by visual verification illustrated in Figures 5-4 and 5-5, where the experimental time-dependent relative crystallinity functions $\theta(t)$ collected at two

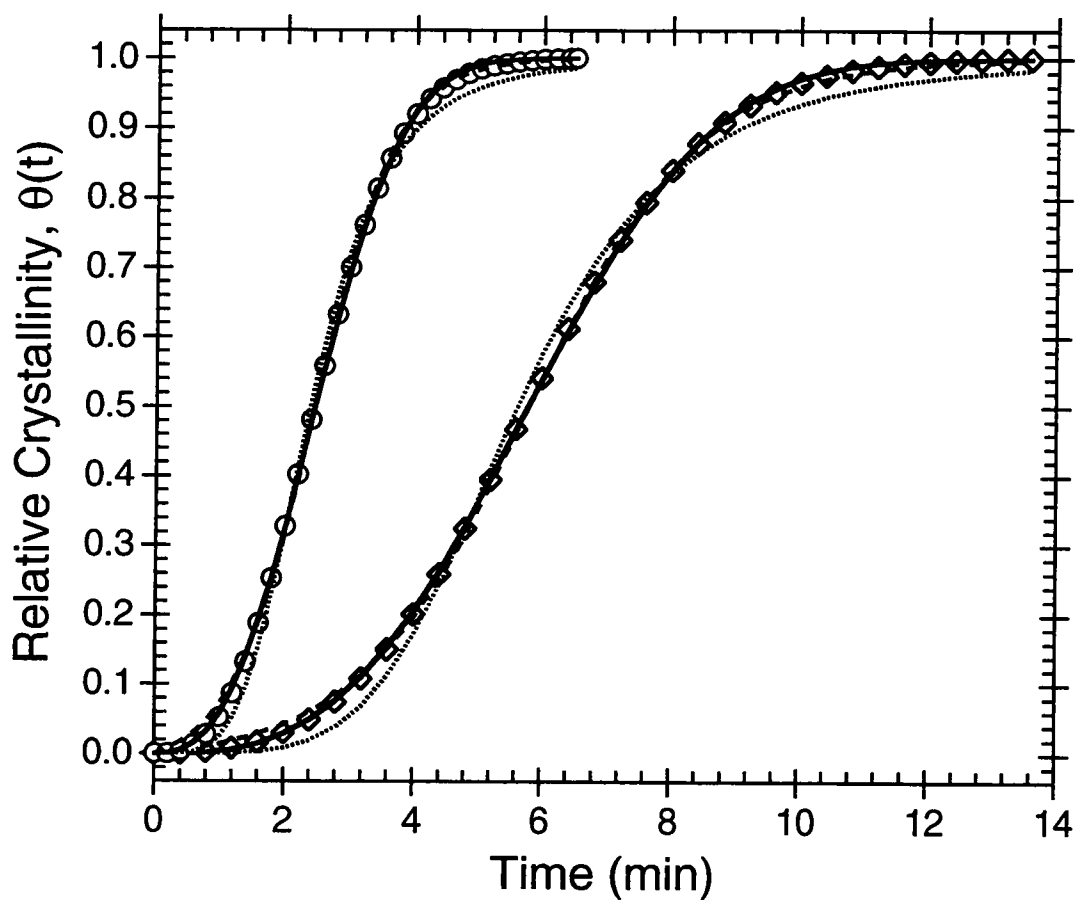


Figure 5-4. Relative crystallinity as a function of time of sPP#1 for 2 different crystallization temperatures: (○) 75°C; (◇) 85°C. The experimental data, shown as points, were fitted to the non-linear multi-variable regression program, where the best fits according to the Avrami, Tobin, and Malkin macrokinetic models are shown as the solid, dotted, and dashed lines, respectively.

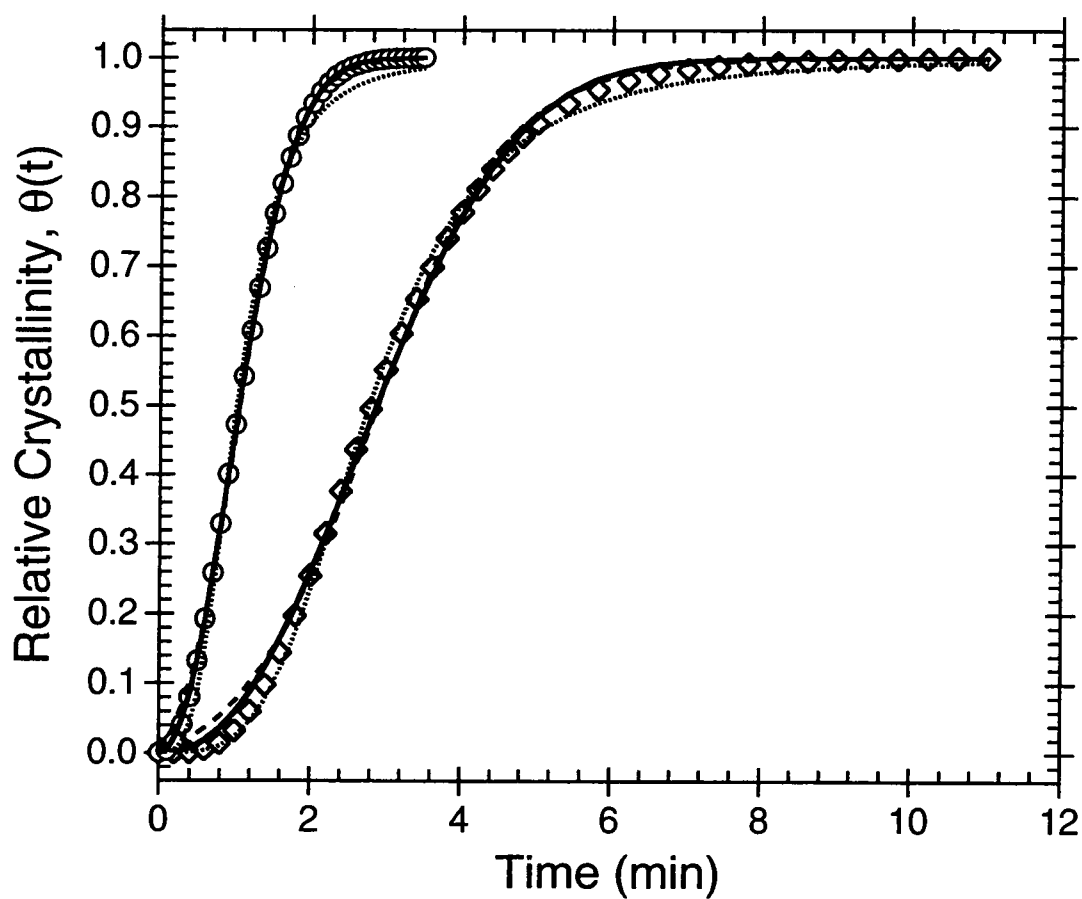


Figure 5-5. Relative crystallinity as a function of time of sPP#3 for 2 different crystallization temperatures: (○) 75°C; (◇) 85°C. The experimental data, shown as points, were fitted to the non-linear multi-variable regression program, where the best fits according to the Avrami, Tobin, and Malkin macrokinetic models are shown as the solid, dotted, and dashed lines, respectively.

crystallization temperatures of 75°C and 85°C are plotted against the best-fitted curves provided by the program. Clearly, the goodness of the fitted curves according to the Avrami and the Malkin models (shown in Figures 5-4 and 5-5 as solid and dashed lines, respectively) is of greater quality than the fitted curve according to the Tobin model (shown in Figures 5-4 and 5-5 as dotted lines). As a result, the Tobin model will not be considered further. In addition, the Avrami model seems to give a better prediction than the Malkin model in the early stage of crystallization (ca. $0.15 \leq \theta(t)$); whereas, the Malkin model seemingly provides a better fit at the later stage of crystallization (ca. $\theta(t) \geq 0.85$).

5.3. Application of the Simultaneous Avrami Model

Applicability of the Avrami and the Malkin models for describing the experimental isothermal crystallization measurements of sPP was verified above. Due to the fact that the Avrami kinetics parameters, n_a and k_a , are very well defined according to Table 5 and that those of the Malkin model, C_0 and C_1 , are not entirely understood (but they are worth looking into, and it is a subject of further investigation), the applicability of the Avrami model for the prediction of the isothermal crystallization will be further discussed.

One of the serious discrepancies which has been raised to question the applicability of the Avrami model is that, in most cases, the analysis of the experimental data based on the Avrami equation leads to fractional values of the Avrami exponent n_a (cf. Table 5-2). The non-integral observations of the Avrami exponent n_a may be explained as follows:

- 1) The discrepancies in the assumptions used in the derivation of the model;
- 2) Inaccuracy in the determination of the onset of the crystallization process (if the onset is set prematurely, the value of the Avrami exponent n_a will be

greater than the actual value, while that of the rate constant k_a will be smaller);

- 3) Changes in the nucleation rate I and growth rate G during the crystallization process (if the values decrease, the value of the Avrami exponent n_a will also decrease);
- 4) Changes in the morphology during the crystallization process (i.e., sheaf-like to spherulitic). This may also include the occurrence of the secondary crystallization in which internal changes in the crystal morphology are experimentally observed [1-3].

In addition to the above explanations, the fractional value of the Avrami exponent n_a may also be elucidated based on the hypothesis that crystalline aggregates grow concurrently from both instantaneous and sporadic nuclei (as opposed to growing from only one type of nuclei, assumed in the original theory), as previously mentioned elsewhere in this study. Indeed, observation made on an optical microscope confirms that for a given crystallization temperature a certain number of nuclei are activated instantaneously, while others are activated sporadically. It should be noted that the observation is valid within the crystallization temperature range of 60°C to 95°C. Based on this experimental observation, the original Avrami equation can be modified to account for both types of transient nucleation. The modified equation, called the "simultaneous Avrami model," can be written as

$$\theta(t) = 1 - \exp(-k_{ai}t^n - k_{as}t^{n+1}), \quad (5-7)$$

where $\theta(t)$ denotes the relative crystallinity as a function of time, and n the morphological dimensionality which ranges from 1 to 3 (i.e., rod, disc, and sphere). k_{ai} and k_{as} are the crystallization rate constants specific for instantaneous and sporadic nucleation, respectively (cf. Table 5-5). It should be noted that a similar equation was first used to explain the fractional values of the Avrami exponent n_a by Banks et al.

Table 5-5. Theoretical description of the Avrami isothermal crystallization rate constant k_a for different types of morphology and transient nucleation mechanisms.

Crystal Morphology	Morphological Dimensionality, n	Isothermal Crystallization Rate Constant ¹⁾ Instantaneous Nucleation, k_{ai} (min ⁻ⁿ)	Sporadic Nucleation, k_{as} (min ⁻⁽ⁿ⁺¹⁾)
Rod	1	N_0GA	$1/2 \cdot IGA$
Disc	2	πN_0G^2D	$\pi/3 \cdot IG^2D$
Sphere	3	$4\pi/3 \cdot N_0G^3$	$\pi/3 \cdot IG^3$

¹⁾ A is constant area, D is the disc thickness, G is the linear crystal growth rate, N_0 is the concentration of predetermined nuclei, and I is the nucleation rate.

[23], but they concluded then that the equation was not satisfactory in accounting for the occurrence of the fractional values of n_a .

Analysis of the isothermal crystallization data based on the simultaneous Avrami model can be done very readily by fitting the $\theta(t)$ function to Equation (5-7) using the non-linear multi-variable regression program, as opposed to the trial-and-error method utilized by Banks et al. [23]. According to the Avrami analysis (cf. Table 5-2), n_a ranges mainly between 2 and 3, suggesting two dimensional growth geometry (perhaps, due to a truncation of the spherulitic structure). Thus, a value of n in Equation (5-7) was chosen to be 2. The crystallization rate constant for instantaneous nucleation process k_{ai} , the crystallization rate constant for sporadic nucleation process k_{as} , and the χ^2 parameter, which were provided by the best fit according to the program, are summarized in Table 5-6. Clearly, the values of both rate constants exhibit a temperature dependence in the same manner as do the rate constants characteristic of the three other models.

Comparison of the χ^2 parameters given in Table 6 with those listed in Tables 5-2 to 5-4 suggests that the quality of the simultaneous Avrami model in describing the isothermal crystallization data is comparable to that of the Avrami model, and is a little better than that of the Malkin model. This further suggests that applicability of the model in describing isothermal crystallization in sPP (and, perhaps, other polymers) is satisfactory. Even though the reasons for the rejection of the similar equation given by Banks et al. [23] were valid, it is postulated in this study that the simultaneous Avrami model may be more suitable than the original Avrami model in describing overall isothermal crystallization in polymers.

Table 5-6. Summary of the overall crystallization kinetics data for syndiotactic polypropylene samples based on the simultaneous Avrami model.

Sample	sPP#1			sPP#3		
T_c (°C)	k_{ai} (min ⁻²)	k_{as} (min ⁻³)	χ^2	k_{ai} (min ⁻²)	k_{as} (min ⁻³)	χ^2
60.0	9.76×10^{-2}	1.06×10^{-1}	0.001	-	-	-
62.5	9.02×10^{-2}	1.04×10^{-1}	0.017	-	-	-
65.0	7.20×10^{-2}	7.31×10^{-2}	0.016	-	-	-
67.5	6.43×10^{-2}	6.27×10^{-2}	0.045	-	-	-
70.0	6.25×10^{-2}	5.65×10^{-2}	0.052	-	-	-
72.5	4.66×10^{-2}	4.41×10^{-2}	0.039	7.75×10^{-1}	2.34×10^{-1}	0.011
75.0	2.93×10^{-2}	3.40×10^{-2}	0.044	5.68×10^{-1}	6.03×10^{-2}	0.009
77.5	6.36×10^{-3}	2.55×10^{-2}	0.015	4.72×10^{-1}	2.11×10^{-2}	0.014
80.0	4.84×10^{-3}	1.63×10^{-2}	0.013	2.62×10^{-1}	1.41×10^{-2}	0.063
82.5	1.27×10^{-3}	7.21×10^{-3}	0.003	1.46×10^{-1}	8.01×10^{-3}	0.176
85.0	1.09×10^{-3}	3.57×10^{-3}	0.015	6.04×10^{-2}	6.95×10^{-3}	0.228
87.5	9.10×10^{-4}	1.40×10^{-3}	0.064	3.35×10^{-2}	2.87×10^{-3}	0.310
90.0	5.50×10^{-4}	4.45×10^{-4}	0.021	8.18×10^{-3}	1.60×10^{-3}	0.132
92.5	2.80×10^{-4}	2.56×10^{-5}	0.188	2.57×10^{-3}	4.62×10^{-4}	0.106
95.0	5.63×10^{-5}	1.09×10^{-5}	0.045	2.68×10^{-4}	1.20×10^{-4}	0.000

5.4. Prediction of Isothermal Crystallization Kinetics

The crystallization kinetics parameters (cf. Tables 5-2, 5-4 and 5-6) determined from limited experimental isothermal measurements can be used to predict the time-dependent relative evolution of the crystallinity $\theta(t)$ at other temperatures. The prediction can be carried out by virtue of the following facts:

- 1) The crystallization rate parameters (i.e., $t_{0.5}^{-1}$, k_a , C_1 , k_{ai} , or k_{as}) determined based on different macrokinetic models exhibit a finite temperature dependence;
- 2) The crystallization rate parameters relate, in one way or another, to the primary nucleation rate I and/or the subsequent crystal growth rate G , especially the crystallization rate parameters of the Avrami and the simultaneous Avrami models (cf. Table 5-5);
- 3) The temperature dependence of the primary nucleation rate I and the subsequent crystal growth rate G are well defined in the literature [24-26]. Even though the temperature dependence of the parameters I and G are different (i.e., $I \propto (\Delta T)^{-2}$ and $G \propto (\Delta T)^{-1}$, respectively), the crystallization rate parameters have often been taken to have similar temperature dependence to that of the subsequent crystal growth rate G (written in the context of the original Lauritzen and Hoffman secondary nucleation theory (LH theory) [25,26]), which can be expressed as

$$\Psi(T) = \Psi_0 \exp\left\{-\frac{\Theta}{R[T_c - (T_g - \delta)]} - \frac{K}{T_c(\Delta T)^f}\right\}, \quad (5-8)$$

where $\Psi(T)$ and Ψ_0 are the respective crystallization rate function (i.e., $t_{0.5}^{-1}$, k_a , C_1 , k_{ai} , or k_{as}) and the respective pre-exponential parameter (i.e., $(t_{0.5}^{-1})_0$, k_{a0} , C_{10} , k_{ai0} , or k_{as0}), respectively. Θ is a parameter related to the activation energy characterizing the molecular diffusion across the melt/crystal interface, while

K is a parameter related to the secondary nucleation. T_c is the crystallization temperature, T_g is the glass transition temperature (ca. -6.1°C [22]), δ is a WLF parameter which indicates the cessation of molecular motion and is often taken to be either ca. 30 K or ca. 50 K, R is the universal gas constant, ΔT is the degree of undercooling (i.e., $\Delta T = T_m^0 - T_c$, where T_m^0 is taken to be 168.7°C [22] (cf. Part 2)), and finally f is a factor used to correct for the temperature dependence of the heat of fusion (i.e., $f = 2T_c / (T_c + T_m^0)$).

It should be noted that a critical analysis of the linear growth rate G of sPP in the context of the LH theory has been discussed in detail in Part 3. The analysis suggested an unmistakable transition from regime II to regime III at the crystallization temperature T_c of 110°C . Since, in this study, the temperature range of interest apparently falls in regime III, the complication which arises from change of the secondary nucleation exponent (i.e., K) due to the change in regimes can be ignored as long as the temperature range of interest is lower than 110°C .

The temperature-dependent crystallization rate function $\Psi(T)$ can be easily determined by fitting the respective crystallization rate parameters (i.e., $t_{0.5}^{-1}$, k_a , C_1 , k_{air} or k_{as}) collected at various crystallization temperatures to Equation (5-8) using the same non-linear multi-variable regression program. As soon as the $\Psi(T)$ function was determined, values of the respective rate parameters at other temperatures can then be estimated. By substitution of the calculated rate constant at a temperature of interest into the appropriate macrokinetic model, the time-dependent relative crystallinity $\theta(t)$ at that temperature can readily be predicted, if the appropriate value of time exponent (i.e., n_s or C_0) is assumed (due to the lack of finite relationship of these parameters with the temperature, and usually assumed to be the *arithmetic mean* of the experimental observations). The discrepancy which may arise from the uncertainty of the time

exponent assumed may be remedied by use of the simultaneous Avrami model, since it does not involve the selection of the dimensionality parameter (provided that changes in crystal morphology do not occur over the temperature range of interest).

In order to obtain the best possible fits for the rate parameters with Equation (5-8), the δ value was chosen to be either 30 K or 50 K, while those of T_g and T_m^0 are fixed as previously noted. In doing so, the only unknown parameters which are provided by the program, once the fit was determined, are Ψ_0 , Θ , and K . Plots of the rate parameters of interest (i.e., $t_{0.5}^{-1}$, k_a , C_1 , k_{ai} , and k_{as}) and their corresponding best fit for both samples are illustrated in Figures 5-6 and 5-7 (for sPP#1 and sPP#3, respectively); whereas, the values of δ , Ψ_0 , Θ , and K , as well as the χ^2 parameter as a result of the best fits are summarized in Table 5-7. Judging from the χ^2 parameters listed in Table 5-7, the goodness of the fits of these rate parameters with Equation (5-8) is very satisfactory. Now that all of the parameters in Equation (5-8) are known, the rate parameters of interest at other temperatures can then be estimated.

Using the kinetics parameters summarized in Table 5-7, the prediction of the time-dependent relative crystallinity functions $\theta(t)$ for $T_c = 85^\circ\text{C}$ and 90°C for both of the sPP samples studied can be demonstrated as illustrated in Figures 5-8 and 5-9 (for sPP#1 and sPP#3, respectively). In general, the quality of the predicted $\theta(t)$ functions is rather disappointing. The deviation of the predicted curve at an arbitrary crystallization temperature may arise from the deviation of the predicted value of the corresponding crystallization rate parameter from the actual value at that temperature. In the Avrami and the Malkin models, another problem exists as a result of the supposition made on the value of the respective time exponent (i.e., n_a or C_0) which has to be fixed (e.g., the average value of the experimental results) when the prediction is carried out. It is fair to state, however, that prediction made for some other crystallization temperatures, where the deviation of the estimated values of the

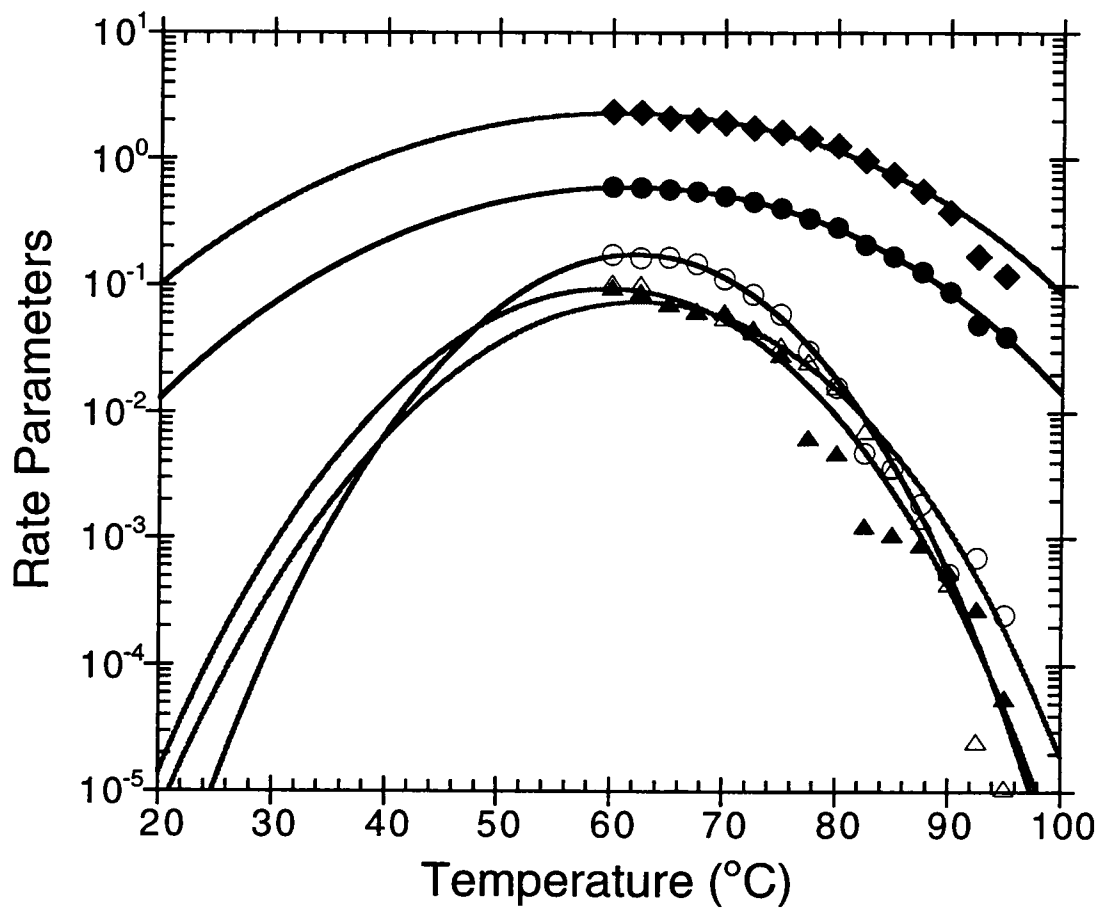


Figure 5-6. The best fitted curves of various crystallization rate parameters of sPP#1 to Equation (5-8). Keys: (●) $t_{0.5}^{-1}$; (O) k_{aj} ; (◆) C_{ij} ; (▲) k_{ai} ; (Δ) k_{as} .

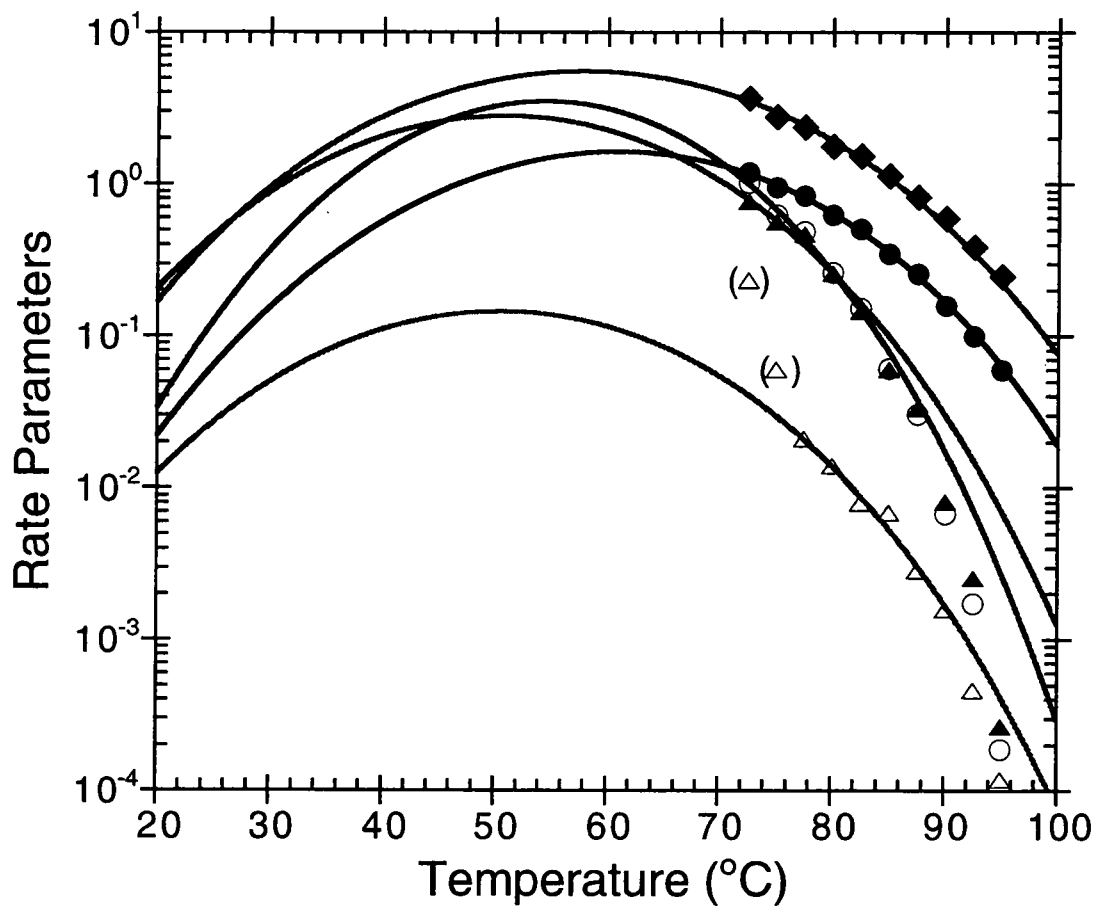


Figure 5-7. The best fitted curves of various crystallization rate parameters of sPP#3 to Equation (5-8). Keys: (●) $t_{0.5}^{-1}$; (○) k_a ; (◆) C_i ; (▲) k_{ai} ; (△) k_{as} .

Table 5-7. The fitting parameters, as provided by the program, for the best possible fits of the respective rate parameters to Equation (5-8).

Ψ	δ (K)	Ψ_0	Θ (cal·mol ⁻¹)	K (K ²)	χ^2
sPP#1					
$t_{0.5}^{-1}$ (min ⁻¹)	50	3.31×10^{13}	2617	6.32×10^5	0.0006
k_a (min ^{-2.75})	50	9.09×10^{42}	8476	1.99×10^6	0.0002
C_1 (min ⁻¹)	50	1.06×10^{12}	2175	5.43×10^5	0.0861
k_{ai} (min ⁻²)	50	7.23×10^{33}	6301	1.65×10^6	0.0004
k_{as} (min ⁻³)	50	4.99×10^{30}	6222	1.44×10^6	n/a
sPP#3					
$t_{0.5}^{-1}$ (min ⁻¹)	50	1.39×10^{16}	2982	7.39×10^5	0.0035
k_a (min ^{-2.75})	50	9.26×10^{25}	3910	1.30×10^6	0.0064
C_1 (min ⁻¹)	30	8.09×10^{12}	1500	6.28×10^5	0.0977
k_{ai} (min ⁻²)	50	5.30×10^{18}	2500	9.79×10^5	0.0091
k_{as} (min ⁻³)	50	6.12×10^{16}	2380	9.49×10^5	n/a

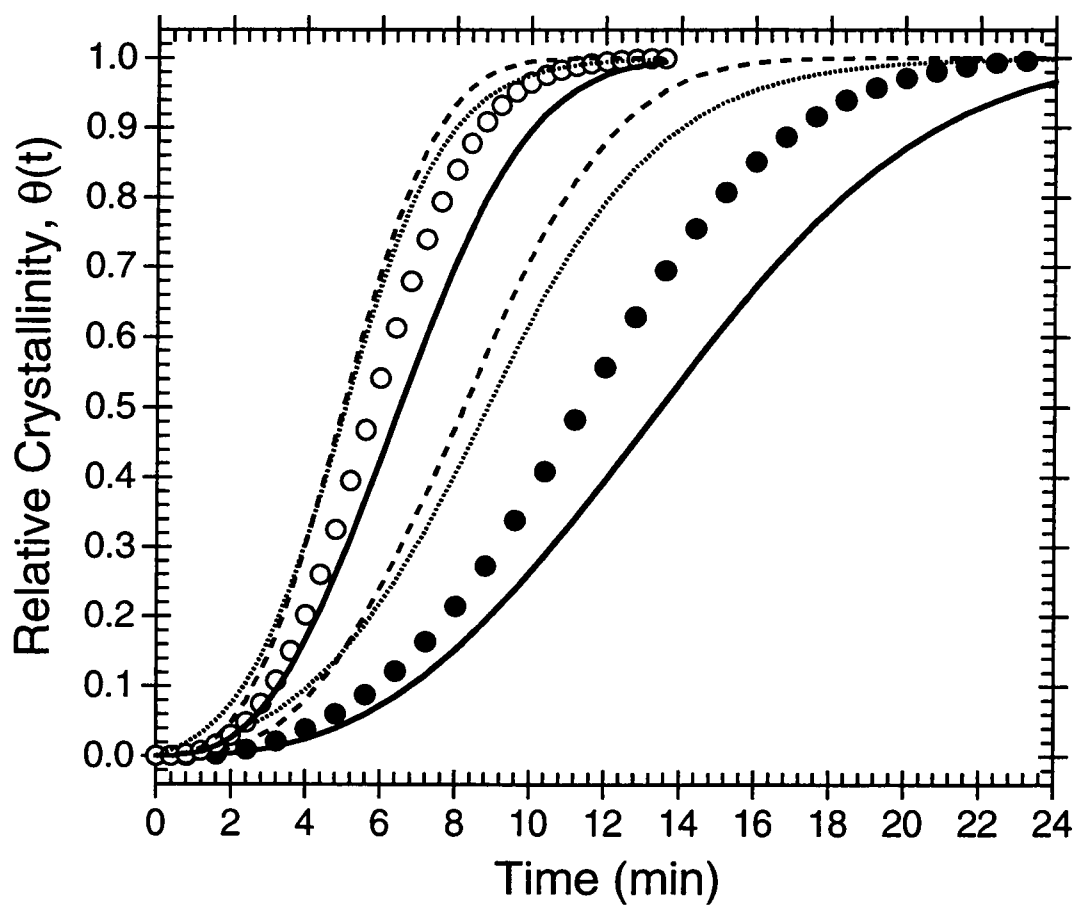


Figure 5-8. Relative crystallinity as a function of time of sPP#1 for 2 different crystallization temperatures: (○) 85°C; (●) 90°C. The experimental data, shown as points, are plotted along with the predicted curves using the Avrami, Malkin, and simultaneous Avrami macrokinetics models (shown as the solid, dotted, and dashed lines, respectively).

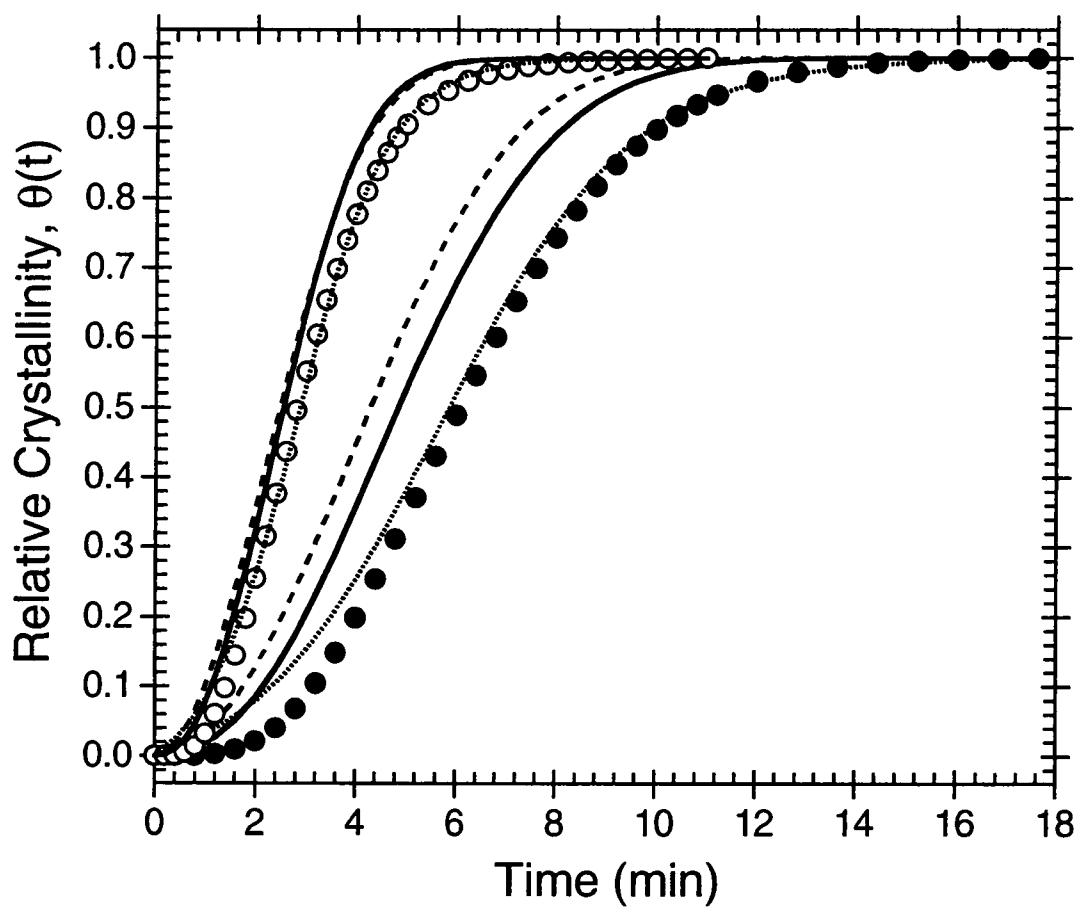


Figure 5-9. Relative crystallinity as a function of time of sPP#3 for 2 different crystallization temperatures: (○) 85°C; (●) 90°C. The experimental data, shown as points, are plotted along with the predicted curves using the Avrami, Malkin, and simultaneous Avrami macrokinetics models (shown as the solid, dotted, and dashed lines, respectively).

corresponding rate parameter (i.e., $t_{0.5}^{-1}$, k_a , C_1 , k_{av} , and k_{as}) from the experimentally observed values is minimal, may be more accurate than what has been demonstrated here.

6. CONCLUSIONS

A non-linear multi-variable regression program was used to fit the isothermal crystallization measurements obtained from the DSC to four macrokinetic models; namely the Avrami, Tobin, Malkin, and simultaneous Avrami models; and was found to give a reliable kinetics results. Judging from the quality of the fit, only the Avrami, the Malkin, and the simultaneous Avrami models were found to describe the time-dependence of the relative crystallinity well, resulting in the rejection of the Tobin model in describing the isothermal crystallization of sPP.

The Avrami exponent was found to be in the approximate range of 2 to 3, suggesting a two dimensional growth from a combination of thermal and athermal nuclei (i.e., instantaneous and sporadic nucleation). All of the crystallization rate parameters (i.e., $t_{0.5}^{-1}$, k_a , k_v , C_1 , k_{av} , and k_{as}) are found to be very sensitive to changes in the crystallization temperature. Within the crystallization temperature range studied (i.e., $60^\circ\text{C} < T_c < 95^\circ\text{C}$), the values of the rate parameters were all found to increase with decreasing temperature, due to the fact that sPP crystallizes faster at lower temperature than at the higher temperature. Comparison with earlier results [20] suggested that the range of temperature in this study falls in the region where nucleation is the rate determining factor. In addition, at the same temperature, sPP#3 was found to crystallize faster than sPP#1, even though its syndiotacticity level is a bit lower. The explanation was given based on the facts that the sPP#3 possesses a lower level of ethylene comonomer defects and that sPP#3 consists of molecular chains of relatively lower molecular mass.

It was shown that all of the crystallization rate parameters (i.e., $t_{0.5}^{-1}$, k_a , k_v , C_1 , k_{av} , and k_{as}) have a definable relationship with crystallization temperature (or degree of undercooling), making it possible to estimate values of the corresponding rate parameters at other temperatures, and hence possible predictions of the isothermal crystallization at those temperatures.

7. REFERENCES

- [1] H.D. Keith and F.J. Padden, *J. Appl. Phys.*, **35**, 1270 (1964).
- [2] H.D. Keith and F.J. Padden, *J. Appl. Phys.*, **35**, 1286 (1964).
- [3] R. Verma, H. Marand, and B. Hsiao, *Macromolecules*, **29**, 7767 (1996).
- [4] A.N. Kolmogoroff, *Izvestiya Akad. Nauk USSR, Ser. Math.*, **1**, 355 (1937).
- [5] W.A. Johnson and K.F. Mehl, *Trans. Amer. Inst. Mining Met. Eng.*, **135**, 416 (1939).
- [6] M. Avrami, *J. Chem. Phys.*, **7**, 1103 (1939).
- [7] M. Avrami, *J. Chem. Phys.*, **8**, 212 (1940).
- [8] M. Avrami, *J. Chem. Phys.*, **9**, 177 (1941).
- [9] U.R. Evans, *Trans. Faraday Soc.*, **41**, 365 (1945).
- [10] M.C. Tobin, *J. Polym. Sci., Polym. Phys.*, **12**, 399 (1974).
- [11] M.C. Tobin, *J. Polym. Sci., Polym. Phys.*, **14**, 2253 (1976).
- [12] M.C. Tobin, *J. Polym. Sci., Polym. Phys.*, **15**, 2269 (1977).
- [13] A.Ya. Malkin, V.P. Beghishev, I.A. Keapin, and S.A. Bolgov, *Polym. Eng. Sci.*, **24(18)**, 1396 (1984).
- [14] K. Ravindranath and J.P. Jog, *J. Appl. Polym. Sci.*, **49**, 1395 (1993).
- [15] J.J.C. Cruz-Pinto, J.A. Martins, and M.J. Oliveira, *Colloid Polym. Sci.*, **272**, 1 (1994).
- [16] B. Wunderlich, In *Macromolecular Physics*, Vol. 2, Academic Press, New York, 1976, pages 132-147.
- [17] J. Rabesiaka and A.J. Kovacs, *J. Appl. Phys.*, **32(11)**, 2314 (1961).
- [18] E. Kreyszig, In *Advanced Engineering Mathematics*, 7th Edition, John Wiley & Sons, New York, 1993, pages 1255-1257.
- [19] P. Supaphol and J.E. Spruiell, *J. Appl. Polym. Sci.*, accepted on April 4, 1999.
- [20] P. Supaphol, J.J. Hwu, P.J. Phillips, and J.E. Spruiell, *SPE-ANTEC Proc.*, 1759 (1997).
- [21] H. Janeschitz-Kriegl, E. Ratajski, and H. Wippel, *Colloid Polym. Sci.*, **277**, 217 (1999).
- [22] P. Supaphol and J.E. Spruiell, *J. Appl. Polym. Sci.*, accepted on April 16, 1999.
- [23] W. Banks, A. Sharples, and J.N. Hay, *J. Polym. Sci.*, **A2**, 4059 (1964).
- [24] B. Wunderlich, In *Macromolecular Physics*, Vol. 2, Academic Press, New York, 1976, Chapter 5.
- [25] J.D. Hoffman, G.T. Davis, and J.I. Lauritzen Jr., In *Treatise on Solid State Chemistry*, Vol. 3, N.B. Hannay (Ed.), Plenum Press, New York, 1976, Chapter 7.
- [26] J.D Hoffman and R.L. Miller, *Polymer*, **38**, 3151 (1997).

PART 6:
ON THE CRYSTALLIZATION AND MELTING BEHAVIOR IN
SYNDIOTACTIC POLYPROPYLENE: THE ORIGIN OF THE
MULTIPLE ENDOTHERMIC MELTING PHENOMENON

1. ABSTRACT

The subsequent melting behavior of syndiotactic polypropylene (sPP) after isothermal crystallization from the melt state has been studied by differential scanning calorimetry (DSC) and wide-angle x-ray diffraction (WAXD) techniques. For isothermal crystallization at high undercoolings, three melting endotherms are observed in the DSC heating scans. The minor endotherm, located close to the corresponding crystallization temperature, has been found to represent the melting of the secondary crystallites formed at the crystallization temperature. The low-temperature melting endotherm corresponds to the melting of the primary crystallites from at the crystallization temperature, while the high-temperature melting endotherm is a result of the melting of the crystallites re-crystallized during a heating scan. The triple-melting behavior observed in subsequent melting endotherms in DSC can then be described as the contributions from: 1) melting of the secondary crystallites and their re-crystallization, 2) partial melting of the less stable fraction of the primary crystallites and their re-crystallization, 3) melting of the primary crystallites, and lastly 4) re-melting of the re-crystallized crystallites formed during the heating scan.

2. INTRODUCTION

Syndiotactic polypropylene (sPP) was first synthesized in the early 1960s by Natta et al. [1,2] based on Ziegler-Natta catalysis, but the resulting polymer contained too high a level of regio-irregular defects (e.g., head-to-head/tail-to-tail type defects) despite a fair level of syndiotactic content. A much improved sPP was successfully synthesized in 1988 by Ewen et al. [3] who reported that highly stereo-regular and regio-regular sPP can be polymerized using a novel metallocene catalysis. The new catalyst systems have made it possible to produce sPP with much improved purity and yields,

which led to renewed interest in both scientific researches [4] and industrial applications [5-8].

Recently, studies on isothermal bulk crystallization and subsequent melting behavior on sPP samples, which were available commercially, using differential scanning calorimetry (DSC) technique have been reported [9,10] (cf. Part 2). According to the results shown in Part 2, subsequent DSC endothermic traces of sPP samples, which have been crystallized isothermally under certain conditions, exhibit two or three distinct melting endotherms, depending on the temperature at which the samples were crystallized. For experimental conditions studied in Part 2, the multiple endothermic melting behavior observed in sPP is likely a result of partial melting, re-crystallization of the less stable crystallites, and re-melting of the re-crystallized crystallites and the normal melting of the primary crystallites formed at the crystallization conditions. Although the melting/re-crystallization/re-melting hypothesis seemed to provide a satisfactory description of the data, a more thorough understanding in the subsequent melting behavior and the origin of the multiple endothermic melting behavior is necessary in order to gain an insight into the crystallization and melting process of sPP.

The multiple melting phenomenon is not only observed in sPP. In fact, various investigators have reported similar observations on a number of semi-crystalline polymers including some flexible polymers, such as polyethylene (PE) [11,12], isotactic polypropylene (iPP) [13,14], trans-1,4-polyisoprene [15], and poly(butylene succinate) (PBS) [16]; and some semi-stiff polymers, such as aliphatic polyamides [17-19], isotactic polystyrene (iPS) [20], syndiotactic polystyrene (sPS) and its blends [21], poly(ethylene terephthalate) (PET) [22-27], poly(butylene terephthalate) (PBT) [28-31], poly(phenylene sulfide) (PPS) [32,33], and poly(aryl ether ether ketones) [34-50].

In order to explain the occurrence of the multiple melting endotherms, a number of hypotheses have been proposed. In the studies of isothermal crystallization under

quiescent conditions (i.e., crystallization is only a function of temperature), the multiple endothermic melting behavior of these semi-crystalline polymers can be designated as a result of one of the following reasons: 1) the presence of two (or more) crystal modifications [13,15], 2) the presence of two (or more) crystalline morphologies [28], 3) the presence of two populations of crystal lamellae of different thicknesses [35,38,40,43-45], and 4) the simultaneous melting/re-crystallization and re-melting of the lamellae initially formed at the crystallization conditions [22,34,37,39,42,46].

Out of these models, the simultaneous melting/re-crystallization/re-melting and the dual-lamellar population models seem to receive much attention in explaining the multiple endothermic melting behaviors in various semi-crystalline polymers which do not exhibit multiple crystal modifications upon crystallizing at the crystallization conditions studied. The simultaneous melting/re-crystallization/re-melting model, first proposed by Holdsworth and Turner-Jones [22], hypothesizes that the primary lamellae formed at the crystallization temperature T_c undergoes a partial melting process which gives rise to an observation of the low melting endotherm (usually observed ca. 10°C above T_c). During the heating scan, the partially melted material undergoes a simultaneous process of re-crystallization into thicker and more perfect lamellae which, upon melting, gives rise to the observation of the high melting endotherm. This model was postulated based primarily on the observation that the magnitude and position of the low endotherm is heating rate dependent. The suitability of the model was questioned by the experimental findings that the occurrence of the high melting endotherm precedes that of the low-temperature endotherm [36,38,47], which clearly contradict the assignment of the low endotherm to the partial melting of the primary lamellae as it was postulated in this model.

The dual-lamellar population model, originally suggested by Cebe and Hong [35] and Bassett et al. [38], hypothesizes that there exists a bimodal distribution of lamellae

of different thicknesses within crystalline aggregates formed at the crystallization conditions studied, with the melting of the thin and the thick lamellae giving rise to the appearance of the low- and high-temperature endotherms, respectively. The two extensions of this model [49] are the dual-lamellar stack model [27,31,40,47,48] and the lamellar insertion model [41,43-45]. According to the dual-lamellar stack model, the distribution of the stacks of thick and thin lamellae is such that they exist in different stacks; whereas, in the lamellar insertion model, they co-exist in the same stacks with the thin lamellae are present in between two thick lamellae. Applicability of these two variants in describing the experimental data is still in controversy, and is very much dependent on the experimental conditions from which the data are obtained and perhaps on the technique used to obtain the data. For a schematic diagram describing the simultaneous melting/re-crystallization/re-melting and the dual-lamellar population models, please see Figure 2 in reference [49].

In recent studies on PET [31] and PBT [27], Hsiao and his colleagues showed that the morphology of both PET and PBT during isothermal crystallization can be best described by a dual-lamellar stack model, in which primary lamellar stacks are formed first (i.e., primary crystallization) followed by the formation of the secondary lamellar stacks inserted between the stacks of primary lamellae (i.e., secondary crystallization). The thickness of the primary lamellae is proven to be thicker than that of the secondary lamellae. On the remark of the triple-melting behavior in PET and PBT upon subsequent melting in DSC, they then concluded that the first endotherm is related to the melting of the secondary crystallites, the middle endotherm is a result of the melting of the primary crystallites, and the third endotherm is due to the melting of crystallites re-crystallized during the heating scan.

In the present study, DSC and x-ray diffraction techniques are used to investigate the melting behavior of sPP after isothermal crystallization under various

crystallization conditions. The aim is to obtain detailed information with regards to the crystallization mechanisms of sPP, and to propose the most probable explanation for the origin of the multiple endothermic melting behavior based on the aforementioned models.

3. EXPERIMENTAL DETAILS

3.1. Materials

The sPP sample (i.e., sPP#4) used in this study was synthesized using a metallocene catalyst and was produced commercially in pellet form by Fina Oil and Chemical Company of La Porte, Texas. Molecular characterization data, which were kindly performed by Dr. Roger A. Phillips and his co-workers of Montell USA, Inc. in Elkton, Maryland, shows the following molecular weight information: $M_n = 81,300$ daltons, $M_w = 171,000$ daltons, $M_z = 294,000$ daltons, and $M_w/M_n = 2.1$. In addition, the syndiotacticity measured by ^{13}C NMR shows the racemic dyad content [%*r*] to be 89.2%, the racemic triad content [%*rr*] to be 84.4%, and the racemic pentad content [%*rrrr*] to be 74.6%. The glass transition temperature T_g was determined to be ca. -6°C [10] (cf. Part 2).

3.2. Sample Preparation

Sliced pellets were melt-pressed between a pair of Kapton films, which in turn were sandwiched between a pair of thick metal plates, in a Wabash compression molding machine preset at 190°C under a pressure of 67 kpsi. After ten minutes holding time, a film of ca. 290 μm thickness was taken out and allowed to cool at ambient condition down to room temperature between the two metal plates. This treatment assumes that previous thermo-mechanical history was essentially erased, and provides a standard crystalline memory condition for the experiments.

3.3. Apparatus and Procedures

3.3.1. Differential Scanning Calorimetry (DSC)

A differential scanning calorimeter (DSC-7, Perkin-Elmer), equipped with internal liquid nitrogen cooling unit reliably providing a cooling rate up to $200^{\circ}\text{C}\cdot\text{min}^{-1}$, was used to record subsequent melting thermograms of sPP after isothermal crystallization at various conditions. All of the recorded melting thermograms were carried out using a scanning rate of $20^{\circ}\text{C}\cdot\text{min}^{-1}$, unless indicated otherwise. Temperature calibration was performed using a pure indium standard ($T_m^0 = 156.6^{\circ}\text{C}$ and $\Delta H_f^0 = 28.5 \text{ J}\cdot\text{g}^{-1}$). The consistency of the temperature calibration was checked every other run to ensure reliability of the data obtained. To make certain that thermal lag between the polymer sample and the DSC sensors is kept to a minimum, each sample holder was loaded with a single disc, weighing $7.1 \pm 0.3 \text{ mg}$, which was cut from the standard film already prepared. It is noteworthy that each sample was used only once and all the runs were carried out under nitrogen purge to minimize thermal degradation.

3.3.2. Wide-angle X-ray Diffraction (WAXD)

Wide-angle x-ray diffraction (WAXD) technique was employed to determine the crystal modification in the samples prepared using similar thermal treatments as described for the DSC samples. The WAXD intensity patterns were collected on a Rigaku-Denki diffractometer equipped with a computerized data collection and analysis system. The monochromatized x-ray beam was $\text{CuK}\alpha$ radiation, with a wavelength $\lambda = 1.54 \text{ \AA}$. The operating condition of the x-ray source was set at a voltage of 35 kV and a current of 40 mA.

4. RESULTS AND DISCUSSION

4.1. Dependence of Subsequent Melting Endotherms on Crystallization Temperature

Figure 6-1 presents a set of subsequent endothermic melting thermograms ($20^{\circ}\text{C}\cdot\text{min}^{-1}$) for sPP samples which were isothermally crystallized from the melt state at crystallization temperatures T_c ranging from 60°C to 95°C with 5°C increment. Each sample was held at a fusion temperature T_f of 190°C for 5 min, which is necessary for complete erasure of previous thermo-mechanical history [51]. After that, the sample was quenched from T_f as fast as possible to T_c , where it was held until the completion of crystallization process. The total holding time required for completion of crystallization at each temperature T_c varies, and was determined earlier [10], based on the assumption that the crystallization ends when no significant change is observed in the heatflow (even though slight change due to secondary crystallization, which is a very slow process, may still be occurring, but the change may not be detectable in the DSC due to high level of noise-to-signal ratio), to be an increasing function of the crystallization temperature (e.g., ca. 4 min at $T_c = 60^{\circ}\text{C}$ and ca. 70 min at $T_c = 95^{\circ}\text{C}$). In fact, the total time interval required for completion of crystallization at each crystallization temperature T_c (including other bulk crystallization kinetics parameters) is mainly controlled by the microkinetics parameters (i.e., the primary and secondary nucleation microkinetics mechanisms) which have finite relationships with the temperature [52-55]. Discussion of the bulk crystallization kinetics for this sPP sample was given elsewhere [10].

According to Figure 6-1, it is apparent that the DSC melting endotherms exhibit double melting phenomena, which are distinguishable in the endotherms recorded for the crystallization temperatures below 90°C . Moreover, the low-melting peak temperature (denoted T_{m1}) clearly increases in its size and sharpness, and its position shifts towards

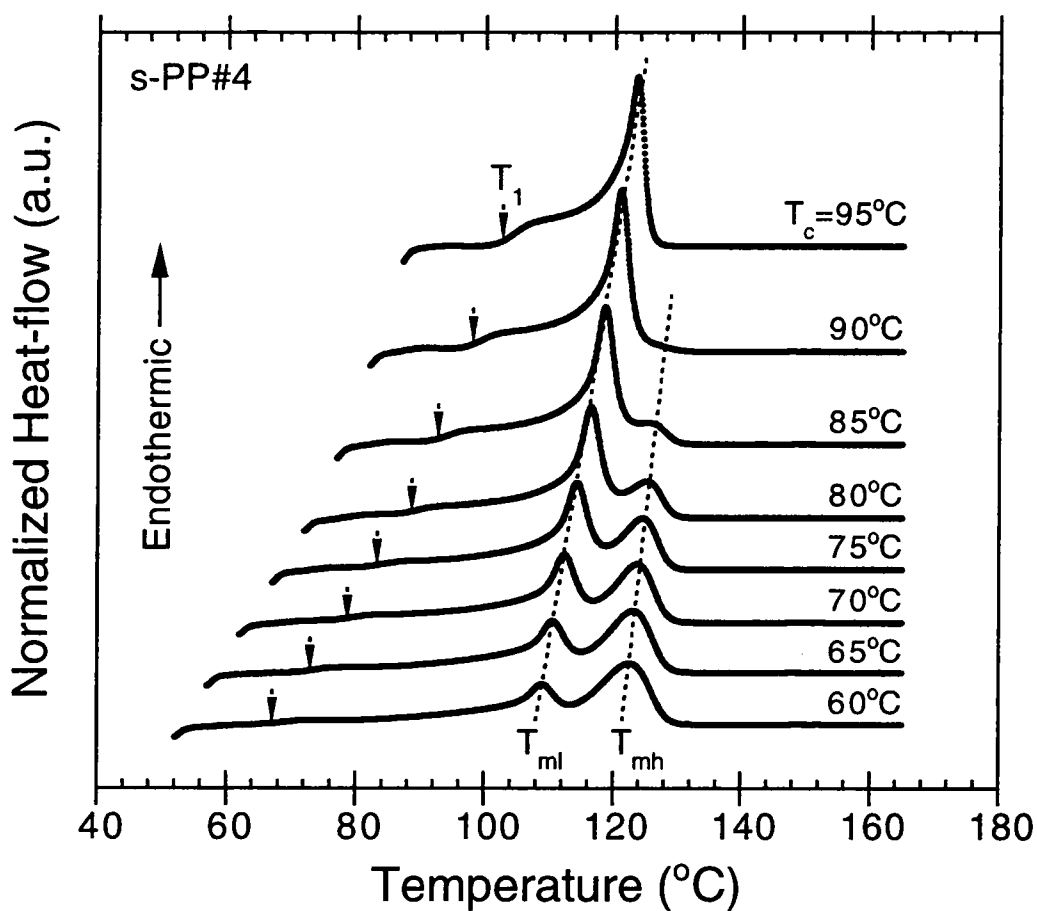


Figure 6-1. Subsequent melting endotherms ($20^\circ\text{C}\cdot\text{min}^{-1}$) of sPP samples after isothermal crystallization from the melt at the specified temperature. Terminologies: T_1 = the minor peak temperature; T_{ml} = the low-melting peak temperature; T_{mh} = the high-melting peak temperature.

higher temperature as crystallization temperature increases. On the contrary, the high-melting peak temperature (denoted T_{mh}) gets smaller with an increase in the crystallization temperature, and even disappears at high crystallization temperatures (e.g., $T_c \geq 90^\circ\text{C}$). Observations of the double-melting endotherms were also previously reported in sPP [56,57], and in syndiotactic poly(propene-co-octene) (sP(P-co-O)) [58], where the double-melting endotherms were observed in sPP below $T_c = \text{ca. } 105^\circ\text{C}$ ($M_n = 53,200$ daltons, $M_w/M_n = 1.1$, $[\%r] = 94\%$, DSC) [56], and below $T_c = \text{ca. } 128^\circ\text{C}$ ($M_n = 104,000$ daltons, $M_w/M_n = 2.3$, $[\%rr] = 97\%$, SAXS) [57], and in s-P(P-co-O) below $T_c = \text{ca. } 116.5^\circ\text{C}$ ($M_n = 73,000$ daltons, $M_w/M_n = 2.1$, $[\%r] = 97\%$, 4% wt. octene co-units, SAXS), respectively. Another interesting characteristic in these endothermic melting thermograms is the observation of the minor endotherm (denoted T_1) located close to the respective crystallization temperature T_c . It should be noted that the presence of the minor melting endotherm is not due to the enthalpic recovery of a physically aged rigid amorphous fraction present in the sample, since the glass transition region of sPP was determined to be ca. -6°C [10] which is very much lower than the temperature range where the minor melting endotherm is observed.

In order to illustrate quantitatively the relationships of these melting endotherms observed in the subsequent heating scans with the crystallization temperature, the following terminologies are used (cf. Figure 6-2): 1) the initial temperature T_{int} refers to the onset temperature of the minor melting endotherm, 2) the minor peak temperature T_1 refers to the apparent peak temperature of the minor melting endotherm, 3) the low-melting peak temperature T_{ml} refers to the peak temperature of the low-temperature melting endotherm, 4) the high-melting peak temperature T_{mh} refers to the peak temperature of the high-temperature melting endotherm, and finally 5) the end temperature T_{end} refers to the final temperature where the last crystalline aggregate melts. These values, extracted from the DSC heating scans shown in Figure 6-1, are

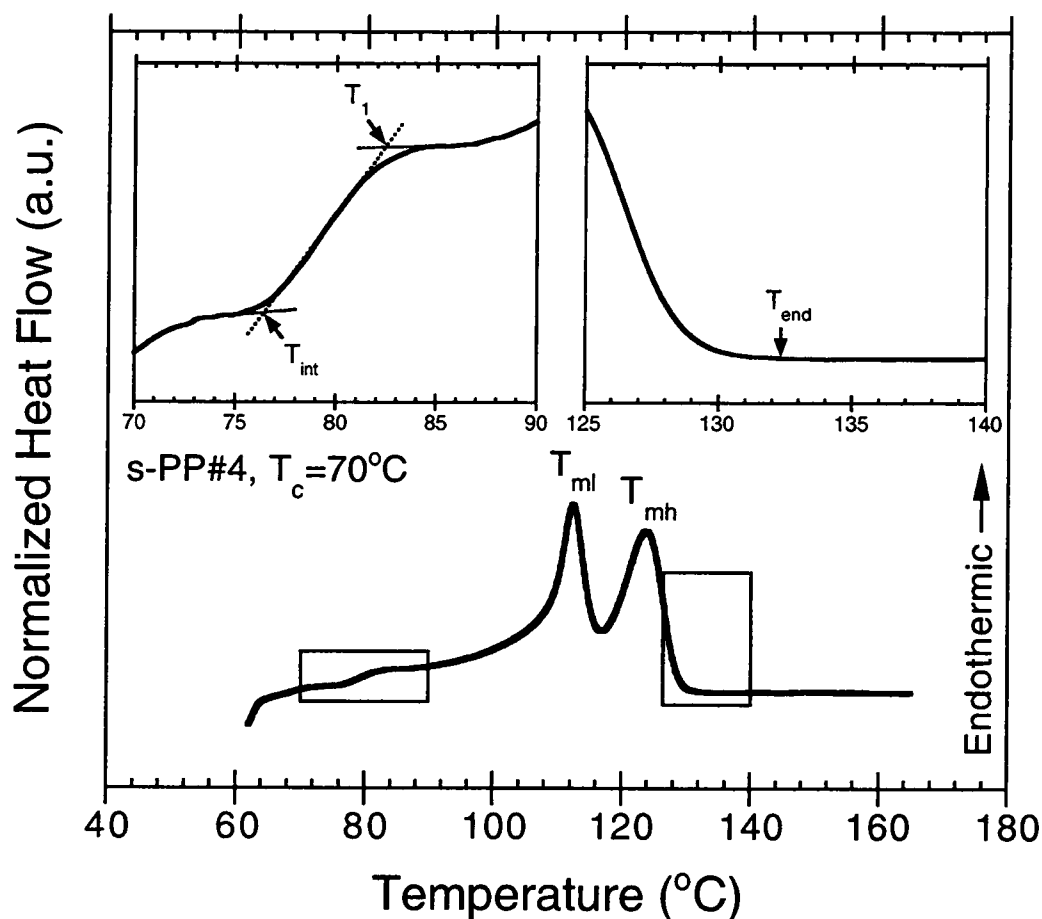


Figure 6-2. The procedure used in this study to determine characteristic temperatures from a subsequent melting endotherm. Terminologies: T_{int} = the initial temperature; T_1 = the minor peak temperature; T_{ml} = the low-melting peak temperature; T_{mh} = the high-melting peak temperature; T_{end} = the end temperature.

summarized in Table 6-1. Plots of these values as a function of crystallization temperature are present in Figure 6-3.

According to Table 6-1 and Figure 6-3, it is apparent that the initial temperature T_{int} and the minor peak temperature T_1 increase steadily with an increase in crystallization temperature. Interestingly, the differences between the values of the initial temperature T_{int} and the minor peak temperature T_1 and the crystallization temperature are found to be nearly constant (i.e., $T_{\text{int}} - T_c = 6.5 \pm 0.3^\circ\text{C}$ and $T_1 - T_c = 11.8 \pm 0.4^\circ\text{C}$). This confirms that the melting always starts at a temperature close to the respective crystallization temperature (ca. $T_c + 6.5^\circ\text{C}$). It is also evident, according to Table 6-1 and Figure 6-3, that the low-melting peak temperature T_{ml} and the high-melting peak temperature T_{mh} both increase steadily with crystallization temperature T_c . The high-melting peak temperature T_{mh} values are less dependent on T_c than the low-melting peak temperature T_{ml} values are. Unlike the other values, the end temperature T_{end} (the average value: $132.1 \pm 0.8^\circ\text{C}$) does not appear to be affected by the changes in the crystallization temperatures. The total enthalpy of fusion ΔH_f , also listed in Table 6-1, slightly increases with increasing crystallization temperature, suggesting that the apparent degree of crystallinity χ_c^{DSC} is an increasing function of the crystallization temperature (within the temperature range studied).

The analysis and the discussion of the multiple endothermic behavior cannot be complete without a proper consideration of whether the samples possess more than one crystal modification within the whole range of crystallization temperatures studied. Figure 6-4 shows WAXD diffractograms for samples isothermally crystallized in a Mettler hot-stage at $T_c = 60, 70, 80, 85, 90,$ and 95°C . Each sample was melted in a Mettler hot-stage at a fusion temperature T_f of 190°C for 5 min, then it was quickly transferred to another Mettler hot-stage, the temperature of which had been set at T_c .

Table 6-1. Variation of the initial temperature T_{int} , the minor peak temperature T_l , the low-melting peak temperature T_{ml} , the high-melting peak temperature T_{mh} , the end temperature T_{end} , and the enthalpy of fusion ΔH_f , as determined from Figure 6-1, with the crystallization temperature T_c .

T_c (°C)	T_{int} (°C)	T_l (°C)	T_{ml} (°C)	T_{mh} (°C)	T_{end} (°C)	ΔH_f (J·g ⁻¹)
60	66.1	72.5	108.9	122.5	132.1	33.1
65	71.0	76.3	110.6	123.0	132.8	33.2
70	76.7	82.3	112.3	123.8	132.4	33.0
75	81.5	86.8	114.2	124.6	132.6	33.3
80	86.9	91.9	116.4	125.3	132.6	33.4
85	91.4	96.5	118.6	-	132.3	33.4
90	96.4	101.6	121.0	-	131.6	34.0
95	101.6	106.7	123.6	-	130.2	34.5

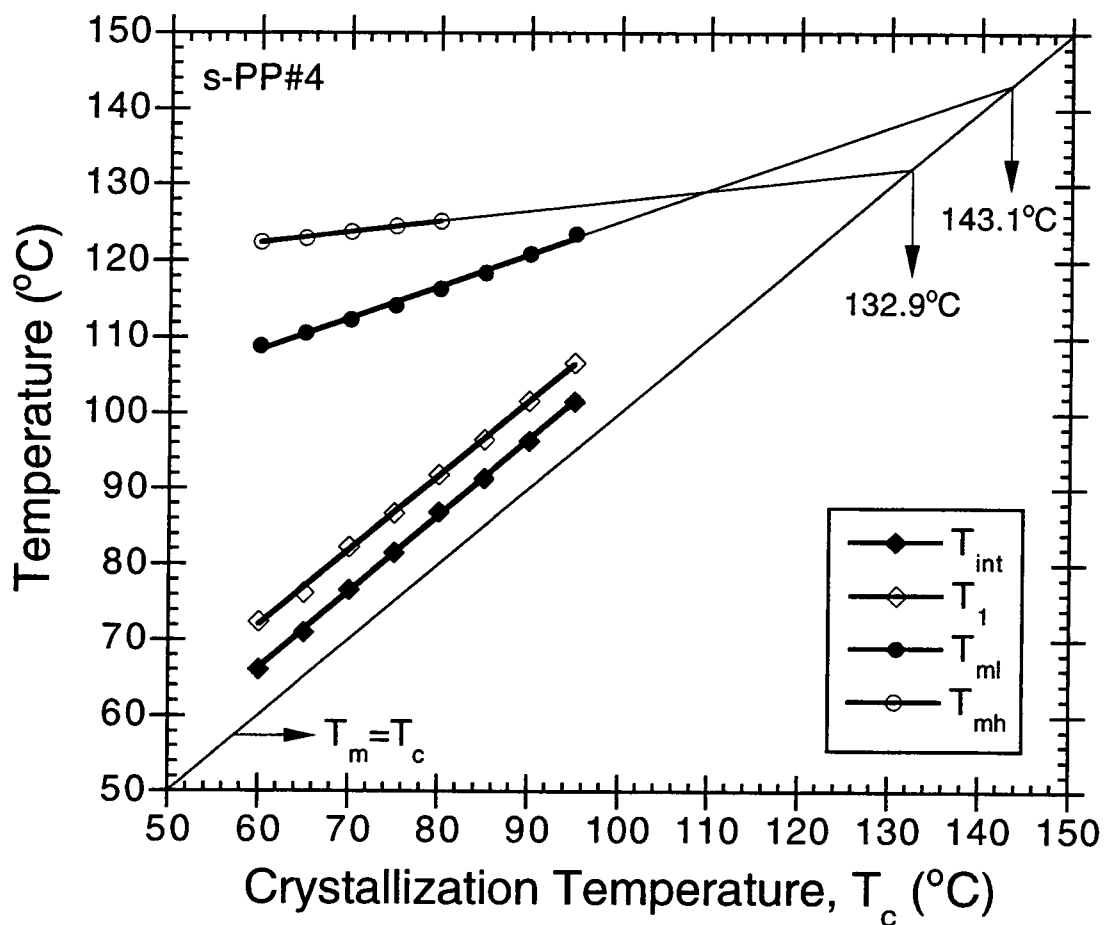


Figure 6-3. Variation of the initial temperature T_{int} , the minor peak temperature T_1 , the low-melting peak temperature T_{ml} , and the high-melting peak temperature T_{mh} as determined from the subsequent melting endotherms in Figure 6-1, with the crystallization temperature.

As soon as the total time required for the completion of the crystallization process at T_c (equivalent to the total time interval the samples spent isothermally in DSC) was reached, the sample was quenched in liquid nitrogen to prevent further change in crystallinity due to the residual thermal energy within the sample.

Before going further into the analysis of the WAXD diffractograms obtained, it is rudimentary to acquire information on all of the possible crystal modifications of sPP available in the literature. To date, four limit-ordered crystalline modifications of sPP have been proposed and described in the literature [59-73]. Of the four crystalline forms, only the molecular chain packing models of the limit-ordered form I [60-63,68,70] and the limit-disordered form I [63,67,70] (after the most recent nomenclature given by De Rosa et al. [74]) can be used to characterize sPP samples which are crystallized under quiescent crystallization conditions from the melt state (or from solution).

The limit-ordered form I is characterized by chains in the $(TTGG)_2$ helical conformation ($s(2/1)_2$ symmetry) fully antichirally packed in an orthorhombic unit cell with axes $a = 14.5 \text{ \AA}$, $b = 11.2 \text{ \AA}$, $c = 7.4 \text{ \AA}$ (cf. Figure 1A in reference [74]). The axes of the helices are in the positions $(0, 0, z)$ and $(\frac{1}{2}, 0, z)$ of the unit cell. The characteristic x-ray peaks in the powder spectrum are observed at $2\theta = 12.2^\circ$, 15.8° , 18.9° , 20.8° , and 24.5° ($d = 7.25$, 5.60 , 4.71 , 4.27 , and 3.63 \AA , respectively), which corresponds to the observations of (200) , (020) , (211) , (121) , and (400) reflection planes, respectively. The space group proposed for this crystal form was $Ibca$ [60,63] (or $P2_1/a$ in the refined model proposed by De Rosa et al. [68]). As revealed by the weakness, or in some cases, by the absence of the (211) reflection at $2\theta = 18.9^\circ$, in samples which were crystallized at low temperatures, it had been concluded that the existence of form I of sPP is controlled by the amounts of disorder present in the packing of the chains [63,67,70], causing a departure from the fully antichiral packing [70]. For samples crystallized at low temperatures, the limit-disordered form I having an orthorhombic unit cell with axes

$a = 14.5 \text{ \AA}$, $b = 5.6 \text{ \AA}$, $c = 7.4 \text{ \AA}$ (cf. Figure 1B in reference [74]) and antichiral packing of chains only along the a axis was described. The space group proposed for this crystal form was $Pcaa$ [60,66] (or $Pca2_1$ in the less symmetric arrangement of chains in the lattice [60]). According to this unit cell, the characteristic x-ray peaks can now be observed at $2\theta = 12.2^\circ$, 15.8° , 20.8° , and 24.5° ($d = 7.25$, 5.60 , 4.27 , and 3.63 \AA , respectively), corresponding to the observations of (200), (010), (111), and (400) reflection planes, respectively.

Let us turn the attention to the WAXD diffractograms shown in Figure 6-4. It is evident that the characteristic crystalline peaks are present at the scattering angles $2\theta = 12.18^\circ \pm 0.03^\circ$, $15.93^\circ \pm 0.03^\circ$, $20.60^\circ \pm 0.08^\circ$, and $24.57^\circ \pm 0.05^\circ$, with the characteristic (211) reflection at $2\theta = 18.9^\circ$ of the limit-ordered form I being absent from all of the WAXD scans. This clearly suggests that the crystalline structure in all of the samples studied can be designated as the limit-disordered form I, and that there is only one crystal modification present in all of the samples studied. As a result, it is logical to rule out the presence of more than one crystal modification as the source of the multiple melting behavior observed in these sPP samples. Owing to the facts that the WAXD scans exhibit only the presence of one crystal structure and that the low-temperature melting endotherm becomes more resolved and shifts towards higher temperature as crystallization increases, while the high-temperature melting endotherm exhibits otherwise, it is reasonable to believe, at this juncture, that the low-temperature melting endotherm is because of the melting process of the primary crystallites formed at the crystallization temperature T_c . The discussion on the occurrence of the minor melting endotherm and the high-temperature melting endotherm will be given in subsequent sections in this study.

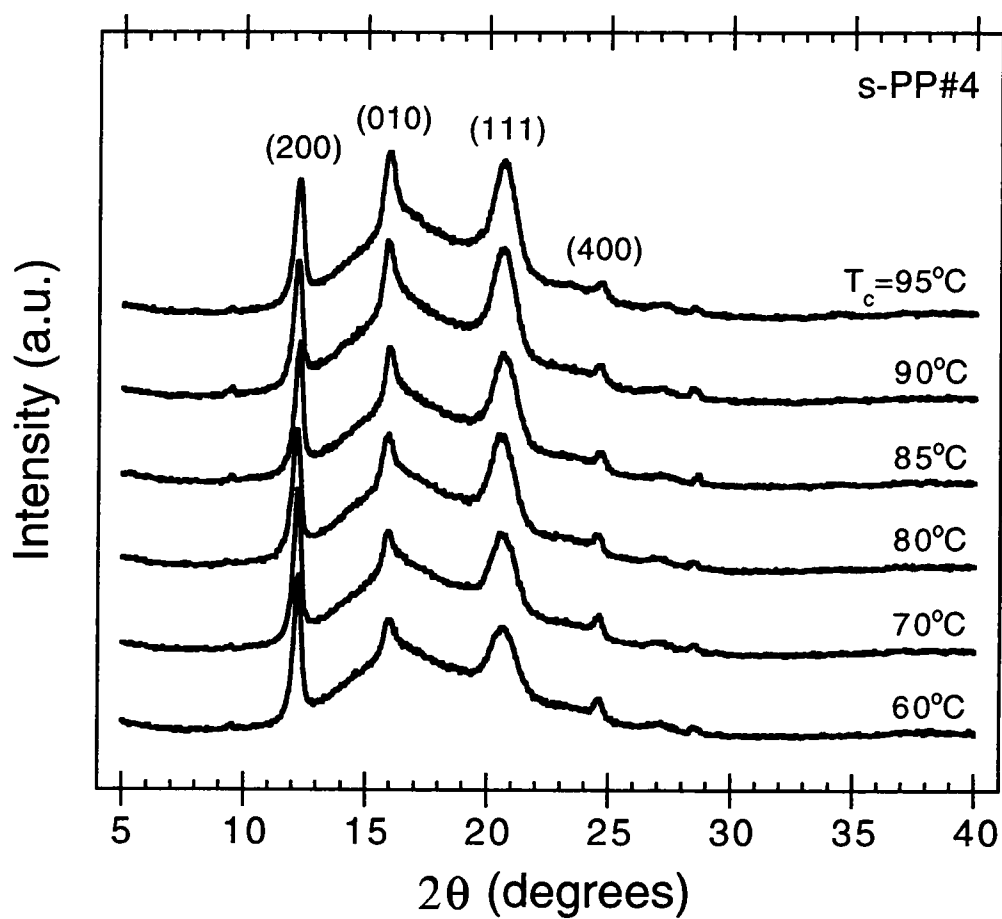


Figure 6-4. Wide-angle x-ray diffractograms of sPP samples isothermally crystallized from the melt at the specified temperature corresponding to the conditions used for the thermal analysis shown in Figure 6-1.

4.2. Dependence of Subsequent Melting Endotherms on Crystallization Time Interval

As mentioned previously, the simultaneous melting/re-crystallization/re-melting and the dual-lamellar population models are the two hypotheses which have received much attention and have been applied to describe the multiple melting phenomena in various semi-crystalline polymers. Since it has been determined in the previous section that the low-temperature melting endotherm, not the minor one, is due to the melting of the primary crystallites formed at T_c , the application of the simultaneous melting/re-crystallization/re-melting model to explain the multiple melting behavior in sPP can be ruled out. This leaves us only one choice: that is the dual-lamellar population model. According to the literature (see, for examples, in references [27,31]), this model proposes that the occurrence of the minor endotherm is a result of the melting of the secondary crystals formed at T_c . It is well established that secondary crystallization is a very slow process and often lags behind the primary crystallization (usually continuing after the impingement of the primary macroscopic crystalline aggregates). If the minor endotherm observed in subsequent melting scans of sPP is indeed due to the melting of the secondary crystals, one would expect that it should not be present in subsequent melting endotherms recorded at the early stage of crystallization (i.e., partial crystallization for short time intervals at T_c).

Figure 6-5 illustrates some representative DSC melting thermograms of sPP (recorded at $20^\circ\text{C}\cdot\text{min}^{-1}$) after isothermal crystallization at $T_c = 75^\circ\text{C}$ for 1.0, 1.5, 1.7, 2.0, 2.5, and 8.0 min, respectively; whereas, Figure 6-6 shows DSC melting thermograms (recorded at $20^\circ\text{C}\cdot\text{min}^{-1}$) after isothermal crystallization at $T_c = 95^\circ\text{C}$ for 15, 20, 25, 30, 40, and 50 min, respectively. At $T_c = 75^\circ\text{C}$, a time interval of at least 0.5 min was required for a melting peak to be observed in the subsequent melting endotherm (not shown). Similarly, a time period of at least 5 min was needed for a melting peak to be

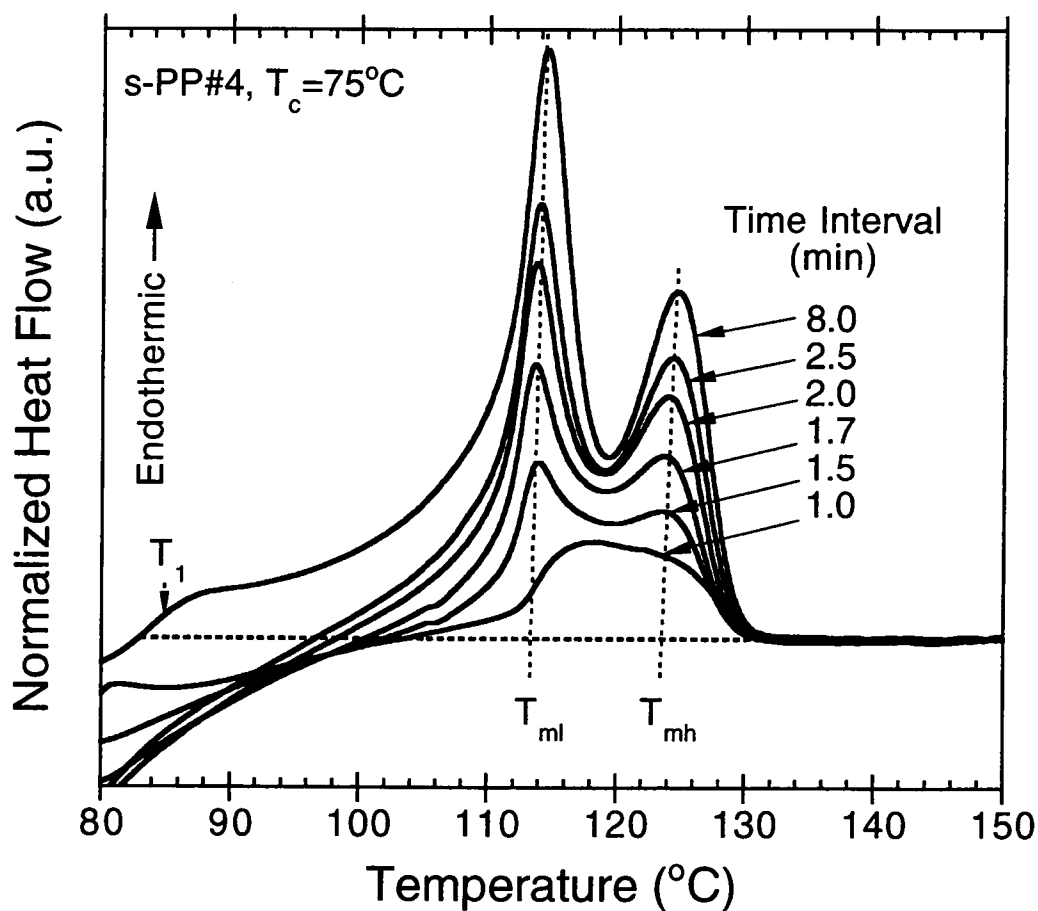


Figure 6-5. Subsequent melting endotherms ($20^\circ\text{C}\cdot\text{min}^{-1}$) of sPP samples after partial and complete crystallization at $T_c = 75^\circ\text{C}$ for different time intervals as indicated. Terminologies: T_1 = the minor peak temperature; T_{ml} = the low-melting peak temperature; T_{mh} = the high-melting peak temperature.

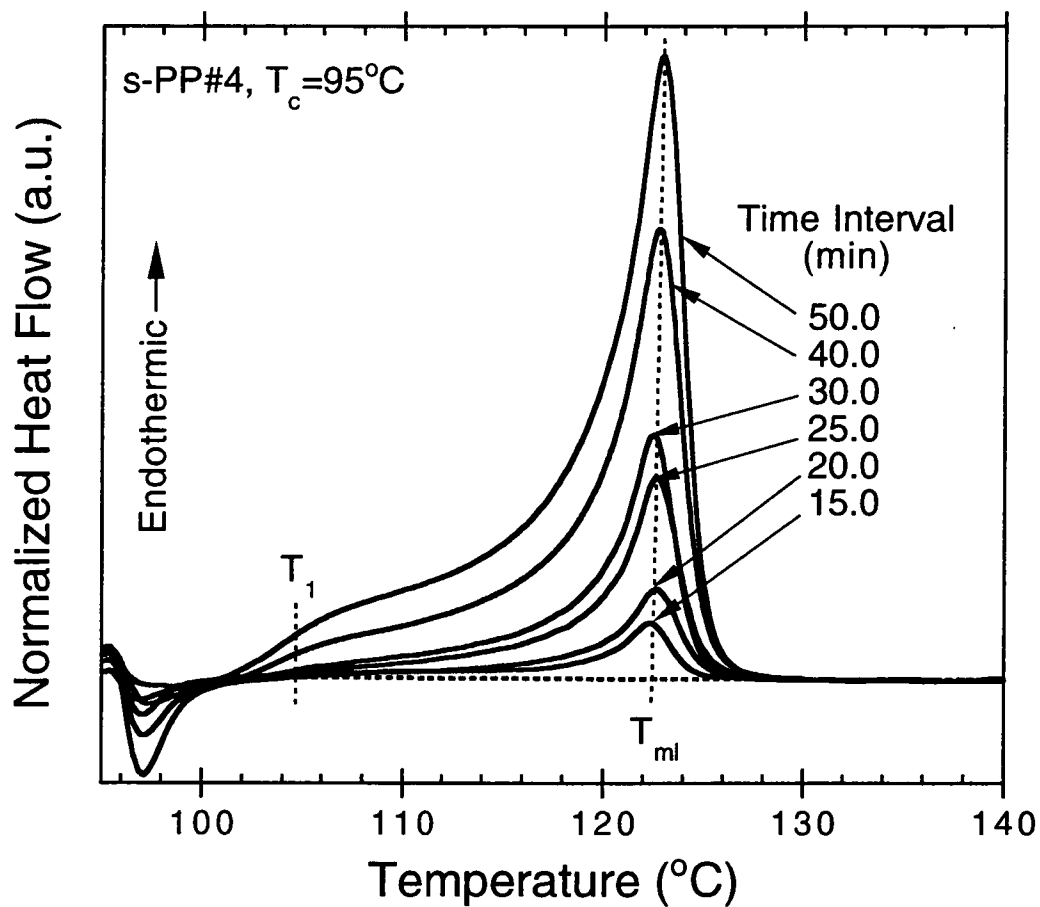


Figure 6-6. Subsequent melting endotherms ($20^{\circ}\text{C}\cdot\text{min}^{-1}$) of sPP samples after partial and complete crystallization at $T_c = 95^{\circ}\text{C}$ for different time intervals as indicated. Terminologies: T_1 = the minor peak temperature; T_{ml} = the low-melting peak temperature.

observed in the subsequent melting endotherm after isothermal crystallization at $T_c = 95^\circ\text{C}$. For the first approximation, the time intervals of ca. 0.5 and 5 min correspond to the induction time t_0 needed for stable crystallites to be formed at $T_c = 75^\circ\text{C}$ and 95°C , respectively.

On further consideration of these melting thermograms recorded after various time intervals at T_c , the occurrence of the secondary crystallization is decisively determinable. At $T_c = 75^\circ\text{C}$, it is clearly seen that the minor endotherm located at the low temperature region is clearly discernable in the DSC thermogram recorded after partial crystallization for 8 min. At $T_c = 95^\circ\text{C}$, the minor endotherm is apparent in the DSC thermograms recorded after partial crystallization for 40 and 50 min. Careful examination in all of the recorded DSC thermograms shows that the appearance of the small endotherms in the DSC thermograms was not clearly observed until after partial crystallization for at least ca. 4 min at $T_c = 75^\circ\text{C}$ and for at least ca. 25 min at $T_c = 95^\circ\text{C}$. The position where the minor endotherm is observed locates close to a temperature where the sample was crystallized, as previously mentioned, and seems to shift to higher temperature with increasing crystallization time interval at the corresponding crystallization temperature.

The facts that the minor endotherm 1) is usually observed at a temperature close to the crystallization temperature, 2) is observed at a later stage of crystallization, and 3) increases in its magnitude and possibly shifts to higher temperature with increasing crystallization time suggest that its existence corresponds to a contribution from a rather slow crystallization mechanism occurring at T_c , which is most likely as a result of the secondary crystallization. At this point, it is possible to establish that the minor endotherm and the low-temperature melting endotherm are caused by the melting of the secondary and primary crystallites formed at T_c , respectively.

In addition to their use for determining the source of the minor endotherm, Figures 6-5 and 6-6 provide us with additional information regarding the melting behavior of sPP. According to Figures 6-5 and 6-6, it is evident that the peak positions of the low-temperature melting endotherm, which is taken as the melting endotherm of the primary crystallites formed at T_c , are essentially unchanged with increasing crystallization time interval. The average values of these peaks are $114.0 \pm 0.3^\circ\text{C}$ for $T_c = 75^\circ\text{C}$ and $120.4 \pm 0.3^\circ\text{C}$ for $T_c = 95^\circ\text{C}$. It has been established in the Gibbs-Thomson equation [54,75] that there is a relationship between the observed melting temperature T_m and the lamellar thickness l_c of the crystallites according to the following equation:

$$T_m = T_m^0 \left(1 - \frac{2\sigma_e}{l_c \Delta H_f^0} \right), \quad (6-1)$$

where T_m^0 is the equilibrium melting temperature (i.e., the melting point of an infinitely thick crystal) for the polymers studied, σ_e is the fold surface free energy, l_c is the lamellar thickness, and ΔH_f^0 is the equilibrium enthalpy of fusion. According to Equation (6-1), this can only be construed to mean that the average thickness of the primary crystallites (as suggested by the position of the peak temperature of the low-temperature melting endotherm) formed at T_c is essentially constant throughout the crystallization process. In other words, the results suggest that the primary crystallites formed at T_c do not thicken during the course of crystallization. This finding agrees extremely well with the observations reported on crystallization behavior of sPP using a real-time SAXS and DSC technique [57,58,76], in which the average lamellar thickness of the primary crystallites of sPP was shown to be constant during both the isothermal crystallization process and subsequent heating to the melting point.

Before going further into the discussion of the origin of the high-temperature melting endotherm, it is important to first establish hypotheses regarding the melting mechanisms of the secondary crystallites formed at T_c during subsequent heating. In

order to do so, the nature of the secondary crystallites have to be first established. This can be carried out base on the two variances [27,31,40,41,43-45,47,48] of the dual-lamellar population model [35,38], and a recent notion on secondary crystallization in polymers proposed by Marand and Alizadeh [77].

It is well-established that overall crystallization in semi-crystalline polymers can be divided into two main processes: primary crystallization and secondary crystallization. Primary crystallization corresponds to the macroscopic development of crystallinity as a result of two consecutive microscopic mechanisms: primary nucleation and secondary nucleation (i.e., subsequent crystal growth). The formation of chain-folded lamellae (i.e., primary nucleation) leads to further growth of the lamellae through the processes of branching and splaying (see, for example, Figure 4 in reference [78]). The degree of branching and splaying is mainly controlled by the degree of undercooling (i.e., the difference between the equilibrium melting temperature and the crystallization temperature: $\Delta T = T_m^0 - T_c$) in an increasing manner. The evidence to this assertion can be seen in a series of atomic force microscopy (AFM) images of the crystal growth in iPS taken by Taguchi et al. [79], in which they showed that the degree of branching and splaying in crystalline aggregates increases with increasing degree of undercooling. This leads to the change of the crystalline aggregates from being a hexagon platelet at $T_c = 210^\circ\text{C}$ to being a dense-branched morphology (spherulitic in 2D) at $T_c = 180^\circ\text{C}$. The primary crystallization is assumed to cease when no further growth of the lamellae can take place. This may be due to the impingement of the crystalline aggregates onto one another.

Secondary crystallization refers to any process which leads to further increase in crystallinity. Two important processes are envisaged: the thickening of the primary lamellae and the formation of secondary lamellae from crystallizable amorphous materials trapped between two different lamellae in the same stack (i.e., inter-lamellar

amorphous layer) or between two different stacks of lamellae (i.e., inter-fibrillar amorphous materials). The thickening mechanism is thermodynamically driven by the reduction of the specific surfaces of the crystals (hence less free energy penalty for the formation of free surfaces), but is hampered by the kinetics factors (e.g., molecular mobility). In the case of copolymers with non-crystallizable co-units, the lamellar thickening is also less favorable due to the *clamping effect* caused by high concentration of the non-crystallizable co-units rejected from the growing lamellae around the basal planes and the growth fronts. This clamping effect was thought by Hauser et al. [58] to be the reason for the observed constancy in the lamellar thickness during the course of crystallization in sPP.

Even though it is obvious that secondary lamellae have to somehow originate from either inter-lamellar or inter-fibrillar crystallizable amorphous materials (or both) trapped within the crystalline aggregates after their impingement to one another, the mechanisms to which the formation of the secondary lamellae are followed are uncertain and are still matters of ongoing research. Explanation of the actual mechanisms may lie on the general understanding of the nature of the inter-lamellar amorphous layers and the inter-fibrillar amorphous materials at certain crystallization conditions.

For crystallization at *high undercoolings*, the facts that 1) the degree of branching and splaying is relatively high, 2) the inter-lamellar amorphous layers are relatively thick, suggest that secondary lamellae may originate from the inter-lamellar amorphous layers, rather than from the free melt between the fibrillar structures (i.e., less inter-fibrillar melt is available due to high order of branching and splaying). Since the inter-lamellar amorphous layers comprise mainly of folds, tie molecular segments, chain-ends, and other rejected non-crystallizable materials, secondary lamellae can only form from tie molecular segments which are constrained at both ends between two different lamellae. In the conditions of conformational constraints, the reduction in the molecular

entropy will cause the apparent equilibrium melting temperature of the particular molecular segments to be higher than normal. Relatively thinner secondary lamellae can therefore become stable at these temperatures. As it is postulated by Marand and Alizadeh [77], the secondary crystallites, in this extreme case, can only originate from a mechanism similar to a *fringed-micelle* or *chain-clustering* (cf. Figure 1 in reference [77]), due to extreme conformational constraints at both ends. On the other hand, for crystallization at *low undercoolings*, the reverse of the reasons given above suggest to us that it is possible for new lamellae to grow from the relatively free melt located between the fibrillar structures, resulting in relatively slight differences between the primary and secondary lamellae formed [77]. For crystallization under intermediate conditions, intermediate situations for the formation of the secondary crystallites after the impingement of the primary crystallites are expected. The characteristics of the secondary crystallites (e.g., its thickness, stability, etc.) will depend greatly on the degree of undercooling and the magnitude of the conformation constraints [77].

Since it has been established that under the same crystallization conditions the thickness of secondary crystallites are thinner than that of the primary crystallites (thus less stability), upon heating these secondary crystallites will melt first. Whether the secondary crystallites are formed in the lamellar insertion or the lamellar stack mode may depend largely on the conditions of crystallization and the types of polymers with which one is dealing. Similar to the crystallization mechanisms, melting mechanisms of both primary and secondary crystals are also complicated. Upon melting, a finite relaxation time is required before a bundle of molecular segments, after the detachment from the crystals, to resume its equilibrium entangled molten state, and this characteristic time varies from one polymer to another. In sPP, previous study [51] (cf. Part 4) indicated that the relaxation time for the segregation of nucleation cluster to its equilibrium molten state (i.e., complete melting) depends strongly on the temperature

where the sample is brought to melt (i.e., fusion temperature T_f) in a decreasing manner with increasing temperature. Since the secondary crystallites are shown to melt close to the crystallization temperature where they are formed due to the thinness and the relatively low stability of the lamellae formed, the relaxation time required for the detached or melted bundles of molecular segments to resume their equilibrium molten state is tremendously large causing the detached bundles of molecular segments to retain their preferred conformational state (i.e., the conformational state they assume in the crystalline phase) and upon further heating in DSC these bundle of molecular segments can act as predetermined nuclei which can re-crystallize during the heating scan.

4.3. Dependence of Subsequent Melting Endotherms on Heating Rate

Without any exceptions, the re-crystallization process during the heating scan must obey the fundamental principles of polymer crystallization, even though the mechanisms behind the process may be completely different. Although the requirement for the formation of primary nuclei may be completely resolved owing to the postulation stated in the previous section that the detached bundle of molecular segments as a result of the melting of the secondary crystallites can act as predetermined nuclei upon heating to the melt state, the following questions may still remain:

- 1) What exactly is the mechanism for the diffusion of molecular segments onto the growth fronts?
- 2) What is the nature of the lamellae formed (whether they are chain-folded, true fringed-micellar, or a mixture of both)?
- 3) Since the re-crystallized lamellae has to grow during a dynamic temperature change, is the thickness of the lamellae formed constant or increasing as the temperature increases?

Whether these questions can be answered is immaterial at this point. One can expect that the extent of re-crystallization process from the crystallizable materials due to the melting of the secondary crystallites depends significantly on the original crystallization temperature where the secondary crystallites were formed, the chemical structure of the polymers studied, and the scanning rate used during the heating scan in DSC. In addition, one can expect that the melting point of these re-crystallized crystals must be higher than that of the primary crystals formed at T_c . The last postulation gives us a confidence that the high-temperature melting endotherms observed in Figures 6-1 and 6-5 are a result of the melting of the re-crystallized crystallites formed during the heating scan in DSC.

To account for the effect of heating rate on the multiple melting behavior of sPP, a separate qualitative experiment was performed, in which the results are presented in Figure 6-7. In this experiment, each sample was isothermally crystallized at 75°C, then its melting thermogram was recorded using 6 different scanning rates, ranging from 5 to 40°C.min⁻¹. It should be noted that before each measurement was carried out at a designated scanning rate, DSC had been well calibrated for that particular scanning rate. It is evident, according to Figure 6-7, that the weight fraction of the high-temperature melting endotherm decreases with increasing heating rate, while that of the lower melting peak increases. This can be explained based on the fact that the rate of re-crystallization depends significantly on the heating rate used during the heating scan. The higher the heating rate used, the shorter the time available for the diffusion of the molecular segments onto the growing re-crystallizing lamellae. In other words, the extent of the re-crystallization is kinetically controlled and decreases with an increase in the heating rate used. This finding is in accordance with what Carfagna et al. [80] found in their work on re-crystallization kinetics of iPP.

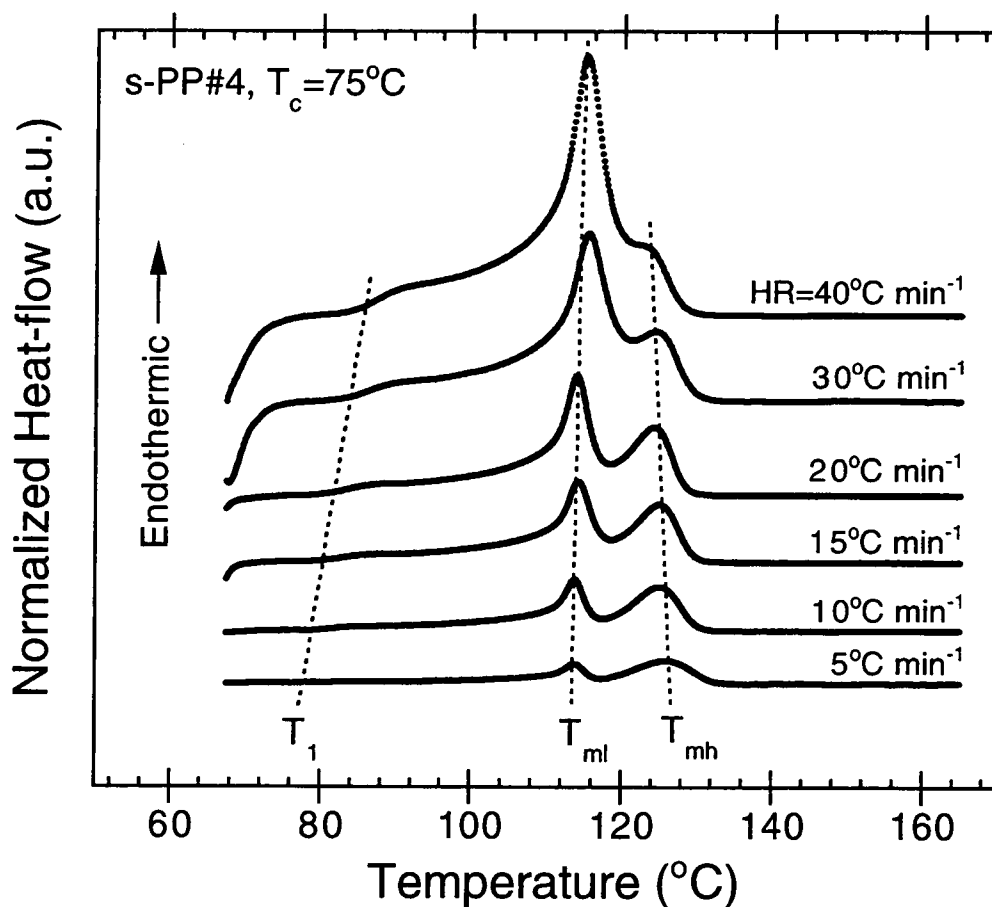


Figure 6-7. Subsequent melting endotherms of sPP samples recorded using different scanning rate ranging from 5 to 40°C·min⁻¹ after complete crystallization at $T_c = 75^\circ\text{C}$. Terminologies: T_1 = the minor peak temperature; T_{ml} = the low-melting peak temperature; T_{mh} = the high-melting peak temperature.

Based on the procedure given in Figure 6-2, quantitative description of subsequent melting endotherms shown in Figure 6-7 is summarized in Table 6-2. It is apparent that both initial temperature T_{int} and the minor peak temperature T_1 increase steadily with an increase in the scanning rate used during the heating scan. It is also clear, according to Table 6-2, that the low-melting peak temperature T_{ml} slightly increases with increasing heating rate used, while the high-melting peak temperature T_{mh} and the end temperature T_{end} are both found to decrease with increasing heating rate used. The reason for the increase in the observed T_{int} , T_1 , and T_{ml} values may be as simple as super-heating effect, while that for the decrease in the observed T_{mh} must be based on a more theoretical ground. As mentioned previously, as the scanning rate during a heating scan in the DSC increases, less time is available for molecular transport onto the growth front of the re-crystallizing crystals. As a result, the re-crystallized crystallites formed at high heating scan rate are less stable than those formed during a DSC heating scan using lower value of the scanning rate, hence the lower value of the observed melting point (i.e., T_{mh}). In addition, the total enthalpy of fusion ΔH_f , also listed in Table 6-2, slightly decreases with an increase in heating rate used, suggesting either that 1) the extent of re-crystallization indeed decreases with increasing heating rate, or that 2) the high-temperature melting endotherm is not solely attributed to the re-melting of the re-crystallized crystals formed from the crystallizable materials due to the melting of the secondary crystals during the heating scan, but also to the re-melting of the re-crystallized crystals formed from the crystallizable materials due to the melting of the less stable fraction of the primary crystallites formed at T_c .

Referring now to Figure 6-5, it has already been established that secondary crystallization does not occur during isothermal crystallization at $T_c = 75^\circ\text{C}$ until at least 4 min holding time was reached. Yet, most of the subsequent melting endotherms after partial crystallization for various holding time intervals less than 4 min (i.e., early stages

Table 6-2. Variation of the initial temperature T_{int} , the minor peak temperature T_1 , the low-melting peak temperature T_{ml} , the high-melting peak temperature T_{mh} , the end temperature T_{end} , and the enthalpy of fusion ΔH_f , as determined from Figure 6-7, with the heating rate used to record the subsequent melting endotherms after complete crystallization at $T_c = 75^\circ\text{C}$.

Heat Rate ($^\circ\text{C}\cdot\text{min}^{-1}$)	T_{int} ($^\circ\text{C}$)	T_1 ($^\circ\text{C}$)	T_{ml} ($^\circ\text{C}$)	T_{mh} ($^\circ\text{C}$)	T_{end} ($^\circ\text{C}$)	ΔH_f ($\text{J}\cdot\text{g}^{-1}$)
5	78.2	81.9	113.3	125.6	133.9	35.8
10	79.4	84.0	113.6	124.9	133.6	34.1
15	79.5	85.9	114.4	124.9	133.5	34.1
20	80.3	86.2	114.0	124.2	132.7	33.9
30	83.0	89.3	115.4	124.2	132.7	33.1
40	84.0	90.2	115.1	123.2	132.0	32.6
114.3 ± 0.8 124.5 ± 0.8 133.1 ± 0.7 34.0 ± 1.1						

of crystallization where only primary crystallization supposedly dominates) also exhibit dual-melting behavior. This suggests to us that melting of the less stable fraction of the primary crystallites may indeed occur, and upon re-melting after re-crystallization it gives rise to the formation of the high-temperature melting endotherm. In order to investigate the impact of the scanning rate during a heating scan on the melting of the less stable fraction of the primary crystallites and its re-crystallization behavior, subsequent melting endotherms after isothermal crystallization for various short time intervals during the early stages of crystallization were recorded as a function of heating rate (cf. Figures 6-8 and 6-9). Quantitative description of the results shown in Figures 6-8 and 6-9 is summarized in Table 6-3.

In Figures 6-8 and 6-9, subsequent melting endotherms after isothermal crystallization at $T_c = 75^\circ\text{C}$ for 1.5 min and at $T_c = 95^\circ\text{C}$ for 15 min are displayed for 5 different heating rates, ranging from 5 to $30^\circ\text{C}\cdot\text{min}^{-1}$, respectively. It is apparent, according to both Figures 6-8 and 6-9, that the minor endotherm does not exist in any of the thermograms recorded, suggesting that appreciable secondary crystallization has not yet occurred during the indicated time interval the samples were held at T_c . The weight and the peak position T_m of the low-temperature melting endotherm in both Figures 6-8 and 6-9 (cf. Table 6-3) slightly increase with increasing heating rate used: those of the high-temperature melting endotherm, however, decrease. In Figure 6-9, it is evident that the high-temperature melting endotherm is present in subsequent melting endotherms recorded using low heating rates (i.e., $\leq 10^\circ\text{C}\cdot\text{min}^{-1}$). This clearly verifies the hypothesis that during the heating scans the less stable fraction of the primary crystallites melts and re-crystallizes and upon further heating the re-crystallized fraction melts again giving rise to the formation of the high-temperature melting endotherm. The extent of the melting and re-crystallization of the primary crystallites depends strongly on the stability of the primary crystallites and the heating rate used.

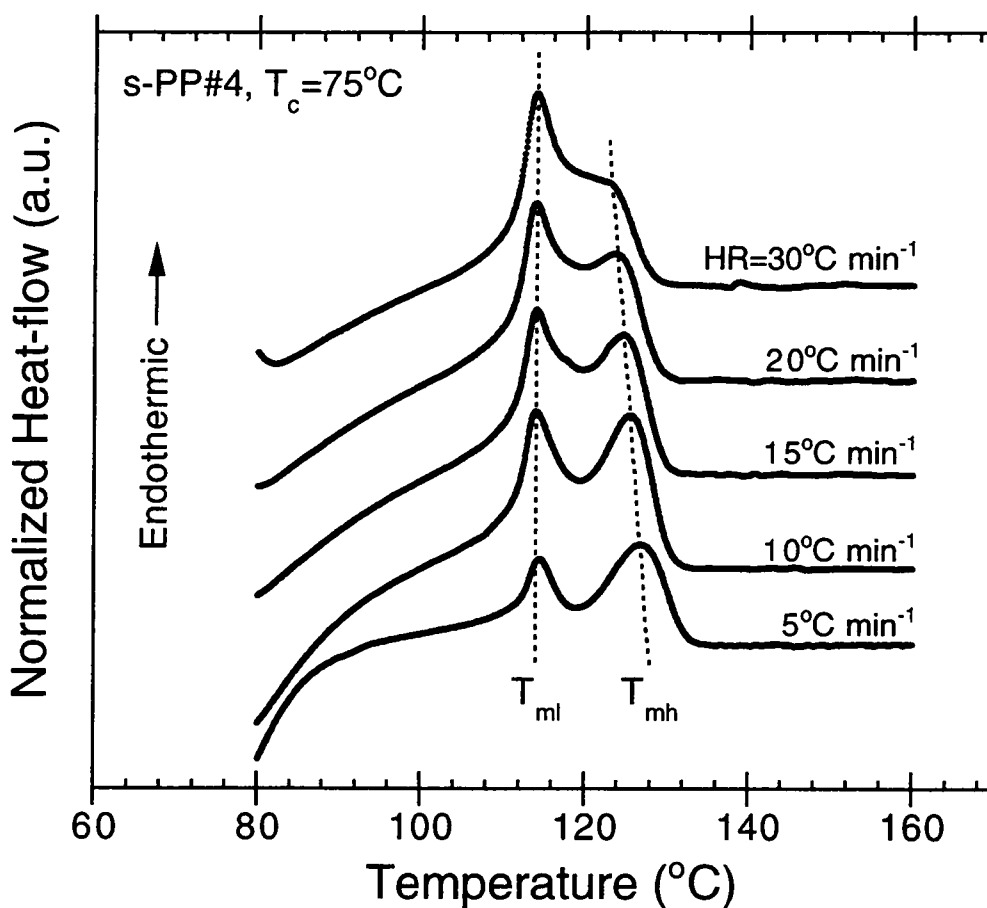


Figure 6-8. Subsequent melting endotherms of sPP samples recorded using different scanning rate ranging from 5 to $30^\circ\text{C}\cdot\text{min}^{-1}$ after partial crystallization at $T_c = 75^\circ\text{C}$ for 1.5 min. Terminologies: T_{ml} = the low-melting peak temperature; T_{mh} = the high-melting peak temperature.

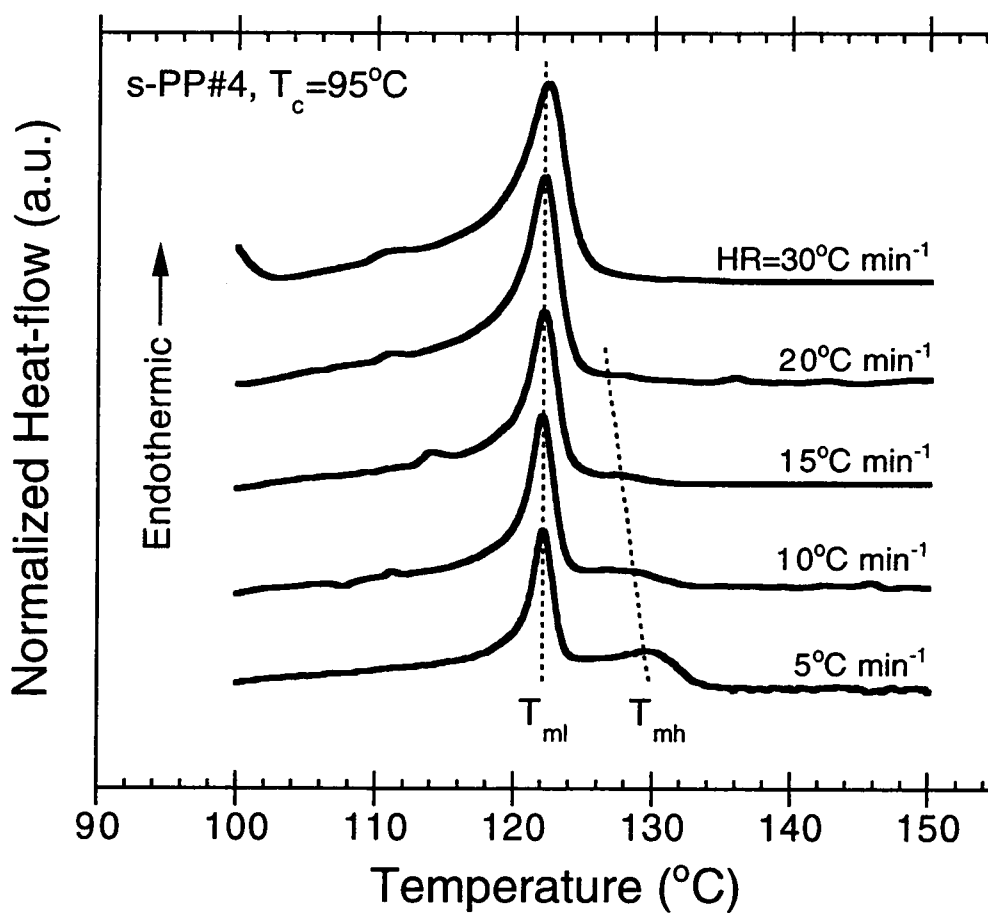


Figure 6-9. Subsequent melting endotherms of sPP samples recorded using different scanning rate ranging from 5 to 30°C·min⁻¹ after partial crystallization at $T_c = 95^\circ\text{C}$ for 15 min. Terminologies: T_{ml} = the low-melting peak temperature; T_{mh} = the high-melting peak temperature.

Table 6-3. Variation of the low-melting peak temperature T_{ml} , the high-melting peak temperature T_{mh} , and the enthalpy of fusion ΔH_f , as determined from Figures 6-8 and 6-9, with the heating rate used to record the subsequent melting endotherms after partial crystallization at $T_c = 75^\circ\text{C}$ for 1.5 min and at $T_c = 95^\circ\text{C}$ for 15 min, respectively.

Heat Rate ($^\circ\text{C}\cdot\text{min}^{-1}$)	$T_c = 75^\circ\text{C}$ for 1.5 min (cf. Figure 6-8)			$T_c = 95^\circ\text{C}$ for 15 min (cf. Figure 6-9)		
	T_{ml} ($^\circ\text{C}$)	T_{mh} ($^\circ\text{C}$)	ΔH_f ($\text{J}\cdot\text{g}^{-1}$)	T_{ml} ($^\circ\text{C}$)	T_{mh} ($^\circ\text{C}$)	ΔH_f ($\text{J}\cdot\text{g}^{-1}$)
5	113.9	126.8	30.6	123.1	130.0	8.7
10	114.0	125.5	23.0	123.1	128.8	3.1
15	114.0	124.6	14.6	123.2	-	2.2
20	114.0	123.6	10.8	123.2	-	2.3
30	114.5	123.3	6.6	123.4	-	1.6
	114.1 ± 0.2	124.7 ± 1.4		123.2 ± 0.1	129.4 ± 0.8	

5. CONCLUSIONS

Subsequent melting thermograms of sPP after isothermal crystallization at various crystallization temperatures exhibit either double- or triple-melting endotherms. For isothermal crystallization at $T_c \leq 90^\circ\text{C}$, triple-melting endotherms were observed in the DSC heating scans ($20^\circ\text{C}\cdot\text{min}^{-1}$); whereas, for isothermal crystallization at $T_c \geq 90^\circ\text{C}$, only double-endotherms were observed. For subsequent melting thermograms exhibiting triple-melting endotherms, the minor and the low-temperature melting endotherms are found to correspond to the melting of the secondary and the primary crystallites formed at corresponding crystallization temperature, respectively; while the high-temperature melting endotherm is found to represent the melting of the re-crystallized crystallites formed during a heating scan in the DSC. The formation of the re-crystallized crystallites is thought to be the re-crystallization of the crystallizable materials due to the melting of the secondary crystallites and to the partial melting of the less stable fractions of the primary crystallites formed at T_c . The observation of the high-temperature melting endotherm is found to depend strongly on the stability of the secondary and the primary crystallites formed and on the scanning rate used to observe the melting behavior.

Based on the analysis, the primary crystallites formed at T_c does not thicken during partial crystallization for various time intervals, at least within the temperature range studied. The thickening process is thought to be a kinetically controlled mechanism in nature. The secondary crystallization is found to occur at a later stage of crystallization process, most likely after the impingement of the macroscopic crystalline aggregates into one another. The formation of the secondary crystallites is thought to occur from either the inter-lamellar crystallizable amorphous materials or from the inter-fibrillar amorphous materials (or both), depending on the crystallization conditions studied. Due to the fact that the minor endotherm is always found to locate close to the

temperature where the sample was crystallized, the thickness of the secondary lamellae has to be thinner than that of the primary lamellae formed at the same temperature. The reason for the relatively thinner secondary lamellae to be stable at the same temperature where the thicker primary lamellae are formed may be attributable to the reduction in the conformational entropy.

6. REFERENCES

- [1] Natta, G.; Pasquon, I.; Corradini, P.; Peraldo, M.; Pegoraro, M.; and Zambelli, A. *Rend. Acc. Naz. Lincei*. **1960**, *28*, 539.
- [2] Natta, G.; Pasquon, I.; and Zambelli, A. *J. Am. Chem. Soc.* **1962**, *84*, 1488.
- [3] Ewen, J.A.; Johns, R.L.; Razavi, A.; and Ferrara, J.D. *J. Am. Chem. Soc.* **1988**, *110*, 6255.
- [4] Rodriguez-Arnold, J.; Bu, Z.; and Cheng, S.Z.D. *J. Macromol. Sci.-Rev. Macromol. Chem. Phys.* **1995**, *C35*, 117.
- [5] Schardl, J.; Sun, L.; Kimura, S.; and Sugimoto, R. *J. Plastic Film & Sheeting* **1996**, *12*, 157.
- [6] Sun, L.; Shamshoum, E.; and DeKunder, G. *SPE-ANTEC Proc.* **1996**, 1965.
- [7] Gownder, M. *SPE-ANTEC Proc.* **1998**, 1511.
- [8] Sura, R.K.; Desai, P.; and Abhiraman, A.S. *SPE-ANTEC Proc.* **1999**, 1764.
- [9] Supaphol, P.; Hwu, J.J.-J.; Phillips, P.J.; and Spruiell, J.E. *SPE-ANTEC Proc.* **1997**, 1759.
- [10] Supaphol, P. and Spruiell, J.E. *J. Appl. Polym. Sci.* accepted on April 16, 1999.
- [11] Alamo, R.G. and Mandelkern, L. *J. Polym. Sci., Polym. Phys.* **1986**, *24*, 2087.
- [12] Freedman, A.M.; Bassett, D.C.; Vaughan, A.S.; and Olley, R.H. *Polymer* **1986**, *27*, 1163.
- [13] Samuels, R.J. *J. Polym. Sci., Polym. Phys.* **1975**, *13*, 1417.
- [14] Alberola, N.; Fugier, M.; Petit, D.; and Fillon, B. *J. Mater. Sci.* **1995**, *30*, 1187.
- [15] Lovering, E.G. and Wooden, D.C. *J. Polym. Sci., A-2* **1969**, *7*, 1639.
- [16] Yoo, E.S. and Im, S.S. *J. Polym. Sci., Polym. Phys.* **1999**, *37*, 1357.
- [17] Liberti, F.N. and Wunderlich, B. *J. Polym. Sci., A-2* **1968**, *6*, 833.
- [18] Bell, J.P.; Slade, P.E.; and Dumbleton, J.H. *J. Polym. Sci., A-2* **1968**, *6*, 1773.
- [19] Xenopoulos, A. and Wunderlich, B. *J. Polym. Sci., Polym. Phys.* **1990**, *28*, 2271.
- [20] Lemstra, P.J.; Kooistra, T.; and Challa, G. *J. Polym. Sci., A-2* **1972**, *10*, 823.
- [21] Woo, E.M. and Wu, F.S. *Macromol. Chem. Phys.* **1998**, *199*, 2041.
- [22] Holdsworth, P.J. and Turner-Jones, A. *Polymer* **1971**, *12*, 195.
- [23] Zhou, C.-X. and Clough, S.B. *Polym. Eng. Sci.* **1988**, *28*, 65.
- [24] Woo, E.M. and Ko, T.Y. *Colloid Polym. Sci.* **1996**, *274*, 309.
- [25] Medellin-Rodriguez, F.J.; Phillips, P.J.; Lin, J.-S.; and Campos, R. *J. Polym. Sci., Polym. Phys.* **1997**, *35*, 1757.
- [26] Tan, S.; Su, A.; Li, W.; and Zhou, E. *Macromol. Rapid Commun.* **1998**, *19*, 11.
- [27] Wang, Z.-G.; Hsiao, B.S.; Sauer, B.B.; and Kampert, W.G. *Polymer* **1999**, *40*, 4615.
- [28] Stein, R.S. and Misra, A. *J. Polym. Sci., Polym. Phys.* **1980**, *18*, 327.
- [29] Blundell, D.J. *Polymer* **1987**, *28*, 2248.
- [30] Kim, H.G. and Robertson, R.E. *J. Polym. Sci., Polym. Phys.* **1998**, *36*, 1757.
- [31] Hsiao, B.S.; Wang, Z.-G.; Yeh, F.; Gao, Y.; and Sheth, K.C. *Polymer* **1999**, *40*, 3515.

- [32] Cheng, S.Z.D.; Wu, Z.-Q.; and Wunderlich, B. *Macromolecules* **1987**, *20*, 2802.
- [33] Huo, P. and Cebe, P. *Colloid Polym. Sci.* **1992**, *270*, 840.
- [34] Blundell, D.J. and Osborn, B.N. *Polymer* **1983**, *24*, 953.
- [35] Cebe, P. and Hong, S.-D. *Polymer* **1986**, *27*, 1183.
- [36] Cheng, S.Z.D.; Cao, M.Y.; and Wunderlich, B. *Macromolecules* **1986**, *19*, 1868.
- [37] Lee, Y. and Porter, R.S. *Macromolecules* **1987**, *20*, 1336.
- [38] Bassett, D.C.; Olley, R.H.; and Raheil, I.A.M. *Polymer* **1988**, *29*, 1745.
- [39] Lee, Y.; Porter, R.S.; and Lin, J.-S. *Macromolecules* **1989**, *22*, 1756.
- [40] Lattimer, M.P.; Hobbs, J.K.; Hill, M.J.; and Barham, P.J. *Polymer* **1992**, *33*, 3971.
- [41] Wang, J.; Alvarez, M.; Zhang, W.; Wu, Z.; Li, Y.; and Chu, B. *Macromolecules* **1992**, *25*, 6943.
- [42] Jonas, A. and Legras, R. *Macromolecules* **1993**, *26*, 813.
- [43] Krüger, K.-N. and Zachmann, H.G. *Macromolecules* **1993**, *26*, 5202.
- [44] Hsiao, B.S.; Gardner, K.H.; Wu, D.Q.; and Chu, B. *Polymer* **1993**, *34*, 3986.
- [45] Hsiao, B.S.; Gardner, K.H.; Wu, D.Q.; and Chu, B. *Polymer* **1993**, *34*, 3996.
- [46] Jonas, A.; Russell, T.P.; and Yoon, D. *Macromolecules* **1995**, *28*, 8491.
- [47] Verma, R.K.; Velikov, V.; Kander, R.G.; Marand, H.; Chu, B.; and Hsiao, B.S. *Polymer* **1996**, *37*, 5357.
- [48] Verma, R.K.; Marand, H.; and Hsiao, B.S. *Macromolecules* **1996**, *29*, 7767.
- [49] Verma, R.K. and Hsiao, B.S. *TRIP* **1996**, *4*, 312.
- [50] Ji, X.-L.; Zhang, W.-J.; and Wu, Z.-W. *J. Polym. Sci., Polym. Phys.* **1997**, *35*, 431.
- [51] Supaphol, P. and Spruiell, J.E. *J. Appl. Polym. Sci.* accepted on April 4, 1999.
- [52] Price, F.P. In *Nucleation*; Zettlemoyer, A.C., Ed.; Marcel Dekker: New York, 1969; Chapter 8.
- [53] Wunderlich, B. In *Macromolecular Physics*; Academic Press: New York, 1976; Vol. 2; Chapter 5.
- [54] Hoffman, J.D.; Davis, G.T.; and Lauritzen Jr., J.I. In *Treatise on Solid State Chemistry*; Hannay, N.B., Ed.; Plenum Press: New York, 1976; Vol. 3; Chapter 7.
- [55] Hoffman, J.D. and Miller, R.L. *Polymer* **1997**, *38*, 3151.
- [56] Rodriguez-Arnold, J.; Zhang, A.; Cheng, S.Z.D.; Lovinger, A.J.; Hsieh, E.T.; Chu, P.; Johnson, T.W.; Honnell, K.G.; Geerts, R.G.; Palackal, S.J.; Hawley, G.R.; and Welch, M.B. *Polymer* **1994**, *35*, 1884.
- [57] Schmidtke, J.; Strobl, G.; and Thurn-Albrecht, T. *Macromolecules* **1997**, *30*, 5804.
- [58] Hauser, G.; Schmidtke, J.; and Strobl, G. *Macromolecules* **1998**, *31*, 6250.
- [59] Corradini, P.; Natta, G.; Ganis, P.; and Temussi, P.A. *J. Polym. Sci.*, **1967**, *C16*, 2477.
- [60] Lotz, B.; Lovinger, A.J.; and Cais, R.E. *Macromolecules* **1988**, *21*, 2375.
- [61] Lovinger, A.J.; Lotz, B.; and Davis, D.D. *Polymer* **1990**, *31*, 2253.

- [62] Lovinger, A.J.; Davis, D.D.; and Lotz, B. *Macromolecules* **1991**, *24*, 552.
- [63] Lovinger, A.J.; Lotz, B.; Davis, D.D.; and Padden, F.J. *Macromolecules* **1993**, *26*, 3494.
- [64] Chatani, Y.; Maruyama, H.; Noguchi, K.; Asanuma, T.; and Shiomura, T. *J. Polym. Sci.*, **1990**, *C28*, 393.
- [65] Chatani, Y.; Maruyama, H.; Asanuma, T.; and Shiomura, T. *J. Polym. Sci., Polym. Phys.* **1991**, *29*, 1649.
- [66] De Rosa, C. and Corradini, P. *Macromolecules* **1993**, *26*, 5711.
- [67] Auriemma, F.; De Rosa, C.; and Corradini, P. *Macromolecules* **1993**, *26*, 5719.
- [68] De Rosa, C.; Auriemma, F.; and Corradini, P. *Macromolecules* **1996**, *29*, 7452.
- [69] Lovinger, A.J. and Lotz, B. *J. Polym. Sci., Polym. Phys.* **1997**, *35*, 2523.
- [70] De Rosa, C.; Auriemma, F.; and Vinti, V. *Macromolecules* **1997**, *30*, 4137.
- [71] Auriemma, F.; De Rosa, C.; Ruiz de Ballesteros, O.; Vinti, V.; and Corradini, P. *J. Polym. Sci., Polym. Phys.* **1998**, *36*, 395.
- [72] De Rosa, C.; Auriemma, F.; Vinti, V.; Grassi, A.; and Galimberti, M. *Polymer* **1998**, *39*, 6219.
- [73] De Rosa, C.; Auriemma, F.; and Vinti, V. *Macromolecules* **1998**, *31*, 7430.
- [74] De Rosa, C.; Talarico, G.; Caporaso, L.; Auriemma, F.; Galimberti, M.; and Fusco, O. *Macromolecules* **1998**, *31*, 9109.
- [75] Brown, R.G. and Eby, R.K. *J. Appl. Phys.* **1964**, *35*, 1156.
- [76] Hugel, T.; Strobl, G.; and Thomann, R. *Acta Polym.* **1999**, *50*, 214.
- [77] Marand, H. and Alizadeh, A. *ACS-PMSE Prepr.* **1999**, *81*, 238.
- [78] Vancso, G.J.; Beekmans, L.G.M.; Trifonova, D.; and Varga, J. *ACS-PMSE Prepr.* **1999**, *81*, 232.
- [79] Taguchi, K.; Miyaji, H.; Izumi, K.; Hoshino, A.; Miyamoto, Y.; and Kokawa, R. *ACS-PMSE Prepr.* **1999**, *81*, 308.
- [80] Carfagna, C.; De Rosa, C.; Guerra, G.; and Petraccone, V. *Polymer* **1984**, *25*, 1462.

PART 7:
ISOTHERMAL MELT- AND COLD-CRYSTALLIZATION KINETICS
AND SUBSEQUENT MELTING BEHAVIOR IN SYNDIOTACTIC
POLYPROPYLENE: A DIFFERENTIAL SCANNING CALORIMETRY
STUDY

1. ABSTRACT

The isothermal melt- and cold-crystallization kinetics and subsequent melting behavior of syndiotactic polypropylene (sPP) were investigated using differential scanning calorimetry (DSC). The overall crystallization kinetics was studied based on the Avrami and Malkin macrokinetic models using a non-linear multi-variable regression program. When plotted as a function of crystallization temperature, the overall crystallization rate parameters for melt-crystallization process exhibited an unmistakable double bell-shaped curve, while those for cold-crystallization process showed the typical bell-shaped curve. Comparison of the overall crystallization rate parameters obtained for both melt- and cold-crystallization processes indicate that crystallization from the glassy state proceeds at a much greater rate than from the melt state. The multiple-melting behavior observed in subsequent melting endotherms is attributed to the contributions from: 1) melting of the secondary crystallites and their re-crystallization, 2) partial melting of the less stable fraction of the primary crystallites and their re-crystallization, 3) melting of the primary crystallites, and lastly 4) re-melting of the re-crystallized crystallites formed during the heating scan. Determination of the equilibrium melting temperature according to the *linear* and *non-linear* Hoffman-Weeks extrapolative methods provides values of ca. 145°C and ca. 182°C, respectively.

2. INTRODUCTION

The syndiotactic form of polypropylene (sPP) has largely been a laboratory curiosity since it was first produced in the 1960s by Natta et al. [1,2]. It has gained more interest in terms of industrial applications since 1988 when Ewen et al. [3] reported that highly stereo-regular and regio-regular sPP can be synthesized using novel metallocene catalysis. Since then, industrial applications of sPP have been extensively explored in areas such as films [4,5], injection molding [6], and melt-spun fibers [7,8].

Other physical properties related to applications have also been investigated and reported [9,10].

Studies related to the crystallization process of semicrystalline polymers are of great importance in polymer processing, owing to the fact that the resulting physical properties are strongly dependent on the morphology formed and the extent of crystallization. It is therefore very important to understand the processing-structure-property inter-relationships of the studied materials, which in this case is sPP. Investigations related to the chain conformation, crystal structure, morphology, and phase transitions in sPP have been reported extensively in recent years. These studies up to 1994 were reviewed and discussed in a publication by Rodriguez-Arnold et al. [11]. Studies which have been carried out in the subject of isothermal crystallization of sPP include the Avrami kinetics of the crystallization process [12-14] (cf. Part 2), the kinetics of the linear growth rates [13,15,16] (cf. Part 3), and the morphology of the single crystals [17].

In this Part, the overall kinetics of crystallization under isothermal quiescent conditions from both the melt and glassy states (i.e., melt- and cold-crystallization processes) and subsequent melting behavior of sPP is thoroughly investigated using differential scanning calorimetry (DSC).

3. THEORETICAL BACKGROUND

The overall crystallization process in semi-crystalline polymers can be divided into two main processes: primary crystallization and secondary crystallization. Primary crystallization corresponds to the macroscopic development of crystallinity as a result of two consecutive microscopic mechanisms: primary nucleation and secondary nucleation (i.e., subsequent crystal growth). The formation of chain-folded lamellae leads to further growth of the lamellae through the processes of branching and splaying

(cf. Figure 4 in reference [18]). The degree of branching and splaying is mainly controlled by the degree of undercooling (i.e., the difference between the equilibrium melting temperature T_m^0 and the crystallization temperature T_c : $\Delta T = T_m^0 - T_c$). In general, branching and splaying increase with an increase in degree of undercooling. The evidence to this assertion can be seen in a series of atomic force microscopy (AFM) images of the crystal growth in iPS taken by Taguchi et al. [19], in which they showed that the degree of branching and splaying in crystalline aggregates increases with increasing degree of undercooling. This leads to the change of the crystalline aggregates from being a hexagon platelet at $T_c = 210^\circ\text{C}$ to being a dense-branched morphology (spherulitic in 2D) at $T_c = 180^\circ\text{C}$. The primary crystallization is assumed to cease when no further addition of molecular stems on a growth face can take place. This may be due to the impingement of the crystalline aggregates onto one another.

Secondary crystallization refers to any process which leads to further increase in crystallinity. Two important processes are envisaged: 1) crystal perfection and/or thickening of the primary lamellae, and 2) formation of secondary lamellae from crystallizable melt trapped between two different lamellae in the same stack (i.e., inter-lamellar crystallizable melt) or between two different stacks of lamellae (i.e., inter-fibrillar crystallizable melt). The thickening mechanism is thermodynamically driven by the reduction of the specific surfaces of the crystals (hence less free energy penalty for the formation of surfaces), but is hampered by the kinetics factors (e.g., molecular mobility). Even though it is obvious that secondary lamellae have to somehow originate from either inter-lamellar or inter-fibrillar crystallizable melt (or both) trapped within the crystalline aggregates (e.g., axialites, spherulites, etc.) [20-22] after their impingement, the mechanisms by which the formation of the secondary lamellae are formed are uncertain and are still matters of ongoing research (e.g., reference [23]).

In order to describe the macroscopic evolution of crystallinity under isothermal quiescent conditions (during the primary crystallization process), a number of mathematical models [24-33] have been proposed over the past sixty years. Even though the contributions from Kolmogoroff [24], Johnson and Mehl [25], Avrami [26-28], and Evans [29] are essentially similar, it is the work of Avrami that has received the most attention and as a result these contributions are frequently referred to as the *Avrami* equation. Based on different approaches, Tobin [30-32] and Malkin et al. [33] arrived at different mathematical models, which are also different from the Avrami model. Recently, a non-linear multi-variable regression program was used to fit the isothermal crystallization measurements from DSC to all of the models mentioned above [34] (cf. Part 5). Only the Avrami and Malkin models were found to be satisfactory in describing the experimental data and this is the reason for the use of only the Avrami and Malkin models to describe experimental data in the present Part.

If $\chi_{c,\infty}$ and $\chi_c(t)$ are the ultimate crystallinity obtained after complete crystallization at a given crystallization temperature T_c and the instantaneous crystallinity after partial crystallization for a given crystallization time t at the same crystallization temperature T_c , respectively, then the Avrami equation [24-29] governing the phase transformation during primary crystallization is given by

$$\frac{\chi_c(t)}{\chi_{c,\infty}} = \theta(t) = 1 - \exp(-k_s t^{n_s}) \in [0, 1], \quad (7-1)$$

where $\theta(t)$ is the relative crystallinity as a function of time, k_s is the Avrami crystallization rate constant, and n_s is the Avrami exponent of time. Both k_s and n_s are constants typical of a given crystalline morphology and type of nucleation for a particular crystallization condition [35]. It should be noted that, according to the original assumptions of the theory, the value of n_s should be integral, ranging from 1 to 4.

Derived based on the notion that the overall crystallization rate equals the summation of the rate at which the degree of crystallinity varies as a result of emergence of the primary nuclei and the rate of variation in the degree of crystallinity as a result of crystal growth, Malkin et al. [33] proposed a totally different form of a macrokinetic equation, which reads

$$\frac{\chi(t)}{\chi_{\infty}} = \theta(t) = 1 - \frac{C_0 + 1}{C_0 + \exp(C_1 t)} \in [0, 1], \quad (7-2)$$

where $\theta(t)$ denotes the relative crystallinity as a function of time. C_0 relates directly to the ratio of the linear crystal growth rate G to the nucleation rate I (i.e., $C_0 \propto G/I$) and C_1 relates directly to the overall crystallization rate (i.e., $C_1 = a \cdot I + b \cdot G$, where a and b are specific constants). Apparently, both C_0 and C_1 are temperature-dependent constants.

Analysis of the experimental data based on the Avrami approach is straight forward. Traditionally, the Avrami kinetics parameters, k_a and n_a , can be extracted from a least-square line fitted to the double logarithmic plot of $\ln[-\ln(1-\theta(t))]$ versus $\ln(t)$; k_a is the anti-logarithmic value of the y-intercept and n_a is the slope of the least-square line. In the case of the Malkin approach, the authors proposed a short-cut method of determining their kinetics parameters, C_0 and C_1 , from those obtained from the Avrami analysis [33]:

$$C_0 = 4^{n_a} - 4, \quad (7-3)$$

and
$$C_1 = \ln(4^{n_a} - 2) \left(\frac{k_a}{\ln(2)} \right)^{1/n_a}. \quad (7-4)$$

Instead of analyzing the experimental data using the traditional procedure mentioned in the previous paragraph, a non-linear multi-variable regression program is utilized to directly fit the experimental data to the Avrami and Malkin models [34]. The corresponding kinetics parameters indicated in each model are automatically provided by the program along with the best fit.

4. EXPERIMENTAL DETAILS

4.1. Materials

The sPP resin (i.e., sPP#1) used in this study was synthesized using metallocene catalysis and was produced commercially in pellet form by Fina Oil and Chemical Company of La Porte, Texas. Molecular characterization data shows the following molecular weight information: $M_n = 76,200$ daltons, $M_w = 165,000$ daltons, $M_z = 290,000$ daltons, and $M_w/M_n = 2.2$. In addition, the syndiotacticity measured by ^{13}C NMR shows the racemic dyad content [%*or*] to be 91.4%, the racemic triad content [%*orr*] to be 87.3%, and the racemic pentad content [%*rrrrr*] to be 77.1%. The glass transition temperature T_g was determined to be ca. -6°C [14] (cf. Part 2).

4.2. Sample Preparation and Technique

Sliced pellets were melt-pressed between a pair of Kapton films, which in turn were sandwiched between a pair of thick metal plates, in a Wabash compression molding machine preset at 190°C under a pressure of 67 kpsi. After ten minutes holding time, a film of $280\ \mu\text{m}$ thickness was taken out and allowed to cool at ambient condition down to room temperature between the two metal plates. This treatment assumes that previous thermo-mechanical history was essentially erased, and provides a standard crystalline memory condition for the experiments.

In this study, a differential scanning calorimeter (DSC-7, Perkin-Elmer) was used to follow isothermal crystallization behavior of sPP. The DSC-7 equipped with internal liquid nitrogen cooling unit reliably provided a cooling rate up to $200^\circ\text{C}\cdot\text{min}^{-1}$. Temperature calibration was performed using an indium standard ($T_m^0 = 156.6^\circ\text{C}$ and $\Delta H_f^0 = 28.5\ \text{J}\cdot\text{g}^{-1}$). The consistency of the temperature calibration was checked every other run to ensure reliability of the data obtained. To make certain that thermal lag between the polymer sample and the DSC sensors is kept to a minimum, each sample

holder was loaded with a single disc, weighed around 4.9 ± 0.3 mg, which was cut from the as-prepared film. It is noteworthy that each sample was used only once and all the runs were carried out under nitrogen atmosphere.

4.3. Methods

For isothermal crystallization from the melt state, each sample was melted in a Mettler hot-stage at a fusion temperature T_f of 190°C for 5 min to ensure complete melting [36] (Part 4). The sample was then transferred as quickly as possible to the DSC cell, the temperature of which was preset at a desired crystallization temperature T_c ranging from 10°C to 95°C . Immediately after complete crystallization at T_c , the sample was heated without prior cooling at a constant scanning rate of $20^\circ\text{C}\cdot\text{min}^{-1}$ to observe its melting behavior. In order to investigate whether or not premature crystallization occurs during sample transfer and thermal stabilization (between sample and the DSC furnace), separate experiments were done in which, instead of waiting for each sample to completely crystallize at the designated crystallization temperature T_c , heating scan was immediately performed on the sample as soon as thermal stabilization was reached. According to these experiments, melting peaks were only observed in subsequent heating scans of samples for experiments carried out at the lowest crystallization temperatures (i.e., $T_c = 10$ and 12.5°C). These findings ascertain that premature crystallization for the majority of the conditions studied (i.e., $15^\circ\text{C} \leq T_c \leq 95^\circ\text{C}$) did not occur, and the data obtained are for the strictly isothermal condition.

For isothermal crystallization from the glassy state, each sample was melted in a Mettler hot-stage at a fusion temperature T_f of 190°C for 5 min to ensure complete melting [36], before being quenched in liquid nitrogen. After submergence in liquid nitrogen for 3 min, the sample was transferred as quickly as possible to the DSC cell, the temperature of which was preset at a desired crystallization temperature T_c ranging

from 8°C to 100°C. Immediately after complete crystallization at T_c , the sample was heated without prior cooling at a constant scanning rate of 20°C·min⁻¹ to observe its melting behavior. In order to investigate whether or not premature crystallization occurs during sample transfer and thermal stabilization, similar separate experiments as described in the previous paragraph were performed. According to these experiments, melting peaks were only observed in subsequent heating scans of samples crystallized at the highest crystallization temperatures studied (i.e., $T_c = 92.5$ and 100°C). These findings indicate that premature crystallization for the majority of the conditions studied (i.e., 8°C ≤ T_c ≤ 87.5°C) did not occur, and the data obtained represent strictly isothermal crystallization from the glassy state.

5. RESULTS

5.1. Crystallization Kinetics

Figure 7-1 shows a typical DSC crystallization exotherm for isothermal crystallization from the melt state of sPP#1 at $T_c = 70^\circ\text{C}$ after complete melting at 190°C for 5 min. Crystallization is assumed to begin at point A, which is preceded by a short period in which the temperature of the sample is equilibrated to T_c . Increasing heat flow due to evolution of the enthalpy of crystallization is evident until a maximum is observed at point B. The rate of evolution of the enthalpy of crystallization depends strongly on the kinetics of the crystallization process, which is very sensitive to changes in crystallization temperature T_c . After point B, crystallization slows down significantly, and the measurement is terminated (i.e., at point C) when no noticeable change in the heat flow is further detected.

Intuitively, during crystallization of semi-crystalline polymers under isothermal conditions, it is assumed that the observed heat flow is directly proportional to the weight of the sample w , the enthalpy of crystallization ΔH_c and the instantaneous

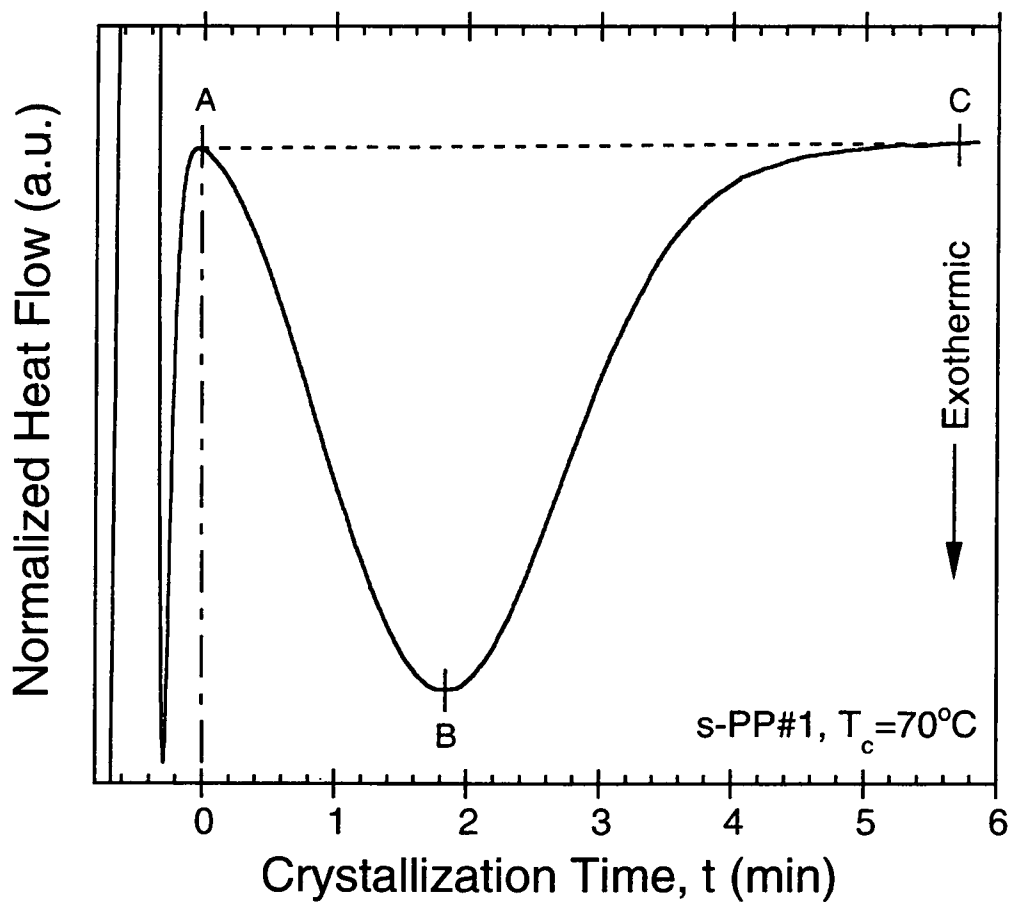


Figure 7-1. Typical crystallization exotherm data of sPP sample isothermally crystallized at $T_c = 70^\circ\text{C}$ from the melt state.

crystallization rate $\dot{\theta}(t)$. The enthalpy of crystallization is the product of the final degree of crystallinity $\chi_{c,\infty}$ and the enthalpy of crystallization of an infinitely thick crystal ΔH_c^0 (i.e., 100% crystalline sample). Consequently, one may write an equation for the heat flow as

$$\dot{Q} = c_1 \cdot w \cdot \chi_{c,\infty} \cdot \Delta H_c^0 \cdot \dot{\theta}(t), \quad (7-5)$$

where c_1 is a combined physical constant specific for each DSC used.

By setting $\dot{q} = \dot{Q}/(c_1 \cdot w \cdot \chi_{c,\infty} \cdot \Delta H_c^0)$, the relative crystallinity $\theta(t)$ can be obtained by integration of the transient normalized heat flow $\dot{q}(t)$ over the course of the crystallization. One finally gets

$$\theta(t) = \int_0^t \dot{\theta}(t') dt' = \int_0^t \dot{q}(t') dt'. \quad (7-6)$$

Figure 7-2 shows a plot of relative crystallization $\theta(t)$ as a function of crystallization time t , which was calculated from the heat flow data shown in Figure 7-1 according to Equation (7-2). An important parameter, which can be readily measured from the relative crystallinity plot similar to Figure 7-2, is the half-time of crystallization $t_{0.5}$, which is defined as the time spent from the onset of the crystallization to the point where the crystallization is 50% complete. It should be noted that the reciprocal value of the crystallization half-time (i.e., $t_{0.5}^{-1}$) is often used to characterize the overall rate of the crystallization process.

In order to obtain kinetics information specific for the Avrami and Malkin models, the experimental relative crystallization data $\theta(t)$ such as that shown in Figure 7-2 are directly fitted to each respective model using a non-linear multi-variable regression program. It is demonstrated in Figure 7-2 for the case of isothermal crystallization at $T_c = 70^\circ\text{C}$ that the experimental data shown can be described by an Avrami equation of the form (denoted in Figure 7-2 as the solid line $\theta_1(t)$):

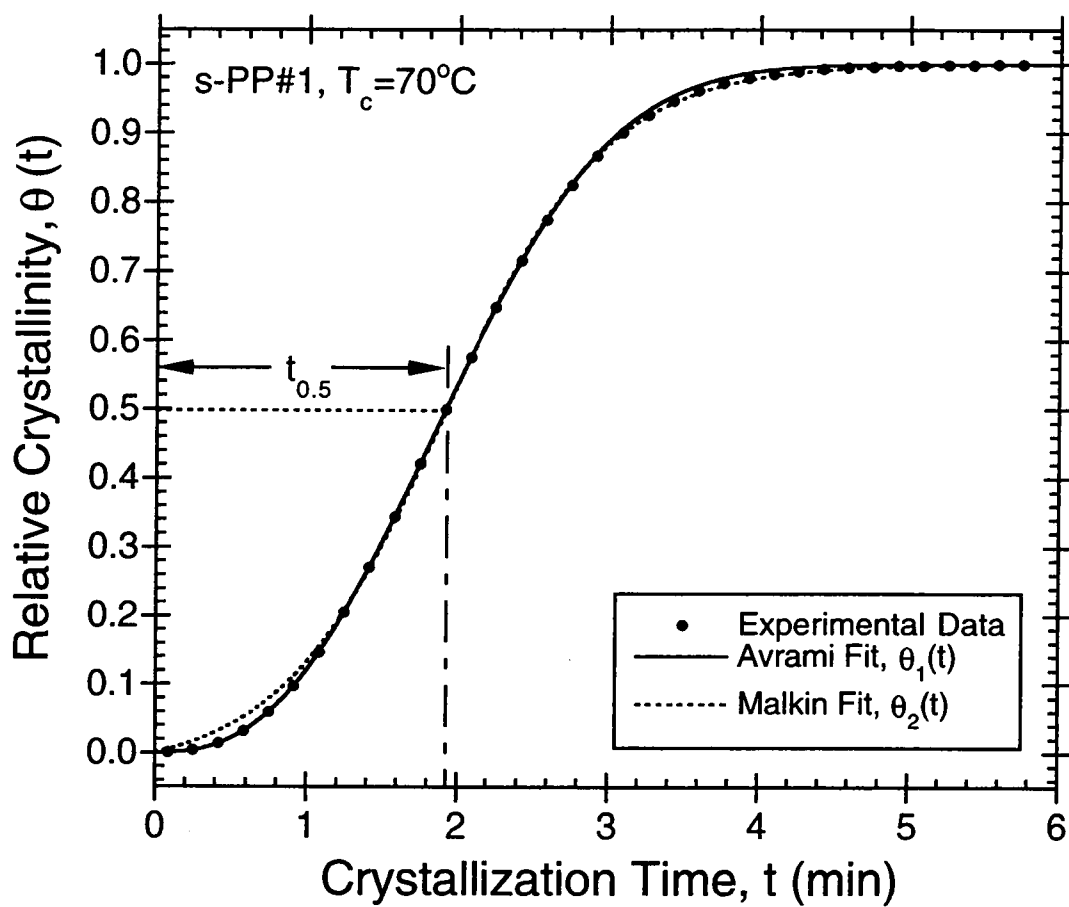


Figure 7-2. Typical relative crystallinity $\theta(t)$ as a function of crystallization time t , calculated from the raw crystallization exotherm data shown in Figure 7-1 according to Equation (7-6).

$$\theta(t) = 1 - \exp(-1.29 \times 10^{-1} \cdot t^{2.58}), \quad (7-7)$$

or it can be described by a Malkin equation of the form (denoted in Figure 7-2 as the dotted line $\theta_2(t)$):

$$\theta(t) = 1 - \frac{37.3}{36.3 + \exp(1.90 \cdot t)}; \quad (7-8)$$

which gives us the values of the corresponding kinetics parameters as the following: the Avrami exponent $n_a = 2.58$, the Avrami rate constant $k_a = 1.29 \times 10^{-1} \text{ min}^{-2.58}$, the Malkin exponent $C_0 = 36.3$, and finally the Malkin rate constant $C_1 = 1.90 \text{ min}^{-1}$. It should be noted that only the data in the range of $\theta(t) \in [0.10, 0.80]$ are used in the analysis.

By repeating the analytical procedure described above on all of the experimental data collected over a wide range of crystallization temperatures T_c , related kinetics parameters (i.e., $t_{0.5}^{-1}$, n_a , k_a , C_0 , and C_1) for describing isothermal crystallization process of sPP#1 at various crystallization temperatures are obtained. Tables 7-1 and 7-2 summarize all of the kinetics parameters considered in this study over a wide range of crystallization temperatures T_c (from 10°C to 95°C for crystallization from the melt state and from 8°C to 100°C for crystallization from the glassy state with 2.5°C increment between each data point). Discussion on the temperature dependence of the kinetics parameters summarized in Tables 7-1 and 7-2 is carried out in detail in the discussion section.

5.2. Subsequent Melting Behavior

Figures 7-3 and 7-4 present two sets of DSC melting endotherms ($20^\circ\text{C}\cdot\text{min}^{-1}$) which were recorded after complete crystallization from the melt and glassy states at different crystallization temperatures, respectively. Referring to all of the subsequent DSC melting endotherms recorded, it is evident that either two or three melting endotherms are observed. Whether two or three melting endotherms are observed depends greatly on the temperature range at which the samples were crystallized. In

Table 7-1. Summary of the overall crystallization kinetics parameters (e.g., the crystallization half-time $t_{0.5}$, the reciprocal half-time $t_{0.5}^{-1}$, the Avrami exponent n_a , the Avrami rate constant k_a , the Malkin exponent C_0 , and the Malkin rate constant C_1) for isothermal crystallization of sPP from the melt state.

T_c (°C)	$t_{0.5}$ (min)	$t_{0.5}^{-1}$ (min ⁻¹)	n_a	k_a (min ⁻ⁿ)	C_0	C_1 (min ⁻¹)
10.0	17.35	0.06	2.82	2.30×10^{-4}	55.0	0.24
12.5	12.38	0.08	4.01	2.92×10^{-5}	277.5	0.46
15.0	8.82	0.11	4.29	6.06×10^{-5}	397.3	0.68
17.5	5.29	0.19	4.04	8.10×10^{-4}	288.0	1.07
20.0	4.14	0.24	4.14	1.90×10^{-3}	327.6	1.40
22.5	3.23	0.31	3.93	6.89×10^{-3}	247.9	1.71
25.0	3.20	0.31	3.88	7.61×10^{-3}	230.4	1.70
27.5	2.61	0.38	3.25	3.07×10^{-2}	97.9	1.76
30.0	2.33	0.43	3.38	3.94×10^{-2}	117.4	2.05
32.5	2.58	0.39	3.70	2.08×10^{-2}	180.8	2.02
35.0	2.70	0.37	3.45	2.28×10^{-2}	128.4	1.81
37.5	2.92	0.34	3.17	2.32×10^{-2}	86.8	1.54
40.0	3.06	0.33	2.84	2.88×10^{-2}	54.0	1.31
42.5	2.82	0.35	2.58	4.73×10^{-2}	36.3	1.29
45.0	2.45	0.41	2.51	7.21×10^{-2}	32.6	1.44
47.5	2.24	0.45	2.56	8.89×10^{-2}	34.7	1.61
50.0	2.04	0.49	2.56	1.13×10^{-1}	35.0	1.77
52.5	1.80	0.56	2.73	1.39×10^{-1}	46.0	2.15
55.0	1.73	0.58	2.70	1.57×10^{-1}	44.0	2.21
57.5	1.67	0.60	2.67	1.77×10^{-1}	41.8	2.26
60.0	1.66	0.60	2.69	1.76×10^{-1}	43.0	2.28
62.5	1.67	0.60	2.70	1.73×10^{-1}	43.9	2.28
65.0	1.72	0.58	2.53	1.76×10^{-1}	33.4	2.07
67.5	1.80	0.56	2.54	1.56×10^{-1}	34.0	1.99
70.0	1.92	0.52	2.58	1.29×10^{-1}	36.3	1.90
72.5	2.10	0.48	2.62	9.89×10^{-2}	38.1	1.75
75.0	2.36	0.42	2.68	6.90×10^{-2}	42.1	1.60
77.5	2.91	0.34	2.96	2.91×10^{-2}	64.5	1.44
80.0	3.50	0.29	3.08	1.46×10^{-2}	76.2	1.24
82.5	4.79	0.21	3.22	4.43×10^{-3}	92.8	0.66
85.0	5.66	0.18	3.00	3.82×10^{-3}	67.8	0.75
87.5	7.51	0.13	2.95	1.81×10^{-3}	63.5	0.56
90.0	10.52	0.10	2.73	1.12×10^{-3}	46.4	0.37
92.5	19.12	0.05	2.46	4.76×10^{-4}	29.7	0.18
95.0	28.24	0.04	2.45	1.96×10^{-4}	29.4	0.12

Table 7-2. Summary of the overall crystallization kinetics parameters (e.g., the crystallization half-time $t_{0.5}$, the reciprocal half-time $t_{0.5}^{-1}$, the Avrami exponent n_a , the Avrami rate constant k_a , the Malkin exponent C_0 , and the Malkin rate constant C_1) for isothermal crystallization of sPP from the glassy state.

T_c (°C)	$t_{0.5}$ (min)	$t_{0.5}^{-1}$ (min ⁻¹)	n_a	k_a (min ⁻ⁿ)	C_0	C_1 (min ⁻¹)
8.0	18.53	0.05	3.50	2.52×10^{-5}	138.6	0.27
10.0	14.13	0.07	4.55	1.35×10^{-5}	695.4	0.45
12.5	8.28	0.12	4.05	1.95×10^{-4}	315.6	0.69
15.0	6.19	0.16	3.93	8.31×10^{-4}	288.6	0.89
17.5	4.20	0.24	3.99	2.26×10^{-3}	268.2	1.33
20.0	2.60	0.38	2.65	5.38×10^{-2}	40.1	1.42
22.5	2.69	0.37	3.77	1.65×10^{-2}	199.9	1.97
25.0	1.96	0.51	3.79	5.27×10^{-2}	206.7	2.71
27.5	1.42	0.71	3.36	2.12×10^{-1}	113.6	3.34
30.0	0.98	1.02	3.11	7.23×10^{-1}	79.8	4.46
32.5	0.51	1.97	1.88	2.38	10.0	4.76
35.0	0.59	1.69	2.97	3.26	65.3	7.08
37.5	0.52	1.91	3.05	4.83	72.5	8.15
40.0	0.41	2.44	2.72	7.71	44.7	9.31
42.5	0.31	3.25	1.86	6.07	9.8	7.86
45.0	0.35	2.85	2.46	8.65	29.1	9.56
47.5	0.27	3.77	2.33	1.51×10^1	24.2	12.25
50.0	0.28	3.63	2.42	1.52×10^1	27.7	12.07
52.5	0.26	3.84	2.45	1.82×10^1	29.1	12.99
55.0	0.30	3.33	2.83	2.02×10^1	51.9	13.14
57.5	0.29	3.44	2.76	2.03×10^1	47.3	13.25
60.0	0.28	3.62	2.69	2.15×10^1	42.4	13.55
65.0	0.27	3.69	2.41	1.59×10^1	27.4	12.36
67.5	0.30	3.34	2.57	1.49×10^1	35.0	11.90
70.0	0.38	2.63	2.34	6.40	23.6	8.36
72.5	0.45	2.21	2.49	4.73	30.6	7.51
75.0	0.36	2.77	1.85	4.48	9.6	6.67
77.5	0.55	1.83	2.41	2.92	27.3	6.10
80.0	0.65	1.54	2.28	1.80	21.8	4.79
82.5	0.90	1.11	2.50	8.65×10^{-1}	31.2	3.82
85.0	1.21	0.82	2.34	4.27×10^{-1}	24.0	2.64
87.5	1.74	0.58	2.63	1.56×10^{-1}	38.4	2.09
92.5	2.32	0.43	2.48	8.53×10^{-2}	30.3	1.49
95.0	2.96	0.34	2.41	5.05×10^{-2}	27.2	1.13
97.5	4.35	0.23	2.49	1.75×10^{-2}	31.3	0.80
100.0	5.59	0.18	2.53	8.82×10^{-3}	33.7	0.64

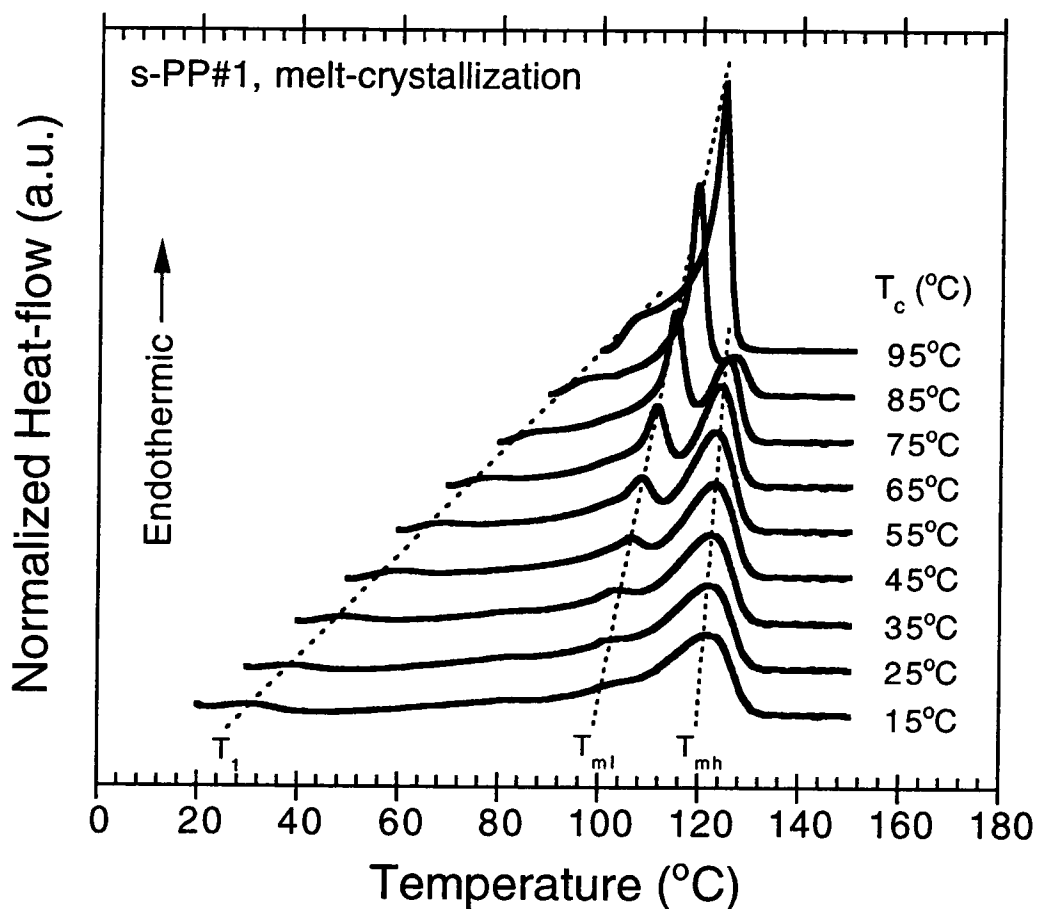


Figure 7-3. Subsequent melting endotherms ($20^\circ\text{C}\cdot\text{min}^{-1}$) of sPP samples after isothermal crystallization from the melt state at the specified temperatures. Terminologies: T_1 = the minor peak temperature; T_{ml} = the low-melting peak temperature; T_{mh} = the high-melting peak temperature.

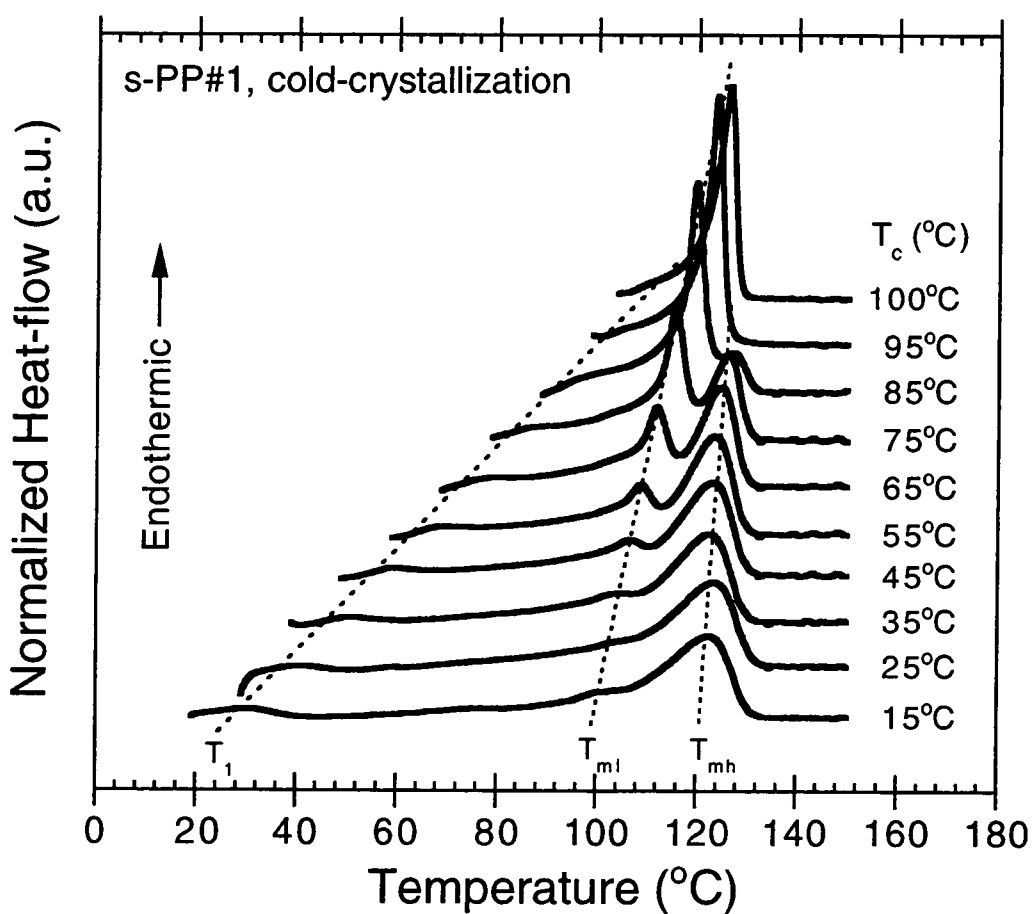


Figure 7-4. Subsequent melting endotherms ($20^\circ\text{C}\cdot\text{min}^{-1}$) of sPP samples after isothermal crystallization from the glassy state at the specified temperatures. Terminologies: T_1 = the minor peak temperature; T_{ml} = the low-melting peak temperature; T_{mh} = the high-melting peak temperature.

this particular sPP resin, three temperature regions for the observation of multiple-melting behavior are envisaged: 1) at low crystallization temperature region (i.e., $T_c < 40^\circ\text{C}$ for both crystallization from the melt and glassy states), only the minor endotherm (located close to the corresponding crystallization temperature) and the high-temperature melting endotherm are observed, 2) at intermediate crystallization temperature region (i.e., $40^\circ\text{C} \leq T_c \leq 85^\circ\text{C}$ for both crystallization from the melt and glassy states), all of the three endotherms (i.e., the minor endotherm, the low-temperature melting endotherm, and the high-temperature melting endotherm) are present, and 3) at high crystallization temperature region (i.e., $T_c > 85^\circ\text{C}$ for both crystallization from the melt and glassy states), only the minor endotherm and the low-temperature melting endotherm are evident.

According to the above experimental observations, melting behavior of sPP is characterized by the presence of three major endothermic peaks; they are 1) the minor endotherm (located close to the corresponding crystallization temperature T_c), 2) the low-temperature melting endotherm, and 3) the high-temperature melting endotherm. Tables 7-3 and 7-4 summarize the peak values of these endotherms (i.e., the minor peak temperature T_1 , the low-melting peak temperature T_{ml} , and the high-melting peak temperature T_{mh} , respectively) of the subsequent DSC melting endotherms after complete crystallization at different crystallization temperatures from the melt and glassy states. The values of the enthalpy of fusion ΔH_f associated with these melting endotherms, and the enthalpy of crystallization ΔH_c associated with crystallization exotherms are also reported in Tables 7-3 and 7-4 for the sake of completeness. Figure 7-5 illustrates plots of the minor peak temperature T_1 , the low-melting peak temperature T_{ml} , the high-melting peak temperature T_{mh} as a function of the crystallization temperature T_c for both crystallization from the melt (shown in Figure 7-5 as various filled geometrical points) and glassy states (shown in Figure 7-5 as various un-filled geometrical points).

Table 7-3. Summary of the minor peak temperature T_1 , the low-melting peak temperature T_{ml} , the high-melting peak temperature T_{mh} , enthalpy of crystallization ΔH_c , and enthalpy of fusion ΔH_f for isothermal crystallization of sPP from the melt state.

T_c (°C)	T_1 (°C)	T_{ml} (°C)	T_{mh} (°C)	ΔH_c (J·g ⁻¹)	ΔH_f (J·g ⁻¹)
10.0	24.9	-	122.3	-27.5	30.0
12.5	29.7	-	122.4	-24.4	29.5
15.0	29.6	-	122.1	-29.3	30.5
17.5	30.7	-	122.3	-24.1	30.2
20.0	33.3	-	122.5	-24.3	29.8
22.5	35.9	-	122.4	-24.1	29.9
25.0	38.9	-	122.4	-23.1	30.6
27.5	41.7	-	122.4	-23.6	31.0
30.0	44.3	-	123.4	-32.6	39.4
32.5	46.8	-	123.5	-33.1	39.6
35.0	50.1	-	123.6	-33.8	39.9
37.5	52.7	-	123.5	-33.5	40.6
40.0	54.9	106.8	123.6	-33.8	40.3
42.5	58.4	106.8	123.7	-33.8	40.1
45.0	59.5	107.3	123.8	-32.9	41.0
47.5	62.4	107.7	123.9	-33.2	39.6
50.0	67.2	108.2	123.7	-33.8	39.4
52.5	67.1	108.3	123.6	-26.2	30.5
55.0	69.1	108.9	123.7	-26.4	33.5
57.5	70.8	109.7	123.9	-26.8	35.5
60.0	73.4	110.3	124.1	-27.3	33.6
62.5	76.4	111.0	124.4	-27.9	34.4
65.0	79.2	112.0	124.9	-28.0	35.9
67.5	81.8	112.8	125.2	-28.7	36.0
70.0	84.3	113.7	125.5	-29.3	36.5
72.5	87.6	114.6	125.8	-30.1	36.3
75.0	90.2	115.5	126.2	-30.7	35.7
77.5	92.4	116.2	126.1	-31.5	35.7
80.0	95.9	117.2	126.4	-31.9	35.9
82.5	97.0	118.2	126.9	-32.1	36.3
85.0	99.3	119.4	127.1	-33.4	37.4
87.5	102.6	121.0	-	-34.5	37.6
90.0	105.2	122.2	-	-35.2	38.0
92.5	107.4	123.6	-	-35.5	39.2
95.0	110.9	125.0	-	-36.1	39.8

Table 7-4. Summary of the minor peak temperature T_1 , the low-melting peak temperature T_{ml} , the high-melting peak temperature T_{mh} , enthalpy of crystallization ΔH_c , and enthalpy of fusion ΔH_f for isothermal crystallization of sPP from the glassy state.

T_c (°C)	T_1 (°C)	T_{ml} (°C)	T_{mh} (°C)	ΔH_c (J·g ⁻¹)	ΔH_f (J·g ⁻¹)
8.0	24.9	-	122.3	-26.2	38.6
10.0	26.4	-	122.3	-21.6	33.7
12.5	28.3	-	121.8	-22.2	31.6
15.0	30.3	-	122.6	-22.9	33.6
17.5	32.9	-	122.4	-24.3	34.3
20.0	35.8	-	122.4	-28.4	35.2
22.5	37.7	-	122.2	-28.6	37.4
25.0	41.1	-	123.5	-27.0	32.3
27.5	43.0	-	123.3	-30.0	33.1
30.0	45.6	-	122.9	-29.9	32.3
32.5	48.9	-	122.5	-26.1	33.9
35.0	50.5	-	122.5	-28.1	33.8
37.5	53.4	-	123.0	-29.5	32.3
40.0	55.8	105.8	123.2	-31.1	36.3
42.5	57.9	106.1	123.4	-32.2	37.2
45.0	58.5	106.7	123.3	-33.8	34.8
47.5	62.7	107.3	123.5	-27.9	36.7
50.0	65.8	107.9	123.5	-33.3	34.0
52.5	67.8	108.6	123.7	-32.8	32.8
55.0	70.4	108.8	123.5	-32.6	34.3
57.5	73.3	109.5	123.6	-32.4	34.3
60.0	75.2	110.3	123.9	-31.2	36.0
65.0	80.5	112.0	124.8	-29.4	34.6
67.5	83.1	112.6	124.9	-30.8	35.4
70.0	86.4	113.5	125.2	-33.3	38.8
72.5	88.0	114.5	125.6	-31.6	35.1
75.0	90.9	115.6	126.1	-29.0	35.3
77.5	93.3	116.7	126.7	-29.2	34.1
80.0	95.4	117.8	127.2	-30.0	34.7
82.5	96.0	118.5	127.1	-30.6	34.0
85.0	100.2	119.7	127.3	-32.5	34.2
87.5	103.6	120.5	-	-33.5	33.9
92.5	108.1	122.7	-	-32.1	35.5
95.0	111.4	123.7	-	-33.2	34.8
97.5	113.0	124.9	-	-34.4	36.3
100.0	115.9	126.3	-	-34.8	37.2

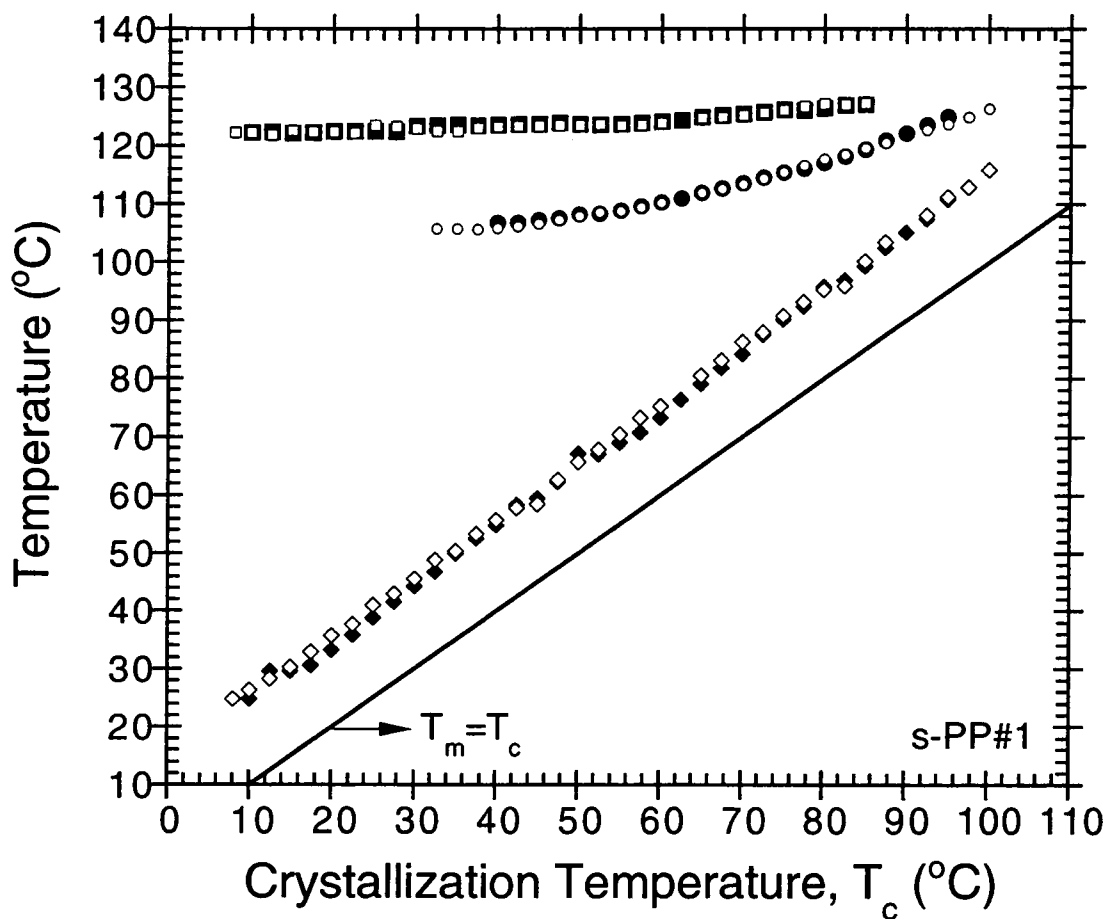


Figure 7-5. Variation of the minor peak temperature T_l , the low-melting peak temperature T_{mv} and the high-melting peak temperature T_{mh} , as determined from the subsequent melting endotherms after complete crystallization from both the melt and glassy states, with the crystallization temperature T_c . Keys: (\blacklozenge), (\bullet), and (\blacksquare) represent T_l , T_{mv} , T_{mh} values for crystallization from the melt states; (\diamond), (\circ), and (\square) represent T_l , T_{mv} , T_{mh} values for crystallization from the glassy states.

According to Figure 7-5, it is apparent that the minor peak temperature T_1 for both crystallization from the melt and glassy states increases steadily with an increase in crystallization temperature. Interesting, the difference between the values of the minor peak temperature T_1 and the corresponding crystallization temperature T_c is found to be nearly constant (i.e., $T_1 - T_c = 14.7 \pm 1.0^\circ\text{C}$ for melt-crystallization data; and $T_1 - T_c = 15.6 \pm 0.6^\circ\text{C}$ for cold-crystallization data). These findings are in parallel to previous finding on sPP#4 resin [37] (cf. Figure 6-3 in Part 6), in which $T_1 - T_c = 11.8 \pm 0.4^\circ\text{C}$ for melt-crystallization data. This confirms that melting always starts at a temperature close to the respective crystallization temperature. It is also apparent, according to Figure 7-5, that the low-melting peak temperature T_{m1} and the high-melting peak temperature T_{m2} illustrate finite dependence on the crystallization temperature T_c in an increasing manner, with the T_{m1} values being more dependent on T_c than the T_{m2} values are. It should be pointed out that the relation between T_{m1} and T_c exhibits slight curvature.

According to Part 6 (cf. reference [37]), the minor endotherm represents the melting of the secondary crystallites formed at T_c . The low-temperature melting endotherm corresponds to the melting of the primary crystallites formed at T_c , while the high-temperature melting endotherm is attributed to the melting of the crystallites re-crystallized during a heating scan. Thus, the multiple-melting (triple-melting) behavior of sPP observed in subsequent melting endotherms in DSC can be best described as the contributions from: 1) melting of the secondary crystallites and their re-crystallization, 2) partial melting of the less stable fraction of the primary crystallites and their re-crystallization, 3) melting of the remaining fractions of the primary crystallites, and lastly 4) re-melting of the re-crystallized crystallites formed during the heating scan. It is important to note that the mechanisms and extent of the re-crystallization process

during a heating scan depends greatly on the stability of the primary and secondary crystallites formed at T_c , and on the heating rate used.

From the values of the peak temperatures summarized in Tables 7-3 and 7-4, it is interesting to note that even though the overall kinetics of the melt- and cold-crystallization processes is totally different (cf. Tables 7-1 and 7-2), the peak temperatures of the low-temperature and high-temperature melting endotherms appear to be very comparable. This indicates that the lamellae formed at T_c either from the melt or glassy state should be of similar thickness, regardless of the difference in the nucleation mechanisms involved (cf. later). In other words, the lamellar thickness of the primary crystals appears to be mainly controlled by the crystallization temperature T_c (or to be exact, the degree of undercooling ΔT).

6. DISCUSSION

6.1. Temperature Dependence of Overall Crystallization Kinetics Parameters

The most fundamental representation of the overall crystallization kinetics data is to plot the reciprocal value of the crystallization half-time (i.e., $t_{0.5}^{-1}$) as a function of the crystallization temperature T_c (cf. Figure 7-6). If the crystallization half-time data can be collected with minimal degree of error over the whole temperature range (i.e., $T_g < T_c < T_m^0$), it is expected according to the secondary nucleation theory of Lauritzen and Hoffman (i.e., LH theory) [38,39], that the temperature dependence of the reciprocal half-time data (i.e., the plot of $t_{0.5}^{-1}$ versus T_c) should exhibit the typical bell-shaped curve, which can be described as a result of the nucleation control effect at low degrees of undercooling (i.e., high crystallization temperatures) and diffusion control effect at high degrees of undercooling (i.e., low crystallization temperatures).

According to Figure 7-6, the plot of $t_{0.5}^{-1}$ versus T_c for $t_{0.5}$ data obtained from isothermal crystallization from the melt state (shown in Figure 6 as filled circles for data

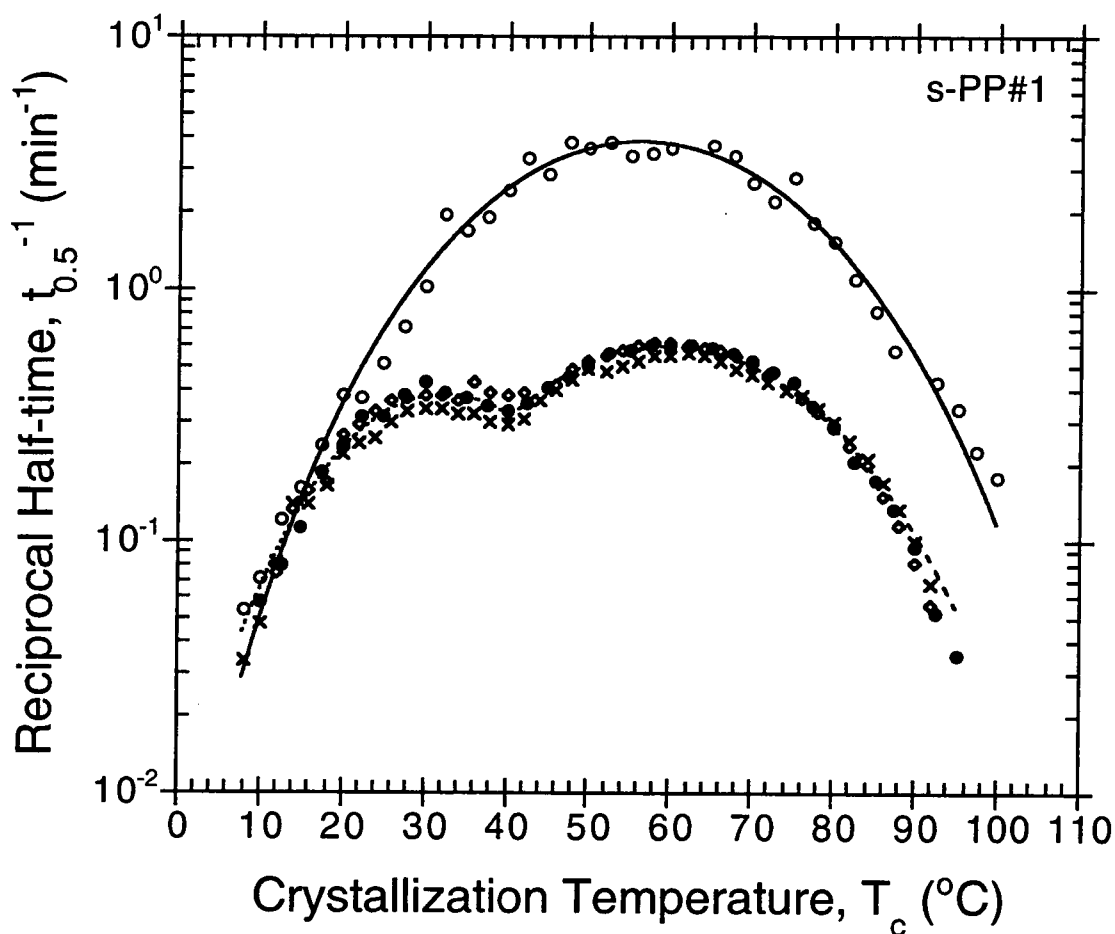


Figure 7-6. Variation of the reciprocal half-time $t_{0.5}^{-1}$ as a function of crystallization temperature T_c : (\diamond) melt-crystallization data taken from reference [40], (\times) melt-crystallization data taken from reference [13], (\bullet) melt-crystallization data measured in this study, and (\circ) cold-crystallization data measured in this study. Different lines represent the best fits of the experimental data.

summarized in Table 7-1) exhibit a *double* bell-shaped curve, while the similar plot for $t_{0.5}$ data obtained from isothermal crystallization from the glassy state (shown in Figure 7-6 as open circles for data summarized in Table 7-2) exhibit the typical bell-shaped curve. In the case of isothermal crystallization from the melt state, the plots of $t_{0.5}^{-1}$ versus T_c for two other different data sets obtained from separate measurements (shown in Figure 7-6 as opened diamonds for data taken from reference [40] and as crosses for data taken from reference [13]) are also included. Interestingly, all of the data sets exhibit a distinct discontinuity in the plot of $t_{0.5}^{-1}$ versus T_c (i.e., at $T_c = \text{ca. } 40^\circ\text{C}$), which clearly separate the plot of $t_{0.5}^{-1}$ versus T_c into two bell-shaped curves. Since it has already been proven that premature crystallization did not occur during sample transfer and thermal stabilization, the fact that excellent agreement is evident in the three data sets indicate that the observation of the double bell-shaped curve is definitely not an artefact, and, to the best of my knowledge, this is the first time that a double bell-shaped curve is observed in a plot of the overall crystallization rate as a function of crystallization temperature T_c .

According to the classical theories of the primary homogeneous nucleation rate I [41,42] and that of the secondary nucleation rate G (i.e., subsequent crystal growth rate) [38,39], the temperature dependence of I and G can be described by exponential equations of the form:

$$I = I_0 \exp\left[-\frac{U^*}{R(T_c - T_\infty)}\right] \exp\left[-\frac{K^I}{T_c(\Delta T)^2 f^2}\right], \quad (7-9)$$

and

$$G = G_0 \exp\left[-\frac{U^*}{R(T_c - T_\infty)}\right] \exp\left[-\frac{K^G}{T_c(\Delta T)f}\right], \quad (7-10)$$

where I_0 and G_0 are pre-exponential terms not strongly dependent on temperature, U^* is the activation energy for molecular segmental transport across the melt/solid interfacial boundary and is commonly given by a universal value of $1,500 \text{ kcal}\cdot\text{mol}^{-1}$ [38], R is the

universal gas constant, T_{∞} is the temperature where the molecular long-range motion ceases and is often taken to be ca. 30 K below the glass transition temperature (i.e., $T_{\infty} = T_g - 30$ K [38]), K^I and K^G are combined factors related to primary homogeneous nucleation and subsequent crystal growth mechanisms, respectively, and f is a factor used to correct for the temperature dependence of the enthalpy of fusion (i.e., $f = 2T_c/(T_m^0 + T_c)$ [38]).

Referring to Equations (7-9) and (7-10), the first exponential term, i.e., $\exp(-U^*/R(T_c - T_{\infty}))$, corresponds to the diffusion of polymer molecules or segments of them from the equilibrium melt onto the growth face. The second exponential term, i.e., $\exp(-K^I/T_c(\Delta T)^2 f)$ in Equation (7-9) or $\exp(-K^G/T_c(\Delta T)f)$ in Equation (7-10), relates to the formation of the critical primary homogeneous and secondary nuclei, respectively. Owing to the competing contributions of the transport and nucleation terms, one expects that there should be a maximum in both of the primary homogeneous and crystal growth rate data at a temperature somewhere between the glass transition temperature T_g and the equilibrium melting temperature T_m^0 , when plotted as a function of the crystallization temperature T_c . Indeed, maxima in the primary homogeneous and crystal growth rate data as a function of crystallization temperature are experimentally observed [43,44], with the maximum in the primary homogeneous nucleation rate data is found at a lower temperature than that of the crystal growth rate data (cf. Figure 1 in reference [44]).

The finding by Okui [44] leads us to believe that the observation of two maxima in the plot of $t_{0.5}^{-1}$ versus T_c for $t_{0.5}$ data obtained from isothermal crystallization from the melt state is a result of the contributions from the maximum in the crystal growth rate at $T_{c,max} = \text{ca. } 60^\circ\text{C}$ and from the maximum in the primary homogeneous nucleation rate at $T_{c,max} = \text{ca. } 30^\circ\text{C}$ with a discontinuity being observed at $T_{c,break} = \text{ca. } 40^\circ\text{C}$. In contrast to the case of crystallization from the melt state, the plot of $t_{0.5}^{-1}$ versus T_c for $t_{0.5}$ data obtained from isothermal crystallization from the glassy state exhibits only one

maximum at $T_{c,max} = \text{ca. } 58^\circ\text{C}$. At this point, it is postulated that, for the crystallization from the melt state, crystallization process is dominated by heterogeneous nucleation mechanisms until the crystallization temperature drops as low as $T_c = \text{ca. } 60^\circ\text{C}$, at which point the contribution from the primary homogeneous nucleation mechanisms start taking effect and increasingly dominates with further decrease in T_c (or further increase in the degree of undercooling ΔT).

Comparison of the overall crystallization rates measured from crystallization from the melt and glassy states (cf. Tables 7-1 and 7-2 and Figure 7-6) indicates that crystallization from the glassy state is much faster than that from the melt state. Since it is expected, based on the LH theory [38,39], that the crystal growth rate is only a function of crystallization temperature T_c , the fact that crystallization from the glassy state is much faster than that from the melt state must be attributable to the much higher contribution from the nucleation mechanisms (i.e., either as an increase in nucleation rate or nucleation density). In other words, the quenching process tremendously increases the total number of activated nuclei and, upon crystallization at T_c , these activated nuclei can act as predetermined homogeneous nuclei (i.e., athermal nucleation mechanism) which greatly enhance the overall crystallization rate [45].

Let us now consider the temperature dependence of other kinetics parameters determined based on the Avrami and Malkin models (cf. Equations 7-1 and 7-2). Figures 7-7 and 7-8 illustrate plots of the Avrami and Malkin exponents for crystallization from the melt and glassy states as a function of crystallization temperature T_c (cf. Tables 7-1 and 7-2). For crystallization from the melt state, both the Avrami and Malkin exponents exhibit a similar temperature dependence. Clearly, the temperature dependence of these parameters can be divided into two regions: 1) low temperature region (i.e., $10^\circ\text{C} \leq T_c \leq 40^\circ\text{C}$), and 2) high temperature region (i.e., $40^\circ\text{C} \leq T_c \leq 95^\circ\text{C}$). In the high temperature region, values of both the Avrami and Malkin

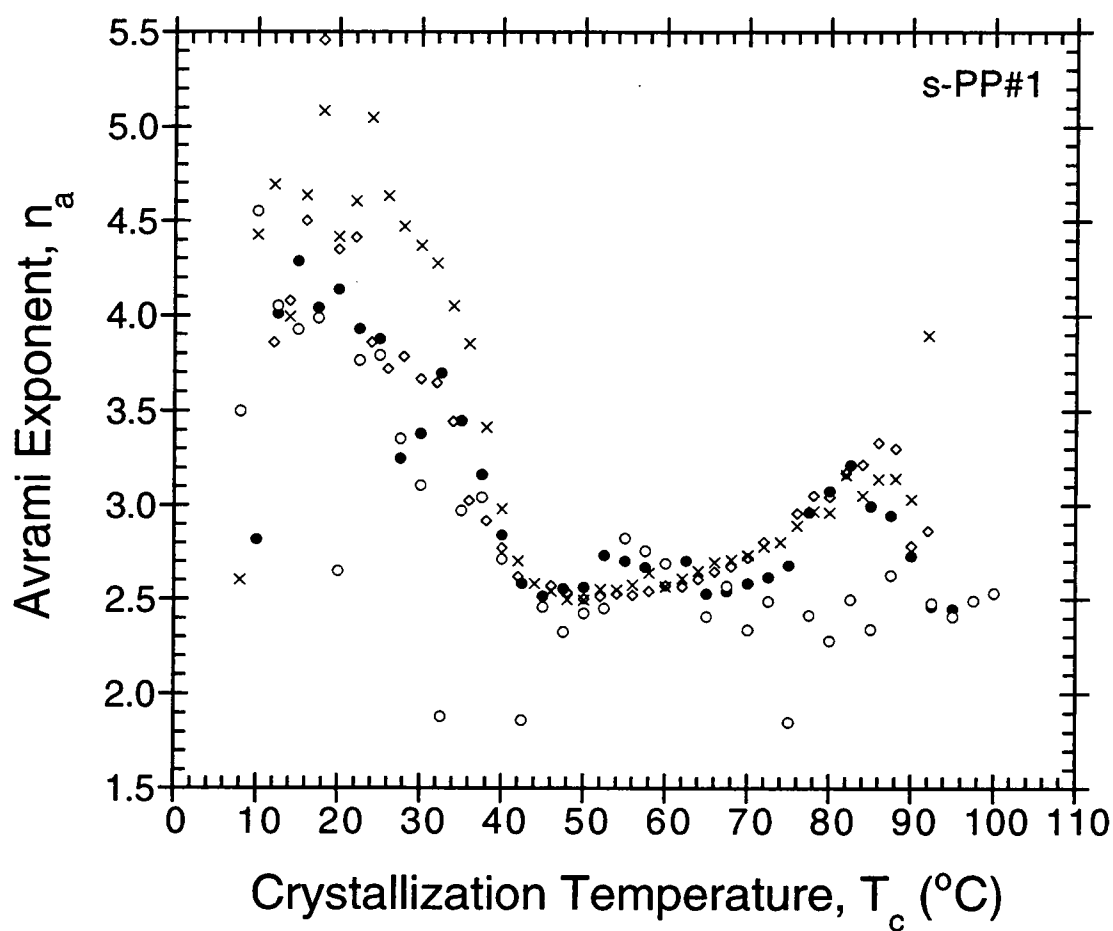


Figure 7-7. Variation of the Avrami exponent n_a as a function of crystallization temperature T_c : (\diamond) melt-crystallization data taken from reference [40], (\times) melt-crystallization data taken from reference [13], (\bullet) melt-crystallization data measured in this study, and (\circ) cold-crystallization data measured in this study.

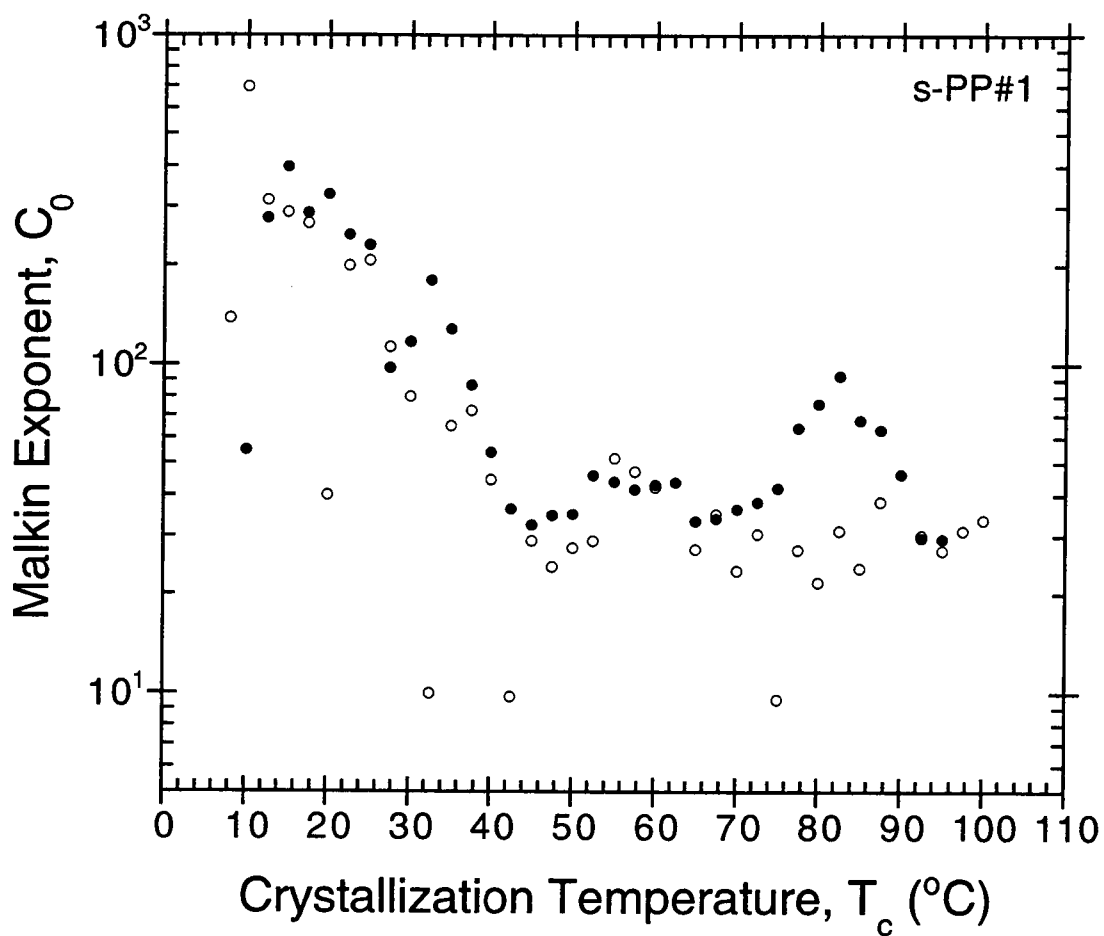


Figure 7-8. Variation of the Malkin exponent C_0 as a function of crystallization temperature T_c : (●) melt-crystallization data measured in this study, and (○) cold-crystallization data measured in this study.

exponents increase with increasing crystallization temperature, with a maximum being observed at $T_c = \text{ca. } 87.5^\circ\text{C}$. In the low temperature region, values of both the Avrami and Malkin exponents increase monotonically with decreasing crystallization temperature. Interestingly, the temperature dependence of the Avrami and Malkin exponents for crystallization from the glassy state appears to be similar to what is observed for the case of crystallization from the melt state. A slight difference can be seen in the high temperature region where both of the Avrami and Malkin exponents appear to be unaffected by changes in the crystallization temperature T_c . The majority of the exponents found for crystallization from the glassy state observed in this range appears to be smaller than those found for crystallization from the melt state (especially, within the T_c range of ca. 60°C to ca. 90°C). According to the classical definition of the Avrami exponent [35], the nucleation mechanisms in crystallization from the glassy state are more instantaneous in time than those in crystallization from the melt state.

Figures 7-9 and 7-10 show plots of the Avrami and Malkin rate constants (i.e., k_a and C_1 , respectively) for crystallization from the melt and glassy states as a function of crystallization temperature T_c . In general, the temperature dependence of these parameters is in accordance with the experimental observation made earlier on the reciprocal values of the crystallization half-time (i.e., $t_{0.5}^{-1}$). This is not surprising, however, since both of the Avrami and Malkin rate constants relate directly to the values of the reciprocal half-time $t_{0.5}^{-1}$ data according to the following equations:

$$k_{a,\text{calc}} = \ln 2 \cdot (t_{0.5}^{-1})^n, \quad (7-11)$$

and
$$C_{1,\text{calc}} = \ln(4^n - 2) \cdot (t_{0.5}^{-1}). \quad (7-12)$$

The Avrami and Malkin rate constants were also calculated according to Equations (7-11) and (7-12) and have found that the difference between the experimental values (cf. Tables 7-1 and 7-2) and the calculated values is lower than 3% on average.

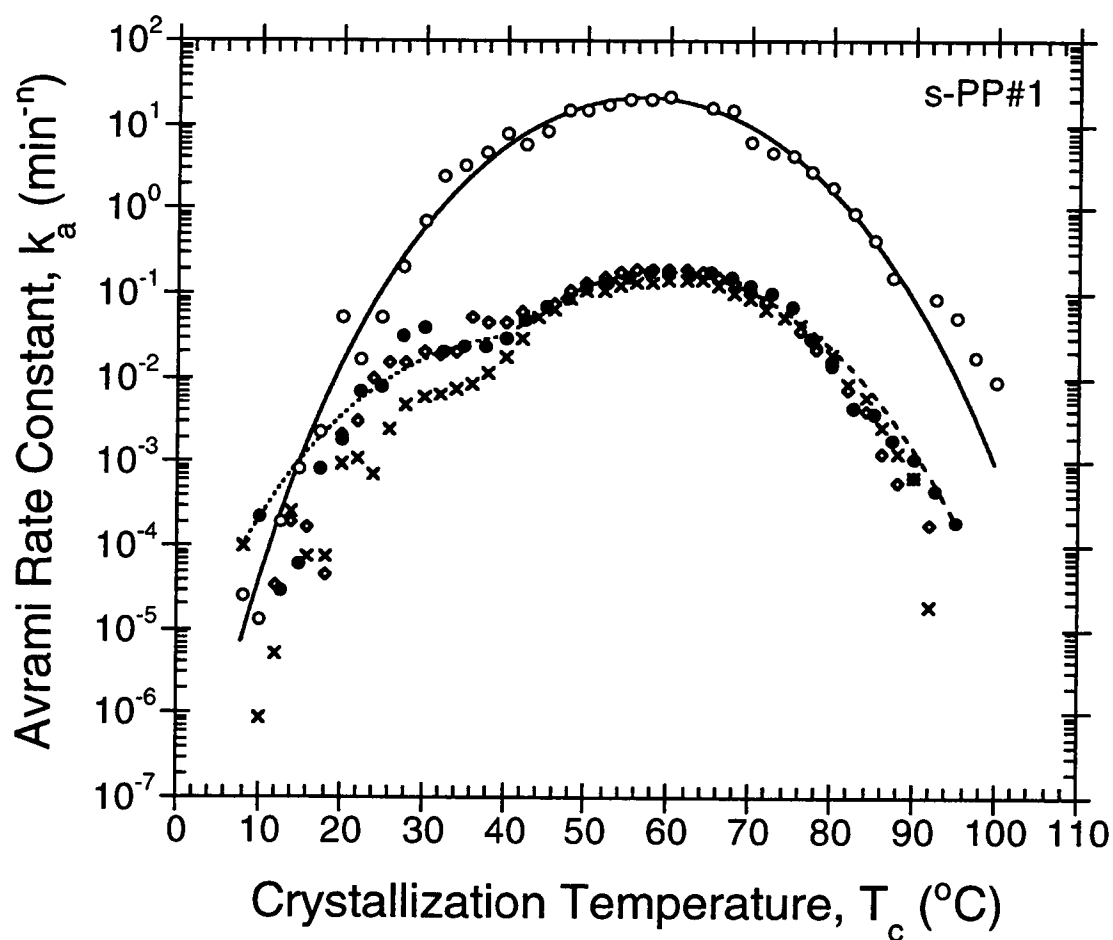


Figure 7-9. Variation of the Avrami rate constant k_a as a function of crystallization temperature T_c : (\diamond) melt-crystallization data taken from reference [40], (\times) melt-crystallization data taken from reference [13], (\bullet) melt-crystallization data measured in this study, and (\circ) cold-crystallization data measured in this study. Different lines represent the best fits of the experimental data.

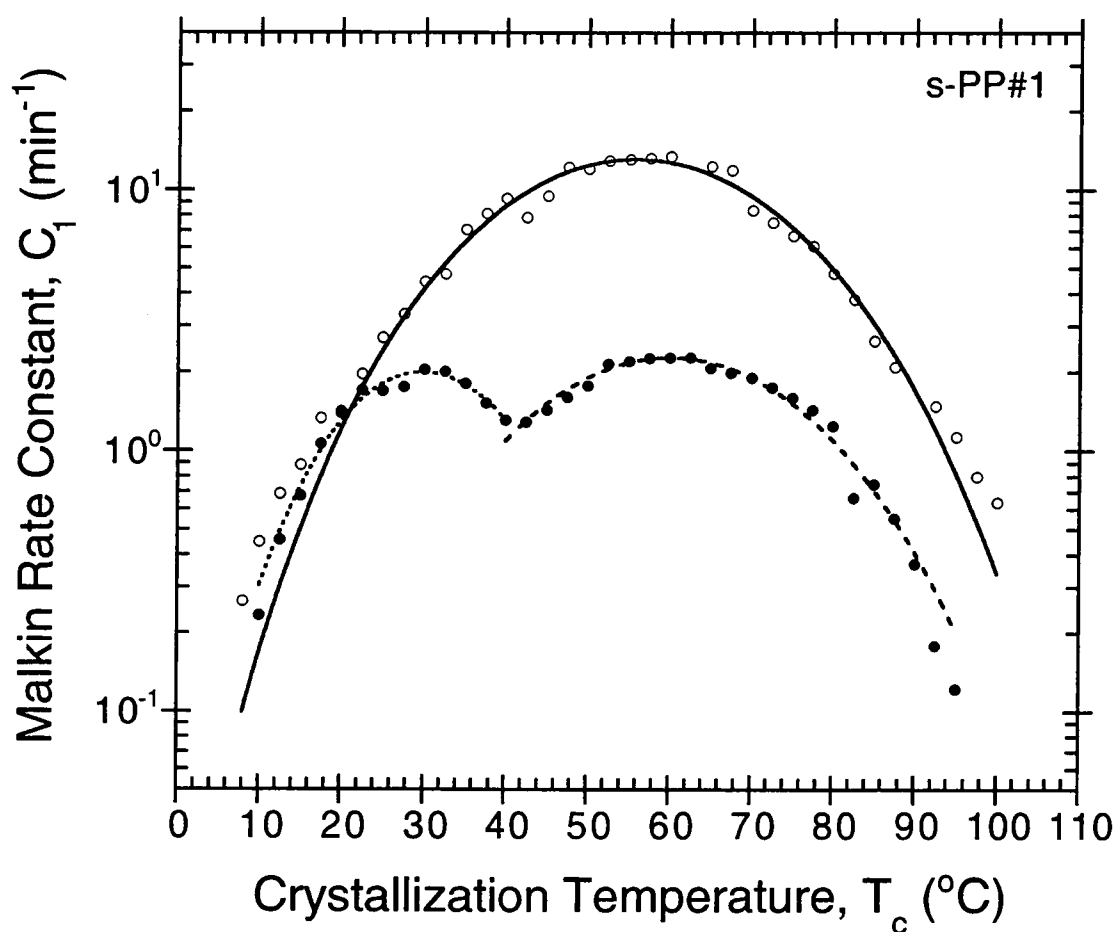


Figure 7-10. Variation of the Malkin rate constant C_1 as a function of crystallization temperature T_c : (\diamond) melt-crystallization data taken from reference [40], (\times) melt-crystallization data taken from reference [13], (\bullet) melt-crystallization data measured in this study, and (\circ) cold-crystallization data measured in this study. Different lines represent the best fits of the experimental data.

Since the overall crystallization rate parameters (e.g., $t_{0.5}^{-1}$, k_a , and C_0) relate, in one way or another, to the primary homogeneous nucleation rate I and/or the subsequent crystal growth rate G and since the temperature dependence of these microscopic mechanisms are well defined in the literature [38,39,41,42] as discussed previously, the temperature dependence of the overall rate parameter can accordingly be quantified and described. Even though the temperature dependence of the parameters I and G are known to have a different temperature dependence (cf. Equations (7-9) and (7-10), respectively), the overall rate parameters have often been taken to have a similar temperature dependence to that of the crystal growth rate G . According to this approximation, the temperature dependence of the overall crystallization rate data (e.g., $t_{0.5}^{-1}$, k_a , and C_0) can therefore be written as

$$\Psi(T_c) = \Psi_0 \exp\left[-\frac{\Theta}{R(T_c - T_\infty)}\right] \exp\left[-\frac{K_3^G}{T_c(\Delta T)f}\right], \quad (7-13)$$

where $\Psi(T_c)$ and Ψ_0 are the respective overall crystallization rate parameter (e.g., $t_{0.5}^{-1}$, k_a , and C_0) and the pre-exponential parameter (e.g., $(t_{0.5}^{-1})_0$, k_{a0} , and C_{00}), respectively, Θ is a parameter related to the activation energy characterizing the molecular transport across the melt/solid interface, K_3^G is a combined factor related to the secondary nucleation mechanisms, and other quantities are the same as previously defined. It is also interesting to determine whether or not the overall rate parameters can be taken a similar temperature dependence to that of the primary homogeneous nucleation rate I . According to such an approximation, the temperature dependence of the overall crystallization rate data (e.g., $t_{0.5}^{-1}$, k_a , and C_0) may be written as

$$\Psi(T_c) = \Psi_0 \exp\left[-\frac{\Theta}{R(T_c - T_\infty)}\right] \exp\left[-\frac{K_4^I}{T_c(\Delta T)^2 f^2}\right], \quad (7-14)$$

where K_4^I is a combined factor related to the primary nucleation mechanisms, and other quantities are the same as previously defined.

According to Equations (7-13) and (7-14), the temperature dependence of the overall rate function $\Psi(T_c)$ can now be quantified by directly fitting the respective overall crystallization rate parameters (e.g., $t_{0.5}^{-1}$, k_a , and C_0) collected at various crystallization temperatures to one of the equations using the same non-linear multi-variable regression program. In order to obtain the best possible fits for the respective overall crystallization rate data, two input parameters have to be pre-defined: 1) the glass transition temperature, $T_g = \text{ca. } -6^\circ\text{C}$ or $\text{ca. } 267 \text{ K}$ [14] (cf. Part 2), and 2) the equilibrium melting temperature, $T_m^0 = \text{ca. } 168.7^\circ\text{C}$ [14] (cf. Part 2). In doing so, the only unknown parameters which are provided by the program, once the best was determined, are Ψ_0 , Θ , K_3^C and K_4^I . The corresponding best fits for all of the overall crystallization rate data (e.g., $t_{0.5}^{-1}$, k_a , and C_0) are also shown in Figures 7-6, 7-9, and 7-10 as different lines; whereas, the values of the Ψ_0 , Θ , K_3^C and K_4^I as the result of the best fits according to Equations (7-13) and (7-14) are summarized in Table 7-5 for the melt-crystallization data and in Table 7-6 for the cold-crystallization data, respectively. It should be noted the dashed line in each figure represents the best fit to the melt-crystallization data in the range of $40^\circ\text{C} \leq T_c \leq 95^\circ\text{C}$, the dotted line represents the best fit to the melt-crystallization data in the range of $10^\circ\text{C} \leq T_c \leq 40^\circ\text{C}$, and the solid line represents the best fit to the cold-crystallization data.

Before going further into the discussion of the thermodynamic melting temperature, it is necessary to establish a comment on a common use of an Arrhenius temperature dependence in describing the temperature dependence of the Avrami rate constant k_a (see, for examples, in references [46-49]), which reads

$$(k_a)^{1/n} = (k_a)_0 \exp\left(-\frac{\Delta E_0}{RT_c}\right), \quad (7-15)$$

where $(k_a)_0$ is a temperature-independent pre-exponential parameter, ΔE_0 is the effective activation energy describing the overall crystallization kinetics, and others variables are

Table 7-5. The fitting parameters, provided by the non-linear multi-variable regression program, for the best possible fits of the respective bulk crystallization rate parameters (e.g., $t_{0.5}^{-1}$, k_a , C_1 and $k_a^{1/n}$) according to Equation (7-13).

Ψ	Ψ_0	Θ (cal·mol ⁻¹)	K (K ²)	r^2
For melt-crystallization data in the range $10^\circ\text{C} \leq T_c \leq 40^\circ\text{C}$				
$t_{0.5}^{-1}$ (min ⁻¹)	1.56×10^{21}	867.5	1.48×10^6	0.9662
$k_a^{1/n}$ (min ⁻¹)	7.80×10^{21}	878.4	1.53×10^6	0.9707
k_a (min ⁻ⁿ)	1.09×10^{22}	1650.4	1.45×10^6	0.7595
C_1 (min ⁻¹)	4.42×10^{30}	1041.5	2.12×10^6	0.9776
For melt-crystallization data in the range $40^\circ\text{C} \leq T_c \leq 95^\circ\text{C}$				
$t_{0.5}^{-1}$ (min ⁻¹)	4.82×10^9	1301.2	4.98×10^5	0.9889
$k_a^{1/n}$ (min ⁻¹)	3.26×10^9	1289.1	4.92×10^5	0.9889
k_a (min ⁻ⁿ)	7.08×10^{26}	3590.7	1.39×10^6	0.9726
C_1 (min ⁻¹)	3.40×10^{10}	1351.4	5.09×10^5	0.9784
For cold-crystallization data				
$t_{0.5}^{-1}$ (min ⁻¹)	7.04×10^9	1082.0	4.89×10^5	0.9851
$k_a^{1/n}$ (min ⁻¹)	9.83×10^9	1085.8	4.92×10^5	0.9885
k_a (min ⁻ⁿ)	4.09×10^{28}	3260.0	1.43×10^6	0.9872
C_1 (min ⁻¹)	4.22×10^{10}	1087.7	5.05×10^5	0.9799

Table 7-6. The fitting parameters, provided by the non-linear multi-variable regression program, for the best possible fits of the respective bulk crystallization rate parameters (e.g., $t_{0.5}^{-1}$, k_a , C_1 and $k_a^{1/n}$) according to Equation (7-14).

Ψ	Ψ_0	Θ (cal·mol ⁻¹)	K (K ²)	r^2
For melt-crystallization data in the range 10°C ≤ T_c ≤ 40°C				
$t_{0.5}^{-1}$ (min ⁻¹)	1.55×10 ⁹	1029.5	5.53×10 ⁷	0.9664
$k_a^{1/n}$ (min ⁻¹)	2.73×10 ⁹	1046.3	5.73×10 ⁷	0.9708
k_a (min ⁻ⁿ)	2.25×10 ¹⁰	1817.5	5.47×10 ⁷	0.7595
C_1 (min ⁻¹)	2.63×10 ¹³	1273.2	7.92×10 ⁷	0.9890
For melt-crystallization data in the range 40°C ≤ T_c ≤ 95°C				
$t_{0.5}^{-1}$ (min ⁻¹)	1.01×10 ⁵	1232.8	1.63×10 ⁷	0.9900
$k_a^{1/n}$ (min ⁻¹)	7.67×10 ⁴	1220.7	1.61×10 ⁷	0.9900
k_a (min ⁻ⁿ)	1.66×10 ¹⁴	3492.8	4.71×10 ⁷	0.9732
C_1 (min ⁻¹)	5.39×10 ⁵	1276.7	1.66×10 ⁷	0.9902
For cold-crystallization data				
$t_{0.5}^{-1}$ (min ⁻¹)	3.11×10 ⁵	1072.8	1.66×10 ⁷	0.9848
$k_a^{1/n}$ (min ⁻¹)	2.84×10 ⁵	1077.0	1.67×10 ⁷	0.9883
k_a (min ⁻ⁿ)	9.95×10 ¹⁵	3231.9	4.92×10 ⁷	0.9879
C_1 (min ⁻¹)	1.41×10 ⁶	1082.5	1.73×10 ⁷	0.9903

the same as previously defined. Apparently, a linear relation is expected when a plot of $(1/n_a)\ln k_a$ versus T_c^{-1} (the unit of T_c is in [K]) is performed, in which the slope is then used to determine the activation energy ΔE_0 . A number of investigators [46-49] claimed to observe a linear relation in the plot of $(1/n_a)\ln k_a$ versus T_c^{-1} . It should be noted however that in those report [46-49] the Avrami rate constant k_a data used to construct the plot were collected within a small range of crystallization temperatures T_c (i.e., $< 10^\circ\text{C}$).

Figure 7-11 illustrates plots of $(1/n_a)\ln k_a$ versus T_c^{-1} for the k_a data collected over a wide T_c range (cf. Tables 7-1 and 7-2). Instead of observing a linear relation in each of the plots, plots similar to those of the reciprocal half-time $t_{0.5}^{-1}$ versus the crystallization temperature T_c (cf. Figure 7-6) are evident. This is not surprising, however, since the Avrami rate constant k_a is known to relate to the reciprocal half-time $t_{0.5}^{-1}$ according to Equation (7-11). To demonstrate this fact, plots of $k_a^{1/n}$ as a function of the crystallization temperature T_c (cf. Figure 7-12) were drawn. Fitting the plots according to Equations (7-13) and (7-14) using the non-linear multi-variable regression program gives the fitting parameters, e.g., Ψ_0 , Θ , K_3^G and K_4^I , which are summarized in Tables 7-5 and 7-6, respectively. Evidently, the resulting fitting parameters are comparable to those obtained from the plots of $t_{0.5}^{-1}$ versus T_c .

The results illustrated in Figure 7-11 apparently indicate that Equation (7-15) can not and should not be used to describe the temperature dependence of the Avrami rate constant k_a . It is important to note that when a set of experimental data is collected over a small T_c range as being carried out in the referenced reports [46-49], a slight curvature observed in the plot of $(1/n_a)\ln k_a$ versus T_c^{-1} can be easily misled as a linear dependence (see, for examples, Figure 3 in reference [47] and Figure 4 in reference [48]), and the degree of the curvature depends on the T_c range in which one is carried out his

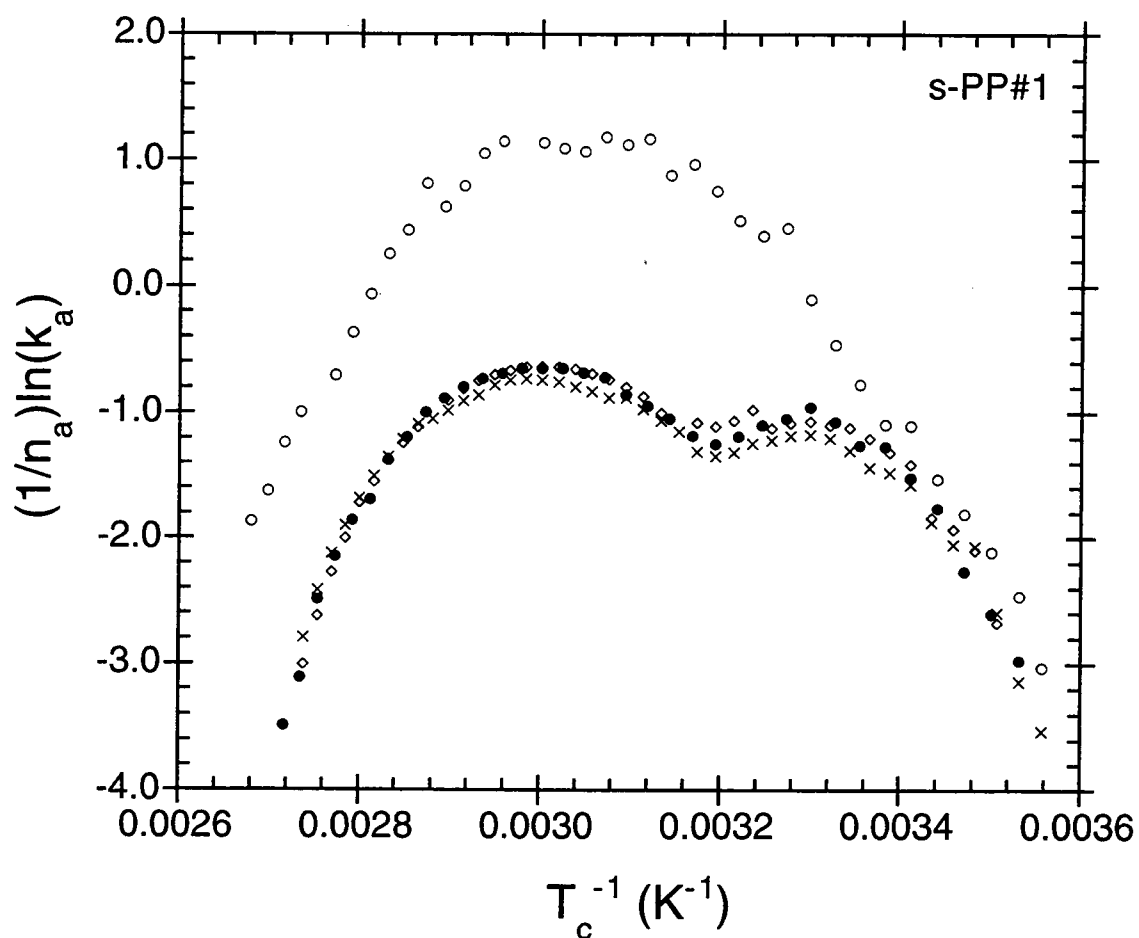


Figure 7-11. Variation of $(1/n_a)\ln k_a$ as a function of the inversed crystallization temperature T_c^{-1} according to Equation (7-15). Keys: (\diamond) melt-crystallization data taken from reference [40], (\times) melt-crystallization data taken from reference [13], (\bullet) melt-crystallization data measured in this study, and (\circ) cold-crystallization data measured in this study.

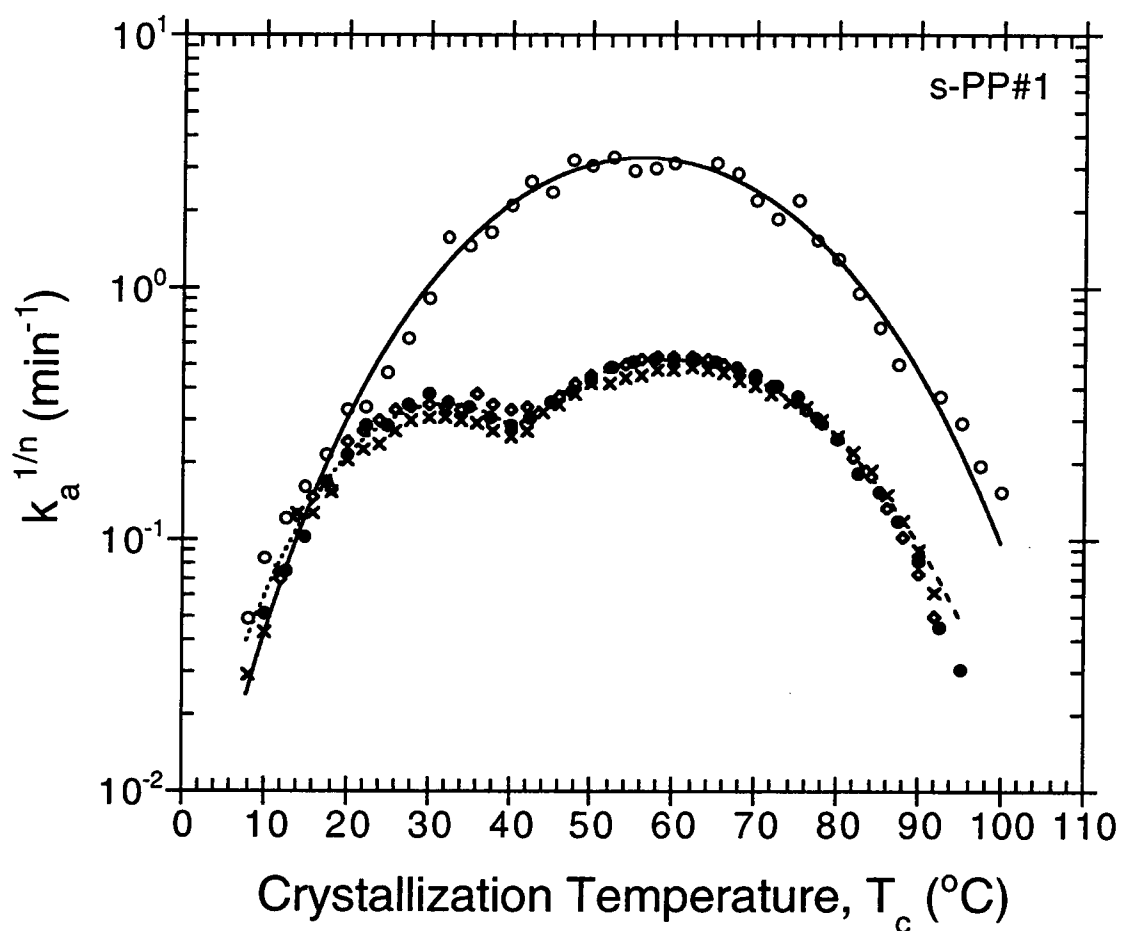


Figure 7-12. Variation of $k_a^{1/n}$ as a function of the crystallization temperature T_c according to Equation (7-15). Keys: (\diamond) melt-crystallization data taken from reference [40], (\times) melt-crystallization data taken from reference [13], (\bullet) melt-crystallization data measured in this study, and (\circ) cold-crystallization data measured in this study.

experiment. Consequently, the ΔE_0 value determined from the plot of $(1/n_a)\ln k_a$ versus T_c^{-1} is not a constant, as it clearly depends on the range of the data used in the construction of the plot. Since the ΔE_0 value is not a constant (for a polymer system), use of the ΔE_0 values to compare the overall crystallization kinetics of different polymer systems is clearly meaningless.

6.2. Determination of the Equilibrium Melting Temperature

As discussed in an earlier report [37] (cf. Part 6) that the values of the low-melting peak temperature T_{m1} correspond to the melting of the primary crystals formed at a specified T_c , thus the T_{m1} values listed in Tables 7-3 and 7-4 are now considered as the melting points T_m of the crystalline aggregates formed in the samples after complete crystallization from the melt and glassy states at T_c . According to a theory derived by Hoffman and Weeks [50], the equilibrium melting temperature T_m^0 (i.e., the melting temperature of infinitely extended crystals) can be obtained by linear extrapolation of observed T_m - T_c data to the line $T_m = T_c$. Mathematically, they arrived at the following equation (hereafter called the *linear* Hoffman-Weeks extrapolation (LHW)):

$$T_m = \frac{T_c}{2\beta} + T_m^0 \left[1 - \frac{1}{2\beta}\right], \quad (7-16)$$

where β is the *thickening ratio*. In other words, β indicates the ratio of the thickness of the mature crystal l_c to that of the initial one l_c^* ; therefore, $\beta = l_c/l_c^*$, which is supposed to always be greater than or equal to 1. It should be noted that the factor 2 in Equation (7-16) suggests that the thickness of the crystals undergoing melting is approximately double that of the initial critical thickness [51].

Figures 7-13 and 7-14 show plots of T_{m1} (or the observed T_m value of the crystallites formed at T_c) as a function of crystallization temperature T_c for the data taken from melt- and cold-crystallization, respectively. It is evident that a slightly upward curvature is discernable in both of the data sets. Intuitively, it is obvious that

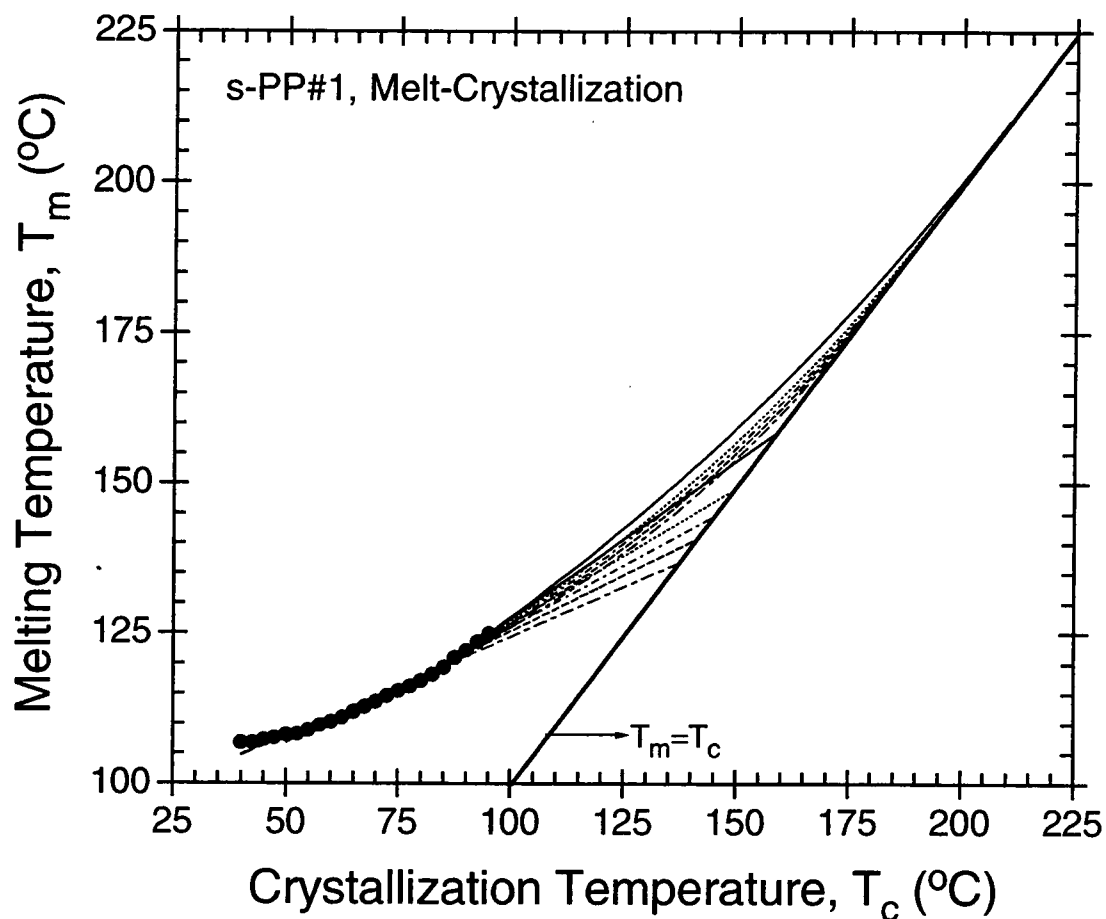


Figure 7-13. Variation of the the melting temperature T_m as a function of the crystallization temperature T_c for isothermal crystallization from the melt state (\bullet), and corresponding *linear* and *non-linear* HW extrapolations shown as straight and curved lines, respectively. Keys: ($- \cdot -$) fitted line for the data range $40^\circ\text{C} \leq T_c \leq 95^\circ\text{C}$, ($- - -$) fitted line for the data range $50^\circ\text{C} \leq T_c \leq 95^\circ\text{C}$, ($\cdot \cdot \cdot$) fitted line for the data range $60^\circ\text{C} \leq T_c \leq 95^\circ\text{C}$, ($- \cdot \cdot \cdot$) fitted line for the data range $70^\circ\text{C} \leq T_c \leq 95^\circ\text{C}$, and ($- - -$) fitted line for the data range $80^\circ\text{C} \leq T_c \leq 95^\circ\text{C}$.

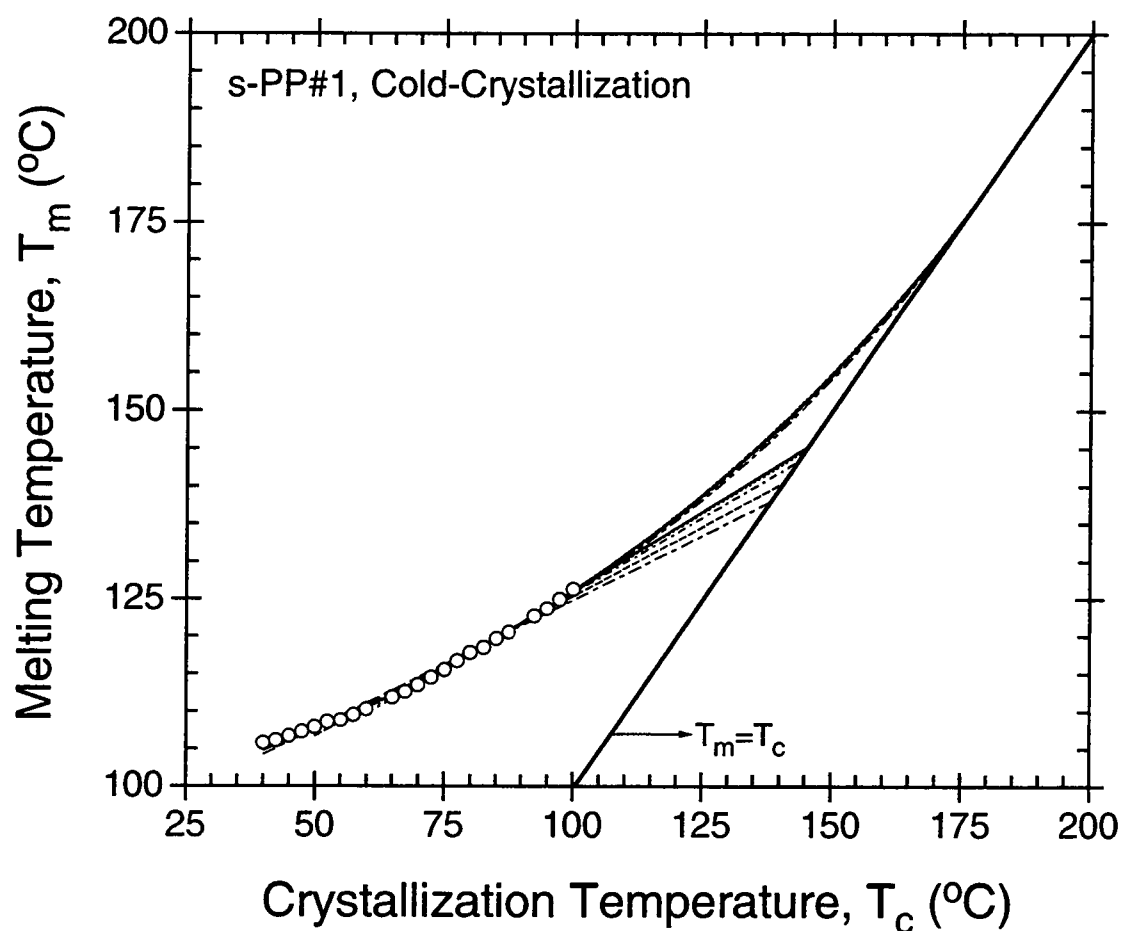


Figure 7-14. Variation of the the melting temperature T_m as a function of the crystallization temperature T_c for isothermal crystallization from the glassy state (\bullet), and corresponding *linear* and *non-linear* HW extrapolations shown as straight and curved lines, respectively. Keys: (---) fitted line for the data range $40^\circ\text{C} \leq T_c \leq 95^\circ\text{C}$, (-·-·) fitted line for the data range $50^\circ\text{C} \leq T_c \leq 95^\circ\text{C}$, (-·-·) fitted line for the data range $60^\circ\text{C} \leq T_c \leq 95^\circ\text{C}$, (·····) fitted line for the data range $70^\circ\text{C} \leq T_c \leq 95^\circ\text{C}$, and (—) fitted line for the data range $80^\circ\text{C} \leq T_c \leq 95^\circ\text{C}$.

the value of the equilibrium melting temperature T_m^{LHW} determined from linear extrapolation of the observed T_m-T_c data to the line $T_m = T_c$ will depend significantly on the range of the data used in the extrapolation (due to the curvature of the data). In this present study, the observed T_m-T_c data were divided into 5 regions accordingly (cf. Table 7-7). Within each region, a *linear* Hoffman-Weeks extrapolation is performed (also shown in Figures 7-13 and 7-14 as different linear lines) and the corresponding values of the equilibrium melting temperature T_m^{LHW} , the lamellar thickening ratio β (i.e., $\beta = 0.5 \times \text{slope}^{-1}$), and the correlation coefficient r^2 (justifying the goodness of the fit) are reported in Table 7-7. It is obvious, according to Table 7-7, that the resulting T_m^{LHW} and β values depend greatly on the range of the observed T_m-T_c data used in the extrapolation.

According to the basis of the *linear* Hoffman-Weeks extrapolative method, the extrapolated T_m^{LHW} value is only valid when the resulting thickening ratio β (calculated from the slope of the linear extrapolation) is equal to or close to 1. As a result, the equilibrium melting temperature T_m^{LHW} determined from the observed T_m-T_c data should lie between 148.7°C and 158.2°C in the case of crystallization from the melt state, and should be higher than 145.3°C in the case of crystallization from the glassy state. Let us pay a closer consideration to the curvature of the observed T_m-T_c data. If it is possible to extend the data range into the higher crystallization temperature region and if the primary crystallites formed at those temperatures do not severely thicken (the probability for crystal thickening increases tremendously with increasing crystallization temperature), it is hypothesized that the observed T_m values should follow the common curvature of the observed T_m-T_c data shown in Figures 7-13 and 7-14 and it should intersect with the line $T_m = T_c$ at the true equilibrium melting temperature T_m^0 of this sPP resin. If this hypothesis is valid, no matter what data range one chooses to perform the *linear* Hoffman-Weeks extrapolation the T_m^{LHW} value obtained will not represent the true

Table 7-7. Summary of the equilibrium melting temperature T_m^{LHW} and the lamellar thickening ratio β as suggested by the *linear* Hoffman-Weeks extrapolative method, and the equilibrium melting temperature T_m^{NLHW} and the parameter a associated with the resulting T_m^{NLHW} value as suggested by the *non-linear* Hoffman-Weeks extrapolative method for the observed T_m - T_c data ranges specified.

T_m - T_c Data Range	T_m^{LHW} (°C)	β	r^2	T_m^{NLHW} (°C)	a	r^2
For melt-crystallization data						
$40^\circ\text{C} \leq T_c \leq 95^\circ\text{C}$	136.6	1.5	0.982	178.0	2.90	0.984
$50^\circ\text{C} \leq T_c \leq 95^\circ\text{C}$	140.6	1.3	0.991	183.3	2.55	0.991
$60^\circ\text{C} \leq T_c \leq 95^\circ\text{C}$	144.3	1.2	0.994	188.2	2.28	0.993
$70^\circ\text{C} \leq T_c \leq 95^\circ\text{C}$	148.7	1.1	0.994	194.4	2.00	0.992
$80^\circ\text{C} \leq T_c \leq 95^\circ\text{C}$	158.2	0.9	0.999	210.2	1.47	0.998
For cold-crystallization data						
$40^\circ\text{C} \leq T_c \leq 100^\circ\text{C}$	137.9	1.5	0.992	177.3	2.93	0.997
$50^\circ\text{C} \leq T_c \leq 100^\circ\text{C}$	140.4	1.3	0.996	179.7	2.76	0.998
$60^\circ\text{C} \leq T_c \leq 100^\circ\text{C}$	143.2	1.2	0.999	181.8	2.61	0.999
$70^\circ\text{C} \leq T_c \leq 100^\circ\text{C}$	144.7	1.2	0.999	182.1	2.59	0.999
$80^\circ\text{C} \leq T_c \leq 100^\circ\text{C}$	145.3	1.2	0.998	180.9	2.67	0.998

equilibrium melting temperature T_m^0 and will always be lower (i.e., $T_m^{\text{LHW}} < T_m^0$). However, the closer is the range of the data to the true equilibrium melting temperature T_m^0 , the smaller is the difference between the true and the extrapolated values (one has to make sure that the observed T_m values obtained at high T_c do not represent the melting temperature of the thickened crystallites formed at that temperature).

It has already been mentioned that a slightly upward curvature is apparent in both of the data sets (cf. Figures 7-13 and 7-14). This upward curvature in the observed T_m - T_c data had also been observed in various other polymer systems (see, for examples, in references [51,52]), thus raising a concern on the assumed constancy of the thickening ratio β . In fact, Weeks [53] pointed out long ago that the increase in observed T_m value with increasing crystallization time is a result of the increase in lamellar thickness, which has a logarithmic dependence on time (although this remark should only be valid for polymers which exhibit significant α -relaxation, e.g., linear PE and iPP). This simply means that the thickening effect is much more severe at higher T_c values (as a result of a combination of high molecular mobility and small relaxation time of the amorphous layer) where prolonged crystallization time is needed for complete crystallization.

Although the non-linearity in the observed T_m - T_c data over wide range of temperature was explained to some extent by Alamo et al. [51], it is the recent contribution by Marand et al. [54] that offers a new method of determining the T_m^0 value based on the observed T_m - T_c data in which the observed T_m data were taken from samples crystallized at different temperatures but with the same *a priori* lamellar thickening coefficient. Derived based on the Gibbs-Thomson equation [38,55] and on the proposition of Lauritzen and Passaglia [56] on stem length fluctuation during chain folding, Marand et al. [54] proposed a new mathematical derivation which states a relationship between the observed melting temperature and the corresponding crystallization temperature. This equation is hereafter called the *non-linear* Hoffman-

Weeks extrapolation (NLHW), and is written in the form:

$$\frac{T_m^0}{T_m^0 - T_m} = \beta^m \frac{\sigma_c^1}{\sigma_c^{GT}} \left[\frac{T_m^0}{T_m^0 - T_c} + \frac{D_2 \Delta H_f^0}{2\sigma_c^1} \right], \quad (7-17a)$$

or in a simpler form:

$$M = \beta^m \frac{\sigma_c^1}{\sigma_c^{GT}} (X + a), \quad (7-17b)$$

where β^m is the thickening coefficient (cf. β in Equation (7-16)), σ_c^{GT} is the basal interfacial free energy associated with a nucleus of critical size including the extra lateral surface energy due to fold protrusion and the mixing entropy associated with stems of different lengths ($\sigma_c^{GT} \equiv$ the basal interfacial free energy as appeared in the Gibbs-Thomson equation [38,55]), σ_c^1 is the interfacial energy associated with the basal plane of the mature crystallite, D_2 is a constant, and all other parameters are the same as previously defined. It is worth noting that for most cases it is safe to assume that $\sigma_c^1 = \sigma_c^{GT}$ [54]. Precautionary remarks regarding the use of the *non-linear* Hoffman-Weeks procedure to estimate the equilibrium melting temperature T_m^0 were addressed in detail in the original publication by Marand et al. [54].

In order to apply Equation (7-17) to analyze the observed T_m - T_c data in real polymer systems, it is required that the observed T_m data be collected from samples crystallized at different temperatures but having the same lamellar thickening coefficient β^m . For each set of the observed T_m - T_c data, corresponding values of M and X in Equation (7-16) can be calculated for a given choice of the equilibrium melting temperature T_m^0 . In case of $\sigma_c^1 = \sigma_c^{GT}$, the *actual* equilibrium melting temperature T_m^0 is taken as the seed T_m^0 value which results in the plot of M versus X being a straight line with slope of unity (i.e., $\beta^m = 1$) and intercept of a (i.e., $a = D_2 \Delta H_f^0 / 2\sigma_c^1$). Since it had been shown in the case of sPP that lamellar thickening does not occur during crystallization, at least within the crystallization temperature range studied [37,57,58],

it is reasonable to assume that the observed T_m data summarized in Tables 7-3 and 7-4 were collected from lamellae having the same thickening coefficient β^n , thus enabling them to be analyzed using this method.

In each of the 5 regions of the observed T_m-T_c data, a *non-linear* Hoffman-Weeks extrapolation is performed (also shown in Figures 7-13 and 7-14 as different curve lines) according to the procedure described in the previous paragraph. The resulting values of the equilibrium melting temperature T_m^{NLHW} , the parameter a associated with the resulting T_m^{NLHW} value, and the correlation coefficient r^2 are summarized in Table 7-7. It is apparent, according to Table 7-7, that the resulting T_m^{NLHW} and a values determined from the melt-crystallization data depend greatly on the range of the observed T_m-T_c data used in the extrapolation; whereas, those determined from the cold-crystallization data do not vary significantly. Comparison of values of the correlation coefficient r^2 summarized in Table 7-7 indicates that the observed T_m-T_c data obtained from crystallization from the melt state are much more scattered than those obtained from crystallization from the glassy state, and this should be the reason for the large variation observed in the resulting T_m^{NLHW} values determined from the melt-crystallization data. If one is to assume that the lamellar thickness is only a function of crystallization temperature T_c (or to be exact, the degree of undercooling ΔT) regardless of the nucleation mechanisms involved, one should be able to determine the true equilibrium melting temperature T_m^0 of the polymer of interest from either melt- or cold-crystallization experiment. If the aforementioned assumption is valid, the true equilibrium melting temperature T_m^0 of this sPP resin should be taken as $T_m^{NLHW} = 181.8^\circ\text{C}$ (judged from the lowest value of the correlation coefficient r^2 of the fit) and the parameter a associated with this T_m^{NLHW} value is 2.61.

7. CONCLUSIONS

In this study, differential scanning calorimetry (DSC) was used to investigate the overall kinetics of melt- and cold-crystallization of sPP under isothermal quiescent conditions and subsequent melting behavior. A non-linear multi-variable regression program was used to fit the isothermal crystallization measurements obtained from the DSC to Avrami and Malkin macrokinetic models. The crystallization kinetics parameters specific to each of the model were obtained along with the best fits, provided by the program.

For crystallization from the melt state, all of the crystallization rate parameters considered (e.g., $t_{0.5}^{-1}$, k_a , and C_0) exhibit an unmistakable double bell-shaped curve when plotted as a function of crystallization temperature T_c , with the two maxima being observed at $T_c = \text{ca. } 30^\circ\text{C}$ and $\text{ca. } 60^\circ\text{C}$ owing to the contributions from the maximum in the crystal growth rate and from the maximum in the primary nucleation rate, respectively, and the discontinuity being observed at $T_c = \text{ca. } 40^\circ\text{C}$. For crystallization from the glassy state however, the typical bell-shaped curve is observed when all of the crystallization rate parameters considered (e.g., $t_{0.5}^{-1}$, k_a , and C_0) were plotted as a function of crystallization temperature T_c , with a maximum being observed at $T_c = \text{ca. } 58^\circ\text{C}$. Comparison of the crystallization rate parameters (e.g., $t_{0.5}^{-1}$, k_a , and C_0) measured from both melt- and cold-crystallization processes indicate that crystallization from the glassy state is much faster than that from the melt state. This clearly suggests that quenching process greatly increases the total number of activated nuclei (or the rate of formation of the nuclei) and, upon subsequent crystallization at T_c , these activated nuclei can act as predetermined homogeneous nuclei which tremendously enhance the overall crystallization rate.

The multiple-melting (triple-melting) behavior of sPP observed in subsequent melting endotherms in DSC can be explained as the contributions from: 1) melting of the

secondary crystallites and their re-crystallization, 2) partial melting of the less stable fraction of the primary crystallites and their re-crystallization, 3) melting of the remaining fractions of the primary crystallites, and lastly 4) re-melting of the re-crystallized crystallites formed during the heating scan. The observation and strength of the high-temperature melting endotherm is found to depend strongly on the stability of the secondary and the primary crystallites formed and on the scanning rate used to observe the melting behavior.

Lastly, analysis of the low-melting temperature according to the *linear* and *non-linear* Hoffman-Weeks extrapolative methods to obtain the equilibrium melting temperature T_m^0 is found to be somewhat sensitive to the range of the observed T_m - T_c data within which the extrapolations were carried out and perhaps to the accuracy of the data obtained. The results also suggest that the *linear* Hoffman-Weeks extrapolation always underestimate the value of the equilibrium melting temperature. As a result, the equilibrium melting temperature T_m^{NLHW} determined from the non-linear Hoffman-Weeks extrapolation may be taken as the better estimate of the true equilibrium melting temperature T_m^0 for this sPP resin (ca. $T_m^0 \cong T_m^{\text{NLHW}} = 181.8^\circ\text{C}$). However, the accuracy of the estimate is still unclear, at least for the case of sPP.

8. REFERENCES

- [1] Natta, G.; Pasquon, I.; Corradini, P.; Peraldo, M.; Pegoraro, M.; and Zambelli, A. *Rend. Acc. Naz. Lincei*. **1960**, *28*, 539.
- [2] Natta, G.; Pasquon, I.; and Zambelli, A. *J. Am. Chem. Soc.* **1962**, *84*, 1488.
- [3] Ewen, J.A.; Johns, R.L.; Razavi, A.; and Ferrara, J.D. *J. Am. Chem. Soc.* **1988**, *110*, 6255.
- [4] Schardl, J.; Sun, L.; Kimura, S.; and Sugimoto, R. *SPE-ANTEC Proc.* **1995**, 3414.
- [5] Schardl, J.; Sun, L.; Kimura, S.; and Sugimoto, R. *J. Plastic Film & Sheeting* **1996**, *12*, 157.
- [6] Sun, L.; Shamshoum, E.; and DeKunder, G. *SPE-ANTEC Proc.* **1996**, 1965.
- [7] Gownder, M. *SPE-ANTEC Proc.* **1998**, 1511.
- [8] Sura, R.K.; Desai, P.; and Abhiraman, A.S. *SPE-ANTEC Proc.* **1999**, 1764.
- [9] Wheat, W.R. *SPE-ANTEC Proc.* **1995**, 2275.
- [10] Wheat, W.R. *SPE-ANTEC Proc.* **1997**, 565.
- [11] Rodriguez-Arnold, J.; Bu, Z.; and Cheng, S.Z.D. *J. Macromol. Sci.-Rev. Macromol. Chem. Phys.* **1995**, *C35*, 117.
- [12] Rodriguez-Arnold, J.; Zhang, A.; Cheng, S.Z.D.; Lovinger, A.J.; Hsieh, E.T.; Chu, P.; Johnson, T.W.; Honnell, K.G.; Geerts, R.G.; Palackal, S.J.; Hawley, G.R.; and Welch, M.B. *Polymer* **1994**, *35*, 1884.
- [13] Supaphol, P.; Hwu, J.J.-J.; Phillips, P.J.; and Spruiell, J.E. *SPE-ANTEC Proc.* **1997**, 1759.
- [14] Supaphol, P. and Spruiell, J.E. *J. Appl. Polym. Sci.* accepted on April 16, 1999.
- [15] Rodriguez-Arnold, J.; Bu, Z.; Cheng, S.Z.D.; Hsieh, E.T.; Johnson, T.W.; Geerts, R.G.; Palackal, S.J.; Hawley, G.R.; and Welch, M.B. *Polymer* **1994**, *35*, 5194.
- [16] Supaphol, P. and Spruiell, J.E. *Polymer* accepted on March 25, 1999.
- [17] Bu, Z.; Yoon, Y.; Ho, R.-M.; Zhou, W.; Jangchud, I.; Eby, R.K.; Cheng, S.Z.D.; Hsieh, E.T.; Johnson, T.W.; Geerts, R.G.; Palackal, S.J.; Hawley, G.R.; and Welch, M.B. *Macromolecules* **1996**, *29*, 6575.
- [18] Vancso, G.J.; Beekmans, L.G.M.; Trifonova, D.; and Varga, J. *ACS-PMSE Prepr.* **1999**, *81*, 232.
- [19] Taguchi, K.; Miyaji, H.; Izumi, K.; Hoshino, A.; Miyamoto, Y.; and Kokawa, R. *ACS-PMSE Prepr.* **1999**, *81*, 308.
- [20] Keith, H.D. and Padden, F.J. *J. Appl. Phys.* **1964**, *35*, 1270.
- [21] Keith, H.D. and Padden, F.J. *J. Appl. Phys.* **1964**, *35*, 1286.
- [22] Verma, R.; Marand, H.; and Hsiao, B. *Macromolecules* **1996**, *29*, 7767.
- [23] Marand, H. and Alizadeh, A. *ACS-PMSE Prepr.* **1999**, *81*, 238.
- [24] Kolmogoroff, A.N. *Izvestiya Akad. Nauk USSR, Ser. Math.* **1937**, *1*, 355.
- [25] Johnson, W.A. and Mehl, K.F. *Trans. Am. Inst. Mining Met. Eng.* **1939**, *135*, 416.
- [26] Avrami, M. *J. Chem. Phys.* **1939**, *7*, 1103.
- [27] Avrami, M. *J. Chem. Phys.* **1940**, *8*, 212.

- [28] Avrami, M. *J. Chem. Phys.* **1941**, *9*, 177.
- [29] Evans, U.R. *Trans. Faraday Soc.* **1945**, *41*, 365.
- [30] Tobin, M.C. *J. Polym. Sci., Polym. Phys.* **1974**, *12*, 399.
- [31] Tobin, M.C. *J. Polym. Sci., Polym. Phys.* **1976**, *14*, 2253.
- [32] Tobin, M.C. *J. Polym. Sci., Polym. Phys.* **1977**, *15*, 2269.
- [33] Malkin, A.Y.; Beghishev, V.P.; Keapin, I.A.; and Bolgov, S.A. *Polym. Eng. Sci.* **1984**, *24*, 1396.
- [34] Supaphol, P. and Spruiell, J.E. *J. Macromol. Sci.-Phys.* accepted on June 1, 1999.
- [35] Wunderlich, B. In *Macromolecular Physics*; Academic Press: New York, 1976; Vol. 2; pp 132-147.
- [36] Supaphol, P. and Spruiell, J.E. *J. Appl. Polym. Sci.* accepted on April 4, 1999.
- [37] Supaphol, P. and Spruiell, J.E. *J. Polym. Sci., Polym. Phys.* submitted for publication.
- [38] Hoffman, J.D.; Davis, G.T.; and Lauritzen Jr., J.I. In *Treatise on Solid State Chemistry*; Hannay, N.B., Ed.; Plenum Press: New York, 1976; Vol. 3; Chapter 7.
- [39] Hoffman, J.D. and Miller, R.L. *Polymer* **1997**, *38*, 3151.
- [40] Supaphol, P. *unpublished research*.
- [41] Turnbull, D. and Fisher, J.C. *J. Chem. Phys.* **1949**, *17*, 71.
- [42] Price, F.P. In *Nucleation*; Zettlemoyer, A.C., Ed.; Marcel Dekker: New York, 1969; Chapter 8.
- [43] Okui, N. *Polym. J.* **1987**, *19*, 1309.
- [44] Okui, N. *J. Mat. Sci.* **1990**, *25*, 1623.
- [45] Janeschitz-Kriegl, H.; Ratajski, E.; and Wippel, H. *Colloid Polym. Sci.* **1999**, *277*, 217.
- [46] Liu, T.; Mo, Z.; Wang, S.; and Zhang, H. *Eur. Polym. J.* **1997**, *33*, 1405.
- [47] Liu, S.; Yu, Y.; Cui, Y.; Zhang, H.; and Mo, Z. *J. Appl. Polym. Sci.* **1998**, *70*, 2371.
- [48] Liu, T.; Mo, Z.; and Zhang, H. *J. Polym. Eng.* **1998**, *18*, 283.
- [49] Lee, S.W. and Cakmak, M. *J. Macromol. Sci.-Phys.* **1998**, *B37*, 501.
- [50] Hoffman, J.D. and Weeks, J.J. *J. Res. Nat'l. Bur. Stand.* **1962**, *A66*, 13.
- [51] Alamo, R.G.; Viers, B.D.; and Mandelkern, L. *Macromolecules* **1995**, *28*, 3205.
- [52] Huang, J.; Prasad, A.; and Marand, H. *Polymer* **1994**, *35*, 1896.
- [53] Weeks, J.J. *J. Res. Nat'l. Bur. Stand.* **1963**, *A67*, 441.
- [54] Marand, H.; Xu, J.; and Srinivas, S. *Macromolecules* **1998**, *31*, 8219.
- [55] Brown, R.G. and Eby, R.K. *J. Appl. Phys.* **1964**, *35*, 1156.
- [56] Lauritzen Jr., J.I. and Passaglia, E. *J. Res. Nat'l. Bur. Stand.* **1967**, *A61*, 261.
- [57] Schmidtke, J.; Strobl, G.; and Thurn-Albrecht, T. *Macromolecules* **1997**, *30*, 5804.
- [58] Hauser, G.; Schmidtke, J.; and Strobl, G. *Macromolecules* **1998**, *31*, 6250.

PART 8:
ISOTHERMAL CRYSTALLIZATION AND MELTING BEHAVIOR OF
SYNDIOTACTIC POLYPROPYLENE: A WAXD/SAXS/DSC STUDY

1. ABSTRACT

The lamellar morphology of isothermally crystallized syndiotactic polypropylene (sPP) samples was investigated using wide-angle x-ray diffraction (WAXD) and small-angle x-ray scattering (SAXS) techniques. The melting behavior of these samples was also investigated using the differential scanning calorimetry technique (DSC). Three methods for the determination of the equilibrium melting temperature T_m^0 , namely the Gibbs-Thomson extrapolation, the *linear* Hoffman-Weeks extrapolation, and the *non-linear* Hoffman-Weeks extrapolation, were employed to evaluate this important thermodynamic parameter.

2. INTRODUCTION

The syndiotactic form of polypropylene (sPP) was first synthesized in the early 1960s by Natta et al. [1,2] based on Ziegler-Natta catalysis, but the resulting polymer contained too high a level of regio-irregular defects (e.g., head-to-head/tail-to-tail type defects) despite a fair level of syndiotactic content. A much improved sPP was successfully synthesized in 1988 by Ewen et al. [3] who reported that highly stereoregular and regio-regular sPP can be polymerized using a novel metallocene catalysis. The new catalyst systems have made it possible to produce sPP with much improved purity and yields, which led to renewed interest in both scientific researches (e.g., [4]) and industrial applications [5-10].

Studies related to crystallization process of semicrystalline polymers are of great importance in polymer processing, owing to the fact that the resulting physical properties are strongly dependent on the morphology formed and the extent of crystallization. It is therefore very important to understand the processing-structure-property inter-relationships of the studied materials, which in this case is sPP. Investigations related to the chain conformation, crystal structure, morphology, and

phase transitions in sPP have been reported extensively in recent years. These studies up to 1994 were reviewed and discussed in a publication by Rodriguez-Arnold et al. [4]. Studies which have been carried out on the subject of isothermal crystallization of sPP include the Avrami kinetics of the crystallization process [11-13] (cf. Part 2), the kinetics of the linear growth rates [12,14,15] (cf. Part 3), and the morphology of the single crystals [16].

In this present part, wide-angle x-ray diffraction (WAXD) and small angle x-ray scattering (SAXS) techniques are employed to determine lamellar morphology information of sPP samples isothermally crystallized at various crystallization temperatures. Differential scanning calorimetry (DSC) technique is used to study the melting behavior of these samples.

3. EXPERIMENTAL DETAILS

3.1. Materials

The sPP resin (i.e., sPP#4) used in this study was synthesized using a metallocene catalyst and was produced commercially in pellet form by Fina Oil and Chemical Company of La Porte, Texas. Molecular characterization data shows the following molecular weight information: $M_n = 81,300$ daltons, $M_w = 171,000$ daltons, $M_z = 294,000$ daltons, and $M_w/M_n = 2.1$. In addition, the syndiotacticity measured by ^{13}C NMR shows the racemic dyad content [%r] to be 89.2%, the racemic triad content [%rr] to be 84.4%, and the racemic pentad content [%rrrr] to be 74.6%. The glass transition temperature T_g was determined to be ca. -6°C [13] (cf. Part 2).

3.2. Sample Preparation

Sliced pellets were melt-pressed between a pair of Kapton films, which in turn were sandwiched between a pair of thick metal plates, in a Wabash compression molding machine preset at 190°C under a pressure of 67 kpsi. After ten minutes holding

time, a film of ca. 290 μm thickness was taken out and allowed to cool at ambient condition down to room temperature between the two metal plates. This treatment assumes that previous thermo-mechanical history was essentially erased, and provides a standard crystalline memory condition for the experiments. The samples used in this study were cut from the as-prepared film, placed between two clean glass slides, brought to melt in a Mettler hot-stage at a fusion temperature T_f of 190°C for 5 min to ensure complete melting [17] (cf. Part 4), and then quickly brought to crystallize isothermally in another Mettler hot-stage calibrated to $\pm 0.5^\circ\text{C}$ in the crystallization temperature T_c range of 30 to 95°C. After complete crystallization at T_c , the samples were quenched in liquid nitrogen to prevent further change in crystallinity due to the residual thermal energy within the samples. Finally, WAXD, SAXS, and DSC techniques were performed on these samples.

3.3. Wide-Angle X-ray Diffraction

WAXD technique was employed to determine the crystal modification and the apparent degree of crystallinity in the samples prepared. The WAXD intensity patterns were collected on a Rigaku-Denki diffractometer (CuK_α radiation, $\lambda = 1.5418 \text{ \AA}$) equipped with a computerized data collection and analytical system. The operating condition of the x-ray source was set at a voltage of 35 kV and a current of 40 mA.

3.4. Small-Angle X-ray Scattering

The SAXS intensity data of the samples prepared were measured on the ORNL 10-m SAXS apparatus [18], which consists mainly of a pinhole-collimated CuK_α x-ray source ($\lambda = 1.54 \text{ \AA}$) operating at 80 mA and 40 kV and a $20 \times 20 \text{ cm}^2$ two-dimensional position-sensitive detector with each virtual cell element of about 3 mm apart. A sample-to-detector distance of 5.12 m was used. The scattered intensity was stored in a 64×64 data array. Corrections were made for instrumental backgrounds, dark

current due to cosmic radiation and electronic noises, and detector non-uniformity and efficiency (via an Fe^{55} radioactive standard which emits γ -rays isotropically) on a cell-by-cell basis. The intensity data were azimuthally averaged at each scattering vector $q = (4\pi/\lambda)\sin(\theta/2)$ (where λ and θ are the x-ray wavelength and the scattering angle, respectively) ranging from 0.058 to 1.004 nm^{-1} , and were converted to an absolute differential scattering cross section by means of pre-calibrated secondary standards [19].

3.5. Differential Scanning Calorimetry

A DSC (DSC-7, Perkin-Elmer) was used to record subsequent melting thermograms of the samples prepared. All of the recorded melting thermograms were carried out using a scanning rate of $20^\circ\text{C}\cdot\text{min}^{-1}$. Temperature calibration was performed using a pure indium standard ($T_m^0 = 156.6^\circ\text{C}$ and $\Delta H_f^0 = 28.5 \text{ J}\cdot\text{g}^{-1}$). The consistency of the temperature calibration was checked every other run to ensure reliability and accuracy of the data obtained.

4. RESULTS

Figure 8-1 shows WAXD diffractograms for sPP samples isothermally crystallized in a Mellter hot-stage at $T_c = 30, 40, 50, 60, 70, 80, 85, 90,$ and 95°C . Apparently, the characteristic crystalline peaks are present at the scattering angles $2\theta = 12.18 \pm 0.03^\circ, 15.93 \pm 0.03^\circ, 20.64 \pm 0.11^\circ,$ and $24.56 \pm 0.04^\circ$. By consulting all of the publications dedicated to crystallographical studies of sPP [20-34], it can be postulated that the results shown in Figure 8-1 can be best described by the limit-disordered form I [26,28,30] (after the most recent nomenclature given by De Rosa et al. [35]), which has an orthorhombic unit cell with axes $a = 14.5 \text{ \AA}, b = 5.6 \text{ \AA},$ and $c = 7.4 \text{ \AA}$ and exhibits an antichiral packing of chains only along the a axis (see Figure 1B in ref. [35]). The space group proposed for this crystal modification was $Pcaa$ [21,27]. According to this unit

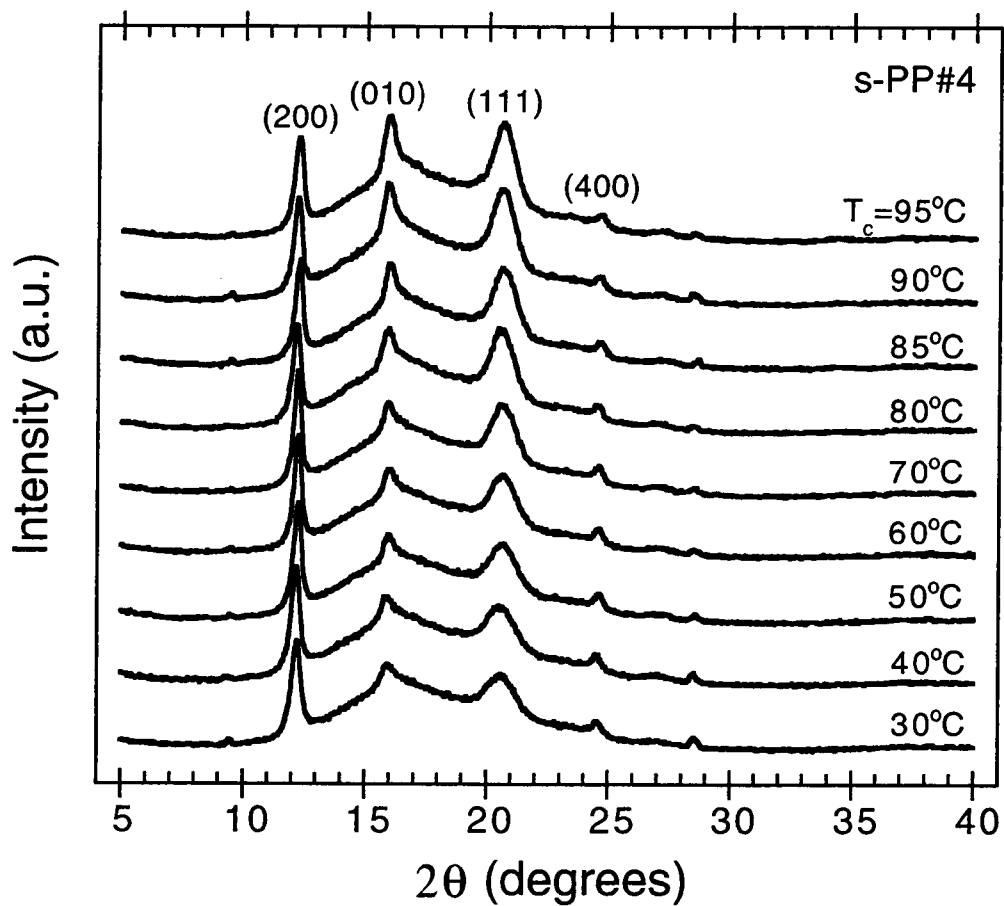


Figure 8-1. WAXD diffractograms of sPP#4 samples isothermally crystallized at various crystallization temperatures T_c ranging from 30°C to 95°C .

cell, the characteristic x-ray peaks are observed at $2\theta = 12.2^\circ$, 15.8° , 20.8° , and 24.5° , corresponding to d -spacing at 7.25, 5.60, 4.27, and 3.63 Å and to reflection planes at (200), (010), (111), and (400), respectively.

WAXD patterns not only indicated to us the crystal modification formed in these samples, but they also suggest to us the apparent degree of crystallinity χ_c^{WAXD} these samples possess. Intuitively, the WAXD degree of crystallinity χ_c^{WAXD} can be determined from the WAXD patterns based on the ratio of the integrated intensities under the crystalline peaks A_c to the integrated total intensities A_t (i.e., $A_t = A_c + A_a$, where A_a = the integrated intensities under the amorphous halo), i.e.,

$$\chi_c^{\text{WAXD}} = \frac{A_c}{A_c + A_a} \in [0, 1]. \quad (8-1)$$

Qualitatively, an increase in size of the crystalline scattering peaks with increasing crystallization temperature (cf. Figure 8-1) suggests to us that the WAXD degree of crystallinity χ_c^{WAXD} is an increasing function of crystallization temperature, at least within the temperature range studied. The quantitative results are summarized in Table 8-1 and will be discussed further in the next section.

Figure 8-2 shows azimuthally averaged SAXS profiles collected on these samples. The raw data are plotted in Figure 8-2 as different geometrical dots, while solid lines drawn through each set of data represent smoothed profiles. The Lorentz-corrected SAXS intensity profiles (i.e., Kratky Plots) of the experimental SAXS intensity profiles (cf. Figure 8-2) are shown in Figure 8-3. With an assumption of a two-phase system comprising crystalline and amorphous fractions with sharp interfaces, the average value of the long period L_B of the lamellar morphology (hereafter called the long period L_B) can be evaluated from the maximum value of the scattering vector q_{max} observed in the Lorentz-corrected SAXS scattering profiles (cf. Figure 8-3). According to Bragg's law and the mathematical definition of the scattering vector q , the long period L_B

Table 8-1. Experimental values of the WAXD degree of crystallinity χ_c^{WAXD} , the maximum scattering vector q_{max} , the long period L_B , the lamellar thickness l_c and the melting temperature T_m .

T_c (°C)	χ_c^{WAXD}	q_{max} (nm ⁻¹)	L_B (nm)	l_c (nm)	T_m (°C)
30	0.28	0.649	9.7	2.7	-
40	0.28	0.618	10.2	2.8	106.0 ± 0.4
50	0.30	0.586	10.7	3.2	107.1 ± 0.2
60	0.30	0.561	11.2	3.3	108.8 ± 0.2
70	0.29	0.533	11.8	3.4	112.1 ± 0.6
80	0.31	0.512	12.3	3.8	116.5 ± 0.7
85	0.33	0.508	12.4	4.1	118.5 ± 0.7
90	0.34	0.501	12.5	4.2	120.8 ± 0.5
95	0.33	0.498	12.6	4.2	123.3 ± 0.7

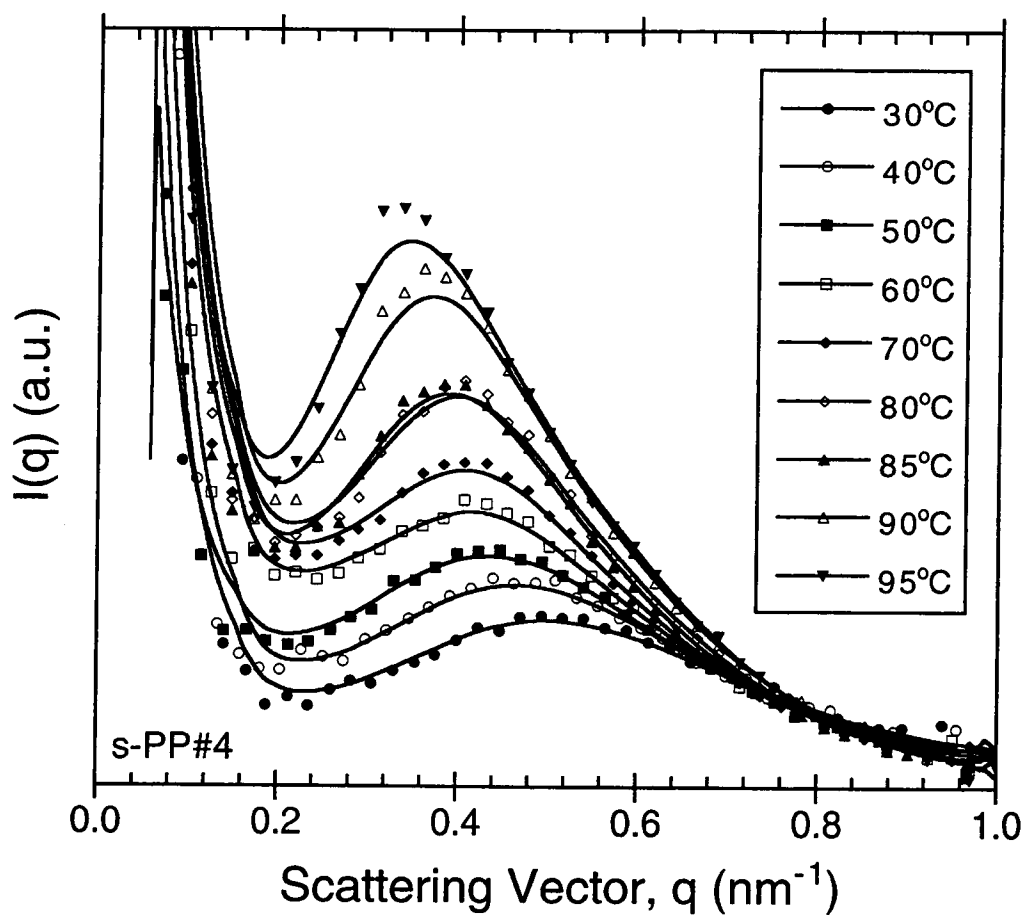


Figure 8-2. Azimuthally averaged SAXS profiles of sPP#4 samples isothermally crystallized at various crystallization temperatures T_c ranging from 30°C to 95°C.

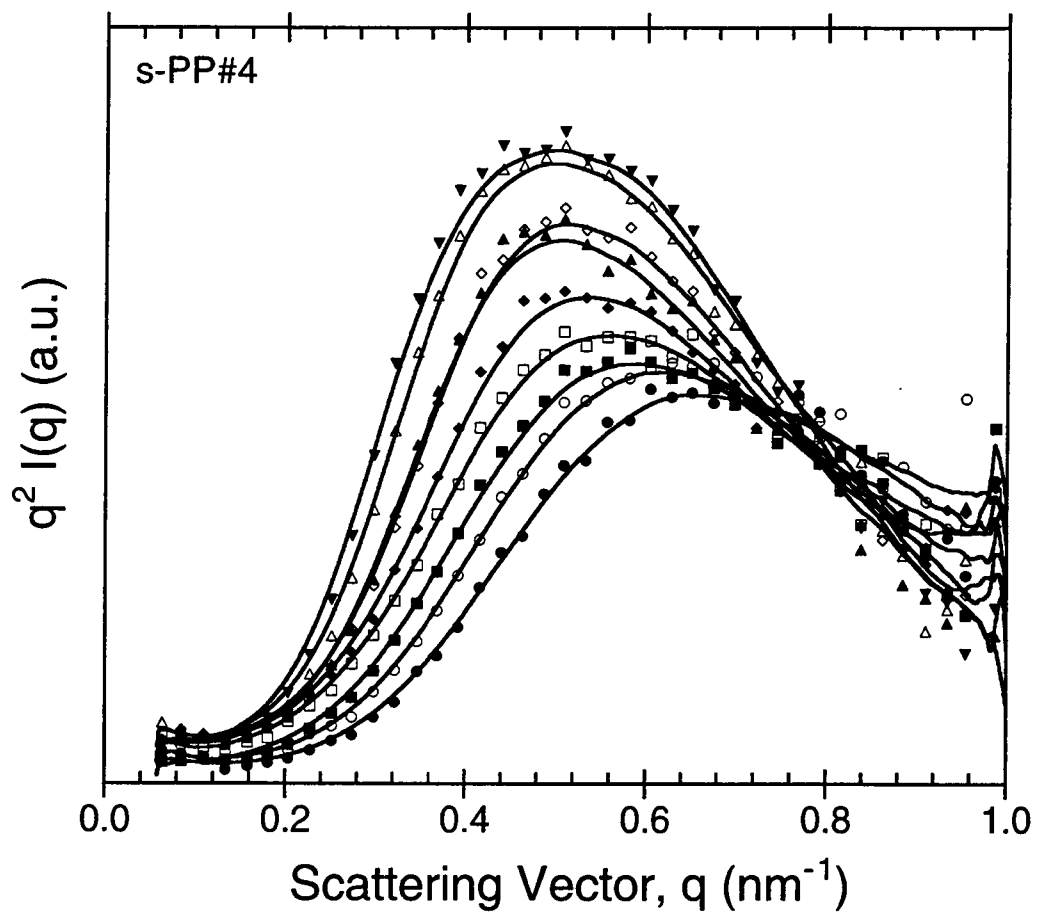


Figure 8-3. Lorentz-corrected SAXS profiles (Kratky plots) of sPP#4 samples isothermally crystallized at various crystallization temperatures T_c ranging from 30°C to 95°C. (Please see Figure 8-2 for legends.)

can then be calculated from the following equation:

$$L_B = \frac{2\pi}{q_{\max}}. \quad (8-2)$$

According to Figure 8-3, the fact that the q_{\max} value decreases with increasing crystallization temperature indicates that the long period L_B increases with increasing crystallization temperature. The quantitative results are summarized in Table 8-1 and will be discussed further in the next section.

Figure 8-4 illustrates the melting behavior of these samples during a heating scan ($20^\circ\text{C}\cdot\text{min}^{-1}$) in DSC. For samples isothermally crystallized at $T_c \leq 90^\circ\text{C}$, three melting endotherms are observed, while only two melting endotherms are present in the sample isothermally crystallized at $T_c = 95^\circ\text{C}$. According to a recent study [36] (cf. Part 6), the minor endotherm (the peak temperature of which is denoted in reference [36] as the minor peak temperature T_1), located close to the corresponding crystallization temperature T_c , represents the melting of the secondary crystallites formed at T_c . The low-temperature melting endotherm (the peak temperature of which is denoted in reference [36] as the low-melting peak temperature T_{mi}) corresponds to the melting of the primary crystallites formed at T_c , while the high-temperature melting endotherm (the peak temperature of which is denoted in reference [36] as the high-melting peak temperature T_{mh}) is attributed to the melting of the crystallites re-crystallized during a heating scan. Thus, the triple-melting behavior of sPP observed in subsequent melting endotherms in DSC can be best described as the contributions from: 1) melting of the secondary crystallites and their re-crystallization, 2) partial melting of the less stable fraction of the primary crystallites and their re-crystallization, 3) melting of the primary crystallites, and lastly 4) re-melting of the re-crystallized crystallites formed during the heating scan.

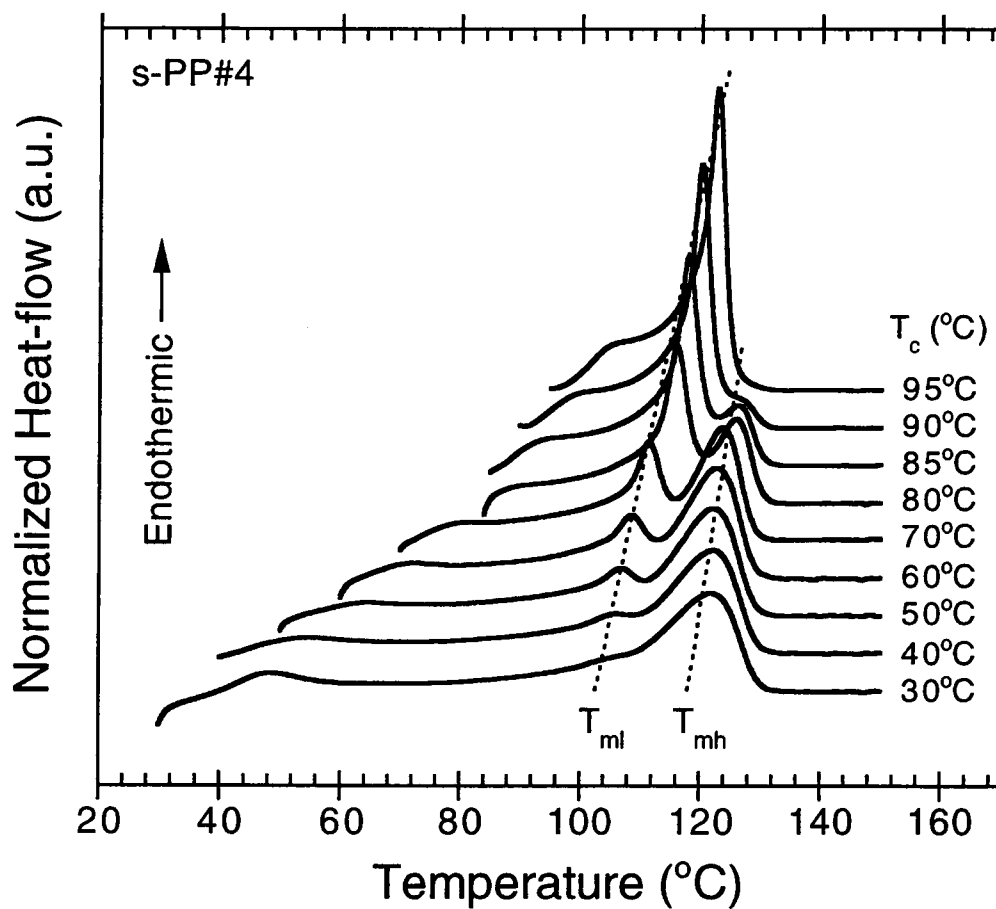


Figure 8-4. Subsequent melting thermograms observed in DSC using a heating rate of $20^{\circ}\text{C}\cdot\text{min}^{-1}$ for sPP#4 samples isothermally crystallized at various crystallization temperatures T_c , ranging from 30°C to 95°C .

5. DISCUSSION

Table 8-1 summarizes values of the WAXD degree of crystallinity χ_c^{WAXD} , the maximum scattering vector q_{max} , the long period L_B , and the melting (peak) temperature of the primary crystallites formed at corresponding T_c (i.e., the peak temperature of the low-temperature melting endotherm $T_{\text{ml}} = T_m$). If the assumption of the two-phase system is valid, the lamellar thickness l_c can be evaluated as the multiplication product of the WAXD degree of crystallinity and the long period, i.e.,

$$l_c = L_B \cdot \chi_c^{\text{WAXD}}. \quad (8-3)$$

The lamellar thicknesses l_c calculated using Equation (8-3) are also summarized in Table 8-1. It is apparent, according to Table 8-1, that the degree of crystallinity χ_c^{WAXD} , the long period L_B , the lamellar thickness l_c , and the melting temperature T_m are all found to increase with increasing crystallization temperature, at least within the temperature range studied. This is owing to the fact that crystals formed at high crystallization temperatures T_c are more stable (thicker) than those formed at lower T_c . Since the lamellar thickness l_c of the primary crystals formed at a given T_c has a definite relationship with the observed melting temperature T_m of these crystals according to the Gibbs-Thomson equation [37]:

$$T_m = T_m^0 \left(1 - \frac{2\sigma_e^{\text{GT}}}{\Delta H_f^0} \cdot \frac{1}{l_c} \right), \quad (8-4)$$

where T_m^0 is the equilibrium melting temperature (i.e., the melting temperature of the crystalline lamellae of infinite thickness), σ_e^{GT} is the interfacial free energy for forming the basal plane of the lamellae, and ΔH_f^0 is the equilibrium enthalpy of fusion for the crystalline phase, the observed melting temperature of the primary crystals is then expected to increase with increasing crystallization temperature T_c . It is worth mentioning that Equation (8-4) is valid only for lamellae whose lateral dimensions (i.e., the width of the growth fronts) are much larger than their thickness, which is generally

true for most cases and it should be applicable to the case of sPP.

According to Equation (8-4), the equilibrium melting temperature T_m^0 of the polymer of interest may be evaluated more accurately by extrapolating a plot of the observed melting temperature T_m versus the reciprocal value of the lamellar thickness l_c^{-1} (i.e., T_m versus l_c^{-1} plot) to $l_c^{-1} = 0$, at which point the y-intercept is taken as the value of the equilibrium melting temperature T_m^0 . Figure 5 shows a Gibbs-Thomson plot of the observed T_m - l_c^{-1} data summarized in Table 8-1. The bulk of the data was fitted to a linear curve-fitting procedure and is given by (i.e., the line $T_m(l_c^{-1})$)

$$T_m(l_c^{-1}) = 166.3 - \frac{189.2}{l_c} \quad (r^2 = 0.979). \quad (8-5)$$

It should be noted that the units of T_m and l_c are in [$^{\circ}\text{C}$] and [nm], respectively. Accordingly, Equation (8-5) gives us the value of the equilibrium melting temperature T_m^{GT} (i.e., $T_m(l_c^{-1} \rightarrow 0)$) to be $166.3 \pm 0.5^{\circ}\text{C}$ (data points at $T_c = 30, 40,$ and 50°C are excluded from the extrapolation: these data points are excluded on the basis that the low-temperature melting endotherms are not well resolved).

According to Equation (8-4), the basal interfacial free energy σ_e^{GT} can also be evaluated from the slope of the line $T_m(l_c^{-1})$ (cf. Equation (8-5)), provided that the value of the equilibrium enthalpy of fusion ΔH_f^0 is *a priori* known. In principle, the value of the equilibrium enthalpy of fusion ΔH_f^0 can be estimated from the observed enthalpy of fusion ΔH_f and a knowledge of the degree of crystallinity, i.e.,

$$\Delta H_f^0 = \frac{\Delta H_f}{\chi_c^{\text{WAXD}}}. \quad (8-6)$$

In this case, the enthalpy of fusion of the sample crystallized at $T_c = 95^{\circ}\text{C}$ (i.e., $\Delta H_f = 36.5 \pm 0.2 \text{ J}\cdot\text{g}^{-1}$) was chosen based on the fact that the enthalpic contribution from the melting of the crystals recrystallized during the heating scan is minimal. According to Equation (8-6), the equilibrium enthalpy of fusion ΔH_f^0 for this particular sPP resin is

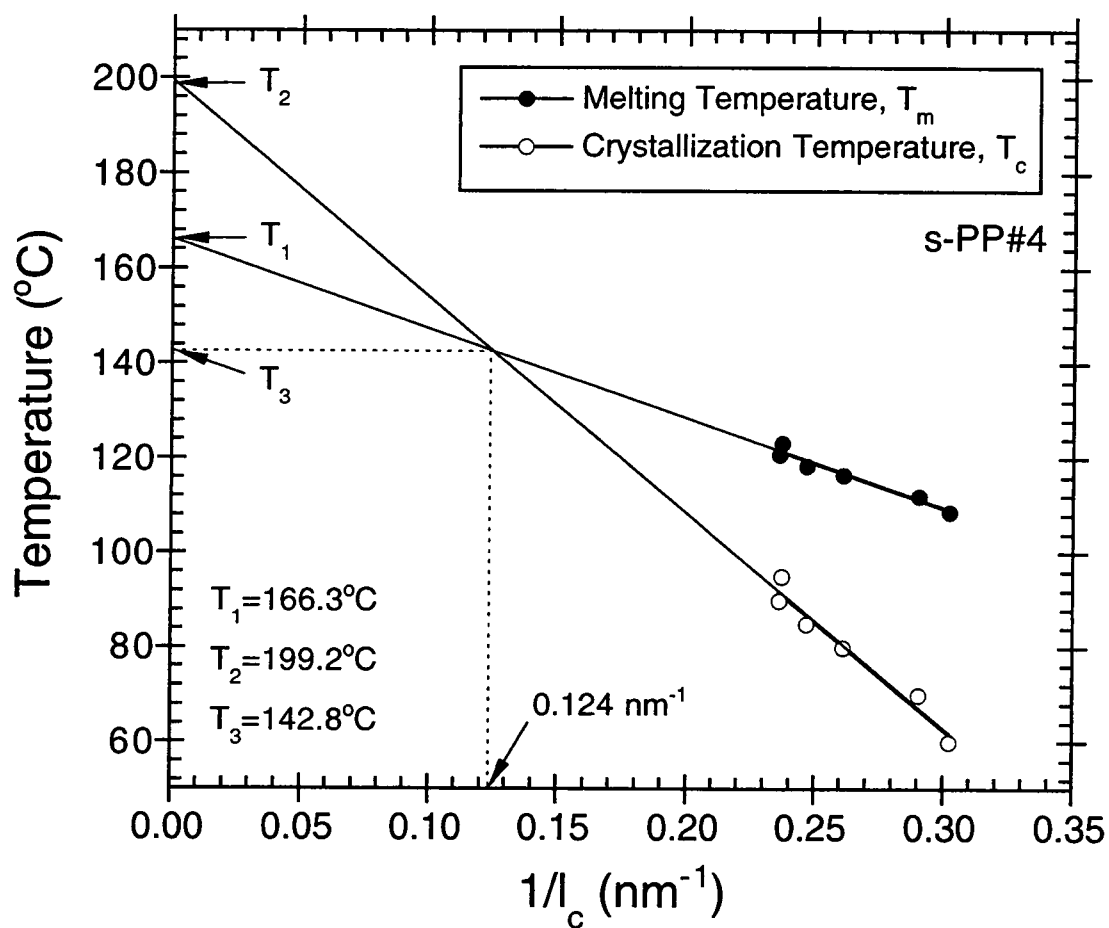


Figure 8-5. Relations between the inverse lamellar thickness l_c^{-1} , the observed melting temperature T_m , and the crystallization temperature T_c obtained for sPP#4 samples isothermally crystallized at various crystallization temperatures T_c ranging from 60°C to 95°C. T_1 represents $T_m(l_c^{-1} \rightarrow 0)$, T_2 represents $T_c(l_c^{-1} \rightarrow 0)$, and T_3 represent T_m^{LHW} .

then found to be $109.3 \pm 0.5 \text{ J}\cdot\text{g}^{-1}$ or $4.6 \text{ kJ}\cdot\text{mol}^{-1}$, and finally gives us the value of the basal interfacial free energy σ_e^{GT} to be $57.8 \pm 0.3 \text{ mJ}\cdot\text{m}^{-2}$.

Analogous to the apparent linear relationship in the plot of the observed $T_m-l_c^{-1}$ data, a plot of the crystallization temperature T_c as a function of the reciprocal value of the lamellar thickness l_c^{-1} , also shown in Figure 8-5, clearly demonstrates that a linear relationship in the $T_c-l_c^{-1}$ data is also observed. Clearly, the bulk of the data can be described by a linear relationship similar to the line $T_m(l_c^{-1})$ (as dictated by Equation (8-4)). When curve-fitting the bulk of the data to a linear relationship similar to that exhibited in Equation (8-5), the following equation (i.e., the line $T_c(l_c^{-1})$) is obtained:

$$T_c(l_c^{-1}) = 199.2 - \frac{454.6}{l_c} \quad (r^2 = 0.981). \quad (8-7)$$

Again, the units of T_c and l_c are in $[\text{°C}]$ and $[\text{nm}]$, respectively. Even though the line $T_c(l_c^{-1})$ does not have theoretical support at this point, some interesting experimental observations related to the relationship between the lines $T_c(l_c^{-1})$ and $T_m(l_c^{-1})$ have to be addressed.

First, a crossing of the lines $T_c(l_c^{-1})$ and $T_m(l_c^{-1})$ at a finite lamellar thickness (i.e., $l_c^{T_c=T_m} = 8.1 \text{ nm}$) is evident in Figure 8-5. By referring to the *linear* Hoffman-Weeks extrapolation method [38] (cf. later), the crossing of the lines $T_c(l_c^{-1})$ and $T_m(l_c^{-1})$ gives us nothing else but the value of the equilibrium melting temperature T_m^0 according to this method (i.e., $T_m^{\text{LHW}} = 142.8\text{°C}$). Clearly, this value is much lower than the value obtained from the Gibbs-Thomson extrapolation (i.e., $T_m^{\text{GT}} = 166.3\text{°C}$ versus $T_m^{\text{LHW}} = 142.8\text{°C}$). The fact that the T_m^{LHW} value was found at a finite value of the lamellar thickness led Schmidtke et al. [39] to suggest that the T_m^{LHW} value only represents the temperature at which point the crystal growth mechanism is free from the kinetic effects such that perfect crystals are immediately formed. Based on this notion, the T_m^{LHW} value obtained from the *linear* Hoffman-Weeks procedure does not necessarily represent the true

equilibrium melting temperature T_m^0 of the polymer of interest, but may be taken as a lower limit (i.e., $T_m^0 > 142.8^\circ\text{C}$ for this particular sPP resin).

Secondly, it was shown in the recent study of Hauser et al. [40] that the relationship between the crystallization temperature T_c and the reciprocal value of the lamellar thickness l_c^{-1} , in the form of the line $T_c(l_c^{-1})$, for sPP and syndiotactic poly(propene-co-octene) (sP(P-co-O)) samples of varying defect contents fall on a common line (cf. Figure 12 in reference [40] or Figure 1 in reference [41]). They found that the extrapolation of the common line $T_c(l_c^{-1})$ to $l_c^{-1} = 0$ gives a value (i.e., $T_c(l_c^{-1} \rightarrow 0) = 193^\circ\text{C}$ according to Equation (31) in reference [39]) approaching the value of the equilibrium melting temperature T_m^0 of a perfect sPP (i.e., $(T_m^0)_{100\%} = 196^\circ\text{C}$) [39,40]. Surprisingly, extrapolation of the $T_c-l_c^{-1}$ data to $l_c^{-1} = 0$ suggests the value of $T_c(l_c^{-1} \rightarrow 0)$ to be 199.2°C , which is very close to the value given by Schmidtke et al. [39]. Comparison of Equation (8-7), which describes the relationship of $T_c-l_c^{-1}$ data of the sPP resin, to Equation (31) in reference [39], which describes the relationship of $T_c-l_c^{-1}$ data of sPP and sP(P-co-O) resins used in references [40,41], indicates that the data line up extremely well on the common line $T_c(l_c^{-1})$ shown in Figure 12 in reference [40] or in Figure 1 in reference [41], with the $T_c-l_c^{-1}$ data being very comparable to those of the sP(P-co-O)15 sample which have a comparable amount of total defects to the sPP sample (i.e., 9.4% (mol of total defects) in sP(P-co-O)15 versus 11.8% (mol of meso defects) in the sample).

Let us now pay a closer attention to the relationship between the observed melting temperature T_m and the crystallization temperature T_c . Two methods have been proposed to describe the observed T_m-T_c data, and obtain the equilibrium melting temperature T_m^0 of the polymer of interest as a result. These methods are 1) *linear* Hoffman-Weeks extrapolation (LHW) [38], and 2) *non-linear* Hoffman-Weeks extrapolation (NLHW) [42].

In the *linear* Hoffman-Weeks extrapolation method, if l_c^* denotes the critical lamellar thickness as dictated in the classical Lauritzen-Hoffman secondary nucleation theory (the LH secondary nucleation theory) [37], in order to prevent the growing crystal from melting at its own crystallization temperature T_c the average initial lamellar thickness l_c^* has to be some number (i.e., δl_c) greater than the critical lamellar thickness. This results in the average initial lamellar thickness l_c^* observed at an arbitrary T_c being in the form:

$$l_c^* = \frac{2\sigma_c}{\Delta f} + \delta l_c \approx \frac{2\sigma_c T_m^0}{\Delta H_f^0 \Delta T} + \delta l_c, \quad (8-8)$$

where Δf is the free enthalpy per unit volume of the crystal and δl_c is a quantity related to very small thickening of the crystals and is a very weak function of temperature.

If the thickening behavior of the crystals can be expressed by an introduction of the thickening ratio $\beta^{\text{LHW}} = l_c/l_c^* \geq 1$ (for a coherent two-dimensional nucleation process), the observed melting point T_m of a crystal which has been thickened by a factor β^{LHW} can be expressed by

$$T_m = T_m^0 \left(1 - \frac{2\sigma_c}{\Delta H_f^0} \cdot \frac{1}{\beta^{\text{LHW}} l_c^*} \right). \quad (8-9)$$

In the case where β^{LHW} equals 1 or δl_c equals 0 (i.e., non-thickening), the crystals growing at an arbitrary crystallization temperature T_c will melt simultaneously (i.e., $T_m = T_c$), thus Equation (8-9) becomes

$$T_c = T_m^0 \left(1 - \frac{2\sigma_c}{\Delta H_f^0} \cdot \frac{1}{l_c^*} \right). \quad (8-10)$$

Based on Equations (8-9) and (8-10), Hoffman and Weeks [38] were able to derive a very useful equation which allows determination of the equilibrium melting temperature T_m^0 from a series of the observed melting temperatures T_m of crystals crystallized at crystallization temperatures T_c :

$$T_m = \frac{T_c}{2\beta^{\text{LHW}}} + T_m^0 \left[1 - \frac{1}{2\beta^{\text{LHW}}} \right]. \quad (8-11)$$

According to Equation (8-6), linear extrapolation of observed T_m - T_c data to the line $T_m = T_c$ yields the equilibrium melting temperature T_m^0 value, and yields the thickening ratio β^{LHW} from the slope. This type of plot is hereafter referred to as the *linear* Hoffman-Weeks extrapolation. The factor 2 in Equation (8-11) suggests that the thickness of the crystals undergoing melting is approximately double that of the initial critical thickness.

The *linear* Hoffman-Weeks extrapolation was carried out on the observed T_m - T_c data listed in Table 8-1 and the result is displayed in Figure 8-6. According to the extrapolation, the equilibrium melting temperature as suggested by this method is found to be $T_m^{\text{LHW}} = 142.8^\circ\text{C}$ with the thickening ratio β^{LHW} and the correlation coefficient of the fit r^2 being 1.2 and 0.998, respectively (cf. long-dashed line in Figure 8-6). If two other sets of the observed T_m - T_c data (which have been measured earlier using DSC (cf. Table 4 in reference [13] (cf. Table 2-4 in Part 2) and Table 1 in reference [36] (cf. Table 6-1 in Part 6)) are included in the extrapolation, the resulting values of T_m^{LHW} , β^{LHW} , and r^2 are respectively found to be 143.9°C , 1.2, and 0.998 (cf. short-dashed line in Figure 8-6). The fact that the difference in the two T_m^{LHW} values is only ca. 1°C suggests to us that the data collected in this study and the other two reports are satisfactorily reliable and accurate.

As mentioned previously, the equilibrium melting temperature as suggested by the LHW extrapolation method (i.e., T_m^{LHW}) does not represent the true equilibrium melting temperature T_m^0 of the polymer of interest, since it was shown in the case that the T_m^{LHW} value was found at a finite value of the lamellar thickness (i.e., $l_c^{T_m=T_c} = 8.1$ nm). Moreover, Marand et al. [42] recently demonstrated using high density polyethylene (HDPE) as the model system that the accuracy of the T_m^{LHW} value to the true equilibrium melting temperature T_m^0 depends significantly on the range of the

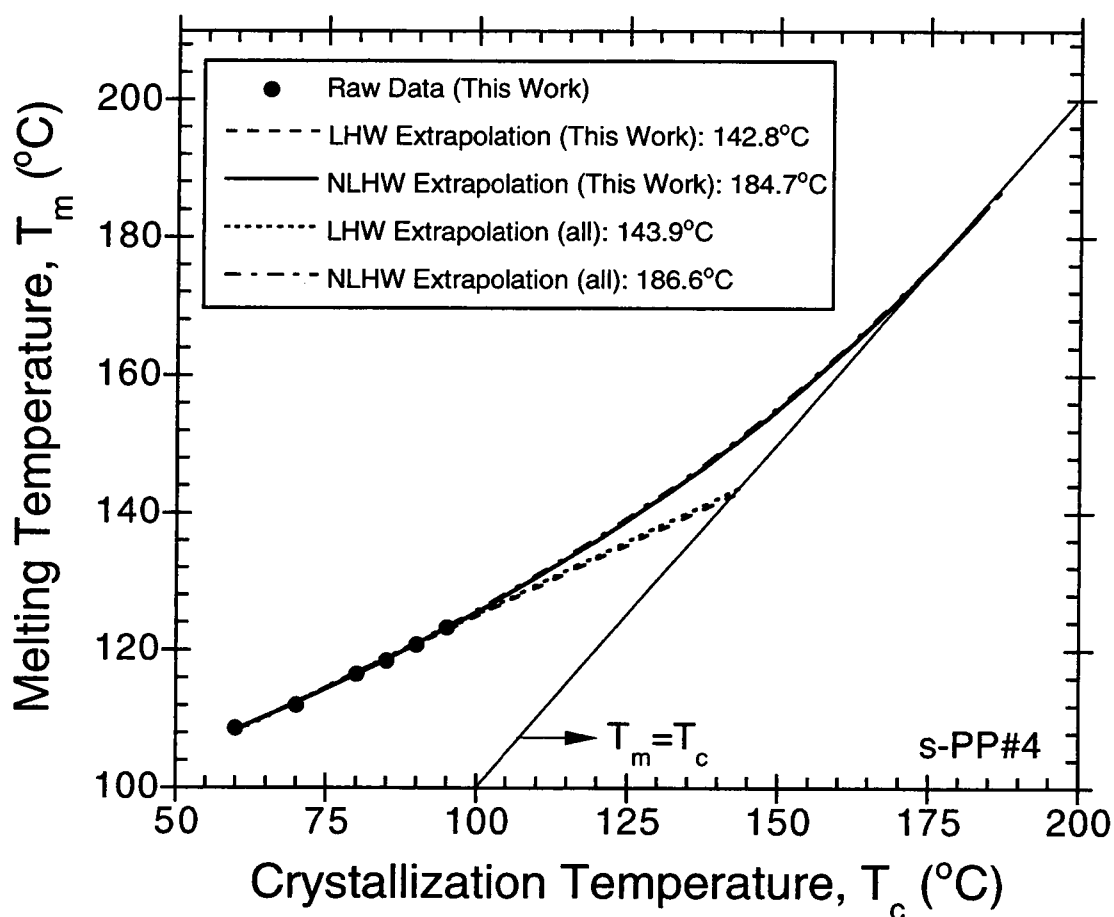


Figure 8-6. Plot of the observed T_m versus T_c (without the data points at $T_c = 30, 40,$ and 50°C). The long-dashed line is the *linear* HW extrapolation based on experimental data points (\bullet). The solid line is the *non-linear* HW extrapolation calculated using $\beta^m = 1, a = 2.34,$ and $T_m^{\text{NLHW}} = 184.7^\circ\text{C}$. The short-dashed line is the *linear* HW extrapolation based on experimental data of this study (\bullet) and those reported earlier in references 13 and 36 (not shown). The alternating-dashed line is the *non-linear* HW extrapolation calculated using $\beta^m = 1, a = 2.25,$ and $T_m^{\text{NLHW}} = 186.6^\circ\text{C}$.

observed T_m - T_c data. The closer this range is to the true equilibrium melting temperature T_m^0 , the better is the accuracy of the T_m^{LHW} value obtained. In practice however, the closer the range of the observed T_m - T_c data is to the true equilibrium melting temperature T_m^0 , the more extensive the lamellar thickening process becomes, especially in the cases of flexible semi-crystalline polymers which exhibit significant α -relaxation (e.g., HDPE, isotactic polypropylene (iPP), etc.).

In HDPE, the lamellar thickening process is responsible for the curvature observed in the observed T_m - T_c data when they are collected over wide enough temperature range and, according to Alamo et al. [43], these data can be divided into three regions. The first region corresponds to the lowest crystallization temperature range. Within this range, the thickness of the crystallites is less sensitive to changes in T_c , therefore the observed T_m is essentially only slightly dependent on T_c . The second region corresponds to the highest crystallization temperature range. Within this range, prolonged crystallization time is needed in order to allow for the completion of the crystallization process. During this time period, the initial nuclei can undergo excessive thickening even before the bulk reaches 5-10% crystallinity [43]. The extent of the thickening process is a function of both time and crystallization temperature. The third region corresponds to the temperature range intermediate to both extremes. In this range, linearity in the plot of observed T_m versus T_c is evident, and it is the region to which the linear Hoffman-Weeks procedure can be applied.

Even though Alamo et al. [43] provided to some extent an explanation on the curvature observed in the T_m - T_c data, they did not provide a solution in order to cope with this experimental fact. Recently, Marand et al. [42] was able to provide a theoretical explanation to the curvature observed in the T_m - T_c data collected over a wide temperature range and provided a convincing demonstration of the new theory on HDPE, which they have chosen as their model system. In addition, the theory provides

a new method of determining the equilibrium melting temperature T_m^0 of the polymer of interest from the observed T_m-T_c data. This method is hereafter called the *non-linear* Hoffman-Weeks extrapolation.

Based on the proposition made by Lauritzen and Passaglia [44] on stem length fluctuations during chain folding, the fold surface free energy associated with a nucleus of critical size σ_e^{GT} accounting for the extra lateral surface free energy due to fold protrusion and for the mixing entropy associated with stems of different lengths (cf. σ_e^{GT} in the Gibbs-Thomson equation) can be expressed as a function of undercooling as

$$\sigma_e^{GT} = \sigma_e^1(1 + \zeta\Delta T), \quad (8-12)$$

where σ_e^1 is the interfacial energy associated with the basal plane of the mature crystallite and can be estimated from the slope of l_c^* versus ΔT^{-1} [37,45], and ζ is a temperature coefficient of roughly 0.0025 K^{-1} estimated for the case of HDPE [37,45]. Using Equation (8-12) as a platform, Marand et al. [42] re-wrote the equation for the initial lamellar thickness (i.e., Equation (8-8)) as

$$l_c^* = \frac{2\sigma_e^1 T_m^0}{\Delta H_f^0 \Delta T} + \frac{2\sigma_e^1 \zeta T_m^0}{\Delta H_f^0} + \delta l_c = \frac{D_1}{\Delta T} + D_2, \quad (8-13)$$

where D_1 and D_2 are constants, and all other parameters are the same as previously defined. Equation (8-13) is able to explain the discrepancy between the thickening parameter measured experimentally (i.e., D_2 in Equation (8-8)) and that calculated based on theoretical consideration (i.e., δl_c in Equation (8-8)) [42].

Combination of Equations (8-4), (8-12) and (8-13) leads Marand et al. [42] to propose a new method, so-called the *non-linear* Hoffman-Weeks extrapolation, for the analysis of observed T_m-T_c data based on the equation of the form:

$$\frac{T_m^0}{T_m^0 - T_m} = \beta^m \frac{\sigma_e^1}{\sigma_e^{GT}} \left[\frac{T_m^0}{T_m^0 - T_c} + \frac{D_2 \Delta H_f^0}{2\sigma_e^1} \right], \quad (8-14a)$$

or in a simpler form:

$$M = \beta^m \frac{\sigma_e^1}{\sigma_e^{GT}} (X + a), \quad (8-14b)$$

where β^m is the thickening ratio and has the same physical meaning as β^{LHW} used earlier, and all other parameters are the same as previously defined. It is worth noting that for most cases it is safe to assume that $\sigma_e^1 = \sigma_e^{GT}$ [42]. Precautionary remarks for using the *non-linear* Hoffman-Weeks procedure were addressed in detail in the original publication by Marand et al. [42].

In order to apply Equation (8-14) for the analysis of the experimental T_m - T_c data in real polymer systems, it is required that the observed T_m data be collected from samples crystallized at different temperatures but having the same lamellar thickening coefficient β^m . For each set of the observed T_m - T_c data, corresponding values of M and X in Equation (8-14) can be calculated for a given choice of the equilibrium melting temperature T_m^0 . For the case of $\sigma_e^1 = \sigma_e^{GT}$, the true equilibrium melting temperature T_m^0 is taken as the seed T_m^0 value which results in the plot of M versus X being a straight line with slope of unity (i.e., $\beta^m = 1$) and intercept of a (i.e., $a = D_2 \Delta H_f^0 / 2 \sigma_e^1$). Since it was shown earlier that lamellar thickening does not occur in sPP during crystallization, at least within the crystallization temperature range studied, it is reasonable to assume that the observed T_m data summarized in Table 8-1 were collected from lamellae having the same thickening coefficient β^m , thus enabling them to be analyzed using this method.

Figure 8-7 shows variation of the M versus X , calculated from the data shown in Table 8-1 according to Equation 8-14, for different choices of the seed temperature. The equilibrium melting temperature as suggested by this method (i.e., T_m^{NLHW}) for this particular sPP sample is found to be 184.7°C (for $\beta^m = 1$). The value of a associated with the resulting T_m^0 value can be determined from the y-intercept of the plot of M versus X and it is found to be 2.34. The *non-linear* Hoffman-Weeks extrapolation of the observed T_m - T_c data summarized in Table 8-1 is also shown in Figure 8-6 as the solid

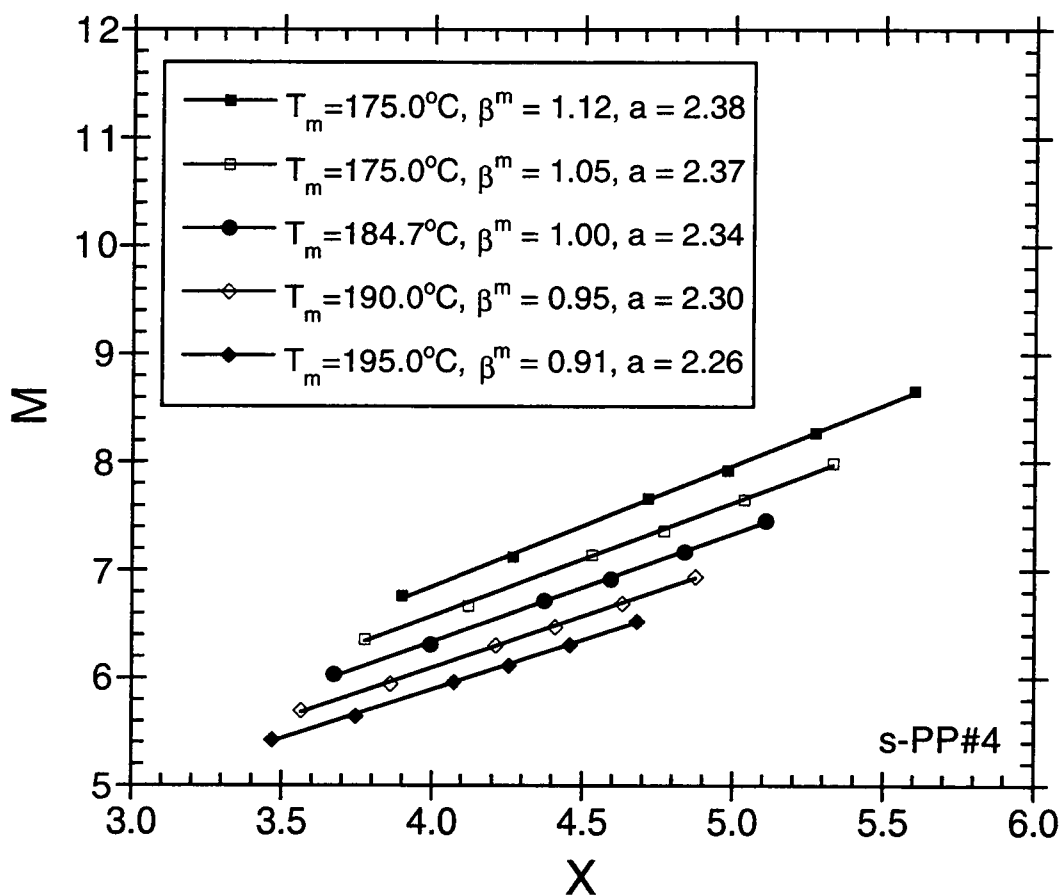


Figure 8-7. Plots of the scaled observed melting temperature $M = T_m^0 / (T_m^0 - T_m)$ against the scaled crystallization temperature $X = T_m^0 / (T_m^0 - T_c)$ for various choices of the seeded equilibrium melting temperature T_m^0 for the observed T_m - T_c data of this study (without the data points at $T_c = 30, 40,$ and 50°C).

line. It should be noted that the correlation coefficient r^2 of the fit obtained for both methods suggest that the *non-linear* Hoffman-Weeks extrapolation gives a better fit to the set of the data than the *linear* Hoffman-Weeks extrapolation does ($r^2 = 0.999$ in NLHW versus $r^2 = 0.998$ in LHW).

Again, if two other sets of the observed T_m - T_c data carried out earlier using DSC (cf. Table 4 in reference [13] (or Table 2-4 in Part 2) and Table 1 in reference [36] (or Table 6-1 in Part 6)) are included in the extrapolation, the resulting values of T_m^{NLHW} , a , and r^2 which result in β^m being 1 are respectively found to be 186.6°C, 2.25, and 0.999. Plots of the M versus X , calculated for all of the data sets, for different choices of the seed temperature are shown in Figure 8-8, while the resulting *non-linear* Hoffman-Weeks extrapolation is also included in plots shown in Figure 8-6 as the alternating-dashed line (raw data for the other two data sets are not shown).

Finally, I would like to end the discussion with the observed temperature dependence of the initial lamellar thickness l_c^* . Since it has been shown in pervious study using DSC technique that lamellar thickness of sPP does not thicken during crystallization process [36] (cf. Part 6), it is reasonable to assume that the initial lamellar thickness l_c^* is equivalent to the experimental values of the lamellar thickness l_c summarized in Table 8-1. This allows one to model the experimental data according to Equation (8-13). In order to use Equation (8-13) to fit the experimental data, *a priori* knowledge of equilibrium melting temperature T_m^0 is required. It is shown, in this study, that by using different methods of determining the equilibrium melting temperature T_m^0 four different values are obtained: 1) from the Gibbs-Thomson extrapolation method, $T_m^{GT} = T_m(l_c^{-1} \rightarrow 0) = 166.3^\circ\text{C}$; 2) from the extrapolation of T_c - l_c^{-1} data to $l_c^{-1} = 0$, $T_c(l_c^{-1} \rightarrow 0) = 199.2^\circ\text{C}$; 3) from the *linear* Hoffman-Weeks extrapolation method, $T_m^{LHW} = 142.8^\circ\text{C}$; and 4) from the *non-linear* Hoffman-Weeks extrapolation method, $T_m^{NLHW} = 184.7^\circ\text{C}$. Of the four values, only $T_m^{GT} = 166.3^\circ\text{C}$ and $T_m^{NLHW} =$

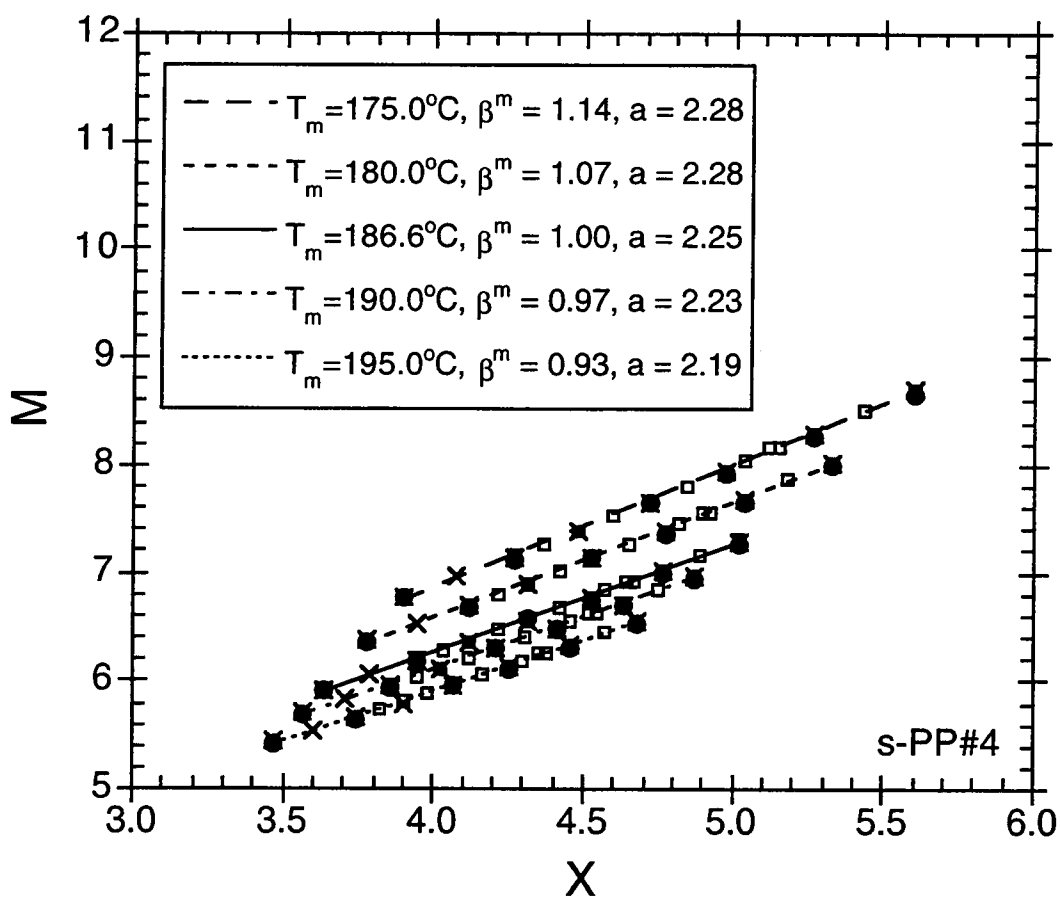


Figure 8-8. Plots of the scaled observed melting temperature $M = T_m^0 / (T_m^0 - T_m)$ against the scaled crystallization temperature $X = T_m^0 / (T_m^0 - T_c)$ for various choices of the seeded equilibrium melting temperature T_m^0 for the observed T_m - T_c data of this study (●) and those reported earlier in references 13 (□) and 36 (×).

184.7°C have solid theoretical basis and either of the values can therefore be taken as the true equilibrium melting temperature T_m^0 of this particular sPP resin. It is not possible, however, to explain the discrepancy between the two values at this point.

Figure 8-9 shows a plot of the lamellar thickness l_c as a function of crystallization temperature T_c (data points at $T_c = 30, 40,$ and 50°C are excluded from the plot). According to the best fit for a given choice of the true equilibrium melting temperature T_m^0 , the temperature dependence of the initial lamellar thickness l_c^* for sPP can be written as

$$l_c^* = \frac{2248.2}{166.3 - T_c} + 11.9 \quad (r^2 = 0.972), \quad (8-15)$$

or

$$l_c^* = \frac{3321.7}{184.7 - T_c} + 6.3 \quad (r^2 = 0.975), \quad (8-16)$$

if choices of $T_m^0 = 166.3$ and 184.7°C are used, respectively. It should be noted that the units of l_c^* and T_c in Equations (8-15) and (8-16) are given in [\AA] and [$^\circ\text{C}$], respectively. Instead, if one is to estimate the temperature dependence of the initial lamellar thickness l_c^* for sPP based on theoretical ground (i.e., $D_1 = 2\sigma_e^1 T_m^0 / \Delta H_f^0$ and $D_2 = 2\sigma_e^1 a / \Delta H_f^0$, where $\sigma_e^1 = \sigma_e^{\text{GT}} = 57.8 \text{ mJ}\cdot\text{m}^{-2}$, $T_m^0 = 184.7^\circ\text{C}$, $\Delta H_f^0 = 4.6 \text{ kJ}\cdot\text{mol}^{-1}$, and $a = 2.34$), one arrives at the following equation:

$$l_c^* = \frac{2100.7}{184.7 - T_c} + 26.6, \quad (8-17)$$

where the units of l_c^* and T_c in Equations (8-15) and (8-16) are given in [\AA] and [$^\circ\text{C}$], respectively. The estimated temperature dependence of the initial lamellar thickness l_c^* for sPP based on Equation (8-17) are also plotted in Figure 8-9 as the solid line. Evidently, the estimated curve over-predicts the size of the initial lamellar thickness l_c^* at a given crystallization temperature. This discrepancy will be a subject of further investigation.

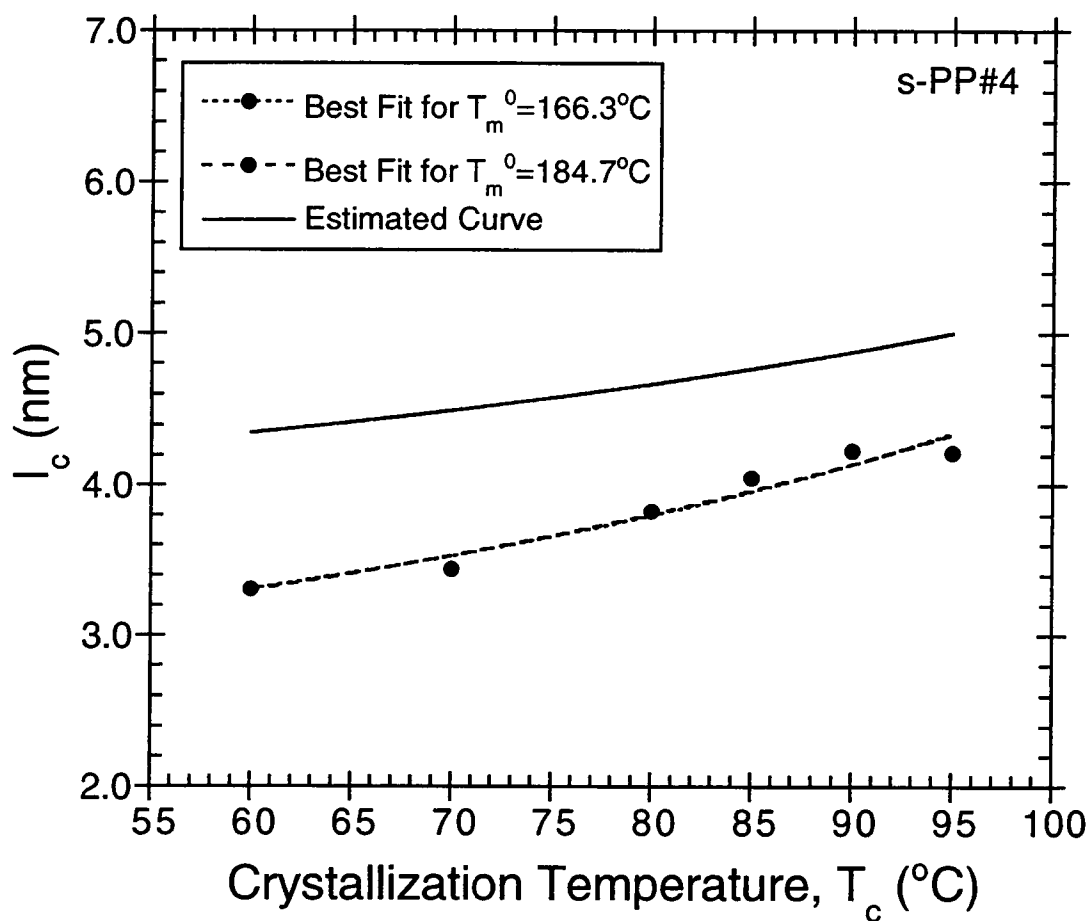


Figure 8-9. Plot of lamellar thickness l_c as a function of the crystallization temperature T_c (without the data points at $T_c = 30, 40,$ and 50°C). The short- and long-dashed lines are the best fits of the experimental data (\bullet) according to Equation (8-13) when T_m^0 is taken as 166.3°C and 184.7°C , respectively. The solid line is the estimated curve calculated according to Equation (8-13) using $\sigma_e^1 = \sigma_e^{\text{GT}} = 57.8 \text{ mJ}\cdot\text{m}^{-2}$, $T_m^0 = 184.7^\circ\text{C}$, $\Delta H_f^0 = 4.6 \text{ kJ}\cdot\text{mol}^{-1}$, and $a = 2.34$.

6. CONCLUSIONS

In this present part, WAXD, SAXS and DSC techniques were employed to investigate the lamellar morphology information and subsequent melting behavior of sPP samples isothermally crystallized at crystallization temperatures ranging from 30°C to 95°C. All of the samples investigated were found to crystallize in the high temperature, orthorhombic limit-disordered form I. The degree of crystallinity χ_c^{WAXD} , the long period L_B , the lamellar thickness l_c , and the melting temperature T_m were all found to increase with increasing crystallization temperature. The equilibrium enthalpy of fusion ΔH_f^0 was found to be $109.3 \pm 0.5 \text{ J}\cdot\text{g}^{-1}$ or ca. $4.6 \text{ kJ}\cdot\text{mol}^{-1}$. The Gibbs-Thomson extrapolation suggested the values of the equilibrium melting temperature T_m^{GT} and the basal interfacial free energy σ_e^{GT} to be ca. 166.3°C and ca. $57.8 \text{ mJ}\cdot\text{m}^{-2}$, respectively, while the *linear* and *non-linear* Hoffman-Weeks extrapolation methods gave the values of the equilibrium melting temperature, T_m^{LHW} and T_m^{NLHW} , to be ca. 142.8°C and ca. 184.7°C, respectively. Finally, the equilibrium melting temperature of perfect sPP sample $(T_m^0)_{100\%}$ was estimated to be ca. 199.2°C.

7. REFERENCES

- [1] Natta, G.; Pasquon, I.; Corradini, P.; Peraldo, M.; Pegoraro, M.; and Zambelli, A. *Rend. Acc. Naz. Lincei*. **1960**, *28*, 539.
- [2] Natta, G.; Pasquon, I.; and Zambelli, A. *J. Am. Chem. Soc.* **1962**, *84*, 1488.
- [3] Ewen, J.A.; Johns, R.L.; Razavi, A.; and Ferrara, J.D. *J. Am. Chem. Soc.* **1988**, *110*, 6255.
- [4] Rodriguez-Arnold, J.; Bu, Z.; and Cheng, S.Z.D. *J. Macromol. Sci.-Rev. Macromol. Chem. Phys.* **1995**, *C35*, 117.
- [5] Wheat, W.R. *SPE-ANTEC Proc.* **1995**, 2275.
- [6] Schardl, J.; Sun, L.; Kimura, S.; and Sugimoto, R. *J. Plastic Film & Sheeting* **1996**, *12*, 157.
- [7] Sun, L.; Shamsoum, E.; and DeKunder, G. *SPE-ANTEC Proc.* **1996**, 1965.
- [8] Wheat, W.R. *SPE-ANTEC Proc.* **1997**, 565.
- [9] Gownder, M. *SPE-ANTEC Proc.* **1998**, 1511.
- [10] Sura, R.K.; Desai, P.; and Abhiraman, A.S. *SPE-ANTEC Proc.* **1999**, 1764.
- [11] Rodriguez-Arnold, J.; Zhang, A.; Cheng, S.Z.D.; Lovinger, A.J.; Hsieh, E.T.; Chu, P.; Johnson, T.W.; Honnell, K.G.; Geerts, R.G.; Palackal, S.J.; Hawley, G.R.; and Welch, M.B. *Polymer* **1994**, *35*, 1884.
- [12] Supaphol, P.; Hwu, J.J.-J.; Phillips, P.J.; and Spruiell, J.E. *SPE-ANTEC Proc.* **1997**, 1759.
- [13] Supaphol, P. and Spruiell, J.E. *J. Appl. Polym. Sci.* accepted on April 16, 1999.
- [14] Rodriguez-Arnold, J.; Bu, Z.; Cheng, S.Z.D.; Hsieh, E.T.; Johnson, T.W.; Geerts, R.G.; Palackal, S.J.; Hawley, G.R.; and Welch, M.B. *Polymer* **1994**, *35*, 5194.
- [15] Supaphol, P. and Spruiell, J.E. *Polymer* accepted on March 25, 1999.
- [16] Bu, Z.; Yoon, Y.; Ho, R.-M.; Zhou, W.; Jangchud, I.; Eby, R.K.; Cheng, S.Z.D.; Hsieh, E.T.; Johnson, T.W.; Geerts, R.G.; Palackal, S.J.; Hawley, G.R.; and Welch, M.B. *Macromolecules* **1996**, *29*, 6575.
- [17] Supaphol, P. and Spruiell, J.E. *J. Appl. Polym. Sci.* accepted on April 4, 1999.
- [18] Wignall, G.D.; Lin, J.-S.; and Spooner, S. *J. Appl. Cryst.* **1990**, *23*, 241.
- [19] Russell, T.P.; Lin, J.-S.; Spooner, S.; and Wignall, G.D. *J. Appl. Cryst.* **1988**, *21*, 629.
- [20] Corradini, P.; Natta, G.; Ganis, P.; and Temussi, P.A. *J. Polym. Sci.* **1967**, *C16*, 2477.
- [21] Lotz, B.; Lovinger, A.J.; and Cais, R.E. *Macromolecules* **1988**, *21*, 2375.
- [22] Lovinger, A.J.; Lotz, B.; and Davis, D.D. *Polymer* **1990**, *31*, 2253.
- [23] Chatani, Y.; Maruyama, H.; Noguchi, K.; Asanuma, T.; and Shiomura, T. *J. Polym. Sci.* **1990**, *C28*, 393.
- [24] Lovinger, A.J.; Davis, D.D.; and Lotz, B. *Macromolecules* **1991**, *24*, 552.
- [25] Chatani, Y.; Maruyama, H.; Asanuma, T.; and Shiomura, T. *J. Polym. Sci., Polym. Phys.* **1991**, *29*, 1649.
- [26] Lovinger, A.J.; Lotz, B.; Davis, D.D.; and Padden, F.J. *Macromolecules* **1993**, *26*, 3494.
- [27] De Rosa, C. and Corradini, P. *Macromolecules* **1993**, *26*, 5711.

- [28] Auriemma, F.; De Rosa, C.; and Corradini, P. *Macromolecules* **1993**, *26*, 5719.
- [29] De Rosa, C.; Auriemma, F.; and Corradini, P. *Macromolecules* **1996**, *29*, 7452.
- [30] De Rosa, C.; Auriemma, F.; and Vinti, V. *Macromolecules* **1997**, *30*, 4137.
- [31] Lovinger, A.J. and Lotz, B. *J. Polym. Sci., Polym. Phys.* **1997**, *35*, 2523.
- [32] Auriemma, F.; De Rosa, C.; Ruiz de Ballesteros, O.; Vinti, V.; and Corradini, P. *J. Polym. Sci., Polym. Phys.* **1998**, *36*, 395.
- [33] De Rosa, C.; Auriemma, F.; Vinti, V.; Grassi, A.; and Galimberti, M. *Polymer* **1998**, *39*, 6219.
- [34] De Rosa, C.; Auriemma, F.; and Vinti, V. *Macromolecules* **1998**, *31*, 7430.
- [35] De Rosa, C.; Talarico, G.; Caporaso, L.; Auriemma, F.; Galimberti, M.; and Fusco, O. *Macromolecules* **1998**, *31*, 9109.
- [36] Supaphol, P. and Spruiell, J.E. *J. Polym. Sci., Polym. Phys.* submitted for publication.
- [37] Hoffman, J.D.; Davis, G.T.; and Lauritzen Jr., J.I. In *Treatise on Solid State Chemistry*; Hannay, N.B., Ed.; Plenum Press: New York, 1976; Vol. 3; Chapter 7.
- [38] Hoffman, J.D. and Weeks, J.J. *J. Res. Nat'l. Bur. Stand.* **1962**, *A66*, 13.
- [39] Schmidtke, J.; Strobl, G.; and Thurn-Albrecht, T. *Macromolecules* **1997**, *30*, 5804.
- [40] Hauser, G.; Schmidtke, J.; and Strobl, G. *Macromolecules* **1998**, *31*, 6250.
- [41] Hugel, T.; Strobl, G.; and Thomann, R. *Acta Polym.* **1999**, *50*, 214.
- [42] Marand, H.; Xu, J.; and Srinivas, S. *Macromolecules* **1998**, *31*, 8219.
- [43] Alamo, R.G.; Viers, B.D.; and Mandelkern, L. *Macromolecules* **1995**, *28*, 3205.
- [44] Lauritzen Jr., J.I. and Passaglia, E. *J. Res. Nat'l. Bur. Stand.* **1967**, *A61*, 261.
- [45] Hoffman, J.D. and Miller, R.L. *Polymer* **1997**, *38*, 3151.

PART 9:

**USE OF DSC MELTING ENDOTHERMS FOR STUDYING
ISOTHERMAL BULK CRYSTALLIZATION OF SEMICRYSTALLINE
POLYMERS AT LOW DEGREES OF UNDERCOOLING: A CASE
STUDY IN SYNDIOTACTIC POLYPROPYLENE**

1. ABSTRACT

In this present study, a technique of using differential scanning calorimeter (DSC) to study crystallization behavior and the kinetics of the process at high crystallization temperatures or low degrees of undercooling is presented, using syndiotactic polypropylene (sPP) as the model system. The technique was carried out based on the observations of, and the measurements of the enthalpy of fusion from, the subsequent melting endotherms after isothermal crystallization for various time intervals. In addition to the determination of crystallization kinetics parameters, the technique allows for an accurate determination of the induction time. It also gives an insight into certain mechanistic aspects of crystallization process as it occurs at different time intervals.

2. INTRODUCTION

Differential scanning calorimetry (DSC) is an excellent tool used to follow thermal transitions of polymers. Since much of the historical significance and many of the applications of DSC, as a thermal analytical device, can be found in an excellent monograph by Wunderlich [1], it is appropriate to start a discussion on uses of DSC in studying crystallization and subsequent melting processes of semicrystalline polymers, some of which can be summarized as the following [2-4]:

- 1) To determine thermodynamic properties associated with the crystallization process (e.g., crystallization temperature T_c , enthalpy of crystallization ΔH_c , etc.), and the kinetics parameters (e.g., the half-time of crystallization $t_{0.5}$, etc.) of crystallization process under both isothermal and non-isothermal conditions.

- 2) To determine thermodynamic properties associated with the melting process (e.g., melting temperature T_m , enthalpy of fusion ΔH_f , etc.), and the kinetics of the melting process.
- 3) To determine the final apparent degree of crystallinity $\chi_{c,\infty}$ in polymer samples after crystallization at the condition of interest.

It is of interest, in this study, to focus on using DSC in studying crystallization, including the kinetics of the process, and subsequent melting behavior of semi-crystalline polymers under isothermal conditions. Traditionally, studies on isothermal crystallization kinetics of polymer in DSC have been based on the information obtained from the crystallization exotherms [2-4]. Though proven to be a very quick and efficient technique, utilization of crystallization exotherms in studying crystallization kinetics can only be applied to certain conditions where the signal can be reliably detected by the instrument. In other conditions, an alternative technique of using subsequent melting endotherms in studying crystallization kinetics had been suggested by Hay and his colleague [2,4].

To the best of my knowledge, there are only very limited number of publications, which utilized the technique of using subsequent melting endotherms in studying crystallization kinetics, available, even though the technique was suggested by Hay and his colleague [2,4] over twenty years ago. Therefore, in the present study, use of subsequent melting endotherms in studying crystallization, including the kinetics of the process, and subsequent melting behavior of semi-crystalline polymers will be critically investigated, using syndiotactic polypropylene (sPP) as the model materials. It will be demonstrated that the technique is suitable for studying crystallization kinetics of polymers at high temperatures (or low degrees of undercooling), where the traditional technique is not applicable. Reliability and applicability of the technique will be tested

by comparing the experimental results, measurements of which are carried out at some temperatures where both techniques can be applied.

3. USE OF DSC IN STUDYING CRYSTALLIZATION OF POLYMERS

3.1. The General Technique of DSC

Figure 9-1 illustrates a typical crystallization exotherm after complete crystallization at $T_c = 77.5^\circ\text{C}$. Crystallization is assumed to begin at point A, which is preceded by a short period in which the temperature of the sample is equilibrated to T_c . Increasing heat flow due to evolution of the enthalpy of crystallization is evident until a maximum is observed at point B. The rate of evolution of the enthalpy of crystallization depends strongly on the kinetics of the crystallization process, which is very sensitive to changes in crystallization temperature T_c . After point B, crystallization slows down significantly, and the measurement is terminated (i.e., at point C) when no more noticeable change in the heat flow is detected.

Intuitively, during crystallization of semi-crystalline polymers under isothermal conditions, it is assumed that the observed heat flow is directly proportional to the weight of the sample w , the enthalpy of crystallization ΔH_c and the instantaneous crystallization rate $\dot{\theta}(t)$. The enthalpy of crystallization is a multiplication product of the final degree of crystallinity $\chi_{c,\infty}$ and the enthalpy of crystallization of an infinitely thick crystal ΔH_c^0 (i.e., 100% crystalline sample). Consequently, one may write an equation for the heat flow as

$$\dot{Q} = c_1 \cdot w \cdot \chi_{c,\infty} \cdot \Delta H_c^0 \cdot \dot{\theta}(t), \quad (9-1)$$

where c_1 is a combined physical constant specific for each DSC used.

By setting $\dot{q} = \dot{Q} / (c_1 \cdot w \cdot \chi_{c,\infty} \cdot \Delta H_c^0)$, the relative crystallinity $\theta(t)$ can be obtained by integration of the transient normalized heat flow $\dot{q}(t)$ over the course of the crystallization. One finally gets

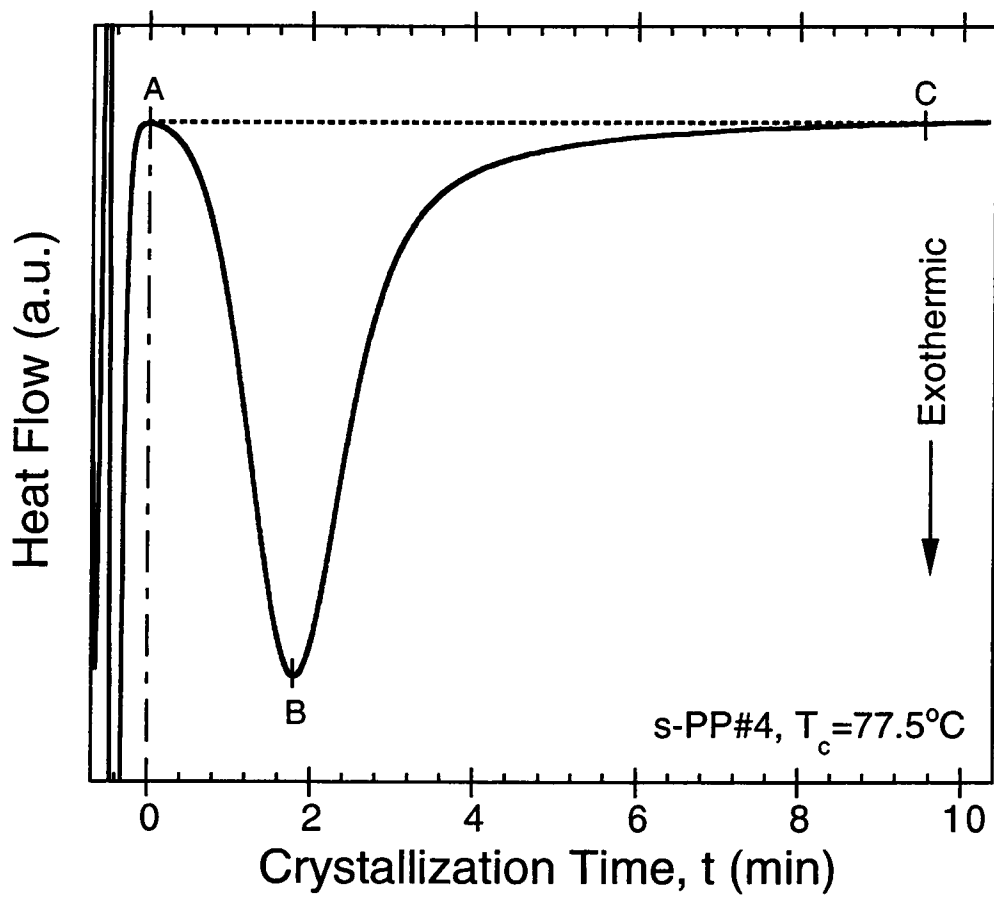


Figure 9-1. Typical crystallization exotherm data of sPP sample isothermally crystallized at $T_c = 77.5^\circ\text{C}$.

$$\theta(t) = \int_0^t \dot{\theta}(t') dt' = \int_0^t \dot{q}(t') dt'. \quad (9-2)$$

Figure 9-2 shows a plot of relative crystallization $\theta(t)$ as a function of crystallization time t , which was calculated from the heat flow data shown in Figure 9-1 according to Equation (9-2). An important parameter, which can be obtained very easily from the relative crystallinity plot similar to Figure 9-2, is the half-time of crystallization $t_{0.5}$, which is defined as the time spent from the onset of the crystallization to the point where the crystallization is 50% complete. It should be noted that the reciprocal of the crystallization half-time (i.e., $t_{0.5}^{-1}$) is often used to characterize the overall rate of the crystallization process.

Even though DSC has been used successfully to follow crystallization of semi-crystalline polymers through crystallization exotherms, a number of limitations associated with the instrument itself needs to be discussed. Since what DSC really measures during the course of crystallization is the rate of evolution of heat, as mentioned previously, the technique is intuitively limited by the sensitivity of the detectors, which somewhat varies from one instrument to another. One of the most important limitations is to use DSC to study isothermal crystallization of polymers at high crystallization temperatures T_c (or at low degrees of undercooling ΔT , defined as $T_m^0 - T_c$). At such conditions, the signal-to-noise ratio becomes too small, causing a problem to the determination of the baseline in the signal obtained. Without a proper baseline, the following problems may arise: 1) inaccuracy in the determination of the onset of crystallization, and hence the inaccuracy in the determination of the induction period t_0 ; and 2) incorrect conversion of the experimental data to the relative crystallization $\theta(t)$, and hence dubious crystallization kinetics parameters obtained.

Due to the aforementioned limitations, the traditional technique of using DSC to follow crystallization of polymers can only be applied within a limited range of

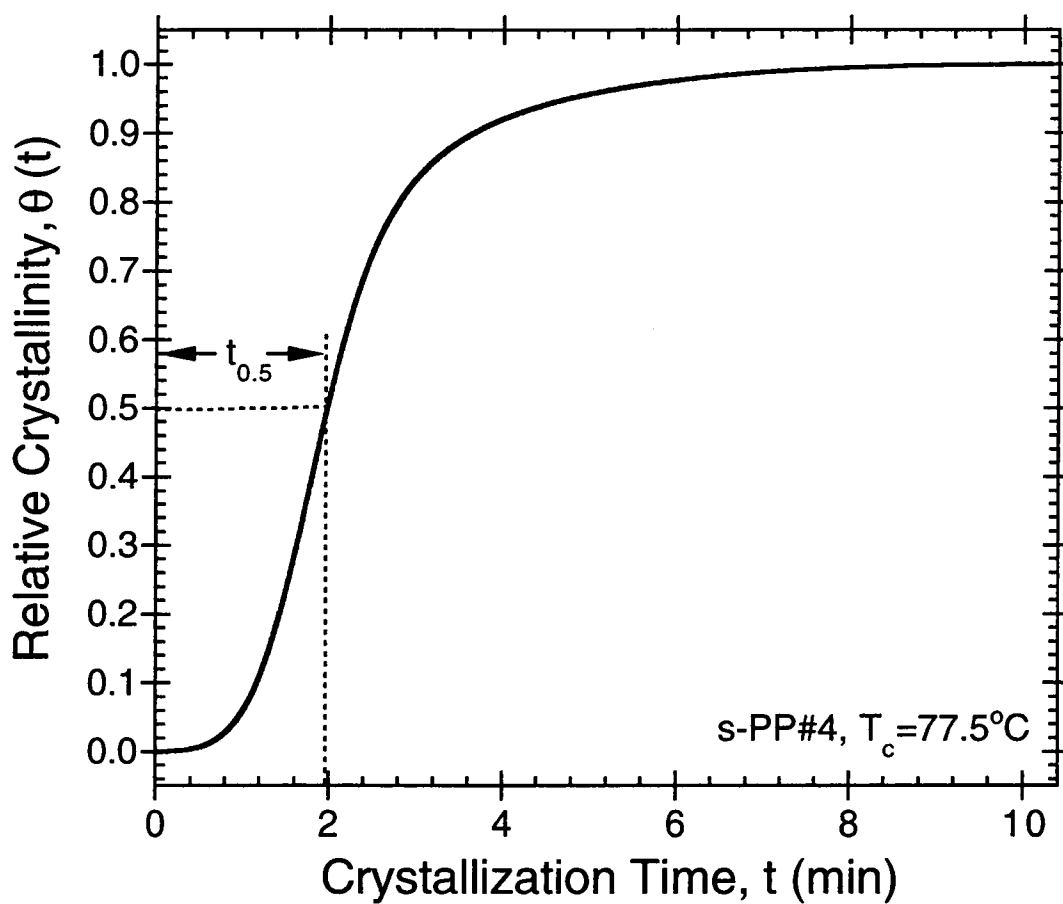


Figure 9-2. Typical relative crystallinity $\theta(t)$ as a function of crystallization time t , calculated from the raw data shown in Figure 9-1 according to Equation (9-2).

crystallization temperatures where the total time for the completion of crystallization does not take too long (this is limited greatly by the sensitivity of the DSC one is using). To overcome this particular problem, it will be demonstrated in this study that it is possible to extend the use of DSC to follow crystallization of semi-crystalline polymers at high crystallization temperatures T_c (or low degrees of undercooling ΔT) by measuring the enthalpy of fusion $\Delta H_{f,t}$ of crystallites developed at T_c during crystallization at various crystallization times (i.e., partial and complete crystallization).

For the first approximation, it is assumed that the crystallization at T_c ends when there is no significant change being observed in $\Delta H_{f,t}$ value after a long crystallization time, that is

$$\lim_{t \rightarrow \infty} \Delta H_{f,t} = \Delta H_{f,\infty} \quad (9-3)$$

where $\Delta H_{f,\infty}$ denotes the final value of enthalpy of fusion of the crystallites formed at T_c . As a result of this assumption (i.e., Equation (9-3)), it is now possible to calculate the relative crystallinity $\theta(t)$ according to the following equation:

$$\theta(t) = \frac{\Delta H_{f,t}}{\Delta H_{f,\infty}}, \quad (9-4)$$

which will be used for further analysis using an appropriate macrokinetics model.

3.2. Determination of Crystallization Kinetics Parameters

In addition to the half-time of crystallization $t_{0.5}$ and its reciprocal value $t_{0.5}^{-1}$, which can be determined directly from the experimental plot of relative crystallinity $\theta(t)$ as a function of crystallization time t , other kinetics parameters can also be determined, using an appropriate macrokinetics model. For the purpose of describing the macroscopic evolution of primary crystallinity under quiescent isothermal conditions, three major models have been proposed thus far. They are 1) the *Avrami model* [5-11], 2) the *Tobin model* [12-14], and 3) the *Malkin model* [15]. Since critical comparison

among the three models in describing the primary crystallization of polymers (in the case of sPP, please see reference [16] (cf. Part 5)) is not of prime concern in this study, only the well known *Avrami model* will be used to analyze the experimental data.

Based primarily on the notion of microscopic mechanisms of primary nucleation and subsequent crystal growth, the Avrami equation describing steady-state isothermal phase transformation is given by [5-11]

$$\theta(t) = \frac{\chi_{c,t}}{\chi_{c,\infty}} = 1 - \exp(-k_a t^{n_a}), \quad (9-5)$$

where $\theta(t)$ denotes the relative crystallinity as a function of time (cf. Equation (9-2)), $\chi_{c,t}$ is the apparent degree of crystallinity at an arbitrary time t during the course of crystallization process, $\chi_{c,\infty}$ is the final apparent degree of crystallinity, k_a is the Avrami crystallization rate constant, and n_a is the Avrami exponent of time. Both n_a and k_a are constants typical of a given crystalline morphology and type of nucleation for a particular crystallization condition [17].

According to the original assumptions of the theory, the value of n_a should be integral, ranging from 1 to 4 [7-9]. Analysis of the experimental data based on the Avrami equation, in most cases however, leads to fractional values of the Avrami exponent n_a . Even though possible explanations for this discrepancy were given elsewhere [16], the non-integral observations of the Avrami exponent n_a may be relieved based on the *simultaneous Avrami model* [16,18], which was postulated on the observations of dual transient nucleation mechanisms (i.e., instantaneous and sporadic nucleation), and the *Ding-Spruiell* version of the Avrami equation [11], which accounts for the fractional values of n_a through the introduction of the *nucleation index* [11].

Analysis of the experimental data based on the Avrami equation is straight forward. The Avrami kinetics parameters, k_a and n_a , can be graphically extracted from a least-square line fitted to the double logarithmic plot of $\ln[-\ln(1-\theta(t))]$ versus $\ln(t)$, where

k_a is taken as the anti-logarithmic value of the y-intercept and n_a the slope of the least-square line. Normally, the kinetics parameters are calculated from the least-square line drawn through the bulk of the data in the range of $0.10 < \theta(t) < 0.80$ (where a straight line portion is usually observed for most semi-crystalline polymers). An alternative method for extracting the kinetics parameters is to fit the experimental data directly to the appropriate macrokinetics models using a non-linear multi-variable regression program (i.e., the data-fitting method), which has proven to be a fast, effective and reliable method of analyzing the kinetics data [16] (cf. Part 5).

4. EXPERIMENTAL DETAILS

4.1. Materials

The sPP sample (i.e., sPP#4) used in this study was synthesized using a metallocene catalyst and was produced commercially in pellet form by Fina Oil and Chemical Company of La Porte, Texas. Molecular characterization data, which were kindly performed by Dr. Roger A. Phillips and his group at Montell USA, Inc. in Elkton, Maryland, shows the following molecular weight information: $M_n = 81,300$ daltons, $M_w = 171,000$ daltons, $M_z = 294,000$ daltons, and $M_w/M_n = 2.1$. In addition, the syndiotacticity measured by ^{13}C NMR shows the racemic dyad content [%*r*] to be 89.2%, the racemic triad content [%*rr*] to be 84.4%, and the racemic pentad content [%*rrrr*] to be 74.6%.

4.2. Sample Preparation

Sliced pellets were melt-pressed between a pair of Kapton films, which in turn were sandwiched between a pair of thick metal plates, in a Wabash compression molding machine preset at a temperature of 190°C and a pressure of 67 kpsi. After ten minutes holding time at the preset condition, a film of ca. 290 μm thickness was taken out and allowed to cool at ambient condition down to room temperature between the

two metal plates. This treatment assumes that previous thermo-mechanical history was essentially erased, and provides a standard crystalline memory condition for our experiments.

4.3. Technique and Experimental Methods

A Perkin-Elmer Series 7 Differential Scanning Calorimeter (DSC7) was used to follow isothermal crystallization and subsequent melting behavior of sPP. The DSC7 equipped with internal liquid nitrogen cooling unit reliably provided a cooling rate up to $200^{\circ}\text{C}\cdot\text{min}^{-1}$. Temperature calibration was performed using a pure indium standard ($T_m^0 = 156.6^{\circ}\text{C}$ and $\Delta H_f^0 = 28.5 \text{ J}\cdot\text{g}^{-1}$). Calibration of the temperature scale was performed every other run to ensure accuracy and reliability of the data obtained. To make certain that thermal lag between the polymer sample and the DSC sensors is kept to a minimum, each sample holder was loaded with a single disc, weighing $7.1 \pm 0.3 \text{ mg}$, which was cut from the standard as-prepared film. It is noteworthy that each sample was used only once and all the runs were carried out under nitrogen purge.

In order to use DSC to follow crystallization behavior of polymers, which in this case is sPP, at high crystallization temperatures T_c (or at low degrees of undercooling ΔT), the proposed technique of measuring the enthalpy of fusion $\Delta H_{f,t}$ in subsequent melting endotherms after isothermal crystallization for various time intervals at T_c will be used in this study. Even though, in this study, the purpose of the technique is to use DSC to study crystallization behavior of sPP at high T_c values, the proposed technique was also applied to observe crystallization behavior and the kinetics of the process at moderate T_c values of 75°C , 90°C , and 95°C for comparison with the results obtained previously [19] (cf. Part 2) based on the traditional technique. The proposed technique was finally applied to study crystallization behavior and its kinetics for $T_c = 100^{\circ}\text{C}$ and 105°C , which can not be studied in the DSC when the traditional technique was used,

due primarily to high level of noise-to-signal ratio observed in the heat flow data. Experimental data were analyzed based on the Avrami equation (cf. Equation (9-5)) using the data-fitting method [16] (cf. Part 5).

5. RESULTS AND DISCUSSION

5.1. Origination of the Proposed Technique

Figure 9-3 illustrates some representative DSC melting thermograms of sPP#4 after partial crystallization at $T_c = 75^\circ\text{C}$ for 1.0, 1.5, 1.7, 2.0, 2.5, and 8.0 min, respectively; whereas, Figure 9-4 shows DSC melting thermograms after partial crystallization at $T_c = 95^\circ\text{C}$ for 15, 20, 25, 30, 40, and 50 min, respectively. The heating rate used in all of the scans was $20^\circ\text{C}\cdot\text{min}^{-1}$. At $T_c = 75^\circ\text{C}$, a time interval of at least 0.5 min was required for a melting peak to be observed in the subsequent melting endotherm (not shown). Similarly, a time period of at least 5 min was needed for a melting peak to be observed in the subsequent melting endotherm after isothermal crystallization at $T_c = 95^\circ\text{C}$. For the first approximation, the time intervals of ca. 0.5 and 5 min correspond to the induction time t_0 needed for stable crystallites to be formed at $T_c = 75^\circ\text{C}$ and 95°C , respectively. It should be kept in mind that accuracy of the observed induction time is likely to vary from one technique (and its sensitivity) used to another. In principle, it is possible, however, to precisely determine the induction time t_0 , but it is a very tedious task and may not be necessary if the precise t_0 value is not of prime concern.

Another interesting phenomenon which can be observed directly from plots of melting thermograms after isothermal crystallization at various time intervals is the occurrence of the secondary crystallization. At $T_c = 75^\circ\text{C}$, it is clearly seen that a small endothermic shoulder (peak) located at the low temperature region is clearly discernable in the DSC thermogram after isothermal crystallization for 8 min. At $T_c = 95^\circ\text{C}$, distinguishable endothermic shoulder (peak) is apparent in the DSC thermograms after

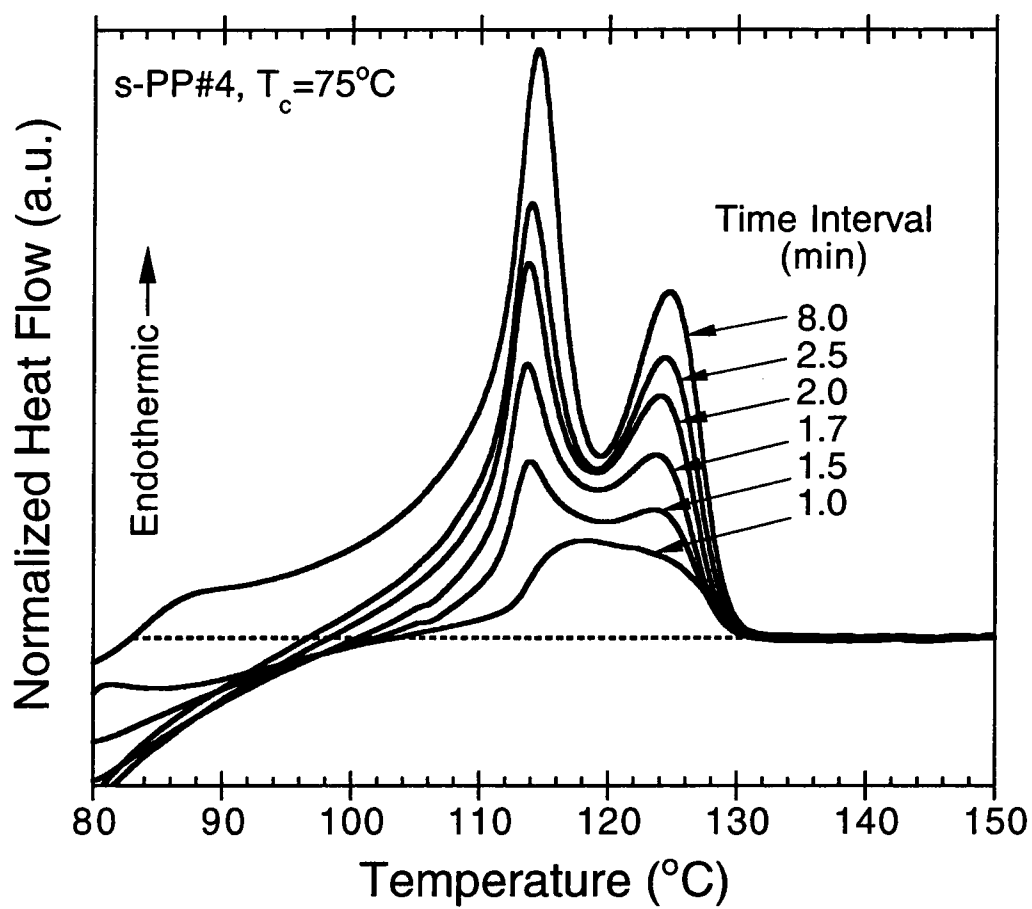


Figure 9-3. DSC subsequent melting endotherms ($20^\circ\text{C}\cdot\text{min}^{-1}$) of sPP samples after partial crystallization at $T_c = 75^\circ\text{C}$ for different time intervals as indicated.

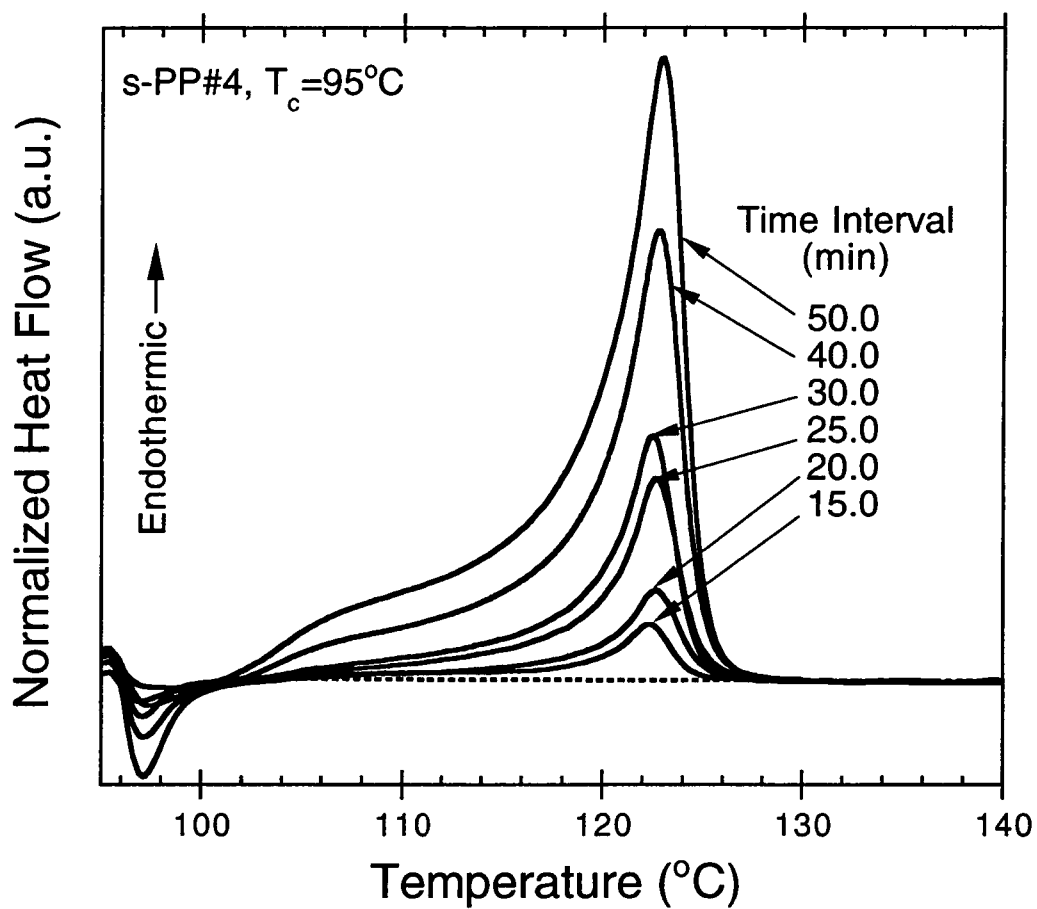


Figure 9-4. DSC subsequent melting endotherms ($20^\circ\text{C}\cdot\text{min}^{-1}$) of sPP samples after partial crystallization at $T_c = 95^\circ\text{C}$ for different time intervals as indicated.

isothermal crystallization for 40 and 50 min. Careful examination of all of the recorded DSC thermograms, however, shows that the appearance of the small endotherms in the DSC thermograms was not clearly observed until an approximate annealing time of ca. 4 min at $T_c = 75^\circ\text{C}$ was reached; whereas, it was ca. 25 min at $T_c = 95^\circ\text{C}$. The position where the small endothermic shoulder is observed in a subsequent melting scan is also interesting, as it always appears close to a temperature where the sample was crystallized (ca. $T_c + 10^\circ\text{C}$).

The facts that the small endotherm 1) is usually observed at a temperature close to the crystallization temperature, 2) is observed at a later stage of crystallization, and 3) increases in its magnitude and possibly shifts to higher temperature with increasing annealing time suggest that the small endotherm is a result of the contribution from a rather slow crystallization mechanism occurring at T_c (i.e., secondary crystallization). Observation of the small endothermic shoulder is not limited to the case of sPP. A number of investigators have reported similar observations in various polymer systems, such as poly(ethylene terephthalate) (PET) [20] and poly(butylene naphthalate terephthalate) (PBNT) copolyesters [21].

Additional important information which can also be observed directly from plots of melting thermograms after partial crystallization at various time intervals is whether or not thickening process occurs during crystallization process in the polymer system studied. In principle, this information can readily be deduced from the position(s) of the primary melting peak(s), which correspond(s) to the primary crystalline aggregates formed during primary crystallization at T_c based on the Gibbs-Thomson equation [22] which correlates the observed melting temperature T_m to the lamellar thickness of the crystallites. The equation is given by

$$T_m = T_m^0 \left(1 - \frac{2\sigma_c}{l_c \Delta H_f^0} \right), \quad (9-6)$$

where T_m^0 is the equilibrium melting temperature (i.e., the melting point of an infinitely thick crystal) of the polymer studied, σ_e is the fold surface free energy, l_c is the lamellar thickness, and ΔH_f^0 is the equilibrium enthalpy of fusion.

It is clearly seen from Figures 9-3 and 9-4 that the positions of the primary melting peak in the subsequent melting endotherms recorded at various time intervals were essentially unchanged, exhibiting the average values of $114.0 \pm 0.3^\circ\text{C}$ for $T_c = 75^\circ\text{C}$ and of $120.4 \pm 0.3^\circ\text{C}$ for $T_c = 95^\circ\text{C}$. According to Equation (9-6), this can only be construed that the thickness of the primary sPP crystallites formed at T_c is essentially constant throughout the crystallization process. This finding agrees extremely well with the observations reported on crystallization behavior of sPP using a real-time SAXS and DSC technique [23-25], in which the original lamellar thickness of sPP is proven to be constant during both the isothermal crystallization and a subsequent heating to the melting point.

It has been shown thus far some possible aspects of using the subsequent melting endotherms recorded after partial crystallization at various time intervals in studying crystallization behavior of sPP, which can very well be applied to other semi-crystalline polymers. At this moment, it is appropriate to elaborate the possibility of using the proposed technique to obtain related crystallization kinetics information. Figure 9-5 shows the relative crystallinity data $\theta(t)$ plotted as a function of time (in logarithmic scale) for $T_c = 75^\circ\text{C}$, 90°C , 95°C , 100°C , and 105°C , respectively. As mentioned previously, the relative crystallinity data $\theta(t)$ were calculated based on the enthalpy of fusion $\Delta H_{t,t}$, measured from the subsequent melting endotherms recorded after isothermal crystallization at various time intervals (see, for examples, Figures 9-3 and 9-4), according to the relationship in Equation (9-4).

By taking a closer examination on the $\Delta H_{t,t}$ data measured from the endotherms such as those shown in Figures 9-3 and 9-4, a couple of possible limitations of the

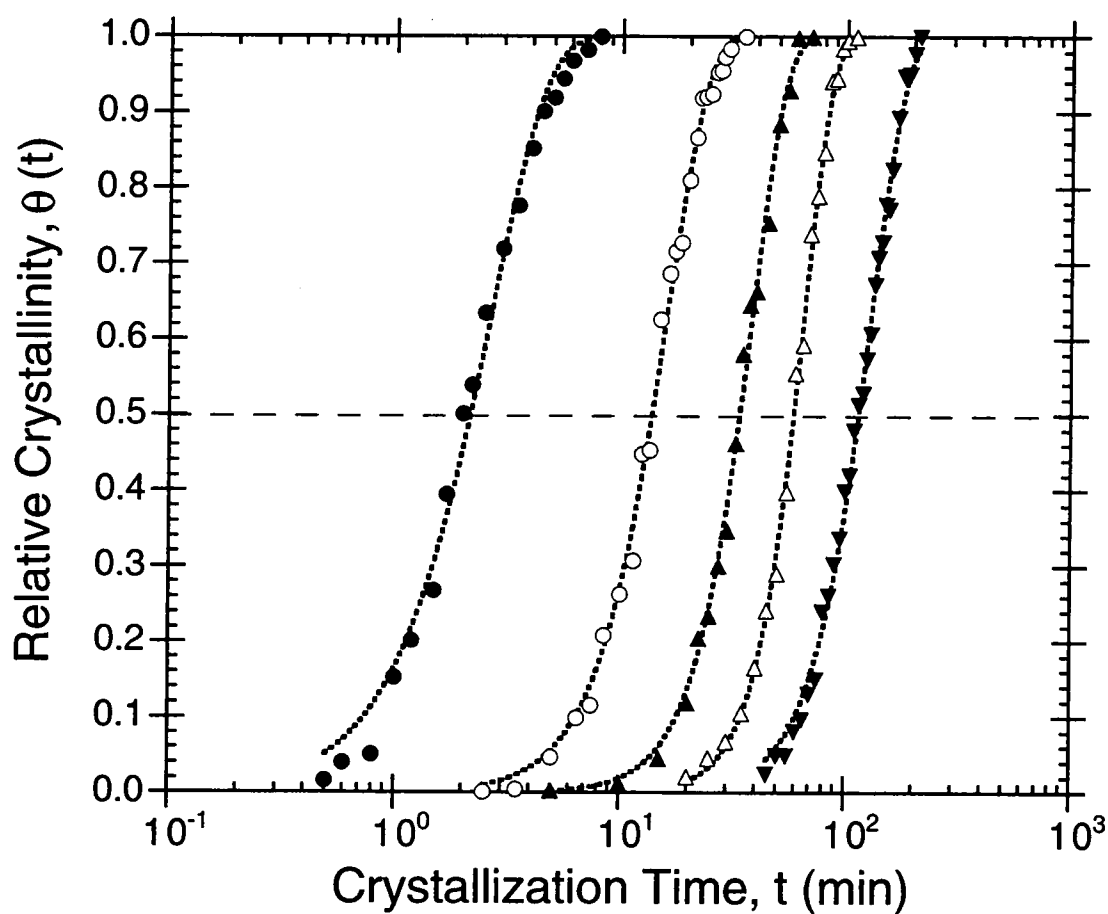


Figure 9-5. Relative crystallinity $\theta(t)$ as a function of crystallization time t (in logarithmic scale) of sPP sample, calculated from enthalpy of fusion ΔH_{t_i} determined from subsequent melting endotherms after isothermal crystallization for various time intervals (cf. Figures 9-3 and 9-4) according to Equation (9-4), for 5 different crystallization temperatures T_c : (●) 75°C; (○) 90°C; (▲) 95°C; (△) 100°C; and (▼) 105°C.

technique need to be addressed. In one, choice of the final value of enthalpy of fusion of the crystalline aggregates formed at T_c (i.e., $\Delta H_{t,\infty}$) can greatly affect the accuracy of the relative crystallinity data $\theta(t)$ obtained. The fact that certain types of secondary crystallization (e.g., crystal perfection and/or lamellar thickening) are slow processes (the mechanisms and the kinetics of these processes are strongly dependent on what type of polymers one is dealing with) which cause a gradual increase in the observed enthalpy of fusion with time makes decisive determination of the final enthalpy of fusion $\Delta H_{t,\infty}$ even more difficult. The problem is even worse in the cases where crystallization occurs at a very high temperature (or low degree of undercooling), since majority of the crystallinity within a growing crystalline aggregate is attributed to the secondary crystallization process.

Another, the procedure used to measure the enthalpy of fusion $\Delta H_{t,t}$ from a melting endotherm also poses another possible problem to the accuracy and reliability of the relative crystallinity data $\theta(t)$ obtained. In this study, the enthalpy of fusion was measured by determining the area under the melting endotherm. The baseline used was taken as the line drawn in parallel to the heat capacity of the polymeric melt (shown in Figures 9-3 and 9-4 as the dotted line). For the technique to be reliable enough, the procedure used to measure the $\Delta H_{t,t}$ data needs to be at least consistent throughout all of the measurements. Different procedures utilized by different experimentalists to determine the $\Delta H_{t,t}$ data also make it difficult to compare data reported from different laboratories. For this reason only, a unified procedure, such as the one used in this study, should be used throughout.

5.2. Determination of Crystallization Kinetics Parameters

As mentioned previously, Figure 9-5 illustrates the relative crystallinity data $\theta(t)$ plotted as a function of time (in logarithmic scale) for $T_c = 75^\circ\text{C}$, 90°C , 95°C , 100°C , and

105°C, respectively. According to Figure 9-5, it is apparent that the values of the induction time t_0 , the crystallization half-time $t_{0.5}$, and the time to reach the final crystallinity increase with increasing crystallization temperature. The induction time t_0 is taken as the time interval the polymeric molecules in the melt state require before stable nuclei can be formed at a studyicular crystallization condition, and by the virtue of this technique it can be determined from the time interval needed for isothermal crystallization at T_c just for a melting peak to be observable in the subsequent melting endotherm (as described in previous section).

The crystallization half-time $t_{0.5}$ can be determined more readily from a plot of $\theta(t)$ versus time t , such as those shown in Figure 9-5. Due to relatively small number of data points acquired at each T_c , it may be necessary to curve-fit the raw data before accurate measurement of the half-time data $t_{0.5}$ can be made. In this study, we directly fitted the raw $\theta(t)$ versus time t data to the Avrami equation (i.e., Equation (9-5)), using a non-linear multi-variable regression program (i.e., data-fitting method). After a curve-fitting was performed on each data set, the crystallization half-time $t_{0.5}$ can be measured as the time interval required for the crystallization process to be half completed (after subtraction of the induction time t_0). Since the Avrami crystallization kinetics parameters, n_a and k_a , are fitting variables, they are automatically provided by the program once the best fit was determined.

Table 9-1 summarizes all of the crystallization kinetics parameters determined from the data shown in Figure 9-5. Related crystallization kinetics parameters (denoted in Table 9-1 as $t_{0.5}^*$, n_a^* , and k_a^*), determined previously based the traditional technique of using crystallization exotherms as basis (i.e., Equation (9-2)) from the relative crystallinity data $\theta(t)$ for moderate crystallization temperatures of 75°C, 90°C, and 95°C, respectively, were also listed for comparison. It should be noted that slight discrepancy between the kinetics parameters reported in reference 19 (cf. Table 2-5) and

Table 9-1. Induction time t_0 and overall Avrami crystallization kinetics data for syndiotactic polypropylene, as determined from the present technique (i.e., $t_{0.5}$, n_a , k_a) and the traditional technique (i.e., $t_{0.5}^*$, n_a^* , k_a^*).

T_c (°C)	t_0 (min)	$t_{0.5}$ (min)	n_a	k_a (min ⁻ⁿ)	$t_{0.5}^*$ (min)	n_a^*	k_a^* (min ⁻ⁿ)
75	0.5	1.58	1.32	3.79×10^{-1}	1.56	2.05	2.75×10^{-1}
90	2.1	11.62	2.10	4.01×10^{-3}	9.80	2.48	2.39×10^{-3}
95	4.9	28.88	2.48	1.65×10^{-4}	30.37	2.91	3.37×10^{-5}
100	7.8	51.12	2.23	2.80×10^{-5}	-	-	-
105	21.5	92.85	3.05	4.18×10^{-6}	-	-	-

those reported in Table 9-1 (i.e., $t_{0.5}^*$, n_a^* , and k_a^*), even though both of the data sets were determined directly from the crystallization exotherms, is due to the fact that those reported in reference 19 (cf. Part 2) were determined from the least-square line fitted to the double logarithmic plot of $\ln[-\ln(1-\theta(t))]$ versus $\ln(t)$, whereas those reported in Table 9-1 were determined using the data-fitting method [16] (cf. Part 5).

According to Table 9-1, it is evident that the induction time t_0 and the crystallization half-time $t_{0.5}$ increase with increasing crystallization temperature. Since the induction time t_0 could not be measured accurately from the crystallization exotherms, comparison between the data obtained from the observation in the crystallization exotherms and those obtained from the observation in the subsequent crystallization endotherms after isothermal crystallization can not be made. On the other hand, the crystallization half-time $t_{0.5}$ as determined from both techniques seem to agree with one another very well, suggesting that the proposed technique of using subsequent melting endotherms in studying crystallization kinetics is at least reliable and applicable to describe isothermal bulk crystallization of sPP at the conditions studied.

In case of the Avrami kinetics analysis, the exponent n_a for primary crystallization is found to be an increasing function of crystallization temperature (within the range studied) and ranges from 1.32 to 3.05. The most likely explanation for the increase of n_a with increasing temperature is based on the fact that the average concentration of athermal nuclei decreases tremendously as the crystallization temperature increases [16,26,27], causing an increase in the number of the homogeneous nuclei at the expense of the number of the heterogeneous nuclei as the crystallization temperature increases. The Avrami rate constant k_a appears to be very sensitive to a change in crystallization temperature, decreasing with an increase in the temperature. This readily suggests that the overall rate of crystallization decreases as crystallization

temperature increases. It should be noted that this observation is only valid when the temperature is in the range where secondary nucleation rate is the rate determining factor (i.e., $T_c \geq \text{ca. } 60^\circ\text{C}$ [19] (cf. Part 2)).

5.3. Further Discussion on the Temperature Dependence of the Induction Time

Recently, a theory for describing temperature dependence of nucleation induction time t_0 was proposed and derived by Lednicky and Muchova [28-33], using the classical theories of primary nucleation [34,35] as basis. The theory offers a way to quantify the induction time data to the primary nucleation theories. The original purpose of the theory is to assess the nature of primary nucleation on foreign surfaces [32,33], e.g., fibers, fillers, etc. Since it is very well known that crystallization in semi-crystalline polymers often starts with primary nucleation on foreign surfaces (or on predetermined nuclei of similar chemical structures), we believe that the theory of the induction time proposed by Lednicky and Muchova [28-33] should be applicable to describe the temperature dependence of the induction time data of sPP, as we shall demonstrate later in this study.

In general, crystallization of polymers from the melt often starts with primary nucleation due to the presence of foreign surfaces, provided that prolonged melting is carried out to ensure complete melting. In heterogeneous nucleation (i.e., crystallization on predetermined surfaces), two mechanisms are involved [29,31,32]: 1) formation of the first layer on the foreign surface which is characterized by the difference in the free energies between the crystallizing species and the surface, and 2) formation of the subsequent layers until the nucleus of critical size is established and the growth process occurs. The induction time t_0 can be expressed as a summation of the time periods for the formation of the first layer (denoted t_h) and for the formation of the subsequent layers (denoted t_s).

Since the time characteristic for each mechanism is inversely proportional to the number of segments capable of nucleation [29,31,32], the equation describing the induction time is given by

$$t_0 = t_h + t_s, \quad (9-7)$$

in which
$$t_h = E_1 \exp\left(-\frac{\Delta G_\eta}{kT_c}\right) \exp\left[\frac{16(\Delta\sigma)\sigma\sigma_c T_m^0}{kT_c(\Delta H_f^0 \Delta T)^2}\right], \quad (9-8)$$

$$t_s = E_2 \left[\frac{2(\Delta\sigma)T_m^0}{(\Delta H_f^0 \Delta T)b_0} - 1 \right] \exp\left(-\frac{\Delta G_\eta}{kT_c}\right) \exp\left[-\frac{4b_0\sigma\sigma_c T_m^0}{kT_c(\Delta H_f^0 \Delta T)}\right], \quad (9-9)$$

where E_1 and E_2 are proportionality constants, ΔG_η is the free energy barrier for the molecular transport across the phase boundary, k is the Boltzman constant, $\Delta\sigma$ is the difference in the interfacial free energy of the crystallizing species and that of the heterogeneous surface, σ is the lateral surface free energy, b_0 is the layer thickness, and others quantities are the same as previously defined.

Muchova and Lednicky [31,32] showed that in some certain circumstances only one of the constituent terms dominates. Specifically, for sufficiently *high* crystallization temperatures, when the number of subsequent layers is much higher than unity (in order for the nucleus to be energetically stable), the time for the formation of the first layer t_h can be neglected. In such a case, the induction time t_0 is approximated by

$$t_0 = E_2 \left[\frac{2(\Delta\sigma)T_m^0}{(\Delta H_f^0 \Delta T)b_0} \right] \exp\left(-\frac{\Delta G_\eta}{kT_c}\right) \exp\left[-\frac{4b_0\sigma\sigma_c T_m^0}{kT_c(\Delta H_f^0 \Delta T)}\right]. \quad (9-10)$$

For some *lower* crystallization temperatures where the number of critical layer approaches unity, the time for the formation of subsequent layers t_s can now be neglected. The induction time t_0 is therefore given by

$$t_0 = E_1 \exp\left(-\frac{\Delta G_\eta}{kT_c}\right) \exp\left[\frac{16(\Delta\sigma)\sigma\sigma_c T_m^0}{kT_c(\Delta H_f^0 \Delta T)^2}\right]. \quad (9-11)$$

It should be noted that, in practice, the transport term, $\exp(\Delta G_\eta/kT_c)$, is often approximated by the William-Landel-Ferry (WLF) equation for viscous flow:

$$\exp\left(\frac{\Delta G_\eta}{kT_c}\right) = \exp\left[\frac{U^*}{R(T_c - T_\infty)}\right], \quad (9-12)$$

where U^* is the activation energy for the transportation of segments of molecules across the melt/solid surface boundary and is commonly given by a universal value of 6,276 J·mol⁻¹ [22], R is the universal gas constant, and T_∞ is the temperature where the molecular motion ceases and is often taken to be about 30 K below the glass transition temperature T_g (ca. -6.1°C for sPP [19]) of the polymer of interest.

In order to approximate the transport term with the WLF expression (i.e., Equation (9-12)) and to account for a temperature dependence of the enthalpy of fusion, Equations (9-10) and (9-11) can be written in a more general form as

$$t_0(T_c) = \frac{\tau_1^1}{(\Delta T)f} \exp\left[\frac{U^*}{R(T_c - T_\infty)} + \frac{K_1^1}{T_c(\Delta T)f}\right], \quad (9-13)$$

and

$$t_0(T_c) = \tau_2^1 \exp\left[\frac{U^*}{R(T_c - T_\infty)} + \frac{K_2^1}{T_c(\Delta T)^2 f^2}\right], \quad (9-14)$$

respectively, where τ_1^1 and τ_2^1 are combined pre-exponential terms, K_1^1 and K_2^1 are combined factors related to nucleation mechanism, and f is a factor used to correct for the temperature dependence of the enthalpy of fusion (i.e., $f = 2T_c/(T_m^0 + T_c)$ [36]).

Figure 9-6 illustrates the relationship of the induction time t_0 as a function of crystallization temperature. Within the temperature range studied, the induction time t_0 increases monotonically as an increase in crystallization temperature. This can be explained based on the fact that, as the crystallization temperature increases, the energy barrier for segments of molecules in the melt state to form clusters of stable nuclei is increasingly enormous, thus requiring longer induction period before the clusters of segments of molecules are able to form stable nuclei. In order to describe the temperature

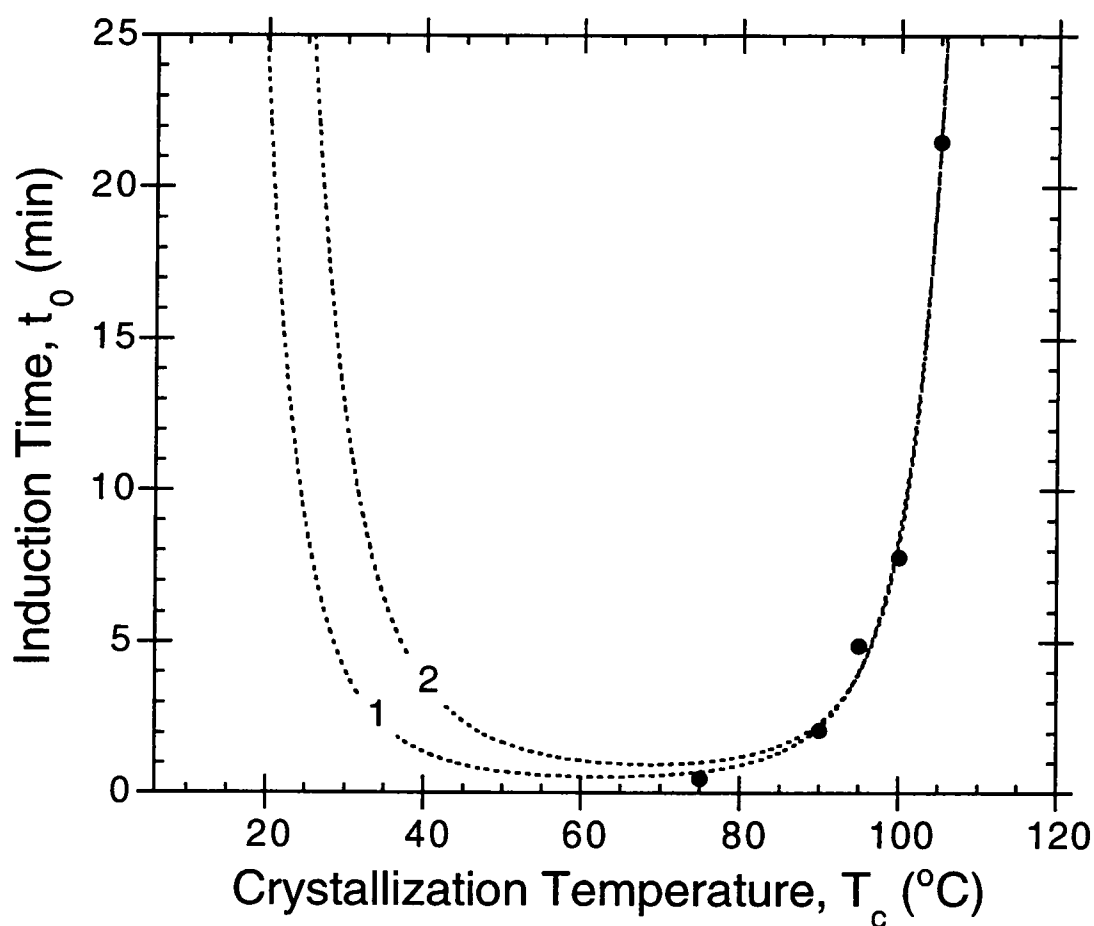


Figure 9-6. Induction time t_0 (cf. Table 9-1) as a function of crystallization temperature T_c of sPP. The dotted line 1 is the best fitted-curve drawn through the bulk of the data after Equation (9-13), while the dotted line 2 is drawn after Equation (9-14). Parameters of the fitted curves: $\tau_1^1 = 2.64 \times 10^{-8} \text{ min} \cdot \text{K}$, $K_1^1 = 4.31 \times 10^5 \text{ K}^2$, $\tau_2^1 = 4.81 \times 10^{-6} \text{ min}$, and $K_2^1 = 1.30 \times 10^7 \text{ K}^3$.

dependence of the observed induction time t_0 , the experimental data are fitted to the approximated equations for *high* and *low* temperature regimes (i.e., Equations (9-13) and (9-14), respectively), using the non-linear multi-variable regression program (shown in Figure 9-6 as lines 1 and 2, respectively). Even though Equation (9-13) seems to give a better fit at the lower end of the data range (i.e., $75^\circ\text{C} \leq T_c \leq 90^\circ\text{C}$), both equations can be used to describe the temperature dependence of the incubation time data in the higher temperature range (i.e., $90^\circ\text{C} \leq T_c \leq 105^\circ\text{C}$) very well.

Interestingly, both equations predict the temperature dependence of the induction time t_0 of having a U-shape curve. When taking a closer look at the theory, it is apparent that this characteristic is mainly mandated by the two exponential terms. The first exponential term, $\exp[U/R(T_c - T_\infty)]$, corresponds to the diffusion of polymer molecules or segments of them from the equilibrium melt across the interfacial boundary onto a growth face. The second term, $\exp[K_i^1/T_c(\Delta T)^i f]$ (where i equals 1 for Equation (9-13) or 2 for Equation (9-14)), relates to the formation of the critical nuclei on the growth face. Intuitively, due to the competing nature of the two exponential terms, a minimum in the composite curve is expected to be observed somewhere between T_∞ and T_m^0 (ca. 168.7°C for sPP [19] (cf. Part 2)). Indeed, a minimum in the composite fitted curve is ostensible in Figure 9-6 at either $T_c = \text{ca. } 60^\circ\text{C}$ or $T_c = \text{ca. } 70^\circ\text{C}$, depending on whether Equation (9-13) or (9-14) is used to describe the data.

5.4. Further Discussion on the Temperature Dependence of the Crystallization Half-time

The most fundamental representation of the bulk crystallization kinetics data is to plot the reciprocal value of the crystallization half-time (i.e., $t_{0.5}^{-1}$) against the crystallization temperature. Figure 9-7 exhibits a plot of the reciprocal half-time of crystallization data, measured using the endothermic technique (cf. Table 9-1 and shown in Figure 9-7 as filled triangles) along with those measured using the exothermic

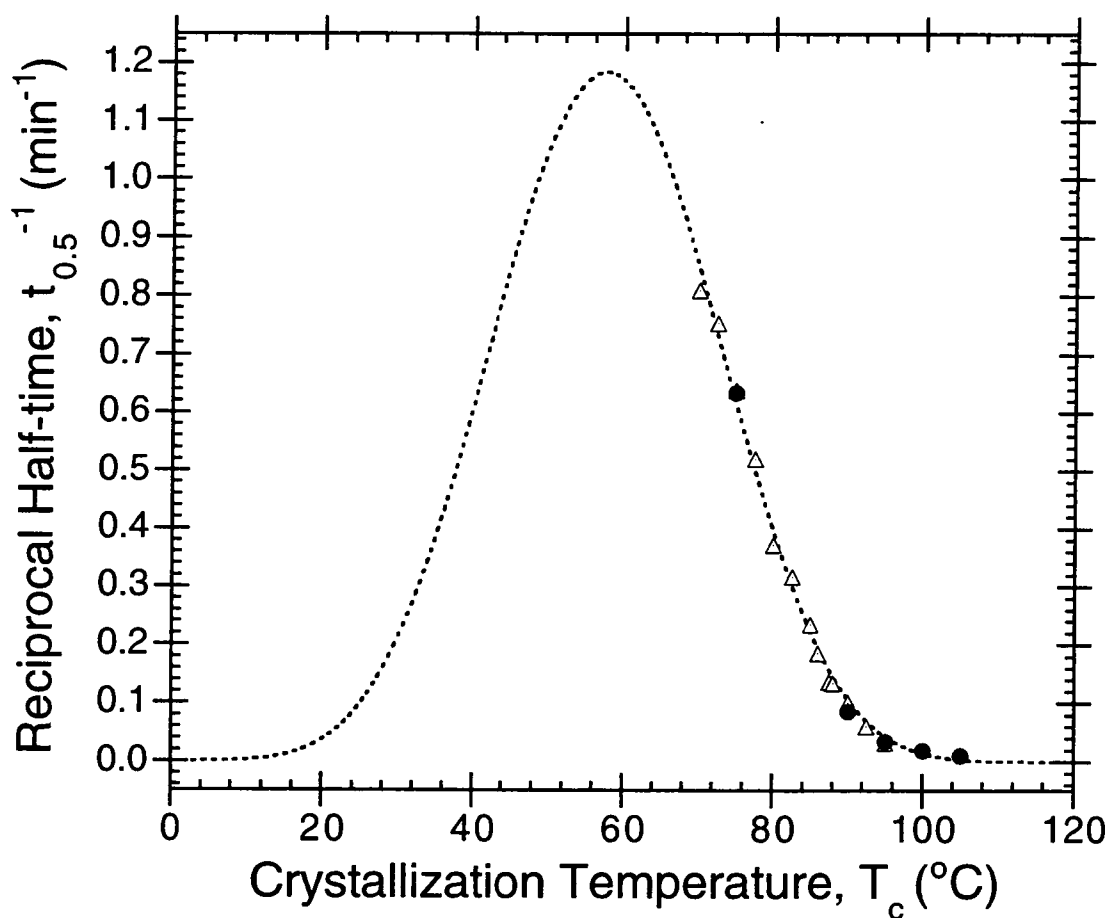


Figure 9-7. Reciprocal half-time $t_{0.5}^{-1}$ as a function of crystallization temperature T_c for sPP. Keys: (●) the data measured from this study (cf. Table 9-1); and (Δ) the data measured from the traditional technique (cf. Table 2-5 in reference [19] (cf. Part 2)). The dotted line is the best fitted curve drawn through the bulk of the data after Equation (9-15). Parameters of the fitted curve: $\Psi_0 = 2.38 \times 10^{12} \text{ min}^{-1}$ and $K_3^1 = 6.38 \times 10^5 \text{ K}^2$.

technique (cf. Table 2-5 in reference [19] and shown in Figure 9-7 as filled circles) as a function of crystallization temperature. Clearly, within the temperature range presented (i.e., $70^{\circ}\text{C} \leq T_c \leq 95^{\circ}\text{C}$), the bulk crystallization rate, as represented by the value of the reciprocal half-time $t_{0.5}^{-1}$, decreases steadily with an increase in T_c .

Since the bulk crystallization rate parameters (e.g., $t_{0.5}^{-1}$) relate, in one way or another, to the primary nucleation rate I and/or the subsequent crystal growth rate G and since the temperature dependence of these microscopic mechanisms are well defined in the literature [22,34,35,37], the temperature dependence of the bulk rate parameter can accordingly be quantified and described. Even though the temperature dependence of the parameters I and G are known to have a different temperature dependence (i.e., $I \propto (\Delta T)^2$ and $G \propto (\Delta T)^1$, respectively), the bulk rate parameters have often been taken the similar temperature dependence to that of the subsequent crystal growth rate G (written in the context of the original Lauritzen and Hoffman secondary nucleation theory (LH theory) [22,37]), which can be expressed as

$$\Psi(T_c) = \Psi_0 \exp\left[-\frac{U^*}{R(T_c - T_\infty)} - \frac{K_3^1}{T_c(\Delta T)f}\right], \quad (9-15)$$

where $\Psi(T_c)$ and Ψ_0 are the bulk crystallization rate parameter (e.g., $t_{0.5}^{-1}$) and the pre-exponential parameter (e.g., $(t_{0.5}^{-1})_0$), respectively, K_3^1 is a combined factor related to the nucleation mechanism, and other quantities are the same as previously defined.

With the aid of Equation (9-15), the temperature dependence of the bulk rate function $\Psi(T_c)$ can now be quantified by directly fitting the experimental data collected at various crystallization temperatures to Equation (9-15) using the same non-linear multi-variable regression program (shown in Figure 9-7 as the dotted line). Apparently, the best fit drawn through the bulk of the data exhibits a bell-shaped curve, which is attributed to the nucleation control effect at high crystallization temperature side (low degrees of undercooling) and the diffusion control effect at low crystallization

temperature side (high degrees of undercooling). Intuitively, from the competing contributions of the transport and nucleation terms, it is expected that a maximum in the composite curve should be observed somewhere between T_{∞} and T_m^0 . Indeed, such a maximum is clearly distinguishable in Figure 9-7 at ca. 60°C. Though the factors controlling the shape of the curves in Figures 9-6 and 9-7 are the same, the facts that Figure 9-6 appears to be U-shaped and that Figure 9-7 appears to be bell-shaped are due to whether or not there is a negative sign present within the exponential terms in Equations (9-13) to (9-15).

6. CONCLUSIONS

We have demonstrated successfully, at least in the case of sPP, that DSC can be used to study crystallization behavior and the kinetics of the process of semi-crystalline polymers at high crystallization temperatures or at low degrees of undercooling, where the traditional technique is not applicable, by measuring the enthalpy of fusion $\Delta H_{t,t}$ observed in subsequent melting endotherms after isothermal crystallization for various time intervals at T_c .

The applications of this technique and its advantages over the traditional one can be recapitulated as the followings:

- 1) The induction period can be determined more accurately, and is taken as the longest time interval the polymer of interest spends at T_c , but does not result in an observation of a melting peak in the subsequent melting endotherms.
- 2) Whether secondary crystallization occurs during the course of crystallization can be determined by observing whether the melting shoulder, which locates close to the crystallization temperature, is shown in the subsequent melting endotherms. The time interval required for the melting shoulder to be observed is taken roughly as the onset (time) of the secondary crystallization.

- 3) Whether lamellar thickening process occurs during the course of crystallization can be determined by observing whether the position of the primary melting peak in the subsequent melting endotherms increases with the increasing time interval the polymer of interest spends isothermally at T_c .
- 4) Related crystallization kinetics parameters can be obtained by analyzing the relative crystallinity data, calculated from ratio of the enthalpy of fusion measured from subsequent melting endotherms after isothermal crystallization at T_c for various time intervals to the final value of the enthalpy of fusion, based on an appropriate macrokinetics model.

This study may not be completed without mentioning about certain disadvantages of the technique, some of which can be summarized as the followings:

- 1) Accuracy of the relative crystallinity data obtained depends significantly on the choice of the final value of the enthalpy of fusion used. To increase the accuracy of the data, a large number of data points are required, but this has proven to be a very tedious process, especially at very high T_c .
- 2) It has been shown in literature that some polymers exhibit a more complex melting behavior than what we observed in sPP, such as in the cases of syndiotactic polystyrene (sPS) [38] and poly(butylene succinate) (PBS) [39]. It is therefore questionable whether the technique will be applicable to describe the crystallization process of those systems, and it is the matter of future researches.

7. REFERENCES

- [1] Wunderlich, B. *J. Therm. Anal.* **1996**, *46*, 643.
- [2] Hay, J.N. and Sabir, M. *Polymer* **1969**, *10*, 203.
- [3] Hay, J.N.; Fitzgerald, P.A.; and Wiles, M. *Polymer* **1976**, *17*, 1015.
- [4] Hay, J.N. *Brit. Polym. J.* **1979**, *11*, 137.
- [5] Kolmogoroff, A.N. *Izvestiya Akad. Nauk USSR, Ser. Math.* **1937**, *1*, 355.
- [6] Johnson, W.A. and Mehl, K.F. *Trans. Am. Inst. Mining Met. Eng.* **1939**, *135*, 416.
- [7] Avrami, M. *J. Chem. Phys.* **1939**, *7*, 1103.
- [8] Avrami, M. *J. Chem. Phys.* **1940**, *8*, 212.
- [9] Avrami, M. *J. Chem. Phys.* **1941**, *9*, 177.
- [10] Evans, U.R. *Trans. Faraday Soc.* **1945**, *41*, 365.
- [11] Ding, Z. and Spruiell, J.E. *J. Polym. Sci., Polym. Phys.* **1997**, *35*, 1077.
- [12] Tobin, M.C. *J. Polym. Sci., Polym. Phys.* **1974**, *12*, 399.
- [13] Tobin, M.C. *J. Polym. Sci., Polym. Phys.* **1976**, *14*, 2253.
- [14] Tobin, M.C. *J. Polym. Sci., Polym. Phys.* **1977**, *15*, 2269.
- [15] Malkin, A.Y.; Beghishev, V.P.; Keapin, I.A.; and Bolgov, S.A. *Polym. Eng. Sci.* **1984**, *24*, 1396.
- [16] Supaphol, P. and Spruiell, J.E. *J. Macromol. Sci.-Phys.*, accepted on June 1, 1999.
- [17] Wunderlich, B. In *Macromolecular Physics*; Academic Press: New York, 1976; Vol. 2; pp 132-147.
- [18] Banks, W.; Sharples, A.; and Hay, J.N. *J. Polym. Sci.* **1964**, *A2*, 4059.
- [19] Supaphol, P. and Spruiell, J.E. *J. Appl. Polym. Sci.*, accepted on April 16, 1999.
- [20] Woo, E.M. and Ko, T.Y. *Colloid Polym. Sci.* **1996**, *274*, 309.
- [21] Wang, C.-S.; Lin, C.-S.; and Lai, N. *Polym. Bull.* **1997**, *39*, 185.
- [22] Hoffman, J.D.; Davis, G.T.; and Lauritzen Jr., J.I. In *Treatise on Solid State Chemistry*; Hannay, N.B., Ed.; Plenum Press: New York, 1976; Vol. 3; Chapter 7.
- [23] Schmidtke, J.; Strobl, G.; and Thurn-Albrecht, T. *Macromolecules* **1997**, *30*, 5804.
- [24] Hauser, G.; Schmidtke, J.; and Strobl, G. *Macromolecules* **1998**, *31*, 6250.
- [25] Hugel, T.; Strobl, G.; and Thomann, R. *Acta Polym.* **1999**, *50*, 214.
- [26] Janeschitz-Kriegl, H. *Colloid Polym. Sci.* **1997**, *275*, 1121.
- [27] Janeschitz-Kriegl, H.; Ratajski, E.; and Wippel, H. *Colloid Polym. Sci.* **1999**, *277*, 217.
- [28] Lednicky, F. and Muchova, M. *Collect. Czech. Chem. Commun.* **1993**, *58*, 2444.
- [29] Muchova, M. and Lednicky, F. *J. Macromol. Sci.-Phys.* **1995**, *B34*, 55.
- [30] Lednicky, F. and Muchova, M. *J. Macromol. Sci.-Phys.* **1995**, *B34*, 75.
- [31] Lednicky, F. and Muchova, M. *J. Macromol. Sci.-Phys.* **1996**, *B35*, 681.

- [32] Muchova, M. and Lednicky, F. *Polymer* **1996**, *37*, 3031.
- [33] Muchova, M. and Lednicky, F. *Polymer* **1996**, *37*, 3037.
- [34] Price, F.P. In *Nucleation*; Zettlemoyer, A.C., Ed.; Marcel Dekker: New York, 1969; Chapter 8.
- [35] Wunderlich, B. In *Macromolecular Physics*; Academic Press: New York, 1976; Vol. 2; Chapter 5.
- [36] Suzuki, T. and Kovacs, A.J. *Polymer J.* **1970**, *1*, 82.
- [37] Hoffman, J.D. and Miller, R.L. *Polymer* **1997**, *38*, 3151.
- [38] Woo, E.M. and Wu, F.S. *Macromol. Chem. Phys.* **1998**, *199*, 2041.
- [39] Yoo, E.S. and Im, S.S. *J. Polym. Sci., Polym. Phys.* **1999**, *37*, 1357.

PART 10:
SUMMARY OF MAJOR CONCLUSIONS AND
RECOMMENDATIONS FOR FUTURE WORK

1. SUMMARY OF MAJOR CONCLUSIONS

The glass transition temperatures determined using a differential scanning calorimeter for all of the sPP resins were found to lie in the range of -5.6 to -6.5°C , with the average value of $-6.1 \pm 0.4^{\circ}\text{C}$. The equilibrium melting temperatures of these resins were estimated using the linear Hoffman-Weeks extrapolative method, and were found to lie in the range of 146.1 to 148.3°C . By assuming that the meso co-units (i.e., stereo-defects) are totally excluded from the crystals, the equilibrium melting temperature of 100% syndiotacticity sPP was estimated to be ca. $168.7 \pm 4.1^{\circ}\text{C}$. Studies of overall crystallization kinetics revealed that the rate of the crystallization for all of the sPP resins is in the following order: sPP#5 > sPP#3 > sPP#2 > sPP#4 > sPP#1. The kinetic crystallizability parameters, which characterize the ability of a polymer to crystallize from the melt state, of these resins were found to range from $0.41^{\circ}\text{C}\cdot\text{sec}^{-1}$ to $2.14^{\circ}\text{C}\cdot\text{sec}^{-1}$. Based on these values, the crystallizability of the sPP resins is in the following sequence: sPP#5 > sPP#2 > sPP#3 > sPP#4 > sPP#1.

Analysis of the linear growth rate data of sPP#1 and other data sets taken from the literature in the context of the Lauritzen-Hoffman secondary nucleation theory suggested an unmistakable regime II-III transition at the crystallization temperature of 110°C . Regardless of the crystal structure (i.e., either the limit-disordered form I or the limit-ordered form I), if the growth is assumed to occur on the *bc* plane, the lateral surface free energy $\sigma = 11.3 \text{ erg}\cdot\text{cm}^{-2}$ and the fold surface free energy $\sigma_e = 63.7 \pm 7.1 \text{ erg}\cdot\text{cm}^{-2}$ were found. On the other hand, if the growth is assumed to occur on the *ac* plane, the fold surface free energy is found to be $\sigma_e = 82.4 \pm 9.1 \text{ erg}\cdot\text{cm}^{-2}$, while the lateral surface free energy is the same as previously noted. The measured crystal growth parameters were found to be sensitive to the values of the input parameters used, especially the equilibrium melting temperature. Qualitatively, it is found that a 2.3%

change in the value of the glass transition temperature leads to an approximately 2.9% change in K_g value, and around 2.6% change in $\sigma\sigma_e$, σ_e , and \bar{q} values. In the case of changes in the equilibrium melting temperature used, it is found that a 2.0% change in its value causes a 29.6% change in K_g value, and around 29.3% change in $\sigma\sigma_e$, σ_e , and \bar{q} values. Alternatively, a 1°C change in the value of the equilibrium melting temperature causes an approximately 4.4% change in K_g , $\sigma\sigma_e$, σ_e , and \bar{q} values. Lastly, a 1% change in the value of the enthalpy of fusion used results in a roughly 1% change in σ value, while other parameters are unaffected. Determination of the equilibrium melting temperature of sPP#1 based on the raw crystal growth rate data in the context of the Lauritzen-Hoffman secondary nucleation theory suggested a value of ca. 178°C. As a result of this equilibrium melting temperature value, the fold surface free energy $\sigma_e = 78.2 \text{ erg}\cdot\text{cm}^{-2}$ was found, for the growth occurring on the bc plane; whereas, the fold surface free energy $\sigma_e = 101.2 \text{ erg}\cdot\text{cm}^{-2}$ was found, for the growth occurring on the ac plane.

Isothermal crystallization behavior of sPP#1 resin after partial or complete melting has been investigated by differential scanning calorimetry. On partial melting, the total concentration of predetermined nuclei N_{tot} was found to decrease with increasing fusion temperature T_f , up to a critical value (i.e., $T_f \approx 160^\circ\text{C}$) where the N_{tot} value approaches a constant (i.e., complete melting). At a specific fusion temperature T_f , the total concentration of predetermined nuclei N_{tot} was found to be a certain decay function with the holding time t_h , characterized by a relaxation time τ , and it was also found to approach a constant value as the holding time t_h becomes long (i.e., complete melting). This constant value of total concentration of predetermined nuclei N_{tot} observed after prolonged melting of the sample at sufficiently high fusion temperature (i.e., $T_f > 160^\circ\text{C}$) is the concentration of infusible heterogeneous nuclei N_0 (e.g.,

impurities, catalyst residues, etc.), and was approximated to be 3.0×10^7 nuclei \cdot cm $^{-3}$ for this particular sPP sample. The relaxation time τ was also found to be a certain decreasing function of fusion temperature T_f , which ranges from 168 min at $T_f = 145^\circ\text{C}$ to 100 min at $T_f = 180^\circ\text{C}$.

Applicability of four macrokinetic models; namely the Avrami, Tobin, Malkin, and simultaneous Avrami models; in describing the time-dependent relative crystallinity data, using sPP as the model system, was tested using a non-linear multi-variable regression program. Based on the quality of the fit, only the Avrami, Malkin, and the simultaneous Avrami models were found to describe the experimental data well, resulting in the rejection of the Tobin model in describing isothermal crystallization data of sPP. Comparison of the Avrami kinetics parameters obtained from the program with those obtained from the traditional analytical procedure suggested that use of non-linear multi-variable regression program in data analysis is satisfactorily reliable.

The subsequent melting behavior of sPP after isothermal crystallization from the melt state was studied in detail using differential scanning calorimetry and wide-angle x-ray diffraction techniques. For isothermal crystallization at high degrees of undercooling (i.e., $T_c \leq 90^\circ\text{C}$), triple-melting endotherms were observed in the DSC heating scans ($20^\circ\text{C}\cdot\text{min}^{-1}$); whereas, for isothermal crystallization at low degrees of undercooling (i.e., $T_c \geq 90^\circ\text{C}$), only double-endotherms were observed. For subsequent melting thermograms exhibiting triple-melting endotherms, the minor and the low-temperature melting endotherms are found to correspond to the melting of the secondary and the primary crystallites formed at corresponding crystallization temperature, respectively; while the high-temperature melting endotherm is found to represent the melting of the re-crystallized crystallites formed during a heating scan. The formation of the re-crystallized crystallites is thought to be the re-crystallization of the crystallizable materials due to the melting of the secondary crystallites and to the

partial melting of the less stable fractions of the primary crystallites formed at the crystallization temperature. The observation of the high-temperature melting endotherm is found to depend strongly on the stability of the secondary and the primary crystallites formed and on the scanning rate used to observe the melting behavior.

The overall kinetics of isothermal melt- and cold-crystallization of sPP#1 resin was thoroughly investigated using a differential scanning calorimeter. The overall crystallization rate parameters (e.g., $t_{0.5}^{-1}$, k_a , and C_0) for melt-crystallization process, when plotted as a function of crystallization temperature, exhibited an unmistakable double bell-shaped curve with the two maxima respectively being observed at the crystallization temperatures of ca. 30 and 60°C and the discontinuity being observed at ca. 40°C; whereas, those for cold-crystallization process showed the typical bell-shaped curve with the maximum being observed at the crystallization temperature of ca. 58°C. It was postulated that the low-temperature maximum is a result of the maximum in the primary nucleation rate, while the high-temperature maximum is a result of the maximum in the crystal growth rate. Comparison of the overall crystallization rate parameters obtained for both melt- and cold-crystallization processes indicate that crystallization from the glassy state proceeds at a much greater rate than from the melt state. This can only be construed that quenching process greatly increases the total number of activated nuclei (or the rate of formation of the nuclei) and, upon subsequent crystallization at arbitrary temperatures, these activated nuclei can act as predetermined homogeneous nuclei which profoundly enhance the overall crystallization rate.

the Lamellar morphology information and subsequent melting behavior of sPP#4 samples isothermally crystallized at crystallization temperatures ranging from 30°C to 95°C were investigated using a combination of wide-angle x-ray diffraction, small-angle x-ray scattering, and differential scanning calorimetry techniques. All of the samples investigated were found to crystallize in the high temperature, orthorhombic

limit-disordered form I. The degree of crystallinity χ_c^{WAXD} , the long period L_B , the lamellar thickness l_c , and the melting temperature T_m were all found to increase with increasing crystallization temperature. The equilibrium enthalpy of fusion ΔH_f^0 was found to be $109.3 \pm 0.5 \text{ J}\cdot\text{g}^{-1}$ or ca. $4.6 \text{ kJ}\cdot\text{mol}^{-1}$. The Gibbs-Thomson extrapolation suggested the values of the equilibrium melting temperature T_m^{GT} and the basal interfacial free energy σ_e^{GT} to be ca. 166.3°C and ca. $57.8 \text{ mJ}\cdot\text{m}^{-2}$, respectively, while the linear and non-linear Hoffman-Weeks extrapolative methods gave the values of the equilibrium melting temperature, T_m^{LHW} and T_m^{NLHW} , to be ca. 142.8°C and ca. 184.7°C , respectively. Finally, the equilibrium melting temperature of perfect sPP sample $(T_m^0)_{100\%}$ was estimated to be ca. 199.2°C .

Lastly, a technique of using differential scanning calorimeter (DSC) to study isothermal crystallization behavior and the kinetics of the process at high crystallization temperatures or low degrees of undercooling was proposed. The technique was carried out based on the observations of, and the measurements of the enthalpy of fusion from, the subsequent melting endotherms after both partial crystallization for various time intervals and after complete crystallization. Comparison of the overall crystallization data obtained from this proposed technique with those obtained from the traditional technique evidently indicated that the proposed technique of using information acquired from subsequent melting endotherms in studying crystallization kinetics is, at least, reliable and applicable to describe isothermal crystallization of sPP#4 resin at the conditions studied. The three major advantages of this technique over the traditional one are 1) increased reliability and accuracy for the determination of the induction period, 2) providing a possibility for the determination of the onset of the secondary crystallization process, and 3) providing a means to determine whether or not lamellar thickening occurs during the course of crystallization at a given crystallization condition.

2. RECOMMENDATIONS FOR FUTURE WORK

The major drawback in this dissertation is that the influence of tacticity on the isothermal crystallization and subsequent melting behavior could not be established. If it is possible to acquire sPP samples having a systematic variation of meso-defects, a thorough investigation of the role of tacticity on 1) the crystallization behavior, 2) the subsequent melting behavior, 3) the equilibrium melting temperature, and 4) the equilibrium heat of fusion, can then be carried out.

It is known that primary crystallization process is a macroscopic development of crystallinity as a result of two consecutive microscopic mechanisms: primary nucleation and secondary nucleation (subsequent crystal growth) mechanisms. Only the kinetics of the subsequent crystal growth mechanism and that of the macroscopic process are usually investigated, owing mainly to the ease of conducting the experiments and to the vast availability of the theoretical and experimental supports. Even though the information obtained from the investigations of these two aspects offers, to some extent, an understanding and insight into the kinetics of the crystallization process, it is the primary nucleation mechanism that is very essential to the understanding of how crystallization starts in the first place. Even though theories have been proposed to describe both the thermodynamic and kinetic aspects of primary nucleation, direct experimental observations are scarce. One main reason for this is that there are numerous factors affecting the nucleation mechanism, e.g., temperature, pressure, stress, and the changes in one or all of these parameters. In order to understand the kinetics of the crystallization process in detail, a complete understanding of the primary nucleation mechanism needs to be established. With this information, thorough investigation into the inter-relation of the microscopic and macroscopic kinetics of isothermal crystallization process can then be obtained.

Even though the information obtained from isothermal measurements may answer many fundamental aspects related to the crystallization process of semi-crystalline polymers, it may not be useful to describe actual conditions occurring during polymer processing, which usually involve changes of external variables (e.g., temperature, pressure, stress, etc). In the case of crystallization under the influence of changes of temperature alone, prediction of the course of crystallization process has been carried out based on the information obtained from isothermal measurements. It has been theoretically proposed very recently that crystallization of semi-crystalline polymers under the influence of changes of any of the external variables, the effects of athermal and transient mechanisms, which are merely absent from pure isothermal process, become significant and dictate the nucleation mechanisms. Due to the significance of these effects in actual polymer processing, it is recommended that the influence of changes of these external variables be investigated thoroughly. Without these informations, understanding of crystallization process of semi-crystalline polymers is far from complete.

VITA

Pitt Supaphol was born in Bangkok, Thailand on February 18, 1970. He attended Saint John Primary School in Bangkok and later got his high school diploma from Bodindecha (Singha Singhaseni) School in Bangkok in March, 1988. He later passed on to Chulalongkorn University, where he received the Bachelor of Engineering in Chemical Engineering in March, 1992. After working for a year in a family business, he entered the Master's program in Polymer Engineering at the University of Tennessee, Knoxville in August, 1993. After receiving his Master of Science degree in May, 1996, he was admitted to pursue the Doctorate of Philosophy in the same program. The Doctorate of Philosophy degree will be awarded officially in December, 1999.

He will start his professional life by joining the faculty of the Petroleum and Petrochemical College, Chulalongkorn University in Bangkok starting from November, 1999.